
University of Sheffield

# 3D-Printed sHAP-PCL Scaffolds as Bone Graft Substitutes for Spinal Fusion Surgery

A thesis submitted in partial fulfilment of the requirements for the degree of Doctor of Philosophy.

Denata Syla

**Department of Materials Science and Engineering**

The University of Sheffield

March 2025

`

# Abstract

Spinal fusion surgery utilising interbody cages with bone autograft is a common treatment for chronic lower back pain when conservative therapy proves ineffective. However, autograft harvesting poses risks, including donor site morbidity, while fusion outcomes are often suboptimal in compromised patients. This study aimed to develop a customisable, osteoconductive bone graft substitute by incorporating magnesium and strontium-substituted hydroxyapatite (sHAP) into polycaprolactone (PCL) composites, intended to replace autografts when contraindicated. To ensure the reproducibility of in vitro testing, a standard operating procedure (SOP) was developed to address cell sensitivity to environmental changes and serum variability. The SOP used a human mesenchymal stem cell (MSC) line under serum-free conditions throughout the project.

Various cell culture parameters were evaluated for their effect on MSC proliferation, including media compositions (serum-free, bovine serum-supplemented, and human serum-supplemented), surface coatings (gelatine and fibronectin), and media change frequencies (partial on day 3, full on day 3, no change in 1 week). Cell proliferation was quantified using a metabolic resazurin assay. For the synthesis of sHAP, multiple formulations with substitution degrees of 5%, 10%, and 20% for Mg and Sr, respectively, were evaluated. Chemical composition, structure, and crystallinity were analysed using ICP-OES, FTIR, and XRD. sHAP was incorporated into 4-arm methacrylated PCL and fabricated into scaffolds via 3D printing. The wettability of different sHAP-PCL composites was analysed via drop-shape analysis, and surface characteristics were examined using SEM. Cytotoxicity of sHAP powders and sHAP-PCL scaffolds was evaluated via a metabolic resazurin assay. Visualisation of cell spreading on scaffolds was performed through actin staining.

Serum-free medium demonstrated comparable cell proliferation to serum-supplemented media, with no medium change necessary over a 1-week culture period. Surface coatings did not significantly impact proliferation. Higher substitution levels increased secondary phase formation, while 20% Mg substitution completely hindered HAP formation. sHAP formulations with 5% Mg, 5% Sr and 10% Mg, 5% Sr exhibited high substituent incorporation with characteristic chemical HAP structure and minimal to no secondary phases. These formulations showed no cytotoxic effects in vitro. The incorporation of sHAP influenced scaffold printability by altering ink rheology, while silica addition potentially reduced hydrophilicity. Scaffolds containing 30% sHAP (5% Mg and Sr) allowed for cell attachment and spreading, demonstrating sustained cell viability and proliferation.

An SOP for serum-free in vitro analysis was established, sHAP was successfully synthesised, and fabrication of sHAP-PCL scaffolds was achieved, advancing the development of customisable fusion cage inserts as potential substitutes for bone autografts.

`

# Dedication

To my family, for believing in me when I could not believe in myself.

`

# Acknowledgements

First, I wish to express my deepest gratitude to my supervisors, Professor Gwendolen Reilly and Professor Frederik Claeyssens. Thank you for this opportunity, for nurturing my academic journey with your support and guidance, and for your invaluable wisdom at every step. I am especially grateful to Professor Reilly for her incredible patience and for going well beyond her duty to ensure my success.

I sincerely thank the European Commission and Marie Skłodowska-Curie Actions for funding this research and making my work possible. My appreciation extends to all members of the SPINNER consortium, particularly Dr Norman Powell, for his skill at resolving every problem encountered. I am also incredibly grateful to Lucia, Laura, Riccardo, Claudio, and the exceptional team at Finceramica for welcoming me during my secondment.

To my fellow ESRs, José, Chloé, Jennifer, Marco, and Cameron, thank you for the great memories at conferences and training events, the laughter that brightened this journey, and the solidarity you provided during difficult times.

I am incredibly grateful to all members of the University of Sheffield, INSIGNEO, and IMSB for imparting the skills and knowledge that enabled my academic development.

My experience was greatly enriched by my lab colleagues Ballad, Tugba, Alice, Areli, and Caitlin, who made me feel instantly welcome and helped in the lab whenever needed. Additional thanks to Boyang for our productive collaboration and to Julie for keeping our lab running smoothly and always being available for a chat if needed.

My gratitude extends to my dear friends for sharing wonderful memories and laughter, providing a comforting presence during challenging times and for dancing the worries away with me. It would not have been the same without you.

Most of all, I wish to acknowledge my beloved family for being my rock throughout. To my siblings, Blinera, Shqiponje, Sylejman, and Albin, your belief in me and unconditional support have been my pillars. Your support for our parents while I pursued my academic goals means more than you know. Especially to my parents, Faik and Florije, mere words cannot describe the depth of my gratitude for your unconditional love and countless sacrifices so I could pursue my academic ambitions. This accomplishment is ours to share. I hope I have made you proud.

# Table of Contents

`

# List of Figures

`

# List of Tables

# Abbreviations

| | |
|---|---|
| 4-PCL | 4-arm poly(ε-caprolactone) |
| 4-PCLM | Methacrylated 4-arm poly(ε-caprolactone) |
| AA-2P | Ascorbic acid 2-phosphate |
| ACP | Amorphous calcium phosphate |
| adj. p | Adjusted p-values |
| ALBP | Acute lower back pain |
| ALIF | Anterior lumbar interbody fusion |
| ALP | Alkaline phosphatase |
| AM | Additive manufacturing |
| ANOVA | Analysis of variance |
| AOF | Animal-origin-free |
| ASTM | American society for testing and materials |
| AT-MSCs | Adipose tissue mesenchymal stem/stroma cells |
| AxLIF | Axial lumbar interbody fusion |
| BMA | Bone marrow aspirate |
| BMAC | Bone marrow aspirate concentrate |
| BM-MSCs | Bone marrow mesenchymal stem/stroma cells |
| BMP | Bone morphogenetic protein |
| BMUs | Bone multicellular units |
| CaSR | Calcium-sensing receptor |
| CD | Chemically defined |
| CDHAP | Calcium deficient hydroxyapatite |
| CFU-M | Colony-forming units macrophage |
| CLBP | Chronic lower back pain |
| CSA | Calcium sulphate anhydrous |
| CSD | Calcium sulphate dihydrate |
| CSH | Calcium sulphate hemihydrate |
| DAPI | 4’,6-diamidino-2-phenylindole dihydrochloride |
| DBM | Demineralised bone matrix |
| DCM | Dichloromethane |
| DCP | Dicalcium phosphates |
| DCPA | Dicalcium phosphate anhydrous |
| DCPD | Dicalcium phosphate dihydrate |

| | |
|---|---|
| Dex | Dexamethasone |
| di$H_2O$ | Deionised water |
| DIW | Direct ink writing |
| DMEM | Dulbecco's modified eagle medium |
| DMP-1 | Dentin matrix protein 1 |
| DMSO | Residual dimethyl sulfoxide |
| DoE | Design of experiments |
| DP | Degree of polymerisation |
| ECM | Extracellular matrix |
| EDTA | Trypsin-ethylenediamine tetraacetic acid |
| EMA | European Medicines Agency |
| ERK | Extracellular signal-regulated kinase |
| Et3N | Triethylamine |
| FAK | Focal adhesion kinase |
| FBS | Foetal bovine serum |
| FDA | Food and Drug Administration |
| FFF | Fused filament fabrication |
| FGF23 | Fibroblast growth factor 23 |
| FTIR | Fourier transform infrared spectroscopy |
| GM | Growth media |
| HAP | Hydroxyapatite |
| HBSS | Hanks balanced salt solution |
| HCl | Hydrochloric acid |
| HEPA | High-efficiency particulate air |
| HLA | Human leukocyte antigen |
| hTERT | Human telomerase reverse transcriptase |
| ICBG | Iliac crest bone graft |
| ICC | Immunohistochemistry |
| ICP-OES | Inductively coupled plasma optical emission spectrometry |
| IFT | Interfacial tension |
| IGF | Insulin-like growth factor |
| IMS | Industrial methylated spirit |
| ISO | International Organisation for Standardisation |
| IUPAC | International Union of Pure and Applied Chemistry |

| | |
|---|---|
| JAK2 | Janus kinase 2 |
| KBr | Potassium bromide |
| LAG | Local autograft |
| LBP | Lower back pain |
| LLIF | Lateral lumbar interbody fusion |
| MAA | Methacrylic anhydride |
| M-CSF | Macrophage colony-stimulating factor |
| MEM | Minimal essential medium |
| MEPE | Matrix extracellular phosphoglycoprotein |
| MgHAP | Magnesium-substituted hydroxyapatite |
| MP | Degree of methacrylation |
| MSCs | Mesenchymal stem/stroma cells |
| Mw | Molecular weight |
| NFATc1 | Nuclear factor of activated T cells 1 |
| NF-κB | Nuclear factor κB |
| NICE | National Institute for Health and Care Excellence |
| NMR | Nuclear magnetic resonance spectroscopy |
| NSAIDs | Non-steroidal anti-inflammatory drugs |
| nsHAP | Non-substituted hydroxyapatite |
| OCP | Octacalcium phosphate |
| OPG | Osteoprotegerin |
| P/S | Penicillin/streptomycin |
| PBS | Phosphate buffered saline |
| PCL | Poly(ε-caprolactone) |
| PCLM | Methacrylated poly(ε-caprolactone) |
| PDGF | Platelet-derived growth factor |
| PDMS | Polydimethylsiloxane |
| PEKK | Poly-ether-ketone-ketone |
| PGA | Polyglycolide |
| PI | Photoinitiator |
| PI3K | Phosphatidylinositol 3-kinase |
| PLA | Polylactide |
| PLGA | Poly(lactide-co-glycolide) |
| PLIF | Posterior lumbar interbody fusion |

| | |
|---|---|
| P-MSCs | Placenta mesenchymal stem/stroma cells |
| ppm | Parts per million |
| RANKL | Receptor activator of nuclear factor κB ligand |
| rhBMP-2 | Recombinant human bone morphogenetic protein 2 |
| ROM | Physiologic range of motion |
| ROP | Ring-opening polymerisation |
| rpm | Revolutions per minute |
| Runx2 | Runt-related transcription factor 2 |
| SCC | Standard cell culture |
| SEM | Scanning electron microscopy |
| SF | Splitting factor |
| SFE | Surface free energy |
| SFM | Serum-free media |
| sHAP | Substituted hydroxyapatite |
| SLBP | Subacute lower back pain |
| SOP | Standardised operating procedure |
| Sox9 | SRY-box transcription factor 9 |
| SrHAP | Strontium-substituted hydroxyapatite |
| stannous octoate | Tin(II) 2-ethylhexanoate |
| STAT3 | Signal transducer and activator of transcription 3 |
| TCP | Tricalcium phosphate |
| TGF | Transforming growth factor |
| TLIF | Transforaminal lumbar interbody fusion |
| UC-MSCs | Umbilical cord mesenchymal stem/stroma cells |
| UV | Ultraviolet |
| VEGF | Vascular endothelial growth factor |
| vol% | Volume percent |
| WCA | Water contact angle |
| WJ-MSCs | Wharton’s jelly mesenchymal stem/stroma cells |
| Wnt | Wingless-related integration site |
| WoA | Work of adhesion |
| wt% | Weight percent |
| XRD | X-ray diffraction |
| βGP | B-glycerol phosphate |

# Collaborative Initiative under the SPINNER Program

The research in this project was conducted within the framework of SPINNER, an innovative doctoral training program funded by the European Union's Horizon 2020 research and innovation programme under the Marie Skłodowska-Curie grant agreement No. 766012. SPINNER represents a multidisciplinary collaborative effort, integrating expertise from industrial partners specialising in biomaterials (Finceramica), medical devices (Aesculap), and computational modelling (Ansys and Adagos), alongside clinical insight from orthopaedic clinicians (National Centre for Spinal Disorders, NCSD) and academic institutions (University of Sheffield and University of Bologna).

The research presented herein was conducted in close collaboration with Finceramica during an industrial secondment, bridging the gap between academic research and industrial application.

The primary objective of SPINNER was to cultivate a cohort of early-stage researchers equipped to advance the field of spinal surgery through the development of novel repair materials and techniques. The work presented in this thesis, focusing on bone graft substitutes for spinal fusion procedures, was one of several interconnected research initiatives within the program. Other projects encompassed the development of osteoinductive coatings for spinal fusion cages, biomechanical and clinical evaluation of lumbar intervertebral disc disease treatments, planning and assessment of techniques for spinal surgeries, computational models for pre-operative planning and patient-specific modelling of the musculoskeletal system.

`

# Preface

In the following chapters, the terms "female" and "male", as well as "women" and "men", "girls", and "boys" are used to refer to the biological genders assigned at birth. It is important to note that these terms are not indicative of individual gender identity. Rather, they serve to describe (patho)physiological differences that can be observed in biological processes within the scope of this thesis. It is with this understanding that these terms are used throughout the subsequent chapters.

`

# Chapter I Introduction

Lower back pain (LBP) stands as a highly prevalent global health issue of growing concern. In 2020 alone, over 600 million individuals worldwide were affected by LBP. As global populations expand and age, both the incidence and ensuing disability from LBP are rapidly rising [1, 2]. Currently, LBP constitutes the foremost driver of rehabilitation demand, emphasising the urgency for viable treatment options [3].

Reflecting its substantial clinical burden, LBP also confers massive economic impacts. It ranked among the top 10 conditions contributing to disability-adjusted life years lost for all age groups, placing fourth for ages 25–49 years [1, 2]. Beyond direct medical costs for diagnosis and hospitalisations, many expenses arise indirectly through lost wages and reduced productivity from prolonged LBP disability [3-5]. Collectively, direct and indirect annual costs of LBP are significant, exceeding $100 billion in the USA alone as of 2006, whereas estimates of €6.6 billion in Switzerland and £12.3 billion in the UK were made [6-8].

Alleviating this escalating epidemic of LBP disability is pivotal not only from a clinical but also socioeconomic perspective. However, guidelines reserve surgical interventions for specific diagnoses or after failed conservative treatment spanning a minimum of two years [9].

Spinal fusion is a surgical treatment for chronic LBP and joins vertebrae using interbody cages filled with bone grafts [10-12]. While bone autografts exhibit good performance in promoting spinal fusion, they are limited in availability and risk donor site morbidities [13-16]. Allografts avoid these issues but carry infection risks and lower fusion success [13, 17, 18]. Bone graft substitutes such as ceramics, cement, composites, and growth factors have emerged to address these limitations. However, they have inadequate strength, poor integration, limited bone formation, and safety concerns for growth factors [19-26]. Thus, autografts remain the gold standard [13, 27].

Selecting appropriate bone grafts and substitutes requires assessing patient and clinical factors against functional graft requirements to promote spinal fusion while avoiding associated comorbidities of current standards [13, 28-32]. This necessitates safer, clinically proven solutions matching autograft efficacy. Exploring innovative options to address this gap motivates the research presented in this thesis.

`

# 1.1. Literature Review

## 1.1.1. Anatomy and Function of the Spine

The spine comprises a complex anatomical structure within the musculoskeletal system. It provides structural support and stability while enabling flexibility and motion for the axial skeleton and head, facilitates the transmission of mechanical loads to the pelvis, and protects the enclosed spinal cord [33, 34]. The spine comprises various tissues and components, including vertebrae, intervertebral discs, muscle, ligaments, vascular tissues, and neural tissues [33, 35]. The vertebral column forms the osseous central axis of the spine axis and comprises 33 vertebrae: 7 cervical, 12 thoracic, 5 lumbar, 5 sacral and 4 coccygeal [33-36]. An overview of its anatomical structure is given in Figure 1.

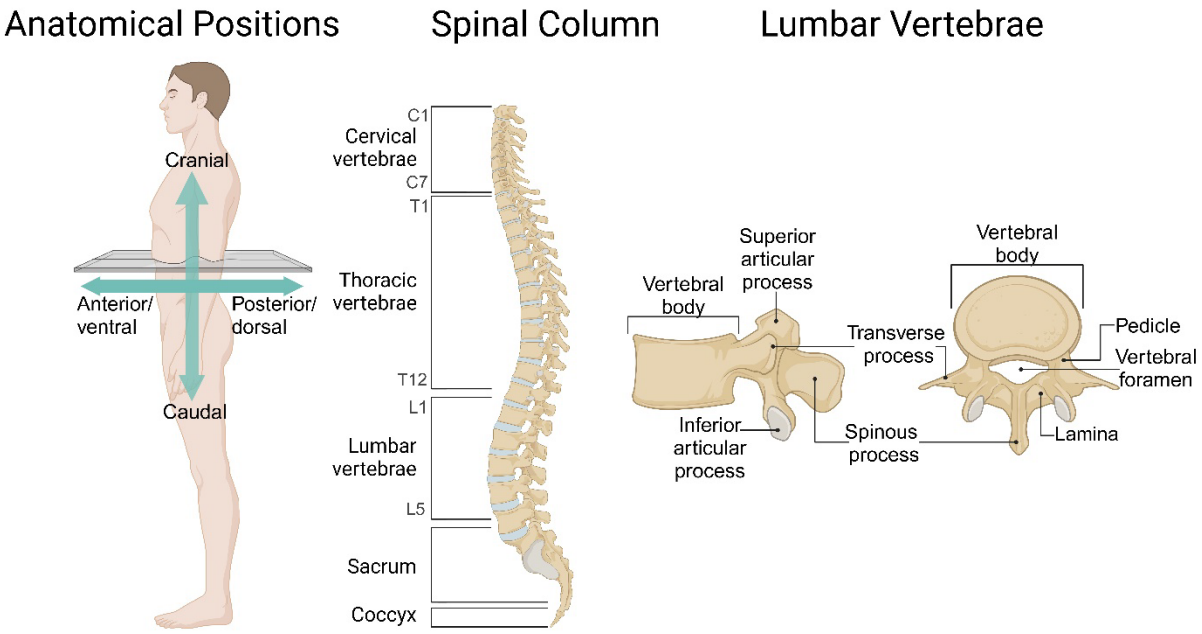


*Figure 1 Anatomical structure of the spine and lumbar vertebrae. From left to right: Anatomical positions, spinal column anatomy, lumbar spine anatomy. Image created on www.biorender.com.*

All vertebrae exhibit several standard morphological features. A typical vertebra (except C1 and C2) can be anatomically divided into two primary constituents: an anterior vertebral body and a posterior vertebral arch [33, 35]. The vertebral body and vertebral arch are composed of central trabecular bone surrounded by a thin peripheral layer of cortical bone. Morphology and dimensions of vertebrae vary by region, with the overall size increasing caudally to accommodate the increasing biomechanical demands of weight-bearing [33].

The vertebral body bears the majority of axial mechanical loads and is cylindrical in shape with varying dimensions along different regions of the spine [33, 34]. The first cervical

vertebra is unique in its absence of a discrete vertebral body [33, 35]. The ventral and dorsal sides of the vertebral body vary in different spine regions. Within the lumbar spine, the ventral body height increases while the dorsal height decreases caudally, contributing to the lordotic curvature characteristic of the lumbar region. The cranial and caudal surfaces of the vertebral body are nearly planar or mildly concave, with a rough trabecular bone surface centrally [33].

The vertebral arch is formed by a ventral pedicle and dorsal lamina on each side, enclosing the vertebral foramen (cylindrical space) that houses the spinal canal [33-35]. The transverse dimensions of the intervertebral foramina are greater in females than in males [33]. The laminae fuse in the midline to form the spinous process, which provides attachments for muscle and ligaments [33, 35]. Articular processes project from the junction of the pedicle and lamina, with the superior articular process oriented dorsally and the inferior oriented ventrally. These processes facilitate articulation with adjacent vertebrae and exhibit variations in morphology and angular orientation across different spinal regions. Transverse processes project bilaterally from the junction of the pedicle and lamina on each side, providing additional attachment points for muscles and ligaments. In the thoracic region, these processes also articulate with the ribs. Additionally, the size of the transverse processes decreases from caudal to cranial cervical levels [33].

The sacrum constitutes a triangular bone formed via the fusion of five rudimentary vertebrae. The coccyx comprises four smaller fused vertebrae [33, 35].

At the lumbosacral junction between L5 and S1, the entire weight of the upper body is transmitted to the pelvis through sacroiliac joints, formed by the articulation between the sacrum and both iliac bones [33-35]. The immobile sacrum also serves as the inferior anchor point for the vertebral column [35].

Except for C1 and C2, all vertebrae up to S1 are interconnected by cartilaginous (symphyses) between the vertebral bodies, synovial joints between their articular processes (zygapophyses), and fibrous joints between the transverse and spinous processes [33]. These joints are reinforced by spinal ligaments, which contribute to biomechanical stability through mechanical constraint and neuromuscular feedback [33, 36].

The intervertebral joints are formed by the articulations between adjoining vertebrae and the intervertebral disc [33, 35]. There are 23 intervertebral discs distributed along the vertebral column [35], exhibiting the lowest thickness in the upper thoracic region and the greatest thickness within the lumbar region [33, 35].

The intervertebral disc is anchored to the vertebral bodies via the bi-layered vertebral endplate, comprised of a bony portion fused to the vertebral body and an overlying cartilaginous layer joined to the intervertebral disc [33, 37]. The endplates prevent protrusion of the hydrated nucleus pulposus into the adjacent vertebral bodies, help to facilitate the diffusion of nutrients into the avascular disc and distribute mechanical loads [33, 34]. The

hyaline cartilaginous endplate consists of chondrocytes embedded within a proteoglycan-collagen extracellular matrix (ECM) (types I and II) [35, 38]. Still, its collagen fibres are arranged parallel rather than oblique to the vertebral end surfaces, as in articular cartilage [38].

The intervertebral disc comprises an inner gelatinous nucleus pulposus surrounded by the peripheral annulus fibrosus [33, 34]. Its anatomical structure is given in Figure 2.

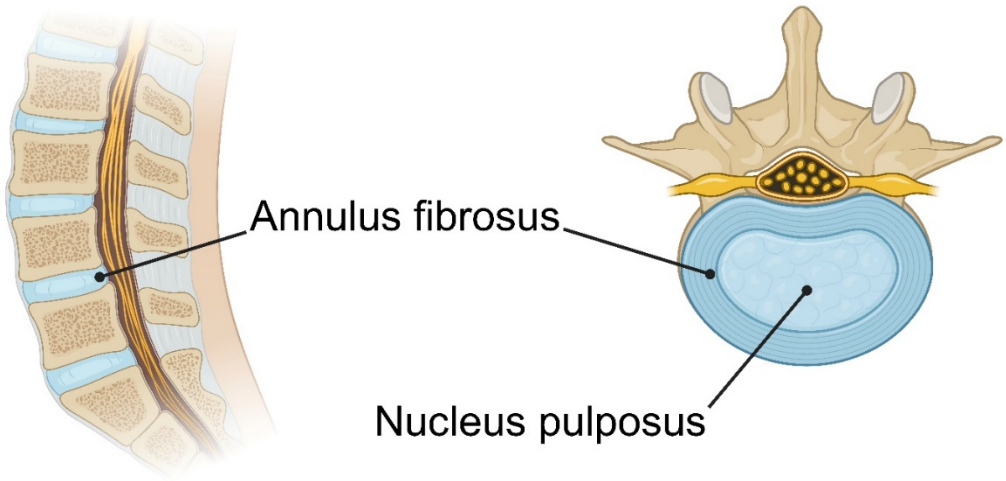


*Figure 2 Anatomy of the intervertebral disc. From left to right: Side view of the spinal column with intervertebral discs, top view of an intervertebral disc. Image created on www.biorender.com.*

The highly hydrated nucleus pulposus (70–90% water content) contains irregularly oriented type II collagen fibres [33, 34]. Its water and proteoglycan composition diminish with age and is replaced by fibrous tissue that impairs its hydrostatic recoil properties [33, 36]. By the fifth decade of life, the fragmented, attenuated annulus fibrosus encapsulates a fibrotic nucleus pulposus [36].

The annulus fibrosus is composed of proteoglycans, collagen, and 10–20 concentric rings of fibrocartilage encircling the nucleus [33, 34]. The annulus fibres are weakest posterolaterally and exhibit the greatest propensity for disc herniation [33].

Intervertebral discs play an essential role in absorbing and distributing compression and shear forces along the spinal column [34]. With age, vascularisation decreases, becoming increasingly reliant on diffusion for nutrition as the tissue becomes avascular by the third decade of life [33, 36].

Zygapophyseal joints, also known as facet joints, formed through the articulation of the inferior and superior articular processes, guide and constrain vertebral motion [33, 35]. Facet joints possess hyaline cartilage surfaces, synovial membranes, and articular capsules [35]. The orientation and morphology of facet joints vary across different spine regions, influencing

the types of movements possible [33, 34]. Significant differences exist in load bearing between the cervical and lumbar spines. In the cervical spine, facet joints support approximately half of the head's weight, while in the lumbar spine, they bear less than one-fifth of the load. This variation in load distribution contributes to the size differences between facet joints and vertebral bodies in the neck and lower back. Facet joints are also responsible for facilitating different types of motion in the spine. In the cervical region, flatter facet joint morphologies allow for smoother sliding motions and greater flexibility, while the larger lumbar facet joints provide enhanced torsional stability. The increased surface area of the lumbar facet joints contributes to greater torsional and shear stability in these spine segments [35].

Fibrous joints connect the transverse processes of adjacent vertebrae. In the thoracic region, they also connect the transverse processes to the ribs via ligaments. Additionally, ligaments connect adjacent vertebrae through the spinous processes. [38].

Functionally, the vertebral column consists of multiple spinal motion segments or functional spinal units, each comprised of two adjoining vertebrae, an intervertebral disc, ligamentous tissues, and facet joints that collectively allow for controlled flexibility and motion [33, 38]. The cervical, thoracic and lumbar regions of the spine allow for flexion and extension, lateral flexion, and horizontal plane (axial) rotation [34]. The physiologic range of motion (ROM) permitted at any particular region is primarily dictated by the shape of the motion segment and variations in local bone, muscle, and ligament structures [34, 35]. The cervical vertebrae are smaller, with flatter facet joints oriented in the transverse plane, enabling greater ROM in all planes compared to the thoracic and lumbar regions [34, 35, 38]. In the thoracic region, articulation with the ribs and frontally oriented facets principally allows for rotation and limited lateral flexion, while extension is restricted by contact with spinous processes [33, 35]. The larger sagittally oriented lumbar facet joints restrict axial rotation but enable flexion, extension, and lateral bending [34, 35]. Ligaments between the transverse processes also limit rotational and lateral flexion ROM [33].

Notably, in the sagittal plane, the spine exhibits distinct curvatures: lordosis in the cervical and lumbar regions characterised by inward curvatures, and kyphosis in the thoracic and sacral regions (sacral and coccygeal vertebrae), displaying outward curvatures [33, 34]. These natural curvatures allow the vertebral column to withstand greater compressive loads than a linear configuration. When these natural curvatures are preserved, compressive forces can be distributed through the tension generated by stretched connective tissues and muscles along each curve's convex side. The flexible curvatures permit controlled “shock absorption” under axial loads rather than rigidly transmitting forces [34]. The kyphotic thoracic and sacral curvatures provide space to accommodate vital thoracic and pelvic viscera [34]. The lordotic lumbar curve is more pronounced in females [33].

`

## 1.1.2. Bone Anatomy and Structure

### Bone Cells

#### Osteoclasts

Osteoclasts are large, multinucleated cells formed by fusion of mononuclear precursor cells [39-44]. They are primarily located on bone surfaces where remodelling or resorption is required, and are only observed in a motile state during bone resorption [39-41, 43, 44]. Osteoclasts are responsible for bone resorption, an essential process for bone modelling during growth and maintaining skeletal integrity in adults [39-44]. They originate from haematopoietic monocyte/macrophage precursors, specifically colony-forming unit macrophages (CFU-M) [39-43, 45]. The key signalling molecules controlling osteoclast recruitment, proliferation, differentiation, and fusion are macrophage colony-stimulating factor (M-CSF) and receptor activator of nuclear factor κB ligand (RANKL). M-CSF initiates signalling cascades through Src and extracellular signal-regulated kinase (ERK), while RANKL binding to its receptor activates transcription factors nuclear factor κB (NF-κB) and nuclear factor of activated T cells 1 (NFATc1). Mature osteoclasts typically survive for a few weeks. After completing bone resorption, osteoclasts undergo apoptosis, triggered by high extracellular calcium levels and signals from osteoblasts. Their lifespan is influenced by factors such as RANKL, M-CSF, and cytokines that activate ERK, phosphatidylinositol 3-kinase (PI3K), Akt, and NF-κB signalling pathways. Steroid hormones such as oestrogens and androgens suppress osteoclast formation and promote apoptosis, whereas glucocorticoids prolong osteoclast lifespan by inhibiting apoptosis, thereby increasing bone resorption and potentially contributing to bone loss [39-41].

#### Osteoblasts

Mature osteoblasts are cuboidal cells with enlarged nuclei and a prominent Golgi apparatus located along the bone surface at sites of active bone formation [39, 41-44]. They originate from inactive bone lining cells or bone marrow mesenchymal progenitors and play a key role in bone formation and mineralisation [39-44]. Mesenchymal progenitors progress through a multistep differentiation pathway, becoming pre-osteoblasts before maturing into osteoblasts. This process is regulated by key transcription factors such as runt-related transcription factor 2 (Runx2) and Osterix, along with signalling pathways including bone morphogenetic protein (BMP) and wingless-related integration site (Wnt)/β-catenin [39, 40, 42]. Mature osteoblasts can follow several fates: differentiation into osteocytes, transformation into bone lining cells, or apoptosis. Approximately 50–70% of osteoblasts undergo apoptosis upon completing their role in bone remodelling [39-41]. Osteoblast survival is supported by

various factors including insulin-like growth factor 1 (IGF-1) and oestrogen, which activate the Wnt, Src/ERK, and PI3K/Akt signalling pathways. Additionally, mechanical loading promotes osteoblast survival by activating protective signalling mechanisms [39].

## Bone Lining Cells

Bone lining cells exhibit a flattened, elongated morphology and cover quiescent bone surfaces [39, 41]. These cells are derived from mature osteoblasts and serve as a source of osteogenic precursors. They can retract from the bone surface, exposing the matrix for remodelling and facilitating the formation of bone multicellular units (BMUs) involved in this process. Additionally, bone lining cells may play a role in regulating calcium exchange between mineralised bone and the bone marrow, although the exact mechanisms remain unclear [39, 41, 42]. Recent studies indicate that the pharmaceutical administration of anabolic agents, such as parathyroid hormone or anti-sclerostin antibodies, can stimulate these cells to convert into active osteoblasts, thereby contributing to rapid bone formation [39].

## Osteocytes

Osteocytes possess a stellate morphology, with dendritic processes extending within the lacunae of the bone matrix [39-42, 44]. They originate from mature osteoblasts that become enclosed in the matrix they produce. Embedded in the mineralised bone matrix [39, 40], osteocytes regulate bone formation, resorption, and mineralisation [39, 40, 44]. Microdamage triggers nearby osteocytes to undergo apoptosis, initiating remodelling [39-42]. These cells indirectly regulate osteoclast formation through signalling pathways involving RANKL, osteoprotegerin (OPG), BMP, and Wnt. They also contribute to bone mineralisation and influence phosphate levels by expressing proteins such as dentin matrix protein 1 (DMP-1), matrix extracellular phosphoglycoprotein (MEPE), and fibroblast growth factor 23 (FGF23) [39]. The differentiation of osteoblasts to osteocytes is regulated by podoplanin and CD44 [39, 40]. As mechanosensory cells, osteocytes translate mechanical signals into biological activity [39-43]. Osteocyte survival is enhanced by mechanical loading, which prevents apoptosis by activating integrin/focal adhesion kinase (FAK)/Src/ERK and Wnt signalling pathways [39]. Ageing is associated with an accumulation of microdamage, a reduction in osteocyte density, and an increase in osteocyte apoptosis. Additionally, hormonal changes such as oestrogen and androgen deficiency, and excess glucocorticoid administration induce osteocyte apoptosis [39, 40].

`

## Hierarchical Structure of Bone

Bone exhibits a hierarchical structural organisation from the nanoscopic to the macroscopic level. This complex, multilevel architecture confers bone with high stiffness and toughness [40, 46, 47]. By weight, bone contains approximately 65% inorganic mineral, 20–25% organic matter (primarily type I collagen, with smaller amounts of types III and V), and 10% non-collagenous proteins, which play crucial roles in regulating various aspects of bone formation [47].

### Macrostructure

At the macroscopic level, bone exists as either cortical or cancellous bone [47]. In the adult human skeleton, cortical bone constitutes approximately 80% of the total bone volume, while cancellous bone comprises the remaining 20%. However, different skeletal locations exhibit varying ratios of cortical to trabecular bone [40, 42]:

- Vertebra: Cortical to trabecular bone ratios = 25:75
- Femoral head: Cortical to trabecular bone ratios = 50:50
- Radial diaphysis: Cortical to trabecular bone ratios = 95:5

#### Cortical Bone

Cortical bone, also known as compact bone, is characterised by its high density and low porosity of 3–5%. It forms the outer bone layer, surrounds the marrow space, and comprises the diaphysis of long bones, providing strength and protection [40, 42, 43, 46, 47]. The periosteum, a fibrous connective tissue, covers the outer cortical surface except at articular regions, whilst the endosteum, a membranous structure, lines the inner surface [42, 43]. Periosteal surface activity is crucial for appositional bone growth and fracture repair [42].

#### Cancellous Bone

Cancellous bone, also known as spongy or trabecular bone, constitutes the inner porous layer of bone, exhibiting a porosity of approximately 25–30% [43]. Despite its lower mechanical strength than cortical bone, the cancellous architecture enables shock absorption and force dissipation. Cancellous bone cushions joint articulations and is essential for metabolic functions due to its higher metabolic activity than cortical bone [40, 42, 46, 47]**.** This type of bone is predominantly found in the metaphyseal regions of long bones, vertebrae, ribs, iliac crest, and other areas, surrounded by the endosteum on its inner layer [40, 42, 43, 46].

### Microstructure

Microscopically, bone can be classified as either lamellar or woven bone, based on the organisation of collagen fibres.

`

Woven Bone

Woven bone is characterised by a disorganised arrangement of collagen fibres and a lattice-like morphology, resulting in significant porosity. Compared to lamellar bone, it exhibits lower mechanical strength. Woven bone typically forms during the early stages of bone development and rapid deposition or remodelling processes. It acts as an initial stabiliser to fulfil immediate structural demands during fracture repair or in response to abnormal loading [42, 43, 46, 47]. Additionally, woven bone is present in conditions of high turnover, such as hyperparathyroidism, Paget's disease, and during initial fluoride treatment [42, 43].

Lamellar Bone

Lamellar bone is the mature bone that replaces woven bone during development and healing [43, 48]. It can be classified as primary bone when deposited de novo on bone or cartilage or as secondary bone when it requires the resorption of pre-existing bone, leading to differences in mechanical and physiological properties [46, 49].

Cortical and trabecular lamellar bone are characterised by lamellae, layers of organised collagen fibres that impart toughness to the bone [43, 46, 47]. In cortical bone, this lamellar organisation manifests in three distinct forms: osteonal, interstitial, and circumferential lamellae, each contributing to the bone's overall structure and function [50].

Cortical circumferential bone is characterised by lamellae arranged in concentric layers around the bone, with limited vascular channels. This structure represents the simplest form of primary bone, deposited during bone growth and remodelling processes [51, 52].

This structure adapts to external stimuli, transforming into osteonal bone during modelling and remodelling [46, 51, 53]. In osteonal bone, lamellae are densely packed into concentric layers within cylindrical osteons, which surround the Haversian channel, a passage for neurovascular bundles. Osteocytes reside in spaces between lamellae, known as lacunae, and are connected by their dendritic processes. Osteons are further distinguished as primary or secondary [46, 53, 54].

Primary osteons develop within primary bone during modelling and remodelling, filling enlarged vascular channels in circumferential laminar bone. These osteons are smaller, measuring 50–100 μm in diameter, containing fewer than 10 lamellae, and lacking a distinct boundary from surrounding bone [46, 53, 54].

Secondary osteons, also known as Haversian systems, form following the resorption of primary osteons during remodelling. In cortical bone, remodelling occurs at the surface or intracortically, necessitating the formation of large resorption cavities due to the bone's density [46, 53-55]. This process increases the number of lamellae, typically between 20 and 25, and enlarges the diameter of secondary osteons to approximately 100–250 μm [46]. Secondary osteons are distinctly separated from surrounding tissue by their outer layer, known as the

cement line, which acts as a boundary for bone resorption. These structural differences result in distinct mechanical properties in secondary osteons compared to primary ones, playing a key role in managing bone fatigue and fracture processes [46, 53, 54].

Interstitial lamellae, found in cortical bone, occupy the spaces between adjacent secondary osteons and are separated from them by cement lines. These lamellae are remnants of incomplete osteons left over from previous remodelling processes and are more vulnerable to microcracks due to their prolonged presence in the bone matrix and consequent higher degree of mineralisation [46, 53].

In cancellous bone, lamellae are arranged into trabeculae, exhibiting either rod-like or plate-like morphology [46, 50, 56]. These structures form a random, irregularly interconnected framework but are oriented along mechanical load paths. Trabeculae are approximately 200 μm in diameter and are composed of lamellar packets, which are groups of lamellae aligned in slightly different directions. Each lamellar packet is bounded by a crenulated cement line. As in cortical bone, osteocytes reside in lacunae between the lamellae and are connected by dendritic processes. However, trabeculae, unlike cortical bone, lack a vascular system and instead receive their blood supply from the adjacent marrow cavity [46, 54]. Trabeculae are interconnected by interstitial lamellae, which enhance their structural support [50, 57].

Due to its loose structure and proximity to the marrow, remodelling in cancellous bone occurs primarily on the trabecular surface. During this process, lamellar packets are replaced by new bone, filling cavities to match the outer layers, though the inner layers may not always align [54]. Consequently, trabecular bone retains its structure during remodelling without increasing thickness [58, 59].

### Nanostructure

At the nanoscale, three polypeptide strands, each approximately 1,000 amino acids long and rich in Gly-X-Y motifs, intertwine to form triple helical structures of tropocollagen. These tropocollagen helices are arranged in parallel to create collagen microfibrils, measuring around 300 nm in length and 1.5 nm in width. The microfibrils aggregate into fibrils approximately 67 nm wide, forming collagen fibres with a diameter of about 150 nm and a length of 10 μm [40, 46].

Lamellae are composed of collagen fibres arranged in sheets of around 9 μm thickness, separated by a 1 μm interlamellar layer. In cortical bone, lamellae are composed of longitudinal mineralised collagen fibrils to withstand tension, while in cancellous bone fibrils are layered laterally to resist compression and are less organised [46, 60-62].

The primary bone mineral that interfaces within collagen fibrils is hydroxyapatite (HAP), a crystalline form of calcium phosphate [40, 42, 43, 46].

HAP formation occurs within extracellular vesicles synthesised by chondrocytes and osteoblasts, creating a protected microenvironment where calcium and phosphate concentrations can sufficiently rise to precipitate crystal formation [42, 43]. Mineralisation of collagen proceeds in two steps [46]:

**Primary mineralisation** entails the initial and rapid deposition of HAP, amorphous precursors, and calcium carbonate. This process occurs through heterogeneous nucleation, which takes place in the gap regions between the ends of collagen sub-units and within the longitudinal spaces between collagen fibrils. This process achieves 65%–70% of total mineralisation within three weeks.

**Secondary mineralisation** follows initial bone formation, during which more mature, plate-like crystalline structures gradually replace the less stable primary mineral crystals. Over time, these crystals continue to mature and align along the orientation of the collagen fibres with their c-axis.

HAP crystals continue to grow in size with age due to changes in mineral composition and ion substitutions, reaching approximately 200 Å in their largest dimension [40, 42, 46]. HAP is abundant in both cortical and cancellous bone but may be less regular in cancellous bone due to the less organised collagen matrix [46]. Various factors, including vitamin D status, can impact mineralisation [42, 63]. The collagen-HAP interaction is synergistic, with collagen providing tensile strength and flexibility, while HAP imparts rigidity and hardness [40, 42, 43, 46]. An overview of the macro to microstructure of bone is illustrated in Figure 3.

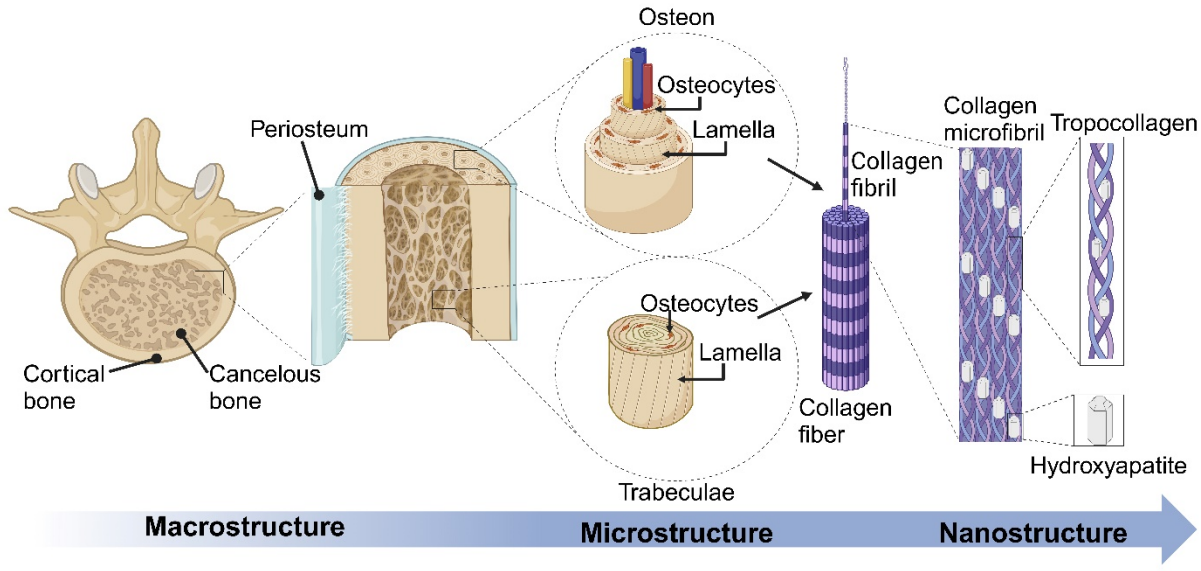


*Figure 3 Macro to microstructure of bone. From left to right: Top view of a vertebrae showing cortical and cancellous bone, cross-section of cortical bone adjacent to cancellous bone, osteon/trabeculae, structure of collagen fibres. Image created on www.biorender.com.*

`

### 1.1.3. Bone Development, Growth, Remodelling, Modelling and Healing

Bone is a dynamic tissue that undergoes longitudinal and radial growth, modelling, remodelling, and healing throughout life to attain size, shape, and structural integrity. While these processes share fundamental cellular mechanisms mediated by osteoclastic resorption and osteoblastic formation, they differ significantly in their spatiotemporal orchestration [48].

*Table 1 Summary of objectives, involved cells, anatomical locations, mechanisms, timings, and effects on bone mass associated with bone development, growth, modelling, remodelling, and healing. Adapted from [48].*

| | **Development and Growth** | **Modelling** | **Remodelling** | **Healing** |
|---|---|---|---|---|
| **Goal** | Bone growth | Alter or maintain bone shape, increase bone mass | Renew bone | Heal bone fractures |
| **Cells** | Osteoclasts, osteoblasts, and their precursors | Osteoclasts or osteoblasts and their precursors | Osteoclasts, osteoblasts, and their precursors | Osteoclasts, osteoblasts, and their precursors |
| **Bone Envelope** | All bone envelopes | Periosteal, endocortical, trabecular | Periosteal, endocortical, trabecular, intracortical | Wherever needed |
| **Mechanism** | Intramembranous ossification or endochondral ossification | Activation-formation or activation-resorption | Activation-resorption-formation | Primary healing via gap healing/contact healing or secondary healing via intramembranous ossification/ endochondral ossification |
| **Timing** | During embryonal development and postnatally until growth plate calcifies | Primarily childhood, but continues throughout life | During embryonal development and postnatally throughout life | On-demand |
| **Net Effect on Bone Mass** | Increase | Increase | Maintain or slight decrease | Maintain |

`

# Bone Development and Growth

## Intramembranous Ossification

Intramembranous ossification is primarily responsible for the embryonic development of flat bones, including the cranium, clavicle, mandible, and scapula. This osteogenic process can also occur postnatally during bone healing. The mechanism comprises several key stages [43, 48, 64-66]:

- **Blastema formation**: Mesenchymal cells condense to form a blastema.
- **Osteoblast differentiation**: Within the blastema, cells differentiate into osteoblasts under the regulation of Wnt signalling. Wnt activation induces β-catenin expression, which promotes Runx2 expression in mesenchymal cells, directing osteoblast differentiation. Chondrocyte differentiation is inhibited by repressing SRY-box transcription factor 9 (Sox9).
- **Ossification centre formation:** Osteoblasts produce disorganised collagen I and other bone matrix proteins, facilitated by Runx2 and Osterix. This results in woven bone formation and the establishment of a primary ossification centre.
- **Osteocyte development:** As more matrix is deposited, some osteoblasts become osteocytes as they become surrounded by the developing matrix. Additional osteoblasts are recruited to continue the formation of woven bone.
- **Maturation:** The matrix becomes mineralised via HAP incorporation. BMUs remodel the primitive woven bone into lamellar bone. Increased Wnt/β-catenin signalling on the bone surface (perichondrium) promotes further osteoblast differentiation, forming cortical bone.
- **Marrow cavity formation:** Growth in some bones leads to a marrow cavity as central osteocytes become distant from the blood supply, prompting blood vessel invasion. Around these vessels, primary osteons develop.

## Endochondral Ossification

Endochondral ossification is the primary mechanism for embryonic development of the axial and appendicular skeleton. This osteogenic process also plays a significant role in postnatal fracture repair. The process comprises several key stages [43, 48, 64-66]:

- **Chondroblast differentiation**: Mesenchymal cells aggregate at bone growth sites and differentiate into chondroblasts, mediated by Sox9.
- **Cartilage template formation:** Chondroblasts produce a collagen II-rich cartilage matrix, which envelops some chondroblasts, transforming them into chondrocytes. A fibrocellular membrane called the perichondrium surrounds the hyaline cartilage template, supplying cells for cartilage expansion.

- **Chondrocyte hypertrophy:** Proliferating chondrocytes progress through a prehypertrophic stage into hypertrophic chondrocytes. This transition is characterised by increased Runx2 expression.
- **Bone collar formation**: Under Runx2 regulation, perichondrium cells differentiate into osteoblasts. These osteoblasts generate a bone collar around the diaphysis, initiating the transformation of the perichondrium into the periosteum. This newly formed periosteum becomes populated with osteogenic precursor cells.
- **Primary ossification centre formation:** The bone collar restricts nutrient diffusion, prompting cartilage calcification and chondrocyte apoptosis. Hypertrophic chondrocytes (before apoptosis) secrete vascular endothelial growth factor (VEGF) and facilitate blood vessel recruitment. These vessels penetrate the bone collar (assisted by osteoclasts) and transport nutrients, osteoclasts, osteoblasts and haemopoietin cells to the cavity. Osteoclasts remove the calcified matrix, and haematopoietic cells form the bone marrow. Osteoblasts then produce new bone on the degraded cartilage matrix, and some hypertrophic chondrocytes transdifferentiate to osteoblasts.
- **Marrow cavity formation**: In certain bones, marrow cavities emerge due to the distance of osteocytes from the nearest vascular supply.
- **Secondary ossification centre formation**: This process follows similar mechanisms as primary ossification and occurs at the epiphyses of long bones, predominantly postnatally.
- **Growth plate formation**: The primary and secondary ossification centres collectively contribute to growth plate formation. This structure comprises two cartilaginous epiphyses connected by a central diaphyseal region housing the bone marrow cavity. It governs longitudinal bone growth and remains active postnatally. The growth plate is organised into distinct zones comprising resting, proliferating, prehypertrophic, and hypertrophic chondrocytes.
- **Bone growth:** Bone growth persists through mechanisms regulated by growth factors such as growth hormone, IGFs, and BMPs. The cartilage template is progressively replaced by woven bone, which is remodelled into lamellar bone. Growth ceases after the growth plate ossifies, typically during late adolescence or early adulthood, leaving the epiphyseal line. Postnatally, thyroid hormones, oestrogen, androgens, glucocorticoids, vitamin D, and leptin contribute to longitudinal bone growth. Oestrogen, in particular, leads to earlier growth cessation in females.

`

## Bone Remodelling

Bone remodelling begins during embryonic development and persists throughout life, renewing bone to maintain strength and mineral homeostasis. This process replaces small regions of old bone with newly synthesised tissue, preventing microdamage accumulation from normal skeletal loading.

At the microscopic level, remodelling occurs in BMUs on cortical and trabecular surfaces. BMUs consist of osteoblasts and osteoclasts that coordinate bone resorption and formation at the same site, thereby preserving bone mass. The remodelling cycle comprises sequential phases (see Figure 4) [41-44, 48, 67-69]:

- **Activation phase:** Osteoclast precursors are recruited and differentiate into mature osteoclasts.
- **Resorption phase:** Bone lining cells retract, exposing the mineralised matrix to osteoclasts. Osteoclasts actively dissolve the inorganic mineral and digest organic collagen fragments.
- **Reversal phase:** Resorption ceases, and bone formation is initiated as the bone matrix releases growth factors, such as transforming growth factor (TGF)-β, platelet-derived growth factor (PDGF), IGF-I, and IGF-II. Mononuclear cells digest the remaining non-mineralised collagen matrix.
- **Formation phase:** Osteoblasts synthesise and secrete a non-mineralised organic matrix called osteoid, composed primarily of type I collagen. The osteoid serves as a template for HAP crystal formation. The mineralisation process occurs in two phases: primary mineralisation and secondary mineralisation.
- **Quiescence phase:** The bone surface is covered by bone lining cells and continues to mineralise.

The entire bone remodelling cycle spans 4–6 months. Once the BMU is remodelled, 50–70% of osteoblasts undergo apoptosis. The remainder become osteocytes or bone lining cells [42, 48, 67].

Coupling refers to the coordinated osteoclast and osteoblast activity within each BMU, while balance refers to the amount of bone resorbed and formed at each site [48]. In a balanced state, resorption always precedes formation, and the amount of bone resorbed equals the amount formed [43, 67]. An imbalance favouring excess osteoclast or osteoblast activity leads to osteopenia, osteoporosis, and osteopetrosis [41].

Remodelling rates are high and generally positively balanced until peak bone mass is attained in the third decade of life. Remodelling rates are higher in females during this time. After age 50, resorption predominates, leading to decreased bone mass [43, 48, 67].

Cellular coupling is regulated by local and systemic genetic, mechanical, nutritional, and hormonal factors to maintain bone homeostasis [41, 43, 44, 48, 68]. Oestrogen deficiency during the peri- to post-menopausal transition causes a negative remodelling balance and strongly predisposes to osteoporosis. Hormone replacement therapy can mitigate increased resorption rates [42, 43].

Remodelling annually renews approximately 5% of cortical and 20% of trabecular bone. Although cortical bone comprises 75% of total bone volume, remodelling rates are 10-fold higher in trabecular bone due to its greater surface area-to-volume ratio. Therefore, 5–10% of total bone is remodelled yearly [43, 48, 67].

In humans, each BMU cycle spans 2–8 months, with the majority of time occupied by bone formation [43, 67]. Approximately 35 million BMUs are in the human skeleton, of which 3–4 million are activated annually. Thus, the skeleton is completely renewed every 10 years [67].

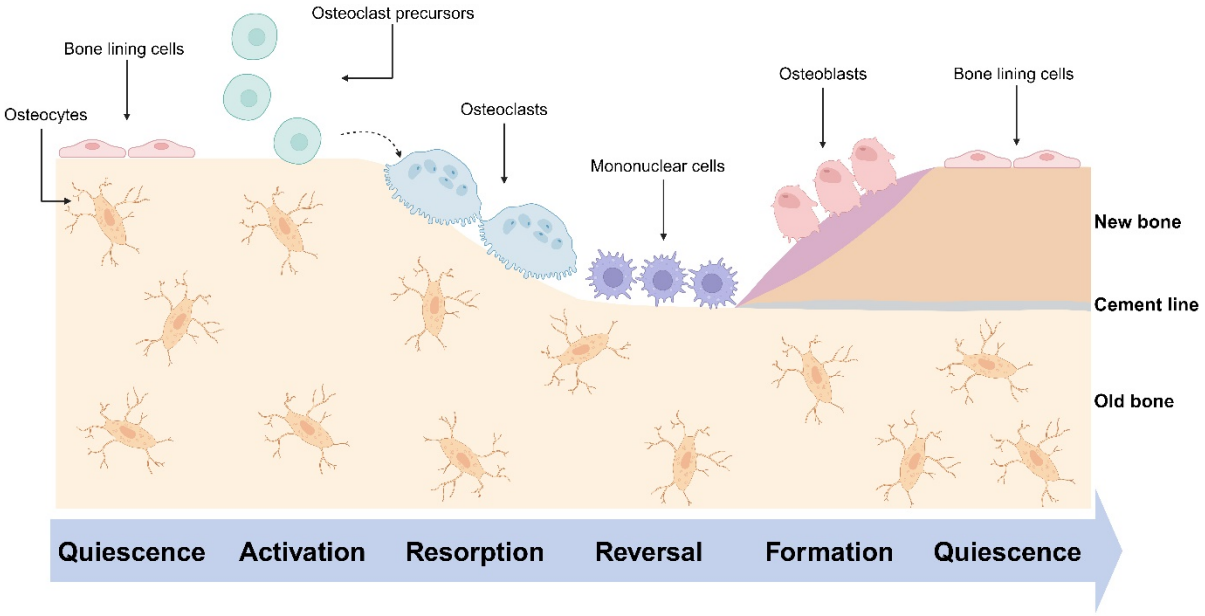


*Figure 4 Different stages of bone remodelling. Image created on www.biorender.com.*

## Bone Modelling

Bone modelling is the process of altering bone structure, primarily during growth and development, to reshape bone and adjust the position of the central bone axis. This process occurs on the periosteal and endocortical surfaces of cortical and trabecular bone surfaces. Structural changes are mediated by osteoblasts for bone formation and osteoclasts for resorption. Unlike remodelling, osteoblast and osteoclast activity in modelling is not coupled; instead, it is systematically organised and coordinated across the skeleton to shape bone. Local mechanical forces sensed by osteocytes initiate modelling; elevated strains trigger

`

modelling on periosteal surfaces to reduce strain, while low strains promote endocortical modelling that removes bone. Following activation, precursor cells are recruited and differentiate into mature osteoblasts or osteoclasts, with formation or resorption continuing until sufficient bone mass is added or removed to normalise local strains. During longitudinal growth, formation and resorption modelling coordinate in the metaphyseal region, with resorption modelling removing periosteal bone and formation modelling adding new endocortical bone. Formation modelling via periosteal apposition is the primary mechanism of radial bone growth throughout life. Although periosteal modelling is most active during growth, it slows in adulthood, countered by endocortical resorptive modelling to maintain cortical thickness. Periosteal modelling is greater in males during puberty due to testosterone, whereas oestrogen inhibits it in females, leading to sex differences in bone diameter. Additionally, factors such as mechanical loading and parathyroid hormone influence bone modelling [48, 70].

## Bone Healing

Bone healing occurs through two primary mechanisms: primary bone healing and secondary bone healing.

### Primary Bone Healing

Primary bone healing occurs when there is stable alignment and minimal movement between fracture fragments, typically through rigid internal fixation. The cortex attempts direct reconnection of the fracture ends, restoring mechanical integrity with little periosteal callus. In humans, direct healing usually requires open reduction and internal fixation and is rare without precise fracture end alignment. It is a gradual process, taking months to years. Primary bone healing proceeds through contact or gap healing [47, 71, 72].

**Contact healing** occurs when fracture ends are precisely aligned and rigidly stabilised through internal or external fixation, facilitating direct communication between bone cells. During this process, osteoclasts resorb damaged bone, while osteoblasts secrete collagen to promote new bone formation [47, 72].

**Gap healing** restores bone integrity across a fracture gap under 800 μm to 1 mm via lamellar bone formation perpendicular to the long axis. Re-vascularised osteons containing osteoprogenitor cells mature into osteoblasts, contributing to lamellar bone formation. Gap healing typically takes 3–8 weeks, influenced by health, age, and fracture severity. Adequate stability through proper immobilisation and fixation is crucial for successful gap healing [47, 72].

`

### Secondary Bone Healing

Secondary healing involves a periosteal and soft tissue response at the fracture site, initiated by bone injury and enhanced by limited fragment motion but inhibited by rigid fixation. This process employs both intramembranous and endochondral ossification concurrently, where intramembranous ossification forms a hard callus peripherally, while endochondral ossification forms a soft callus at the fracture. This process occurs in different subsequent stages (see Figure 5) [40, 47, 71]:

- **Inflammation**: The initial stage is marked by clotting and haematoma formation. Platelet activation releases cytokines such as VEGF, TGF-β, and PDGF, recruiting neutrophils and macrophages with a peak response at 24 h
- **Soft Callus Formation:** Stimulated cells generate new blood vessels, fibroblasts, and supporting cells. The haematoma is replaced by fibrocartilage collagen, stabilising the bone ends, with peak activity occurring at 7–10 days.
- **Hard Callus Formation:** Osteoclasts and perivascular mesenchymal stem cells (MSCs) invade the cartilage template. Osteoclasts degrade the cartilage, while MSCs differentiate into osteoblasts to form woven bone, with peak activity around 14 days.
- **Remodelling:** Woven bone is gradually replaced by lamellar bone through osteoclastic resorption and osteoblastic formation, starting after 3–4 weeks and potentially continuing for years.

Ageing reduces healing potential due to declining cellular activity. In diabetes, hyperglycaemia and hypoinsulinemia lead to impaired chondrogenesis and osteogenesis, reversed by insulin treatment or local delivery. Osteoporosis drugs such as bisphosphonates prolong endochondral ossification and delay remodelling, resulting in a larger, stronger callus. Furthermore, nonsteroidal anti-inflammatory drugs (NSAIDs) inhibit prostaglandins, delaying healing [40, 47].

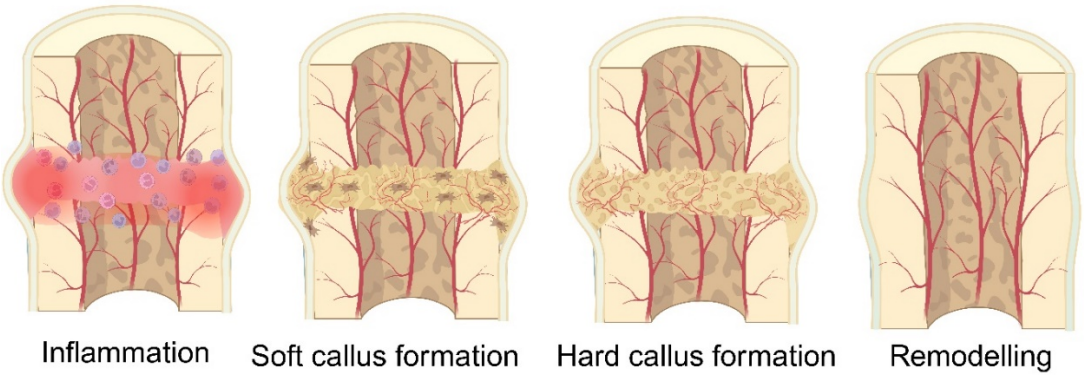


*Figure 5 Stages of secondary bone healing. From left to right: Inflammation, soft callus formation, hard callus formation, remodelling. Image created on www.biorender.com.*

`

## 1.1.4. Back Pain

The term "back pain" is predominantly synonymous with "low back pain" among most experts, excluding neck and thoracic pain from this classification [73]. This perspective is reflected in the literature, which predominantly focuses on lower back pain. Consequently, this section will focus on understanding the burden, risks, diagnosis, and treatment of lower back pain. However, it is important to note that this emphasis does not undermine the significance of addressing neck and thoracic pain, particularly in the context of spinal fusion interventions.

Lower back pain (LBP) is a complex health concern, affecting the lives of numerous individuals globally. Due to its high prevalence and the challenges associated with its treatment, it constitutes a substantial clinical, economic, and societal burden.

### Definition, Classification, and Prevalence

LBP is typically characterised by pain, muscle tension, or stiffness localised between the costal margin and the inferior gluteal folds, often radiating into the leg. LBP is categorised into two primary types: specific and non-specific [74]. Specific LBP is further classified as nociceptive or neuropathic pain [75]. Nociceptive pain arises from actual or potential damage to non-neural tissues, activating nociceptors, and is commonly associated with conditions such as osteoporosis, rheumatoid arthritis, fractures, or tumours. Neuropathic pain originates from lesions or pathology affecting the somatosensory nervous system, as observed in herniated nuclei pulposi [74, 75]. Conversely, non-specific LBP cannot be attributed to a distinct underlying cause, with approximately 90% of patients diagnosed via exclusion of specific pathology [74]. Central sensitisation, characterised by heightened pain sensitivity, is considered non-specific LBP due to its ambiguous origin but may coexist with specific LBP. Neuropathic pain can present with central sensitisation, resulting in widespread pain hypersensitivity. Similarly, nociceptive and central sensitisation pain may co-occur, where disproportionate pain levels arise alongside identifiable nociceptive sources [75]. An overview of different pain types is illustrated in Figure 6.

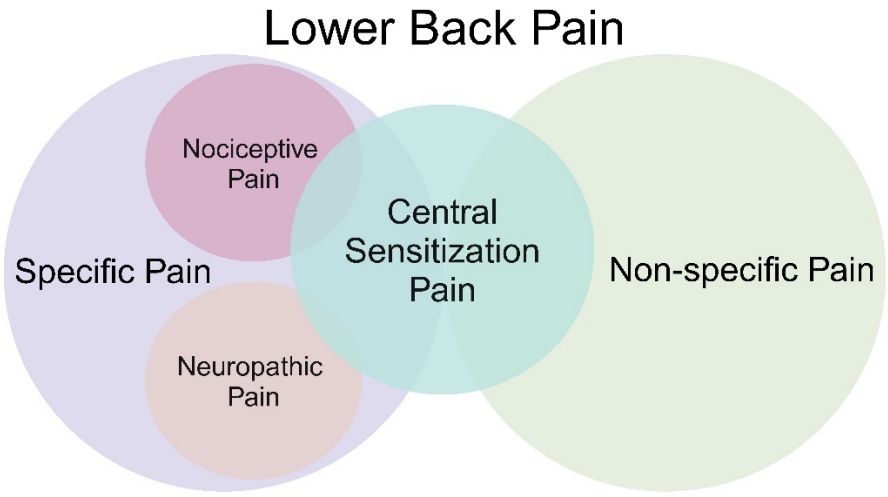


*Figure 6 Illustration of different LBP categories. Image created on www.biorender.com.*

LBP is categorised by duration: acute (ALBP), lasting less than six weeks; subacute (SLBP), lasting six weeks to three months; and chronic (CLBP), persisting beyond three months [74]. The onset of these symptoms results from a complex interaction of multifactorial risk factors.

## Risk Factors

Given its widespread prevalence, a considerable number of individuals will experience at least one episode of LBP in their lifetime, with many facing persistent or recurrent issues [74, 76]. Several risk factors are linked to the modulation, prevalence, and recurrence of LBP (Figure 7) [77].

Research indicates a significant role of genetic factors in experiencing an LBP episode [78-83].

Additionally, several studies have demonstrated a connection between LBP and psychological factors such as depression and stress [79, 84, 85].

The social environment is also critical in influencing LBP. Social isolation has been shown to correlate with LBP-related disability [86] positively. Similarly, it was found that the work environment presents a complex relationship with LBP [87, 88].

The presence of comorbidities was associated with increased LBP prevalence. Conditions such as diabetes, psoriasis, overweight, obesity, and smoking have been linked to a higher incidence of back pain [89-91], with smoking showing a greater incidence in adolescents than adults [91].

Physical factors were also found to play a role in LBP occurrence. A high-energy diet has been positively associated with LBP, whereas a high-protein diet has shown a negative association [92]. Higher levels of fitness were associated with reduced LBP [93]. There is ongoing debate about whether deconditioning, through reduced strength and overall fitness,

is a cause or effect of chronic low back pain, but a bidirectional relationship is likely despite limited research [94]. Additional physical factors linked to LBP recurrence include awkward postures, prolonged sitting, and a history of more than two previous LBP episodes [76]. An overview of risk factors is illustrated in Figure 7.

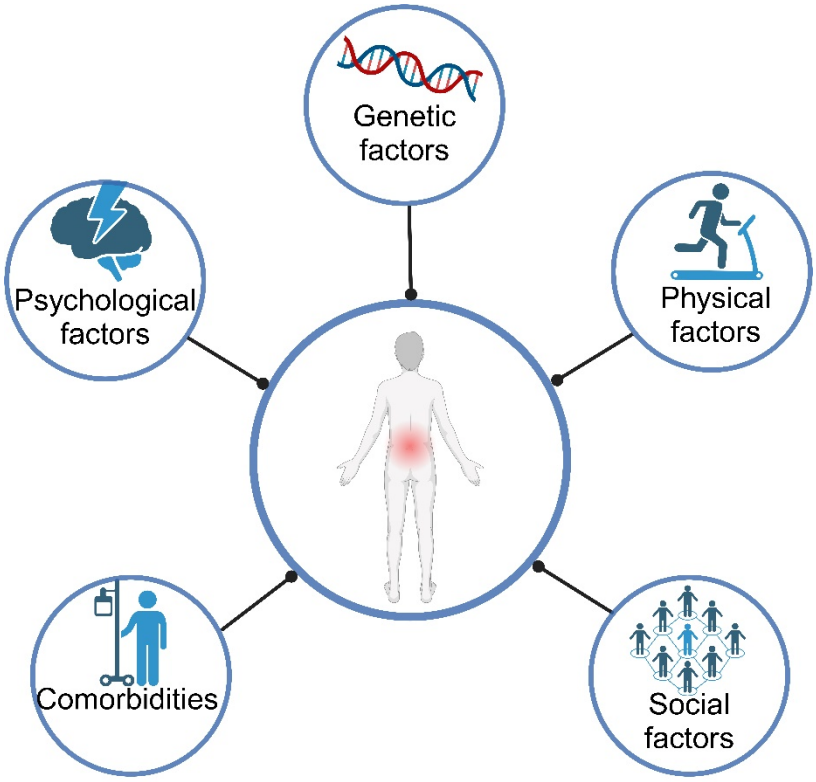


*Figure 7 Risk factors for LBP. Image created on www.biorender.com.*

## Prevalence and Social-Economic Impact

LBP stands as a highly prevalent global health concern. According to the Global Burden of Disease Study 2019, in 2020 LBP affected 619 million people worldwide. This condition accounted for 69 million years lived with disability (YLDs) globally, representing the primary contributor to YLDs, accounting for 7.7% of the total burden. Notably, LBP ranked among the top 10 leading causes of disability-adjusted life-years (DALYs) globally across all age groups, reaching the fourth position in global DALYs for individuals aged 25–49 [1, 2].

LBP is not limited to adults; its prevalence extends to adolescents. It was observed to be more prevalent among girls than boys, with sex disparities becoming more pronounced with age. Among adolescents, back pain accounted for 37% of reported pain causes [95]. While LBP can affect individuals of all age groups, its incidence increases notably with increasing years, peaking around the age of 85 [2]. Its prevalence by age and sex is visualised in Figure 8.

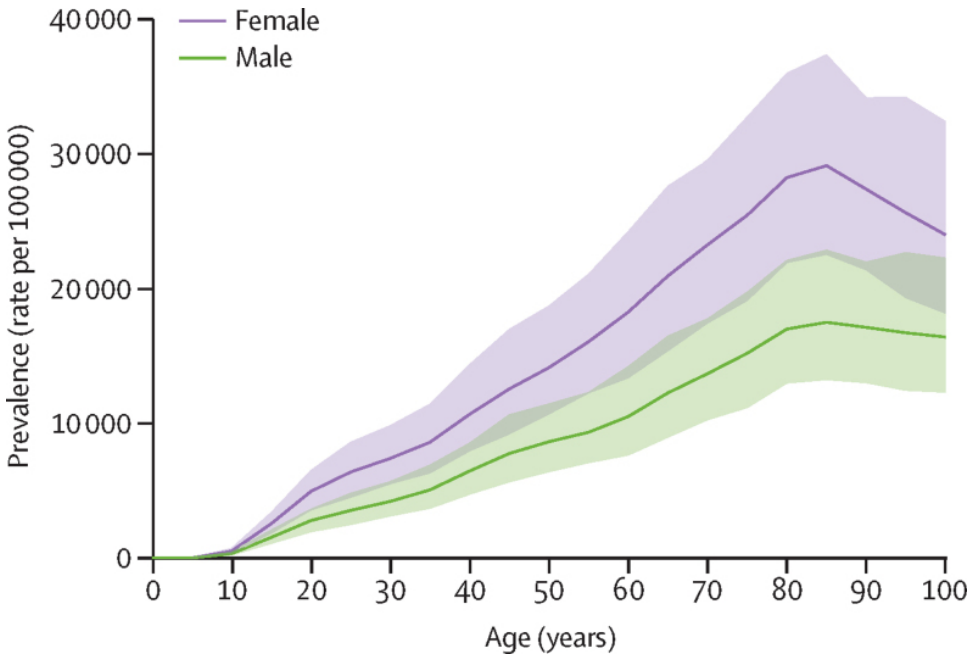


*Figure 8 Prevalence of LBP by age. X-axis: Age in years; Y axis: Prevalence per 100,000. From [2].*

Due to population growth and ageing, the incidence of disability resulting from LBP is rapidly increasing. Notably, LBP stands as the foremost health condition driving demand for rehabilitation services [3].

A study revealed that the median duration for recovery in terms of pain relief and return to work following an episode of ALBP was 59 days. Six weeks after the initial presentation to primary care, the cumulative probability of recovery was 39.0%, increasing to 57.4% by 12 weeks and further to 71.8% by one year [96]. Nevertheless, as the duration of pain and disability increases, the prognosis becomes less favourable. After six months of sick leave, fewer than 50% will successfully return to work, and after two years of absence, the likelihood of returning significantly diminishes. Recurrence of acute episodes affects 20–44% of patients within one year in the working population, with lifetime recurrences reaching up to 85% [97].

In North America, Europe, and the Western Pacific, the pooled annual hospitalisation rate for lower back pain was estimated at 3.2% [98]. The economic burden of LBP extends beyond hospitalisation, encompassing both direct and indirect costs. Direct costs include medical expenses related to diagnosis, treatment, and management, such as doctor visits, hospital stays, medications, procedures, and medical devices. Indirect costs reflect the economic burden on society through reduced production and income, including missed workdays, reduced work capacity, early retirement, caregiver time, and premature death [3-5].

Using population metrics from the respective years, the per capita economic impact varies significantly across countries [99].

`

In 2006, the USA reported total annual costs exceeding $100 billion ($335 per capita), with $20 billion in direct costs (excluding medications and diagnostic tests) and $50 billion in indirect costs. Notably, less than 5% of patients experiencing an episode of LBP annually account for 75% of total costs [6].

Switzerland's 2005 estimates showed total costs of €6.6 billion (€887.6 per capita), comprising €2.6 billion in direct healthcare costs and €4.1 billion in indirect costs [7].

In the UK, a 1998 cost-of-illness study revealed total costs of £12,300 million (£210 per capita), with £1,632 million in direct costs and £10,668 million in indirect costs [8].

Individual episodes of back pain also carry substantial economic implications. A Swedish study (2008-2011) estimated the mean total cost per episode at €2,753, with 67% attributed to indirect costs [100].

Research has shown that recurrent back pain increased the likelihood of health-related employment exit by 51% compared to those without back pain [101]. In Australia, early retirement due to back problems was associated with an 87.35% decrease in total assets when present [102].

These findings underscore the critical societal and individual burden of lower back pain, emphasising the importance of prompt treatment.

# Diagnosis and Treatment

## Diagnosis

Official medical organisations in respective countries provide guidelines for LBP diagnosis and treatment. These guidelines recommend clinical assessment via triage with physical examination, imaging, and evaluation of psychosocial factors, as presented in Figure 9 [103, 104]. In the UK, guidelines are provided by the National Institute for Health and Care Excellence (NICE). The following steps are recommended to exclude any underlying causes and assess for prognostic indicators [105]:

- **Initial assessment:** A medical history should be taken, and the patient should be interviewed to understand their symptoms and how they impact various aspects of their daily life, including work, relationships, sleep, and psychological well-being.
- **Physical examination:** Posture, gait, spine deformities, localised spinal tenderness, limitations in ROM, and neurological anomalies are assessed.
- **Risk stratification:** If no cause is detected, it is advisable to employ a risk stratification screening tool to better understand the potential severity of the condition.
- **Use of imaging:** X-ray or other imaging tests should generally be avoided in primary care for diagnosing non-specific low back pain. They should only be employed if there is reason to suspect a specific underlying issue.

`

- **Specialist referral:** Depending on clinical judgment, arrangements for emergency hospital admission or referral to a specialist should be made if there are any concerning signs (red flags) or if an underlying cause is suspected.

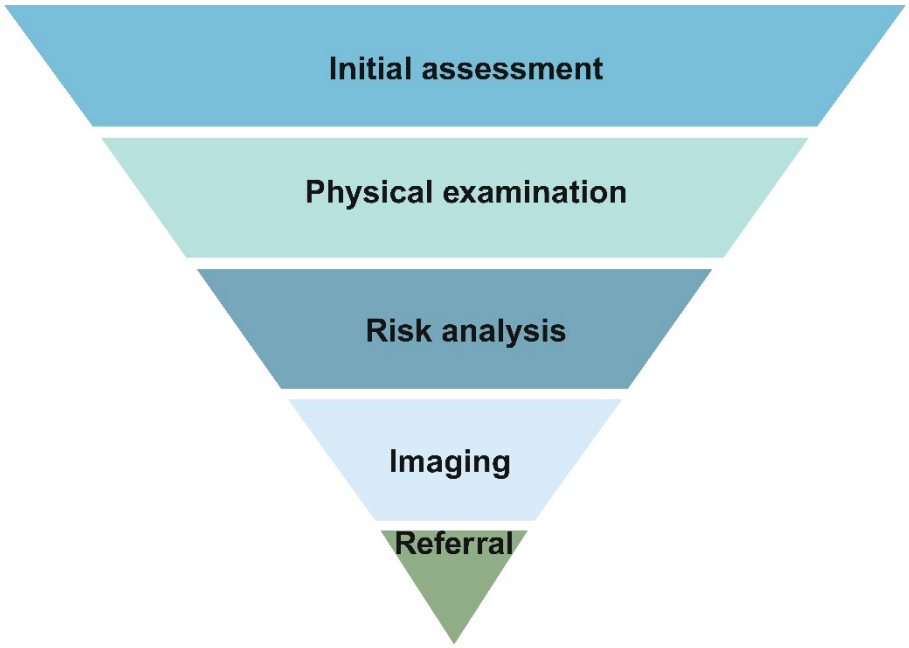


*Figure 9 Treatment pyramid for LBP. Image created on www.biorender.com.*

The concept of flag identification was developed to classify risk factors associated with poor outcomes in patients with LBP [106-108].

Red flags (e.g. unexpected weight loss) indicate possible serious spinal pathology (e.g. spinal tumour) and are obtained from patient history, interview, and physical examination [108-110]. There are 163 signs and symptoms documented as red flags in the book: “Red Flags and Blue Lights: Managing Serious Spinal Pathology” [110, 111]. The identification of red flags guides clinical decision-making, with their absence supporting conservative management in primary care, while their presence necessitates specialist referral and advanced imaging, such as magnetic resonance imaging [109, 112].

Psychological factors known as yellow flags, such as negative attitudes, fear-avoidance behaviours, depression, and unsupportive work environments, are linked to the development of chronic pain and disability [106, 109, 112]. Early identification of yellow flags can help recognise patients at risk of chronicity, enabling intervention through cognitive-behavioural therapy, coordinated care, and workplace adjustments [107, 108]. If untreated, these factors can result in prolonged work disability [106]. Orange refer to abnormal psychological responses that meet diagnostic criteria for conditions such as major depressive disorder or post-traumatic stress disorder, necessitating referral to mental health specialists [107].

`

Blue flags relate to a worker's perception of a stressful, unsupportive, or highly demanding work environment, such as a perceived lack of control over tasks or inadequate social support at work [107, 108].

Black flags refer to workplace conditions or compensation policies that may affect disability outcomes, often requiring administrative or legal intervention [107, 108].

The flag system aims to guide decision-making about referral, imaging, medication, activity recommendations, and psychosocial interventions to diagnose and treat spinal pathologies and prevent chronic LBP disability [106-112]. Table 2 presents an overview of the different flags and their underlying causes.

*Table 2 Summary of different flag identification types. From [107].*

| Flag | Nature | Examples |
|---|---|---|
| Red | Signs of serious pathology | Cauda equina syndrome, fracture, tumour |
| Orange | Psychiatric symptoms | Clinical depression, personality disorder |
| Yellow | Beliefs, appraisals, and judgments | Unhelpful beliefs about pain: indication of injury as uncontrollable or likely to worsen<br>Expectations of poor treatment outcome, delayed return to work |
| | Emotional responses | Distress not meeting criteria for diagnosis of mental disorder<br>Worry, fears, anxiety. |
| | Pain behaviour (including pain coping strategies) | Avoidance of activities due to expectations of pain and possible re-injury<br>Over-reliance on passive treatments (hot packs, cold packs, analgesics) |
| Blue | Perceptions about the relationship between work and health | Belief that work is too onerous and likely to cause further injury<br>Belief that workplace supervisor and workmates are unsupportive |
| Black | System or contextual obstacles | Legislation restricting options for return to work<br>Conflict with insurance staff over injury claim<br>Overly solicitous family and health care providers<br>Heavy work, with little opportunity to modify duties |

## Treatment

The stepwise management of LBP begins with conservative approaches, including self-care strategies (such as the use of heating pads), exercise, stress reduction techniques [113, 114], and physical therapy [9, 115], prior to considering more invasive interventions. If conservative measures prove ineffective, pharmacological options such as NSAIDs, antidepressants, anticonvulsants, and opioids may be employed for pain relief. [113, 116-119]. Other conservative treatment methods include spinal injections and prolotherapy [117, 120, 121]. If symptoms persist, minimally invasive procedures such as nucleoplasty, neuroplasty, and annuloplasty may be considered [122-127]. Subsequent options encompass laminectomy

`

procedures [128, 129] and motion preservation surgeries [130, 131]. Minimally invasive techniques are preferred when fusion is deemed necessary [132-135]. In severe, recalcitrant cases that do not respond to previous interventions, more radical spinal corrective surgeries may be performed, including pedicle subtraction osteotomy, sacropelvic fixation, vertebral column resection, or spinal fusion with instrumentation [136-138]. However, European guidelines recommend surgical treatment only after two consecutive years of unsuccessful conservative management [9].

### 1.1.5. Spinal Fusion: Definitions and Historical Development

#### Spinal Fusion Surgery

Spinal fusion is a surgical treatment for various spinal disorders that compromise structural integrity and stability, including spondylolisthesis, spondylolysis, degenerative disc disease, trauma, infections, tumours, and post-decompression instability. The procedure entails the fusion of at least two vertebrae by inserting a graft or cage into the intervertebral space following the discectomy of the affected spinal segment. Subsequently, the graft and intervertebral space are stabilised using fixation devices such as pedicle screws, plates, or spacers. Spinal fusion aims to eliminate painful motion and enhance stability by fusing the unstable vertebral segments. The two primary indications for the procedure are: 1) the management of primary pathologies affecting the structural spine, including fractures, tumours, infections, inflammatory conditions, or degeneration, and 2) supplemental stabilisation following decompression procedures that further destabilise the spine [10-12].

Cervical fusion is employed to address a variety of pathological conditions, including fractures, radiculopathy, and myelopathy resulting from disc herniation or spondylosis. It also serves to stabilise the subaxial cervical spine in cases of traumatic injury, infection, neoplasia, or degenerative disease [139, 140]. Interbody fusion of the cervical spine can utilise a posterior, anterior, or combined anterior and posterior approach. The anterior fusion technique involves the insertion of an intervertebral cage and anterior plating, facilitating decompression [139, 141]. In contrast, posterior fusion employs pedicle screw fixation to achieve reduction and stabilisation through a posterior approach. Posterior fusion is often utilised when instability is not adequately managed by anterior fusion alone, providing stabilisation in cases where anterior approaches are unsuitable [140, 141]. The choice between approaches depends on the need for decompression versus the ease of achieving reduction. Although combined anterior and posterior approaches can provide adequate decompression and enhanced stability, they also confer greater surgical trauma and complexity [141].

`

The indications for thoracic fusion encompass a range of pathological entities, including traumatic disorders, infections, neoplasms, degenerative conditions, and deformities such as scoliosis and kyphosis [142]. Thoracic spinal fusion can utilise an anterior or posterior surgical approach [143]. The anterior approach involves performing a discectomy or disc shortening if necessary. A graft or cage may be inserted to prevent thoracolumbar kyphosis, and rods are utilised to restore kyphosis. Notably, the anterior approach is superior to the posterior approach for restoring normal thoracic kyphosis [144]. Conversely, the posterior approach entails discectomy followed by the insertion of an interbody cage. The cage is then filled with bone graft or substitute and secured with pedicle screws. Fusion can be performed with or without fixation [141, 145]. Importantly, posterior approaches avoid invading the thoracic or abdominal cavities, making them technically easier and associated with fewer complications than anterior approaches [141]. For patients with preoperative hyperkyphosis, a posterior approach should be considered [144].

Lumbar interbody fusion techniques are employed in the treatment of various spinal pathologies affecting the lumbar region, including scoliosis, spondylolisthesis, vertebral fractures, and advanced disc degeneration. The primary objectives of these interventions are to restore spinal alignment and decompress neural elements by increasing the intervertebral foraminal space. Multiple surgical approaches have been developed to achieve these goals, each with distinct advantages and indications. The primary techniques include:

- **Posterior Lumbar Interbody Fusion (PLIF):** Involves bilateral laminectomy, discectomy, and bone graft implantation via a posterior approach.
- **Transforaminal Lumbar Interbody Fusion (TLIF):** Utilises a unilateral facetectomy for graft insertion through the neural foramen.
- **Anterior Lumbar Interbody Fusion (ALIF):** Employs an anterior approach for implant insertion.
- **Lateral Lumbar Interbody Fusion (LLIF):** Utilises a lateral approach for implant placement.
- **Axial Lumbar Interbody Fusion (AxLIF):** Implements an axial approach for spacer insertion.

The latter three techniques (ALIF, LLIF, and AxLIF) facilitate indirect neural decompression through their respective approaches [12]. A schematic representation of these surgical techniques, detailing their anatomical approaches, is provided in Figure 10.

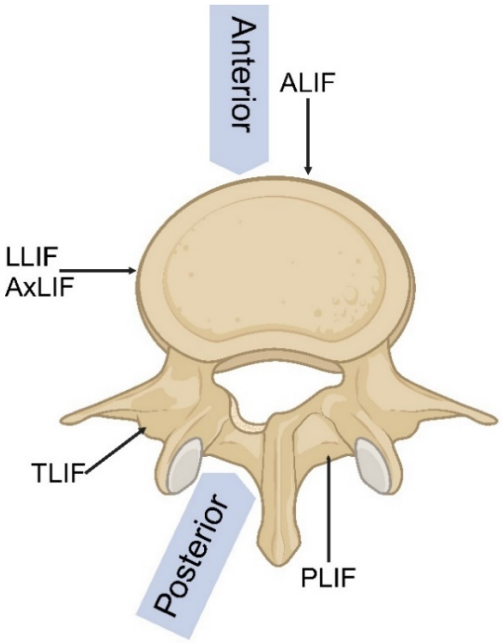


*Figure 10 Different interbody fusion approaches. Image created on www.biorender.com.*

To enhance construct stability, supplementary fixation hardware may be implemented, including pedicle screws, rods, and interspinous clamps. Figure 11 illustrates an anterior spinal fusion with cage implantation and pedicle screw stabilisation.

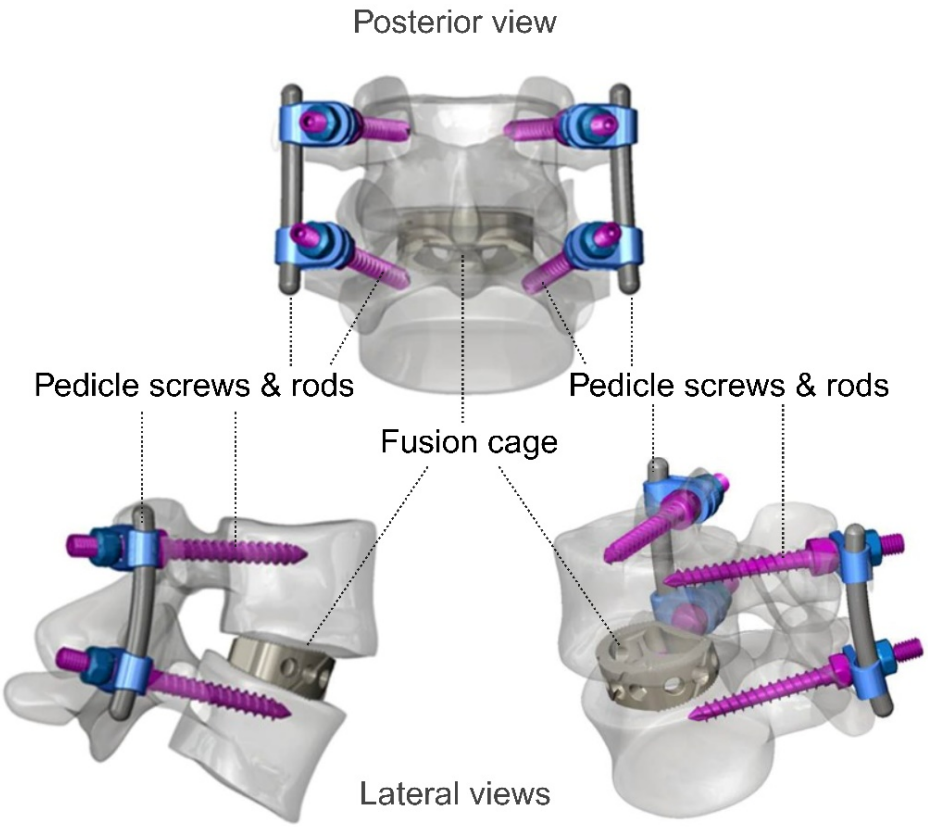


*Figure 11 Example of lumbar interbody fusion with a cage and pedicle-screw stabilisation, shown in posterior and lateral views. Adapted from [146].*

`

Spinal fusion surgery has demonstrated positive economic outcomes in the treatment of LBP. A study examining patients who underwent lumbar spinal fusion in the USA reported significant improvements in workplace productivity: at-work performance increased from 16% to 29% within 12 months post-surgery, while monthly time lost due to reduced work performance decreased from 19.8% to 9.7% over the same period [147].

Additionally, a Swedish study found that successful spine surgery led to substantial cost savings, with average monthly societal costs decreasing by €1,010 between the first and third year post-surgery [148].

## Historic Review of First Developments to Current Techniques

Ancient references to the treatment of spinal deformities have laid the foundation for modern spinal interventions, including spinal fusion surgery. One of the earliest mentions can be traced back to ancient Hindu mythological epics (3500 BC to 1800 BC), in which Lord Krishna is said to have corrected the hunchback of a devotee using axial traction [149]. Hippocrates (460 BC to 377 BC) also employed axial traction to rectify spinal deformities, pioneering specialised apparatuses such as the Hippocratic ladder and board [149, 150].

*Figure 12 Hippocratic apparatuses for spinal deformity correction. The Hippocratic ladder (left) uses gravity with the head downward, while the Hippocratic board (right) applies pressure using body weight. From [150].*

`

Paul of Aegina (625–690) is believed to have performed one of the earliest laminectomies on patients with spinal cord injuries. In one of his writings, he describes making incisions in the compressing bone to alleviate pressure on the spinal cord [151].

These ancient practices established the foundation for the sophisticated techniques employed in contemporary spine surgery.

In the 19$^{th}$ century, the rise of tuberculosis led to substantial bone damage, initially described as Pott's disease [152]. This necessitated an increased demand for spinal treatments, resulting in exponential advancements in the field. The evolution of spinal fusion techniques can be classified into those with or without instrumentation, the latter primarily involving bone grafts. However, modern practices predominantly utilise a combination of both to achieve the best therapeutic outcomes.

## Spinal Fusion without Instrumentation

An important milestone in non-instrumental spinal fusion was achieved in 1911 when Russell Hibbs published his work on bone graft-mediated spinal fusion. Hibbs employed a posterior approach, grafting autologous bone over the spinous processes and laminae. Despite its success, this technique had limitations, as the spine could re-bend without external support, resulting in curve progression [153]. To address this issue, a cast designed by Risser [154], also known as the Risser cast, was introduced, applying rigid pressure to the ribcage post-surgery until fusion was achieved. This combined approach achieved an impressive spinal fusion success rate of 74.6% [155].

Fred Albee's work in 1911 further developed Hibbs' spinal fusion technique. Bone was harvested from the patients' tibiae and placed between the segments of the spinous processes, secured in position with sutures [156]. Albee also advanced surgical techniques by creating various surgical tools for spine surgery, including the Albee Bone Mill, which reduced the time required for harvesting bone for autografts [157].

Advancements continued with Ralph Cloward, who introduced modifications to Hibbs' approach in response to high rates of spinal fusion failure and pseudoarthrosis. Cloward performed a partial laminectomy to remove the degenerated disc, followed by the implantation of allogeneic bone grafts obtained from a tissue bank into the evacuated intervertebral space. The allografts were shaped into wedges to fit the interbody gap and secured in place using gelatine foam [158, 159].

In 1932, Mixter and Barr performed the first intentional discectomy, a procedure that laid the foundation for future spinal fusion techniques, which is still in use today [160].

`

### Spinal Fusion with Instrumentation

The evolution of instrumentation to complement spinal fusion began with Jules Guerin, who, in 1839, was the first to attempt surgical correction in patients with scoliosis using braces; however, this technique demonstrated only partial success, as frequent revisions were necessary [161].

In 1891, Hadra became the first to successfully stabilise cervical vertebrae in a patient experiencing progressive neurological decline due to a cervical spine fracture using wires [162]. Later, similar wires were employed by German surgeon Dr Fritz Lange in 1909, who conducted the first spinal fusion surgeries for scoliosis [163].

A significant milestone in the surgical treatment of spinal conditions was achieved in 1962 with the development of the Harrington rod by Paul Harrington. This was the first technique to provide effective treatment for scoliosis, utilising a concave-distraction method with rods and hooks that offered rigidity and support for spinal fusion. However, it also resulted in flattening of the spine in the sagittal and coronal planes [164].

Later advancements introduced pedicle screws, further enhancing the stability and effectiveness of spinal fusion procedures [165, 166].

The first spinal fusion device was reported by Wagner et al., designed by co-author Bagby, and was used for the treatment of cervical vertebral malformation in horses via cervical fusion [167]. This device and Bagby's proposal to utilise it with bone autografts in human spinal procedures marked a significant milestone in the field [168]. Alongside Stephen Kuslich, Bagby pioneered the Bagby-Kuslich method for lumbar interbody fusion, demonstrating promising outcomes in clinical trials [169]. This innovative device was subsequently patented by Bagby [170].

## 1.1.6. Bone Grafts and Substitutes in Spinal Fusion Surgery

### Bone Graft/Substitute Requirements

The material requirements depend on the intended application. Generally, bone grafts and their substitutes are expected to provide structural support and/or facilitate bone formation. These characteristics can be categorised as osteoinductive, osteoconductive, and osteogenic, described as follows [171-175]:

- **Osteoconductive materials**: Provide a passive porous scaffold to support or direct bone formation through cell ingrowth, facilitate vascularisation, and provide a network for cell attachment.

`

- **Osteoinductive materials**: Induce recruitment and differentiation of stem cells into osteogenic cells through the provision of signals.
- **Osteogenic materials**: Supply viable cells stem cells with osteogenic potential, which directly lay down new bone.

Various types of grafts and substitutes exhibit these characteristics to varying degrees, making these attributes important considerations in the selection of a suitable graft or substitute. Table 3 provides an overview of different bone grafts and their properties based on their source, location, and preparation.

*Table 3 Different properties of autografts and allograft.*

| Bone Graft | Structural Strength | Osteoconduction | Osteoinduction | Osteogenesis |
|---|---|---|---|---|
| **Autograft** | | | | |
| *Cancellous* | - | +++ | +++ | +++ |
| *Cortical* | +++ | ++ | ++ | ++ |
| *BMA* | - | ± | + | ++ |
| **Allograft** | | | | |
| *Cancellous* | | | | |
| Frozen | - | ++ | + | - |
| Freeze-Dry | - | ++ | + | - |
| *Cortical* | | | | |
| Frozen | +++ | + | - | - |
| Freeze-Dry | + | + | - | - |
| *DBM* | - | + | ++ | - |

To optimise clinical application, the ideal bone graft or substitute should possess osteoconductive, osteoinductive, and osteogenic properties. However, autografts are currently the only option exhibiting all three properties [175, 176]. Most bone graft substitutes provide only osteoconduction. Consequently, the addition of growth factors is critical for imparting osteoinduction. Similarly, the inclusion of cellular components such as bone marrow aspirate (BMA) enables osteogenesis [174].

## Definitions, Advantages and Disadvantages

Bone grafts and substitutes can be derived from autologous, allogeneic, and xenogeneic sources (see Figure 13). Each source presents specific advantages and disadvantages, which will be discussed in detail.

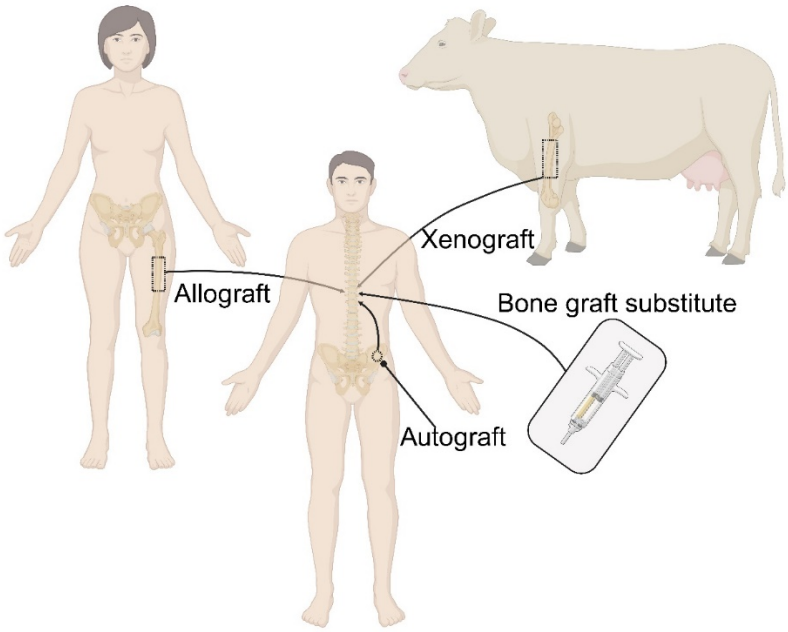


*Figure 13 Sources of materials for bone grafting. Image created on www.biorender.com.*

## Bone Grafts

Bone grafts play a crucial role in orthopaedic procedures by providing structural support and promoting new bone formation. Cancellous bone, recognised for its high osteogenic potential, significantly contributes to this process, whereas cortical bone has a comparatively lower osteogenic capacity while offering greater strength. These grafts serve as scaffolds and gradually undergo replacement through creeping substitution [13, 14]. Unlike cortical bone, cancellous bone undergoes faster revascularisation [14]. Bone grafts are commonly used in various formats, including bone chips, powder, pastes, or putties [13, 14, 18, 177, 178].

### Autografts

Autografts, sourced from the patient's own body, are considered the "gold standard" in orthopaedic applications. Although their availability is limited, they offer osteoinductive, osteoconductive, and osteogenic properties. Common harvest sites include the tibia, fibula, and ilium [13].

Despite their proven efficacy, autografts present certain limitations. Their success is influenced by patient age, health status, graft harvesting techniques, and donor site selection. Additionally, complications such as haematoma, pain, and infections can arise at the donor site [15, 16]. A retrospective cohort study of nearly 14,000 spinal fusion patients treated between 2010 and 2012 compared outcomes between those receiving iliac crest bone grafts (ICBG) and those who did not. The findings showed that patients with ICBG experienced higher transfusion rates, longer operation times, and extended hospital stays, although adverse event rates were similar across both groups [179]. Despite its drawbacks, the iliac

`

crest remains the primary source for autografts in spinal fusion, with a recent study reporting higher MSC concentrations in the anterior iliac crest than the distal tibia and calcaneus [180, 181]. Table 4 provides an overview of commonly used autograft harvest sites, highlighting their advantages and disadvantages.

*Table 4 Commonly used harvest sites for autologous bone grafts with their advantages and disadvantages. From [182].*

| Source | Advantages | Disadvantages |
|---|---|---|
| Iliac crest | Large bone volume, rich source of progenitor cells and growth factors, easy access, providing both cancellous and cortical bones | Nerve, arterial, and urethral injury, increased blood loss, haematoma, infection, chronic post-operative donor site pain, high patient morbidity, high recovery time, large scar, hip subluxation, pelvic fractures, costly, local infection |
| Distal radius | Lower bone turnover than iliac crest, lower post-operative pain than the iliac crest, easy to harvest, small incision is needed | Superficial radial nerve injury, fracture, infection |
| Tibia | Easy to access, less operative time, and less gait disturbance than the iliac crest | Fracture risk, less bone volume than iliac crest, infection |

Another form of autograft is autologous bone marrow aspirate (BMA), commonly harvested from the iliac crest but also obtainable from other anatomical sites, including the sternum, posterior ilium, anterior ilium, or vertebral body [176, 183-186]. BMA can be directly injected or implanted at sites requiring bone formation [185] and contains a heterogeneous mixture of cells, including haematopoietic and mesenchymal lineage cells, white and red blood cells, platelets, endothelial cells, adipocytes, fibroblasts, osteoblasts, osteoclasts, and MSCs [176, 184-186]. However, BMA has limitations, particularly its relatively low stem cell content, which is further reduced in older individuals. To increase stem cell concentration, BMA can be processed by centrifugation to generate bone marrow aspirate concentrate (BMAC), which shows a five-fold increase in MSC concentration compared to unprocessed BMA, though the final cell yield depends on patient factors and technique [176, 185, 186]. Despite this, the low progenitor cell count in BMAC suggests its contribution to bone healing is likely due to growth factor release rather than direct engraftment [29, 186]. Additionally, BMA lacks structural support and must be combined with a carrier such as ceramic or allograft to facilitate effective integration [29, 183]. Furthermore, BMA tends to disperse from the graft site, which can be mitigated by incorporating it into demineralised bone (DMB) matrix to improve retention and efficacy [29, 176, 185].

`

Allografts

Allografts, derived from donor bone, offer a viable alternative to address the limitations associated with autografts, particularly in situations where autografts are inadequate or unsuitable, such as in paediatric or high-risk patients [13, 17]. The growing demand for allografts prompted Bush and Garber to explore various methods for preserving bone tissue, leading to the establishment of the first tissue bank in 1949 [187, 188]. Since then, allograft distribution has been facilitated through regional tissue banks, ensuring procurement, sterile processing, and donor screening to minimise disease transmission risks. However, complete elimination of such risks remains challenging [18]. Bone can be stored and sterilised in several forms. It can be harvested in a clean, nonsterile environment, sterilised by irradiation, strong acid, or ethylene oxide, and freeze-dried for storage. Under sterile conditions, bone can be deep-frozen for preservation at temperatures ranging from −70°C to −80°C. Fresh-frozen allografts retain strength better, while freeze-dried allografts offer longer storage convenience [13].

Allografts are commonly harvested from deceased donors and are routinely harvested during total hip arthroplasty from the femoral heads and the proximal metaphyseal region of the femur from living donors [189]. These allografts can be utilised alone or supplemented with small amounts of autologous bone to enhance osteogenesis [13].

Despite the benefits of allografts, including their availability in various sizes and forms, the avoidance of donor-site morbidity, and the preservation of host structures, a clinical study has shown significantly lower success rates in lumbar fusion procedures with allografts than autografts, whether used alone or in combination [18].

Demineralised bone matrix (DBM) constitutes a demineralised form of allograft bone. It is derived from cadaveric or live donor bone, similar to standard bone allografts. Following initial sterilisation, allograft bone undergoes demineralisation, typically via hydrochloric acid, to remove the inorganic mineral content. This leaves behind a collagenous matrix scaffold composed primarily of type I collagen (with minor type IV and X collagen) as well as small amounts of calcium, cellular debris, and non-collagenous proteins such as BMPs. DBM offers an osteoconductive collagen scaffold and osteoinductive potential through growth factors such as BMPs [19, 20, 171]. Commercially available DBM is found in various forms, including injectable pastes, sheets, and mouldable putties, often enhanced with carriers to improve handling and retention at the surgical site [19, 20]. Its advantages include avoiding donor site morbidity from autograft harvesting and its ready availability in different forms, with minimal risk of disease transmission due to extensive processing [19, 20, 171].

However, allografts are not without limitations. Allografts, including DBM, carry a risk of disease transmission, as evidenced by documented cases of transmission through donor sources [190]. Moreover, the absence of antigenic matching can provoke a dose-dependent

immune response, leading to delays in vascularisation and the activities of osteoblasts and osteoclasts [27]. Additionally, DBM lacks inherent structural integrity and mechanical strength, and its osteoinductive potential is highly variable [19, 20, 191, 192]. Studies have shown that osteoinductivity is dose-dependent and influenced by residual calcium content, particle size, and donor age [191, 192]. BMP levels also vary between DBM batches and manufacturers, contributing to variability in osteoinductive potential [193].

Xenografts

Xenograft bone grafts involve the transplantation of bone tissue across different species, commonly from animals to humans. They offer advantages including a virtually unlimited supply, controlled donor biology, absence of donor site morbidity, and cost-effectiveness compared to human-derived allografts [194-196]. However, xenografts have several disadvantages. Similar to allografts, they lack osteoinductive properties and predominantly possess osteoconductive properties. Additionally, there is a risk of potential zoonotic disease transmission due to inherent immunogenicity resulting from species differences. The immune response is triggered by the alpha-Gal epitope present in animal cells but absent in humans, leading to high graft rejection rates, poor integration with host bone, and often necessitating revision surgery [194-197].

To mitigate immune reaction and disease transmission risks, xenografts undergo processing techniques combining alkaline chemical baths and ultra-high temperature treatment around 300°C. This removes organic components and antigens while preserving mechanical strength, porosity, and microarchitecture [194, 195, 198]. Nevertheless, complete eradication of animal antigens remains challenging, and residual organic antigens may provoke inflammatory reactions [194, 198].

Moreover, xenografts can pose challenges for patients whose religious beliefs conflict with certain healthcare procedures. There are also ethical concerns regarding animal welfare [197].

## Bone Graft Substitutes

Interest in bone graft substitutes has spiked in recent years. The risks and shortcomings of autografts and allografts have driven research toward advancements in synthetic replacements.

The primary objective of bone graft substitutes is to either replace or supplement traditional bone grafts, thereby circumventing the limitations of autografts and the risks of allografts [13]. Bone graft substitute biomaterials serve as osteoconductive scaffolds to support bone cell migration and attachment. Additionally, some bone grafts provide osteoinductive signals to stimulate osteoprogenitor differentiation and bone formation [13, 29].

`

Despite these advances, autografts remain the "gold standard" against which substitutes are compared for bone repair applications [13, 27]. Current research focuses on developing an ideal substitute that matches the performance of autografts.

## Biological Mechanisms of Bone Graft/Substitute Incorporation

Graft incorporation, irrespective of its source or structural composition, follows two distinct pathways of intramembranous and endochondral ossification, each characterised by five key stages [14, 175, 182, 199, 200]:

- **Inflammation**: The initial response of the host to a graft/substitute is inflammation, characterised by the recruitment of immune cells and formation of fibrous granulation tissue. This phase typically lasts for 7–14 days.
- **Vascularisation**: Vascularisation follows as vascular buds grow into the graft. Membranous bone tissue forms near decorticated bone, followed by chondrogenesis and endochondral ossification.
- **Osteoinduction**: Osteoinduction is characterised by increased vascularisation and the appearance of differentiated osteoblasts and chondroblasts. New bone forms peripherally on the graft while central resorption continues.
- **Osteoconduction**: Around 4–5 weeks after implantation, osteoconduction begins as host tissue infiltrates into the graft by creeping substitution. Within the fusion mass, a centralised zone of endochondral interface develops. While this phase may persist for several months in cancellous grafts, it can extend for years in cortical grafts. During this stage, the graft serves as a scaffold for the ingrowth of host cells, offering structural support until the host tissue can bear weight.
- **Remodelling**: This phase initiates at 6–10 weeks, as a cortical rim forms on the peripheral layer of the graft alongside increased bone marrow activity and secondary spongiosa. The cortical rim widens, and the spongiosa extends towards the centre until the remodelling process is complete, typically within one year. The mechanical loads to which the graft is exposed substantially influence this phase.

The mechanism of incorporation varies based on graft composition and immunogenicity. Autogenous cancellous bone, characterised by its porous structure and abundance of osteoblasts, undergoes rapid revascularisation and integration. In contrast, dense cortical bone lacks essential endosteal cells, leading to delayed incorporation initiated by osteoclasts through creeping substitution, which can result in prolonged necrosis [176, 185]. While all grafts have an initial inflammatory response, in allografts, a specific lymphocytic reaction follows the initial immune response. This leads to fibrous encapsulation of cancellous

grafts and necrosis of cortical grafts, where the dense structure of cortical grafts further restricts vascularisation. Consequently, allogeneic grafts are incorporated more slowly, relying on appositional bone growth on the necrotic scaffold. Graft incorporation is influenced by various local factors (e.g. stability and vascularity) and systemic factors (e.g. smoking, steroid use, and nutritional status). Overall, autogenous cancellous bone demonstrates the fastest incorporation, followed by cortical, allogeneic cancellous, and cortical grafts [185].

# Historic Evolution

## Bone Grafts

Evidence of bone grafting dates back to the Neolithic era, with findings of defects in frontal bone repaired using a gold plate. The first documented bone grafting was performed by Meekeren in 1668, who repaired a skull defect in a soldier with a dog bone. However, the graft had to be removed due to protests from the church [201].

Philips von Walter performed the first recorded autograft in 1820, who reported transferring autologous bone from the femur to a patient's skull in a case study. The term "bone graft" was first documented by Leopold Ollier in 1861 in his publication, “Traité de la régénération des os” [202].

In 1879, William Macewen performed the first human allograft transfer, reconstructing the right humerus of a boy with fragments of donor tibia [203].

DBM was first utilised in 1889 when Senn employed DBM derived from bovine tibiae to repair cranial and long bone defects in human patients [204]. Later in 1961, John Sharrad used decalcified autologous bone for spinal fusion in three children with scoliosis in Sheffield, demonstrating successful fusion [205].

In 1892, Dreesmann performed the first successful synthetic bone graft using gypsum (calcium sulphate) to fill bone defects in patients in Germany [206].

Since these early advances, there has been growing interest in the use of autografts, allografts, and synthetic alternatives to promote bone healing and fusion, particularly in spinal surgery, where adequate bone fusion is critical for clinical success.

As previously mentioned, Hibbs pioneered the use of bone grafts in spinal fusion in 1911 and was the first to use autografts harvested from the spinous processes [153].

A few years later, Cloward successfully introduced fresh bone allografts from a tissue bank for spinal fusion surgery [158, 159], followed by Sharrad's use of DBM [205].

While there are no reported uses of complete xenografts for spinal fusion, one study analysed the application of bovine-derived apatite (Orthoss®) in 27 patients undergoing spinal fusion procedures, achieving a successful fusion rate of 85% [207].

`

## Bone Morphogenic Protein

A significant leap in bone graft substitutes was marked by Marshall Urist's landmark paper, where he described bone formation by autoinduction. Urist's observation that decalcified bone stimulated new bone growth when implanted into non-bony sites in rats revolutionised the understanding of osteogenesis [208]. This discovery led to the knowledge that BMP in bone matrix plays a crucial role in promoting bone formation [209]. Shortly after, BMP could be firstly cloned [210], resulting in a surge in their application for orthopaedic purposes, including routine use in spinal fusion procedures [211-217].

In 2002, recombinant human BMP-2 (rhBMP-2) was approved for use in lumbar spinal fusion by both the Food and Drug Administration (FDA) in the USA and the European Medicines Agency (EMA) in Europe [218, 219]. However, safety concerns emerged due to serious complications associated with BMP use in spinal fusion [21]. Reports indicated that rhBMP-2 use in lumbar interbody fusion resulted in vertebral bone resorption in 69% of patients [23]. Additionally, there was a six-fold increased risk of retrograde ejaculation following anterior lumbar interbody fusion with BMP-2 [22]. Other complications were related to the off-label usage of BMP-2 in anterior cervical spine fusion included cervical swelling, wound healing issues, dysphagia or hoarseness, epidural haematoma, seroma, and ectopic bone formation [23-26]. In response to these complications, the FDA issued a warning in 2008 regarding the off-label use of BMP-2 in the cervical spine [220].

## Calcium Phosphates

Calcium phosphates were first introduced as bone graft substitutes by Shima et al. in 1979, who employed tricalcium phosphate for cervical fusion. However, the results were suboptimal, leading to the conclusion that it was biochemically and biomechanically unsuitable for this purpose, although it paved the way for further research in this area [221]. Later, in 1984, Cook et al. evaluated HAP as a graft material for spinal fusion in canines [222], followed by Koyama and Handa's clinical application of HAP spacers for anterior cervical spine fusion in 1986 [223]. These advancements have broadened the options for spinal fusion procedures. Since its initial use in spinal fusion, HAP has frequently been employed as a bone graft substitute in clinical settings, yielding positive outcomes. In a clinical study, a mixture of nanocrystalline HAP, autograft bone and BMA was used as filler in an interbody fusion device for lumbar fusion, demonstrating excellent outcomes comparable to those achieved with autograft bone alone [224]. In another study, a hydroxyapatite-beta-tricalcium phosphate filler was used in lumbar fusion and compared to an autograft control. The results indicated a 100% fusion rate in all patients, with no significant difference between the synthetic filler and autografts [225]. Figure 14 provides an overview of significant historical milestones in the development of spinal fusion and the use of bone graft substitutes.

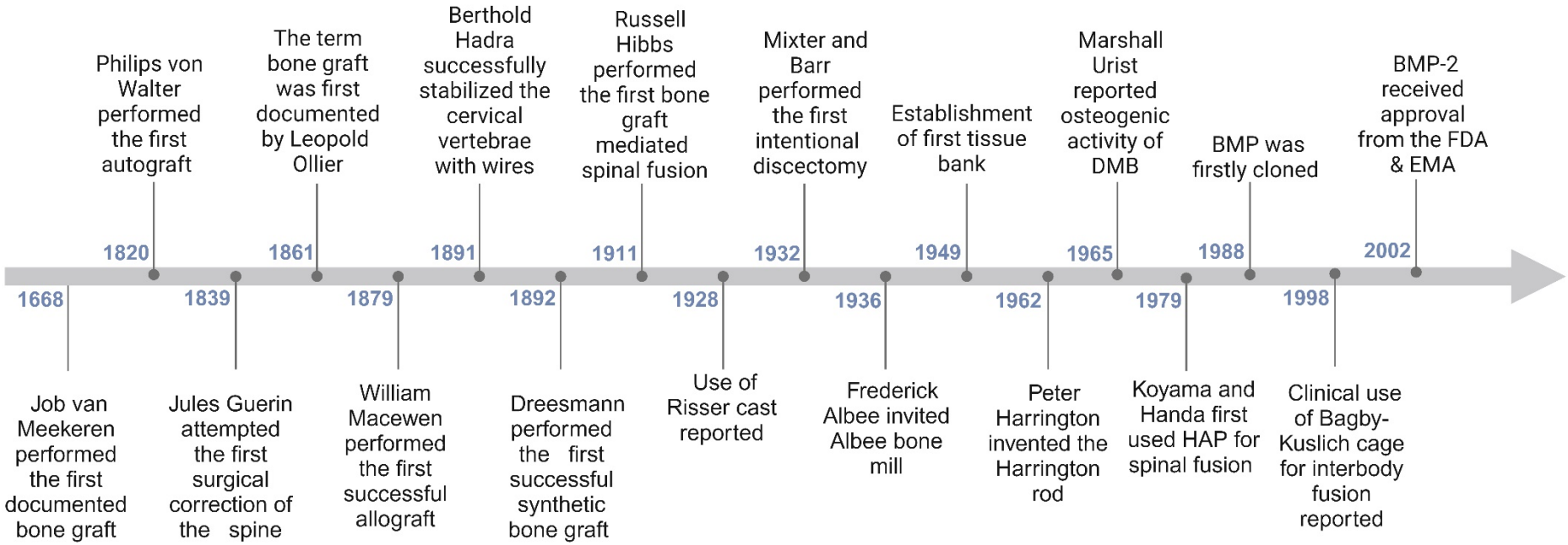


*Figure 14 Historical landmarks in the development and use of bone grafts and substitutes for spinal fusion. Image created on www.biorender.com.*

`

## Choice of Bone Graft/Substitute

Selecting a suitable bone graft or substitute is a critical decision in orthopaedic practice. The ideal graft or substitute should exhibit osteogenic, osteoinductive, and osteoconductive properties [28, 175, 226]. Additionally, substitutes must demonstrate biocompatibility, bioresorbability, structural similarity to natural bone, user-friendliness, and cost-effectiveness [28, 175, 226].

Several factors influence the selection of bone grafts or substitutes, including patient-specific considerations such as autograft availability and physical characteristics such as age and comorbidities [13, 30-32].

Functional requirements also need evaluation, based on the intended use, such as the necessity for void filling, mechanical support, and promotion of bone healing [28, 29, 227]. Moreover, varying success rates across different clinical settings, particularly spinal fusion, highlight the need for context-specific considerations [228-231].

Consequently, the effectiveness of a bone graft substitute in one clinical context may not necessarily apply to a different anatomical site.

In light of these considerations, various commercially available bone graft alternatives exist for orthopaedic applications, differing in composition, mechanism, and attributes. These alternatives may serve as substitutes, completely replacing autografts; extenders, augmenting graft volume and providing structural reinforcement; or enhancers, conferring additional fusion properties such as osteoinductivity. Frequently, these components are combined to optimise the graft's osteogenic, osteoinductive, and osteoconductive potential [29, 232, 233]. Figure 15 presents a schematic overview of a proposed decision-making pathway for selecting bone grafts or their substitutes. It is important to note that this pathway is not a standardised clinical guideline but a conceptual framework based on the current literature and understanding of the field.

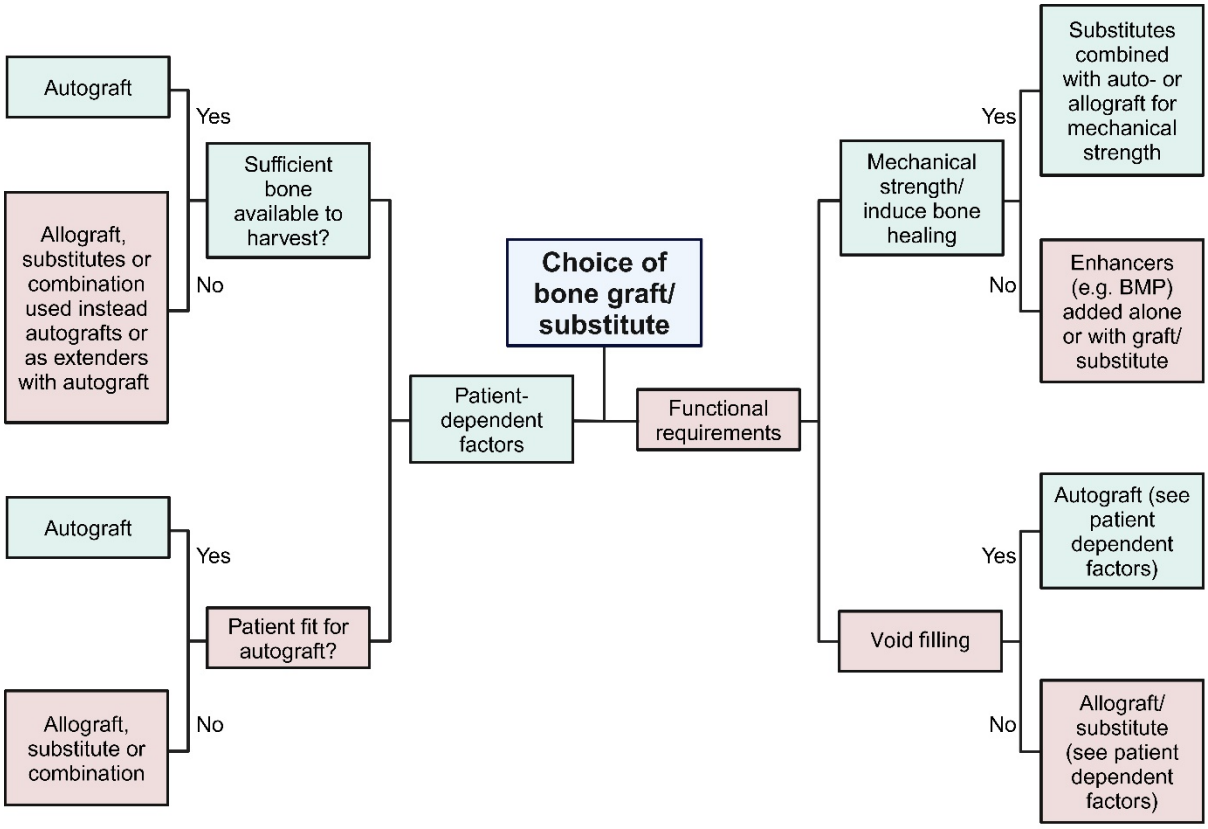


*Figure 15 Decision pathway for the choice of bone grafts vs substitutes as filler for spinal fusion cages. Image created on www.biorender.com.*

## Currently Available Commercial Bone Grafts Substitutes

In the USA, the FDA requires premarket authorisation for medical devices, with specific regulations applying to combination products containing drugs or cells. In contrast, Europe adopts a more streamlined approach, where notified bodies certify devices against European standards without premarket approval. However, similar to the USA, Europe imposes strict authorisation protocols through the EMA for drugs and cell-based products before they can enter the market [234]. Table 5 presents a comprehensive, though not exhaustive, overview of bone graft substitutes currently available in the USA and Europe. These substitutes have been utilised in clinical studies for spinal fusion, and their levels of evidence are classified as I-III according to established guidelines [235]. The listed manufacturers represent present entities, accounting for mergers or acquisitions over time. In most clinical studies, substitutes have been employed alongside autografts, functioning primarily as extenders rather than replacements for ICBG or local autografts (LAG). LAG is harvested from the patient's decompressed laminae, facets, and spinous processes during spinal fusion. It possess similar mechanical and physiological properties to ICBG without necessitating additional surgical procedures. The incorporation of this local bone, routinely obtained during decompression, provides significant benefits with minimal associated costs and morbidity [233, 236, 237].

*Table 5 An overview of commercially available bone grafts/substitutes and their application in clinical studies.*

| Product Information | | | Clinical Studies | | | | | | | | |
|---|---|---|---|---|---|---|---|---|---|---|---|
| **Manufacturer and Product** | **Material** | **Delivery Format** | **Formulation** | **Control/ Comparison** | **Surgery** | **Follow-up [months]** | **Patient Number** | **Outcome** | **Study Design** | **Level of Evidence** | **Ref** |
| Medtronic (Watford, UK Grafton™ | Demineralised bone (fibre/non-fibre) | Matrix, strips, putty, paste, crunch | Grafton™ + ICBG | ICBG | PLF | 24 | 120 | Test ≈ control | Prospective Cohort | II | [228] |
| | | | Grafton™ + local autograft | ICBG | PLF | 24 | 108 | Test ≈ control | Retrospective cohort | III | [238] |
| | | | Grafton™ + allograft | ICBG | Anterior cervical fusion | 18 | 77 | Test (less fusion and graft collapse) < control | Prospective cohort | II | [229] |
| | | | Grafton™ + BMA + local autograft or Grafton + ICBG | ICBG | PLF | 24 | 73 | Test ≈ control | Prospective cohort | II | [239] |
| | | | Grafton ™+ local autograft | ICBG | PLF | 24 | 46 | Test ≈ control | Prospective randomised | I | [240] |
| Stryker (Newbury, UK Vitoss® | β-tricalcium phosphate | Foam, morsels, blocks | Vitoss® + local autograft | ICBG | Posterior scoliosis correction and fusion | 48 | 40 | Test ≈ control | Prospective randomised | I | [241] |
| Wright Medical Technology (Pulford, UK OsteoSet™ | Calcium sulphate | Pellets, beads | OsteoSet™ + BMA and ICBG intra-patient control | Local autograft + BMA and ICBG intra-patient control | PLF | 24 | 43 | Test (less fusion) < control | Prospective randomised | I | [242] |
| | | | OsteoSet™ + local autograft | ICBG | PLF or posterior sacral fusion | 12 | 40 | Test ≈ control | Prospective randomised | I | [243] |
| | | | OsteoSet™ + local autograft | ICBG | PLF | 33 | 74 | Test ≈ control | Prospective case-control | III | [244] |

`

| | | | | | | | | | | |
|---|---|---|---|---|---|---|---|---|---|---|
| NuVasive Inc., (San Diego, California, USA) AttraX® putty | Biphasic calcium-phosphate | Putty | AttraX® putty | ICBG | XLIF | 2 | 45 | Test ≈ control | Prospective, randomised | I | [245] |
| | | | AttraX® putty | ICBG + local autograft | Thoracolumbar PLF | 2 | 100 | Test ≈ control | Case-control | III | [246] |
| Cerapedics Inc., (Westminster, Colorado, USA) i-Factor™ | P-15 osteogenic cell-binding peptide, bound to an inorganic bone mineral | Putty | i-Factor™ + cortical allograft ring | Local autograft + cortical allograft ring | Anterior cervical fusion | 2 | 319 | Test ≈ control | Randomised controlled | I | [247] |
| ZimVie (Westminster, Colorado, USA) Pro-Osteon® | HAP | Granules, blocks, wedges | Pro-Osteon® 500R with local autograft and BMA | ICBG | PLF | 1 | 57 | Test ≈ control | Prospective randomised | I | [230] |
| | | | ProOsteon® 200 blocks | ICBG | Anterior cervical fusion | 2 | 29 | Test ≈ control in fusion but more graft collapse in test group | Prospective randomised | I | [231] |
| DePuy (Leeds, UK ViviGen® and DBX® | Cellular allograft (ViviGen®)<br><br>Demineralised bone matrix DBX® | | ViviGen® | DBX® | Anterior cervical fusion | 1 | 53 | ViviGen® ≈ DBX® | Retrospective cohort | III | [248] |

`

## 1.1.7. Calcium Ceramics for Hard Tissue Repair

Ceramics are inorganic, non-metallic materials composed of bonded metallic and non-metallic elements, typically displaying a crystalline structure [249]. Ceramic-based biomaterials are widely used in biomedicine as bone graft substitutes [10, 231, 245, 246, 250-254]. These materials possess several advantageous properties, including biodegradability with composition-dependent degradation rates [255], osteoconductive capabilities, and the ability to promote osteogenic differentiation despite lacking inherent osteoinductive properties [183, 256-261]. Additionally, ceramics are non-immunogenic due to their biological inertness, eliminating the risk of inflammatory immune responses. Their sterilisability ensures biosafety for clinical applications, and their widespread availability further enhances their utility in the medical field [183, 261].

However, ceramics alone demonstrate limited mechanical performance. While they offer high compressive strength, their poor fracture toughness and tensile strength restrict their use, especially in load-bearing regions of the skeleton [183, 261].

Ceramic biomaterials constitute a major portion of the synthetic graft market, representing 60% of available options. These include calcium phosphates, calcium sulphates, and bioactive glasses [262]. Commercially available products frequently feature mixed calcium salts, such as calcium phosphate cements. These mouldable materials, consisting of calcium phosphates and an aqueous curing agent, can be shaped to fit various bone defects [29, 261].

### Calcium Sulphates

Calcium sulphates constitute calcium minerals with incorporated sulphate ions, described by the general chemical formula $CaSO_4$ ($xH_2O$), where x accounts for related hydrates. They exist in three primary polymorphic forms: calcium sulphate anhydrous (CSA) with the formula $CaSO_4$, calcium sulphate dihydrate (CSD) with the formula $CaSO_4$ $2H_2O$, and calcium sulphate hemihydrate (CSH) with the formula $CaSO_4$ ½ $H_2O$. CSH presents in α and β forms, the former requiring less water, forming denser cements [263, 264]. Due to its superior mechanical properties, α CSH is primarily used as a bone void filler. Calcium sulphates are naturally occurring minerals [263]. Plaster of Paris, consisting of CSH synthesised by heating CSD to 160°C, is one commonly used form [264]. As an inexpensive and widely available synthetic bone substitute, calcium sulphate is offered in various forms, including hard pellets or injectable viscous fluids that harden in vivo. A key advantage of calcium sulphate is its ability to fill bone voids percutaneously through liquid application. However, due to its rapid resorption occurring typically within one to three months, which is faster than the natural rate of bone growth, calcium sulphate is unsuitable for spinal fusion applications [29, 183, 261, 265, 266]. It is often combined with other synthetic bone substitutes

and growth factors to enhance performance. Additionally, calcium sulphate shows potential for loading with antibiotics to treat osteomyelitis caused by multidrug-resistant bacteria [265].

## Calcium Phosphates

Calcium phosphates represent a class of calcium salt compounds characterised by varying ratios of calcium ions and phosphate groups. They form the primary inorganic component of mammalian skeletal structures, including bones and teeth [29, 267]. Their properties depend on their composition and crystal lattice structure [265].

Amorphous calcium phosphate (ACP) consists of hydrated calcium phosphate salts with minimal or no three-dimensional order, typically represented by the formula $Ca_3(PO_4)_2\ xH_2O$, where x indicates hydration level [267-270]. The Ca/P ratio of ACP ranges from 1.18 to 2.50, influenced by environmental factors such as temperature, pH, and ion concentration [269, 271, 272]. ACP is believed to be a precursor to HAP and maintains stable concentrations in vivo under physiological conditions [273, 274]. Synthetically, ACP forms transiently during apatite precipitation and can be converted to apatite through hydrolysis [268, 275, 276]. Due to its high instability, ACP rapidly transforms into HAP upon contact with aqueous solutions [277-279]. Its high solubility promotes utility in coatings and self-setting cement [267, 272].

Dicalcium phosphates (DCP), with the general formula $CaHPO_4\ (xH_2O)$, are calcium hydroxide-neutralised phosphoric acids with a Ca/P ratio of 1. They encompass dicalcium phosphate dihydrate (DCPD), with the formula $CaHPO_4\ 2H_2O$, known as brushite, and dicalcium phosphate anhydrous (DCPA) with the formula $CaHPO_4$, known as monetite [264, 267, 268, 277]. Brushite is found exclusively in pathological calcifications, whereas monetite is rare in biological systems [268, 277, 280]. DCPs can serve as intermediates in apatite formation at lower pH levels, undergoing hydrolysis to HAP [267, 268, 281-284].

Despite their utility in self-setting bone repair cement, DCPs have limited clinical application due to their short setting time, poor injectability, rapid biodegradation, and weaker mechanical properties [267, 285].

Tricalcium phosphate (TCP), with the formula $Ca_3(PO_4)_2$ and a Ca/P ratio of 1.5, exists in α or β form depending on its structural organisation. Both forms are stable at room temperature, with α-TCP forming when cooled from a molten state above 1125°C and β-TCP forming below 800°C through precipitation, conversion from α-TCP, or heating of calcium-deficient HAP. TCP does not occur naturally in biological systems. Due to its high solubility, TCP is frequently used in bone graft substitutes, cements, and coatings, particularly where rapid resorption is advantageous. Combining TCP with HAP as biphasic calcium phosphate allows modulation of its biodegradation rate [261, 267, 268, 280]. After implantation, TCP partially converts to HAP, which slows its degradation. β-TCP has a more porous structure but weaker mechanical properties than HAP [265].

`

Octacalcium phosphate (OCP), with the formula $Ca_8(HPO_4)\ 2(PO_4)_4\ 5H_2O$ and a Ca/P ratio of 1.33, is a hydrated calcium phosphate with alternating apatitic and hydrated layers. OCP often forms as an unstable transient intermediate from DCPD during HAP precipitation at low pH and can be hydrolysed into HAP. It is involved in physiological processes as a precursor to biological apatite and is found in pathological calcifications. OCP is utilised in cement and composites to enhance bioactivity [264, 267-270, 277, 280, 286, 287].

HAP holds paramount importance among calcium phosphates owing to its significant biological role. Synthesised stoichiometric HAP differs from biological HAP, the latter being calcium deficient and referred to as calcium-deficient HAP (CDHAP). HAP constitutes the most stable calcium phosphate, with the slowest degradation rate at pH levels above four. It is commonly used in bone grafts, implant coatings, and cement, particularly when long-term stability is required [261, 267-269, 278, 280]. Although primarily osteoconductive, HAP exhibits osteogenic differentiation capability [288, 289], mediated by surface topography-induced autophagy through mTOR signalling [290]. A more detailed description of HAP characteristics is provided in the next section.

The properties of these materials vary significantly with environmental conditions. Table 6 summarises the Ca/P ratios of the aforementioned calcium phosphates.

*Table 6 Chemical formulas and Ca/P ratios of different calcium phosphate compounds.*

| **Compound** | **Abbreviation** | **Chemical Formula** | **Ca/P Molar Ratio** |
|---|---|---|---|
| Amorphous calcium phosphates | ACP | $Ca_3\ (PO_4)_2\ xH_2O,\ x = 3–4.5;$ 15–20% $H_2O$ | 1.18–2.50 |
| Dicalcium phosphate dehydrate (brushite) | DCPD | $CaHPO_4\ 2H_2O$ | 1.0 |
| Dicalcium phosphate anhydrous (monetite) | DCPA | $CaHPO_4$ | 1.0 |
| Octacalcium phosphate | OCP | $Ca_8(HPO_4)_2\ (PO_4)_4\ 5H_2O$ | 1.33 |
| α and β-Tricalcium phosphate | α/ β -TCP | $Ca_3(PO_4)_2$ | 1.5 |
| Calcium-deficient hydroxyapatite | CDHAP | $Ca_{10-x}(HPO_4)_x(PO_4)_{6-x}(OH)_{2-x}$ $(0 < x < 1)$ | 1.5–1.67 |
| Hydroxyapatite | HAP | $Ca_{10}(PO_{4)6}(OH)_2$ | 1.67 |

The solubility order of these calcium ceramics is as follows: DCPD > DCPA > ACP > α-TCP > β-TCP > CDHAP > OCP > HAP [280, 291].

Each material confers distinct strengths, with the optimal calcium ceramic selection dependent on the intended application and desired attributes. A recent systematic review on ceramic materials employed as cage fillers in spinal fusion surgeries of 1332 patients found ceramics demonstrated an overall 86.4% lumbar spine fusion rate, suggesting ceramic-based scaffolds as an effective bone graft extender for spinal fusion [292].

`

## 1.1.8. Hydroxyapatite

### Stoichiometric Hydroxyapatite

HAP is the most common calcium phosphate with a stoichiometric apatite phase. The International Union of Pure and Applied Chemistry (IUPAC) name is pentacalcium hydroxide tris(orthophosphate). It possesses a Ca/P molar ratio of 1.67, which is chemically stable under ambient conditions and pH from 4 to 14. The empirical formula is $Ca_5(PO_4)_3OH$, while the unitary cell formula is $Ca_{10}(PO_4)_6(OH)_2$ [293-296].

HAP is characterised by distinct a-, b- and c-axes with corresponding Miller index lattice planes. Plane a is parallel to the a-axis, also denoted the [100] plane. Plane b is parallel to the b-axis, or [010] plane. Plane c parallels the c-axis, represented by the [001] plane (Figure 16A+B) [297, 298]. The planes possess different charges owing to their composition and atomic organisation. The a/b planes are rich in $Ca^{2+}$ and positively charged, while the c-planes contain more $PO_4^{3-}$ and $OH^-$ and are negatively charged. Consequently, these planes exhibit different properties regarding biocompatibility and degradation [293, 298, 299].

The HAP crystalline matrix comprises unit cells, each containing two subunits and two formula units. Each unit cell is composed of 44 atoms in a complex arrangement (Figure 16C+D) [300]:

Phosphorus is configured in $PO_4^{3-}$ tetrahedral groups with $P^{5+}$ ions at the centre, surrounded by four oxygen atoms at the vertices. The $PO_4$ tetrahedra are linked via shared oxygen atoms [293, 294, 300].

Each unit cell possesses two non-equivalent Ca sites, denoted Ca I and Ca II, based on their location. Ca I sites are in aligned columns, while Ca(II) sites are centred within equilateral triangles situated on the screw axis, constituting the calcium tunnels where $OH^-$ ions are longitudinally arranged parallel to the c-axis. $Ca^{2+}$ ions are coordinated through shared oxygen atoms of the $PO_4^{3-}$ tetrahedra. The calcium tunnels facilitate ion mobility along the columnar axes [294, 299-301].

In Ca I sites, four $Ca^{2+}$ per unit cell are arranged in columns parallel to the c-axis surrounded by nine oxygen atoms belonging to six $PO_4^{3-}$ tetrahedra. In Ca II sites, six $Ca^{2+}$ per cell unit are coordinated to six oxygen atoms belonging to five $PO_4^{3-}$ groups and one $OH^-$ forming two equilateral triangles oriented along the c-axis [294, 299-301].

This structural arrangement may exhibit variations, as studies have identified notable differences between the surface and bulk composition of HAP [302, 303].

Two polymorphic crystal forms have been reported for HAP: (a) hexagonal symmetry with space group P63/m and lattice constants a = b = 9.418 Å, c = 6.881 Å at an interaxial angle γ = 120°; and (b) monoclinic symmetry with space group P21/b and lattice parameters a = 9.4214 Å, b = 2a, c = 6.8814 Å, γ = 120° [293, 294, 299, 300, 304]. Hexagonal HAP is

most common, though monoclinic HAP is more ordered and thermodynamically stable. Both share a 1.67 Ca/P ratio but differ in $OH^-$ orientation. In hexagonal HAP, adjacent $OH^-$ point opposite directions, while monoclinic HAP $OH^-$ have the same direction within a column but opposite directions between columns [269, 293, 300, 304-307]. This orientation induces strain in hexagonal HAP, which can be alleviated by substitutions or vacancies, rendering hexagonal HAP rarely stoichiometric [269, 296]. Common mechanisms include phosphate protonation to $HPO_4^{2-}$ and $OH^-$ removal. The non-stoichiometric formula accounting for bulk $HPO_4^{2-}$ moieties and $OH^-$ vacancies counterbalancing $Ca^{2+}$ deficiency is : $Ca_{10-x}(HPO_4)_x(PO_4)_{6-x}(OH)_{2-x}\ nH_2O$ [302, 308]. Despite structural similarities, the monoclinic and hexagonal forms differ in physicochemical properties, such as dissolution kinetics and diffusion along the OH– columns, due to their structural distinctions [305].

HAP can exhibit various morphologies, such as plate-like or rod-like, with crystals predominantly growing along the c-axis to yield a rod-like morphology (Figure 16A+B) [293, 299, 304].

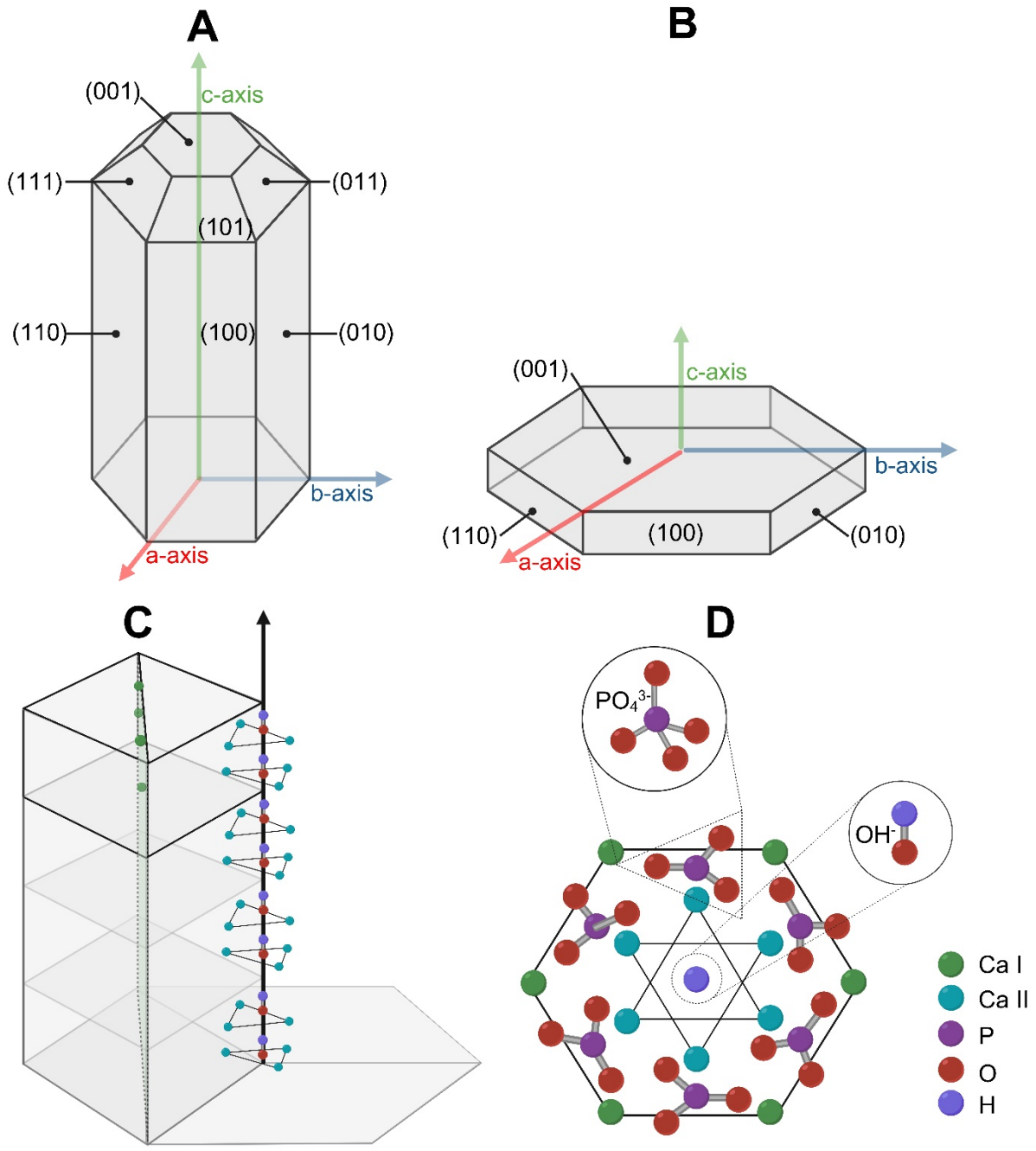


*Figure 16 The structure of HAP. A+B) Different axes and planes. A) Needle-like HAP. B) Plate-like HAP. C) Overview of HAP unit cell structure along the c-axis of HAP. D) Ionic structure of HAP projected and centred along the c-axis. Image created on www.biorender.com.*

`

## Biological Hydroxyapatite

Biological HAP is compositionally distinct from stoichiometric HAP, harbouring various ionic substitutions within the $Ca^{2+}$, $PO_4^{3-}$, and $OH^-$ loci in the lattice or adsorbed on the surface, necessary to maintain homeostatic physiological functions [298, 300, 309-311]. Biological HAP is calcium-deficient, with approximately 20% $Ca^{2+}$ substitution [298, 309, 312]. Ion composition varies with age and tissue type (bone, dentin, and enamel), with their approximate concentrations presented in Table 7 in weight percent (wt%) and parts per million (ppm).

*Table 7 Composition of human enamel, dentine, and bone. Adapted from [310].*

| | Enamel | Dentine | Bone |
|---|---|---|---|
| **Ca (wt%)** | 37.6 | 40.3 | 36.6 |
| **P (wt%)** | 18.3 | 18.6 | 17.1 |
| **CO2 (wt%)** | 3.0 | 4.8 | 4.8 |
| **Na (wt%)** | 0.70 | 0.1 | 1.0 |
| **K (wt%)** | 0.05 | 0.07 | 0.07 |
| **Mg (wt%)** | 0.2 | 1.1 | 0.6 |
| **Sr (wt%)** | 0.03 | 0.04 | 0.05 |
| **Cl (wt%)** | 0.4 | 0.27 | 0.1 |
| **F (wt%)** | 0.01 | 0.07 | 0.1 |
| **Zn (ppm)** | 263 | 173 | 39 |
| **Ba (ppm)** | 125 | 129 | |
| **Fe (ppm)** | 118 | 93 | |
| **Al (ppm)** | 86 | 69 | |
| **Ag (ppm)** | 0.6 | 2 | |
| **Cr (ppm)** | 1 | 2 | 0.33 |
| **Co (ppm)** | 0.1 | 1 | <0.025 |
| **Sb (ppm)** | 1 | 0.7 | |
| **Mn (ppm)** | 0.6 | 0.6 | 0.17 |
| **Au (ppm)** | 0.1 | 0.07 | |
| **Br (ppm** | 34 | 114 | |
| **Si (ppm)** | | | 500 |
| **Ca/Pa** | 1.59 | 1.67 | 1.65 |

Substitutions play important roles in bone metabolism in vivo, induce lattice strain and $OH^-$ vacancies (less than 50% filled), reducing crystallinity and stability while increasing reactivity and osteoclastic resorption compared to synthetic HAP. Vacancies enable $OH^-$ mobility, facilitating crystal restructuring during bone remodelling [300, 312].

These substitutions likely yield hexagonal over monoclinic biological HAP by providing inverted $OH^-$ orientations [305, 313]. In contrast to stoichiometric HAP, biological apatite is hydrated with loosely bound or bridging structural water within the apatite crystal [314].

Biological HAP exhibits different morphologies in vivo due to differences in local environments. Tooth enamel exhibits a predominant uniaxial growth along the preferred c-axis in a hydrophobic milieu without cellular involvement, forming rod-shaped crystals. In contrast, bone HAP grows along the a/b axes, creating plate-like crystals, despite c-axis growth being

`

more favourable, owing to the hydrophilic microenvironment and bone cell-mediated deposition/resorption restricting extensive growth along the c-axis (Figure 16A+B). While bone and dentin HAP particles are nano-sized in all dimensions, enamel crystals are nano-sized in diameter but micro-sized in length [312].

## Substituted Hydroxyapatite

HAP has gained increasing attention in recent years due to the increasing demand for porous bone implants. A growing trend toward partial ionic substitutions in HAP aims to replicate bone mineral composition better while modifying dissolution rates, cell attachment, osseointegration, and biocompatibility [294, 295, 304, 315]. Due to stoichiometric flexibility, the HAP structure can accommodate substitutions of various ions for the $Ca^{2+}$, $PO_4^{3-}$, and $OH^-$ sites without altering its configuration. This allows for a reduction of the Ca/P ratio down to 1.3 while maintaining crystallographic symmetry [294, 295, 300, 312].

Possible substitution ions are listed in Table 8. Cations can replace $Ca^{2+}$, while anions can substitute for $OH^-$ or $PO_4^{3-}$ sites [294, 308]. Substitution can be expressed with the general chemical formula $Me_{10}(XO_4)_6(Y)_2$, where [294]:

- Me represents monovalent, divalent or trivalent cations,
- $XO_4$ denotes tetravalent, trivalent or divalent anions,
- Y denotes monovalent or divalent anions.

*Table 8 Examples of common HAP substitution sites.*

| **$Me^{2+}$** | **$XO_4^{3-}$** | **$Y^-$** | **Ref** |
|---|---|---|---|
| $Mg^{2+}$ | $SiO_4^{3-}$ | $Cl^-$ | [316-318] |
| $Sr^{2+}$ | $SO_4^{3-}$ | $F^-$ | [319-321] |
| $Mn^{2+}$ | $CO_3^{2-}$ | $CO_3^{2-}$ | [322, 323] |
| $Na^+$ | $SeO_3^{2-}$ | | [324, 325] |
| $Zn^{2+}$ | | | [317] |
| $K^+$ | | | [326] |

During substitution, small cations and smaller quantities of larger cations may occupy the Ca I site, whereas large cations typically occupy the Ca II site [308]. Due to the differing valences of the substituent ions, some $OH^-$ group positions may remain vacant to preserve electroneutrality [294, 308].

Substituent incorporation in HAP can occur in three principal locations, each with distinct implications for biological function [327]:

- **Bulk lattice integration:** Substituents incorporated within the HAP crystal structure may have minimal direct impact on osteogenesis but can potentially modulate solubility and exert biological effects upon release during dissolution.
- **Surface localisation**: Substituents on the HAP surface can enhance cellular adhesion and the metabolic activity of adsorbed cells.

`

- **Loose surface association:** Ions loosely bound to the HAP surface may directly influence cellular function through modulation of protein biosynthesis and enzymatic activity.

## Magnesium Substitution

Magnesium is involved in many biological processes. Physiologically, Mg is the main ion substituting for Ca in biological apatite at approximately 1 wt% [328]. Early investigations found that Mg contents are higher during the early stages of mineralisation [329]. Mg deficiency in animal models led to osteopenia, osteoporosis, bone fragility, impaired bone growth during development and lower ossification around bone grafts [330-333]. As a substituent in HAP, it enhances osteogenic potential through miR-16 micro RNA inhibition [334]. Magnesium-substituted hydroxyapatite (MgHAP), marketed as SINTlife® by Finceramica, is commercially available [335]. Recent studies on spinal fusion have shown that MgHAP exhibits comparable efficacy to autografts and superior efficacy than DBM-MgHAP in an ovine spinal fusion model [336]. A prospective clinical study employing this bone graft for spinal fusion via TLIF reported fusion rates of 62% after 2–18 months [337]. Numerous research groups have explored the substitution of HAP with Mg in recent years [316, 338-346], with an overview provided in Table 9.

`

*Table 9 Overview of research with MgHAP and their outcomes.*

| Theoretical Mg | Experimental Mg | Chemical and Structural Analysis | In Vitro/In Vivo Analysis | Ref |
|---|---|---|---|---|
| 5 wt%,<br>10 wt% | 1.23 ± 0.01 wt%,<br>2.32 ± 0.25 wt% | Decreased crystallinity with increasing Mg substitution | MgHAP 2.32 ± 0.25 wt% Mg cytotoxic on MG-63 cells but not rat MSCs | [338] |
| 6 mol%,<br>12 mol%,<br>16 mol% | | Decreased crystallinity with Mg substitution<br>Particle agglomeration | Higher MG-63 cell proliferation, alkaline phosphatase (ALP) activity, osteogenic gene expression and serum protein adsorption with MgHAP vs HAP<br>Best performance of 12 and 16% MgHAP | [339] |
| 0.72 wt%<br>1.23 wt%<br>2.46 wt%<br>12.3 wt% | 0.59 wt%<br>1.12 wt%<br>2.12 wt%<br>6.13 wt% | MgHAP nano-rods<br>Decreased crystallinity, increased particle size, hydration and degradation with increasing Mg substitution | MgHAP is non-cytotoxic to endothelial cells and osteoblasts<br>Enhanced cell adhesion with increasing Mg substitution | [340] |
| 5 mol%,<br>10 mol%,<br>15 mol%,<br>20 mol% | | Needle-like MgHAP<br>Decreased crystallinity with increasing Mg substitution | Higher solubility of MgHAP vs HAP in simulated body fluid | [341] |
| 5 mol%,<br>10 mol%,<br>20 mol% | 1.33 mol%,<br>2.48 mol%,<br>4.74 mol%, | Decreased crystallinity and nanoparticle size with increasing Mg substitution | Higher pre-osteoblast cell attachment, osteogenic activity, increased solubility in simulated body fluid of MgHAP vs HAP | [316] |
| 4.8 mol%<br>9.1 mol%<br>16.7 mol%<br>23.1 mol%<br>28.6 mol%<br>33.3 mol%<br>37.5 mol%<br>100 mol% | | Water adsorption<br>Particle agglomeration<br>Decreased crystallinity, increased surface area with increasing Mg substitution<br>28.6 and 33.4 mol% had secondary phases<br>No HAP from 37.5 mol% | | [342] |
| 0.6 wt%<br>1.2 wt%<br>2.4 wt% | 2.4 wt% substitution deviated from the theoretical value | Needle-like MgHAP<br>Decreased crystallinity and particle size with increasing Mg substitution | | [343] |
| 1 mol% | | Agglomeration<br>Pure MgHAP | Antimicrobial efficacy against P. aeruginosa, S. aureus, and C. albicans microbial strains | [344] |
| 1 mol%,<br>3 mol%,<br>5 mol% | | Decreased crystallinity with increasing Mg substitution<br>$OH^-$ and $Ca^{2+}$ deficiency | | [345] |
| 15 mol%,<br>20 mol%,<br>25 mol%,<br>30 mol% | 5.7 mol%,<br>7.5 mol%,<br>13.3 mol%,<br>13.7 mol% | Decreased crystallinity and particle size, increased surface adsorption, hydration and agglomeration with Mg substitution | Higher solubility of 5.7 mol% MgHAP vs HAP in HBSS<br>MgHAP biocompatible in vivo: enhanced osteoconductivity and resorption vs HAP in rabbits | [346] |

## Strontium Substitution

Strontium is physiologically present in bone and is found in higher concentrations in regions with high metabolic turnover [328]. Treating osteoporotic, oestrogen-deficient rats with strontium significantly increased bone density and prevented bone loss [347]. Owing to these properties, oral strontium administration (as chloride, ranelate, or lactate) is utilised in osteoporosis management, as low doses can stimulate bone formation, enhance mineral density, suppress resorption, and ultimately increase bone mass and functionality [348-354]. Nevertheless, severe adverse reactions, including cutaneous toxicity, acute coronary syndrome, and venous thromboembolism, have been associated with strontium ranelate, leading to regulatory restrictions by the EMA [355-358]. As a substituent in HAP, strontium enhances osteogenic potential through activation of the calcium-sensing receptor (CaSR) and its downstream Janus kinase 2 (JAK2)/Signal Transducer and Activator of Transcription 3 (STAT3) signalling pathway [359]. A meta-analysis has indicated that strontium-substituted calcium phosphates improve in vivo performance in animal models of bone repair [360]. Numerous studies have investigated strontium-substituted hydroxyapatite (SrHAP) [319, 361-369], of which a summary is provided in Table 10.

`

*Table 10 Overview of research with SrHAP and their outcomes.*

| Theoretical Sr | Experimental Sr | Chemical and Structural Analysis | In Vitro/In Vivo Analysis | Ref |
|---|---|---|---|---|
| 0.19 Sr/Ca ratio | 0.13 Sr/Ca ratio of | 1.66 (Sr + Ca)/P ratio<br>Higher crystallinity of SrHAP vs HAP | Higher solubility of SrHAP vs HAP in HBSS | [361] |
| 0.3 mol%,<br>1.5 mol%,<br>15 mol% | 0.31 mol%,<br>1.57 mol%,<br>15.33 mol% | At 15.33 mol%: Decreased crystallinity, increased particle size with increasing Sr substitution | | [362] |
| 10 mol%,<br>20 mol%,<br>30 mol% | 9.25 mol%,<br>18.94 mol%,<br>29.40 mol% | Fabricated SrHAP polymer drug carrier fibres via electrospinning with 97.21% drug loading efficiency | Increased solubility with Sr substitution<br>2.36%/day drug release | [363] |
| 5 wt%<br>10 wt%<br>with each<br>1.5 wt% Mg<br>0.2 wt% Zn<br>0.2 wt% Si | | Lower particle size increased surface area with increasing Sr substitution | Higher solubility of SrHAP vs HAP | [364] |
| 5 wt%,<br>10 wt% | 3.3 wt%,<br>7.1 wt% | Lower crystallinity, increased zeta potential with increasing Sr substitution<br>Sr 5 wt% = rod shape,<br>10 wt% = needle shape | Non-cytotoxic to fibroblasts<br>Higher solubility with increasing Sr substitution<br>10 wt% best antimicrobial properties against E. coli and S. aureus | [365] |
| 0.78 wt%,<br>2.07 wt%,<br>4.09 wt%, | 0.56 ± 0.06 wt%,<br>1.41 ± 0.14 wt%,<br>3.10 ± 0.30 wt% | Rod-like shape<br>Lower particle size and crystallinity with increasing Sr substitution | Increased osteoblast differentiation vs HAP | [366] |
| 1 mol%,<br>5 mol%,<br>10 mol% | 1.8 mol%,<br>6.2 mol%,<br>11.0 mol% | Lower HAP phase and increased ACP with increasing Sr substitution<br>Higher solubility of 5% SrHAP compared to HAP only | Higher solubility for 5% SrHAP vs HAP<br>Higher kidney cell viability with 1 mol% SrHAP vs HAP and 5% SrHAP | [367] |
| 3 mol%,<br>5 mol%,<br>10 mol%,<br>20 mol%,<br>30 mol%,<br>50 mol%,<br>70 mol%,<br>90 mol%,<br>100 mol% | 1 mol%<br>3 mol%,<br>7 mol%,<br>18 mol%,<br>27 mol%,<br>49 mol%,<br>71 mol%,<br>93 mol%,<br>100 mol% | Elongated crystal morphology, decreased surface area with increasing Sr substitution<br>Increasing Sr substitution → more Ca II incorporation<br>Decreased crystallinity at lower Sr substitution vs HAP, increased again with higher substitution | | [368] |
| 5 mol%,<br>10 mol%,<br>20 mol% | | | Enhanced osteogenic and angiogenic activity of MSCs and human umbilical vein endothelial cells with SrHAP vs control and HAP | [369] |
| 50 mol%<br>100 mol% | 30 ± 1 mol%<br>63 ± 1 mol% | Needle-shaped<br>Decreased crystallinity and particle size for 50% Sr vs HAP | Non-cytotoxic to pre-osteoblasts<br>Higher solubility of 50% SrHAP compared to HAP only | [319] |

`

## Magnesium and Strontium Co-Substitution

The incorporation of Mg into HAP is limited, as Mg only partially substitutes for Ca in the crystal lattice and destabilises the HAP structure, resulting in the formation of secondary phases [370, 371]. Sr substitution in HAP has achieved higher incorporation rates than Mg [371, 372]. Lima et al. [372] demonstrated the difficulty of Mg incorporation into the HAP crystal lattice due to the discrepancy in ionic radius between $Mg^{2+}$ and $Ca^{2+}$. Only approximately 10% of the target Mg amount was substituted, while approximately 25% of the target Sr was incorporated. Although both MgHAP and SrHAP increased HAP solubility, MgHAP elicited a greater effect. While MgHAP increased fibroblast density, it also exhibited higher apoptosis levels than SrHAP [372]. In another study, the co-substitution of Mg and Sr (at the levels: 1% Mg with 9% Sr, 5% Mg with 5% Sr, 1% Mg with 19% Sr, 5% Mg with 15% Sr, and 10% Mg with 10% Sr) decreased HAP crystallinity and increased specific surface area and secondary phases, with Mg causing a greater effect. Additionally, sole Mg substitution led to a higher prevalence of secondary phases [370]. Geng et al. synthesised Sr/Mg co-substituted HAP (at 5%, 10%, 20% and 25%, respectively) and found that crystallinity significantly decreased with increasing overall degree of substitution, especially at higher $Mg^{2+}$ concentrations. However, the incorporation of Sr counterbalanced the effects of Mg to a small extent, slightly increasing crystallinity compared to MgHAP alone. Mg incorporation destabilised the HAP lattice parameters and decreased thermal stability, likely by adsorbing to crystal surfaces and inhibiting growth along the c-axis. In contrast, $Sr^{2+}$ ions demonstrated complete substitution for $Ca^{2+}$ ions in the HAP lattice. $Mg^{2+}$ ions only partially substitute for $Ca^{2+}$ due to the difference in ionic radii. In vitro, biocompatibility assays demonstrated favourable cell viability and the highest osteogenic activity for HAP co-substituted with 10% $Mg^{2+}$ and 20% $Sr^{2+}$ compared to other substitution levels investigated. [373].

Landi et al. synthesised HAP co-substituted with Mg and Sr as a prospective bone graft substitute material. The release of $Mg^{2+}$ ions from the HAP matrix was beneficially prolonged by incorporating $Sr^{2+}$. Compared to pure HAP and MgHAP, the co-substituted material exhibited increased osteoblast viability and expression of osteogenic proteins in vitro [374]. Another study demonstrated that 0.5% Mg and 0.5% Sr (among the 0.5 and 1% tested) co-substituted HAP achieved the best crystallinity and cell proliferation among the substitution degrees investigated [375]. Furthermore, Mg/Sr-HAP coatings were found to significantly enhance the corrosion resistance of Ti-6Al-4V alloy surfaces [376].

HAP co-substituted with $Mg^{2+}$ and $Sr^{2+}$ has exhibited favourable biocompatibility and promoted osteogenic differentiation compared to pure HAP in multiple studies [372-374]. Although different groups have worked on substitution for HAP, an optimal substitution degree

for the combined substitution with Mg and Sr suitable as bone graft substitutes has yet to be defined [370-374].

## 1.1.9. Thermodynamic Principles

The crystallisation of HAP initiates with the nucleation of particles in a supersaturated solution, followed by crystal growth. The thermodynamic principles governing these processes will be described in this section.

### Supersaturation

Supersaturation serves as the thermodynamic driving force for both nucleation and growth. It is defined as the concentration of solutes at a specific pressure, temperature, and pH that exceeds the theoretical equilibrium of a solid and its constituent ions. This condition can be represented in several ways. One representation is with the supersaturation σ, described by [377, 378]:

$$\sigma = \frac{\Delta\mu}{kT}$$

where $\Delta\mu$ is the chemical potential difference, $k$ is the Boltzmann constant, and $T$ is the absolute temperature.

An alternative form of representation is with the supersaturation ratio $S$ [378, 379]:

$$S = \frac{IP}{K_{SP}}$$

where $IP$ is the actual ion activity product, and $K_{sp}$ is the solubility product.

When S < 1, the solution is undersaturated; when S = 1, the solution is saturated; and when S > 1, the solution is supersaturated.

The supersaturation ratio is related to the supersaturation via the following equation [378]:

$$\sigma = \ln S$$

Kinetic factors, including temperature and pH, influence the saturation terms. Consequently, the solubility of a solute in a solution varies with changes in these factors, as illustrated by the solubility curves in Figure 17. These curves divide the diagram into the following regions [378]:

- **Undersaturated region:** The solution's concentration is below the equilibrium amount of the solute, allowing for continued dissolution with no possibility of precipitation.
- **Supersaturated region:** The concentration of the solution exceeds the equilibrium amount. This region is divided into two zones: the metastable zone, where precipitation is improbable without seed crystals, and the labile zone, in which spontaneous

precipitation without a seed is possible but not inevitable. The curves separating these zones are referred to as follows [377, 378]:

- **Solubility curve:** Divides the undersaturated and supersaturated region with clearly defined points at S = 1, where the solvent is in equilibrium with the solution.
- **Supersolubility or spinoidal curve:** Separates the metastable and labile zones and is influenced by kinetic factors such as agitation, pH, and temperature.

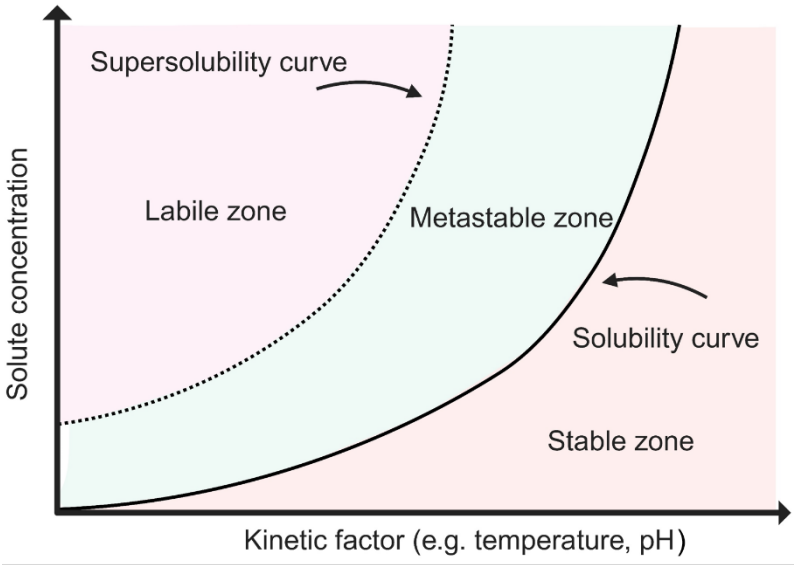


*Figure 17 Solubility and supersolubility curves as functions of solution concentration and kinetic variables. Image created on www.biorender.com.*

## Nucleation

Nucleation, which includes primary, secondary, and homogeneous/non-homogeneous forms, refers to the spontaneous formation of nuclei essential for crystal growth [377, 380].

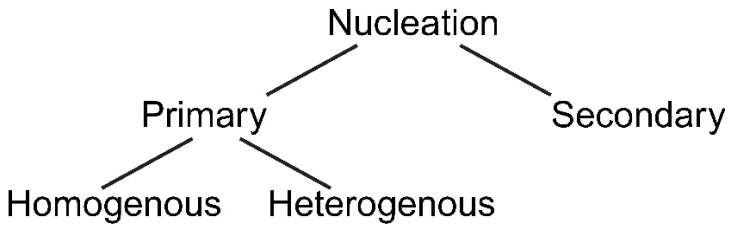


*Figure 18 Overview of different forms of nucleation.*

`

The driving force for nucleation is the difference in Gibbs free energy (ΔG) between the liquid and the solid, determined by enthalpy (ΔH), entropy (ΔS), and temperature (T) with the following equation [381]:

$$\Delta G = \Delta H - T\Delta S$$

A reaction occurs spontaneously when ΔH is negative, and ΔS is positive. If both ΔH and ΔS are negative, spontaneity is observed at low temperatures. Conversely, when both are positive, spontaneity occurs at high temperatures [382].

Alternatively, ΔG can be expressed as the sum of surface free energy ($\Delta G_{SFG}$) and the excess free energy ($\Delta G_{vol}$) by [380, 381]:

$$\Delta G = \Delta G_S + \Delta G_{vol}$$

Assuming that a spherical particle with the radius r is formed, ΔG can be expressed as [380, 381]:

$$\Delta G = 4\pi r^2 \gamma + \frac{4}{3} 3\pi r^3 \Delta G_v$$

where $\gamma$ represents the interfacial tension between the solid surface and the solution, and $\Delta G_v$ denotes the free energy change of the conversion per unit volume.

In a solution with a particle concentration below the supersaturation threshold, collisions form small clusters, which subsequently dissolve due to a kinetic energy barrier. As available energy increases (by increasing supersaturation or temperature), clusters with larger radii form until a stable radius is achieved, allowing them to overcome a critical energy barrier. Nucleation decreases supersaturation, thereby halting the formation of new nuclei and the dissolution of nuclei below the critical size. In the previous equation, the first term represents the energy required for nucleation, while the second term indicates the energy decrease upon nucleation. Consequently, the sum of these energies increases until a maximum is reached and subsequently declines [380, 383]. The critical radius ($r_c$), at which ΔG reaches its maximum, is described by [380, 381, 384]:

$$r_c = -\frac{2\gamma}{\Delta G_v}$$

The corresponding energy at $r_c$, $\Delta Gr_c$ is represented by:

$$\Delta G_{rc} = \frac{\frac{16}{3}\pi \gamma^3}{\Delta G_v^2}$$

Once this energy barrier is crossed, the metastable state, as seen in Figure 17, is reached [385]. The correlation between supersaturation and particle size is described by the Gibbs-Thomson relationship. As supersaturation increases, the free energy curve is lowered due to a reduced entropy of phase transformation, which diminishes the critical radius value beyond which particle stability is achieved. Consequently, $\Delta G_{rc}$ can be expressed as [379, 380, 386, 387]:

$$\Delta G_{rc} = \frac{16\,\pi\,\gamma^3\,v^2}{(k\,T\ln S)^2}$$

where v represents the molecular volume.

## Heterogeneous Nucleation

Nucleation can be influenced by impurities or the reaction vessel, which can aid in the nucleation process by reducing the activation energy but not the critical radius, thereby increasing the nucleation rate. For heterogeneous nucleation, the free energy change in a crucial nucleus ($\Delta G'_{rc}$) is expressed as [380, 381, 388]:

$$\Delta G'_{rc} = \Phi\,\Delta G_{rc}$$

where Φ is a factor dependent on the wettability, θ and described by [380, 389]:

$$\Phi = \frac{(2 + \cos\theta)(1 - \cos\theta)^2}{4}$$

At a wetting angle of θ = 180°, Φ = 1, $\Delta G'_{rc} = \Delta G_{rc}$, therefore nucleation is not influenced by the foreign particle's presence. For wetting angles between θ = 0° and θ = 180°, $\Delta G'_{rc} < \Delta G_{rc}$, suggesting that heterogeneous nucleation is more spontaneous than homogeneous nucleation.

## Secondary Nucleation

Secondary nucleation refers to the initiation of crystallisation, primarily influenced by the presence of existing crystals of the same material, which can lower the energy barrier for nucleation. This phenomenon is characterised by various patterns [377, 380, 383, 388]:

- **Initial or dust breeding**: Small crystallites form on the surface of seed crystals during growth or due to fragmentation, acting as nucleation sites when introduced into the solution. The nucleation rate remains independent of solution supersaturation or stirring rate.
- **Needle or polycrystalline breeding:** High supersaturation leads to the formation of needle-like or dendritic crystals, which fragment in solution to create irregular polycrystalline aggregates that serve as nucleation centres.
- **Contact nucleation (microabrasion):** Microabrasion occurs when crystals collide with contact materials, resulting in surface damage and the generation of secondary nucleation sites.
- **Collision or attrition breeding (macroabrasion**): High stirring speeds cause macroabrasion of crystals, rounding their edges and corners, leading to fragments that function as nucleation sites.

`

- **Impurity concentration gradient nucleation:** Impurities suppress primary nucleation, leading to secondary nucleation when the incorporation of impurities into the growing crystal creates a concentration gradient.
- **Nucleation due to fluid shear:** The boundary layer between the crystal and solution can produce crystal nuclei, which are removed due to fluid shearing.

## Nucleation Theories

Ostwald Rule and Classical Nucleation Theory

Ostwald's rule of stages suggests that the first phase to form is not the most thermodynamically stable but metastable phase. The transition to the thermodynamically stable phase occurs through a series of high-energy intermediate states, eventually reaching equilibrium [390]. Based on macroscopic observations, Ostwald's theory assumed that the appearance of the next stage coincides with the disappearance of the previous stage (Figure 19A, black full line) [391].

Classical nucleation theory later introduced the concept of a critical nucleus size, where growth becomes energetically favourable once this threshold is surpassed. This critical size is determined by the interplay between volume-free energy, which drives growth, and surface-free energy, which inhibits it. The theory assumes that clusters grow through the ordered addition of monomers, aligning with the structure of the bulk crystal. Similar to Ostwald's model, the initial precipitate may not represent the thermodynamically stable phase but the kinetically favoured one, which can later transform into a more stable form. Additionally, multiple metastable phases may form simultaneously rather than in a sequential cascade [392-395].

The growth rate of different phases varies with initial supersaturation. If the growth rates of different phases do not fall within the same order of magnitude, influenced by kinetic factors, the phase composition can be influenced [391].

Non-Classical Nucleation Theory with Pre-Nucleation Clusters

Ostwald's theory holds primarily at lower supersaturation levels, where a limited ion availability leads to fewer nuclei, which can grow sufficiently large to transform into a metastable phase. However, at higher supersaturations, this process is hindered by the simultaneous formation of multiple small nuclei, which are insufficiently developed to resemble a crystalline calcium phosphate structure [396].

Recent studies have identified these initial clusters as calcium triphosphate pre-nucleation clusters, with the chemical formulas $Ca(HPO_4)_3^{4-}$ and $Ca(HPO_4)_2(H_2PO_4)^{3-}$. These clusters incorporate calcium to generate ACP. Pre-nucleation complexes have excess free energy associated with surface ions, which reduces the free-energy barrier for nucleation

[397]. Recent findings indicate that ion pair associations in aqueous environments facilitate pre-nucleation cluster formation, which grow into larger aggregates as more calcium is introduced, overcoming electrostatic repulsion [398].

In contrast to classical pre-critical nuclei, pre-nucleation clusters exhibit greater size and are considered thermodynamically stable, existing in equilibrium with free ions. Upon further calcium addition, these stable pre-nucleation clusters transition into a metastable state, eventually transforming into ACP [399-402].

Crystallisation pathways depend on the free energy of different polymorphs, each with distinct minima. The observation of Ostwald's step rule is likely when the surface energy of the metastable polymorph is significantly smaller than that of the stable phase (Figure 19B, black full line). High supersaturation with respect to multiple polymorphs may yield small free-energy barriers, leading to the simultaneous formation of multiple phases. In such systems, transformations must occur to form single phases (Figure 19B red dotted line) [403].

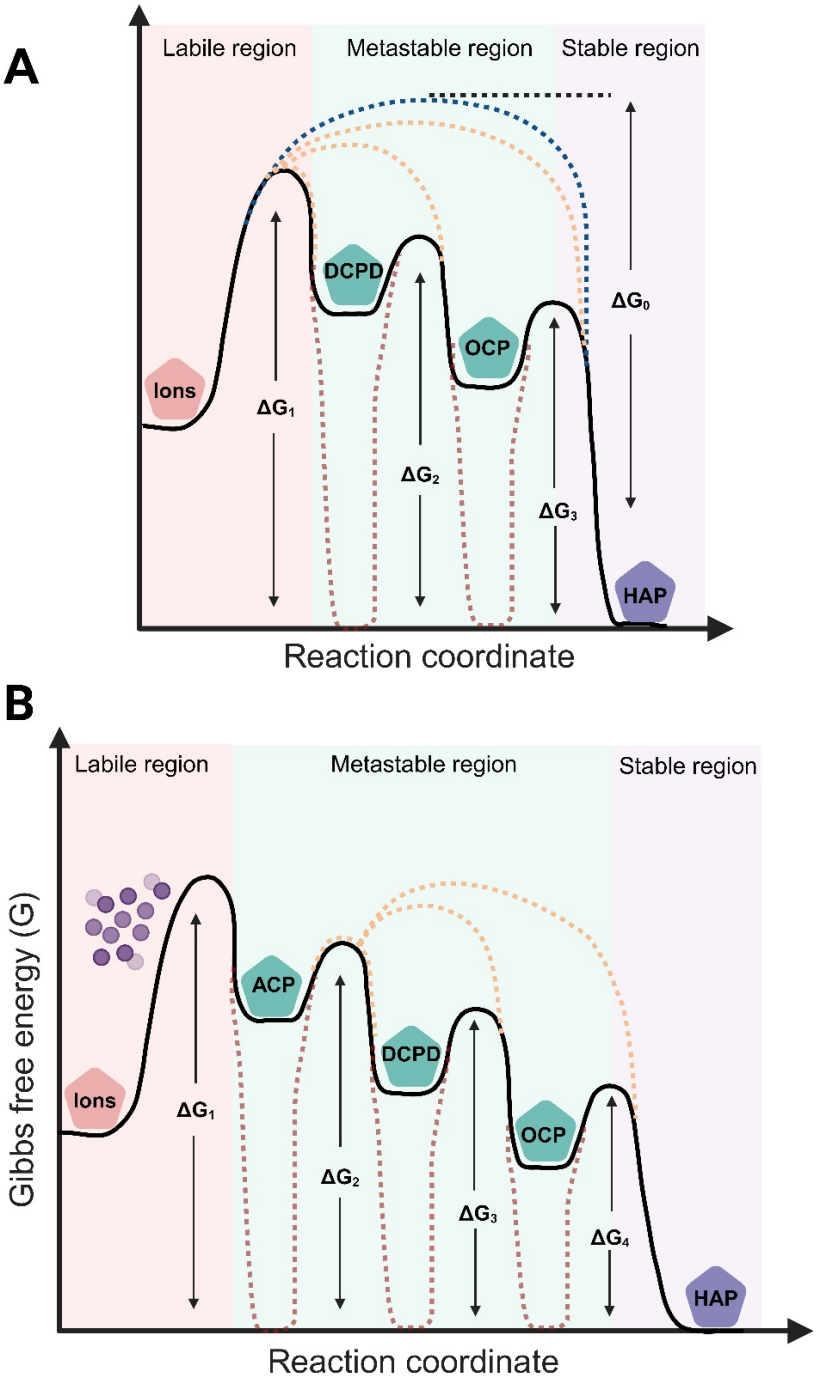


*Figure 19 HAP formation pathways with classical and non-classical nucleation theory. A) Classical nucleation theory: HAP forms directly without metastable phases (blue dashed line), with metastable phases in cascade (full black line) or with metastable phase(s) forming in parallel (orange dashed lines). B) Non-classical nucleation theory from pre-nucleation clusters: Pre-nucleation clusters (purple spheres) transform to ACP with metastable phases forming in cascade (full black line) or with metastable phase(s) forming in parallel (orange dashed lines) before transforming to HAP. X-axis = reaction coordinate. Y-axis = changes in Gibbs free energy. Green pentagons = metastable phases, purple pentagons = stable phases. Image created on www.biorender.com.*

`

## 1.1.10. Polymers for Hard Tissue Repair

### Natural Polymers

Natural polymers, such as chitosan, alginate, and collagen, represent a diverse group of biologically derived materials known for their intrinsic biocompatibility and functional properties [404]. Chitosan, a polysaccharide sourced from crustacean shells or fungal cell walls, has been shown to enhance mineralisation and promote osteogenic differentiation in vitro [405-409]. In vivo, chitosan/HAP/collagen composite scaffolds have induced osteogenesis in a rabbit bone defect model [410]. Alginate, an anionic polysaccharide extracted from brown algae, is biocompatible and biodegradable [411]. When combined with HAP, alginate has improved cell proliferation, osteogenic differentiation, and mineralisation in vitro [412, 413], and facilitated mineralisation in a rat calvarial bone defect model in vivo [414]. Collagen, derived from animal sources or produced through recombinant expression, has shown enhanced osteogenic differentiation in vitro when combined with HAP [415-418] and promoted osteogenesis in vivo in a rat calvarial defect model using collagen membranes [419]. Self-assembling hydrogel peptides, such as Puramatrix™, have been employed as scaffolds for bone repair, demonstrating the potential to stimulate osteogenic differentiation in vitro and osteogenesis in vivo [420-423].

Despite their advantageous properties, the inherent variability of natural polymers poses challenges in achieving consistent and reproducible material properties, limiting their reliability in biomedical applications [404].

### Synthetic Polymers

Unlike their natural counterparts, synthetic polymers are laboratory-synthesised materials offering precise control over structural and functional properties. This customisability makes them attractive for biomedical applications, particularly in bone scaffold engineering, where tuneable chemical, physical, and mechanical characteristics are critical. Among such polymers, polylactide (PLA), polyglycolide (PGA), their copolymer poly(lactide-co-glycolide) (PLGA), and poly(ε-caprolactone) (PCL) stand out due to their biocompatibility, mechanical strength, and FDA approval [424-428].

These polymers undergo degradation via the hydrolysis of ester linkages, allowing for tuneable degradation rates influenced by their composition, structure, and molecular weight [429]. The degradation hierarchy follows PGA > PLGA > PLA > PCL, with PGA degrading within weeks, whilst PCL exhibits the greatest stability [430-432].

An in vitro study demonstrated that PLA/HAP scaffolds maintain immunological inertness whilst promoting osteogenic differentiation of human MSC [425]. PGA/HAP scaffolds have shown successful osteogenesis, mineralisation and controlled biodegradation in a rabbit

model [433]. PLGA has demonstrated promising results in composites with calcium phosphate ceramics. In vitro, PLGA combined with HAP supported the attachment and proliferation of endometrial stem cells [424]. In vivo, PLGA combined with β-TCP facilitated successful spinal fusion in a rat model [434]. Clinical applications of PCL-β-TCP cages have achieved 95.2% fusion rates [435], highlighting the potential of polymer-ceramic composites to replace traditional bone grafts in spinal fusion procedures effectively.

## Polycaprolactone

PCL is an aliphatic semicrystalline polyester comprised of hexanoate repeat units, possessing a melting point of 59–64°C and a glass transition temperature of −60°C. It is commonly synthesised via ring-opening polymerisation (ROP) of ε-caprolactone, a cyclic monomer, using ionic and metal catalysis. This elastic polymer exhibits high elongation at breakage and tuneable stiffness for various biomedical applications [427, 428, 436, 437]. Notably, its slow degradation time of 2–5 years renders it suitable for applications requiring prolonged degradation kinetics, such as spinal fusion [431, 432, 436].

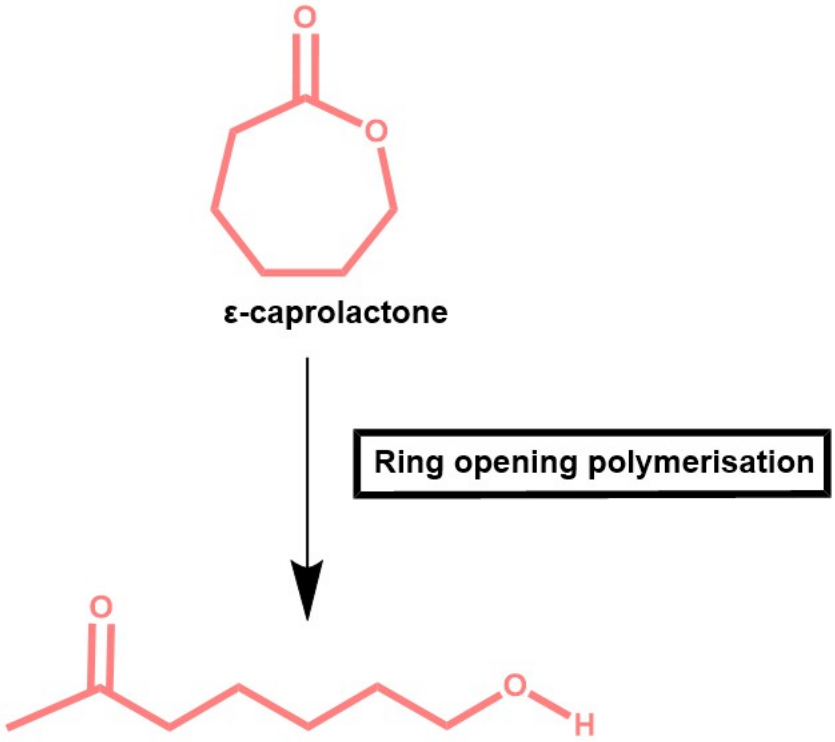


*Figure 20 Ring-opening polymerisation of ε-caprolactone.*

Clinically, PCL has been employed in nasal corrections [438], as a drug carrier for subdermal contraceptive implants [439], and in biodegradable surgical sutures [440]. However, as a standalone material, PCL presents challenges, including slow degradation and a lack of intrinsic bioactivity or sufficient cell attachment sites [441-443].

`

Incorporating HAP into the PCL polymer matrix was found to improve its performance. HAP-PCL composites have demonstrated enhanced compressive modulus, surface roughness, and wettability [426, 444-450]. In vitro studies on HAP-PCL composites have shown enhanced cell attachment, biocompatibility, proliferation, and osteogenic differentiation [426, 443, 446, 447, 451-453], while in vivo, these composites have demonstrated increased osteogenesis and improved cell differentiation [452, 453]. The versatility of PCL makes it a prime candidate for 3D-printed bone graft scaffolds, with HAP incorporation enhancing ink recovery and reducing pore size in printed scaffolds [449, 454, 455].

PCL offers the flexibility to be synthesised in various architectures, including linear, star-shaped, and Y-shaped configurations, allowing for tuneable properties based on the application [456-459]. Star-shaped PCL polymers, in particular, possess smaller hydrodynamic radii than their linear counterparts, enhancing renal excretion efficiency [460]. Increasing the number of polymer arms enhances tensile strength, although mechanical properties tend to diminish with higher molecular weights or uneven arm numbers [461, 462].

Additionally, PCL can undergo further functionalisation via methacrylation, enabling the formation of biocompatible, crosslinked networks [456]. Methacrylated PCL supports extrusion-based printing, with cell viability rates exceeding 91% in resultant scaffolds, as demonstrated by Samson et al. [463]. Additionally, methacrylation also offers the potential to fine-tune the degradation rate by controlling the degree of methacrylation [459].

### 1.1.11. 3D Printing for Bone Tissue Engineering

Additive manufacturing (AM) has emerged as a transformative approach in bone tissue engineering, offering significant advantages over conventional fabrication methods [464-466]. Traditional techniques, such as solvent casting, particle leaching, phase separation, and electrospinning, are often limited by the use of toxic organic solvents, incomplete removal of residual particles, non-homogeneous material distribution and extended fabrication times [467]. In contrast, AM technologies provide precise control over scaffold architecture and composition. According to the International Standardisation Organisation (ISO) and the American Society for Testing and Materials (ASTM), as specified in ISO/ASTM 52900, these technologies can be classified into seven categories based on their manufacturing process: material extrusion, vat photopolymerisation, material jetting, sheet lamination, powder bed fusion, directed energy deposition, and binder jetting. Each category encompasses various technologies that utilise materials in solid, powdered, or liquid form to create 3D objects layer by layer through mechanisms such as solidification from a molten state, polymerisation, lamination, melting, and binding [467-470].

These advanced methods enable the production of highly precise, intricate structures with controlled pore size and interconnectivity, crucial in promoting osteogenesis and vascularisation for bone tissue engineering [467, 471, 472]. AM facilitates rapid, cost-effective fabrication of patient-specific implants, allowing for customisation based on individual requirements. Furthermore, the enhanced control over scaffold architecture ensures homogeneity throughout the scaffold, improving cell attachment and osteogenic differentiation [467, 473-475].

The versatility of AM in bone tissue engineering is evident in its ability to incorporate multiple materials and bioactive agents, paving the way for advanced, multifunctional bone implants that can more effectively mimic the complex structure and composition of natural bone tissue [476].

Bone tissue engineering has witnessed significant commercial advancement, with several companies harnessing AM to produce and commercially distribute bone implants. Oxford Performance Materials stands out as a pioneer in the field, with their customisable OsteoFab® implants made from poly-ether-ketone-ketone (PEKK) approved for use in Europe and the USA [477]. Recently, Cerhum has received FDA and European approval for MyBone, a custom 3D-printed HAP implant designed to treat severe facial deformations, demonstrating promising osseointegration in a clinical case series [478, 479]. Similarly, Dimension Inx has made significant strides with their FDA-approved CMFlex, a 3D-printed implant composed of PLG and HAP particles for oral and maxillofacial applications, showing positive initial clinical results [480]. While awaiting full FDA approval, Ossiform has received its premarket notification for bone implants developed for regeneration and research using β-TCP [481, 482]. Osteopore has secured FDA and European approval for aXOpore®, a PCL-TCP construct for the treatment of critical-sized segmental defects, with initial clinical studies indicating favourable outcomes in bone regeneration [483, 484]. Lastly, BellaSeno has obtained European authorisation for its PCL-based, 3D-printed custom implants, demonstrating promising results with good bone restoration in a clinical case study [485-487].

## Material Extrusion

Material extrusion has emerged as a prominent technique in bone tissue engineering [488]. This methodology involves the sequential deposition of materials along predetermined paths, designed using computer-aided design (CAD) software, to fabricate three-dimensional constructs [489]. The process typically entails the extrusion of material from a reservoir or thermal unit through a nozzle or orifice in the x-y plane on the collection platform. Following the deposition of each layer, either the extrusion head or the collection platform adjusts in the z-axis by a predetermined increment to accommodate subsequent layers [490, 491]. Material extrusion can be categorised in direct ink writing and fused filament fabrication.

Fused Filament Fabrication (FFF) employs thermoplastic materials and composites, primarily in filament form, but also as pellets and powders. Filament feedstock is conveyed from the spool into the print head via roller-driven stepper motors, whereas pellets and powders are transported via rotating screws, pistons, or pneumatic pressure. In the print head, the material is melted to a semi-liquid state and deposited onto the collection platform, where it fuses with the previous layer and rapidly solidifies through heat dissipation [489, 490, 492-496]. A schematic representation of this printing process is shown in Figure 21.

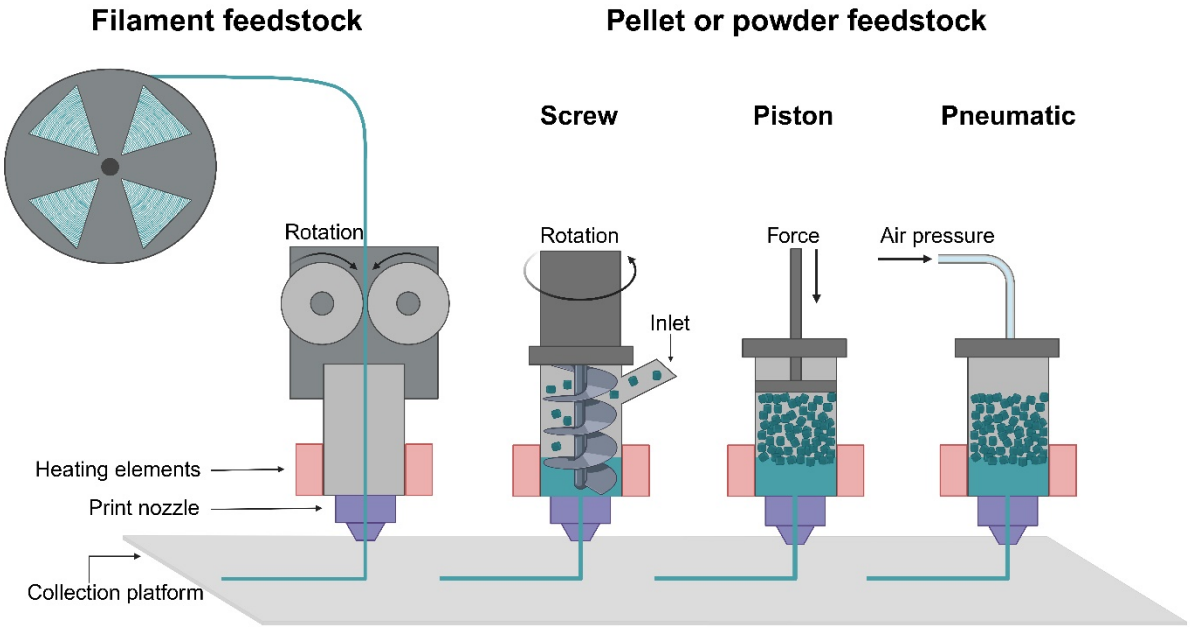


*Figure 21 Illustration of the fused deposition modelling process using different feedstock and extrusion techniques. Image created on www.biorender.com.*

Direct ink writing (DIW) operates at or near room temperature, enabling the processing of liquid and semi-liquid materials. This technique accommodates a broad range of materials, including polymers, ceramics, and composites, provided the ink exhibits suitable rheological properties for extrusion and structural retention [497]. Bioprinting represents a specialised DIW variant employing cell-laden bioinks formulated with non-cytotoxic materials to maintain cell viability [498, 499].

During the process, the material is extruded from the reservoir onto the platform via a rotating screw, piston, or pneumatic pressure, where it undergoes solidification [500-502]. Screw-based systems are generally less suitable for bioprinting due to high shear forces that compromise cell viability [503]. Some bioprinting systems employ a coaxial delivery mechanism to introduce a crosslinking agent to the bioink before deposition, facilitating in situ crosslinking [504, 505]. A schematic of the DIW process is illustrated in Figure 22.

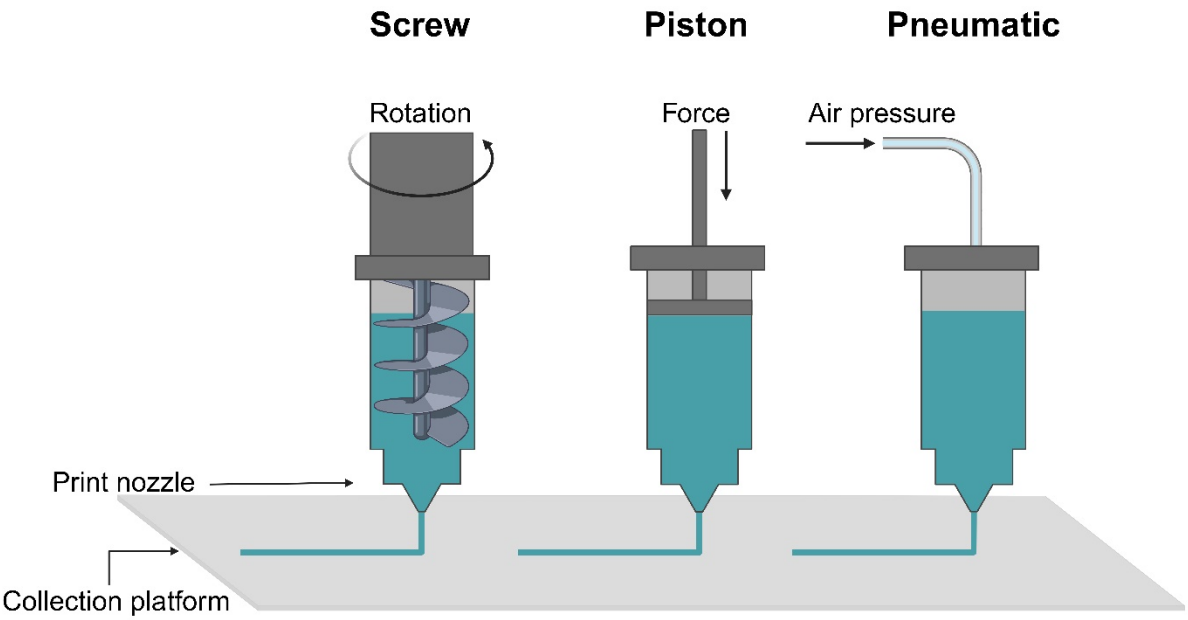


*Figure 22 Illustration of the direct ink writing process via screw, piston, and pneumatic extrusion. Image created on www.biorender.com.*

Solidification mechanisms are governed by material characteristics and comprise physical and chemical processes:

**Physical processes:**

- pH-induced coagulation [506]
- Precipitation [507]
- Ionic crosslinking [508, 509]
- Solvent evaporation [510]
- Freezing or lyophilisation [511, 512]
- Temperature-initiated sol-gel transitions [513]

**Chemical reactions:**

- Ultraviolet (UV)-initiated crosslinking [514, 515]
- Temperature-induced polymerisation [516]
- Enzymatic polymerisation when applicable (e.g. fibrin polymerisation) [517, 518]

The efficacy of FFF and DIW processes is highly dependent on material rheological properties. Optimal materials exhibit shear-thinning behaviour or viscoelasticity, enabling extrusion while maintaining post-deposition structural integrity through rapid viscosity recovery [519-522]. This characteristic is particularly crucial for bioinks, minimising cell damage from

shear stress during printing [523]. Notably, cells within the bioink may contribute to shear-thinning behaviour, with the magnitude varying with cell density [524].

Printing parameters, including temperature, pressure, deposition rate, and nozzle geometry (shape and diameter), can significantly influence the ink printability and shape fidelity of deposited layers [519-522].

Consequently, parameter optimisation is critical for process enhancement and achieving the targeted structural outcomes in bone tissue engineering applications.

## 1.1.12. In Vitro Testing of Bone Graft Substitutes

Prior to the development of in vitro testing techniques, the evaluation of human physiology and pathophysiology, particularly in medical and pharmaceutical research, historically relied on animal models [525]. However, ethical concerns surrounding animal experimentation in biomaterial assessment led to significant paradigm shifts in research approaches. The introduction of the 3Rs framework (reduce, refine, replace) in the 1959 publication "The Principles of Humane Experimental Technique" established foundational guidelines promoting minimal animal usage and alternative testing strategies [526]. Consequently, cell cultures have emerged as a valuable preliminary testing platform for biomaterial safety and efficacy [527].

Biocompatibility assessment represents a critical determinant in biomaterial development and clinical safety protocols. Multiple national and international standards require biocompatibility testing of biomaterials using cell cultures. ISO 10933-1 ("Biological Testing of Medical Devices—Part 1: Guidance on Selection of Tests") consolidates these requirements, classifying devices by [528]:

- Body contact type: Surface (e.g. contact lenses), external (e.g. dental cement), or implanted (e.g. prostheses)
- Tissues localisation: Epithelial, endothelial, bone, cartilage, etc.
- Exposure duration: Limited (<24 h), prolonged (24–30 h), or permanent (>30 h)

ISO 10993-5 mandates initial cytotoxicity testing for all devices to evaluate metabolism, replication, adhesion and antigen expression [528]. Beyond these baseline requirements, materials must demonstrate application-specific functional capabilities. For bone biomaterials, this typically encompasses structural support and osteogenic potential [529, 530].

The bone graft substitute developed in this project was designed as a potential cage filler for spinal fusion applications. Structural support is not required within a load-bearing cage system; instead, facilitating cell attachment and promoting bone ingrowth is essential. The PCL-HAP composite material developed for this purpose leverages HAP's osteoconductive

properties, while its surface topography and substitution characteristics offer potential support for osteogenic differentiation [290, 334, 359, 531].

While a comprehensive preliminary evaluation should include both ISO-standard biocompatibility testing MSCs that can be sourced from diverse tissues and assessment of osteoconductive and osteoinductive properties, this project's initial evaluation focused on examining cell attachment and metabolic activity on fabricated scaffolds.

## The Choice of Cells

First identified by Friedenstein in 1966 [532], MSCs exhibit the capacity to differentiate into chondrogenic, osteogenic, and adipogenic lineages when provided with appropriate in vitro or in vivo cues [533]. MSCs can be sourced from diverse tissues, such as bone marrow (BM-MSCs), umbilical cord blood (UC-MSCs), Wharton's jelly (WJ-MSCs), adipose tissue (AT-MSCs), and placenta (P-MSCs) [534, 535]. However, isolation success, immunophenotype, proliferation, and differentiation potential vary by tissue source [534, 536, 537].

Ongoing discussions of MSC heterogeneity have led to the proposal of the alternative term "mesenchymal stromal cells" to avoid implying uniformity [538]. The International Society for Cellular Therapy has defined the following minimal criteria for MSCs [539]:

- Plastic adherence under standard culture conditions
- Expression of surface antigens CD73, CD90, CD105
- Lack of CD11b, CD14, CD34, CD45, CD79, CD19, human leukocyte antigen (HLA)-DR
- In vitro differentiation into osteoblasts, adipocytes, chondroblasts

### Immortalised vs Primary Cells

Primary cell cultures are derived directly from native tissues by enzymatic/mechanical dissociation or spontaneous outgrowth from explants. Under optimised conditions, they retain proliferative capacity and closely mimic tissue physiology in vivo [528, 540-542]. With repeated passaging, primary cultures can generate finite cell lines or strains [542-544]. The proliferative potential of primary cells progresses through three phases [545]:

- Phase I: Limited proliferation before the first passage
- Phase II: Rapid cell proliferation
- Phase III: Gradual senescence

MSCs undergo replicative senescence following repeated in vitro passaging, ceasing division after finite population doublings [545]. Primary MSC cultures also exhibit heterogeneous behaviour, with spontaneous osteogenic commitment observed during the expansion of human MSCs [546]. Variability in MSC characteristics exists among different

donors [543, 547, 548] and is further influenced by lifestyle factors [549]. Additionally, donor age contributes to variability, with higher passage numbers achieved in younger donors. BM-MSCs from donors aged up to ~15 years exhibited an average doubling time of 28 ± 1.7 and 10.3 ± 1.0 passages, whereas those from donors aged 59–75 years exhibited only 16.5 ± 1.0 doublings and 2.4 ± 0.5 passages [550]. Furthermore, tissue source plays a critical role, as BM-MSCs exhibit earlier senescence than UC-MSCs or AT-MSCs [537, 551].

In contrast, immortalised cell lines are either tumour-derived or artificially manipulated to acquire indefinite proliferation, facilitating extensive passaging. These cell lines provide several advantages, including abundant homogeneous cell populations, cost-effectiveness, user-friendliness, and reduced ethical constraints [528, 552, 553]. Consequently, they serve as a valuable platform for reproducible in vitro analyses [554].

However, the validity of extrapolating findings from genetically modified or tumour-derived cultures to primary cells in vivo is a significant concern due to their inadequate representation of native physiological conditions. Nonetheless, immortalised cell lines can be an effective tool for initial screening, which can then be validated using primary cells [528, 555].

## Cell Culture Media

Cell culture relies on medium to provide essential nutrients, growth factors, and regulatory molecules for cell growth and maintenance. The first basal medium, Minimal Essential Medium (MEM), was developed in 1959 and included 13 amino acids, 8 vitamins, 6 ionic species, and glucose [544, 556]. The composition of standard cell culture medium encompasses [544, 556, 557]:

- Water
- Inorganic salts and trace elements (iron, manganese, zinc, selenium, copper)
- Balanced salt solution ($Na^+$, $Ca^{++}$, $Mg^{++}$, $K^+$) to maintain pH and cellular homeostasis
- Energy sources (glucose and glutamine)
- Essential amino acids (L-arginine, L-histidine, L-isoleucine, L-leucine, L-lysine, L-methionine, L-phenylalanine, L-threonine, L-tryptophan, L-valine, L-cysteine, L-tyrosine, L-glutamine)
- Non-essential amino acids (L-alanine, L-asparagine, L-aspartic acid, L-glutamic acid, L-glycine, L-proline, L-serine)
- Vitamins as coenzyme constituents (folic acid, niacinamide, pyridoxal, pantothenate, riboflavin, thiamine) and lipid synthesis substrates (choline and inositol)

`

- Serum-containing hormones, attachment/binding factors, membrane permeability regulators, lipids, enzymes, micronutrients, trace elements, buffers, free radical scavengers, protease inhibitors, mitogens

Different cell types and cell lines have specific requirements for these factors and nutrients. Meeting these essential needs is critical for preserving the desired cellular phenotype. Traditional media were originally formulated for immortalised cancer-derived cell lines, which can tolerate various compositions. However, these formulations often prove suboptimal for more specialised cells, such as stem cells [544].

The culture of eukaryotic cells in vitro typically relies on serum supplementation. However, the undefined biological complexity and variability of sera introduce significant challenges in experimental reproducibility and interpretation. Research has shown that the origin of sera significantly affects the biological properties of human MSCs. These effects extend to key cellular processes, including metabolic activity, colony-forming efficiency, proliferation rate, differentiation potential, and immunomodulatory functions [558-560].

Foetal bovine serum (FBS), a commonly used supplement in standardised medium, presents its challenges. FBS has been observed to lead to stronger variability in different batches of BM-MSCs compared to serum-free media [561], possibly due to the inherent heterogeneity of MSCs [538]. This variability extends to differences between FBS batches and suppliers. Research has shown that media supplemented with FBS from a single supplier can exhibit batch-to-batch variations that affect cell proliferation [562]. Additionally, FBS from different suppliers have been found to induce varying ALP activity, thereby influencing the osteogenic differentiation of human MSCs [563]. In human cancer epithelial cells, supplier-specific FBS caused variability in immune response cytokine expression [564]. FBS from certain suppliers has been reported to induce spontaneous mineralisation in cell-free silk fibroin scaffolds [565]. These issues of variability and undefined composition affect experimental design and result interpretation. Additionally, the use of FBS raises ethical concerns in cell culture practices [566]. In response to these challenges, alternative media formulations have been developed. Current available media options include [544]:

- Classical media: Universal formulations with FBS.
- Serum-free media (SFM): Lacking serum but containing serum-derived components
- Animal-origin-free (AOF) media: No animal-origin components, replaced by recombinant alternatives.
- Chemically defined (CD) media: Components with precisely defined and specified chemical compositions.

The choice of medium is contingent upon cell type specificity and research objectives. Each of these media types has distinct advantages and disadvantages, outlined in Table 11.

`

*Table 11 Advantages and disadvantages of the different media. Adapted from [544].*

| | **Classical with Serum** | **SFM** | **AOF** | **CD** |
|---|---|---|---|---|
| **Advantage** | Well-established formulations<br>Available in multiple formats<br>Universal culture system | Performance consistency | Performance consistency<br>Potential cost-effectiveness<br>Regulatory friendly | Performance consistency<br>Potential cost-effectiveness<br>Regulatory friendly |
| **Disadvantage** | Requires serum<br>Variable performance dependent on serum lot and % used<br>Not regulatory friendly | Dependency on origin of components<br>May contain animal-derived components<br>May not be regulatory-friendly<br>May require various degrees of adaptation | May contain recombinant proteins and peptides<br>May require various degrees of adaptation | Attachment-independent cells only<br>Requires cell adaptation<br>Some companies mislabel products as CD instead of AOF |

While addressing ethical concerns associated with the use of FBS, human serum introduces source and concentration-dependent variability in MSC culture. A study has shown that a medium with human autologous serum promotes higher proliferation of human MSCs compared to a medium supplemented with FBS, while allogenic serum leads to growth arrest and cell death. Gene expression analyses revealed that at late passages, FBS upregulated cell cycle inhibition transcripts in MSCs and induced greater differentiation, while autologous serum maintained more stable gene expression [567]. Further research has demonstrated that 10% autologous human serum performs at least as well as 10% bovine serum in terms of isolation and expansion of human MSCs. In comparison, lower concentrations (1% and 3%) of autologous serum appear inferior [568]. In the pursuit of xeno-free alternatives, Blázquez et al. showed that human MSCs maintained multipotency and genetic stability in a defined xeno-free medium derived from human plasma, exhibiting enhanced proliferation compared to xenogeneic MSC-specific media [569]. In another study, osteogenic differentiation of MSCs was observed in a culture medium supplemented with human platelet lysate [570].

Efforts in the development of SFM have yielded promising results. Ansari et al. formulated an SFM by supplementing Dulbecco's Modified Eagle Medium (DMEM) with various components, demonstrating that its efficacy for MSC attachment, survival, differentiation, and ECM deposition is comparable to that of FBS-containing media [571]. Another study found that a commercial serum-free medium (PRIME-XV SFM) supported higher growth rates of human MSCs than FBS-supplemented media while also reducing variability among different MSC batches [561]. However, it is important to acknowledge that

different SFM formulations can have varying effects on MSC characteristics. A study identified differences in population doubling time, yield, potency, colony-forming ability, differentiation potential, and immunosuppressive properties among various SFM formulations [572].

Additional supplements are typically required for the induction of osteogenic differentiation. The standard protocol involves treating a confluent monolayer of MSCs with a combination of dexamethasone (Dex), ascorbic acid 2-phosphate (AA-2P), and β-glycerol phosphate (βGP) [573].

## 1.1.13. The Necessity for a Standard Operating Procedure

To maintain a specific cell phenotype in vitro, it is critical to provide tailored essential requirements for each cell line. While certain cell types, such as cancer lines, tolerate diverse conditions, this does not apply to most stem cells [544].

To achieve experimental reproducibility, the use of homogeneous cell populations, sourced from either established cell lines or species-matched donor tissues, is imperative, as cellular origin influences metabolic characteristics. Notably, goat-derived MSCs demonstrated higher proliferation rates and glucose metabolism than human and mouse MSCs [574]. Even within the same species, MSCs harvested from different anatomical sites can exhibit significant functional variations under identical culture conditions [575].

The implementation of a standardised operating procedure (SOP) is essential for maintaining cell phenotype and behaviour. Research has shown that cells from the same sources manifest molecular heterogeneity and functional variability when cultured across different laboratory environments with varying culture medium compositions, commercial suppliers, and cellular seeding densities [576].

MSCs are highly responsive to their microenvironment, adapting to substrate properties, medium composition, and culture conditions by modulating their behaviour, phenotype, and secretory profile. The secretome, a diverse array of bioactive molecules released by these cells, mediates cellular communication via paracrine and autocrine signalling pathways that govern cell fate determination [577, 578]. In vitro studies have extensively documented the factors secreted by MSCs under various conditions [579-587].

Substrate stiffness has been demonstrated to influence the composition of the MSC secretome. BM-MSCs cultured on stiffer substrates (100 kPa) secreted factors that promote MSC proliferation, whereas those on softer substrates (0.2 kPa) released factors that facilitate osteogenesis, adipogenesis, angiogenesis, and macrophage phagocytosis [581]. Additionally, the topography and composition of substrate surfaces influence cellular signalling pathways. For instance, when hematopoietic stem cells were cultured on substrates with varying microcavity sizes, smaller cavities primarily affected autocrine signalling, while larger ones

modulated paracrine signalling. The addition of fibronectin coating enhanced both signalling mechanisms while reducing cellular proliferation [582]. In another study, human BM-MSCs cultured on collagen I matrices preferentially differentiate toward osteogenic lineages while exhibiting limited adipogenic potential [588]. Similarly, the application of collagen coating in cultures of immortalised AT-MSCs modulated the secretion of numerous factors, increasing the production of 60 while decreasing 17 others [579].

Cell seeding density is another critical parameter, as it directly influences growth kinetics and metabolic activity. A study with BM-MSCs revealed that lower initial seeding densities (100 cells/cm$^2$) result in extended lag phases, slower proliferation, and increased consumption of glucose, lactate, glutamine, and glutamate, than higher seeding densities (1000 cells/cm$^2$) [589]. Interestingly, research with immortalised AT-MSCs at varying densities ($1.4 \times 10^4$, $2.4 \times 10^4$, $3.8 \times 10^4$ cells/cm$^2$) has shown the highest factor secretion at intermediate densities [579].

The composition of the culture medium profoundly affects MSC behaviour and secretome profiles. Research examining various serum-free media formulations for BM-MSCs demonstrated different outcomes in doubling time, cell yield, potency, colony formation, differentiation potential, and immunosuppressive properties while maintaining consistent marker expression [572]. Analysis of MSC secretomes in various media conditions, including xeno-free and human platelet lysate-supplemented media, revealed distinct metabolic patterns and growth factor consumption [583]. The presence of serum substantially affects growth factor concentrations in human MSC secretomes [584, 585]. For instance, WJ-MSCs exhibited enhanced production of proteins linked to angiogenesis, neurogenesis, osteogenesis, and cell proliferation in serum-containing medium compared to serum-free conditions [585]. Additionally, reducing FBS levels from 20% to 0% increased human protein expression while decreasing bovine protein content in BM-MSC secretomes [586]. The use of FBS alternatives and supplements also creates variations in cell behaviour and secretome profiles. Human AT-MSCs displayed modified growth factor profiles when cultured with fresh frozen human plasma compared to plasma-free conditions [590]. When exposed to immunomodulatory factors, immortalised adipose-derived MSCs showed a greater than 50% increase in cytokine production [579]. The addition of common supplements, including platelet-derived growth factor, ascorbic acid, transferrin, and fibroblast growth factor-2, was been found to influence proliferation and differentiation in a human MSC cell line [591].

Medium volume and change frequency can further affect cell behaviour and secretome composition. The depth of the culture medium, determined by vessel geometry and medium volume, affects oxygen availability, with shallower medium levels facilitating higher oxygen concentrations [592, 593]. This depth can be affected by medium change frequency, as longer intervals between changes can lead to evaporation, influencing oxygenation levels [594].

`

Cellular oxygen requirements vary based on consumption rates influenced by cell size and growth kinetics, with larger, rapidly proliferating cells typically requiring more oxygen due to their greater volume and protein content [595]. Oxygen levels significantly influence MSC signalling and metabolism. A study has shown that hypoxic conditions (1% $O_2$) in immortalised AT-MSCs alter secretome composition, decreasing some factors while slightly increasing other factors involved in angiogenesis. However, cell surface markers remained unchanged [579]. Additional research with BM-MSCs has demonstrated that both anoxic (0.1% $O_2$) and hypoxic (5% $O_2$) conditions enhance paracrine signalling [596], while moderate hypoxia (8% $O_2$) increases proliferation and differentiation compared to normoxic conditions [597]. The method (partial/full) and frequency of medium changes affect secretome composition and nutrient levels by removing inhibitory metabolites and growth factors. Research showed that high glucose levels (25 mM) enhance MSC cell line proliferation while primarily affecting mineralisation in primary cells [598]. Low glucose levels (0.2 g/l) combined with reduced FBS (2%) decreased human exfoliated deciduous teeth stem cell proliferation and increased apoptosis while enhancing chondrogenic differentiation potential and reducing osteogenic differentiation [599]. In AT-MSCs, serum starvation altered mitochondrial metabolism, increasing reactive oxygen species while reducing succinate dehydrogenase activity [587]. Research has shown that both stimulating and inhibitory effectors influence stem cells through autocrine and paracrine signalling [582]. A study using a kidney fibroblastic cell line demonstrated that replacing used serum-containing (calf serum) medium with fresh serum-containing medium enhanced cell metabolism. Interestingly, replacing fresh serum-containing medium with fresh serum-free medium also increased metabolism, suggesting the coexistence of both stimulatory and inhibitory molecules in serum [600]. Further research demonstrated that murine stem cells undergo cell cycle arrest at different G1 phases under various conditions: high cell density (10% FBS), serum deprivation (0.5% FBS), and nutrient deprivation (isoleucine-deficient, 10% FBS). This arrest significantly impacts differentiation potential, as cells in later arrest stages cannot differentiate even with differentiation-promoting medium until cell cycle progression resumes. While nutrient addition can reverse the effects of serum and nutrient deprivation, cells arrested due to high density remain unable to differentiate. Notably, cells grown in human plasma arrested at lower densities in the early G1 phase and spontaneously differentiated into non-terminal stage adipocytes, demonstrating that FBS exerts stronger inhibitory effects and necessitates higher cell densities [601].

Partial medium change provides an alternative to complete replacement and has successfully supported human adipose-derived stem cell expansion [602]. In bovine myoblast cultures under serum-free conditions, partial (75%) media replacement yielded higher cell numbers than complete (100%) media changes [603].

These findings emphasise the importance of developing well-defined, customised SOPs for each cell line to ensure experimental reproducibility, especially for managing the complex sensitivity of MSCs to their microenvironment.

## 1.2. Project Aims and Objectives

The primary aim of this project was to develop a novel biomaterial by incorporating magnesium and strontium-substituted hydroxyapatite into polycaprolactone. This composite material was designed to serve as a customisable, non-cytotoxic alternative to conventional auto- and allograft fillers for spinal fusion applications. Additionally, the project aimed to establish scalable, cost-effective methods for sHAP synthesis and composite fabrication suitable for industrial production, alongside developing an SOP for reproducible in vitro testing. To achieve these aims, the following key objectives were pursued:

1. Standardisation of cell culture protocols for in vitro evaluation of sHAP and composite scaffolds:

- Comparison of serum-free and serum-containing media for MSC expansion.
- Evaluation of ECM cell culture dish coatings on cell adhesion and proliferation.
- Assessment of the effect of various media change regimens on cell proliferation.

2. Refinement of continuous sHAP synthesis methods and production of sHAP powders:

- Development of a scalable, continuous sHAP synthesis method.
- Determination of suitable magnesium and strontium substitution levels in HAP.
- Evaluation of sHAP cytotoxicity in vitro.

3. Fabrication and characterisation of sHAP-PCL composites:

- Incorporation of sHAP into PCL and assessment of composite cytotoxicity.
- Refinement of formulation and process parameters to enhance printability.
- Fabrication of scaffolds via 3D extrusion printing.
- Assessment of scaffold cytotoxicity in vitro.

`

# Chapter II Materials and Methods

This chapter describes the materials and experimental methods used throughout this project.

## 2.1. Materials

All equipment and consumables used in this project are detailed in Table 12 and Table 13, respectively. Reagents were used according to supplier specifications unless otherwise noted.

*Table 12 List of equipment used.*

| Equipment | Model | Manufacturer |
|---|---|---|
| Analytical balance | ABJ 320-4NM | Kern & Sohn (Germany) |
| Analytical balance | CP225D | Sartorius (UK) |
| Autoclave, portable | Vario 3028 | Dixons Surgical Instruments (UK) |
| Autosampler | Cetac ASX-520 | Thermo Fisher Scientific (UK) |
| Bench top centrifuge | R-8C | Remi Group (India) |
| Class II safety cabinet | SafeFAST Top 209-D | FASTER S.r.l (Italy) |
| $CO_2$ incubator | BB15 | Thermo Fisher Scientific (UK) |
| $CO_2$ incubator, water-jacketed | Forma™ series II 3111 | Thermo Fisher Scientific (UK) |
| Confocal microscope | LSM 510 META | Zeiss (Germany) |
| Counting chamber | Improved Neubauer 2x bright | Scientific Laboratory Supplies (UK) |
| Drop shape analyser | DSA100 | KRÜSS GmbH (Germany) |
| Dropping funnel system | Pyrex™ Quickfit™ | Thermo Fisher Scientific (UK) |
| Drying and heating chamber | FD53 | Binder (Germany) |
| Extrusion printer | BioBot 1 | Allevi (USA) |
| Field emission scanning electron microscope | Nova NanoSEM 450 | FEI (USA) |
| Freezer (−80°C) | C340-86 | Eppendorf (UK) |
| Freezer (−80°C) | ULT1386-9-V34 | Revco Technologies (UK) |
| Freezing container | Mr Frosty™ for up to 18 cryovials | Thermo Fisher Scientific (UK) |
| FTIR spectrometer | Nicolet™ Apex KBr with iZ10 module | Thermo Fisher Scientific (UK) |
| Fume cabinet | FLC CDS | Clean Air Limited (UK) |
| Hydraulic press for FTIR analysis | CrushIR™ | Pike Technologies (USA) |
| ICP-OES spectrometer | iCAP 7000 series | Thermo Fisher Scientific (UK) |
| Liquid nitrogen tank | Biorack 3000 | Statebourne Cryogenics (UK) |
| Magnetic hotplate stirrer | MR Hei-Tec | Heidolph Instruments (Germany) |
| Microcentrifuge | MiniSpin 5702 | Eppendorf (UK) |
| Mixing column, ⅜ ” outer diameter with 32 elements | Koflo 3/8-32 316 SS | Cole-Parmer Instrument Company (USA) |

`

| | | |
|---|---|---|
| Mixing column, ½ ” outer diameter with 21 elements | Koflo 1/2-21 316 SS | Cole-Parmer Instrument Company (USA) |
| Nuclear magnetic resonance spectrometer | Avance III™ 400 MHz | Bruker (UK) |
| Peristaltic pumps | 120S and 323 | Watson Marlow (UK) |
| pH meter | pH 7 Vio with XS 201 T electrode | XS Instruments (Italy) |
| Plate reader | Infinite® F200 pro | Tecan (Austria) |
| Rocking shaker | ROCKER 2D | IKA (UK) |
| Rotary evaporator | Rotavapor® R II | Buchi (UK) |
| Safety cabinet | Airstream® AC2–6E1 | Esco (UK) |
| Separation funnel with PTFE key | Pyrex™ | Thermo Fisher Scientific (UK) |
| Three-neck round-bottomed flask | Quickfit™ | Thermo Fisher Scientific (UK) |
| Ultrasonic bath | UR 1 | Retsch GmbH (Germany) |
| Ultrasonic processor (HAP synthesis) | UP400St | Hielscher (Germany) |
| Ultrasonic processor (ink preparation) | UP100H | Hielscher (Germany) |
| Ultraviolet light curing system | S2000 | OmniCure (UK) |
| Vacuum aspiration system | Safevac | Scientific Laboratory Supplies (UK) |
| Water bath | SBB Aqua12 Plus | Grant Instruments (UK) |
| Water purification system | | Elga (USA) |

*Table 13 List of consumables used.*

| Consumable | Manufacturer |
|---|---|
| 12 and 48-well plates, flat bottom, cell-culture treated and sterile, Nunc™ Thermo Scientific™ | Thermo Fisher Scientific (UK) |
| 20 gauge tapered tip | Metcal (UK) |
| 3-(Trimethoxysilyl)propyl methacrylate (98%) | Thermo Fisher Scientific (UK) |
| 48-well plates, flat bottom, non-treated and sterile, CytoOne® | Starlab (France) |
| 6-diamidino-2-phenylindole dihydrochloride for fluorescence analysis (≥95.0%) | Sigma-Aldrich (UK) |
| 96-well plates without lid, clear with a flat bottom, non-treated and non-sterile | Greiner Bio-One (UK) |
| Aluminium foil | Sigma-Aldrich (UK) |
| Azowipe™ | VWR (UK) |
| Calcium hydroxide, ERBApharm, Ph.Eur.-USP certified (97.8%) | CARLO ERBA Reagents S.A.S. (France) |
| Conical polypropylene centrifuge tubes, sterile (15 ml) | Appleton Woods (UK) |
| Costar™ 24-well plates, flat bottom, cell-culture treated and sterile, Corning™ | Thermo Fisher Scientific (UK) |
| Cryo.s™ cryovials, skirted with internal thread, sterile (1 ml, 4 ml) | Greiner Bio-One (UK) |
| Deuterated chloroform | Sigma-Aldrich (UK) |
| Dichloromethane stabilised with amylene for HPLC, Fisher Chemical™ | Thermo Fisher Scientific (UK) |
| Dimethyl sulfoxide, Hybri-Max™ (≥99.7%) | Sigma-Aldrich (UK) |
| Diphenyl(2,4,6-trimethylbenzoyl)phosphine oxide/2-hydroxy-2-methylpropiophenone blend | Sigma-Aldrich (UK) |
| Dulbecco's Modified Eagle Medium, high glucose with GlutaMAX™ supplement | Thermo Fisher Scientific (UK) |
| Easy Reader™ conical polypropylene centrifuge tubes, sterile, Fisherbrand™ (50 ml) | Thermo Fisher Scientific (UK) |
| Ethanol, AR certified for analysis (≥99.8%) | Thermo Fisher Scientific (UK) |
| Fibronectin solution, human (1 mg/ml) | PromoCell (UK) |
| Foetal bovine serum, FCS-SA | Labtech (UK) |
| Formaldehyde, ACS reagent (37 wt% in $H_2O$ with 10–15% methanol stabiliser) | Sigma-Aldrich (UK) |
| Glass rectangular coverslips, Fisherbrand™ | Thermo Fisher Scientific (UK) |
| Gloves | Scientific Laboratory Supplies (UK) |
| Hanks' Balanced Salt Solution with sodium bicarbonate, without phenol red | Scientific Laboratory Supplies (UK) |
| HDK® H30 pyrogenic silica (>99.8%) | Wacker Chemie (UK) |
| HENKE-JECT® single-use syringes, 2-piece with Luer lock tip, sterile (10 ml) | VWR (UK) |
| Human Mesenchymal-XF Expansion Medium | Merck (UK) |
| Hydrochloric acid, AR certified for analysis (1.18 g/ml, 37%) | Thermo Fisher Scientific (UK) |
| Hydrogen peroxide solution, Suprapur® (30%) | Thermo Fisher Scientific (UK) |
| Hydroxyapatite powder, synthetic, <200 nm particle size (≥97%) | Sigma-Aldrich (UK) |
| Industrial methylated spirit (99%) | Thermo Fisher Scientific (UK) |
| Isopropanol, extra pure, SLR Fisher Chemical™ | Thermo Fisher Scientific (UK) |
| Lead-free autoclave indicator tape, STERIS™ | Thermo Fisher Scientific (UK) |

| | |
|---|---|
| Magnesium nitrate hexahydrate, BioUltra (≥99%) | Sigma-Aldrich (Germany) |
| Methacrylic anhydride with 2,000 ppm topanol A as inhibitor (≥98%) | Sigma-Aldrich (UK) |
| Methanol, AR certified for analysis, Fisher Chemical™ | Thermo Fisher Scientific (UK) |
| Nitric acid, BAKER ANALYZED™ J.T.Baker® ACS reagent (69.0–70.0%) | Avantor™ Performance Materials (USA) |
| Orthophosphoric acid, ISO-ACS-Reag.Ph.Eur.-USP certified (86%) | CARLO ERBA Reagents S.A.S. (France) |
| Penicillin-streptomycin solution (10,000 units penicillin and 10 mg streptomycin/ml in proprietary citrate buffer) | Sigma-Aldrich (UK) |
| Pentaerythritol (99%) | Sigma-Aldrich (UK) |
| PES syringe filter, sterile, Fisherbrand™ (0.2 µm) | Thermo Fisher Scientific (UK) |
| Phalloidin-TRITC (≥90%) | Sigma-Aldrich (UK) |
| Phosphate buffered saline tablets | Scientific Laboratory Supplies (UK) |
| Plain microscope slides, Corning™ | Thermo Fisher Scientific (UK) |
| Potassium bromide for IR spectroscopy, Uvasol® | Merck (UK) |
| Premium microcentrifuge tubes, Fisherbrand™ (1.5 ml) | Thermo Fisher Scientific (UK) |
| Presept tablets | Scientific Laboratory Supplies (UK) |
| Resazurin sodium salt, Santa Cruz Biotechnology | Insight Biotechnology (UK) |
| Serological pipettes, individually wrapped and sterile (5 ml, 10 ml, 25 ml) | Greiner Bio-One (UK) |
| Silicone oil for oil baths (−40–200°C) | Thermo Fisher Scientific (UK) |
| SINTlife® MgHAP powder | Finceramica (Italy) |
| Specimen containers with cap, individually wrapped and sterile (120 ml) | Elkay Laboratory Products (UK) |
| StemMACS™ MSC Expansion Medium Kit XF, human | Miltenyi Biotec (Germany) |
| Strontium nitrate, ACS reagent (≥99%) | Sigma-Aldrich (Germany) |
| Sulphuric acid, BAKER ANALYZED™ J.T.Baker® (95-97%) | Thermo Fisher Scientific (UK) |
| SureOne™ micropoint (0.1–5 µl and 100–1250 µl) and bevelled (1–200 µl) pipette tips, non-filtered and non-sterile, Fisherbrand™ | Thermo Fisher Scientific (UK) |
| T-75 cell culture flasks with filter cap, cell-culture treated and sterile | Sarstedt (Germany) |
| Tin(II) 2-ethylhexanoate (≥98%) | Sigma-Aldrich (UK) |
| Toluene, AR certified for analysis, Fisher Chemical™ | Thermo Fisher Scientific (UK) |
| Triethylamine (≥99.5%) | Sigma-Aldrich (UK) |
| Triton™ X-100, laboratory grade | Sigma-Aldrich (UK) |
| Trypan blue solution (0.4%) | Gibco (UK) |
| Trypsin-ethylenediamine tetraacetic acid solution with phenol red (0.25% porcine trypsin and 0.02% ethylenediamine tetraacetic acid in Hanks' Balanced Salt Solution) | Sigma-Aldrich (UK) |
| Type B bovine gelatine, tissue culture grade (2% in $H_2O$) | Sigma-Aldrich (UK) |
| Water protect C 6000.1 | VWR (UK) |
| ε-caprolactone (97%) | Sigma-Aldrich (UK) |

`

## 2.1.1. Reagent Compositions

Reagents were prepared using analytical grade chemicals unless otherwise specified. The compositions of prepared reagents were as follows:

- Industrial methylated spirit (IMS) solution: 70 volume percent (vol%) in deionised water ($diH_2O$)
- Presept cell neutralisation solution: ~5 mg/ml water
- Phosphate buffered saline (PBS): 1 tablet in 200 ml $diH_2O$
- Resazurin stock solution: 10 mM in $diH_2O$
- Resazurin working solution: 10 vol% resazurin stock solution in Hanks' Balanced Salt Solution (HBSS)
- Nitric acid washing solution: 29 ml nitric acid and 0.2 ml Triton X-100 in 970 ml $diH_2O$
- 7N nitric acid solution: 450.74 ml nitric acid in 1000 ml $diH_2O$
- Hydrochloric acid (HCl) washing solution: 1 M in $diH_2O$
- Piranha solution: 75 vol% sulphuric acid in hydrogen peroxide
- Toluene solution: 10 wt% in 3-(Trimethoxysilyl)propyl methacrylate
- Ethanol solution: 70 vol% in $diH_2O$
- Formaldehyde fixing solution: 3.7 vol% in PBS
- Immunohistochemistry (ICC) buffer: 0.1 vol% Triton X-100 in PBS
- 4',6-diamidino-2-phenylindole dihydrochloride (DAPI) stock solution: 10 mg/ml $diH_2O$
- DAPI working solution: 0.01 vol% DAPI stock solution in PBS
- Phalloidin-TRITC stock solution: 0.5 mg/ml absolute methanol
- Phalloidin working solution: 0.1 vol% phalloidin-TRITC stock solution in ICC buffer

## 2.1.2. Cell Line

The cell line utilised in this project was Y201, an immortalised human MSC line derived from the bone marrow. Y201 MSCs constitutively express the interleukin-7 receptor CD317 and harbour the human telomerase reverse transcriptase (hTERT) gene. This cell line exhibits tri-lineage potency capable of differentiation towards adipogenic, osteogenic, and chondrogenic lineages [555]. The University of York generously provided the Y201 hTERT-MSC line.

`

# 2.2. Methods

## 2.2.1. Cell Culture

### Aseptic Working Techniques in Cell Culture

Aseptic techniques were employed throughout all cell culture experiments to maintain experimental integrity. All procedures were performed in a Class II biosafety cabinet with high-efficiency particulate air (HEPA)-filtered laminar flow to ensure a sterile working environment. The following steps were implemented to minimise contamination risk:

- **Hygiene and personal protective equipment:** Hands were thoroughly washed, and a clean lab coat covering the arms up to the wrists was worn. Gloves were worn over the lab coat cuffs.
- **Safety cabinet setup:** The cabinet was turned on, the sash opened, and airflow allowed to stabilise before beginning work.
- **Disinfection:** Gloves were sprayed with 70% IMS upon cabinet entry and changed periodically during prolonged work sessions or when contaminated. All surfaces and items introduced into the cabinet were cleaned with 70% IMS and azo wipes™.
- **Sterility**: All items in direct contact with cells were verified sterile through protective covers, autoclave tape indicators, or manufacturer certification. Temperature-sensitive reagents were sterilised using 0.2 µm filters. Sterile vessels sealed sterile equipment, and cell culture dishes were only opened inside the cabinet.
- **Sterile techniques**: Work was conducted in the cabinet's central airflow region. Direct contact with sterile items was avoided, and proper pipetting technique was maintained by preventing surface contact. Vessels remained closed until needed, and handling over-exposed containers was avoided. Spills were immediately cleaned with azo wipes™ and 70% IMS.

### Preparation of Growth Media

During cell expansion and in vitro experiments, growth medium (GM) was used to support cell growth and maintain cells in an undifferentiated state without additional stimuli. To reduce potential bacterial contamination, an antibiotic penicillin-streptomycin (P/S) solution was added to the GM, resulting in final concentrations of 100 U/ml penicillin and 100 µg/ml streptomycin in the medium. GM volumes varied according to experimental requirements and are detailed in the respective experimental sections.

`

### Serum-Free Growth Medium

Serum-free cell culture was conducted with the StemMACS™ MSC Expansion Medium Kit XF, containing base medium and supplement. Under aseptic conditions, the serum-free GM was prepared by combining the base medium, supplement, and 1% P/S solution. The prepared medium was gently mixed by inversion and aliquoted into sterile 100 ml containers to minimise contamination risk. Aliquots were stored at 4°C for use within one week or at −20°C for long-term storage, according to manufacturer guidelines [604].

### FBS-Containing Growth Medium

For medium containing FBS, DMEM GlutaMAX™, pre-supplemented with high glucose to enhance cell viability and mitigate ammonia build-up, served as the base medium [605, 606]. The FBS-GM was prepared by supplementing DMEM with 10% (v/v) FBS and 1% P/S solution. The prepared medium was gently mixed, aliquoted into sterile 100 ml containers, and stored at 4°C for up to 4 weeks, following the recommended shelf life of FBS [607].

### Human-Serum Growth Medium

Human Mesenchymal-XF Expansion Medium, a pre-supplemented human serum-based medium, was used for human serum culture conditions. The medium was supplemented with 1% P/S solution, gently mixed and aliquoted into 100 ml sterile containers wrapped in aluminium foil to prevent light exposure. According to manufacturer guidelines, aliquots were initially stored at −20°C, then transferred to 4°C for use within one month [608].

## Cell Seeding for Expansion

Vials of cryopreserved cells (1–3 million cells/vial in 1–3 ml suspension) were rapidly thawed and diluted with 7–9 ml pre-warmed FBS-GM. The suspension was centrifuged for 5 min at 1000 revolutions per minute (rpm) to separate cells from the cryopreservation medium. The resultant cell pellet was resuspended in appropriate GM and transferred to T75 flasks containing 10 ml GM total volume. Even cell distribution was achieved through gentle rocking and rotation. Cultures were maintained at 37°C, 5% $CO_2$ and 95% humidity. After 24 h, a complete medium exchange was performed to remove residual dimethyl sulfoxide (DMSO) from cryopreservation. Medium replacement frequency varied by formulation: every 2–3 days for FBS-containing medium and weekly for serum-free conditions. Cells were passaged at approximately 90% confluence for continued expansion, experimental use, or cryopreservation for future use.

`

## Detaching Adherent Cells and Preparing Cell Suspensions

To detach adherent cells, the culture medium was discarded, and the cell layer was rinsed twice with 10 ml HBSS to remove any residual medium. Cells were then covered with 5 ml of 0.25% trypsin-ethylenediamine tetraacetic acid (EDTA) solution and incubated under culture conditions to facilitate enzymatic detachment, which was monitored microscopically. Detachment time varied by the expansion medium: up to 5 min for serum-free and 10 min for serum-supplemented medium. Gentle tapping of the culture vessel facilitated detachment. After successful detachment, trypsin-EDTA activity was neutralised by adding 10 ml of FBS-GM. The cell suspension was then transferred to a 50 ml conical tube and centrifuged for 5 min at 1000 rpm to separate the cells from the GM/trypsin-EDTA solution. Cells were subsequently resuspended in GM for in vitro experiments or cryopreservation medium for freezing.

## Cell Counting

Viable cell quantification utilised Trypan Blue exclusion. Prior to use, a glass hemocytometer and coverslip were cleaned with 70% IMS and assembled with the coverslip affixed by observing Newton's rings. A counting suspension was created by mixing 20 µl of the cell suspension with an equal volume of Trypan Blue. This mixture was then loaded into each chamber of the hemocytometer under the coverslip. Under a 100x microscope objective, live, unstained cells within each of the 16 squares in one chamber were counted, including those touching the right and bottom boundaries. This process was repeated for the second chamber.

## Cell Passaging

When cell cultures reached 70–90% confluency, they were passaged to facilitate further expansion. The passage number was incremented with each detachment and documented on the new flasks. To passage the cells, a cell suspension was prepared as previously described. This suspension was then redistributed into multiple new T75 flasks, each receiving a minimum of 1 million cells in 10 ml fresh GM. Uniform cell seeding was achieved through gentle rocking and rotation of the flasks. Passaged cultures were then returned to the incubator for continued expansion.

## Well Plate Coatings

Cell culture plates were coated with ECM proteins to assess their effects on cell adhesion and proliferation. For gelatine coating, 48-well plates were incubated with 0.1% (w/v) bovine gelatine in sterile di$H_2O$ for 30 min at room temperature. Fibronectin coating was performed using 0.001% (w/v) human fibronectin in sterile PBS for 1 h at room temperature.

`

Following incubation, coating solutions were aspirated, and plates were dried under sterile conditions before cell seeding.

## Cell Seeding for In Vitro Experiments

For in vitro experiments, cell suspensions were prepared as previously described, and viable cell counts were performed to determine the appropriate seeding density. A standardised seeding density of 4000 cells/cm$^2$ was used for all in vitro experiments, based on internal establishment for the cell type. This calculation accounted for the bottom surface area of the well plates. The specific surface area considered for scaffolds is stated in the corresponding sections of each experiment. Unless otherwise noted, each experimental group was seeded in triplicate, with an additional cell-free blank. As detailed in the corresponding sections, the media formulation used depended on the specific experimental requirements. Media volumes were 1 ml per well in 12-well plates, 800 µl in 24-well plates, and 500 µl in 48-well plates, unless otherwise specified.

## Cell Cryopreservation

Highly confluent cells not intended for further expansion, and surplus cells from in vitro experiments were cryopreserved for future use. Cells were detached as previously described, and the cell pellet was resuspended in fresh cryopreservation medium (90% FBS, 10% DMSO) at a density of 1°x°10$^5$ to 3°x°10$^5$°cells/ml. The cell suspensions were then transferred to cryovials, placed in a Mr Frosty™ freezing container and frozen at −80°C for 24 h before being transferred to −196°C for long-term storage.

## Resazurin Reduction Assay for Cell Metabolic Activity

The resazurin reduction assay was used to assess cell metabolic activity. This method relies on the ability of viable cells to convert the blue, non-fluorescent dye resazurin into the pink fluorescent product resorufin through mitochondrial dehydrogenase enzymes [609] (Figure 23A). Resorufin diffuses into the surrounding medium rather than accumulating in cells, contributing to the assay's low toxicity and allowing for continued culture or additional analyses [610, 611].

For the assay, the medium was aspirated from cell culture plates, and wells were washed twice with HBSS. For scaffold-free experiments, the same plates were used to add the resazurin working solution. For 3D experiments, scaffolds were transferred to a new plate before adding the working solution to ensure that only cells attached to the scaffold were measured. To protect the light-sensitive assay, the working solution was added under minimal light and plates were loosely covered with aluminium foil before incubation at 37°C and 5%

`

$CO_2$ for 2 h. After incubation, the resazurin solution changed colour from blue-violet to pink, with the degree of change proportional to metabolic activity (Figure 23).

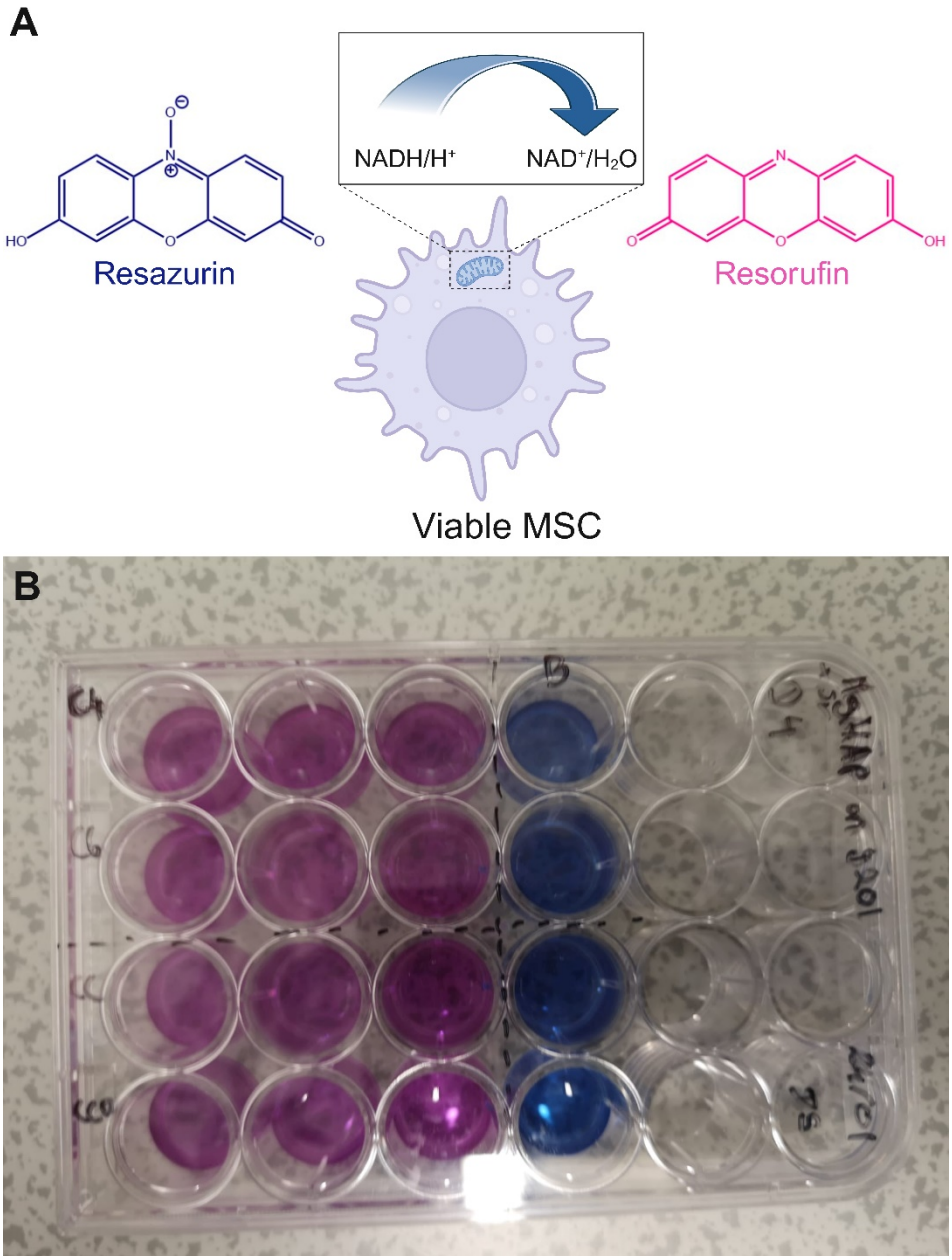


*Figure 23 A) Resazurin assay reaction principle. B) Resazurin solution on Y201 MSCs (violet: cells; blue: blanks) after 2 h incubation. Image created on www.biorender.com.*

A 200 µl aliquot from each well was then transferred in triplicate to a 96-well plate, following a specific pattern to prevent interference from adjacent wells' fluorescence (Figure 24).

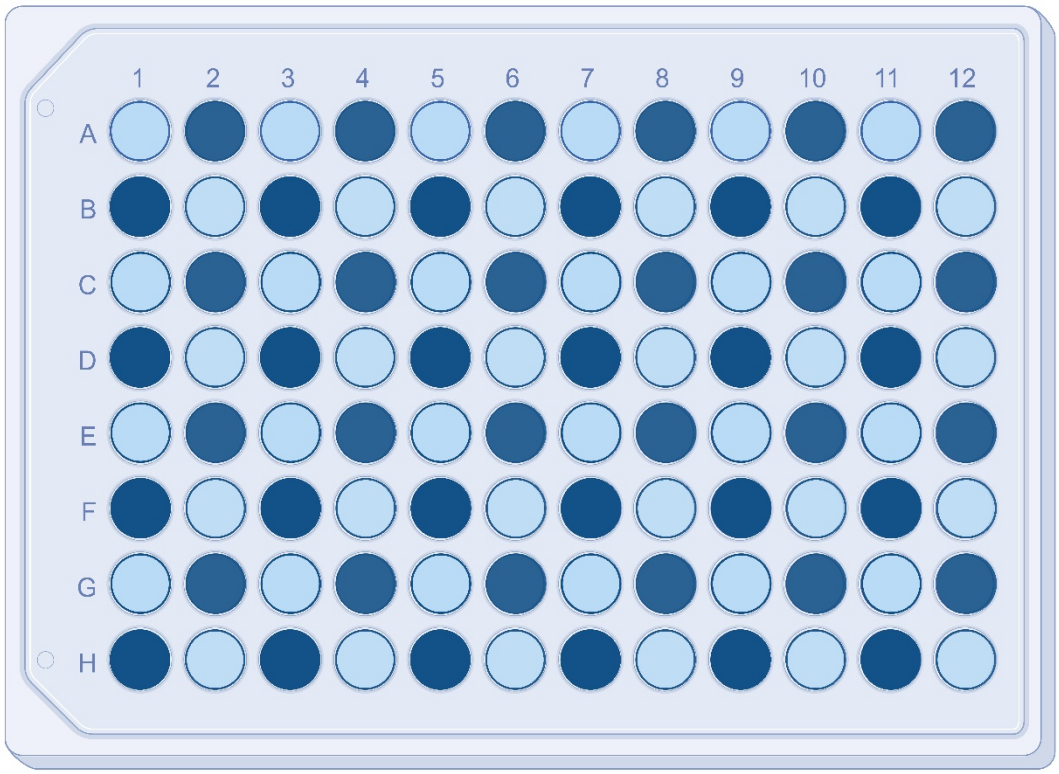


*Figure 24 Pipetting pattern for resazurin working solution in a 96-well plate. Image created on www.biorender.com.*

The 96-well plates were analysed in a plate reader at an excitation wavelength of 540 nm and an emission wavelength of 590 nm. The average fluorescence value (in arbitrary units) for each sample was corrected with the background fluorescence of cell-free blanks. These corrected values were used to determine the relative metabolic activity. After analysis, cell culture plates were washed twice with HBSS and either prepared for further analysis or replenished with fresh medium for continued experimentation.

## 2.2.2. Synthesis and Evaluation of Hydroxyapatite

### Preparation of Precursor Phases

Precursor ions for non-substituted (nsHAP) and substituted HAP (sHAP) precipitation were sourced from orthophosphoric acid ($H_3PO_4$) for phosphorus, calcium hydroxide ($Ca(OH)_2$) for calcium, magnesium nitrate ($MgN_2O_6$) for magnesium, and strontium nitrate ($SrN_2O_6$) for strontium. Cation precursors (Ca, Mg, Sr) were combined in the basic phase, while the phosphate precursor formed the acidic phase. An overview of the ion sources and the phase they were incorporated is given in Table 14.

`

*Table 14 Ion sources for HAP synthesis.*

| Ion | Ion Source | Phase |
|---|---|---|
| Ca | $Ca(OH)_2$ | Basic |
| P | $H_3PO_4$ | Acidic |
| Mg | $MgN_2O_6$ | Basic |
| Sr | $SrN_2O_6$ | Basic |

Precursor quantities were calculated to achieve a final Ca concentration of 0.54 mol, with P ions proportioned to maintain a 1.66 Ca/P ratio. Mg and Sr quantities were determined as mol% replacements of Ca according to the intended substitution degrees. The selected solvent was di$H_2O$ due to its ability to produce smaller particles with improved dispersibility and needle-like HAP formation, which favours in vitro osteoblast differentiation [612, 613].

The acidic phase was prepared by combining $H_3PO_4$ (31.85 g) with di$H_2O$ (500 ml). For the basic phase, $Ca(OH)_2$ (40 g) was dissolved in di$H_2O$ (500 ml). For sHAP synthesis, $Ca(OH)_2$ quantities were adjusted for substituents as per Table 15, and di$H_2O$ volume was reduced to 300 ml. Mg and Sr precursors were individually mixed with di$H_2O$ (100 ml each) before addition to the calcium phase. Table 15 provides an overview of precursor amounts used for each targeted formulation. Chemical impurities were not accounted for in formulations Mg20Sr20, Mg5Sr20, Mg20Sr5, and Mg5Sr5 (in the 5-20% substitution range), while adjustments were made in formulations Mg5Sr5 (in the 5-10% substitution range), Mg5Sr10, Mg10Sr5, and Mg10Sr10.

*Table 15 Quantities of $MgN_2O_6$, $SrN_2O_6$, $Ca(OH)_2$, and $H_3PO_4$ for the synthesis of sHAP at different substitution degrees. Formulations adjusted for impurities are denoted with "A".*

| Acronym | Mg [%] | Sr [%] | Ca [%] | $MgN_2O_6$ [g] | $SrN_2O_6$ [g] | $Ca(OH)_2$ [g] | $H_3PO_4$ [g] |
|---|---|---|---|---|---|---|---|
| Mg20Sr20 | 20 | 20 | 60 | 27.69 | 22.85 | 24 | 31.85 |
| Mg5Sr20 | 5 | 20 | 75 | 6.92 | 22.85 | 30 | 31.85 |
| Mg20Sr5 | 20 | 5 | 75 | 27.69 | 5.71 | 30 | 31.85 |
| Mg5Sr5 | 5 | 5 | 90 | 6.92 | 5.71 | 36 | 31.85 |
| Mg5Sr5$^A$ | 5 | 5 | 90 | 6.92 | 5.71 | 36.81 | 37.03 |
| Mg5Sr10$^A$ | 5 | 10 | 85 | 6.92 | 11.43 | 34.76 | 37.03 |
| Mg10Sr5$^A$ | 10 | 5 | 85 | 13.85 | 5.71 | 34.76 | 37.03 |
| Mg10Sr10$^A$ | 10 | 10 | 80 | 13.85 | 11.43 | 32.72 | 37.03 |

All precursor phases were prepared on the same day to minimise carbonation under atmospheric conditions and were continuously stirred to prevent particle sedimentation and aggregation.

## Development of a Continuous Synthesis Method

To enable scalable, uninterrupted HAP production, several continuous synthesis systems were developed, as summarised in Table 16.

*Table 16 Overview of different synthesis methods used in this chapter.*

| Acronyms | Synthesis Method |
|---|---|
| C1 | Mixing column with $^{3}/_{8}$ inch OD under sonication |
| BPT | Bifurcation plastic tube under sonication |
| BGT | Bifurcation glass tube under sonication |
| B2B | Beaker-to-beaker under sonication |
| FCR | Flow-cell reactor |
| C2 | Mixing column with ½ inch OD under sonication |

## Synthesis via the C1 Column Method

During the synthesis process, the acidic and basic precursors were continuously mixed to prevent particle settling and aggregation. The precursors were transported through plastic tubing via peristaltic pumps to a bifurcation connector, where they combined. The combined precursors then passed through a stainless steel mixing column (outer diameter $^{3}/_{8}$ “) consisting of a series of fixed right- and left-handed mixing elements to facilitate blending. This mixing column was submerged in a sonication water bath operating at 100% amplitude and power. After passing through the column, the synthesised precursor suspension was collected in a beaker. A schematic of this synthesis process is provided in Figure 25.

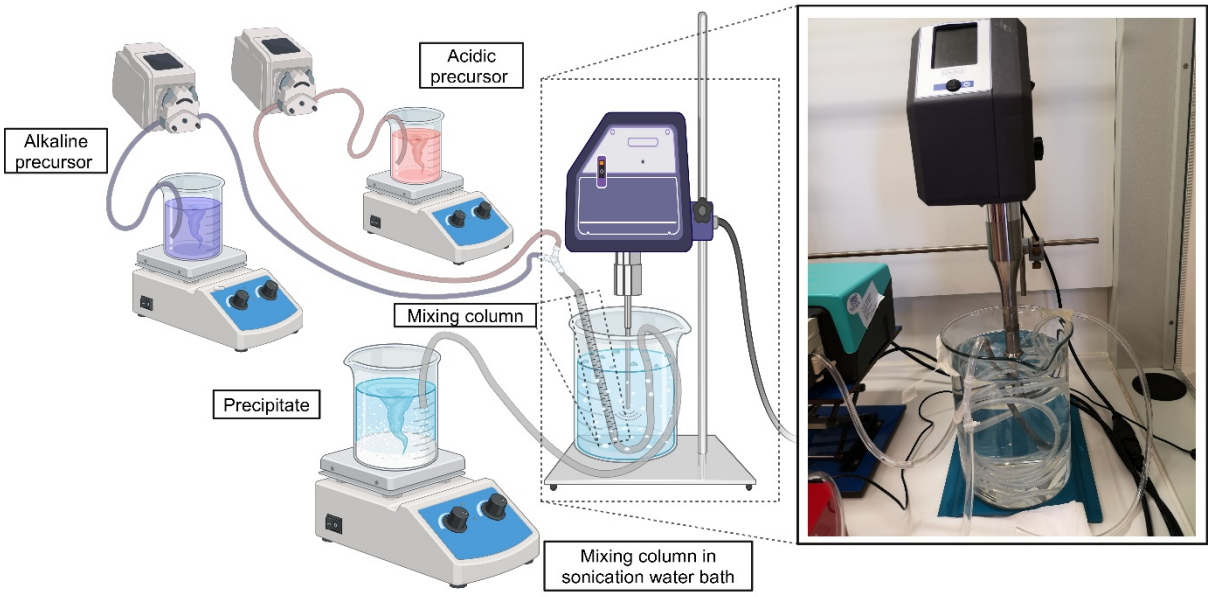


*Figure 25 Schematic of the synthesis with the C1 column method. Alkaline and acidic precursors were transported through a mixing column in a sonication water bath and collected in a beaker. Image created on www.biorender.com.*

## Synthesis via the BPT Bifurcation Tube Method

In contrast to the C1 column-based synthesis approach, the BPT method eliminated the mixing column. Instead, the combined acidic and basic precursors passed through plastic tubing submerged in a sonication water bath operating at 100% amplitude and power after

their initial combination at the bifurcation point. A schematic of this BPT synthesis process is provided in Figure 26.

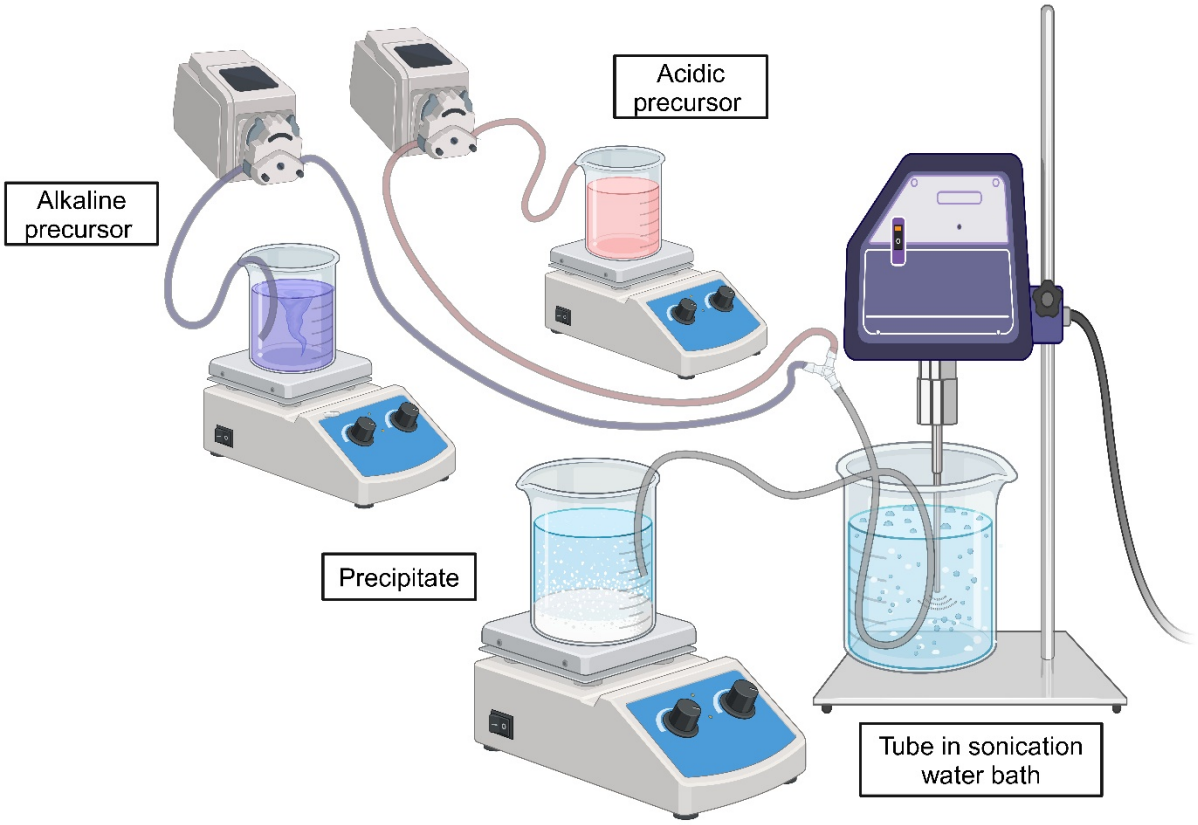


*Figure 26 Schematic of the synthesis with the BPT method. Alkaline and acidic precursors were transported through a tubing system in a sonication water bath and collected in a beaker. Image created on www.biorender.com.*

### Synthesis via the BGT Bifurcation Tube Method

In contrast to the BPT method's plastic bifurcation tube, the BGT approach utilised a glass bifurcation tube with a larger diameter to avoid clogging. The bifurcation tube and subsequent plastic tubing, where the combined precursors flowed, were submerged in a sonication water bath operating at 100% amplitude and power. A schematic of this BGT process is given in Figure 27.

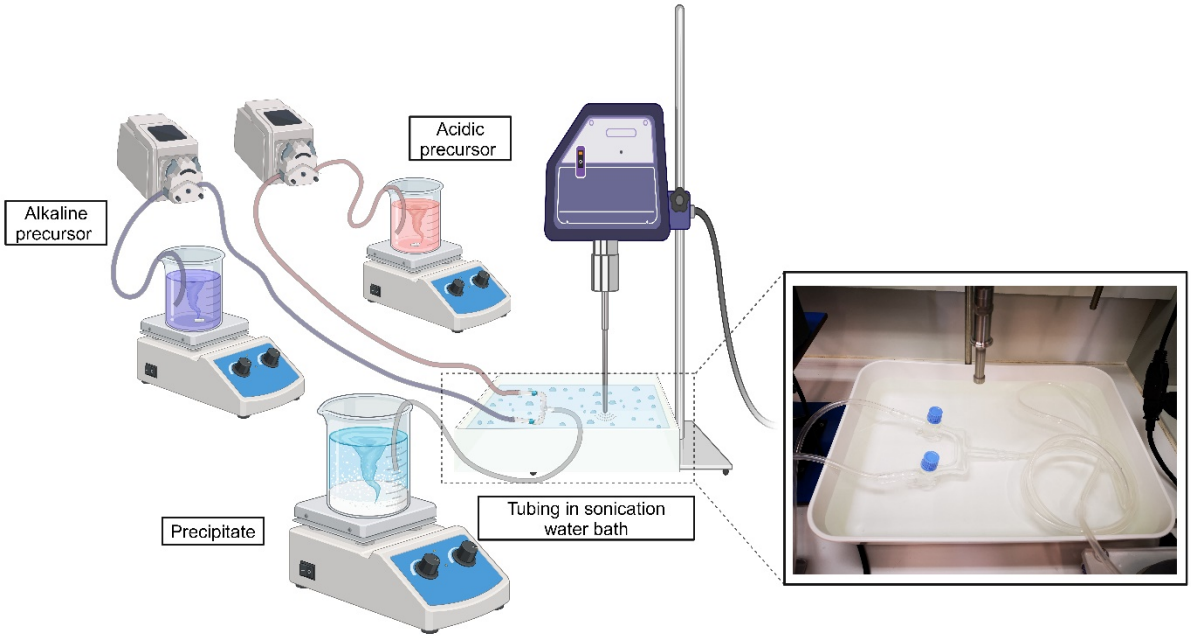


*Figure 27 Schematic of the synthesis with the BGT method. Alkaline and acidic precursors were transported through a tubing system in a sonication water bath and collected in a beaker. Image created on www.biorender.com.*

### Synthesis via the B2B Method

In this setup, the precursors were transported separately into an open beaker and mixed using an overhead stirrer. The beaker was submerged in a sonication water bath operating at 100% amplitude and power. A schematic is provided in Figure 28.

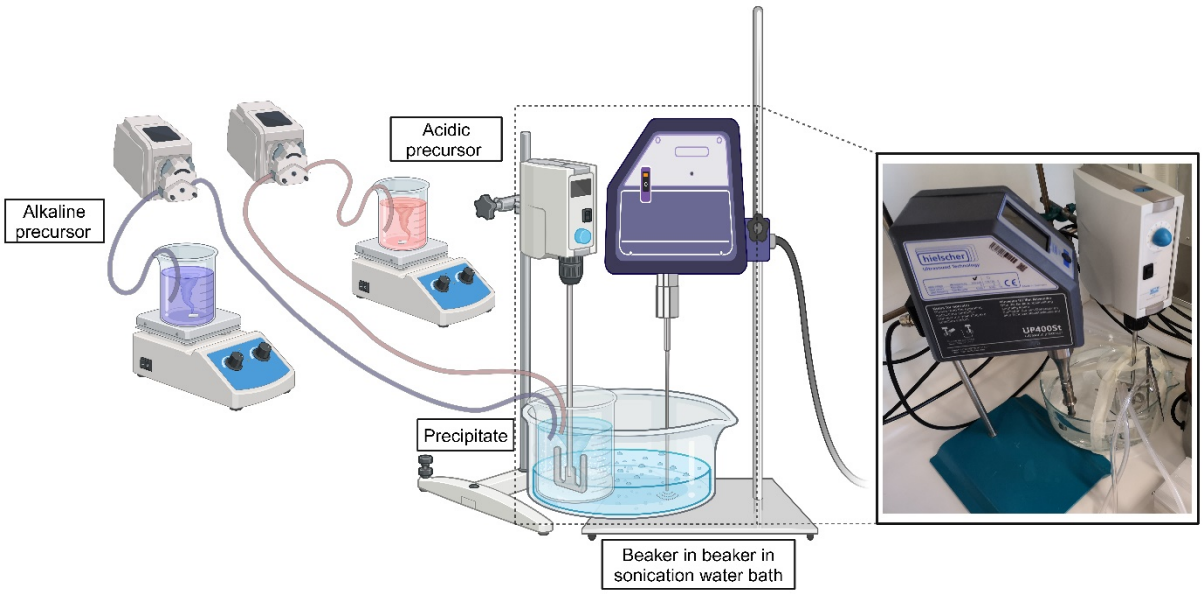


*Figure 28 Schematic of the synthesis with the B2B method. Alkaline and acidic precursors were transported through a tubing system in a beaker placed in a sonication water bath. Image created on www.biorender.com.*

`

## Synthesis via the Flow-Cell Method

In this approach, precursors were combined in a plastic bifurcation tube before entering a sonication flow cell chamber, where they underwent direct sonication at 100% amplitude and power. The flow cell was filled through a lower inlet and emptied through a higher outlet, ensuring continuous contact of the suspension with the probe before being released. A schematic of this process is shown in Figure 29. The temperature within the flow cell reached approximately 50°C during synthesis. Sonication in the flow cell led to cavitation formation through the creation and collapse of vacuum bubbles, which have been shown to influence chemical reactions, especially in the synthesis of nanoparticles, where they can facilitate particle size reduction [614].

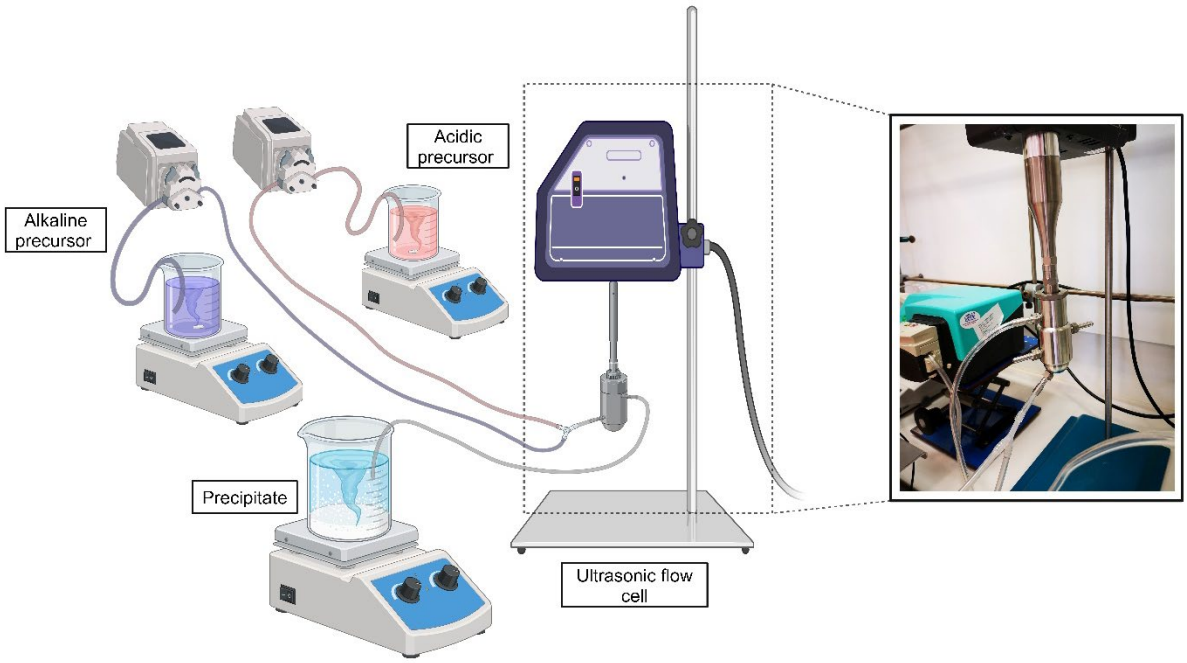


*Figure 29 Schematic of the synthesis with the flow cell method. Alkaline and acidic precursors were transported via a tubing system into a flow cell and collected in a beaker. Image created on www.biorender.com.*

## Synthesis via the C2 Synthesis Column

Similar to the C1 column method, this C2 approach used a column with a larger diameter (outer diameter ½") to mitigate clogging. The precursors were transported through plastic tubing (4.8 mm inner diameter) via two peristaltic pumps, set to a flow rate of 1.38 ml/s to a connector, and then into a larger tube (12.7 mm inner diameter) connected to the column. The suspension was collected in a beaker after passing through the column. A schematic is provided in Figure 30.

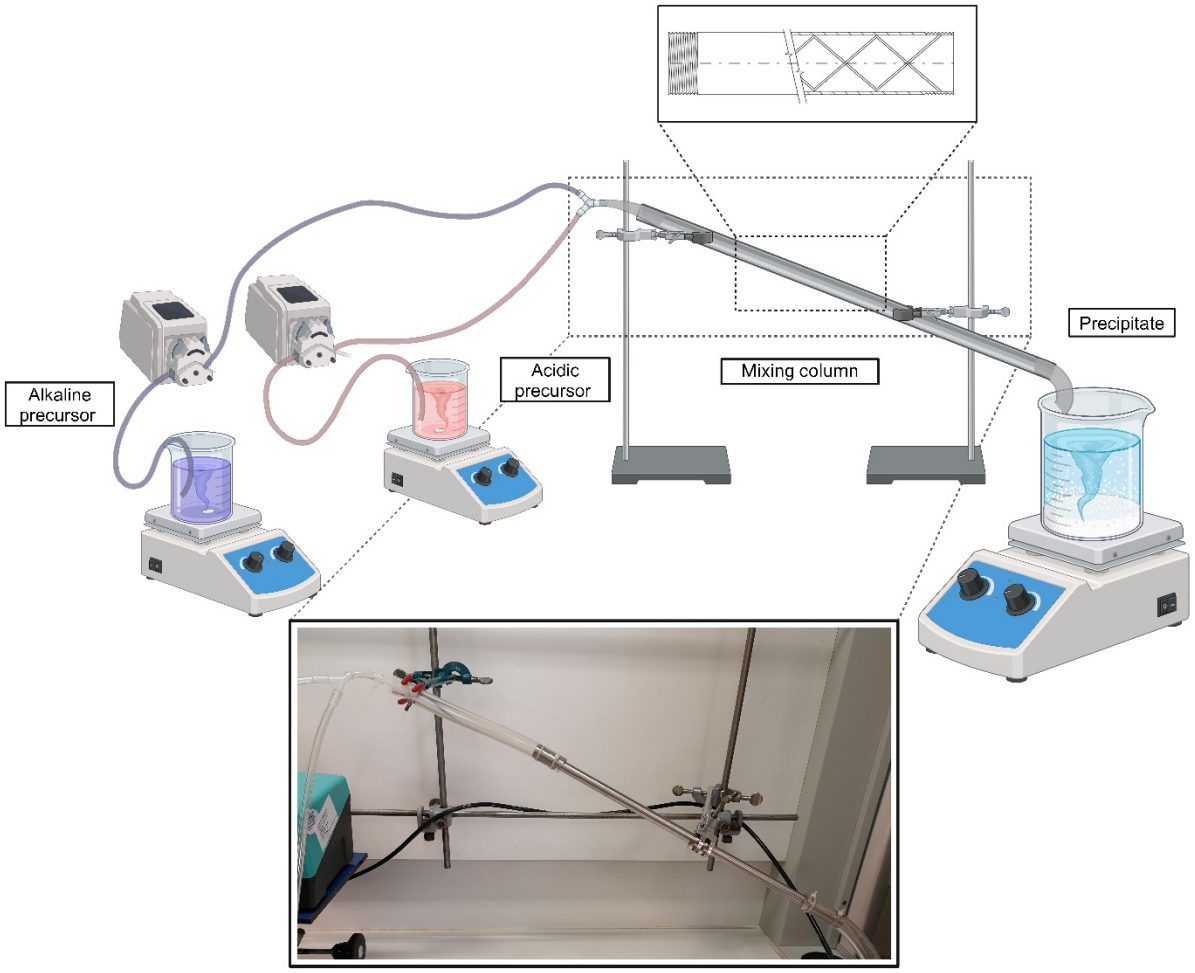


*Figure 30 Schematic of synthesis with C2 column method. Alkaline and acidic precursors were transported through a mixing column and collected in a beaker. Image created on www.biorender.com.*

## Processing

Following synthesis, the suspension underwent incubation with continuous stirring on a magnetic stirrer at a constant temperature of 37°C. After incubation, the suspension was subjected to a series of processing steps:

1. **Filtration**: The suspension was divided into 50 ml aliquots and centrifuged at 6000 rpm for 10 min to separate the solid and liquid phases. The supernatant was discarded.
2. **Washing**: The solid phase was washed three times to remove residual reactants. Each wash involved re-suspending the solid in di$H_2O$, followed by centrifugation.
3. **Drying**: The washed solid pellets were dried in an oven at 40°C for approximately 24 h until completely dry.
4. **Grinding**: The dried solid pellets were manually pulverised using a grinder.

The pH of the supernatant was measured after synthesis, incubation, and each washing step to monitor changes in acidity/alkalinity. These processing steps were consistently applied across all synthesis methods and concentrations investigated. A schematic of the post-synthesis processing is provided in Figure 31.

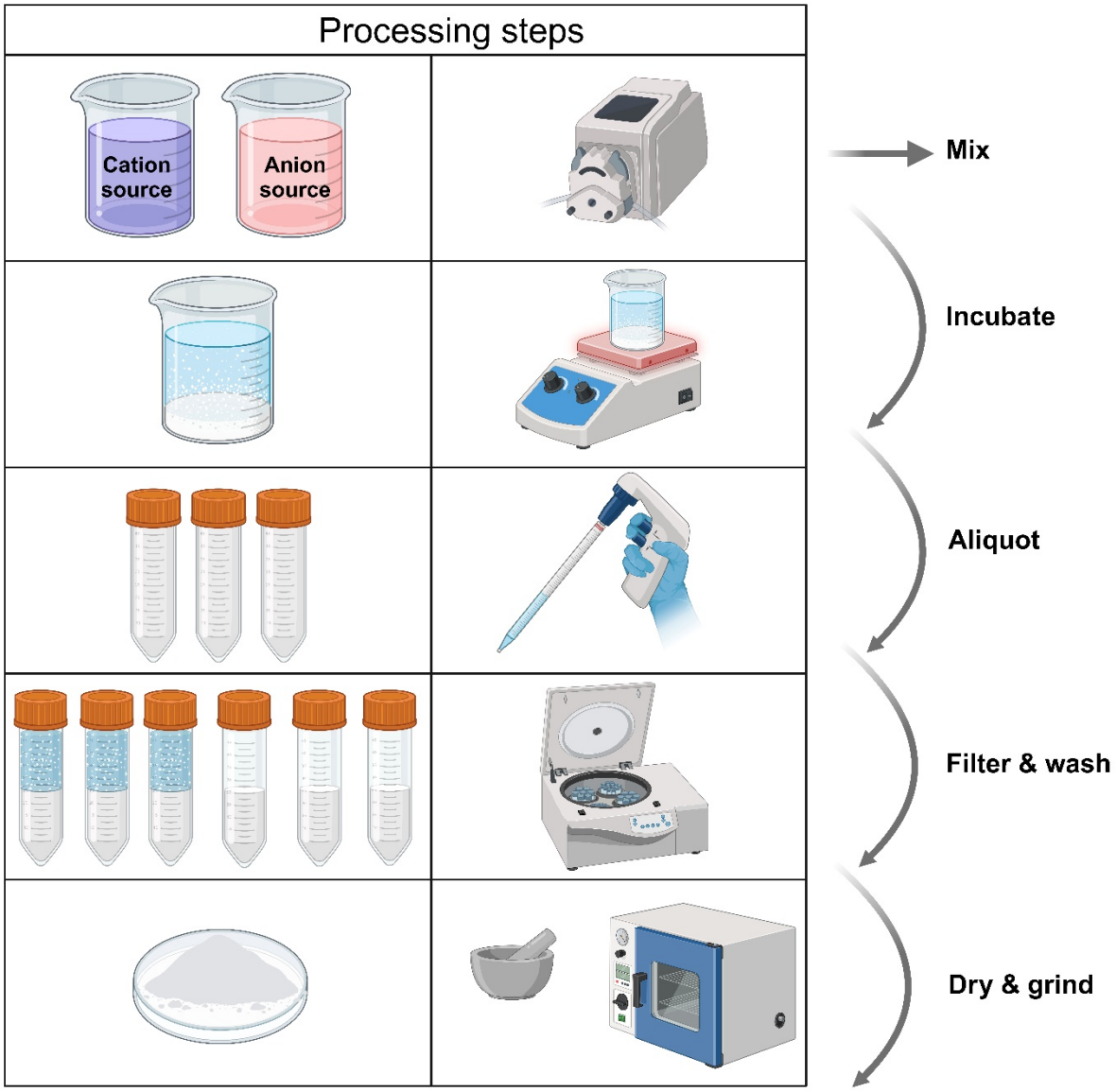


*Figure 31 Processing steps of precipitates after synthesis. Image created on www.biorender.com.*

## ICP-OES Analysis

Inductively coupled plasma optical emission spectrometry-optical emission spectrometer (ICP-OES) is a widely used analytical technique that determines the elemental composition of samples. It is based on the principle of exciting atoms in a plasma state, causing them to emit characteristic radiation when returning to their ground state. This emitted

`

radiation, containing distinct wavelengths, is detected and measured by a spectrometer, allowing for the identification and quantification of elements present in the sample [615].

Prior to ICP-OES analysis, all glassware (volumetric flasks, pipettes) was thoroughly cleaned with nitric acid washing solution, rinsed with di$H_2O$, and dried at 125°C for 1 h, in accordance with the laboratory's SOP. Standard curves were established for the quantification of Ca, P, Mg, and Sr in precipitates. A series of standards (Table 17) were prepared from internal stock solutions, with yttrium added as an internal standard to compensate for instrumental and matrix-related variations.

*Table 17 Concentrations of standards in ppm.*

| | Ca | P | Mg | Sr |
|---|---|---|---|---|
| **STD 1** | 20 | 10 | 1 | 1 |
| **STD 2** | 30 | 20 | 5 | 5 |
| **STD 3** | 50 | 30 | 10 | 10 |
| **STD 4** | 100 | 50 | 20 | 20 |
| **STD 5** | 125 | 100 | 30 | 30 |

Standard solutions were prepared by combining specific volumes of stock solutions with 7 N nitric acid and the internal standard, as detailed in Table 18.

*Table 18 Volumes of stock solutions [ml] used to prepare standards with varying concentrations. A) Derived from a 10 ppm internal stock dilution. B) Derived from a 200 ppm internal stock dilution. Y = internal standard.*

| | Ca | P | Mg | Sr | Nitric Acid | Standard[B] |
|---|---|---|---|---|---|---|
| **STD 1** | 2 | 1 | 10[A] | 10[A] | 2 | 1 |
| **STD 2** | 3 | 2 | 0.5 | 0.5 | 2 | 1 |
| **STD 3** | 5 | 3 | 1 | 1 | 2 | 1 |
| **STD 4** | 10 | 5 | 2 | 2 | 2 | 1 |
| **STD 5** | 12.5 | 10 | 3 | 3 | 2 | 1 |
| **Blank** | / | / | / | / | 2 | 1 |

For sample preparation, approximately 20 mg (± 5 mg) of the synthesised material was mixed with 2 ml 7 N nitric acid and 10 ml di$H_2O$. The suspension was then sonicated for 10 min at full power in a sonication water bath to ensure homogeneous dispersion and breakdown of large particles [616].

## FTIR Analysis

Fourier transform infrared spectroscopy (FTIR) is a widely used analytical technique that detects the energy-dependent oscillation of atoms relative to their equilibrium positions, allowing for the identification of chemical bonds and functional groups. The method operates by exciting molecular vibrations with infrared radiation and measuring the resulting absorption or transmission spectra [617].

`

For FTIR analysis, samples weighing 0.5–1.0 mg were combined with 100 mg of potassium bromide (KBr), manually ground into a fine powder, and compacted into a disc using a hydraulic press at 8 t for 50 s. The disc was then analysed using an FTIR spectrometer, with each sample undergoing 64 scans at a resolution of 4 $cm^{-1}$ to determine absorbance. A blank measurement was taken prior to sample analysis. If the highest peak in the absorbance spectrum exceeded one, the experiment was repeated with a reduced sample amount to comply with the Beer-Lambert Law [617, 618]. Graphs were plotted using the Origin 2019 software (OriginLab Corporation, USA).

## $CO_3^{2-}/PO_4^{3-}$ Ratio and Splitting Factor Calculations

FTIR analysis was used to conduct a semi-quantitative assessment of the carbonate content through ratios of carbonate to phosphate ($CO_3^{2-}{}_{1420}/PO_4^{3-}{}_{1033}$) and carbonate to hydroxyl ($CO_3^{2-}{}_{1420}/OH^-{}_{3572}$), following a previous methodology [619]. Peak areas were integrated at specific wavenumbers: 1420 $cm^{-1}$ for $CO_3^{2-}$ (baselined at 1520–1350 $cm^{-1}$), 1033 $cm^{-1}$ for $PO_4^{3-}$ (baselined 900–1180 $cm^{-1}$), and 3572 $cm^{-1}$ for $OH^-$ (baselined 3800–2500 $cm^{-1}$). Ratios were calculated by dividing the $CO_3^{2-}$ area by the $PO_4^{3-}$ or $OH^-$ area. A schematic of the peak areas used for the calculations is presented in Figure 32.

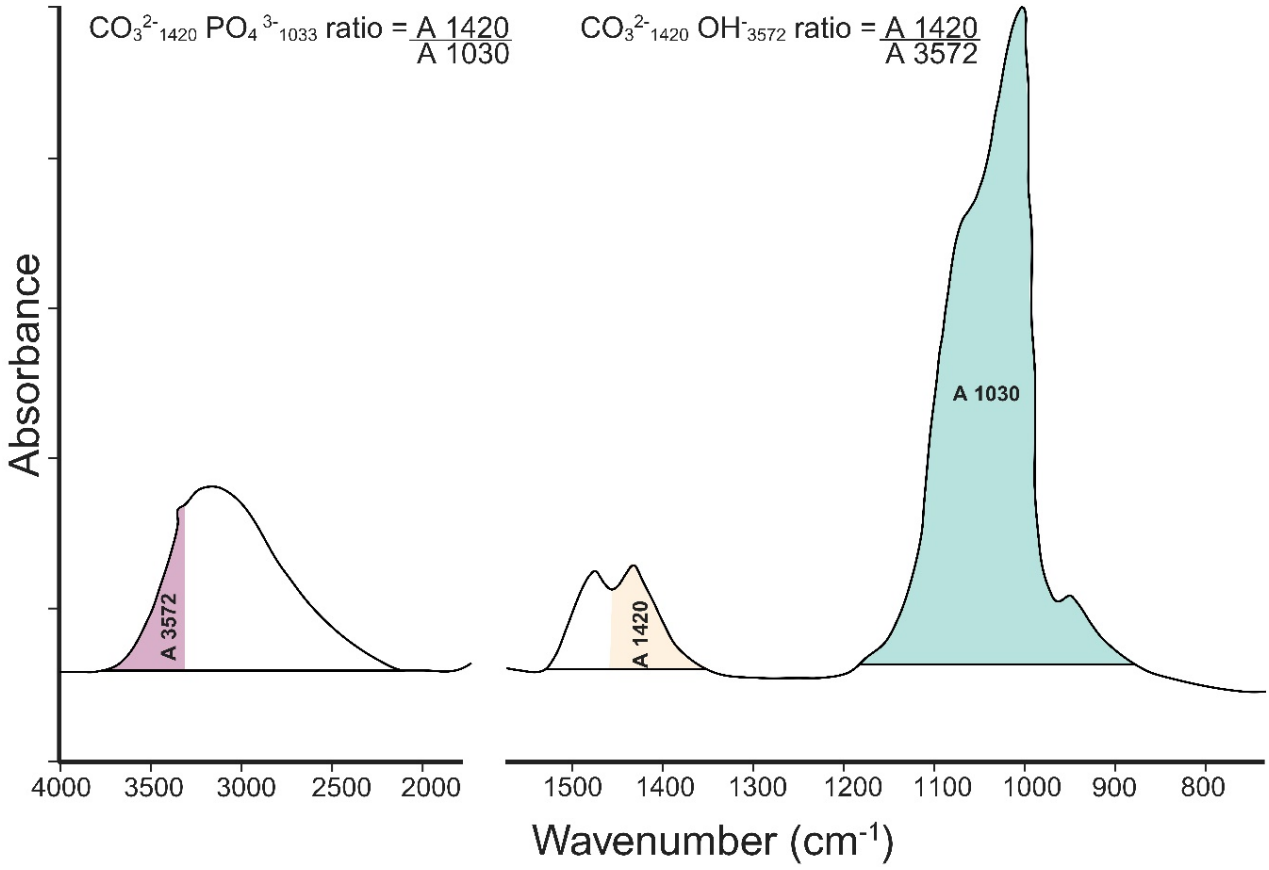


*Figure 32 Illustration highlighting the peak areas of $CO_3^{2-}$, $PO_4^{3-}$ and $OH^-$ bands in an FTIR spectrum for calculating the $CO_3^{2-}{}_{1420}$ $PO_4^{3-}{}_{1033}$ and $CO_3^{2-}{}_{1420}$ $OH^-{}_{3572}$ ratios. Image created on www.biorender.com.*

`

Additionally, the splitting factor (SF) was calculated as a quantitative measure to estimate the crystalline nature of the material [620-622]. The SF quantifies the split in the $PO_4$ bond bending peaks, which correlates positively with increasing crystallinity, and is calculated using the formula [623]:

$$SF = \frac{a+b}{c}$$

where “a” and “b” represent the absorbance at 603 and 565 $cm^{-1}$, respectively, and “c” represents the absorbance of the valley between the peaks (see Figure 33) [622]. Prior to calculations, a baseline of 480 and 660 $cm^{-1}$ was subtracted from the absorbance values.

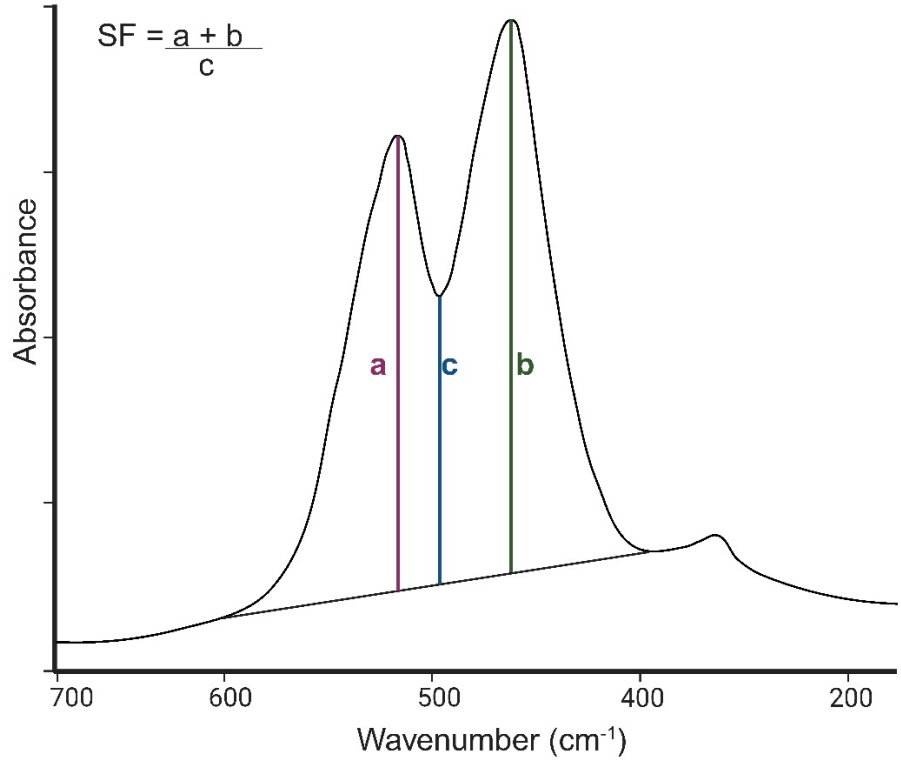


*Figure 33 Illustration of the $PO_4$ bands in an FTIR spectrum for calculating the SF. Image created on www.biorender.com.*

Peak values and integral surface areas for the $CO_3^{2-}/PO_4^{3-}$ ratio and SF factor calculations were derived from the Origin 2019 software.

## XRD Analysis

X-ray diffraction (XRD) analysis is a widely used technique that provides insights into the crystalline structure of materials. The principle involves directing X-rays at a crystalline sample, causing the X-rays to diffract based on the atomic arrangement within the material. The resulting diffraction pattern can be analysed to determine the structure and composition of the crystalline substance [624].

`

In this project, the XRD analysis of all samples was conducted by an external contractor, Specialchimica (S.A.S.).

## Biological Testing of sHAP

An in vitro assessment was conducted to evaluate the cytotoxicity of the synthesised sHAP powders at a total concentration of 1000 µg/ml cell culture medium.

### Preparation of sHAP Suspensions

The sHAP stock suspensions used for in vitro analysis were prepared by dispersing gamma-sterilised sHAP powders in di$H_2O$ at a 10 mg/ml concentration. Previous research has demonstrated that gamma-sterilisation does not compromise the structural integrity of HAP [308]. To ensure uniform particle dispersion, the suspensions underwent a two-step sonication process in an ultrasonic water bath at 100% amplitude for 15 min, followed by 1 min vortex mixing, repeated in two intervals.

### In Vitro Experiments

The in vitro assessment was conducted using Y201 MSCs seeded in 24-well plates at 4000 cells/$cm^2$ density and cultured in 720 µl of GM per the established SOP. In addition to the experimental groups with sHAP treatment, standard cell culture (SCC) controls and blanks were included to enable comparisons and account for any background interference from the sHAP powders and medium during light-sensitive assays. Analysed groups comprised:

- Mg5Sr5C: Cells treated with Mg5Sr5 sHAP
- Mg5Sr5B: No cells, Mg5Sr5 sHAP
- Mg10Sr5C: Cells treated with Mg10Sr5 sHAP
- Mg10Sr5B: No cells, Mg10Sr5 sHAP
- SCC: Cells only
- B: Medium only

The plate layout is illustrated in Figure 34.

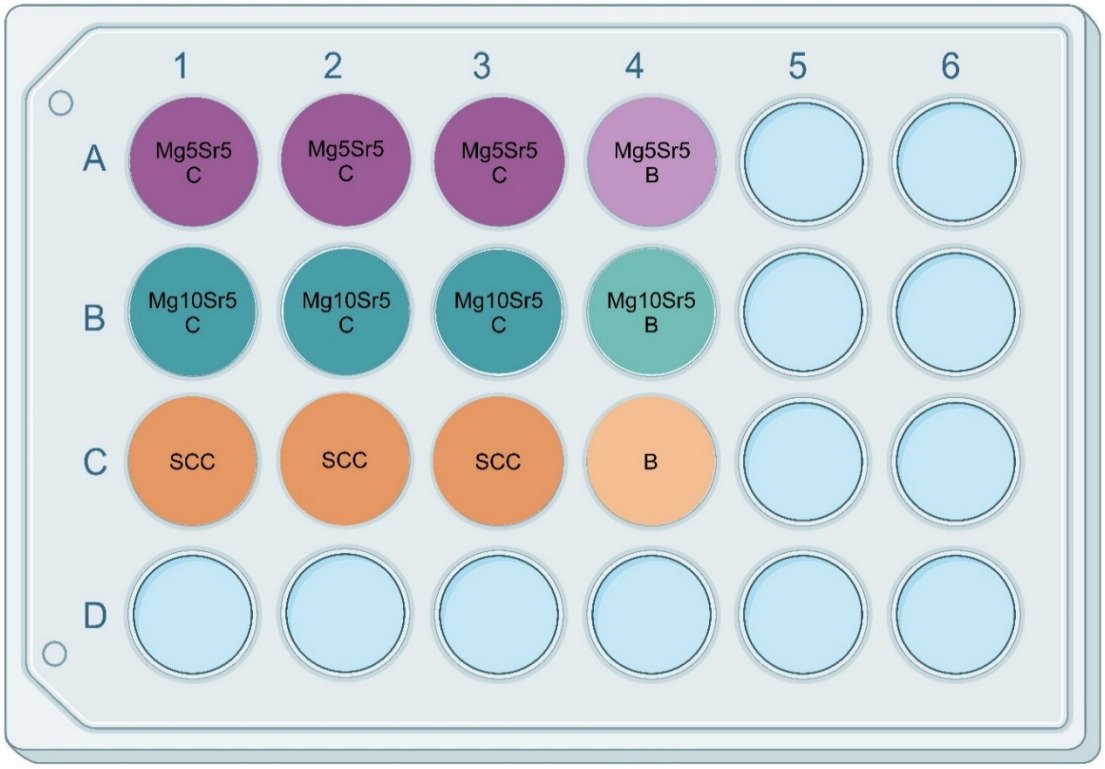


*Figure 34 Plate organisation for in vitro testing of sHAP. Image created on www.biorender.com.*

On day, two post-seeding, experimental groups were treated with sHAP. Transwell inserts with a 1 µm pore size were aseptically placed into the wells of these groups using sterile tweezers. The sHAP suspensions were vortex-mixed for 1 min, and 80 µl was added to the corresponding transwells to achieve a final concentration of 1 mg/ml medium in the experimental groups, while SCC control wells received 80 µl of di$H_2O$. The experimental setup is illustrated in Figure 35.

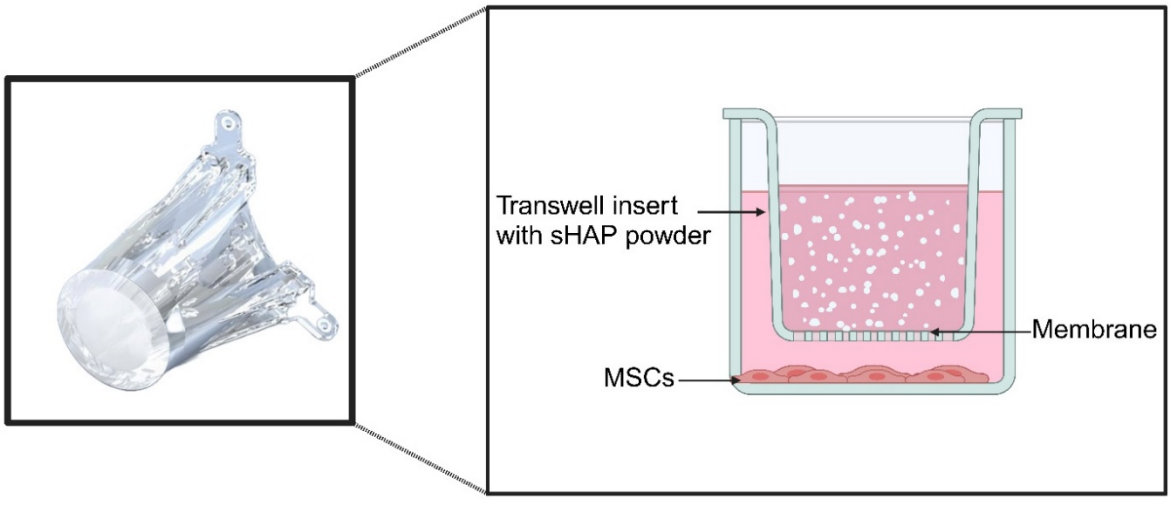


*Figure 35 Schematic of a transwell set-up. Image created on www.biorender.com.*

`

## 2.2.3. PCL Synthesis and Methacrylation

### Synthesis of 4-arm PCL

The synthesis of 4-arm PCL (4-PCL) was conducted through an ROP process, employing ε-caprolactone as the monomer, pentaerythritol as the initiator, and tin(II) 2-ethylhexanoate (stannous octoate) as the catalyst (Figure 36).

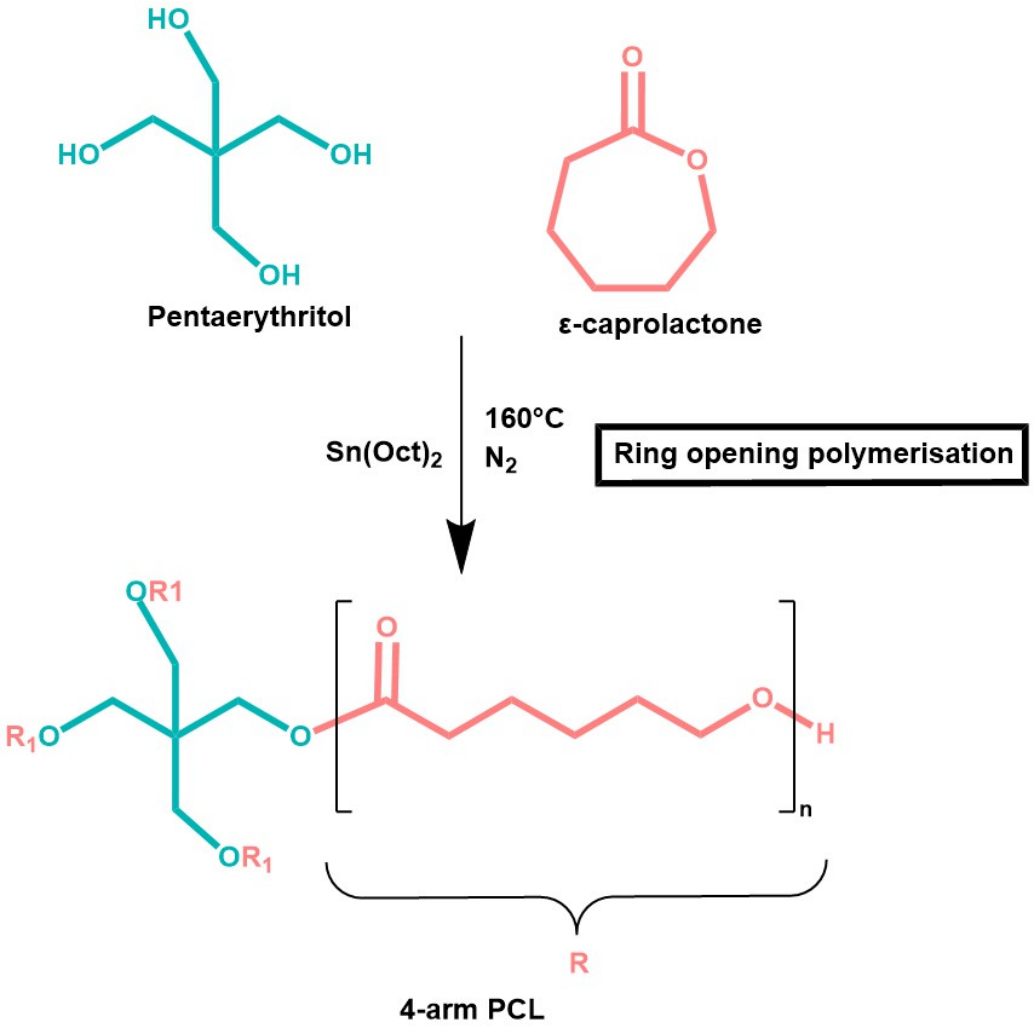


*Figure 36 The chemical reaction of 4-PCL synthesis via ROP, n = 2 (theoretically).*

The procedure followed a method previously described by Dikici et al. [457]. In a controlled nitrogen atmosphere, a homogeneous mixture of 12 g pentaerythritol (molecular weight (Mw) = 136.15 g/mol) and 80.49 g ε-caprolactone (Mw = 114.14 g/mol) was introduced into a three-neck, round-bottomed flask. The reaction vessel was immersed in a silicone oil bath and heated to 160°C while being continuously stirred at 200 rpm using a magnetic stirrer. Once pentaerythritol had fully dissolved (~30 min), and the solution was clear, a single drop (~30 µl) of stannous octoate (1.25 g/ml) was introduced via the central neck of the flask. A schematic of the synthesis process is shown in Figure 38.

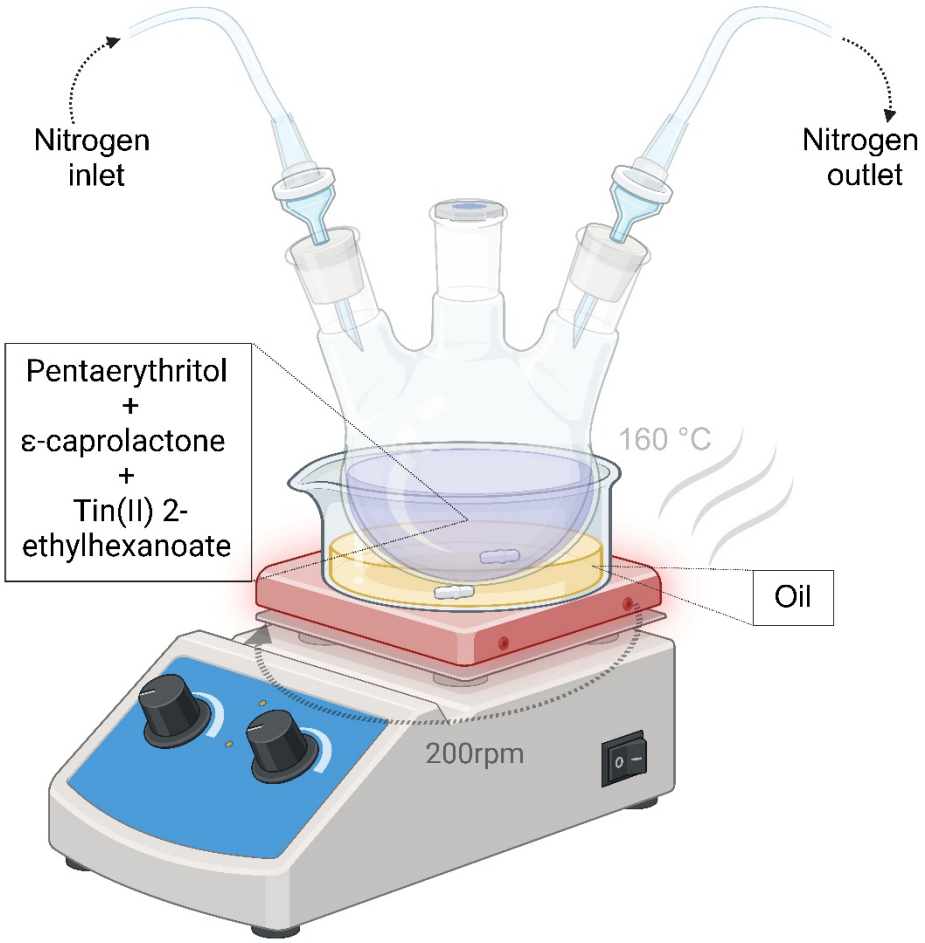


*Figure 37 Schematic of the synthesis of 4-PCL with a three-neck, round-bottomed flask and heat plate. Image created on www.biorender.com.*

The reaction mixture was maintained under these conditions overnight to facilitate the formation of 4-PCL oligomers. Following the reaction period, the flask was removed from the oil bath and allowed to cool gradually to ambient temperature. Following previous literature, this protocol was designed to achieve a polymerisation degree of two repeats per arm [457].

## PCL Methacrylation

Following synthesis, 4-PCL oligomers were functionalised by introducing photo-crosslinkable methacrylate groups to the hydroxyl-terminated ends, adhering to the protocol described by Dikici et al. [457] and Field et al. [459]. A schematic representation of the chemical reaction for the methacrylation functionalisation is illustrated in Figure 38.

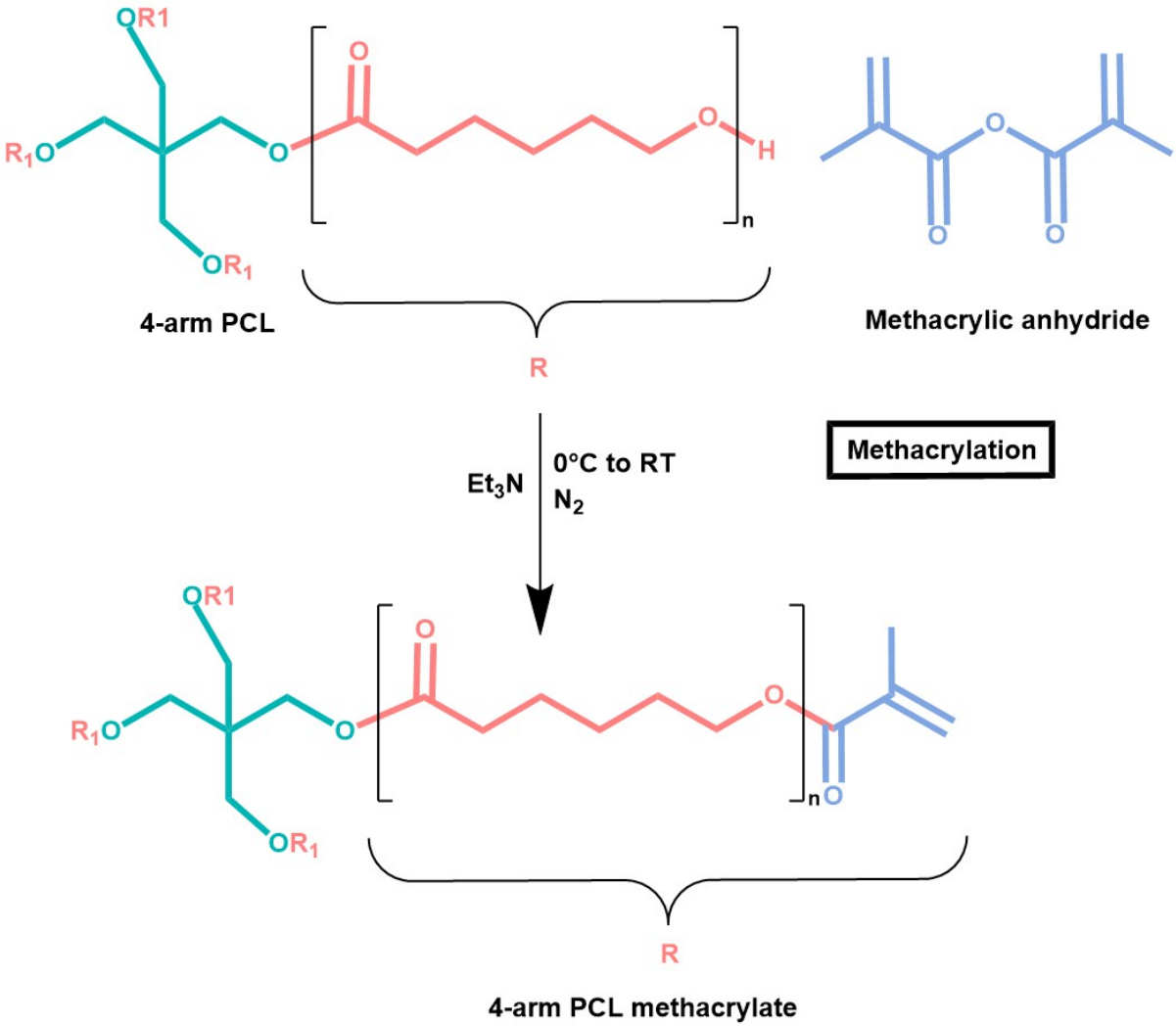


*Figure 38 The chemical reaction of 4-PCL methacrylation, n = 2 (theoretically).*

The methacrylation process began with the dissolution of 91 g of synthesised 4-PCL oligomers (Mw = 1049.3 g/mol) in 300 ml of dichloromethane (DCM) under ambient conditions. This solution was then transferred to a 3-necked round-bottomed flask under nitrogen flow, followed by the addition of 52.65 g triethylamine ($Et_3N$) (Mw = 101.19 g/mol). An additional 200 ml of DCM was introduced to ensure complete dissolution, and the reagents were continuously stirred at 375 rpm while cooled in an ice bath. Next, 80.22 g methacrylic anhydride (MAA) (Mw = 154.16 g/mol) was dissolved in 100 ml of DCM and added to the reaction mixture via a dropping funnel system at approximately 1 drop/s. A schematic of the methacrylation process is shown in Figure 39.

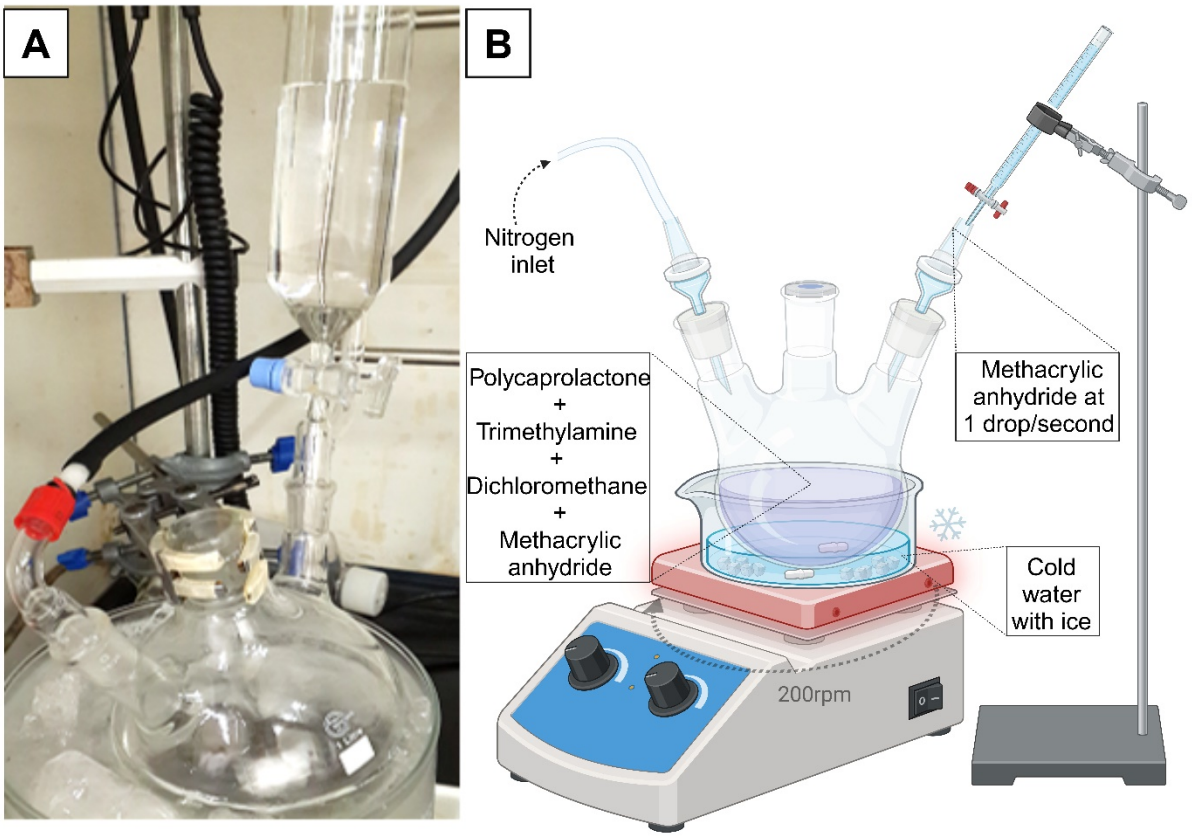


*Figure 39 Schematic of the methacrylation of 4-PCL with a three-neck, round-bottomed flask and magnetic stirrer. Image created on www.biorender.com.*

Once all the MAA solution was added, the ice bath was removed, and the system was allowed to reach ambient temperature while the mixture was left to stir overnight under dry and dark conditions.

To eliminate $Et_3N$, MAA, and salt residues, methacrylated 4-PCL underwent a series of washing steps. Initial washing was performed in a separation funnel (Figure 40A) by adding 100 ml of 1 M HCl washing solution to the polymer mixture, shaking the funnel three times, and allowing phase separation. After phase separation, the polymer/DCM mixture was drained via the valve while the upper acid phase was discarded. This process was repeated three times with 300 ml 1 M HCl washing solution, followed by two washes with di$H_2O$ to remove residual salts. The majority of the solvent was then extracted using a rotary evaporator, with the round flask shielded from light via aluminium foil (Figure 40B).

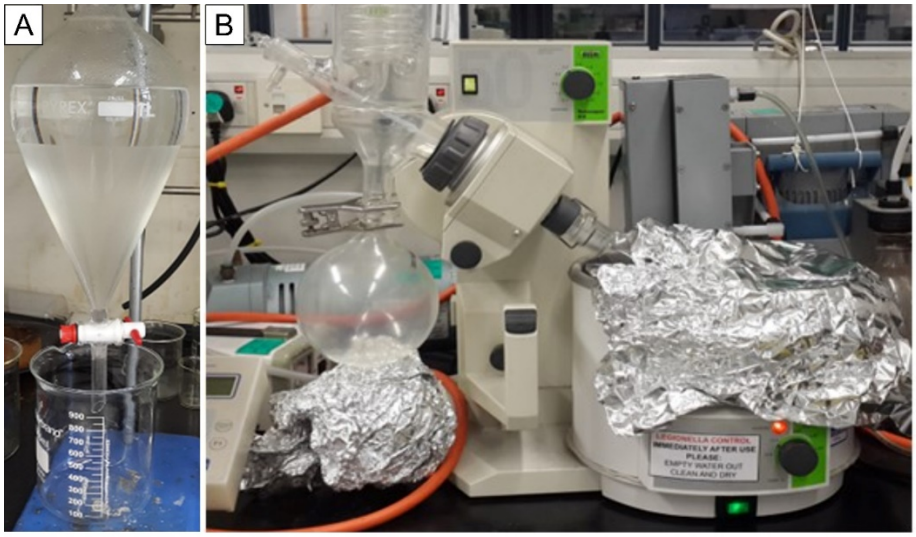


*Figure 40 Washing setup after PCL methacrylation. A) Glass separation funnel for the removal of DCM. B) Rotary evaporator for the removal of undesired solvents.*

Residual DCM was removed via precipitation with 100% methanol. Methanol was added at 10x the PCL solution volume and stored at −80°C overnight until the methacrylated PCL (PCLM) precipitated at the bottom, allowing separation from the upper DCM-methanol phase. Fresh methanol was then added and mixed to break up the PCLM precipitate, and these steps were repeated three times. Final solvent removal was performed via rotary evaporation, and PCLM was stored at −20°C.

Based on previous literature, assuming the desired degree of polymerisation was achieved, this process should have resulted in a 50% degree of methacrylation [457, 459].

## Analysis of Chemical Structures of 4-PCL and PCLM

To analyse the chemical structures of PCL and PCLM and determine the degree of methacrylation in PCLM, $^{1}$H nuclear magnetic resonance spectroscopy (NMR) was employed.

This technique operates on the intrinsic quantum spin property of atomic nuclei, generating magnetic moments. Under an applied magnetic field, nuclei with low spin energy align with the field, while those with high spin energy oppose it. Upon exposure to a radiofrequency pulse within this magnetic field, protons transition to a higher energy state, emitting detectable resonance energy as they return to a lower energy state. The NMR principle is illustrated in Figure 41 [625].

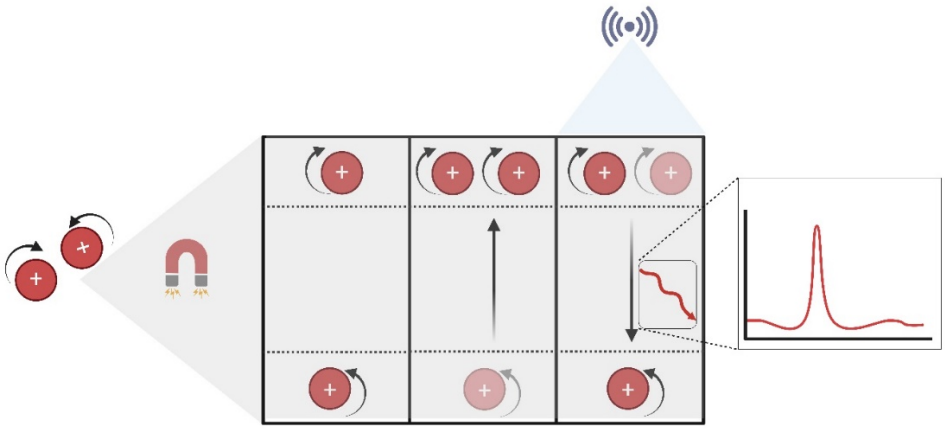

*Figure 41 Schematic of the NMR principle. Image created on www.biorender.com.*

For NMR analysis, samples were prepared by dissolution in 1% (w/v) deuterated chloroform ($CDCl_3$). Spectra were recorded at 25°C on a proton spectrometer, with receiver gain set to 80.6 for increased sensitivity and a spectral width set to 8.2 kHz. Data were collected at an excitation frequency of 400 MHz with a 1 s recycle delay and a 30° pulse width of 9.5 µs. A total of 65,500 data points with a dwell time of 60.8 µs were collected over an acquisition time of 4.0 s and 32 transients. The resulting spectra were processed with the MestReNova 14.0.0 software (Mestrelab, Spain), with chemical shift values referenced to $CDCl_3$ at 7.27 ppm.

## Preliminary Screening with HAP-PCLM Films/Discs

Following PCLM synthesis, sHAP was incorporated into the polymer matrix for the fabrication of composite scaffolds. In all sHAP/HAP-PCLM composites used in this project, synthesised methacrylated 4-PCL was employed, henceforth referred to as methacrylated PCL, PCLM, or simply the polymer.

Cytotoxicity evaluation of HAP-PCLM was conducted using commercially available nsHAP (particle size <200 nm) due to limited sHAP availability. Multiple formulations were evaluated with varying HAP:PCLM ratios. Diphenyl(2,4,6-trimethylbenzoyl)phosphine oxide/2-hydroxy-2-methylpropiophenone was used as the photoinitiator (PI) at 2 wt% relative to PCLM, with HAP concentrations varied as detailed in Table 19. The components were manually mixed and subjected to sonication to achieve homogeneous dispersion and eliminate agglomerates, producing a paste-like consistency.

*Table 19 Concentrations of HAP and PCLM used for preliminary experiments.*

| HAP [wt%] | PCLM [wt%] |
|---|---|
| 0 | 100 |
| 10 | 90 |
| 20 | 80 |
| 30 | 70 |

`

## Synthesis of HAP-PCLM Films

Initial testing was performed on HAP-PCLM films. Films were fabricated using surface-treated glass coverslips (13 mm diameter). The surface treatment protocol comprised Piranha solution cleaning for organic impurity removal, followed by a rinse with 100% methanol for residue elimination. The coverslips were then immersed in 10% toluene solution for 30 min to functionalise the surface with C=C groups, enabling chemical bonding with C=C groups in HAP-PCLM and ensuring uniform photocuring. Prior to use, excess toluene solution was removed by methanol washing, and the coverslips were dried.

For film fabrication, a single droplet (~30 µm) of HAP-PCLM was deposited onto a glass slide, and a treated coverslip was placed on top, forming a “sandwich” structure. The structure was UV-irradiated at 405 nm and 100% intensity for 15 s on each side, using a UV source operating at 40 W/cm$^2$. The cured film was then separated from the glass slide, yielding circular films of 13 mm diameter. Figure 42 illustrates a schematic of the fabrication process.

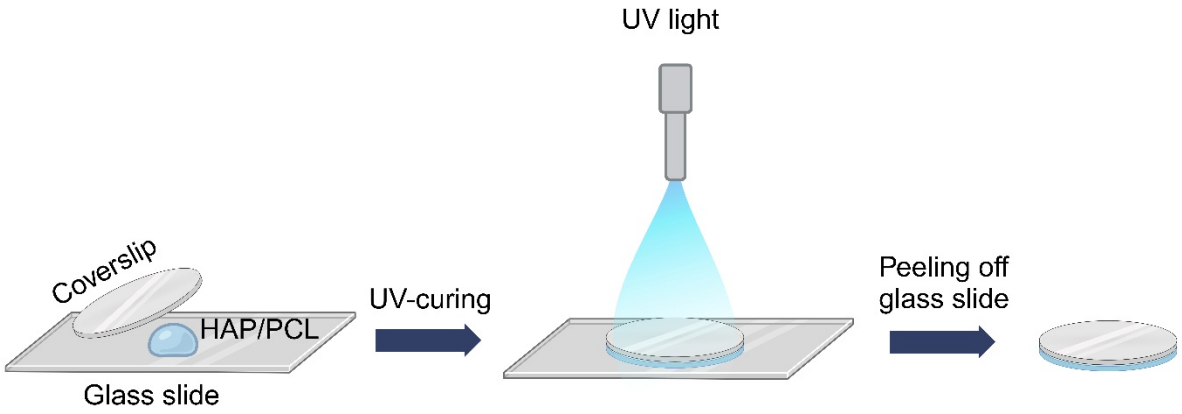


*Figure 42 Schematic of HAP-PCLM film synthesis via the “sandwich” procedure. Image created on www.biorender.com.*

## Synthesis of HAP-PCLM Discs

Following initial 2D cytotoxicity testing on HAP-PCLM films, an intermediate assessment was conducted using larger HAP-PCLM discs. While not a true 3D cell culture, this approach involved seeding cells in a monolayer on bulk scaffolds to evaluate cytotoxicity in a configuration more representative of future 3D scaffolds.

HAP-PCLM discs were fabricated using polydimethylsiloxane (PDMS) moulds consisting of two components: the bottom mould, which contained three disc-shaped chambers interconnected by channels for the flow of injected HAP-PCLM, and the top cover, with openings (injection sites) for introducing the HAP-PCLM composite (Figure 43). The HAP-PCLM composite was injected into the mould via the injection sites. It was cured at 405 nm and 100% intensity for 15 s on each side, using a UV source operating at 40 W/cm$^2$, producing discs 9 mm in diameter and 3 mm in height.

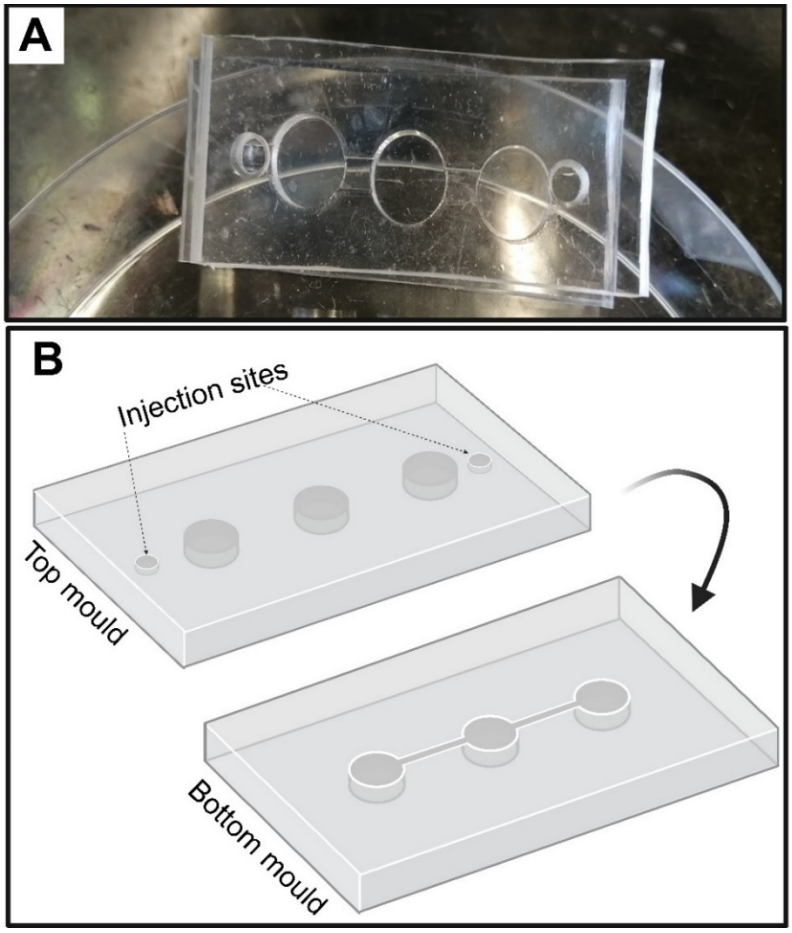


*Figure 43 A) Photograph of the PDMS mould. B) Sketch of the PDMS mould. Image created on www.biorender.com.*

## In Vitro Testing of HAP-PCLM Films and Discs

Films and discs were evaluated in vitro for cytotoxicity using Y201 MSCs. To eliminate non-crosslinked residues, samples were washed in 100% methanol on a rocker for three days. A subsequent 70% methanol wash served dual purposes of sterilisation and further reduction of residual monomers. Films were washed for three days without methanol replacement, while discs were washed for one week with one methanol replacement to ensure thorough removal of unbound components from the dense scaffolds.

Following sterilisation, films on glass coverslips were aseptically transferred to 12-well plates, and discs were placed in 24-well plates. Both were rinsed twice with sterile di$H_2O$ to eliminate residual methanol.

Prior to cell seeding, films were immersed in 300 µl GM and discs in 400 µl GM for 45 min, allowing medium-bound proteins to adhere to the film surface and promote cell attachment. After medium removal, cells were seeded onto films/discs at a density of 4000 cells/$cm^2$, accounting for the top surface area of films or the exposed top and lateral surfaces of the discs (Figure 44).

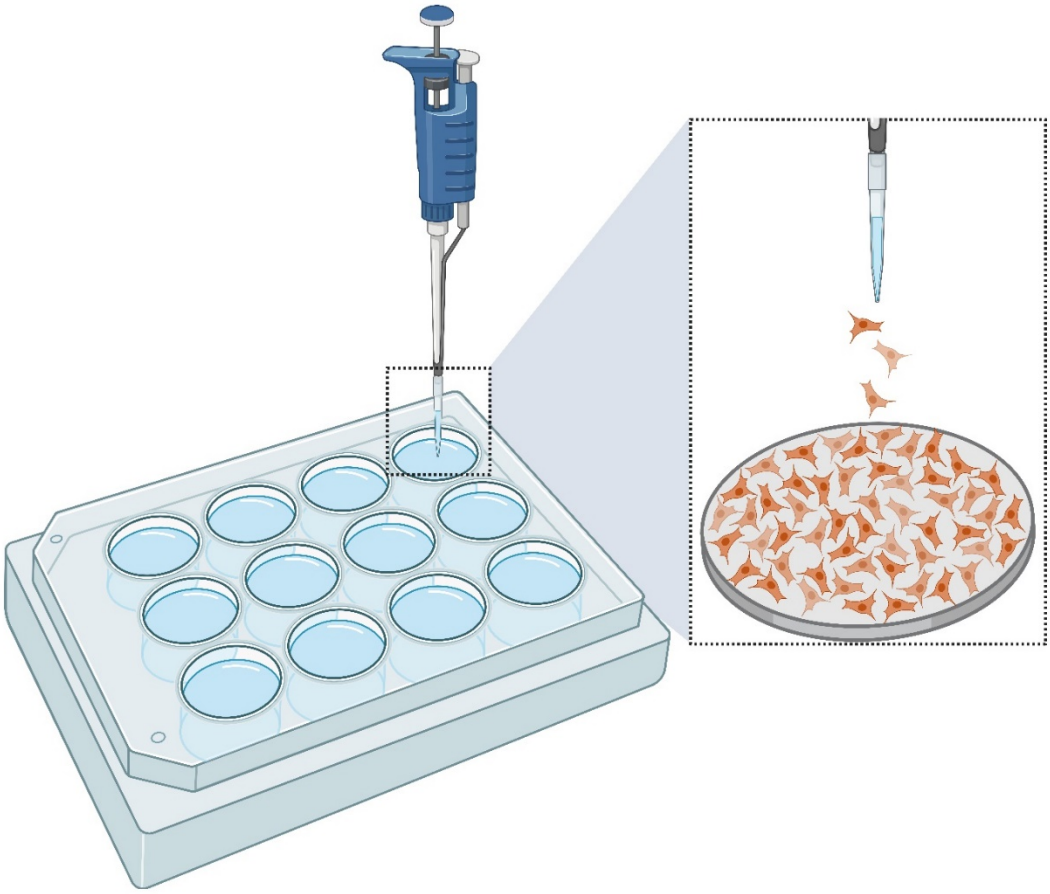

*Figure 44 Schematic of cell seeding on films in well plates. Image created on www.biorender.com.*

Control samples included films/discs without cells and cells seeded directly onto the well plates (SCC). All samples were cultured in GM as per the SOP. Analysed groups comprised:

- 0% HAP C: Cells on 0% HAP/100% PCLM films/discs
- 0% HAP B: No cells, 0% HAP/100% PCLM films/discs
- 10% HAP C: Cells on 10% HAP/90% PCLM films/discs
- 10% HAP B: No cells, 10% HAP/90% PCLM films/discs
- 20% HAP C: Cells on 20% HAP/80% PCLM films/discs
- 20% HAP B: No cells, 20% HAP/80% PCLM films/discs
- 30% HAP C: Cells on 30% HAP/70% PCLM films/discs
- 30% HAP B: No cells, 30% HAP/70% PCLM films/discs
- SCC: Cells only
- B: Medium only

`

The plate layouts for films and discs are illustrated in Figure 45 and Figure 46, respectively.

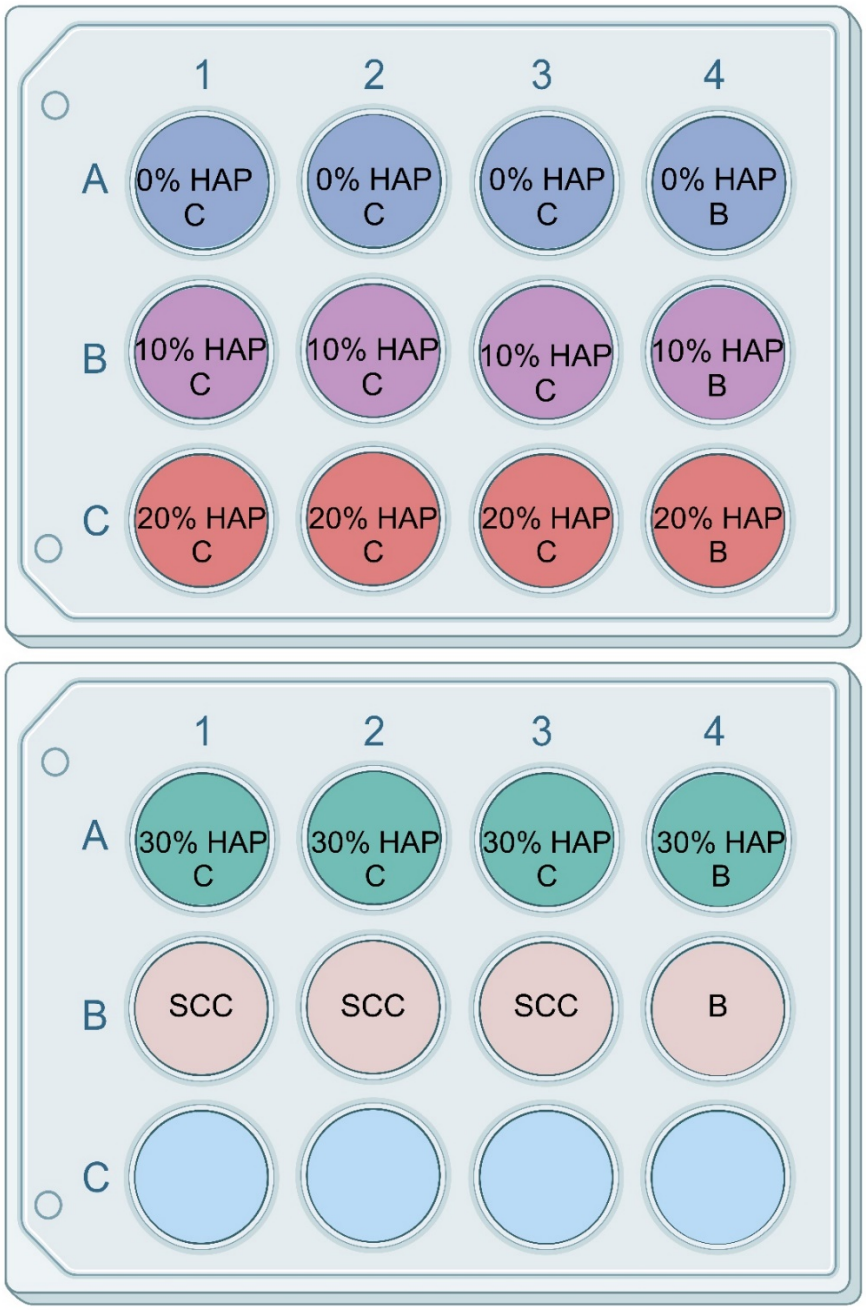


*Figure 45 Plate organisation for in vitro testing of HAP-PCLM films. Image created on www.biorender.com.*

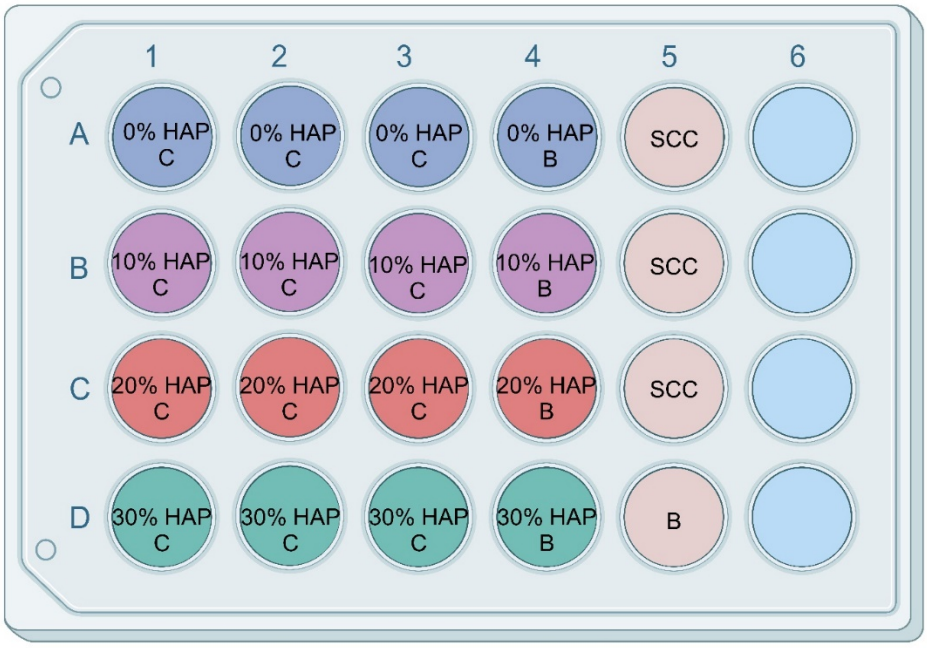


*Figure 46 Plate organisation for in vitro testing of HAP-PCLM discs. Image created on www.biorender.com.*

## Fabrication of Complex 3D Scaffolds

Following the verification of HAP-PCLM's non-cytotoxicity in preliminary film assessments, the focus shifted to fabricating more complex structures suitable for bone graft applications.

Preliminary testing established provisional printing parameters using commercially available HAP. The initial ink formulation comprised PCLM, 50 wt% HAP, and 2 wt% PI (both relative to PCLM) and was extruded at 50 psi and 21°C. The composition was later modified by incorporating MgHAP (SINTlife®), which necessitated the addition of pyrogenic silica ($SiO_2$) nanoparticles to achieve printability. The final ink formulation comprised PCLM with 30 wt% MgHAP, 1.5 wt% $SiO_2$ (relative to MgHAP), and 2 wt% PI, and printing was conducted at 50 psi and 21°C.

### Printing of sHAP-PCLM Scaffolds

Following the establishment of baseline printing parameters and the formulation of a shear-thinning ink with HAP/MgHAP-PCLM, sHAP was incorporated in inks for subsequent in vitro evaluation. PCLM was liquefied at ambient temperature and combined with varying amounts of Mg5Sr5 and Mg10Sr5 sHAP, along with $SiO_2$ and PI. The specific amounts are outlined in Table 20.

`

*Table 20 Different ink formulations for 3D-printed scaffolds.*

| sHAP [wt%] | SiO2 [wt%] | PI [wt%] | PCLM [wt%] |
|---|---|---|---|
| 0 | 0 | 2 | 98 |
| 10 | 1.5 | 2 | 87.85 |
| 20 | 1.5 | 2 | 77.7 |
| 30 | 1.5 | 2 | 67.55 |
| 40 | 1.5 | 2 | 57.4 |
| 50 | 1.5 | 2 | 47.25 |

Inks were mixed using a magnetic stirrer, with further sonication for 10 min to disperse aggregates and ensure thorough blending. The prepared inks were then loaded into a 10 ml syringe and extruded through a 20 gauge tapered nozzle (0.61 mm inner diameter), wrapped in aluminium foil to prevent premature curing. The syringe was placed in one of the two temperature-controlled cylindrical extruders. The G-code for the scaffold design was generated via the Repetier-Host V1.6.1 software (Repetier, Germany). The scaffolds were printed in a layer-by-layer pattern, forming a two-layer woodpile structure with final dimensions of 7.5 × 7.5 × 0.69 mm, as shown in Figure 47.

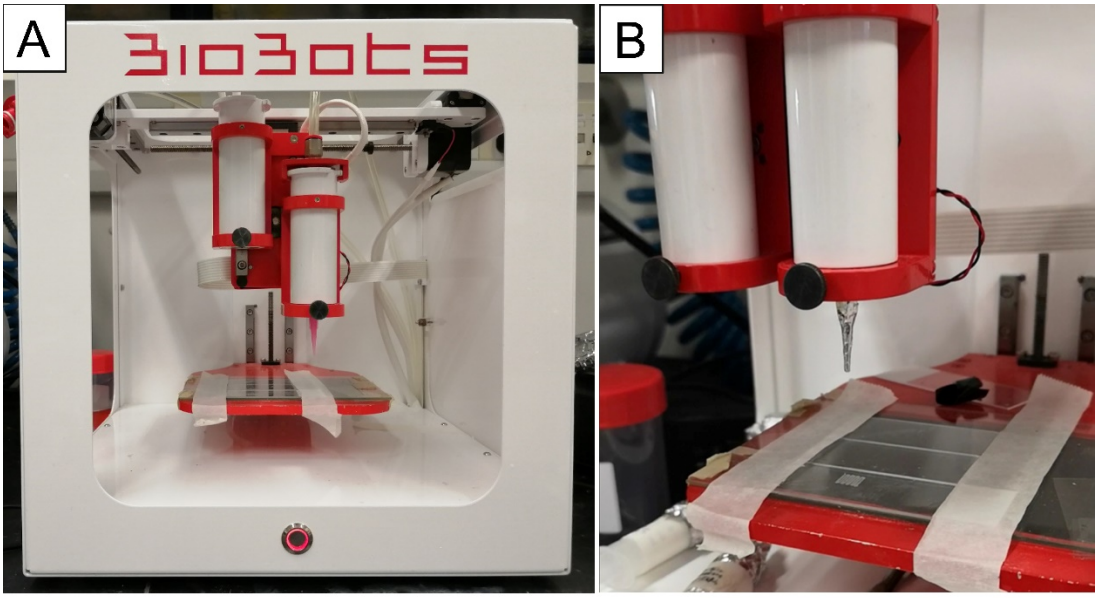


*Figure 47 A) 3D printer setup for scaffold fabrication. B) Scaffold printing process showing extrusion through one of the top-mounted cylindrical nozzles.*

The printing process was adapted to accommodate varying viscosities of the different ink formulations by adjusting pressures and speeds accordingly. The ink containing 50 wt% Mg5Sr5 sHAP exhibited higher viscosity and was maintained at 30°C, while all other inks were kept at 25°C in the reservoir before printing. Printing parameters were managed through the Allevi-provided Bioprint software. Further details can be found in Table 21.

`

*Table 21 Printing parameters used for different sHAP-PCL formulations.*

| sHAP [wt%] | Pressure [psi] | Temperature [°C] | Speed [mm·s$^{-1}$] |
|---|---|---|---|
| 0 | 5 | 25 | 1 |
| 10 | 15 | 25 | 0.8 |
| 20 | 20 | 25 | 0.8 |
| 30 | 30 | 25 | 0.8 |
| 40 | 40 | 25 | 0.8 |
| 50 | 75 | 30 | 0.6 |

Following printing, scaffolds were cured for 15 s on each side under a UV light at 405 nm and 100% exposure intensity.

## SEM Analysis of 3D-printed Scaffolds

3D-printed scaffolds composed of Mg5Sr5 sHAP and PCLM were analysed using scanning electron microscopy (SEM) at a beam energy of 3 kV to visualise the scaffold microstructure.

## Surface Mapping via ImageJ

The distribution and homogeneity of Mg5Sr5 sHAP particles within the scaffolds were assessed through surface mapping of grey-scale SEM images. SEM images were captured from scaffold sections measuring approximately 3 mm × 2 mm at a magnification of 50×. These images were analysed using the ImageJ software (National Institutes of Health, USA) and transformed into 3D surface plots using an ImageJ extension [626]. To gain a comprehensive assessment of sHAP distribution, the analyses were conducted at two levels: first, on the entire SEM images of the scaffold sections, and second, on a smaller focused region within each image, measuring approximately 300 × 300 µm.

## Surface Characterisation

The dependence of surface hydrophilicity on varying formulations was characterised using polymer composite films. Quantitative surface characterisation included the measurement of water contact angle (WCA), interfacial tension (IFT), and work of adhesion (WoA). The formulations examined were as follows: sHAP-PCLM (Mg5Sr5 and Mg10Sr5), nsHAP-PCLM, PCLM compounded with silica at a wt% equivalent to sHAP substitution, and pure PCLM. A detailed overview of the test groups and their respective quantities is provided in Table 22.

`

*Table 22 Composition ratios in various test groups for surface analysis.*

| Group | PCLM [wt%] | (s)HAP [wt%] | $SiO_2$ [wt%] | PI [wt%] |
|---|---|---|---|---|
| 10% Mg5Sr5 sHAP-PCLM | 87.85 | 10 | 1.5 (to HAP) | 2 |
| 30% Mg5Sr5 sHAP-PCLM | 67.55 | 20 | 1.5 to HAP) | 2 |
| 50% Mg5Sr5 sHAP-PCLM | 47.25 | 30 | 1.5 to HAP) | 2 |
| 10% Mg10Sr5 sHAP-PCLM | 87.85 | 10 | 1.5 to HAP) | 2 |
| 30% Mg10Sr5 sHAP-PCLM | 67.55 | 20 | 1.5 to HAP) | 2 |
| 50% Mg10Sr5 sHAP-PCLM | 47.25 | 30 | 1.5 to HAP) | 2 |
| 10% HAP-PCLM | 87.85 | 10 | 1.5 to HAP) | 2 |
| 30% HAP-PCLM | 67.55 | 20 | 1.5 to HAP) | 2 |
| 50% HAP-PCLM | 47.25 | 30 | 1.5 to HAP) | 2 |
| 0.15% Silica-PCLM | 97.85 | 0 | 0.15 (to PCLM | 2 |
| 0.45% Silica-PCLM | 97.55 | 0 | 0.45 (to PCLM | 2 |
| 0.75% Silica-PCLM | 97.25 | 0 | 0.75 (to PCLM) | 2 |
| PCLM | 98 | 0 | 0 | 2 |

Films were fabricated following the previously described “sandwich” procedure, with 1 ml of sample per group added onto a glass slide to create rectangular films. For the analysis, approximately 30 µl of $H_2O$ was deposited at five randomly selected non-overlapping locations for each group. The measurements were taken using a drop shape analyser at 20°C. Using the acquired WCA and IFT values between the surfaces and $H_2O$, alongside the known surface free energy of $H_2O$ [627], the surface free energy (SFE) of each polymer blend was determined via the Young’s formula [628]:

$$\gamma_{SFE(P)} = \gamma_{SFE(L)} + \gamma_{IFT} * \cos\theta_{WCA}$$

where $\gamma_{SFE(P)}$ represents the surface free energy of the polymer, $\gamma_{SFE(L)}$ the surface free energy of $H_2O$, $\gamma_{IFT}$ denotes the interfacial free energy and $\cos\theta_{WCA}$ the water contact angle.

## In Vitro Testing of sHAP-PCLM Scaffolds

To assess cytotoxicity, scaffolds were subjected to in vitro testing, using Y201 MSCs. Non-crosslinked residues were removed via a 3-day wash in 100% methanol, followed by sterilisation in 100% ethanol for 3 days. The sterilised scaffolds were aseptically transferred into untreated 24-well plates and rinsed twice with sterile di$H_2O$ to remove any residual ethanol.

Prior to cell seeding, scaffolds were pre-conditioned by immersion in 400 µl GM for 45 min to promote protein adsorption onto the scaffold surface. After pre-treatment, the medium was aspirated, and cells were seeded onto the scaffolds at a density of 4000 cells/$cm^2$, calculated based on the bulk surface area of a scaffold (Figure 48). Seeded scaffolds were cultured in GM under standard incubation conditions. A seeding control was established by culturing cells at the same density directly on treated well plates.

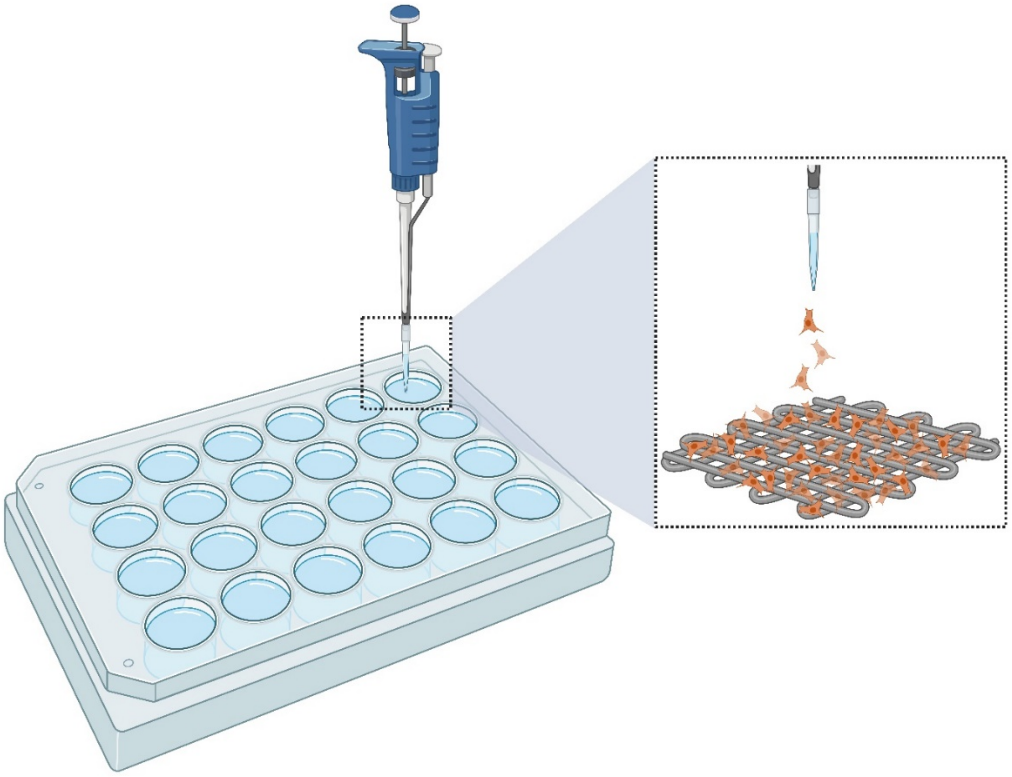

*Figure 48 Schematic of cell seeding on scaffolds in cell culture plates. Image created on www.biorender.com.*

### Actin and Nucleus Staining

Actin and nucleus staining were employed to visualise the attachment, spatial distribution, and morphology of Y201 MSCs on scaffolds. Nuclei were labelled with DAPI, and actin structures were visualised with phalloidin. First, scaffolds were fixed to preserve cellular structure. The culture medium was removed, and scaffolds were washed twice with PBS, followed by a 30-min incubation in 500 µl of formaldehyde fixing solution under a fume hood. After fixation, scaffolds were washed twice with PBS.

To permeabilise the cell membranes for staining, scaffolds were incubated in 500 µl ICC buffer for 10 min, followed by two PBS washes. Next, the DAPI working solution was added and incubated for 15 min at room temperature in the dark. After incubation, the DAPI solution was removed, and scaffolds were washed twice with PBS. The scaffolds were then incubated with phalloidin working solution for 30 min at room temperature in the dark. After staining, the solution was removed, and scaffolds were washed once with PBS. Finally, scaffolds were submerged in PBS and protected from direct light until visualisation. Fluorescent images were captured with a confocal microscope and analysed using the MetaMorph® Microscopy Automation and Image Analysis Software (Molecular Devices LLC, UK).

`

## 2.2.4. Statistical Analysis

Statistical analyses were performed using GraphPad Prism (GraphPad, USA). Normality was assessed via Kolmogorov-Smirnov or Shapiro-Wilk tests. Parametric or nonparametric tests were selected based on data normality and equality of variances. Tests included one-sample t-test, Wilcoxon, one-way analysis of variance (ANOVA), two-way ANOVA, Mann-Whitney, and Kruskal-Wallis. Significance was set at $p < 0.05$. For ANOVA multiple comparisons, adjusted p-values (adj. p) indicated significant differences between factor levels when adj. $p < 0.05$. Figures display means, with error bars as standard deviations, unless stated otherwise. Further statistical test details are available in relevant sections and the appendix.

`

# Chapter III Establishment of an SOP for the Culture of Y201 MSCs

## 3.1. Aims and Objectives

This chapter focused on developing a standardised operating procedure for culturing Y201 MSCs, driven by two primary aims: to establish suitable expansion conditions for in vitro experiments in this project and to develop a serum-free protocol that enhances reproducibility while addressing ethical concerns. The following objectives were addressed to evaluate factors influencing cell expansion:

- Evaluation of different cell culture media formulations
- Assessment of various media change protocols
- Comparison of cell culture dish coatings to uncoated surfaces

## 3.2. Introduction

In biomedical research, in vitro models play a crucial role in providing initial insights into the biocompatibility, osteogenicity, osteoinductivity, and osteoconductivity of bone biomaterials [528, 629-631]. These models reduce the need for animal studies during early research stages and address ethical concerns [525-527]. Despite their advantages, reproducibility for in vitro assays remains challenging due to variability introduced by varying cell culture conditions [572, 575, 576, 579, 632]. To ensure reliable and comparable results across studies, stringent standardisation of protocols is essential.

MSCs are commonly used for in vitro assessments of bone biomaterials due to their role in bone formation and their capacity for osteogenic differentiation in vitro and in vivo [533, 633]. However, the limited lifespan of primary MSCs in vitro (typically 2-12 passages) and their inherent heterogeneity across tissues and donors restrict their long-term use in experiments [534, 536, 537, 543, 547-551]. As an alternative, immortalised MSC lines provide prolonged proliferation, cost-effectiveness, ease of use, and reduced ethical concerns while enabling reproducible preliminary studies. Although immortalised lines may not fully replicate primary cell behaviour, they are invaluable in screening studies before further validation with primary cells [528, 552-555, 634, 635].

Different cell culture media play an important role in maintaining various cell types. While certain cell types, such as cancer cells, can tolerate variability in culture media, this resilience does not apply to most stem cells [544]. Therefore, standardised media must be defined for each cell type. Serum-supplemented media, particularly of xenogenic origin, such

as FBS, can introduce variability that compromises reproducibility [538, 561-565, 572, 636, 637]. Alternatives, such as human serum-supplemented media, which more closely mimic the in vivo human environment, and serum-free media, which improve reproducibility by eliminating serum-associated variability, have been shown to support MSC proliferation and yield comparable or superior outcomes to FBS-based formulations [561, 567, 568, 571, 583, 634, 635, 638-640].

A cell's interaction with its microenvironment is a critical determinant of its fate. MSCs modulate their behaviour, phenotype, and secretory profile in response to substrate properties [577, 578]. While commercially available culture dishes are typically surface-treated to enhance cell attachment, some cell types benefit from additional coatings, such as ECM proteins, to promote attachment and proliferation [641, 642].

The frequency and extent of media changes further impact cellular function by regulating nutrient levels and removing inhibitory metabolites and stimulatory growth factors [582, 600, 601].

This variability in the cellular response under varying cell-culture conditions underscores the necessity of standardised protocols to ensure experimental reproducibility.

To evaluate suitable conditions for cell expansion, serum-free and human serum-based media were compared with conventional FBS-supplemented media, alongside assessments of different substrate coatings and media change protocols.

## 3.3. Experimental Overview

The impact of GM composition, media change frequency, and ECM coatings on the attachment and proliferation of Y201 MSCs was evaluated in vitro using a metabolic resazurin assay at three different time points during a 1-week culture period. Three GM formulations were tested: BM3 with FBS, HSM with human serum, and CD1 as a serum-free medium. Media change frequency was assessed using three protocols: no media replacement (NM), partial media replacement with a 50% exchange on day 3 (PM), and full media replacement with a complete exchange on day 3 (FM). Additionally, tissue culture dishes were pre-coated with bovine gelatine (GC), human fibronectin (FC) or left uncoated (NC). An overview of the experimental conditions is provided in Table 23.

`

*Table 23 Overview of experimental conditions for the SOP development.*

| Growth Media | |
|---|---|
| **Media Name** | **Media Formulation** |
| BM3 | DMEM GlutaMAX™ + 10% FBS |
| HSM | Human Mesenchymal-XF Expansion Medium |
| CD1 | StemMACS™ MSC Expansion Media |

| Media Change | |
|---|---|
| **Acronym** | **Change Frequency** |
| NM | No media replacement during a 1-week culture period |
| PM | Partial media replacement on day 3 (50% media exchanged) |
| FM | Full media replacement on day 3 (100% media exchanged) |

| ECM Coating | |
|---|---|
| **Acronym** | **Coating Description** |
| NC | No ECM coating |
| GC | ECM coating with bovine gelatine |
| FC | ECM coating with human fibronectin |

## 3.4. Results

Figure 49 presents the metabolic activity profiles for the tested coating substrates, media formulations, and media change frequencies. Across all feeding protocols, HSM showed the highest metabolic activity on days 1 and 4, while CD1 supported the overall highest activity by day 7. Distinct interactions between media change frequency, coating type, and media formulation influenced the kinetics of metabolic activity.

In conditions without media replacement, BM3 and CD1 showed steady metabolic activity increase from days 1–7, with FC and GC coatings yielding higher activity than NC. Conversely, HSM displayed a rapid metabolic activity increase on day 4, followed by an activity plateau in FC and a decline in GC and NC on day 7.

Under partial media replacement, BM3 exhibited similar metabolic activity levels to no medium change conditions with GC and FC but experienced a decline with NC on day 7. In HSM, the metabolic activity remained comparable to no medium change conditions, with increased activity levels in GC. CD1 exhibited lower metabolic activity on day 4 across all substrates compared to no medium change conditions, increasing comparable to no medium change levels for FC and GC by day 7, with minimal increase observed for NC.

Under full medium replacement, BM3 supported metabolic activity levels similar to no medium change. HSM demonstrated activity levels comparable to partial and full medium change protocols without substrate-specific decreases. In CD1, metabolic activity was similar to a partial medium replacement, with increased activity for NC.

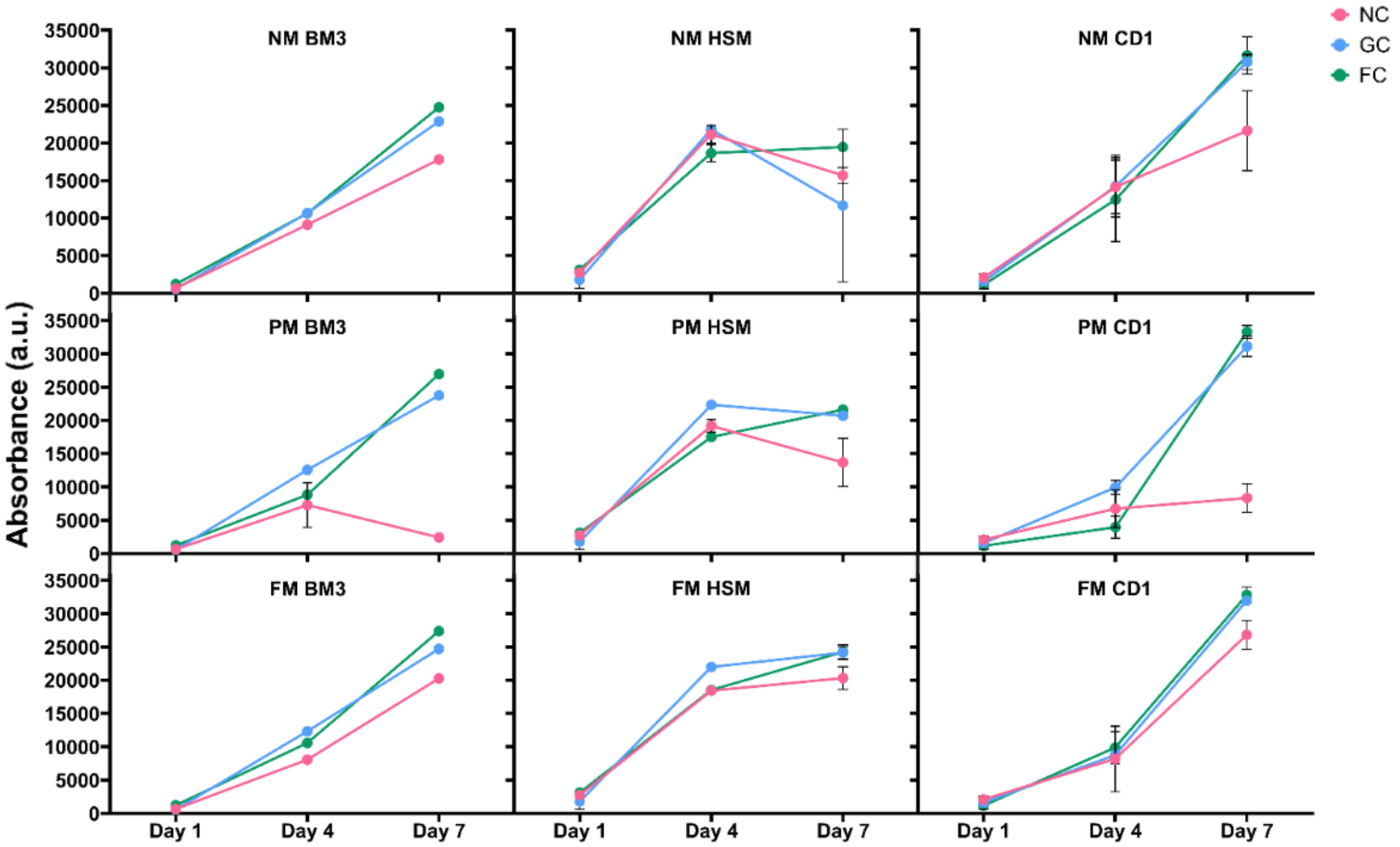


*Figure 49 Y201 MSC metabolic activity with different media formulations (BM3, HSM, CD1), media change protocols (NM, PM, FM) and surface coatings (NC, GC, FC). X-axis: Days 1–7; Y-axis: Absorbance (arbitrary units). Data presented as mean ± SD (n = 3).*

`

## 3.5. Discussion

This chapter focused on developing a serum-free expansion protocol to establish standardised conditions for in vitro assays in subsequent chapters while addressing ethical concerns and variability associated with serum-supplemented media [538, 561-565, 572, 636, 637].

The Y201 MSC line was selected due to its trilineage differentiation capacity and phenotypic stability up to passage 80 [555], overcoming the donor and tissue variability and early senescence associated with primary MSCs [534, 536, 537, 543, 547-551].

Variable cell line responses to culture media necessitated the evaluation of multiple media formulations, as cellular behaviour and phenotype can differ between media types [575, 576]. Three media formulations were analysed: standard DMEM supplemented with FBS, which is the recommended medium for Y201 MSC maintenance and widely used for MSC culture [555, 643-646]; HSM, a specialised human-serum medium formulated for MSC expansion and maintenance [634, 635], and CD1, a validated serum-free medium that has demonstrated successful MSC culture outcomes in previous studies [583, 638-640].

Despite inherent MSC plastic adherence properties [528], fibronectin and gelatine surface coatings were assessed for their potential to enhance cellular performance under varying media formulations and feeding protocols. Previous studies have documented these substrates' capacity to promote MSC proliferation and differentiation [647-650].

Metabolic activity analysis (Figure 49) revealed media-specific patterns. CD1 demonstrated peak metabolic activity on day 7 across all media change protocols, consistent with its formulation for MSC expansion [604]. HSM exhibited the highest activity on day 4, reflecting its design for rapid expansion [608], while BM3 maintained consistent metabolic activity with a marginal increase under full media change conditions. Metabolic activity variations across media change protocols likely stemmed from growth factor dynamics. CD1's stable metabolic activity without medium change aligns with supplier recommendations of weekly media replacement [604]. Lower metabolic activity on day 4 with full and partial medium changes may have resulted from growth factor removal during day 3 medium change, with activity recovery by day 7 through renewed factor secretion. HSM's metabolic activity plateau or decline by day 7 potentially indicated cellular transition to a pre-differentiation state, consistent with previous findings of human plasma-supplemented medium inducing non-terminal pre-differentiation states at lower cell densities compared to FBS-supplemented medium [601]. Metabolic activity remained stable with full medium changes, aligning with the manufacturer's 2-3 day change recommendation [608]. BM3's slightly enhanced metabolic activity under full medium change conditions aligns with FBS's complex inhibitory and stimulatory factors, where media stagnation can lead to nutrient depletion and inhibitory factor

accumulation [600, 601]. Y201 MSCs demonstrated minimal metabolic inhibition during a 1-week culture with no or partial BM3 medium changes.

Well plate coating enhanced metabolic activity, particularly evident by day 7. Fibronectin and gelatine demonstrated comparable performance, though fibronectin showed superior results in BM3 on day 7. Previous studies confirm fibronectin's role in improving MSC attachment, spreading [651], and stemness maintenance [652] while reducing differentiation potential in FBS-containing media [653], potentially explaining the higher metabolic activity observed.

Variations in proliferation across culture conditions indicate suboptimal cellular adaptation to artificial microenvironments, characterised by inconsistent nutrient and growth factor levels. These conditions can induce cellular stress responses, leading to reduced proliferation and premature senescence, underscoring the need for cell line-specific standardised protocols [654].

## 3.6. Established Cell Culture Conditions

Based on peak metabolic activities observed on day 7, CD1 was selected as the standard cell culture medium for subsequent experiments. Following supplier recommendations for 7-day cultures, the no medium change protocol was adopted, as it preserved higher metabolic activity on day 4 than partial or full medium changes. For cultures extending beyond 7 days, medium replacement was conducted on day 7 following established internal protocols.

Despite fibronectin and gelatine coatings demonstrating higher metabolic activity than non-coated wells, non-coated cell culture dishes were adopted as the project standard due to CD1's superior performance over BM3 and HSM, even without surface coatings. Furthermore, using uncoated dishes ensures compatibility with scaffold-based experiments, where surface coatings could influence the interpretation of scaffold properties.

`

## 3.7. Summary and Conclusion

This chapter aimed to establish an SOP for in vitro experiments conducted within this project.

Various cell culture media types, including human and bovine serum-supplemented and a serum-free alternative, were comparatively evaluated. Additionally, the effects of different media change frequencies (no media change, full media change, and partial media change) were assessed. CD1 demonstrated the highest metabolic activity with no medium change, with reduced activity observed under partial or full medium change protocols. BM3 performance was comparable but marginally inferior across all feeding strategies. HSM exhibited high initial metabolic activity that plateaued or declined.

This chapter also investigated the impact of fibronectin and gelatine coatings on culture dishes compared to uncoated surfaces. While coatings enhanced metabolic activity, uncoated plates still supported adequate cellular metabolism.

CD1 without medium changes or surface coatings provided good conditions for cell attachment and proliferation, establishing it as the standard culture system for subsequent in vitro experiments.

An SOP, based in part on the findings of this chapter, was developed as a deliverable for the SPINNER project and is included in the appendix. This SOP represents a collaborative effort, integrating cell expansion insights from this project with Jose Rodriguez's contributions to cell differentiation.

`

# Chapter IV Synthesis of Mg and Sr Substituted Hydroxyapatite

## 4.1. Aims and Objectives

This chapter focused on the synthesis of sHAP for subsequent incorporation within composite scaffolds. The primary objectives were to develop a continuous synthesis method that facilitates apatite formation, enables the incorporation of target ions, and maintains crystalline integrity. Additionally, the chapter aimed to investigate the impact of varying substitution degrees on the elemental and structural properties of sHAP and their effect on cell viability. To achieve these objectives, the following steps were undertaken:

- Evaluation of different continuous synthesis methods for sHAP.
- Determination of suitable substitution degrees by assessing their influence on sHAP properties.
- In vitro assessment of sHAP powders to evaluate their effect on cell viability.

## 4.2. Introduction

HAP is widely employed in orthopaedic applications to facilitate bone regeneration, primarily due to its exceptional osteoconductive properties [231, 250-254]. While HAP lacks intrinsic osteoinductive capabilities, as it does not actively recruit osteoprogenitor cells [289, 655, 656], numerous studies have demonstrated its ability to promote osteogenic differentiation in vitro [256-258]. Additionally, when combined with stem cells, HAP has been shown to induce ectopic bone formation in vivo [289].

Synthetic HAP represents a stoichiometric apatite phase, characterised by a Ca/P molar ratio of 1.67 and the chemical formula $Ca_{10}(PO_4)_6(OH)_2$ [293-295]. In contrast, naturally occurring apatites in bone and dentin are non-stoichiometric, exhibiting a variable calcium and phosphate ion ratio, which results in calcium-deficient HAP [309]. Stoichiometric HAP exhibits a rigid crystalline structure and slow degradation rate, limiting its bioactive properties [657-659]. Alterations to the Ca/P ratio can disrupt the crystalline structure, promoting material dissolution. Consequently, calcium-deficient HAP, with a Ca/P ratio of 1.60, exhibits increased bioactivity compared to stoichiometric HAP [659].

Ion substitution during HAP synthesis allows for the achievement of calcium-deficient HAP, influencing degradation rates and facilitating the release of biologically relevant ions. This approach provides a means to engineer customised HAP with desirable properties [364, 660, 661].

While bone grafts composed of single-substituted HAP have demonstrated good biological performance in various in vitro and in vivo studies [338, 339, 346, 662-664], they may not satisfy all multifunctional requirements for clinical applications. Several research groups hypothesise that co-substituted HAP could further enhance the beneficial effects of individual substituents [374, 665, 666].

Mg is the predominant ion replacing Ca in biological apatite, playing a crucial role in bone remodelling. Research has revealed notably higher Mg levels during the initial stages of calcification in bone remodelling [667]. Moreover, studies indicate Mg levels decrease with age [668, 669]. Furthermore, Mg is well-documented for stimulating osteoblast activity and promoting bone formation [670].

Sr, another naturally occurring ion in bone, is predominantly found in regions of high metabolic activity [671]. It has been shown to enhance osteoblast proliferation and differentiation while simultaneously suppressing osteoclast activity and promoting bone matrix formation [347, 672]. Currently, strontium-based medications are utilised for osteoporosis treatment [348-351], and Mg-HAP is commercially available as a synthetic graft substitute for bone regeneration [335].

Co-substitution of Mg and Sr in HAP increases solubility and bioactivity, promoting cell viability and osteogenic differentiation [295, 315, 370, 372-374]. Mg inhibits apatite crystal growth, producing smaller crystals with enhanced surface activity and bioavailability [328], whereas Sr stabilises the HAP structure [370, 372].

Continuous hydrothermal synthesis has been established for HAP production [673, 674]. Anwar et al. utilised a continuous hydrothermal method to synthesise Mg-substituted HAP [675]. However, no research has been conducted on the continuous synthesis of Mg- and Sr-substituted HAP, an approach with potential implications for high-throughput production. Based on these insights, Mg and Sr were selected as substituents for sHAP synthesis using a continuous system.

`

## 4.3. Experimental Overview

Substitution degrees of 2.5 and 10 mol% for Mg and 5 and 20 mol% for Sr were initially selected based on literature findings. Previous studies indicate Mg substitution is typically constrained to approximately 10 mol%, while Sr can be incorporated at levels up to 25 mol% [372]. Mg substitution at 2.5 mol% has been shown to induce lower lattice strain and smaller particle size than higher concentrations [676, 677]. For Sr substitution, 10 mol% exhibited optimal osteogenic activity in MSCs within the 5–20 mol% range [369] and demonstrated favourable antimicrobial properties [365]. Moreover, co-substitution with 10 mol% Mg and 20 mol% Sr has been reported to show superior osteogenic activity compared to alternative co-substitution ratios (5%, 10%, 20%, and 25% for Mg and Sr, respectively) [373].

Due to unsatisfactory initial results and to ensure equivalent substitution degrees for comprehensive comparison, new substitution degrees were selected as outlined in Table 24.

*Table 24 Mg and Sr substitution degrees [mol%] employed for sHAP synthesis.*

| Acronym | Mg | Sr |
|---|---|---|
| Mg20Sr20 | 20 | 20 |
| Mg5Sr20 | 5 | 20 |
| Mg20Sr5 | 20 | 5 |
| Mg5Sr5 | 5 | 5 |
| Mg5Sr10 | 5 | 10 |
| Mg10Sr5 | 10 | 5 |
| Mg10Sr10 | 10 | 10 |

Synthesis systems described in section 2.2.2 were evaluated using nsHAP, followed by sHAP synthesis via the established C2 method. Incubation times post-synthesis were assessed for precipitates generated through the flow cell method using nsHAP. Suspensions were processed either immediately ($T_0$) or after incubation periods of 2 h ($T_2$), 6 h ($T_6$), and 24 h ($T_{24}$).

The in vitro cytotoxicity of synthesised sHAP powders was evaluated using a resazurin assay. Initial testing employed commercial MgHAP (SINTlife®) at 10, 505, and 1000 µg/ml medium to determine the maximum non-cytotoxic concentration due to limited sHAP availability. Based on the absence of cytotoxicity across all tested MgHAP concentrations, the highest concentration was selected for subsequent sHAP testing.

`

## 4.4. Results

This section presents the experimental findings on the synthesis of Mg and Sr co-substituted HAP. Various synthesis methods, parameters, and HAP formulations were evaluated, with detailed results provided in the subsequent sections and the appendix.

### 4.4.1. HAP Synthesis Systems

A key project objective was the development of a continuous chemical precipitation method for sHAP synthesis with potential for industrial upscaling. Table 25 comprehensively details the investigated synthesis methods, encountered challenges, implemented solutions, and outcomes. Based on these results, the C2 column method was selected as the standard synthesis approach for subsequent experiments.

*Table 25 Overview of synthesis methods, problems, solutions, and outcomes.*

| Method | Remarks and Issues | Implemented Solutions and Improvements | Outcome |
|---|---|---|---|
| BBT | Clogging, gelatinous phase formed | Reduced saturation | Persistent clogging, method rejected |
| BGT | Clogging, gelatinous phase formed | Reduced saturation | Persistent clogging, method rejected |
| B2B | Difficult to operate, gelatinous phase formed | Method rejected | |
| FCR | Release of ultrasonic probe debris | Covered ultrasonic probe | Covering ineffective, methods rejected |
| C1 | Clogging, gelatinous phase formed | Reduced saturation, cleaned column | Persistent clogging, method rejected |
| C2 | Air in vessels, high flow rate needed, gelatinous phase formed | Tube priming<br>Filtration and washing | Tube priming enabled flow and reduced free air.<br>Filtration and washing reduced gelatinous phase.<br>Method accepted. |

Synthesis attempts using BBT, BGT, B2B, and FCR methods encountered clogging issues, rendering them unsuitable as standard synthesis protocols. Furthermore, all methods except FCR yielded a gelatinous precipitate alongside the granular precipitate, primarily observed in nsHAP or low substitution formulations (Mg5Sr5) (Figure 50).

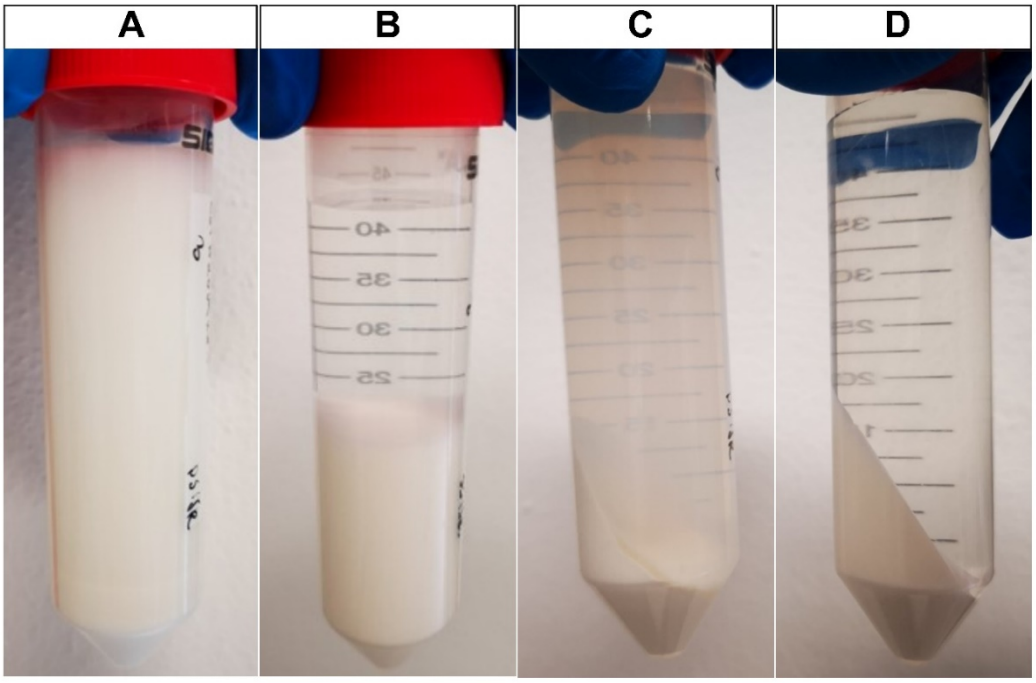


*Figure 50 Precipitates after synthesis via the C2 method. A) nsHAP after 24 h incubation. B) sHAP (Mg10Sr10) after 24 h incubation. C) nsHAP after 24 h incubation and processing. D) sHAP (Mg10Sr10) after 24 h incubation and processing.*

Filtration and washing partially reduced the gelatinous phase, as illustrated in Figure 51.

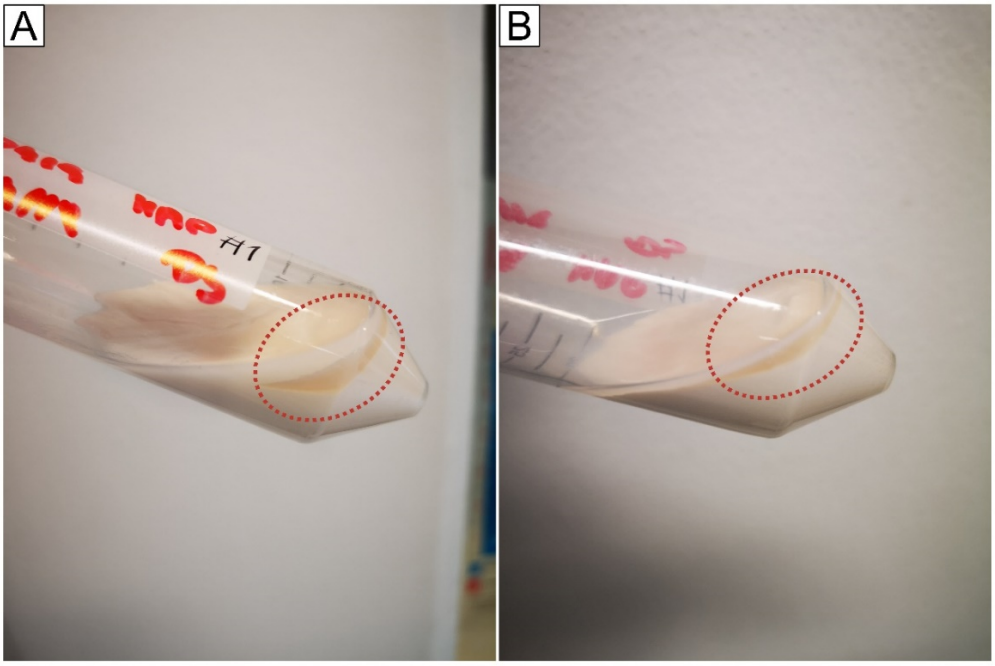


*Figure 51 Gelatinous phase in nsHAP precipitate. A) After 24 h incubation and filtration. B) After 24 h incubation, filtration and washing. Dashed red circles indicate the gelatinous precipitate.*

`

Synthesis with the FCR method produced precipitates without a gelatinous phase and showed potential for upscaling. However, ultrasonic probe abrasion introduced debris contamination of unknown composition into the precipitates (Figure 52), rendering FCR unsuitable for potential in vivo applications.

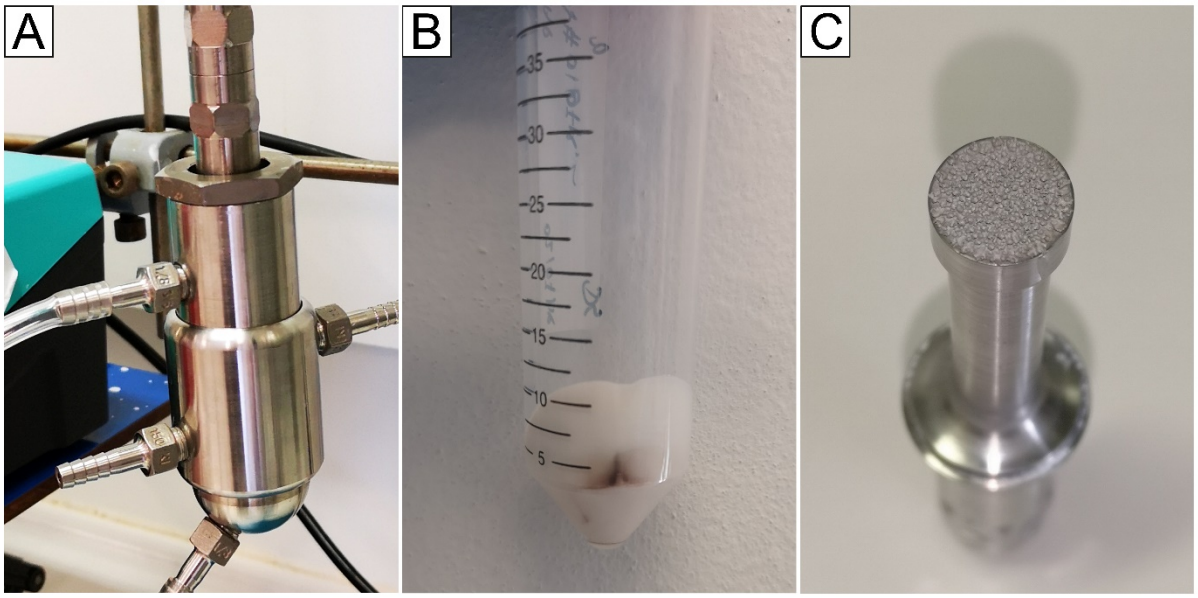


*Figure 52 Release of ultrasonic probe debris with the FCR synthesis method. A) Flow cell reactor. B) Debris particles in precipitate after filtration and washing. C) Abrasion of ultrasonic probe.*

The C2 method was identified as the most effective approach. Gelatinous phase reduction was achieved through filtration and washing. Flow was improved by tube priming through manual compression until saturation with the suspension, which enabled reduced flow rates and the elimination of air entrapment.

`

## 4.4.2. General FTIR Peak Assignment

FTIR spectral analysis characterises functional groups within materials, providing insights into chemical composition and structural properties. This technique provides quantifiable data on lattice structure, impurities, and crystallinity of HAP through analysis of the functional group ratios. The primary chemical groups identified in the FTIR spectra of calcium phosphates encompass $PO_4^{3-}$, $OH^-$, $CO_3^{2-}$, and $HPO_4^{2-}$ [678-681].

Phosphate bands in HAP exhibit four vibrational modes (v1–v4), identifiable in FTIR spectra, corresponding to [682-684]:

- v1 P-O symmetric stretching
- v2 O-P-O bending
- v3 P-O antisymmetric stretching
- v4 O-P-O bending

In contrast, phosphate bands in brushite display eight vibrational modes (v1 to v8) corresponding to [679, 685-687]:

- v1 (P)O-H stretching
- v2 P-O stretching
- v3 P-O(H) stretching
- v4 O-P-O(H) bending
- v5 P-O-H bending
- v6 P-O stretching
- v7 O-P-O(H) bending
- v8 O-P-O(H) bending

HAP is characteristically anhydrous, with water limited to adsorbed $H_2O$ on calcium-deficient HAP. Conversely, brushite contains intrinsic water molecules exhibiting one libration and three vibrational modes corresponding to [679, 685-688]:

- v1 symmetric O-H stretching
- v2 H-O-H bending
- v3 asymmetric O-H stretching

Carbonate bands exhibit four vibrational modes (v1–v4), of which three (v1–v3) are detectable by FTIR, with v2 and v3 being the most prominent. Carbonate ions can substitute for either phosphate (B-type substitution) or hydroxyl groups (A-type substitution) [676, 684].

Detailed information on associated wavelengths and other ion groups is provided in Table 26.

`

*Table 26 FTIR band assignments for brushite and HAP from the literature. Commas separate distinct peaks within the same vibrational mode, while ranges indicate variations in reported peak positions.*

| | HAP | | Brushite | |
|---|---|---|---|---|
| **Assignment** | **Wavenumber [$cm^{-1}$]** | **References** | **Wavenumber [$cm^{-1}$]** | **References** |
| **v1 of $PO_4$** | 960–962 | [304, 682-684, 689] | 2930–2936, 2380–2392, 2270, 2140 | [679, 685, 687, 688] |
| **v2 of $PO_4$** | 474–475, 462 | [304, 682-684, 689] | 1000–1005, 984–988 | [679, 685-688] |
| **v3 of $PO_4$** | 1087–1092, 1072, 1048–1046, 1032 | [304, 682-684, 689] | 871–880 | [679, 685-688] |
| **v4 of $PO_4$** | 601–603, 561–575 (merged) | [304, 682-684, 689] | 569–583 | [679, 685-688] |
| **v5 of $PO_4$** | | | 1200, 1207–1217, 785–790 | [679, 685-688] |
| **v6 of $PO_4$** | | | 1135–1140, 1123–1125, 1068–1075, 1057–1065 | [679, 685-688] |
| **v7 of $PO_4$** | | | 519–528, 535–543 | [679, 685, 686, 688] |
| **v8 of $PO_4$** | | | 394–400, 418–420 | [679, 685, 686] |
| **O-H stretching** | 3572 | [304, 682, 689, 690] | | |
| **OH libration** | 630–632 | [304, 682, 689] | | |
| **$H_2O$ libration** | | | 612, 661–665, 675–675 | [679, 685-688] |
| **v1 or v3 of $H_2O$** | | | 3541–3548, 3490 3280–3282, 3160–3166 | [679, 685, 688] |
| **v2 of $H_2O$** | | | 1720, 1649–1652 | [679, 685-688] |
| **HAP adsorbed $H_2O$** | 3500, 1630–1634 | [365, 691] | | |
| **$HPO_4^{2-}$** | 873–875, 1093–1091 | [323, 365, 678, 692] | | |
| **physisorbed $CO_2$** | 2347 | [690, 693] | | |
| **gaseous $CO_2$** | 2359, 2344 | [690, 693] | | |
| **v3 $CO_3^{2-}$ A-type** | 1454–1465, 1540–1550 | [323, 365, 619, 676, 690, 693-695] | | |
| **v3 $CO_3^{2-}$ B-type** | 1410–1422, 1447–1470 | [323, 365, 619, 676, 690, 693, 694, 696] | | |
| **v2 $CO_3^{2-}$ A-type** | 878–880 | [323, 676] | | |
| **v2 $CO_3^{2-}$ B-type** | 871–873 | [323, 694, 696] | | |
| **Residual nitrates** | 1380 | [323] | | |

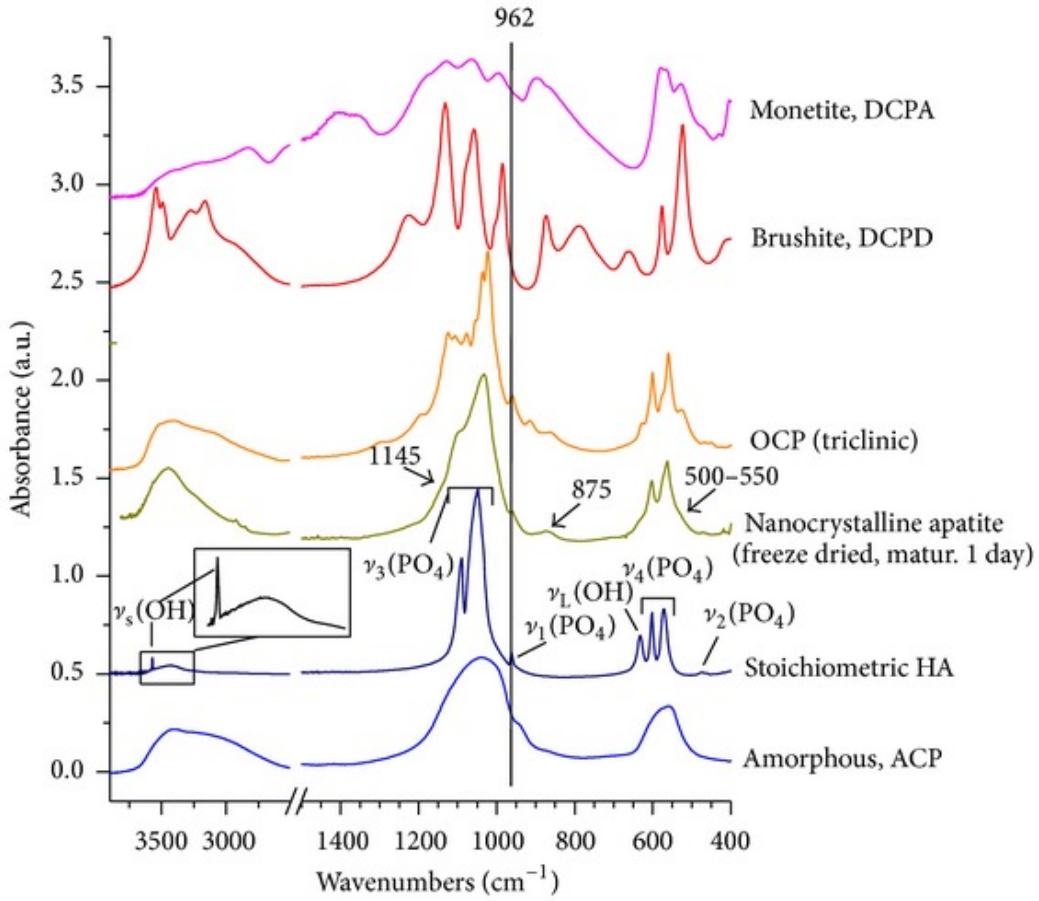


*Figure 53 FTIR reference spectra for various calcium phosphates. From [689].*

### 4.4.3. 24 h-Incubation Achieved Near-Stoichiometric HAP Ca/P Ratio

Given the reported influence of incubation time on synthesis outcomes [697-700], different incubation times were evaluated for non-substituted HAP (nsHAP) synthesised via the flow cell method: immediately after synthesis ($T_0$) and incubation periods of 2 h ($T_2$), 4 h ($T_4$) and 24 h ($T_{24}$). Changes in pH were monitored, Ca/P ratios were determined via ICP-OES analysis, and FTIR was employed to identify characteristic HAP functional groups.

Monitoring pH before and after processing at various incubation times served as an indicator of crystal maturation and ion dissolution dynamics [397, 402, 701, 702]. Unprocessed samples at $T_{24}$ exhibited a slightly lower pH than shorter incubation periods. Following filtration and washing, all incubation periods demonstrated a pH decline, with $T_{24}$ showing a more pronounced pH drop. $T_{24}$ exhibited the most substantial pH drop after filtration and the first washing step, maintaining a stable pH in subsequent washes. The pH decreased mainly

during the initial washing step for shorter incubation times, with minor changes observed thereafter (Figure 54).

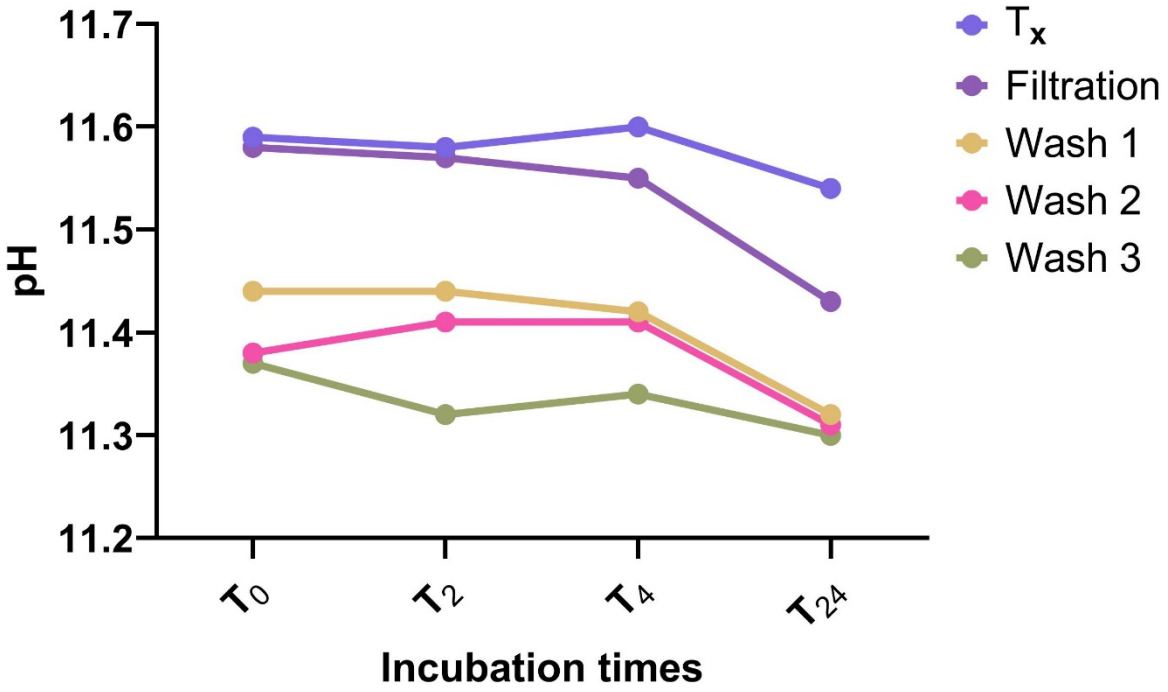


*Figure 54 pH development of nsHAP at different incubation times and processing steps. X-axis: Incubation times (0–24 h); Y-axis: Mean pH values. Legend: $T_x$ = after incubation, Filtration = after filtration, Wash 1–3 = after sequential washing steps*

FTIR peak assignments were made per the references listed in Table 26. Analysis of spectra (Figure 55) confirmed the presence of characteristic HAP functional groups across all investigated incubation times.

All incubation times showed adsorbed water with broad peaks at 3700–2500 $cm^{-1}$ and distinct peaks at 3440–3442 $cm^{-1}$ and ~1636 $cm^{-1}$ attributed to adsorbed $H_2O$. Peaks at ~1420 and ~1473 $cm^{-1}$ were assignable to v3 B-type $CO_3^{2-}$ incorporation into the lattice structure. Vibrational bands corresponding to $PO_4^{3-}$ were observed for v3 P-O stretching at ~1096 and 1033 $cm^{-1}$, for v1 P-O stretching at 962 $cm^{-1}$, for v2 O-P-O bending at ~472 $cm^{-1}$, and for v4 O-P-O bending at ~602 and ~564 $cm^{-1}$. Furthermore, OH was identified as a weak stretch across all incubation times at ~3572 $cm^{-1}$ (as a shoulder to the broad $H_2O$ band) and libration at ~630 $cm^{-1}$ (as a shoulder to v2 $PO_4^{3-}$ bands). Peaks observed at ~872 $cm^{-1}$ could be attributed to v2 B-type $CO_3^{2-}$ or $HPO_4^{2-}$. At $T_4$, additional peaks at 2359 and 2341 $cm^{-1}$ were assigned to adsorbed gaseous $CO_2$.

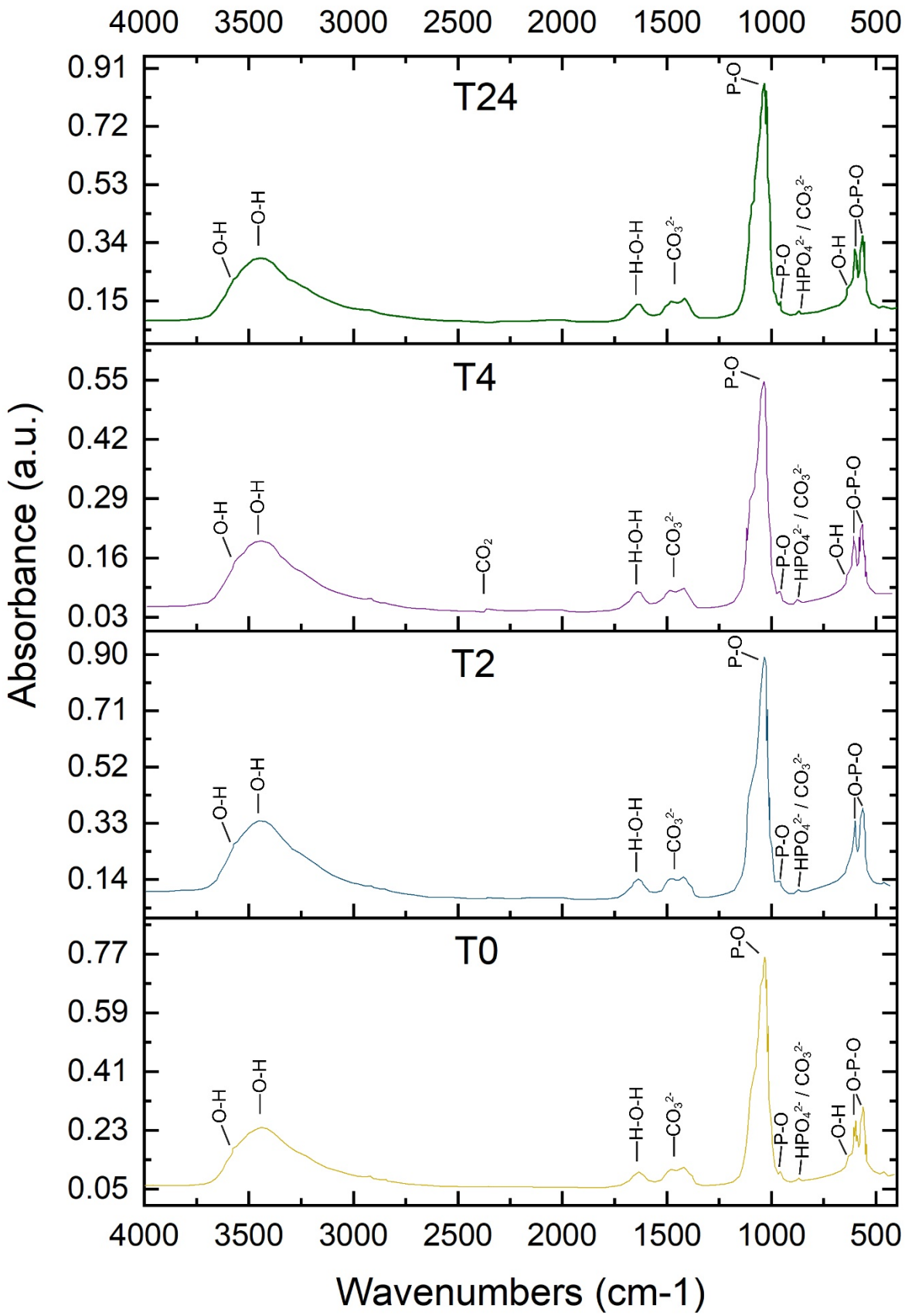


*Figure 55 FTIR spectra of nsHAP at different incubation times. X-axis: Wavenumbers ($cm^{-1}$); Y-axis: Absorbance (arbitrary units).*

Carbonate-to-phosphate ratio ($CO_3^{2-}{}_{1420}$/ $PO_4^{3-}{}_{1033}$) analysis revealed a consistent decline over incubation time, characteristic of first-order reaction kinetics. Conversely, the carbonate-to-hydroxyl ratio ($CO_3^{2-}{}_{1420}$/ $OH^-{}_{3572}$) demonstrated a decrease from $T_0$ to $T_4$, with a slight increase at $T_{24}$ (Figure 56).

Splitting factor calculations exhibited consistent values at $T_0$ and $T_2$, followed by an increase at $T_4$ and a decrease at $T_{24}$ below $T_0$ levels. These observations suggest an initial increase and subsequent reduction in crystallinity (Figure 56).

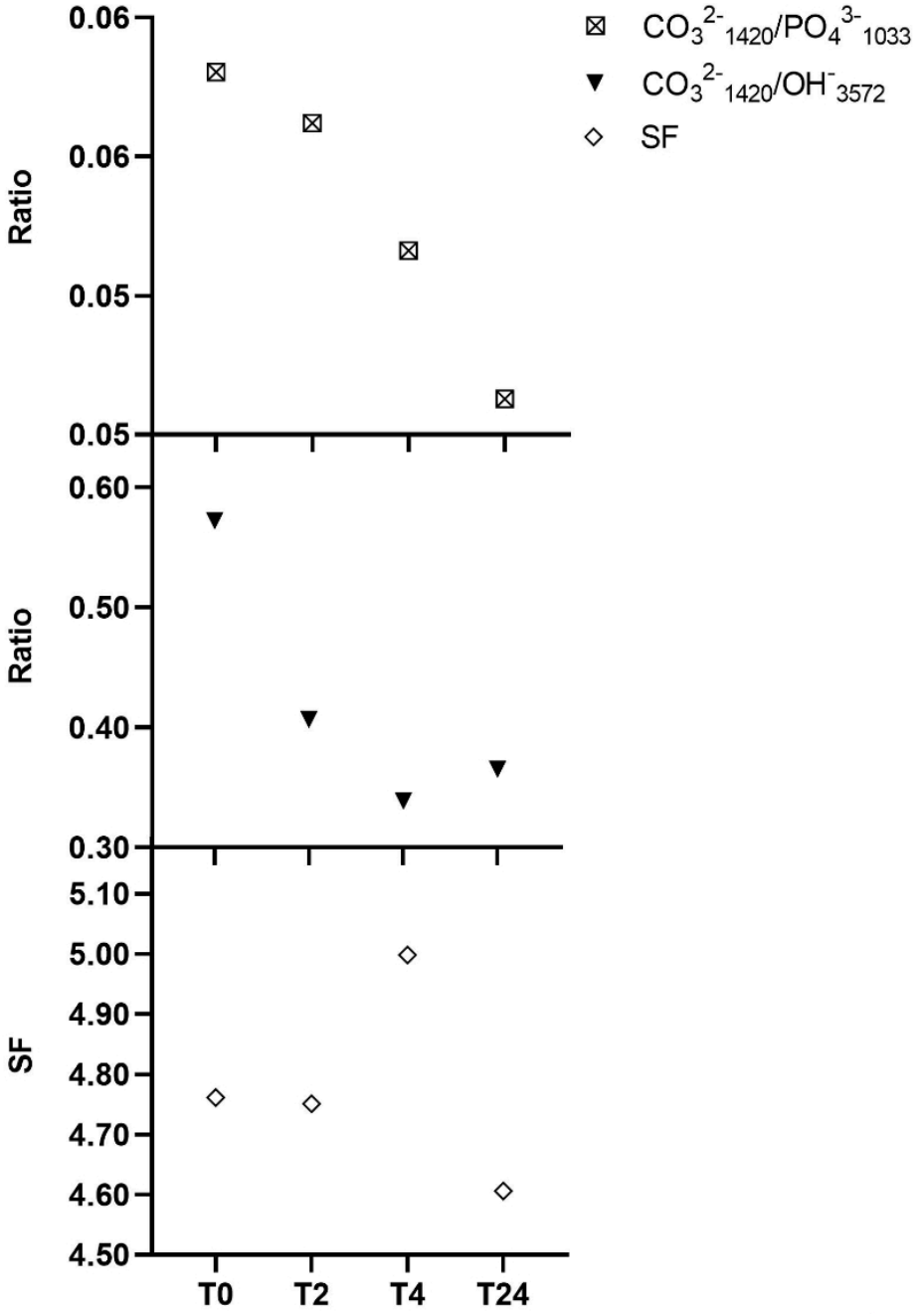


*Figure 56 Calculations of $CO_3^{2-}{}_{1420}$/ $PO_4^{3-}{}_{1033}$ and $CO_3^{2-}{}_{1420}$/ $OH^-{}_{3572}$ ratios and SF. X-axis: Incubation time (0–24 h); Y-axis: Ratios/SF (arbitrary units).*

`

Ca/P ratio analysis demonstrated a consistent decline with prolonged incubation time. A significant deviation was observed at $T_{24}$, compared to shorter incubation times, suggesting convergence towards the characteristic Ca/P ratio of stoichiometric HAP with increasing incubation time (Figure 57).

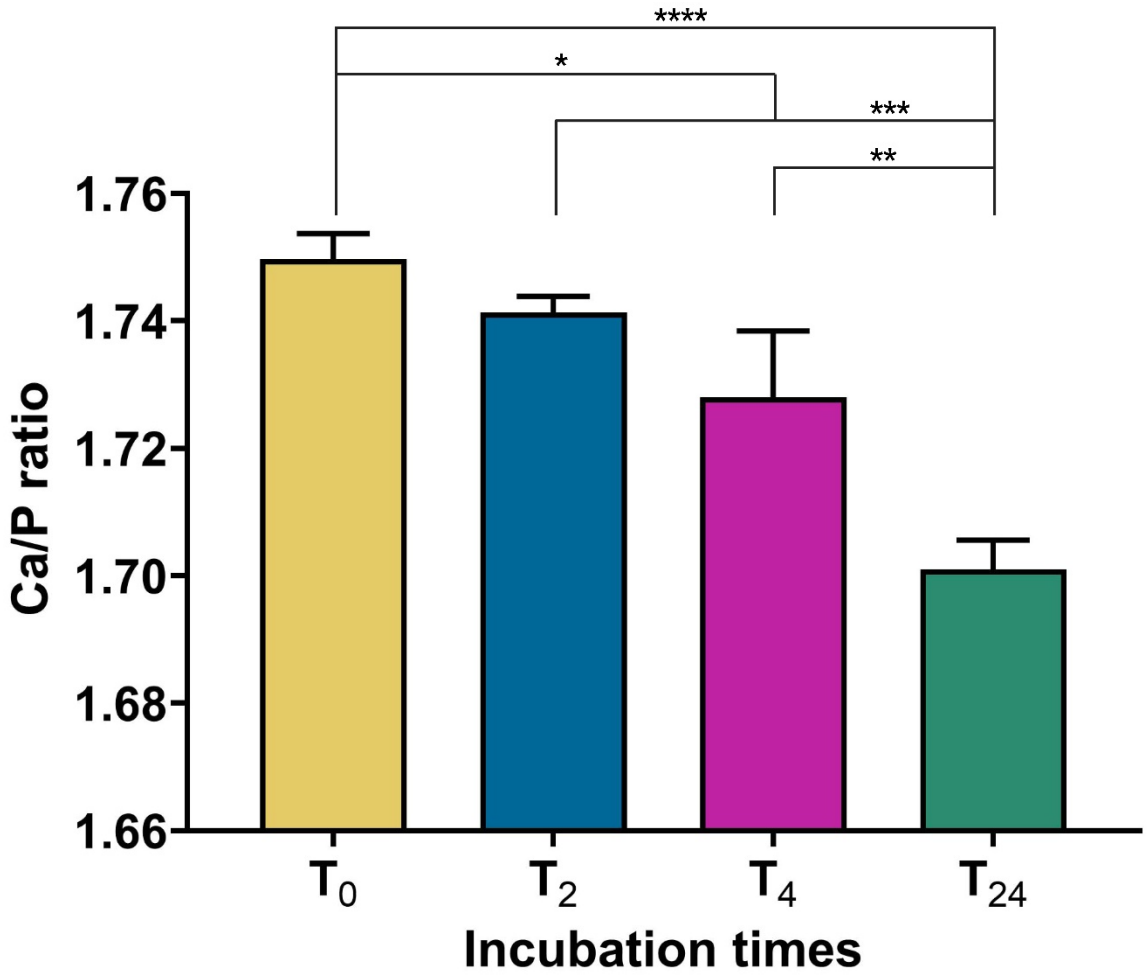


*Figure 57 Ca/P ratio of nsHAP at different incubation times from ICP-OES analysis. X-axis: Incubation times (0–24 h); Y-axis: Ca/P ratios. Data presented as mean ± SD (n = 3, ** adj. p< 0.01, *** adj. p< 0.001, **** adj. p< 0.0001).*

### 4.4.4. Synthesis of Mg/Sr-Substituted HAP with Varying Substitution Degrees

Another objective of this project was to evaluate different substitution degrees to determine formulations suitable for incorporation in a polymer matrix. Selection criteria prioritised substituent incorporation efficiency, Ca/P ratio, and phase purity. The results for all

`

investigated formulations, including Ca/P ratios and phase compositions, are summarised in Table 27.

*Table 27 Overview of ratios and phase compositions for all formulations synthesised via the C2 synthesis method.*

| Formulation | Achieved (Ca+Mg+S)/P Ratio | Phases |
|---|---|---|
| Mg20Sr20 | 1.14 | 72.4% brushite, 27.6% ACP, 0% HAP |
| Mg5Sr20 | 1.44 | 100% HAP |
| Mg20Sr5 | 1.42 | 19.4% brushite, 71.2% ACP, 9.4% HAP |
| Mg5Sr5 | 1.59 | 23.2% brushite, 76.8% HAP |
| Mg5Sr5–A | 1.51 | 3.8% brushite, 96.2% HAP |
| Mg5Sr10 | 1.46 | ~more HAP than Mg10Sr10 but less than Mg10Sr5 |
| Mg10Sr5 | 1.44 | 4.1% brushite, 95.9% HAP |
| Mg10Sr10 | 1.36 | 28.7% brushite, 71.3% HAP |

## HAP Substitution with 20% Mg Reduced Synthesis Success

This section presents the results of substitution experiments exploring formulations with 5% and 20% Mg and Sr. Syntheses were conducted using the C2 column method, with precursor phases adjusted to a 0.54 mol calcium concentration, targeting a final (Ca+Mg+Sr)/P ratio of 1.66. Specific formulation quantities are detailed in Table 15. Each formulation underwent synthesis and characterisation in duplicate, with triplicate assessment per group (n = 2 × 3).

The pH of each formulation was monitored at key intervals: immediately post-synthesis ($T_0$), after 24 h incubation ($T_{24}$), and following filtration and washing steps (Figure 58). All formulations exhibited normal distribution (Kolmogorov-Smirnov test). Statistical comparisons between incubation times were performed via one-way ANOVA, with results summarised in Table 33 in the appendix.

Except for Mg20Sr20, all formulations exhibited a significant pH decrease after 24 h incubation (adj. p-values in Table 33). For Mg20Sr20, the pH steadily increased during processing (adj. p = 0.0175), while other formulations maintained stable pH levels with only minor fluctuations. Overall, higher substitution levels were associated with more acidic environments, while lower substitution levels yielded more alkaline environments. Comparative analysis of Mg5Sr20 and Mg20Sr5 revealed that pH shifts depend on total substitution quantity and individual Mg and Sr substitution magnitudes. Directly after synthesis, Mg5Sr20 exhibited higher pH levels than Mg20Sr5 despite having the same total substitution degree.

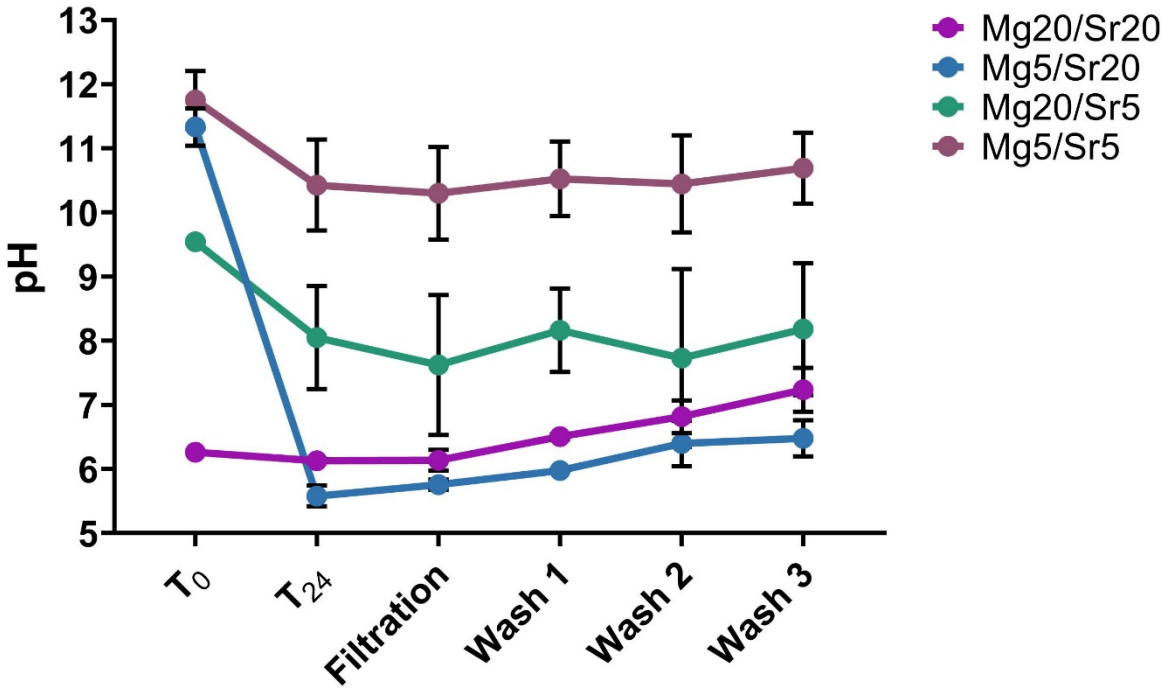


*Figure 58 pH development of sHAP formulations in the 5–20% substitution range at different time points and processing steps. X-axis: Time points and processing steps ($T_0$ = after synthesis, $T_{24}$ = after 24 h incubation, Filtration = after filtration, Wash 1–3 = after sequential washing steps); Y-axis: Mean pH values. Data presented as mean ± SD (n = 6).*

FTIR analysis (Figure 59) was performed to identify characteristic functional groups within the wavelengths typically associated with HAP and other calcium phosphates (Table 26).

In the Mg20Sr20 formulation, adsorbed water manifested as a broad peak spanning the ~3700–2500 $cm^{-1}$ range. Peaks on top of the broad water bands presented as sharp peaks at 3544 and 3486 $cm^{-1}$, and weak peaks at 3321 and 3173 $cm^{-1}$ were attributed to v1/v3 O-H stretching of $H_2O$. Peaks at 2360 and 2337 $cm^{-1}$ were assigned to gaseous surface $CO_2$. A peak at 1653 $cm^{-1}$ corresponded to v2 H-O-H bending of $H_2O$. The weak peak at 1383 $cm^{-1}$ was associated with $NO^{3-}$ residues. A subtle peak at 1220 $cm^{-1}$ could be attributed to v5 P-O-H bending vibrations. Sharp peaks with strong absorbance at 1134 $cm^{-1}$ and 1059 $cm^{-1}$ were linked to v6 P-O stretching vibrations. Peaks with weaker absorbance at 1005 and 982 $cm^{-1}$ were assigned to v2 P-O stretching. The peak at 870 $cm^{-1}$ corresponded to v3 P-O(H) stretching rather than v2 $CO_3^{2-}$ due to the lack of $CO_3^{2-}$ peaks in the 1400–1600 $cm^{-1}$ region. The peak at 792 $cm^{-1}$ was identified as v5 P-O-H bending, and the peak at 668 $cm^{-1}$ was identified as OH libration of $H_2O$. Additionally, peaks at 575 and 527 $cm^{-1}$ were associated with v4 O-P-O(H) bending and v7 O-P-O(H) bending, respectively. Compared to the reference spectrum (Figure 53), the spectrum of this formulation markedly deviated from HAP in the

reference spectrum. The broad $H_2O$ peak in the 3700–2500 $cm^{-1}$ region, along with the four sharp bending and stretching vibrations, the peak at 1653 $cm^{-1}$, the quadruple P-O split peak in the 1200–900 $cm^{-1}$ region, and the double P-O split peak in the 900–700 $cm^{-1}$ region, were characteristic of brushite. The calculation of the splitting factor for this formulation was not feasible due to the absence of distinct phosphate bands at 603 and 565 $cm^{-1}$.

The Mg5Sr20 formulation exhibited adsorbed water as a broad peak within the ~3700–2500 $cm^{-1}$ range. A distinct peak at 3424 $cm^{-1}$ was assignable to the v1/v3 O-H stretching of $H_2O$ or adsorbed $H_2O$ in HAP. Another peak at 1635 $cm^{-1}$ was assignable to v2 H-O-H bending of $H_2O$ or adsorbed $H_2O$ in HAP. A very weak peak, indicative of lattice O-H stretching vibrations, was observed at 3566 $cm^{-1}$. A weak peak at 2359 $cm^{-1}$ could be attributed to gaseous surface $CO_2$. Peaks at 1457 and 1418 $cm^{-1}$ were identified as B-type v3 $CO_3^{2-}$ vibrations. The weak peak at 1384 $cm^{-1}$ was attributed to $NO^{3-}$ residues. Vibrational peaks corresponding to v3 P-O stretching were observed at 1038 $cm^{-1}$, v1 P-O stretching at 961 $cm^{-1}$, and v4 O-P-O bending at 602 and 563 $cm^{-1}$. The peak at 875 $cm^{-1}$ could be assigned to $HPO_4^{2-}$ and/or v2 B-type $CO_3^{2-}$ vibrations within the lattice. The observed peaks corresponded to characteristic HAP peaks, as illustrated in Figure 53 and described in Table 26, confirming HAP presence. The splitting factor of 3.81 was notably lower than that of nsHAP.

In the Mg20S5 formulation, a broad peak observed in the range of ~3700–2500 $cm^{-1}$ corresponded to $H_2O$ vibrations accompanied by a weak shoulder at 3539 $cm^{-1}$ and a peak at 3483 $cm^{-1}$ assignable to v1/3 O-H stretching of $H_2O$. A sharp peak at 1648 $cm^{-1}$ was identified as v2 H-O-H bending of $H_2O$. Weak peaks at 1432 and 1382 $cm^{-1}$ were associated with v3 B-type $CO_3^{2-}$ vibrations and $NO^{3-}$ residues, respectively. The weak shoulder at 1222 $cm^{-1}$ could be attributed to v5 P-O-H bending vibrations, and the strong peak at 1059 $cm^{-1}$ could be assigned to v6 P-O stretching. The 874 $cm^{-1}$ peak could be attributed to v3 P-O(H) stretching or v2 B-type $CO_3^{2-}$, and the broad, weak peak at 785 $cm^{-1}$ to v3 P-O(H) stretching. Furthermore, the 576 $cm^{-1}$ and 530 $cm^{-1}$ peaks were assigned to v4 O-P-O(H) bending and v7 O-P-O(H) bending, respectively. The spectrum of this formulation did not align with characteristic HAP peaks. While minor peaks potentially attributable to brushite were detected, including the weak shoulder at 3539 $cm^{-1}$ and the broader peaks at 3483 $cm^{-1}$ and 3405 $cm^{-1}$, these peaks were insufficiently pronounced to suggest that brushite is the predominant phase. The observed peaks were broader and exhibited less splitting than known crystalline calcium phosphates, with no distinct, strong infrared bands corresponding to a specific crystalline calcium phosphate. However, the observed symmetry of the bands suggested that the spectrum likely represented an amorphous calcium phosphate [276, 703-705]. The splitting factor could not be calculated due to the absence of the required phosphate bands at 603 and 565 $cm^{-1}$ in the spectrum.

`

In the Mg5Sr5 formulation, adsorbed water appeared as a broad peak in the ~3700–2500 $cm^{-1}$ region, with a distinct peak at 3544 and 3486 $cm^{-1}$ attributable to v1/v3 O-H stretching of $H_2O$. Another $H_2O$ peak, attributed to the v2 H-O-H bending, was observed at 1645 $cm^{-1}$. The shoulder adjacent to the broad water band at 2921 $cm^{-1}$ was identified as v1 (P)O-H stretching. Peaks at 2360 and 2341 $cm^{-1}$ indicated gaseous surface $CO_2$ vibrations, whereas the peaks at 1423 and 1467 $cm^{-1}$ were assigned to v3 B-type $CO_3^{2-}$ lattice vibration. A band at 1385 $cm^{-1}$, corresponding to $NO^{3-}$ residues, was detected, consistent with previous spectra. The weak peak at 1218 $cm^{-1}$ was assigned to v5 P-O-H bending, and the shoulder at 1135 $cm^{-1}$ to v6 P-O stretching. The strong peak at 1059 $cm^{-1}$ was associated with v3 or v6 P-O stretching. The shoulder at 986 $cm^{-1}$ was associated with v2 P-O stretching. The weak peak at 874 $cm^{-1}$ was attributed to either v3 P-O(H) stretching in brushite, $HPO_4^{2-}$ in HAP or v2 B-type $CO_3^{2-}$. The broad peak at 789 $cm^{-1}$ was attributed to v5 P-O-H bending. Peaks at 602 and 574 $cm^{-1}$ were assigned to v4 O-P-O bending, whereas the 528 $cm^{-1}$ peak corresponded to v7 O-P-O(H) bending vibrations. The spectrum of this formulation showed high absorbance for water vibrations. Peaks characteristic of lattice water in brushite were observed at 3544 $cm^{-1}$ and 3486 $cm^{-1}$ but were less distinct compared to the Mg20Sr20 formulation and the reference in Figure 53. Furthermore, the $H_2O$ bending vibration at 1645 $cm^{-1}$ exhibited higher absorbance than Mg5Sr20 but remained weaker and broader than the distinct peak in brushite observed in formulation Mg20Sr20. Additionally, the peaks at 1218 $cm^{-1}$, 1135 $cm^{-1}$, 1059 $cm^{-1}$, and 986 $cm^{-1}$ aligned with brushite peaks, though very weak, except for the peak at 1059 $cm^{-1}$ which presented as shoulder rather than a separate peak characteristic for brushite. The P-O stretch at 874 $cm^{-1}$, typical for brushite, was also broader with a weaker absorbance than in Mg20Sr20. In the lower frequency region, v4 vibrations at 602 $cm^{-1}$ and 574 $cm^{-1}$ were characteristic of HAP, and the peak at 528 $cm^{-1}$ with brushite, though much weaker than in Mg20Sr20. This formulation indicated the presence of both HAP and brushite, with generally weaker brushite-attributable peaks suggesting HAP as the predominant phase despite the higher number of brushite peaks. The overlap of some brushite peaks may have obscured characteristic HAP vibrations, limiting the detection of HAP peaks. XRD results support this conclusion. The splitting factor for this formulation was 3.70.

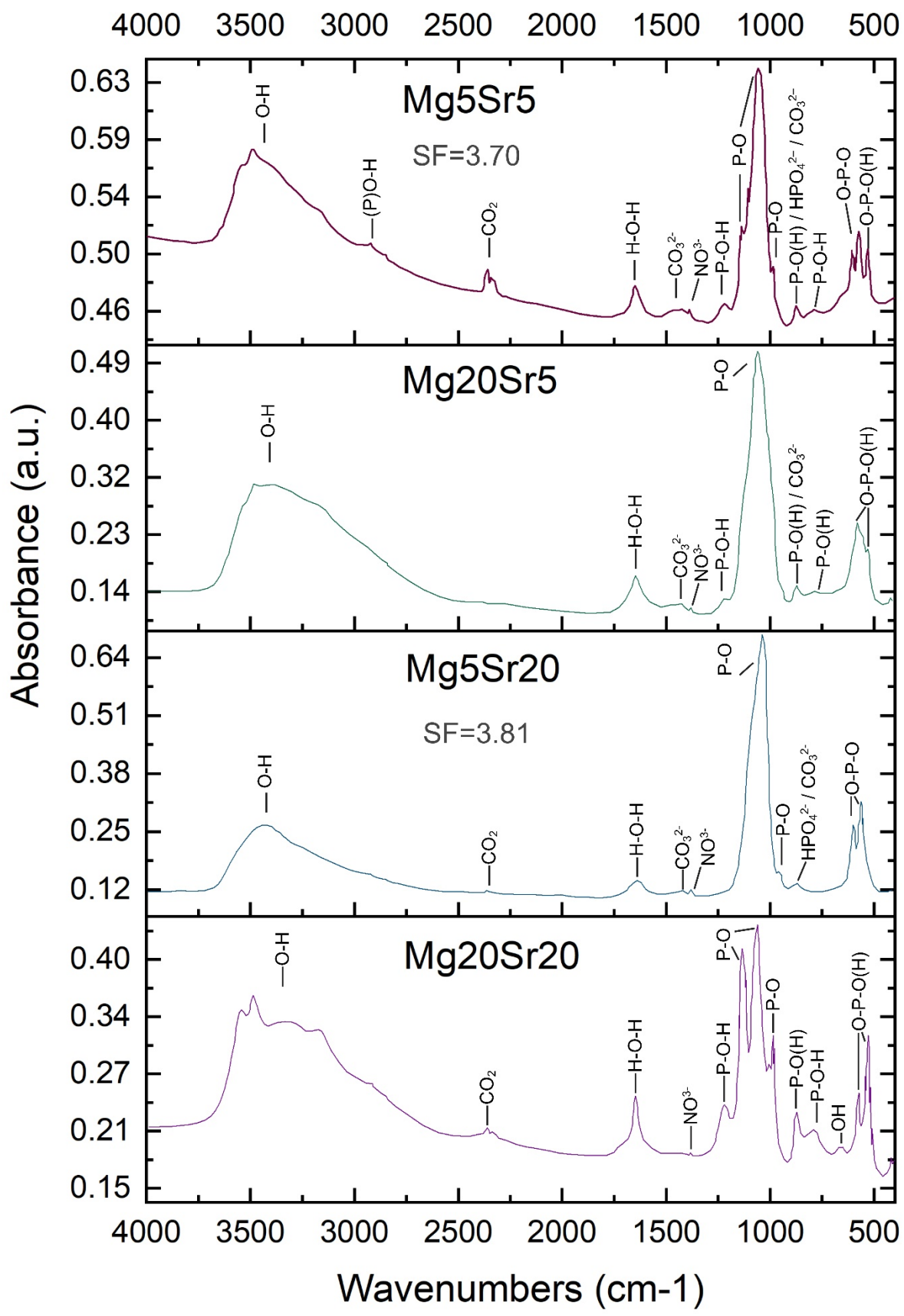


*Figure 59 FTIR spectra and splitting factors (SF) of sHAP formulations in the 5–20% substitution range. X-axis: Wavenumbers ($cm^{-1}$); Y-axis: Absorbance (arbitrary units).*

`

The incorporation efficiency rates for Ca, Mg, Sr, and P were calculated to assess the effect of individual and total substituent quantities on ion incorporation, using the achieved wt% from ICP-OES analysis and hypothetical values based on anticipated formula weights (Figure 60). Normal distribution was confirmed for all formulations using the Kolmogorov-Smirnov test. Deviations from hypothetical values were determined via a one-sample t-test, with group comparisons conducted through two-way ANOVA. Comprehensive statistical results are presented in Table 34 in the appendix.

All formulations demonstrated significant deviations in achieved incorporation compared to the hypothetical calculated values (adj. p-values in Table 34), with two exceptions: Mg5Sr20 showed no significant difference between achieved and anticipated values for Ca and P, and formulation Mg5Sr5 for P.

A comparison of Ca incorporation rates across different formulations revealed that the degree of Ca incorporation was more dependent on the individual quantities of Mg and Sr than the total substitution level. Mg20Sr20 and Mg5Sr5 formulations demonstrated similar Ca incorporation, while Mg5Sr20 exhibited significantly higher Ca incorporation than Mg20Sr5.

Individual Mg and Sr quantities and the total substitution level influenced Mg incorporation. Formulations with 5% Sr exhibited significantly higher Mg incorporation than those with 20% Sr. Reducing Mg substitution from Mg20Sr5 to Mg5Sr5 further increased Mg incorporation.

The amount of Sr in the formulation predominantly influenced Sr incorporation. Formulations containing 5% Sr exhibited significantly higher Sr incorporation than those with 20% Sr. The quantity of MG did not notably affect Sr incorporation.

P incorporation was lowest in the Mg20Sr5 formulation, with similar rates observed in all other formulations.

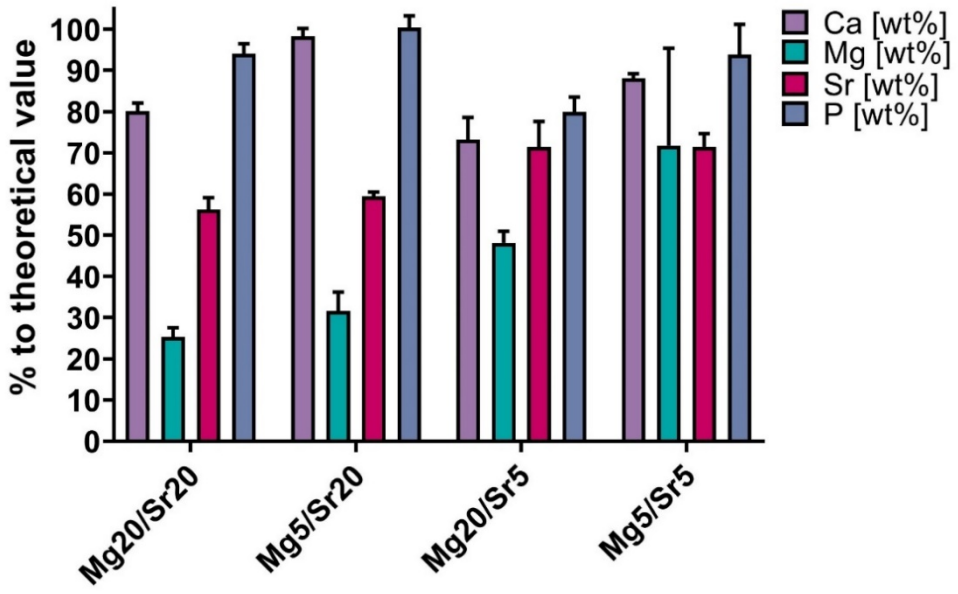


*Figure 60 Ion incorporation efficiency for Ca, Mg, Sr, and P of sHAP formulations in the 5–20% substitution range. X-axis: Different formulations; Y-axis: Incorporation efficiency in % to theoretical values. Data presented as mean ± SD (n = 6).*

Substitution degrees, quantified as mol% Mg or Sr relative to the total Ca+Mg+Sr incorporated, were determined from ICP-OES analysis results. Substitution rates were calculated from achieved and anticipated substitution values (Figure 61). The Kolmogorov-Smirnov test confirmed normal distribution for all formulations. Deviations from theoretical values were assessed using one-sample t-tests, with group comparisons performed via two-way ANOVA. Statistical results are summarised in Table 35 in the appendix.

Except for Mg in the Mg5Sr5 formulation, all other formulations demonstrated significant deviations from their theoretical values (adj. p-values in Table 35). Most formulations exhibited Mg and Sr substitution rates below anticipated levels, with Sr substitution in Mg20Sr5 slightly exceeding the expected substitution degree.

A significant interaction between theoretical and achieved Mg and Sr substitution was observed. The rate of Mg substitution was significantly higher (adj. $p < 0.0001$) in 5% Sr formulations than 20% Sr formulations at constant Mg levels. Similarly, the rate of Sr substitution was significantly higher (adj. p-values in Table 35) in 20% Mg formulations than 5% Mg formulations at constant Sr levels.

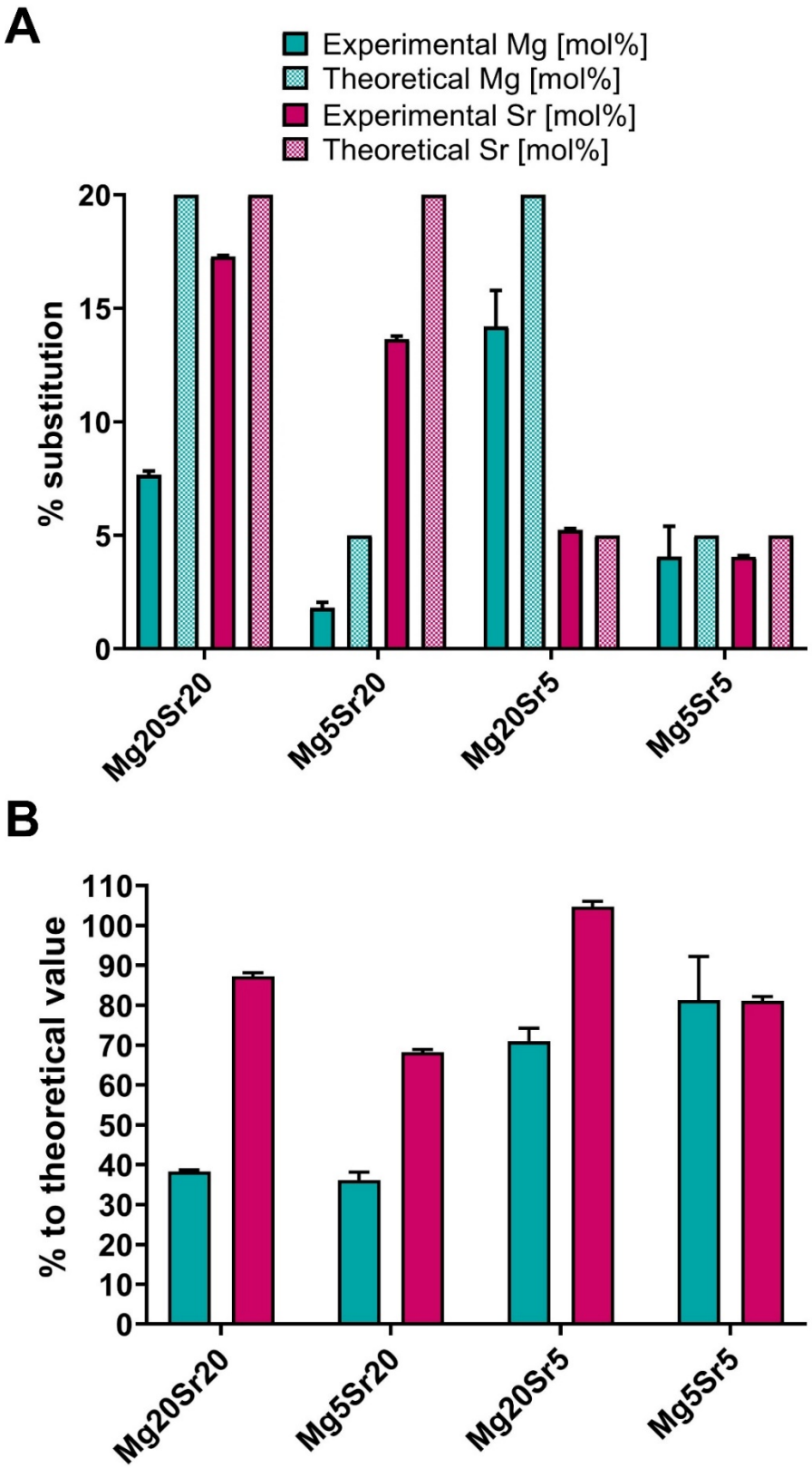


*Figure 61 Mg and Sr substitution degrees of sHAP formulations in the 5–20% substitution range. A) Experimental (solid bars) versus theoretical (dashed bars) Mg and Sr substitution. B) Substitution efficiency relative to theoretical values; X-axis: Different formulations. Y-axis: Mean %. Data presented as mean ± SD (n = 6).*

These findings suggest an inverse relationship between the Mg substitution rate and the co-substituent proportion and a direct relationship between the Sr substitution rate and the co-substituent proportion.

The Ca/P ratio, which varies among calcium phosphates, provides valuable insights into precipitate composition. Ca/P and (Ca+X)/P ratios, where X denotes one or more ions substituting for Ca, were calculated from Ca, P, Mg, and Sr concentrations measured by ICP-OES (Figure 62).

The Kolmogorov-Smirnov test confirmed normal distribution across all formulations. Ratio comparisons between and within formulations were performed via two-way ANOVA. Detailed statistical comparisons are presented in Table 36 in the appendix.

Formulations exhibited distinct elemental ratios. The (Ca+Mg+Sr)/P ratio was highest in Mg5Sr5 and lowest in Mg20Sr20 (adj. $p < 0.0001$), with similar values observed in Mg5Sr20 and Mg20Sr5. Variations in the Ca/P, (Ca+Mg)/P, (Ca+Sr)/P, and (Ca+Mg+Sr)/P ratios were determined by relative cationic (Ca, Mg, Sr) and anionic (P) ion incorporation.

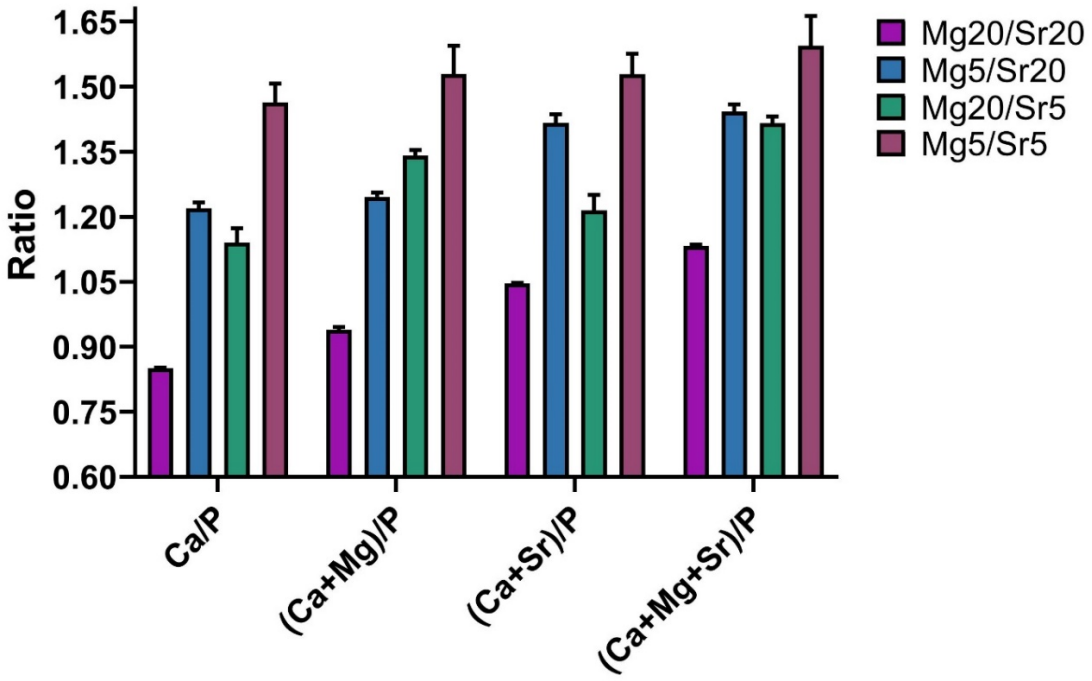


*Figure 62 Ratios of sHAP formulations in the 5–20% substitution range. X-axis: Ca/P, (Ca+Mg)/P, (Ca+Sr)/P, and (Ca+Mg+Sr)/P ratios; Y-axis: Ratio values. Data presented as mean ± SD (n = 6).*

XRD analysis was conducted by an external contractor to evaluate the phase composition and crystallinity of the precipitates from each formulation, thereby assessing the efficiency of HAP synthesis. The analysis provided the wt% of distinct calcium phosphate phases and their corresponding average crystallinity values (Table 28). Statistical analysis

`

was not possible due to the limited sample size. HAP formation was achieved in all formulations except Mg20Sr20. Among the formulations, Mg5Sr20 demonstrated the highest HAP content, followed by nsHAP and Mg5Sr5. In addition to HAP, other calcium phosphates were identified. Brushite was present in all groups except Mg5Sr20, which exclusively precipitated HAP. An amorphous phase was detected in Mg20Sr20 and Mg20Sr5, where minimal or no HAP was observed.

The crystallinity of nsHAP and Mg5Sr5 was comparable, with Mg5Sr20 demonstrating the lowest crystalline content. Due to the low crystalline phase presence, crystallinity could not be determined for Mg20Sr20 and Mg20Sr5.

*Table 28 Calcium phosphate phase composition [wt%] and crystallinity of precipitates from sHAP formulations in the 5–20% substitution range.*

| HAP Formulation | Brushite | Amorphous Phase | HAP | Crystallinity [± 0.5%] |
|---|---|---|---|---|
| nsHAP | 18.8 | - | 81.2 | 27.9% |
| Mg20Sr20 | 72.4% | 27.6% | - | - |
| Mg5Sr20 | - | - | 100% | 25.1% |
| Mg20Sr5 | 19.4% | 71.2% | 9.4% | - |
| Mg5Sr5 | 23.2% | - | 76.8% | 28.2% |

The findings in this section demonstrate that the Mg5Sr5 formulation achieved the highest total ion incorporation and (Ca+Mg+Sr)/P ratio. Increasing Mg substitution to 20% enhanced Sr incorporation but reduced HAP precipitation (Mg20Sr5), with complete HAP absence at 20% Mg and Sr substitution (Mg20Sr20).

## HAP Substitution with 5–10% Mg and 5% Sr Yielded High Purity and Ion Incorporation

This section summarises the outcomes of substitution experiments with 5% and 10% Mg and Sr content. Syntheses were carried out using the C2 column method, with precursor phases adjusted to 0.54 mol calcium concentration, targeting a final (Ca+Mg+Sr)/P ratio of 1.66. Specific quantities for each formulation are provided in Table 15. Synthesis and characterisations were repeated once and assessed in triplicate (n = 1 × 3).

The pH of each formulation was recorded at three time points: immediately after synthesis ($T_0$), following 24 h incubation ($T_{24}$), and post-processing ($T_{PP}$) (Figure 63). The limited sample size prevented the assumption of normal distribution. Statistical analysis of pH variations across incubation times was conducted using one-way ANOVA, with results summarised in Table 37 in the appendix.

Immediately after synthesis, formulations with 5% Mg substitution exhibited significantly higher pH values (~12) than 10% Mg formulations (~8.5) (adj. $p < 0.0001$). All formulations exhibited significant pH reduction after 24 h incubation (adj. $p < 0.0001$).

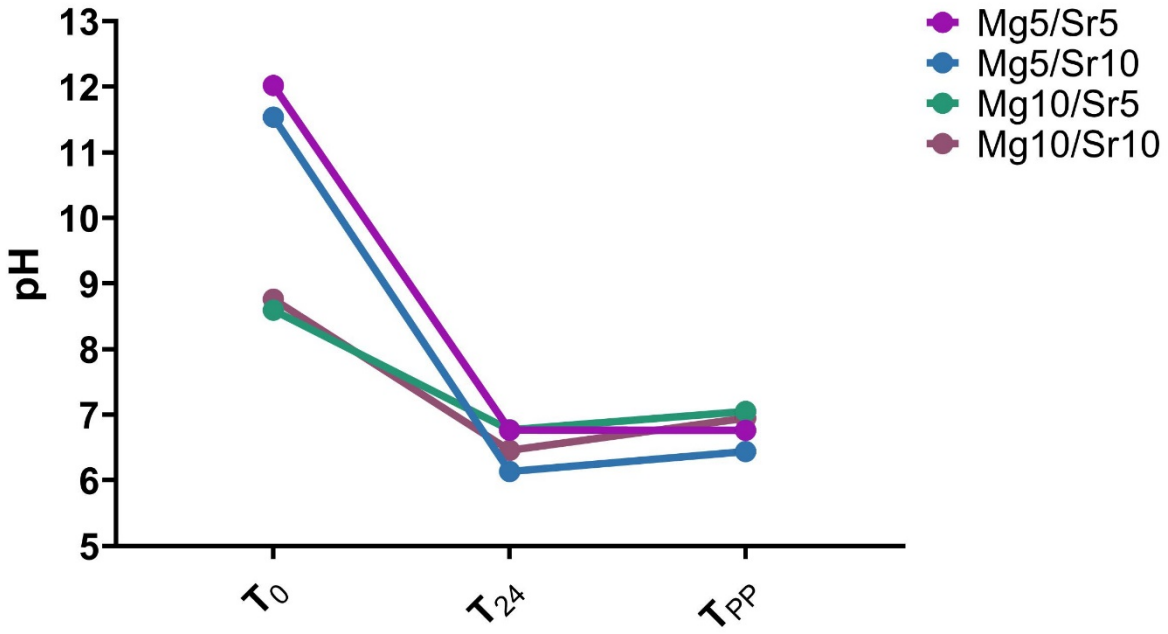


*Figure 63 pH development of sHAP formulations in the 5–10% substitution range at different time points and after processing. X-axis: Time points and processing ($T_0$ = after synthesis, $T_{24}$ = after 24 h incubation, $T_{PP}$ = after processing); Y-axis: pH changes. Data presented as mean ± SD (n = 3).*

FTIR analysis was conducted to identify key functional groups at characteristic wavelengths, enabling the determination of the precipitate composition (Figure 64). Peak assignments were made according to Table 26.

In the Mg5Sr5 formulation, a broad peak of adsorbed water was observed within the~3700–2500 $cm^{-1}$ range, with an absorption maximum at 3423 $cm^{-1}$ attributed to v1/v3 O-H stretching of $H_2O$. A weak shoulder to the broad water band at 3567 $cm^{-1}$ was assigned to O-H stretching. Additionally, peaks at 2360 and 2342 $cm^{-1}$ were associated with gaseous surface $CO_2$. A peak at 1647 $cm^{-1}$ was attributed to v2 H-O-H bending of $H_2O$. The peaks at 1447 and 1420 $cm^{-1}$ were identified as v3 B-type $CO_3^{2-}$ vibrations. The peak at 1384 $cm^{-1}$ corresponded to $NO^{3-}$ residues. The shoulder at 1090 $cm^{-1}$ and the strong peak at 1033 $cm^{-1}$ were identified as v3 P-O stretching vibrations, whereas a subtle shoulder at 960 $cm^{-1}$ was assigned to v1 P-O stretching. The peak observed at 875 $cm^{-1}$ could be attributed to v2 B-type $CO_3^{2-}$ or $HPO_4^{2-}$ modes. The weak peak at 669 $cm^{-1}$ could be assigned to $H_2O$ libration, the peaks at 603 and 563 $cm^{-1}$ to v4 O-P-O bending, and the weak peak at 469 $cm^{-1}$ to v2 O-P-O bending.

The spectrum for this formulation displayed peaks characteristic of HAP, as shown in Figure 53 and assigned according to Table 26. The splitting factor, measured at 3.79, was the highest within the 5–10% substitution range but remained lower than nsHAP's.

In the Mg5Sr10 formulation, adsorbed water exhibited a broad peak within the range of ~3700–2500 $cm^{-1}$, with a maximum at 3417 $cm^{-1}$ and a shoulder at 3541 $cm^{-1}$ attributed to v1/v3 O-H stretching of $H_2O$. A broad peak at 2349 $cm^{-1}$ was attributed to gaseous surface $CO_2$. A peak observed at 1648 $cm^{-1}$ was assignable to v2 H-O-H bending of $H_2O$. Peaks at 1449 and 1420 $cm^{-1}$ were identified as v3 $CO_3^{2-}$ vibrations, and a weak peak at 1384 $cm^{-1}$ was associated with $NO^{3-}$ residues. A shoulder at 1220 $cm^{-1}$ was assigned to v5 P-O-H bending, whereas a weak shoulder at 1091 $cm^{-1}$ and a strong peak at 1029 $cm^{-1}$ were assigned to v3 P-O stretching vibrations. The weak shoulder at 952 $cm^{-1}$ was attributed to v1 P-O stretching. A peak at 874 $cm^{-1}$ was attributed to either v2 B-type $CO_3^{2-}$, $HPO_4^{2-}$ in HAP, or v3 P-O(H) stretching, and the broad peak at 785 $cm^{-1}$ was attributed to v5 P-O-H bending in brushite. Peaks in the lower wavelength region at 602 and 563 $cm^{-1}$ were identified as v4 O-P-O vibrations, whereas the small peak at 529 $cm^{-1}$ was attributed to v7 O-P-O(H) bending. Furthermore, the shoulder at 460 $cm^{-1}$ corresponded to v3 P-O vibration modes.

This formulation displayed predominantly HAP characteristics with weak v5 and v7 peaks, indicating minor brushite presence. The splitting factor was calculated as 3.59.

Formulation Mg10Sr5 exhibited a broad peak corresponding to adsorbed water within the range of ~3700–2500 $cm^{-1}$, with a peak maximum at 3424 $cm^{-1}$ due to v1/v3 O-H stretching of $H_2O$. Peaks at 2360 and 2342 $cm^{-1}$ were attributed to gaseous surface $CO_2$. A peak at 1644 $cm^{-1}$ was assigned to v2 H-O-H bending of $H_2O$. Peaks at 1450 and 1421 $cm^{-1}$ were attributed to v3 B-type $CO_3^{2-}$ vibrations, and the peak at 1384 $cm^{-1}$ was attributed to $NO^{3-}$ residues. The weak shoulder at 1095 $cm^{-1}$ and the strong peak at 1031 $cm^{-1}$ corresponded to v3 P-O stretching, whereas the weak shoulder at 952 $cm^{-1}$ was attributed to v1 P-O stretching. A peak at 876 $cm^{-1}$ was assignable to either v3 P-O(H) stretching, v2 B-type $CO_3^{2-}$ or $HPO_4^{2-}$. The subtle peak at 669 $cm^{-1}$ was assigned to $H_2O$ libration, the peaks at 602 and 562 $cm^{-1}$ to v4 O-P-O bending, and the small peak at 471 $cm^{-1}$ to v2 O-P-O bending vibrations.

The spectrum for this formulation exhibited peaks characteristic of HAP, with a splitting factor calculated as 3.47.

Similar to spectra in previous formulations, Mg10Sr10 exhibited a broad band of adsorbed water in the higher wavenumber region of ~3700–2500 $cm^{-1}$, with a peak maximum at 3443 $cm^{-1}$, a distinct shoulder at 3535 $cm^{-1}$, and a weaker shoulder at 3164 $cm^{-1}$ attributable to v1/v3 O-H stretching of $H_2O$. Peaks at 2349 and 2283 $cm^{-1}$ were assigned to gaseous surface $CO_2$. A peak at 1649 $cm^{-1}$ was identified as the v2 H-O-H bending mode of $H_2O$. The peak at 1423 $cm^{-1}$ was identified as v3 B-type $CO_3^{2-}$ vibrations, and the small peak at 1384 $cm^{-1}$ was attributed to $NO^{3-}$ residues. A shoulder at 1225 $cm^{-1}$ was assigned to v5 P-O-H bending, whereas a weaker shoulder at 1091 $cm^{-1}$ and a strong peak at 1035 $cm^{-1}$ were attributed to v3 P-O stretching modes. The peak at 874 $cm^{-1}$ was assignable to either v2 B-type $CO_3^{2-}$, $HPO_4^{2-}$ in HAP, or v3 P-O(H) stretching. The broad peak at 789 $cm^{-1}$ was attributed to v5 P-O-H

rotation. The weak peak at 673 $cm^{-1}$ could be assigned to $H_2O$ libration, the peaks at 600 and 561 $cm^{-1}$ to v4 O-P-O bending, and the adjacent peak at 528 $cm^{-1}$ to v7 O-P-O(H) bending.

This formulation exhibited characteristic HAP peaks, with weaker v5 and v7 brushite peaks that were stronger than in Mg5Sr10, indicative of HAP as the predominant phase with minor brushite presence. The splitting factor was calculated as 3.00.

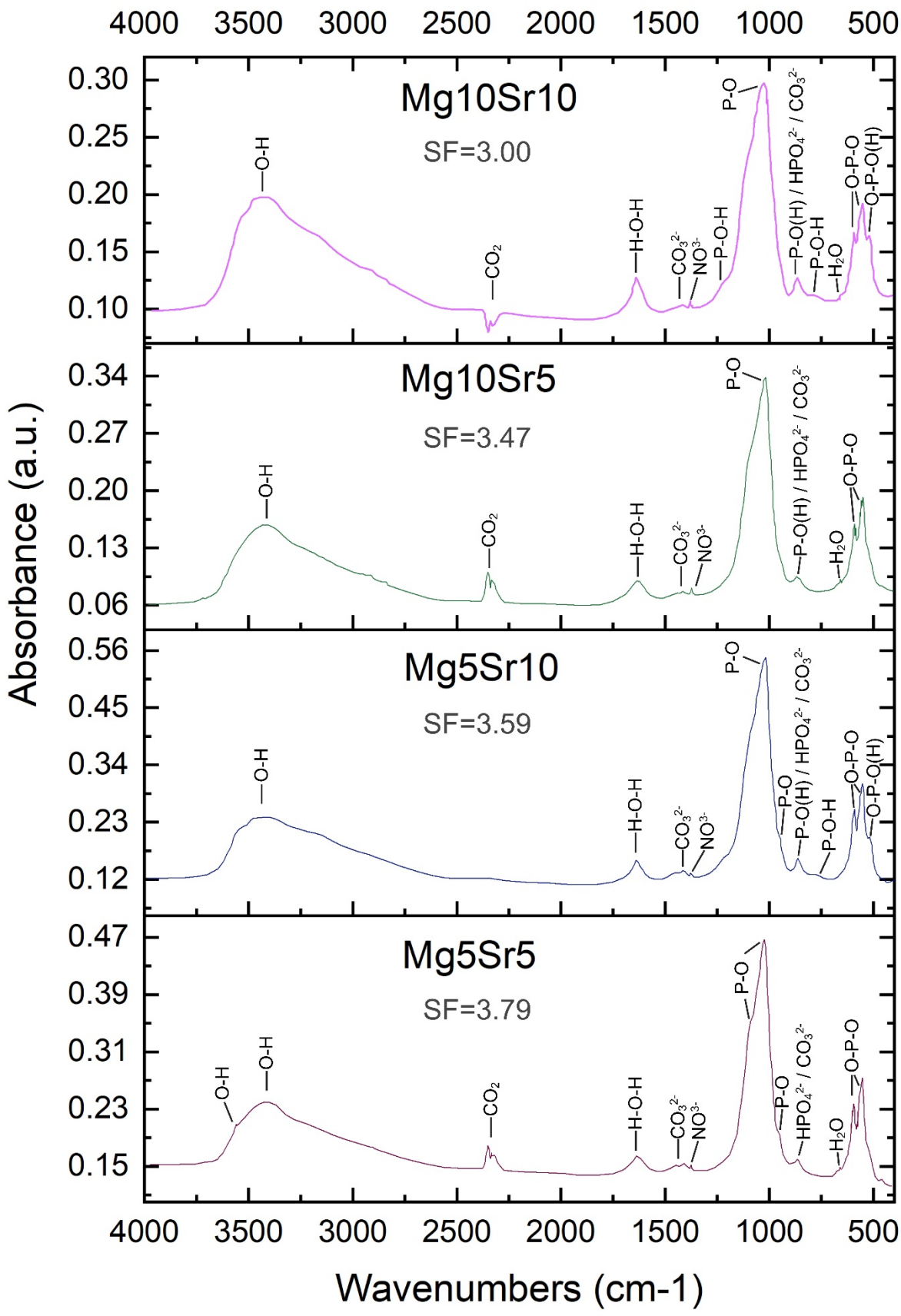


*Figure 64 FTIR spectra and splitting factors (SF) of sHAP formulations in the 5–10% substitution range. X-axis: Wavenumbers ($cm^{-1}$); Y-axis: Absorbance (arbitrary units).*

`

As previously described, the effect of individual and combined substituents on the efficacy of ion incorporation was analysed from calculated Ca, Mg, Sr, and P incorporation rates (Figure 65).

Most formulations followed a normal distribution (Shapiro-Wilk test), except for Mg10Sr10 with respect to Sr [wt%] due to the small sample size. Deviations from theoretical values were assessed via one-sample t-tests, with inter-group comparisons performed using two-way ANOVA. A summary of the statistical results is provided in Table 38 in the appendix.

All formulations exhibited significant deviations between achieved and calculated ion incorporation values (adj. p-values in Table 38), except Mg5Sr10, showing no significant differences for Ca and P incorporation.

The Ca incorporation rate was primarily influenced by the magnitude of combined Mg and Sr substitution, with the lowest rate observed in the Mg10Sr10 formulation (adj. $p < 0.0001$). Mg5Sr10 and Mg10Sr5 demonstrated Ca incorporation rates similar to Mg5Sr5. Mg itself influenced Ca incorporation, with Mg5Sr10 showing higher rates than Mg10Sr5 (adj. $p = 0.0018$).

Similar to the previous substitution range, the degree of Sr substitution influenced the rate of Mg incorporation. Mg incorporation rates were significantly higher (adj. $p < 0.0001$) in formulations with 5% Sr than those with 10% Sr. Formulations containing 5% and 10% Mg exhibited similar Mg incorporation rates, provided the Sr substitution level remained constant.

The Sr incorporation rate was significantly lower (adj. $p < 0.0001$) in formulations with 10% Sr than those with 5% Sr.

The Mg10Sr10 formulation displayed the lowest P incorporation rate (adj. $p < 0.0001$).

`

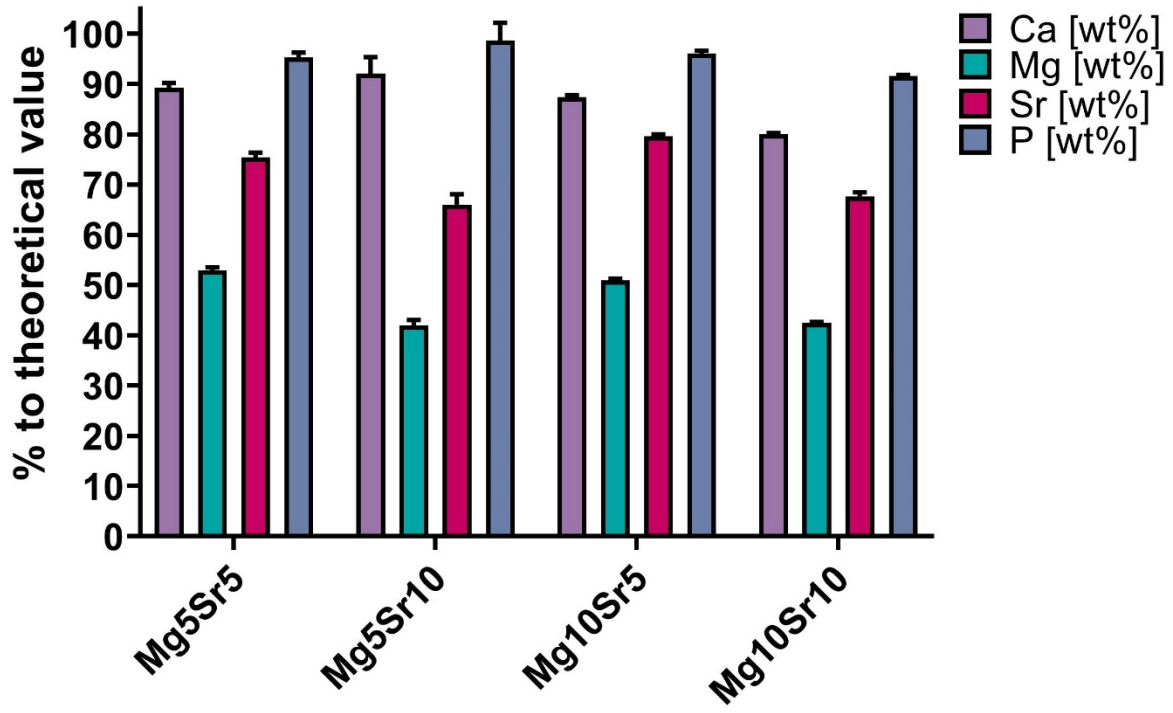


*Figure 65 Ion incorporation efficiency for Ca, Mg, Sr, and P of sHAP formulations in the 5–10% substitution range. X-axis: Different formulations; Y-axis: Incorporation efficiency in % to theoretical values. Data presented as mean ± SD (n = 3).*

The Mg and Sr substitution rates relative to total Ca+Mg+Sr mol% were calculated and compared to theoretical values (Figure 66). Most formulations exhibited normal distribution (Shapiro-Wilk test), except for Mg5Sr10 Mg [mol%] due to limited sample size. Divergences from theoretical values were assessed via one-sample t-tests, with inter-formulation comparisons performed using two-way ANOVA (results summarised in Table 39 in the appendix).

All formulations demonstrated significant differences between experimental and predicted Mg and Sr substitution rates (adj. p-values in Table 39).

The magnitude of Mg and Sr substitution in the formulations influenced the substitution rates for both ions. The Mg substitution rate was higher (adj. $p < 0.0001$) in formulations with 5% Sr than those with 10% Sr. In formulations with 10% Sr, the Mg substitution rate was higher at 10% Mg than 5% (adj. $p < 0.0001$). The Sr substitution rate was greater in formulations with 10% Mg than those with 5% Mg (adj. p-values in Table 39) and higher with 5% Sr than 10% Sr at constant Mg levels (adj. $p < 0.0001$).

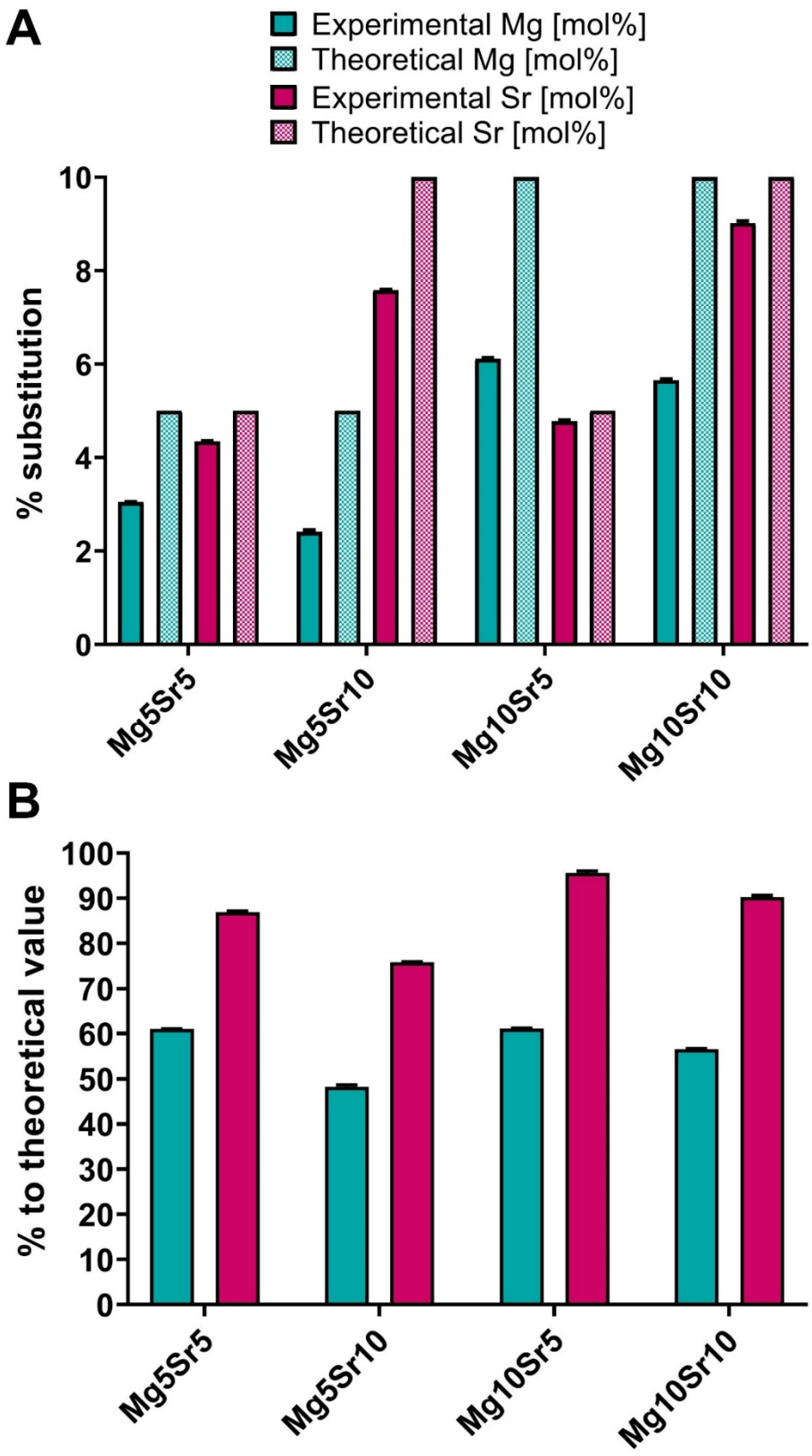


*Figure 66 Mg and Sr substitution degrees of sHAP formulations in the 5–10% substitution range. A) Experimental (solid bars) versus theoretical (dashed bars) Mg and Sr substitution. B) Substitution efficiency relative to theoretical values. X-axis: Different formulations; Y-axis: Mean %. Data presented as mean ± SD (n = 3).*

`

The Ca/P and (Ca+X)/P ratios were calculated as previously described. All formulations exhibited normal distributions (Shapiro-Wilk test). Comparisons within groups were performed using two-way ANOVA, with results summarised in Table 40 in the appendix.

Although the targeted (Ca+Mg+Sr)/P ratio of 1.66 was not achieved in any formulation, the highest (Ca+Mg+Sr)/P ratio was observed in Mg5Sr5, and the lowest in Mg10Sr10 (adj. $p < 0.0001$). The (Ca+Mg+Sr)/P ratio in Mg5Sr10 was higher than in Mg10Sr5 (adj. $p < 0.0001$). A similar pattern was observed for Ca/P ratios across all formulations (adj. $p < 0.0001$) (Figure 67).

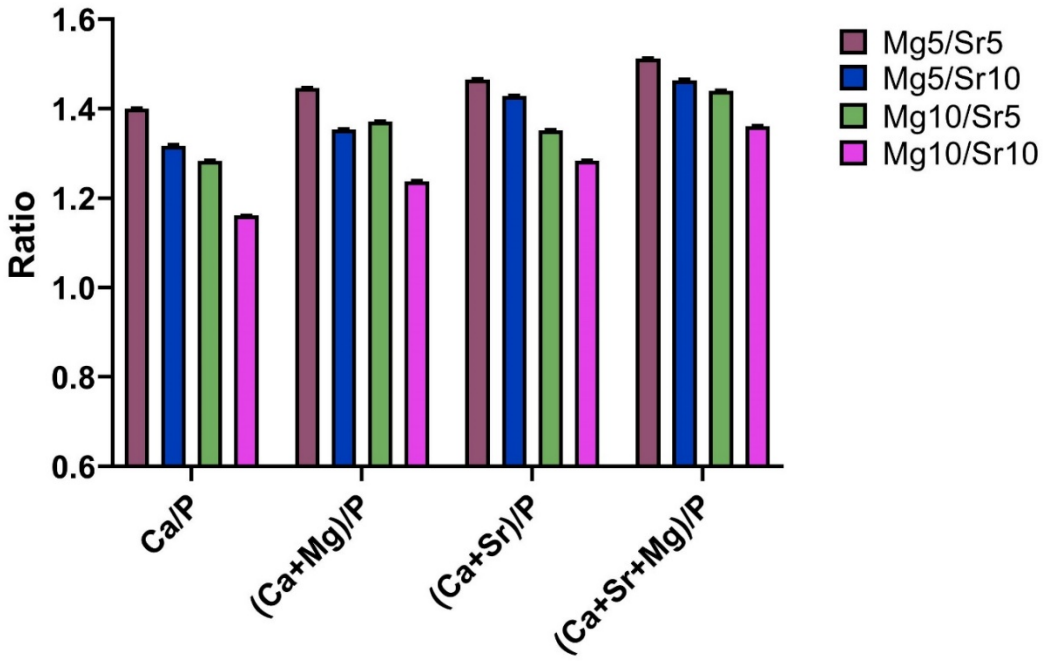


*Figure 67 Ratios of sHAP formulations in the 5–10% substitution range. X-axis: Ca/P, (Ca+Mg)/P, (Ca+Sr)/P, and (Ca+Mg+Sr)/P ratios; Y-axis: Ratio values. Data presented as mean ± SD (n = 6).*

The phase composition and crystallinity of all formulations, except for Mg5Sr10, were assessed by an external contractor (Table 29).

The results revealed high HAP phase precipitation, exceeding 90%, in Mg5Sr5 and Mg10Sr5, with brushite levels below 5%. Mg10Sr10 also exhibited high HAP formation at 71.3%, although this was lower than the other groups, with a higher brushite content of 28.7%. Crystallinity values were similar across all formulations, with the Mg5Sr5 formulation achieving the highest crystallinity.

Although XRD analysis was not conducted for the Mg5Sr10 formulation, FTIR analysis provided evidence of HAP formation alongside the presence of brushite, though at lower levels than in Mg10Sr10 and higher than in Mg10Sr5. Based on these results, it is assumed that the wt% of HAP in the Mg5Sr10 formulation was between 71.3% and 95.9%.

`

*Table 29 Calcium phosphate phase composition [wt%] and crystallinity of precipitates from sHAP formulations in the 5–10% substitution range.*

| HAP Formulation | Brushite | Amorphous Phase | HAP | Crystallinity [± 0.5%] |
|---|---|---|---|---|
| Mg5Sr5 | 3.8% | - | 96.2% | 29.7 |
| Mg10Sr5 | 4.1 | - | 95.9 | 26.2 |
| Mg10Sr10 | 28.7% | - | 71.3% | 24.2% |

The findings presented in this section confirm the successful precipitation of Mg and Sr-sHAP in three of the four synthesised formulations. Formulations Mg5Sr5 and Mg10Sr5 exhibited the highest HAP phase composition, crystallinity, substituent incorporation, and (Ca+Sr+Mg)/P ratios.

Consequently, these formulations demonstrated the most favourable characteristics and were selected for subsequent cytotoxicity testing prior to polymer matrix incorporation for scaffold fabrication.

### 4.4.5. Mg5Sr5 and Mg10Sr5 sHAP Exhibited No Cytotoxicity to Y201 MSCs

As previously described, the cytotoxicity of sHAP formulations Mg5Sr5 and Mg10Sr5 was evaluated on Y201 MSCs using a transwell system. Prior to conducting experiments with these formulations, the maximum permissible HAP concentration without cytotoxic effects was determined using commercially available MgHAP (SINTlife®) at concentrations of 10 µg/ml, 505 µg/ml, and 1000 µg/ml in cell culture medium.

Potential cytotoxicity-induced variations in metabolic activity were assessed using the resazurin assay, comparing MgHAP-treated Y201 MSCs to untreated standard cell culture (SCC) controls (Figure 68).

This analysis was repeated once, with each group assessed in triplicate (n = 1 × 3). Results are presented as x-fold change, with statistical analysis conducted on non-normalised raw data. Shapiro-Wilk test confirmed normal distribution across all groups. Inter-group and time point comparisons were performed using two-way ANOVA. A summary of the statistical results is provided in Statistical Results for Cytotoxicity Testing with MgHAP and sHAP

Table 41 in the appendix.

All concentrations demonstrated a significant increase (adj. $p < 0.0001$) in metabolic activity between time points. No statistically significant inter-group differences were observed on days 1 and 7. On day 4, significant differences between SCC and concentrations Min (adj. $p = 0.0079$) and Med (adj. $p = 0.0167$) were identified, with SCC exhibiting slightly lower metabolic activity.

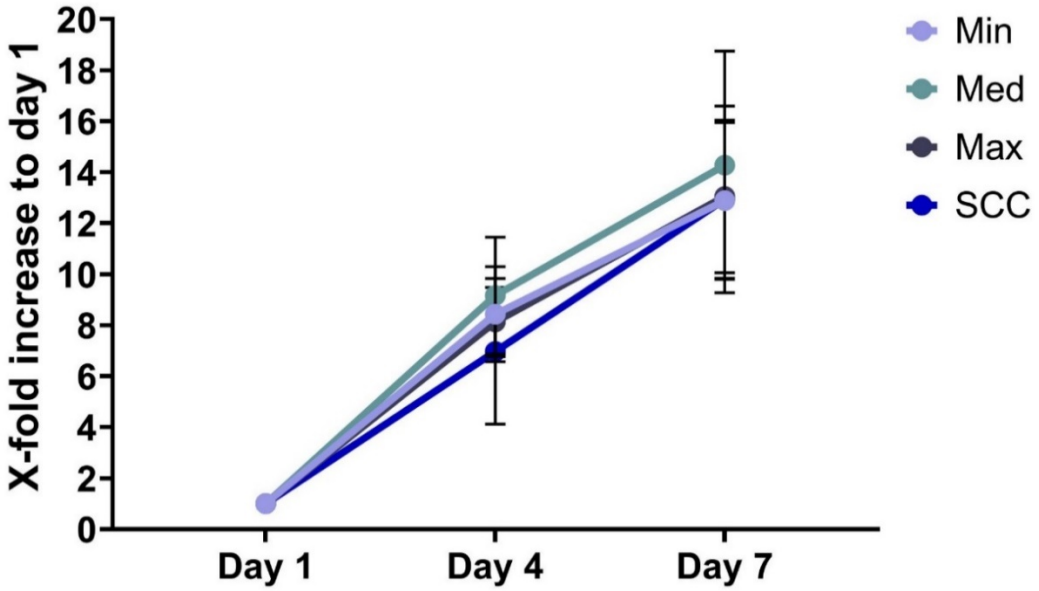


*Figure 68 Y201 MSCs metabolic activity with MgHAP (SINTlife®) treatment at different concentrations (Min = 10 µg/ml, Med = 505 µg/ml, Max = 1000 µg/ml) compared to a control (SCC). X-axis: Days 1–7; Y-axis: X-fold increase to day 1. Data presented as mean ± SD (n = 6).*

These findings suggest an absence of MgHAP cytotoxicity towards Y201 MSCs within the tested concentration range.

Following confirmation of non-cytotoxicity at the maximum tested MgHAP concentration (Figure 68), an in vitro cytotoxicity evaluation of sHAP Mg5Sr5 and Mg10Sr5 was performed at 1000 µg/ml. The metabolic activity of Y201 MSCs treated with sHAP Mg5Sr5 and Mg10Sr5 was quantitatively compared against the SCC control (Figure 69b).

This analysis was conducted twice, with each group assessed in triplicate (n = 2 × 3). Results were normalised to day 1, with statistical analyses performed on non-normalised data. The Shapiro-Wilk test confirmed normal distribution across all groups. Comparisons between groups and time points were performed using two-way ANOVA. Comprehensive statistical results are detailed in Table 42 in the appendix.

Metabolic activity significantly increased (adj. $p < 0.0001$) across all groups between time points. No significant inter-group variations were detected on day 1. On day 4, both sHAP formulations exhibited significantly higher metabolic activity than SCC (adj. $p < 0.0001$). A significant difference (adj. $p = 0.0251$) was also observed between Mg5Sr5 and Mg10Sr5, with Mg5Sr5 showing marginally higher metabolic activity. On day 7, a significant (adj. $p = 0.0018$) difference in metabolic activity was only detected between Mg10Sr5 and SCC, with SCC yielding marginally higher metabolic activity.

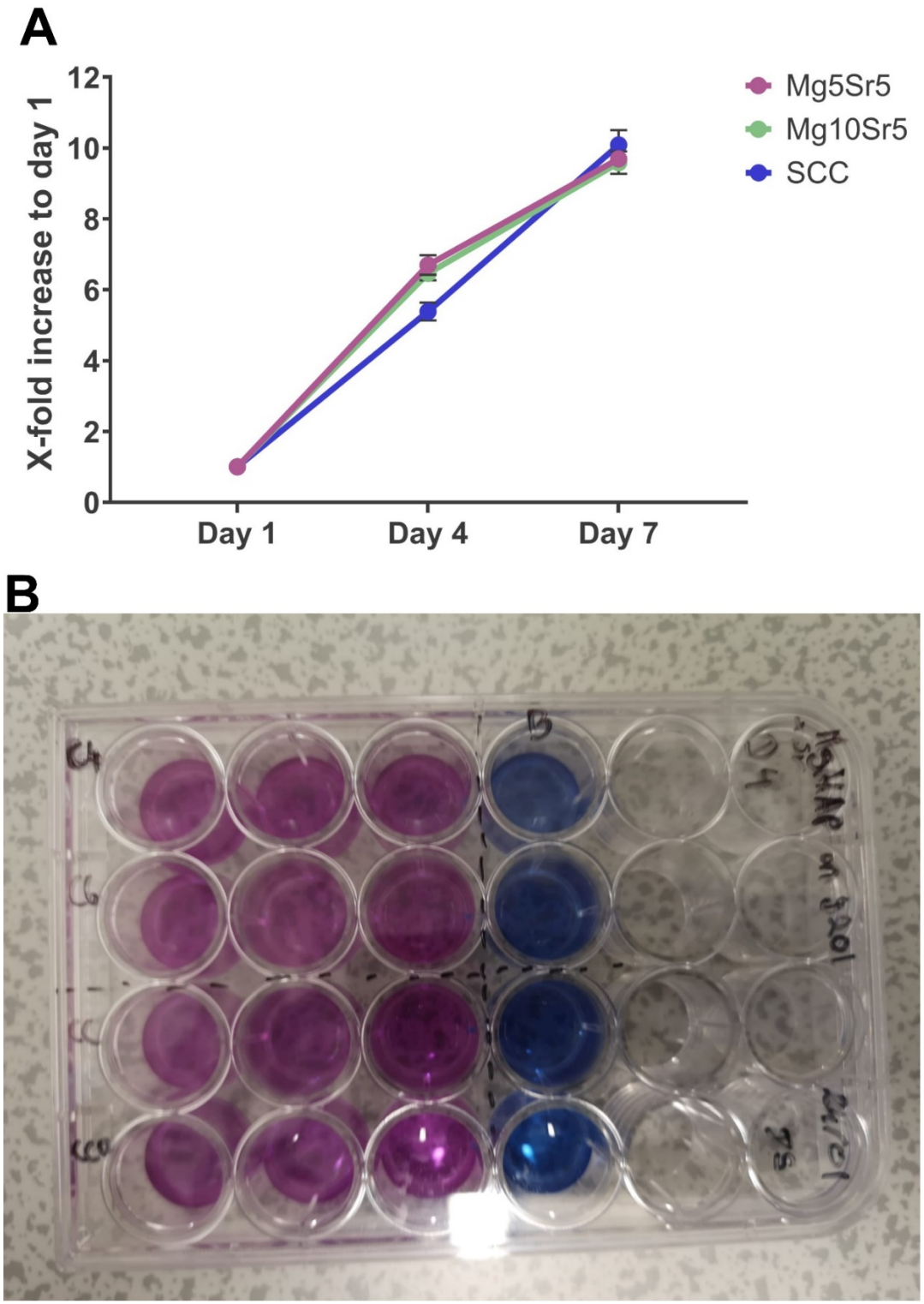


*Figure 69 Y201 MSCs metabolic activity with Mg5Sr5 and Mg10Sr5 treatment at 1000 µg/ml versus control (SCC). A) Metabolic activity development. X-axis: Days 1–7; Y-axis: X-fold increase to day 1. Data presented as mean ± SD (n = 3). B) Cell culture plate after 1.5 h resazurin incubation. Pink wells indicate cell presence; blue wells are blanks (no cells).*

The findings indicate that sHAP formulations Mg5Sr5 and Mg10Sr5 are non-cytotoxic towards Y201 MSCs at 1000 µg/ml medium concentration.

`

# 4.5. Discussion

## 4.5.1. Clogging, Particle Release and Gelatinous Phase

Synthesis attempts using the BPT, BGT, and C1 methods were unsuccessful due to clogging, rendering these approaches unsuitable for further use. The formation of blockages was likely attributed to $Ca(OH)_2$ suspension supersaturation, promoting calcium hydroxide growth via Ostwald ripening [706]. Chemical interactions leading to $Ca(OH)_2$ and calcium phosphate adhesion to stainless steel and glass surfaces may have further obstructed the mixing column and reaction vessels [707-709].

The FCR synthesis method resulted in ultrasonic probe abrasion and release of debris into precipitates. This may be attributed to hydrogen embrittlement induced by hydrogen diffusion from $Ca(OH)_2$ and $H_3PO_4$ at solubility limits, reportedly pronounced at temperatures above ~80°C and pH levels <3 or >12 [710-713].

Except for the FCR method, all methods listed in Table 16 produced a gelatinous phase concurrent with the granular precipitate, occurring only in non-substituted or minimally substituted (Mg5Sr5) formulations. The gelatinous phase volume decreased after 24 h incubation and further reduced following processing. The observed gelatinous phase during HAP precipitation is consistent with literature reports and is associated with rapid mixing, elevated Ca/P ratios, and alkaline pH. This phase characterised as a highly soluble and amorphous intermediate, transitions into more crystalline structures with Ca/P ratios of 1.22–1.48, exhibiting properties of both HAP and brushite [714-718]. Boulet et al. demonstrated increased solubility of gelatinous phases formed at higher Ca/P ratios, with further reduction upon washing [715], aligning with observations made in this project. Tung et al. reported the presence of a gel-like phase as an intermediate during HAP precipitation at neutral pH, dependent on the concentration of phosphate present (Figure 70). The phosphate concentration of 325 mM used in this project aligns with the concentration-dependent observations by Tung et al. [719].

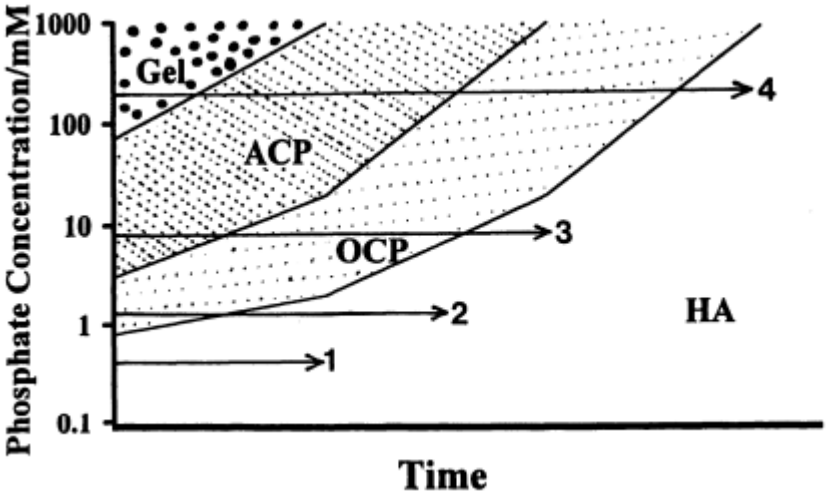


*Figure 70 Formation and conversion of different calcium phosphates as a function of phosphate concentration [log P] at neutral pH. Conversion stages: 1: log P = 0.24 mM, 2: log P = 1.2 mM, 3: log P = 4.2 mM, 4: log P > 100 mM. From [719].*

The observed gelatinous phase likely represents an ACP precursor phase, forming predominantly at high Ca/P ratios characteristic of ACP metabolic intermediates [720]. This phase was only visible in non-substituted or minimally substituted HAP samples, suggesting that alkaline pH contributed to the formation of this gelatinous phase, as previously suggested by another study [720]. Reducing the amount of $Ca(OH)_2$, thereby lowering the pH, eliminated the phase at higher substitution levels. Another explanation for a gel-like phase is the high concentration of calcium ions, facilitating multiple nucleation sites for initial ACP formation, subsequently transforming to HAP. The reduction of this phase after 24 h incubation suggests incomplete transformation kinetics, indicating insufficient time for complete structural conversion. The absence of a gel-like phase and the clear precipitate supernatant observed using the FCR method suggests that other factors, such as high temperature and vigorous mixing, accelerate HAP precipitation. The potential presence of ACP in the gelatinous phase, alongside the confirmed detection of both ACP and brushite in the precipitates, suggests that non-classical nucleation mechanisms may be involved in HAP formation under these conditions.

## 4.5.2. Incubation Time

Various incubation times were evaluated to determine the most favourable duration. It is important to note that incubation time experiments were conducted using the FCR method, while substitution experiments employed the C2 column method. Furthermore, synthesis

using the FCR method generated a slurry temperature of approximately 50°C, measured immediately after collection from the flow cell.

Following 24 h incubation, the pH marginally decreased from 11.59 to 11.54, consistent with literature reports of phosphate species deprotonation [278, 397, 402, 701, 702, 721]. Rapid HAP precipitation likely facilitated $HPO_4^{2-}$ incorporation into the lattice and surface adsorption, as documented in previous studies [275, 397, 402, 702]. Additionally, subsequent processing induced pH variations primarily attributed to $HPO_4^{2-}$ and $OH^-$ surface release, with pH stabilisation occurring more rapidly after 24 h incubation.

The Ca/P ratio at $T_0$ exhibited a high average of 1.75, decreasing to 1.701 after 24 h while remaining above the theoretical value of 1.66. Literature reports HAP Ca/P ratios up to 1.95, with variations dependent on precursor composition [722]. The Ca/P ratio decline potentially resulted from incorporated $CO_3^{2-}$ release. Higher Ca/P ratios have been associated with $CO_3^{2-}$ substituting for $PO_4^{3-}$, a process enhanced under alkaline pH and rapid addition rates [690, 723, 724]. Changes in $CO_3^{2-}{}_{1420}/PO_4^{3-}{}_{1033}$ ratios align with the declining Ca/P ratio, further supporting the substitution of $CO_3^{2-}$ for $PO_4^{3-}$, as indicated by the ~1420 $cm^{-1}$ band.

Similarly, the $CO_3^{2-}{}_{1420}/PO_4^{3-}{}_{1033}$ ratio decreased from $T_0$ to $T_4$, followed by a minor increase at $T_{24}$. Greater $CO_3^{2-}$ incorporation in $PO_4^{3-}$ sites potentially induced strain due to calcium vacancies and the larger atomic diameter of carbon (0.76 Å) compared to phosphorus (1.10 Å) [725]. Strain could facilitate $OH^-$ removal via ion channels [726], explaining the transient $OH^-$ increase with $CO_3^{2-}$ decrease. Additionally, $HPO_4^{2-}$ incorporation and Ca vacancies may have disrupted the charge balance, compensated by $OH^-$ removal [727, 728]. This suggests that the removal of $CO_3^{2-}$ reduced lattice strain, potentially allowing greater $OH^-$ incorporation. The slight ratio increase at $T_{24}$ could stem from surface $CO_3^{2-}$ formation from adsorbed $CO_2$, initially detected at $T_4$.

Splitting factor analysis revealed an initial sharp increase after 4 h incubation, potentially indicating structural maturation [275, 722], followed by a decline at 24 h, consistent with previous observations [729]. This decrease may result from $CO_3^{2-}$ removal, generating lattice vacancies and facilitating $Ca^{2+}$ release. Prior research documented reduced HAP crystallinity associated with $Ca^{2+}$ loss [730]. Consequently, the decreased crystallinity potentially stemmed from $Ca^{2+}$ release induced by $CO_3^{2-}$ removal, which could also account for the reduction in the Ca/P ratio with increasing incubation time.

FTIR analysis revealed no secondary phases at any time point during incubation, suggesting rapid HAP precipitation. The literature reports that high temperatures reduce ACP formation time and accelerate ACP hydrolysis to HAP [401, 720]. Additionally, the lifetime of ACP is pH-dependent, with rapid reduction above pH 12 [731, 732].

`

Consequently, the high temperature and pH of the employed synthesis method likely accelerated ACP formation and rapid hydrolysis to HAP, preventing the detection of an intermediate ACP phase.

## 4.5.3. Substitution Degree

Multiple formulations were investigated to evaluate Mg and Sr incorporation into the lattice structure and phase formation and to determine a suitable substitution degree for sHAP synthesis. Table 30 provides a comprehensive summary of experimental results obtained using the C2 column method. Initially, the purity of precursors (97.8% for $Ca(OH)_2$ and 86% for $H_3PO_4$) was unaccounted for but corrected for formulations across substitution degrees ranging from 5% to 10%. To distinguish between formulations, the Mg5Sr5 substitution within the 5–10% range is designated as Mg5Sr5–A, reflecting adjustments for precursor impurities, compared to Mg5Sr5 in the 5–20% substitution range.

`

*Table 30 Overview of results from substitution experiments at different substitution degrees using the C2 column method. $T_0$ = after synthesis, $T_{24}$ = after 24 h incubation, $T_{PP}$ = after processing.*

| Formulation | pH $T_0$ | pH $T_{24}$ | pH $T_{PP}$ | Experimental Mg/P Ratio | Achieved (Ca+Mg+S)/P Ratio | Phases | Remarks |
|---|---|---|---|---|---|---|---|
| nsHAP 24 h incubation, filtration, | 12.4 | | | - | 1.53 (Ca/P ratio) | 18.8% brushite 81.2% HAP | Actual Ca/P mixing ratio: 1.89<br><br>Cloudy supernatant and gelatinous phase |
| Mg20Sr20 | 6.27 | 6.13 | 7.24 | 0.33 | 1.14 | 72.4% brushite 27.6% ACP 0% HAP | Actual (Ca+Mg+S)/P mixing ratio: 1.89 |
| Mg5Sr20 | 11.33 | 5.58 | 6.48 | 0.07 | 1.44 | 100% HAP | |
| Mg20Sr5 | 9.54 | 8.28 | 8.18 | 0.27 | 1.42 | 19.4% brushite 71.2% ACP 9.4% HAP | |
| Mg5Sr5 | 11.75 | 10.43 | 10.69 | 0.06 | 1.59 | 23.2% brushite 76.8% HAP | Actual (Ca+Mg+S)/P mixing ratio: 1.89<br><br>Cloudy supernatant and gelatinous phase |
| Mg5Sr5-A | 12.02 | 6.77 | 6.76 | 0.06 | 1.51 | 3.8% brushite 96.2% HAP | Cloudy supernatant and gelatinous phase |
| Mg5Sr10 | 11.54 | 6.13 | 6.44 | 0.06 | 1.46 | More HAP than Mg10Sr10 but less than Mg10Sr5 | |
| Mg10Sr5 | 8.59 | 6.77 | 7.05 | 0.12 | 1.44 | 4.1% brushite 95.9% HAP | |
| Mg10Sr10 | 8.76 | 6.46 | 6.95 | 0.13 | 1.36 | 28.7% brushite 71.3% HAP | |

`

Distinct calcium phosphate phases, namely HAP, brushite, and ACP, were identified through FTIR and further validated by XRD analysis. The precipitation of these phases is governed by the energy barrier (ΔG), with the lowest ΔG phases precipitating first. The order of precipitation and the transformation pathway are influenced by several parameters. In this project, the Ca/P ratio, substitution degree, and pH were recognised as potential variables affecting these processes.

## 4.5.4. The Ca/P Mixing Ratio

As outlined in Table 30, Mg5Sr5-A exhibited higher HAP content and lower brushite content than Mg5Sr5. Additionally, the synthesis of nsHAP at a Ca/P ratio of 1.89 did not yield phase-pure HAP, with a higher presence of brushite when compared with Mg5Sr5-A. Previous studies observed that high supersaturation, high Ca/P mixing ratios, and more alkaline pH levels favour HAP synthesis via initial ACP formation [276, 720]. Consequently, formulations with a higher Ca/P ratio, such as nsHAP and Mg5Sr5, synthesised at alkaline pH, were anticipated to precipitate via the kinetically favoured ACP intermediate. This would result in a higher proportion of HAP, with minimal ACP remaining due to rapid ACP hydrolysis, rather than the observed presence of brushite. Recent studies have highlighted the influence of the Ca/P mixing ratio on the HAP synthesis pathway by modulating Ca and P ligand binding. One study demonstrated that the Ca/P mixing ratio influences ACP transformation via bidentate or monodentate Ca-P binding geometries. Precursors with P > Ca primarily exhibited monodentate binding, while those with Ca > P favoured bidentate binding. Bidentate geometries facilitated the transformation of ACP to HAP and brushite, whereas monodentate geometries enabled direct ACP conversion to HAP [697]. Another study reported accelerated ACP to HAP phase transformation in collagen fibrils at lower Ca/P ratios due to predominantly monodentate Ca/P binding [733].

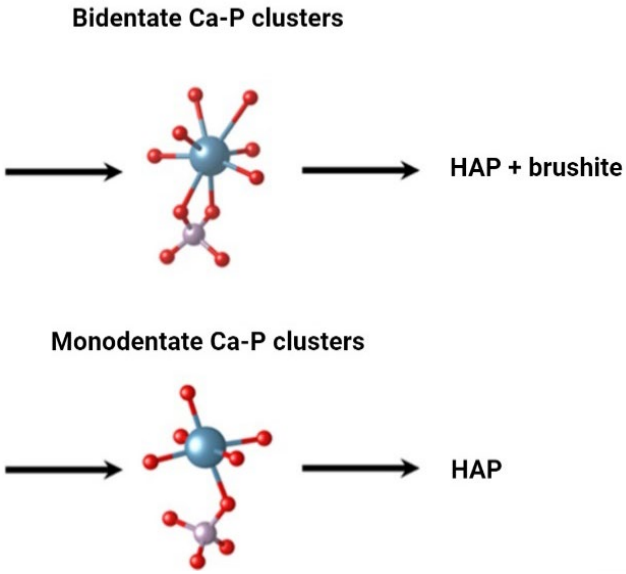


*Figure 71 Illustration of HAP formation via bidentate and monodentate Ca-P binding geometries in Ca-P clusters. Blue = calcium, purple = phosphorus, red = oxygen. Adapted from [697].*

Under the applied synthesis conditions, HAP formation likely occurred via initial ACP and brushite intermediates. The initial ACP to brushite ratio is hypothesised to be modulated by substitution degrees and Ca/P molar ratios, with a potentially higher ratio at lower Ca/P concentrations. ACP was not detected in most formulations, attributable to its rapid transformation into HAP during the 24-h incubation period.

## 4.5.5. The Effect of pH

The pH modulates precursor ion availability by influencing precipitation and dissolution equilibria, thereby altering equilibrium constants. Figure 72 illustrates the pH-dependent $H_3PO_4$ species and their relative abundances.

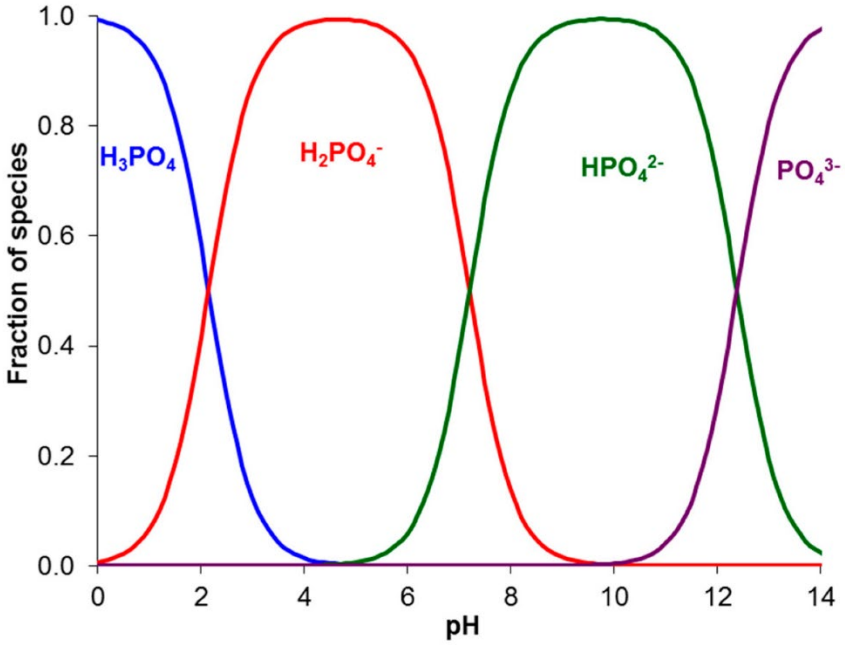


*Figure 72 Mole fraction distribution of phosphoric acid species of $H_3PO_4$ dissociation as a function of pH. X-axis: pH; Y-axis: mole fractions. From [734].*

Such pH variations consequently modulate calcium phosphate synthesis pathways and outcomes. A research group calculated the activity of various calcium phosphate species across different pH conditions, as illustrated in Figure 73 [722].

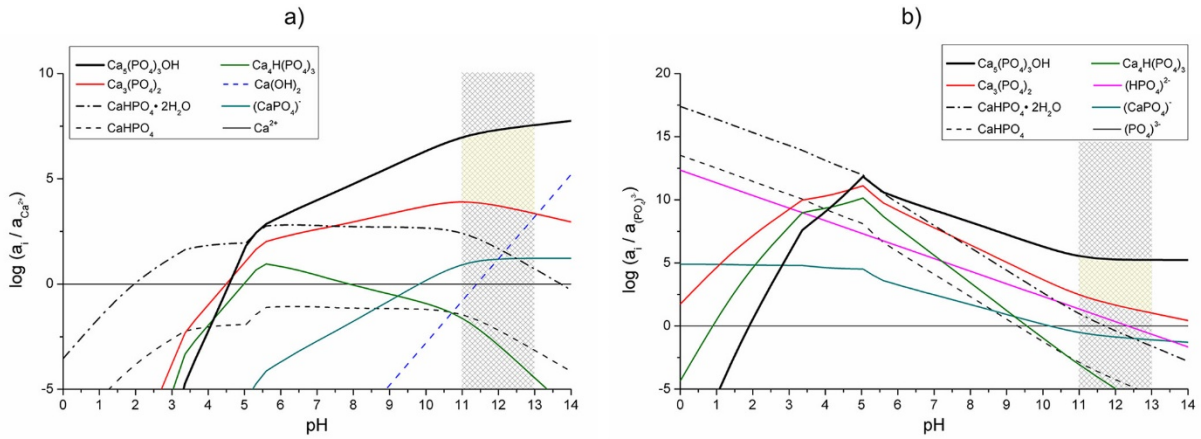


*Figure 73 Relative activity of calcium phosphate species as a function of pH. A) Relative to $Ca^{2+}$. B) Relative to $PO_4^{3-}$. From [722].*

Variations in pH were observed across different formulations during synthesis, incubation, and processing. Substitution ranges of 5–20% demonstrated higher pH levels than the 5–10% ranges, as seen by Mg5Sr5 and Mg5Sr5–A comparisons. Unaccounted precursor impurities resulted in an actual (Ca+Mg+Sr)/P mixing ratio of 1.89 for Mg5Sr5, deviating from the targeted 1.66. Consequently, Mg5Sr5-A exhibited a more pronounced pH reduction after 24 h incubation, primarily due to $H_3PO_4$ precursor dissociation.

Substantial pH declines were observed after 24 h incubation for some formulations. While literature reports pH reduction after incubation due to deprotonation or detachment of surface $HPO_4^{2-}$ dissociating into $H^+$ and $PO_4^{3-}$ [278, 397, 402, 701, 702, 721], the observed pH shifts exceeded previous findings. High supersaturation likely facilitated instantaneous multi-ion cluster formation from species present in suspension. At the observed pH levels, $H_3PO_4$ precursors predominantly existed as $H_2PO_4^-$ and $HPO_4^{2-}$, with $PO_4^{3-}$ primarily forming under alkaline conditions (Figure 72). Cluster formation potentially proceeded through $Ca^{2+}$/$Mg^{2+}$/$Sr^{2+}$ and $H_2PO_4^-$ and/or $HPO_4^{2-}$ interactions, temporarily reducing free $H^+$ levels and increasing pH. Upon reaching supersaturation, nucleation initiated, with clusters smaller than the critical size potentially dissolving and releasing $H^+$ during incubation, reducing pH.

Comparisons between formulations Mg5Sr20 and Mg20Sr5 and between formulations Mg5Sr10 and Mg10Sr5 revealed different pH values after synthesis (Table 30), despite equivalent $Ca(OH)_2$ quantities within each comparative set. This discrepancy could have originated from different precipitation behaviours. $Mg(OH)_2$ preferentially precipitates at pH 8.7–12.5, below the precipitation pH of $Ca(OH)_2$ at 2–14 [735], while $Sr(OH)_2$ precipitates at pH ~13.5 [736]. Additionally, $Mg(OH)_2$ exhibits lower solubility than $Ca(OH)_2$, potentially trapping $OH^-$, thereby inhibiting further increases in pH [737, 738]. Such phenomena may have contributed to reduced Mg levels during initial precipitation, as observed in the Mg20Sr5 formulation. While Mg5Sr10 and Mg10Sr5 converged to comparable pH after 24 h incubation, Mg5Sr20 and Mg20Sr5 maintained distinct acidic and alkaline pH values, respectively.

As anticipated, Mg5Sr5 and Mg20Sr20 exhibited the highest and lowest post-synthesis pH values, respectively, within the 5–20% substitution subset. All formulations except Mg20Sr20 showed pH reductions after 24 h incubation. The stable pH of Mg20Sr20 may reflect the incorporation of $HPO_4^{2-}$ into its structure without deprotonation. XRD analysis confirmed that this formulation predominantly comprised brushite, which contains hydrogen phosphate ($HPO_4^{2-}$), with minimal deprotonation contributions expected. Mg5Sr5 and Mg20Sr5 demonstrated comparable pH decreases after 24 h, despite substitution degrees suggesting a more pronounced pH drop for Mg20Sr5, potentially attributable to $Mg(OH)^2$ precipitation dynamics. Previous research reported 50% lattice phosphate incorporation in nanocrystalline HAP, with remaining surface phosphate groups comprising 1/3 $HPO_4^{2-}$ moieties and 2/3 water-surrounded phosphate groups [739]. Another study indicated early Ca-P precipitation aggregates predominantly comprise $[Ca(HPO_4)_3]_4$ and $[Ca(H_2PO_4)(HPO_4)_2]_3$ clusters transitioning to $[Ca_2(HPO_4)_3]_2$ ACP entities [397]. While Mg5Sr5 achieved high HAP quantities, Mg20Sr5 exhibited minimal HAP formation (~10%) with substantially more ACP. Although both formulations may have initiated through similar ACP-mediated mechanisms, Mg5Sr5 likely underwent ACP-to-HAP transformation, whereas Mg may have inhibited or delayed this conversion in Mg20Sr5. As expected, Mg5Sr20, which achieved 100% HAP

formation, demonstrated the most pronounced pH reduction, primarily attributed to $HPO_4^{2-}$ removal. Processing induced mild pH fluctuations in Mg5Sr5 and Mg20Sr5, likely resulting from $HPO_4^{2-}$ and $OH^-$ release from hydrated surface layers. Conversely, Mg20Sr20 and Mg5Sr20 exhibited continuous pH increases, also associated with $HPO_4^{2-}$ and $OH^-$ release. In acidic pH ranges, released $HPO_4^{2-}$ ions predominantly protonate to $H_2PO_4^-$, representing the most stable configuration. Consequently, $OH^-$ and $HPO_4^{2-}$ release would induce pH increases. Unlike Mg20Sr20, Mg5Sr20 eventually stabilised after the second wash, potentially attributable to lower surface hydration than Mg20Sr20's high brushite composition with substantial hydration.

In the 5–10% substitution range, Mg5Sr5-A exhibited the highest post-synthesis pH, while Mg10Sr10 demonstrated the lowest. After 24 h incubation, all formulations converged to comparable pH levels (Table 30).

Variations in pH are known to influence the stability of specific calcium phosphate phases [740]. Brushite formation occurs at pH 4–8 [276, 741], with ACP formation observed at pH 6.6 and above, with kinetic favourability increasing at higher pH levels [276, 731, 732, 741, 742]. Both brushite and ACP can form near neutral pH [743], and the inclusion of foreign ions such as Mg has been shown to facilitate ACP synthesis at pH 6 [744]. Consistent with literature-reported kinetically favourable pH conditions, Mg20Sr20 comprised primarily brushite, while Mg20Sr5 was predominantly ACP. The formation of brushite due to Ca-P binding geometries was previously explained. At higher pH, $H_3PO_4$ precursor dissociation reduces $HPO_4^{2-}$ ion concentrations due to equilibrium shifts, promoting $PO_4^{3-}$ generation. Highly alkaline conditions are expected to reduce intermediate $HPO_4^{2-}$-containing phases. However, at high pH, the $Ca(OH)_2$ equilibrium potentially restricts free $Ca^{2+}$ ion availability necessary for HAP precipitation, thereby facilitating brushite formation [722].

Formulation Mg5Sr20 was the only one to achieve 100% HAP formation, surpassing the HAP phase composition of nsHAP precipitates. This outcome may be attributed to the pronounced pH decrease from alkaline to acidic levels. As previously mentioned, the Ca/P ratio influences Ca and P binding through monodentate or bidentate configurations, initially forming brushite and/or ACP. If brushite and ACP initially formed under high pH conditions for this formulation, ACP may have transitioned to HAP, while brushite could have converted to ACP before subsequently forming HAP. Prior research has shown that brushite can transition to ACP, which converts to HAP under neutral to alkaline conditions [745]. The subsequent pH decrease to acidic levels may have further driven the conversion of residual ACP to HAP. This sequential transformation pathway likely enabled complete phase conversion within the 24-h incubation period, resulting in 100% HAP formation.

`

## 4.5.6. Mg and Sr Substitution

The present work demonstrated that higher combined levels of Mg and Sr substitution reduced the incorporation of Ca and P into the HAP lattice, with higher Mg levels particularly hindering integration. Conversely, lower Mg and higher Sr substitution (Mg5Sr10 and Mg5Sr20) enhanced Ca and P uptake, even resulting in phosphate excess, as previously reported [746]. These effects may be attributed to differences in ionic radii. The larger atomic radius of Sr (1.13 Å) compensated for the smaller radius of Mg (0.65 Å), replacing Ca (0.99 Å), promoting Ca lattice incorporation [362, 747]. However, HAP calcium deficiency following Sr substitution has been documented [722]. Further observations indicated that Sr limited Mg substitution, while Mg facilitated Sr incorporation, likely due to their ionic radii. The larger atomic radius of Sr compared to Ca potentially induced strain upon substitution, decreasing Mg incorporation [362]. Conversely, the smaller radius of Mg compared to Ca may have alleviated strain during Sr replacement, enabling greater Sr integration [747]. Lower Ca incorporation at higher substitution degrees may also relate to pH effects. Literature demonstrated lower Ca/P ratios in ACP at reduced pH due to $HPO_4^{2-}$ [748]. Consequently, ACP with lower Ca/P ratios would generate HAP with lower Ca/P ratios. Additionally, surface adsorption of phosphate has been shown to further decrease the Ca/P ratio after washing steps [749].

Anticipated Mg and Sr substitution degrees were not achieved across formulations, with Mg substitution being the lowest, consistent with prior research [694]. Even in the Mg20Sr20 brushite-predominant formulation, limited Mg and Sr incorporation was observed. Previous studies documented restricted Mg incorporation into brushite, substituting approximately 20%, while Sr replacement reached up to 38% [750, 751]. Unincorporated Mg has been observed to adsorb onto brushite surfaces [752]. The consistently lower experimentally achieved Mg substitution, even in predominantly non-HAP formulations, may relate to preferential Ca over Mg incorporation, stemming from higher CaP solubility than MgP phases [753]. Beyond solubility factors, released Mg during HAP transformation could have contributed to reduced Mg substitution rates. Prior research identified gradual magnesium release after nucleation, attributed to hindered HAP formation kinetics [754].

Varying Mg and Sr substitution degrees influenced ion incorporation, crystallinity, and phase transformation. The splitting factor in nsHAP was higher than in sHAP, indicating reduced crystallinity with substitution. Previous studies demonstrated substitution-induced crystallinity reduction due to Ca vacancies and $HPO_4^{2-}$ charge compensation-inducing strain. This effect was more pronounced with increasing substitution degree [362, 368, 676, 703, 755, 756]. Mg5Sr5 displayed lower splitting factors than Mg5Sr20 despite lower total substitution. This could be attributed to superimposition by the v2 brushite phosphate band at 573 $cm^{-1}$ on

the 565 $cm^{-1}$ region or strontium's larger atomic diameter, stabilising the lattice structure by compensating Ca vacancies. Prior research showed that Mg and Sr co-substitution yielded higher crystallinity than Mg-only substitution. Conversely, Mg potentially obstructs OH channels, limiting ion movement and reducing $HPO_4^{2-}$ deprotonation and crystallinity [746]. Higher pH during Mg5Sr5 synthesis may also contribute, as decreasing HAP crystallinity with increasing pH has been previously reported [690]. Among sHAP precipitates, Mg5Sr5-A exhibited the highest splitting factor, while Mg10Sr10 had the lowest. Notably, Mg10Sr5 showed a lower splitting factor than Mg5Sr10 despite FTIR spectra indicating higher HAP content in Mg10Sr5. This discrepancy may stem from Mg's smaller atomic radius destabilising the lattice. The reduction of HAP crystallinity due to Mg substitution has been extensively documented [341, 676, 691, 754, 757]. Under conditions comparable to this study, a decline in HAP crystallinity was observed at 10 mol% Mg substitution [341], with a 70% reduction at 15 mol% Mg substitution [676].

Precipitates with metastable intermediates, such as ACP and brushite, were observed in formulations with higher Mg substitution. The inhibitory effect of Mg on the transformation of ACP and brushite to HAP has been extensively reported [753, 758-760]. Recent research indicates inhibition primarily results from surface-adsorbed rather than lattice-incorporated Mg, with an approximate 3:1 adsorption-to-incorporation ratio [702]. One study reported 90% Mg ion surface adsorption following MgHAP synthesis [761]. Kinetic analyses of brushite transformation have demonstrated that Mg delays or impedes brushite to HAP conversion through surface adsorption without affecting brushite growth [752, 762]. Additionally, Mg has been shown to suppress HAP nucleation rates in supersaturated Ca–P solutions [718]. Considering high Mg levels and deviations in targeted compared to achieved Mg incorporation in Mg20Sr20 and Mg20Sr5 formulations, uncontrolled surface Mg adsorption likely inhibited or delayed ACP and brushite to HAP transformation. The lower Mg excess in Mg20Sr5 (due to higher incorporation success) may have permitted limited HAP formation through reduced surface interference. Such an inhibitory effect on HAP formation has not been reported for Sr. Previous studies found that precipitation of Sr-substituted calcium phosphates occurs without ACP formation [763, 764]. Another reason for Mg's inhibitory mechanism could be its molecular structure. Mg binds water molecules more tightly than Ca and possesses two hydration shells, yielding a hydrated radius ~400x larger than its non-hydrated form, compared to only ~25x for Ca [747]. Increased hydration levels in Mg-HAP compared to nsHAP have been confirmed by previous studies [340, 691]. These hydration levels lead to energy changes affecting the endothermic ACP to HAP transition [764, 765]. Brushite to HAP conversion represents another endothermic reaction, progressing more rapidly under alkaline than neutral pH conditions [282]. Lattice restructuring exhibits higher activation barriers than crystal growth or dissolution [766]. Consequently, excessive surface hydration may prevent the hydrolysis of

highly hydrated ACP and brushite surfaces, as observed in the Mg20Sr20 and Mg20Sr5 formulations. The transformation of ACP to HAP occurs at the ACP surface, which acts as a template for HAP nucleation. Adsorbed Mg may obstruct this template, inhibiting the transformation process [718]. Previous studies have shown that the Mg/Ca ratio influences the effect of Mg on phase transformation kinetics. One study reported that a 0.25 Mg/Ca ratio extended HAP formation time from 6 to over 30 h [760]. Boskey and Posner documented transformation times of 18 min at 0.004 Mg/Ca molar ratio, 45 min at 0.02, and 53 min at 0.04, while no conversion occurred when the Mg/Ca ratio exceeded 0.2 [759]. Consistent with these findings, Mg20Sr20 and Mg20Sr5 formulations with Mg/Ca ratios above 0.2 displayed negligible or no HAP formation.

## 4.6. Summary and Conclusion

This chapter focused on the synthesis of sHAP via a continuous synthesis system for subsequent composite material integration, which will be explored in subsequent project chapters. Various methods for sHAP synthesis were evaluated. A flow-cell reactor with direct ultrasonic probe contact yielded promising results but was deemed unsuitable for clinical applications due to the release of uncharacterised particles. While less effective than the flow-cell reactor, an alternative mixing column approach met the project's experimental requirements. Post-synthesis conditions were established as 24 h incubation at 37°C under continuous stirring.

Multiple sHAP formulations with 5, 10, and 20 mol% Mg and Sr substitutions were investigated. At 20 mol% Mg substitution, HAP formation was minimal or absent. Higher substitution levels were associated with reduced ion incorporation, a lower (Ca+Mg+Sr)/P ratio, and decreased overall crystallinity. The HAP formation pathway was influenced by substitution degree, precursor (Ca+Mg+Sr)/P ratio, and synthesis pH, highlighting the need for further systematic studies to optimise synthesis parameters.

The metabolic activity of Y201 MSCs was assessed to evaluate the cytotoxicity of synthesised Mg5Sr5 and Mg10Sr5 sHAP formulations. Neither formulation exhibited cytotoxic effects on MSC metabolic activity at a 1 mg/ml medium concentration.

Based on favourable physicochemical characteristics and no observed cytotoxicity, Mg5Sr5 and Mg10Sr5 were identified as the most suitable formulations for further development as biomaterial composites.

`

# Chapter V Incorporation of sHAP in a Polycaprolactone Matrix

## 5.1. Aims and Objectives

This chapter investigated the incorporation of sHAP into a polymer carrier for the fabrication of customisable biomaterial scaffolds using 3D extrusion printing. Different formulations were assessed for cytotoxicity, and printing parameters were adjusted to identify the most suitable settings for successful scaffold printing. The objectives were achieved through the following steps:

- Adaptation of ink formulation by incorporating varying sHAP concentrations and a shear-thinning additive.
- Adjustment of printing parameters, including nozzle temperature, printing speed, and layer width.
- In vitro evaluation of scaffold cytotoxicity.

## 5.2. Introduction

Scaffold design must address essential functional requirements specific to the intended application. In this project, the scaffold serves as a temporary template facilitating bone tissue regeneration, requiring gradual degradation to allow replacement by new tissue. Several factors must be considered during scaffold design [767]:

1. Biocompatibility: The scaffold and its derivatives must not exhibit cytotoxicity, induce an immune response in the host, or provoke thrombogenic and carcinogenic reactions [767, 768].
2. Bioactivity: The scaffold should interact with the host tissue. Within the scope of this project, this could include the differentiation of stem cells towards the osteogenic lineage and the promotion of sHAP precipitation and crystallisation, thereby strengthening the bond with the host bone tissue [767, 769].
3. Biodegradability: The scaffold must degrade progressively as new tissue forms, enabling integration and replacement by regenerating cells [767].
4. Morphological Structure: A frequently employed 3D scaffold design is the woodpile structure, with a 0°/90° lay-down pattern. This structure provides pores to support cell migration, large surface areas for attachment and growth, and high mechanical properties due to reduced interlayer slipping [767, 770, 771].

`

5. Mechanical Compatibility: Scaffolds must possess a stiffness similar to the host tissue while providing sufficient load-bearing capacity to ensure functionality and compatibility with the surrounding environment [767].

Although comprehensive scaffold evaluation for these requirements remains critical for clinical translation, this project focused on developing a scaffold with such potential. The primary objective was to identify and implement a literature-validated material that is compatible with key scaffold requirements. Research emphasised woodpile-structured scaffold fabrication, prioritising cell attachment potential and verifying the absence of apparent cytotoxicity.

Various materials meeting the above-described criteria have been used for bone scaffold fabrication, with PCL standing out as one of the most commonly used polymers [772, 773]. PCL is an aliphatic polyester typically synthesised through ionic or metal-catalysed ROP of ε-caprolactone. Widely used in biomedical fields such as tissue engineering, drug delivery, wound dressing, and dentistry, PCL exhibits excellent biocompatibility, securing FDA approval for multiple medical applications [426, 427]. A key advantage of PCL is its biodegradability, facilitated by microorganisms and enzymes, supporting its sustainability and suitability for in vivo biomedical applications [427]. The degradation rate of PCL is modulated by molecular weight, crystallinity, and morphological properties. Additionally, its stiffness can be tailored, enabling versatile scaffold fabrication [428]. PCL is highly versatile despite its limitations as a standalone polymer, including slow degradation and lack of bioactivity and cell adhesion sites [441]. It can be processed in various forms utilising techniques ranging from traditional methods, such as solvent casting and porogen leaching, to advanced approaches, such as additive manufacturing [772, 773].

AM has emerged as a prominent technique for 3D scaffold fabrication in bone tissue engineering, offering precise control over scaffold morphology and customisation. Common AM methods include stereolithography, selective laser sintering, fused deposition modelling, and extrusion printing. Careful material-technique pairing is essential to ensure compatibility and performance [426, 467, 770].

HAP has emerged as a promising biomaterial for 3D-printed bone scaffolds, with extensive research groups utilising additive manufacturing techniques for scaffold fabrication [774-778].

Polymer/ceramic composites have been successfully employed to overcome the brittleness of ceramics while enhancing the stiffness of thermoplastic polymers and reinforcing softer polymers for extrusion printing [779-784]. 3D-printed HAP-PCL scaffolds have shown promising results in bone tissue engineering, with comprehensive in vitro [426, 441, 452, 784, 785] and in vivo [452, 785, 786] studies demonstrating improved cell proliferation and bone

ingrowth. This synergistic combination of materials offers the potential for advancing bone tissue engineering and regenerative medicine.

Due to its biocompatibility and versatility, PCL is an excellent polymer matrix for sHAP incorporation in the fabrication of 3D-printed scaffolds.

## 5.3. Experimental Overview

High-temperature fabrication of sHAP-PCL scaffolds poses challenges, including loss of nanostructure, increased crystallinity, and transformation of sHAP to stoichiometric HAP and β-TCP, rendering such methods unsuitable for preserving the desired properties [787]. To preserve sHAP integrity, 3D extrusion printing under (near) ambient temperature was selected for scaffold fabrication, necessitating specialised ink formulations for precise extrusion and subsequent crosslinking via physical or chemical processes [506-508, 510-513, 516, 517].

Star-shaped 4-arm PCL was selected over linear PCL due to its superior physiochemical properties [459, 460]. To enable photocrosslinking for scaffold solidification, PCL was functionalised with methacrylate groups, facilitating UV-induced crosslinking in the presence of a photoinitiator [459].

Preliminary cytotoxicity evaluation of varying HAP-PCLM formulations was conducted using commercial HAP in 2D scaffold configurations, including films and discs. Following confirmation of non-cytotoxic properties, research progressed to 3D-printed scaffold development.

Extrusion-based scaffold fabrication necessitates the precise control of ink rheology. The ink must exhibit high viscosity at rest and pseudoplastic behaviour under stress to ensure precise extrusion and shape retention until crosslinking occurs [767]. The temperature-sensitive PCLM enabled viscosity modulation through reservoir and collector temperature control. The addition of silica further enhanced ink shear-thinning properties, reducing viscosity during extrusion while maintaining structural integrity after printing. Previous studies have demonstrated silica's capability to increase zero-shear viscosity, exhibit shear-thinning behaviour, provide biocompatibility, and improve mechanical characteristics, including enhanced tensile strength and fracture toughness [788-791]. Initial printing parameters were established using commercial HAP and MgHAP before proceeding with sHAP formulations Mg5Sr5 and Mg10Sr.

In vitro evaluation was performed on scaffolds containing 30 wt% sHAP Mg5Sr5.

`

## 5.4. Results

An overview of the methodological approach in this chapter is outlined in Table 31. It provides information on the experiments conducted, identifies encountered issues, describes implemented solutions, and reports the consequent outcomes.

*Table 31 Overview of used methods with encountered problems, implemented solutions and their outcomes.*

| **Method Assessment Overview** | | | |
|---|---|---|---|
| **Method** | **Remarks and Issues** | **Implemented Solutions and Improvements** | **Outcome** |
| In vitro testing of HAP-PCLM films | Poor cell attachment | Pre-soaking in GM | Improvement |
| | Uneven cell distribution after seeding | Droplet cell seeding | No improvement |
| | | Rocking of well plates after cell seeding | Improvement |
| In vitro testing of HAP-PCLM discs | No cell attachment and apoptosis | Prolonged washing with ethanol | No improvement |
| Preparation of (s)HAP-PCLM blends | Difficulty in dissolving (s)HAP and agglomerate formation | Dissolving (s)HAP in 100% isopropanol | Isopropanol did not evaporate |
| | | Sonication to dissolve (s)HAP | Improvement |
| Printing with sHAP-PCLM inks | Viscosities of inks too high/low for printing: | Addition of $SiO_2$ for shear thinning, adjustment of ink reservoir temperature, pressure, and printing speed | Partial improvement |
| In vitro testing of sHAP-PCLM scaffolds | Insufficient cell attachment on scaffolds | Droplet cell seeding | No improvement |
| | | Drying scaffolds before seeding | No improvement |
| | | Attachment of scaffolds to wells via surface tension | No improvement |
| | | Usage of non-treated well plates | No improvement |

`

### 5.4.1. Methacrylated PCL Could be Successfully Synthesised

4-PCL was synthesised via ROP, followed by the functionalisation of the hydroxyl-terminated ends with methacrylate groups. The chemical composition and structure of 4-PCL and its methacrylated derivative (4-PCLM) were characterised via $^{1}$H NMR spectroscopy using $CDCl_3$ as the reference.

$^{1}$H NMR spectroscopy revealed characteristic structures of (methacrylated) 4-PCL, confirming the successful synthesis and methacrylation. The degree of polymerisation (DP) and methacrylation (MP) were also quantified to assess synthesis efficiency.

Spectral resonances are visualised as peaks in plots, with the x-axis representing chemical shift frequency (δ) in ppm and the y-axis indicating signal intensity.

Figure 74 presents the $^{1}$H spectra of 4-PCL and 4-PCLM. Spectral analysis focused on chemical shift regions and peak multiplicity to determine the molecular environment. Chemical shift assignments (H1−H8) were made based on resonance characteristics, with different functional groups contributing to distinct resonances within specific chemical shift regions [792]. Other research groups have previously reported on the molecular characterisation of PCL using NMR spectroscopy [793, 794].

Distinct proton signals characterised the PCL backbone: Methylene protons adjacent to ester group oxygen resonated at approximately 4 ppm (H1), while methylene protons neighbouring the carbonyl carbon appeared at around 2.5 ppm (H2). Resonances at approximately 1.6 ppm corresponded to four hydrogen atoms within two methylene groups (H3), and central methylene protons were identified at about 1.3 ppm (H4).

Distinct proton signals were also observed for end groups: Peaks at approximately 3.5 ppm were associated with the terminal methylene proton (H5) near the hydroxyl group. In comparison, signals at 1.87 ppm indicated methyl protons (H6) in the methacrylate region. Signals in the area of approximately 6−5.5 ppm were attributed to methylidene (H7+8). A comprehensive summary of these peak assignments and their characteristics is presented in Table 32.

*Table 32 NMR spectral resonance assignments and characteristics.*

| Assignment | Feature | Moiety | δ[ppm] | Multiplicity | Compound | Group |
|---|---|---|---|---|---|---|
| H1 | Repeating unit/ copolymer linkage | C-$CH_2$-O- | ~4 | Multiplet | Methylene | Alkyl |
| H2 | Repeating unit | C-$CH_2$-C- | ~2.25 | Multiplet | Methylene | Alkyl |
| H3 | Repeating unit | C-$CH_2$-C- | ~1.6 | Multiplet | Methylene | Alkyl |
| H4 | Repeating unit | C-$CH_2$-C- | ~1.3 | Multiplet | Methylene | Alkyl |
| H5 | End group | -$CH_2$-O- | ~3.5 | Triple | Methylene | Alkyl |
| H6 | End group | $CH_3$ | 1.87 | Single | Methyl | Alkyl |
| H7 | End group | C = $CH_2$ | ~6-5.50 | Multiplet | Methylidene hydroxyl hydrogen | Alkenyl, hydroxyl |
| H8 | End group | C = $CH_2$ | ~6-5.50 | Multiplet | Methylidene | Alkenyl |

The successful methacrylation of 4-PCL was confirmed by H6–9 peaks representing methyl and methylidene end groups (Figure 74, with a detailed spectrum in Figure 90 in the appendix). These spectral chemical shifts corroborated findings from previous methacrylation research [457, 795-798].

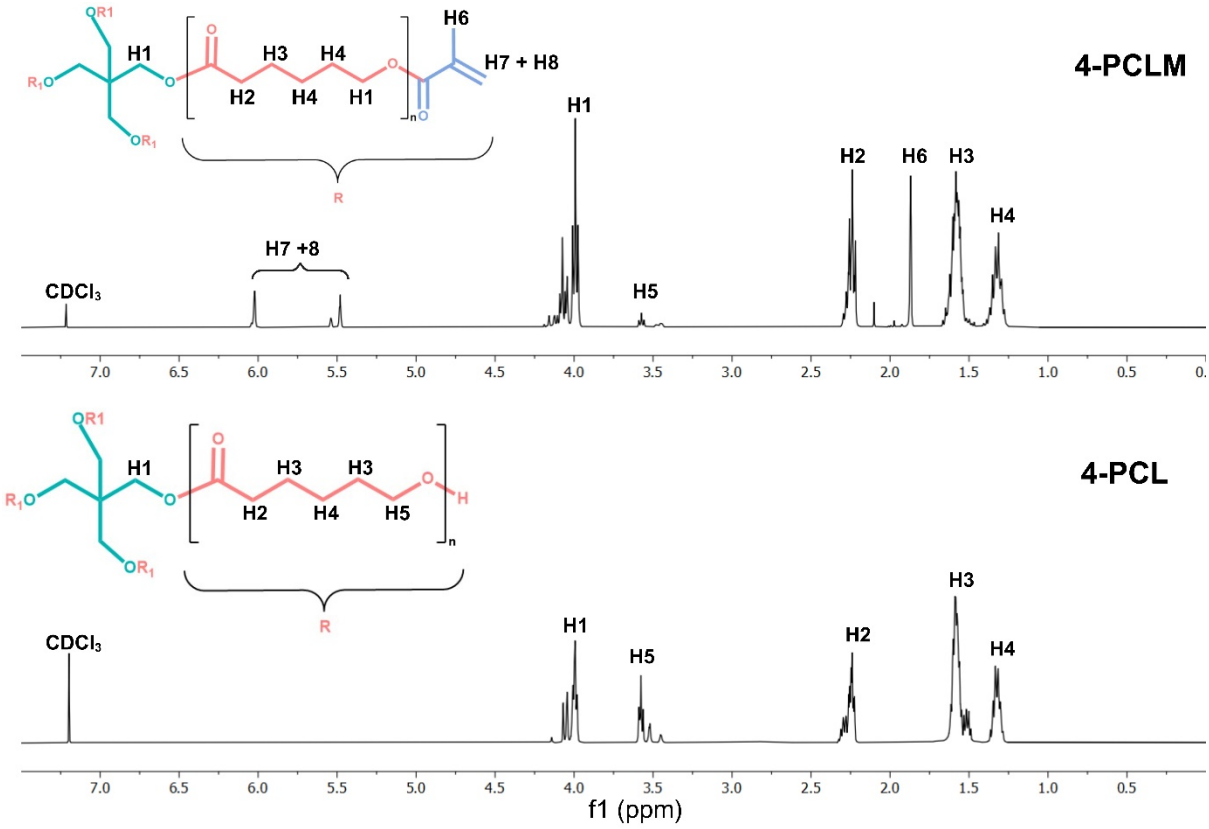


*Figure 74 NMR Spectra of 4-PCLM and 4-PCL with schematic representation of peak allocation.*

`

Peak integration was performed to quantify hydrogen atom proportions within distinctive chemical environments. Integral values were categorised by assigned regions, with comprehensive chemical shift and integral data detailed in Table 43 of the appendix. In the anticipated 4-PCLM chemical structure, the H6 group comprises three hydrogen protons. In comparison, the H7 + H8 groups contain two hydrogen protons, establishing a theoretical H7 + H8 to H6 ratio of 2:3. This ratio serves as a critical indicator of methacrylate group integrity, with deviation potentially signifying structural degradation. The calculated integral area ratio matched the expected 2:3 value, confirming the preservation of methacrylate groups. Methacrylation induces notable changes in the chemical environment of H5 protons. The adjacent ester group generates a deshielding effect, causing signal shifts towards the higher energy region, resulting in overlap with chemically equivalent H1 signals. Nonetheless, the coexistence of H5 groups with H6–8 groups indicates the presence of non-methacrylated PCL regions, suggesting methacrylation efficiency was less than 100%.

The average methacrylation degree was quantified by establishing an equation based on the introduction of methacrylate groups, characterised by hydroxyl end loss and H5 proton energy shift. This shift occurs for each of the 4-PCLM arms when two H7 + H8 protons and three H6 protons are introduced, causing three H5 hydrogen protons to deviate from their standard chemical shift region. DM directly correlates with the hydrogen atom ratio between H6–8 and H5. This relationship is represented by the following equation:

$$\overline{DM} = \frac{3\,DM}{2(4\text{-}DM)}$$

where "DM" quantifies methacrylate regions within a 4-PCL molecule. The number of hydroxyl-connected H5 protons is represented as "4−DM". Given the coexistence of H6 and H7 + H8 groups in these regions, only one group is required to calculate DM, with H6 chosen as the reference. The values "3" and "2" correspond to the protons in the respective groups. Establishing the correlation between the H5 to H6 proton ratio yielded the following equation:

$$\frac{3\,\overline{DM}}{2\left(4\text{-}\overline{DM}\right)} = \frac{\int H6}{\int H5}$$

By solving this equation, the calculated value of DM approximates to ”2.76”. In a fully methacrylated 4-PCL molecule, DM would equal “4”. Consequently, the percentage degree of methacrylation was determined through the following equation:

$$\overline{DM\%} = \frac{\overline{DM}}{4} \times 100$$

Solving for this equation revealed a DM of approximately 69%.

To establish the average number of caprolactone units polymerised per pentaerythritol arm, DP was calculated utilising the molar volume ratio between repeat units and end groups, a methodology employed by previous research groups [799, 800]. Initially, the relative molar

volume (m) of repeat unit regions at H2, H3, H4, and methacrylic end group regions at H6–8 was calculated through the following equation:

$$\bar{m}\ [mol] = \frac{\sum \int H(x)}{\sum P\ (x)}$$

where H(x) represents the sum of integral areas for repeat units at H2–4 and end groups at H6–8, while P(x) denotes the corresponding proton count in these regions. Proton numbers from Table 43 in the appendix were adjusted to account for the DM in end units. The calculated molar volume enabled the determination of the average number of repeat units per molecule through the formula:

$$\overline{DP} = \frac{\bar{m}\ (repeat\ units)}{\bar{m}\ (end\ groups)}$$

The DP calculation yielded 2.69, indicating an average of approximately three repeat units per PCL arm. During 4-PCL synthesis, a monomer-to-initiator ratio of 8:1 was employed, targeting a molecular weight of 1049.3 g $mol^{-1}$, theoretically corresponding to a DP of two per arm.

Polymer molecular weight, influenced by molecular chain length diversity, is a key determinant of its physical properties. NMR offers a precise and accessible approach to molecular weight determination, requiring no calibration and providing high sensitivity for high-molecular weight polymers without necessitating highly resolved peaks [800]. Using adjusted proton numbers for DP and DM in the formula weight, the number-average molecular weight was calculated as 1,664.64 g/$mol^{-1}$.

### 5.4.2. HAP-PCLM Films Exhibited No Cytotoxicity to Y201 MSCs

Cytotoxicity of HAP-PCLM films was assessed in vitro on Y201 MSCs. Figure 75 presents optical microscope images of Y201 MSCs cultured on a 50% HAP-PCLM film for 7 days. Cells adhered to the film surface, exhibiting the characteristic elongated fibroblastoid morphology typical of this cell type [801]. High-density cell populations were evident on well plate surfaces surrounding the film. The culture medium remained clear, suggesting no apparent cell death via apoptosis or necrosis.

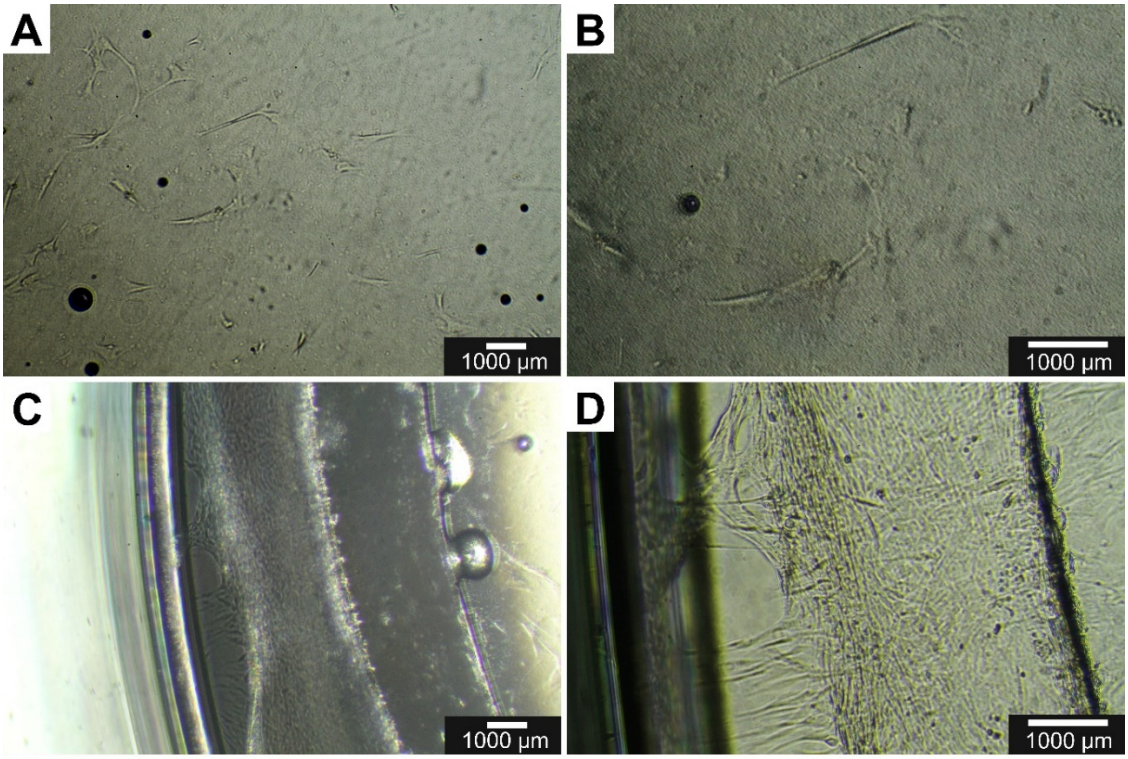


*Figure 75 Optical microscope images of Y201 MSCs cultured on 50% HAP-PCLM films for 7 days. A) Cells at 50 × magnification. B) Cells at 100 × magnification. C) Cells on the edge of a film at 50 × magnification. D) Cells on the edge of a film at 100 × magnification.*

Cytotoxicity in Y201 MSCs was evaluated via the resazurin assay, comparing metabolic activity on HAP-PCLM and pure PCLM films with the SCC control (Figure 76).

This analysis was repeated once, with each group assessed in triplicate (n = 1 × 3). Results are presented as x-fold change, with statistical analysis conducted on non-normalised raw data. Shapiro-Wilk test confirmed normal distribution across all groups. Inter-group and time point comparisons were performed using two-way ANOVA.

All groups exhibited significant increases ($p < 0.0001$) in metabolic activity across time points. Variations among film types were identified, which may have resulted from differences in initial cell seeding density or cell attachment efficiency, as indicated by the comparable growth slopes observed in the control group.

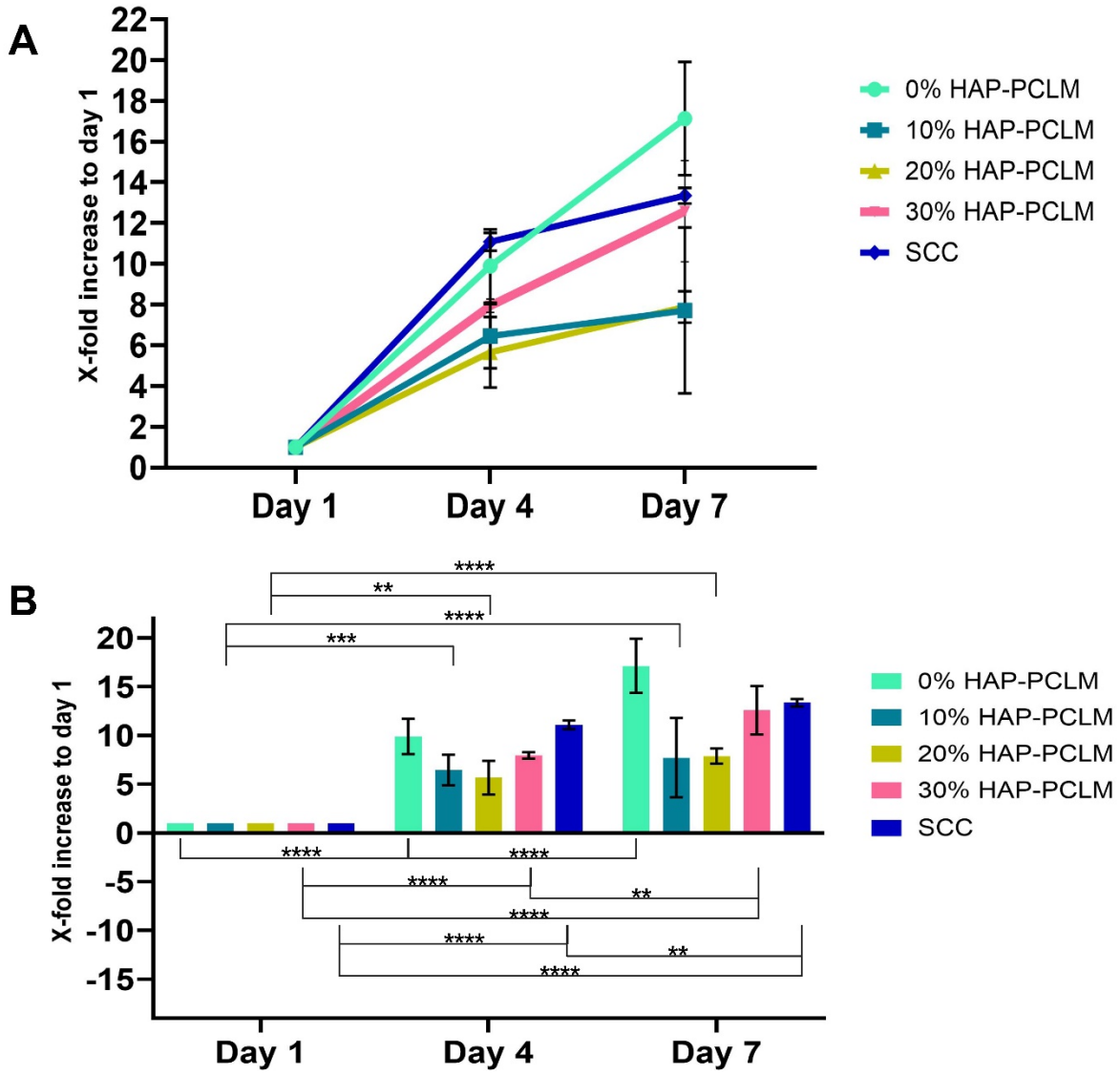


*Figure 76 Y201 MSCs metabolic activity on HAP-PCL films. Results are represented as a line graph (A) and a bar graph (B). X-axis: Days 1–7; Y-axis: X-fold increase to day 1. Data presented as mean ± SD (n = 3, ** p < 0.01, *** p < 0.001, **** p < 0.0001).*

These data demonstrate that HAP-PCLM films supported Y201 MSCs attachment and did not negatively impact metabolic activity, suggesting that cytotoxicity was absent at the tested HAP-PCLM composite concentrations.

`

### 5.4.3. Silica and HAP/sHAP Incorporation Altered Wettability Properties

Surface wettability was evaluated on films fabricated via the previously described "sandwich" method. Different polymer blends, including PCLM alone, HAP/sHAP-PCLM and PCLM with silica, were characterised using a drop shape analyser. WCA and WoA were measured, and IFT was automatically determined based on WCA measurements using di$H_2O$. SFE was calculated from IFT values and the known surface free energy of di$H_2O$.

Measurements were performed five times on different film regions. Shapiro-Wilk test confirmed normal data distribution across most groups, with exceptions noted for 30% HAP in IFT and 30% sHAP Mg5Sr5 and Mg10Sr5 in SFE. The effects of blend composition, substitution degree, and silica incorporation on surface properties were evaluated via one-way and two-way ANOVA and Kruskal-Wallis tests.

The incorporation of different HAP types (commercial HAP/sHAP Mg5Sr5 and Mg10/Sr5), silica, and their respective concentrations notably influenced water contact angle WCA, WoA, IFT, and SFE, as detailed in subsequent sections.

Figure 77 illustrates cumulative images of di$H_2O$ droplets on various PCLM blend surfaces exhibiting different WCAs.

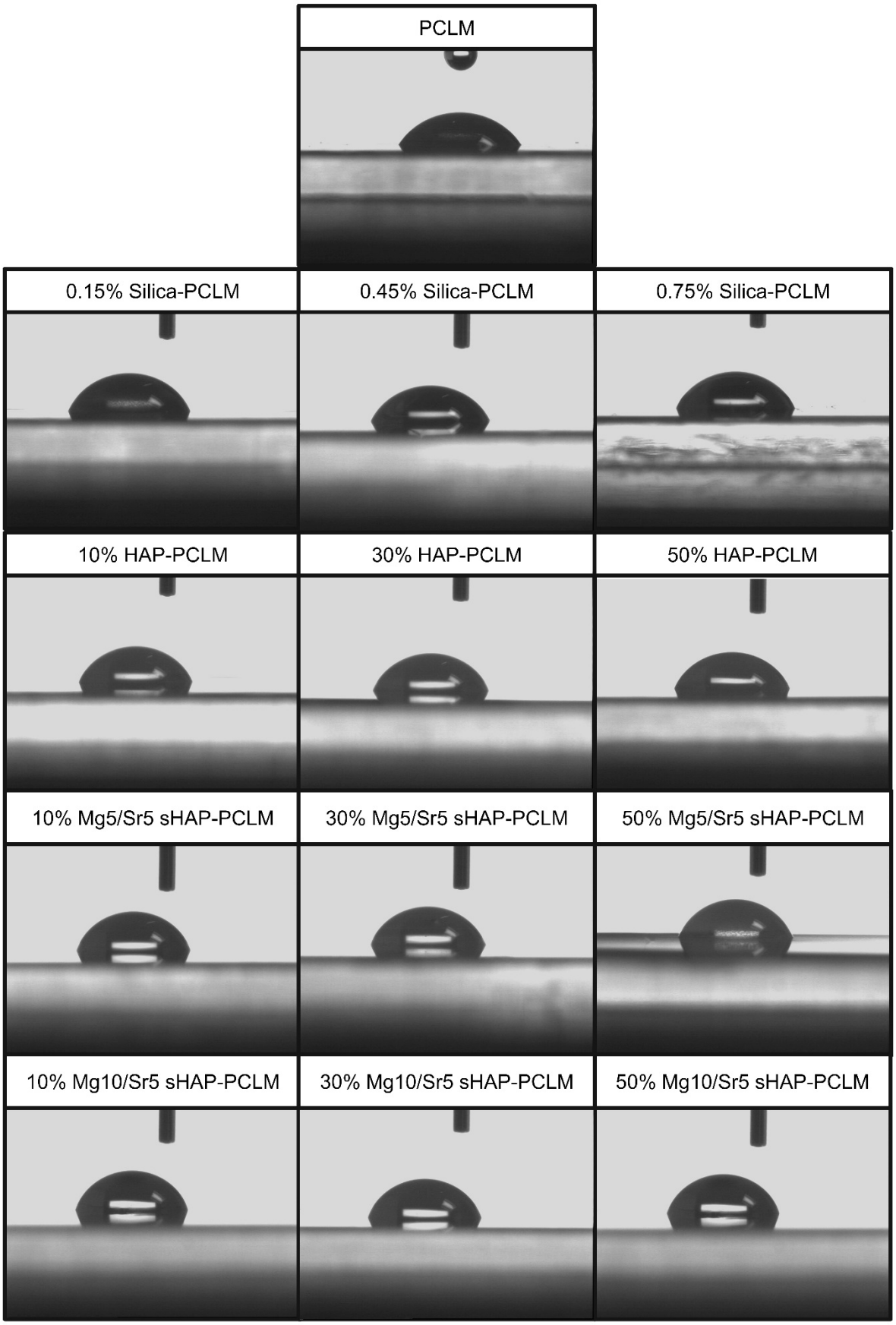


*Figure 77 Images of di$H_2O$ droplets on different PCLM blends with varying water contact angles.*

`

## WCA

One-way ANOVA revealed significant effects ($p < 0.0001$) of HAP, sHAP, and silica incorporation compared to pure PCLM. Two-way ANOVA indicated that HAP/sHAP incorporation significantly increased WCA ($p < 0.0001$), primarily attributed to HAP variations ($p < 0.0001$) rather than incorporation degree ($p = 0.3032$). Despite the overall insignificant contribution of incorporation degree, inter-degree differences were observed among formulations. HAP-PCLM exhibited increased WCA from 10% to 30% HAP incorporation, subsequently plateauing. Conversely, Mg5Sr5 sHAP-PCLM showed a WCA decline from 10% to 50% HAP, while Mg10Sr5 sHAP-PCLM decreased from 30% to 50%. Silica incorporation significantly increased WCA from 0.15% to 0.45% ($p = 0.0096$) (Figure 78). All formulations maintained WCA below 90°, indicating hydrophilicity [802].

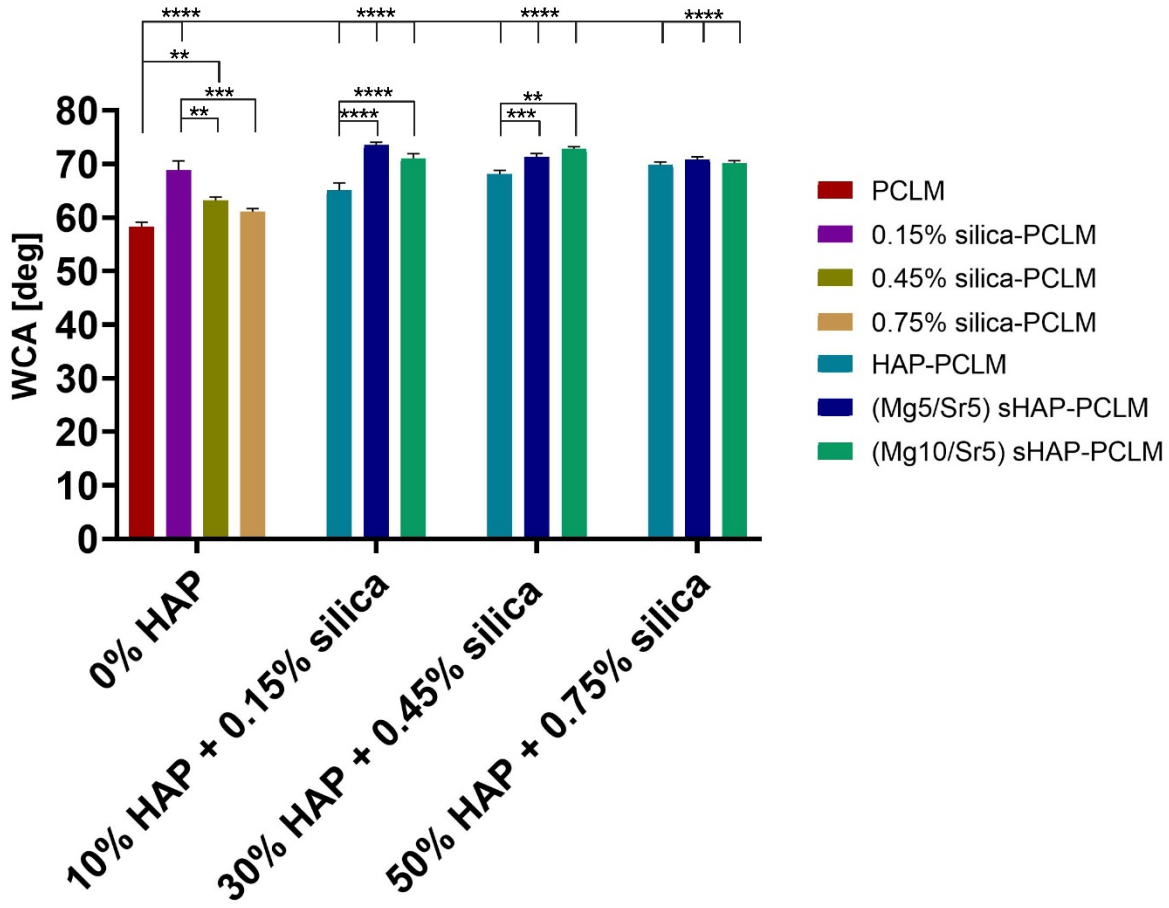


*Figure 78 Water contact angles of different PCLM blends. X-axis: %-HAP/silica incorporation; Y-axis: WCA in degrees. Data presented as mean ± SD (n = 5, ** p < 0.01, *** p < 0.001, **** p < 0.0001).*

`

## IFT

Unlike WCA, one-way ANOVA and Kruskal-Wallis tests revealed no significant differences between HAP/sHAP and PCLM alone. However, 0.75% silica incorporation significantly increased IFT compared to PCLM ($p = 0.0008$). Two-way ANOVA and Kruskal-Wallis test (after data transformation) revealed significant effects of both HAP type ($p < 0.0001$) and incorporation degree ($p = 0.0456$) on IFT with formulation-dependent variations. Mg5Sr5 demonstrated significantly higher IFT at 30% and 50% incorporation than Mg10Sr5 ($p = 0.0002$), while both sHAP formulations showed lower IFT than HAP-PCLM at 10% incorporation ($p < 0.0001$). At 30% incorporation, HAP-PCLM showed higher IFT than sHAP Mg10Sr5 ($p = 0.0027$), although non-normal distribution of 30% HAP-PCLM samples may have influenced this result. Notably, only HAP-PCLM exhibited incorporation degree-dependent IFT changes, with a significant decrease from 30% to 50% ($p < 0.0001$) (Figure 79).

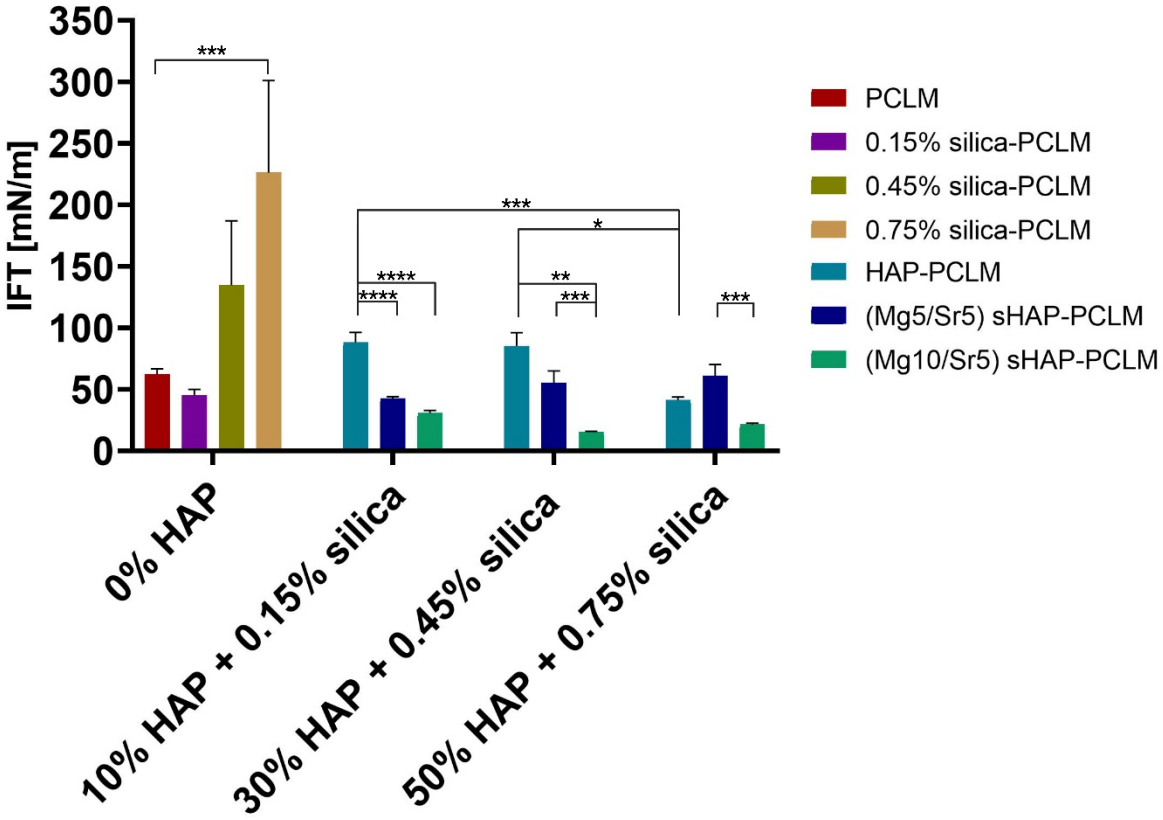


*Figure 79 Interfacial tension of different PCLM blends. X-axis: %-HAP/silica incorporation; Y-axis: IFT in mN/m. Data presented as mean ± SD (n = 5, * p < 0.05, ** p < 0.01, *** p < 0.001, **** p < 0.0001).*

`

## WoA

HAP/sHAP incorporation significantly reduced WoA values compared to PCLM alone, as demonstrated by one-way ANOVA ($p < 0.0001$). Silica incorporation decreased WoA significantly at 0.15% ($p < 0.0001$) and 0.45% ($p = 0.0025$) compared to PCLM alone, with 0.15% exhibiting lower values than 0.45% ($p = 0.0086$) and 0.75% ($p = 0.0009$).

Two-way ANOVA identified significant differences between HAP types ($p < 0.0001$). At 10% concentration, HAP-PCLM demonstrated higher WoA than both sHAP types ($p < 0.0001$), with Mg5Sr5 showing higher values than Mg10Sr5 ($p = 0.0410$). At 30%, HAP-PCLM exhibited higher WoA than Mg5Sr5 ($p = 0.0065$) and Mg10Sr5 ($p < 0.0001$), as shown in Figure 80.

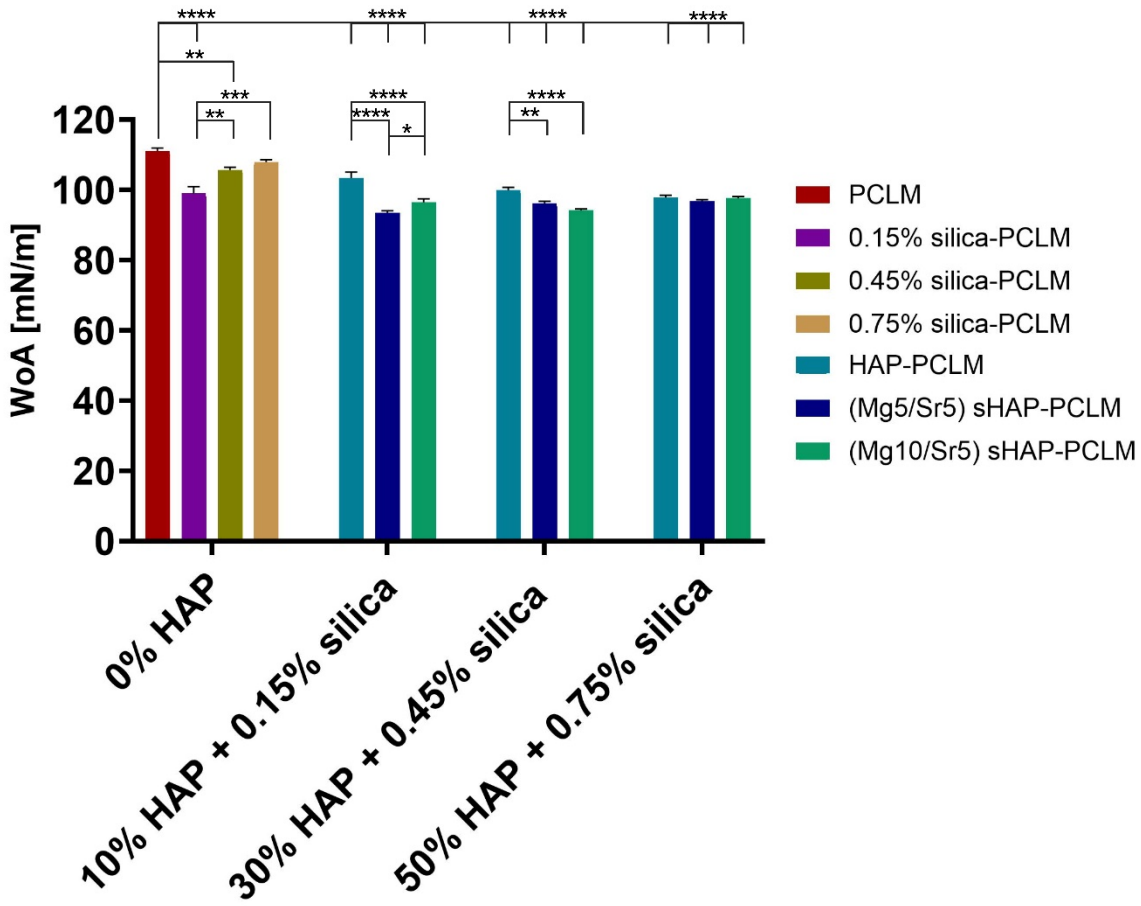


*Figure 80 Work of adhesion of different PCLM blends. X-axis: %-HAP/silica incorporation; Y-axis: WoA in mN/m. Data presented as mean ± SD (n = 5, ** p < 0.01, *** p < 0.001, **** p < 0.0001).*

`

**SFE:**

One-way ANOVA and Kruskal-Wallis tests revealed no significant differences between most HAP groups and PCLM alone, except for 30% Mg10Sr5 sHAP, which showed significantly lower SFE ($p = 0.0434$). Two-way ANOVA and Kruskal-Wallis test (after data transformation) showed no significant substitution degree effect, but sHAP type significantly influenced SFE ($p = 0.0334$). Specifically, sHAP Mg10Sr5 exhibited significantly lower SFE than HAP at 30% ($p = 0.0434$). Notably, the 30% Mg10Sr5 data demonstrated a non-normal distribution, potentially influencing these findings (Figure 81).

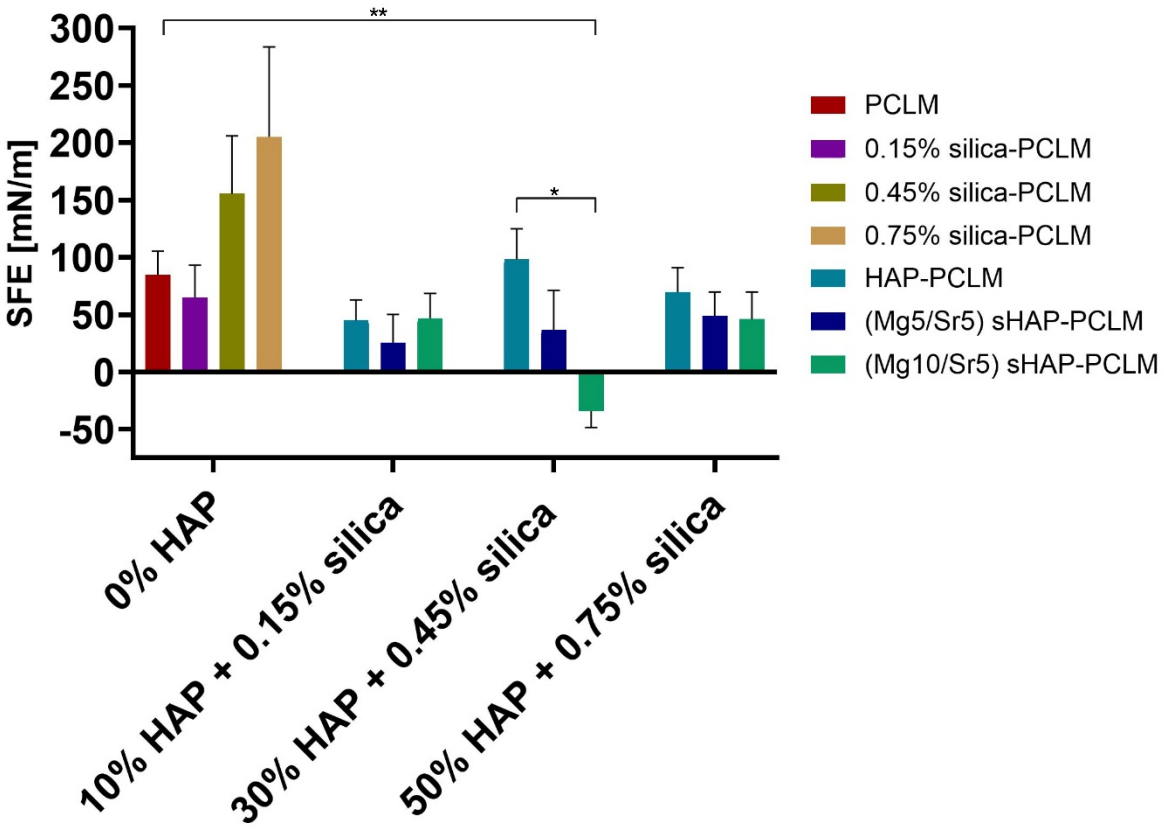


*Figure 81 Polymer surface free energies of different PCLM blends. X-axis: %-HAP/silica incorporation; Y-axis: SFE in mN/m. Data presented as mean ± SD (n = 5, * p < 0.05, ** p < 0.01).*

## 5.4.4. Incorporation of sHAP Enhanced Printability and Scaffold Properties

Scaffolds were fabricated via 3D printing using Mg5Sr5 sHAP-PCLM inks at varying concentrations, with printing parameters adjusted for each composition.

`

Scaffold morphology and surface topography were assessed through optical imaging (Figure 82 A–F) and SEM analysis (Figure 82 a–b). The results revealed that the degree of sHAP incorporation influenced ink printability, scaffold structure, and surface topography.

PCLM inks without sHAP exhibited poor printability, failing to achieve the desired morphological integrity due to liquid-like consistency. SEM analysis revealed smoother surface structures compared to sHAP-containing scaffolds. Increasing the sHAP content to 10% marginally improved printability but resulted in non-uniform filament width and filament dragging. Gradual increase in sHAP concentration from 10 wt% to 50 wt% enhanced printability and scaffold morphology through increased ink viscosity. Extruded filaments demonstrated improved definition, characterised by more uniform filament width, reduced run-out and decreased interlayer merging. SEM images indicated increasing surface roughness with higher sHAP incorporation. At 50 wt% sHAP, the highest printing resolution was achieved, with filaments exhibiting sharper edges and width consistency at turning points, closely matching straight filament widths. Slight bottom-layer filament dragging persisted, potentially attributable to increased ink viscosity and top-layer interaction.

With increasing sHAP content, the colour of scaffolds transitioned from translucent to white, as shown in Figure 82.

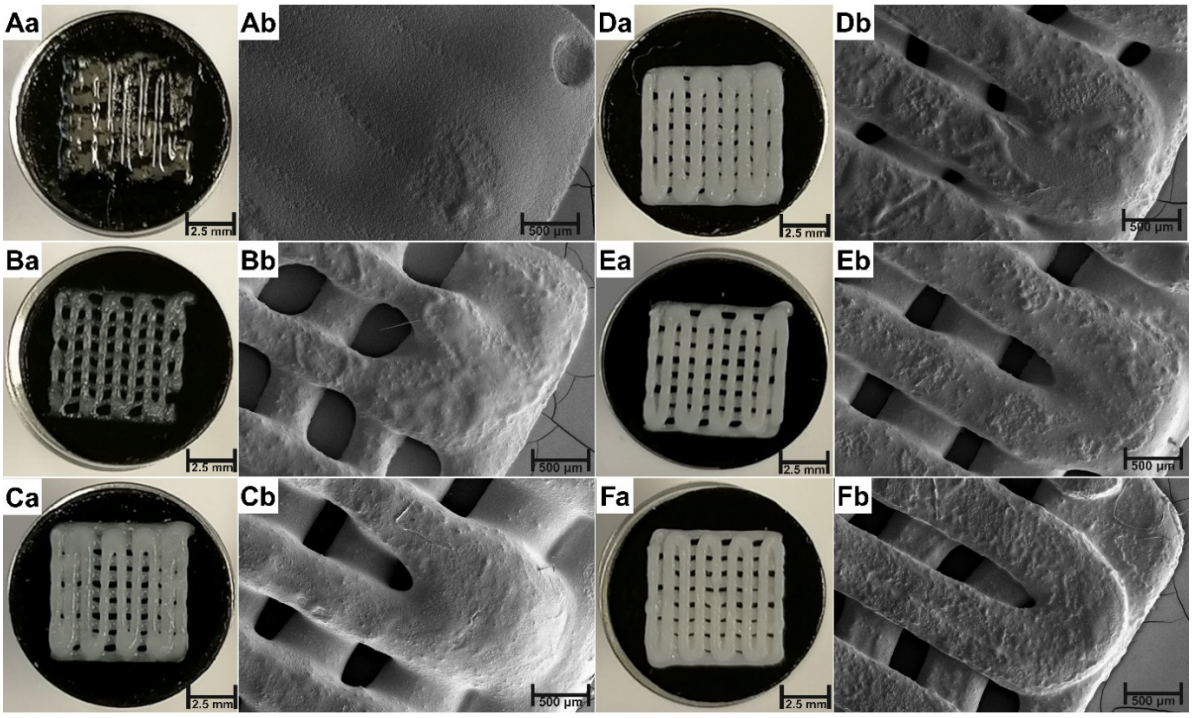


*Figure 82 Photograph and SEM images of sHAP-PCLM scaffolds with varying amounts of sHAP Mg5Sr5. A) 0% sHAP-PCLM, B) 10% sHAP-PCLM, C) 20% sHAP-PCLM, D) 30% sHAP-PCLM, E) 40% sHAP-PCLM, F) 50% sHAP-PCLM. a) Photograph of scaffolds after printing, b) SEM images at 500 × magnification. Prepared by Boyang Liu in collaborative research.*

`

An ImageJ extension was used to generate 3D plots of the sHAP distribution from SEM images. Figure 83 and Figure 84 display these plots, with left-hand images representing larger scaffold sections (3 mm × 2 mm) derived from the SEM images in Figure 82 and right-hand images showing a smaller region (300 × 300 µm) within these images.

A distinct difference between pure PCLM scaffolds and those incorporating sHAP was observed. Peak distribution and intensity increased with higher sHAP concentration, making overlapping peaks more evident. The 50% sHAP concentration exhibited the most pronounced differences compared to PCLM alone.

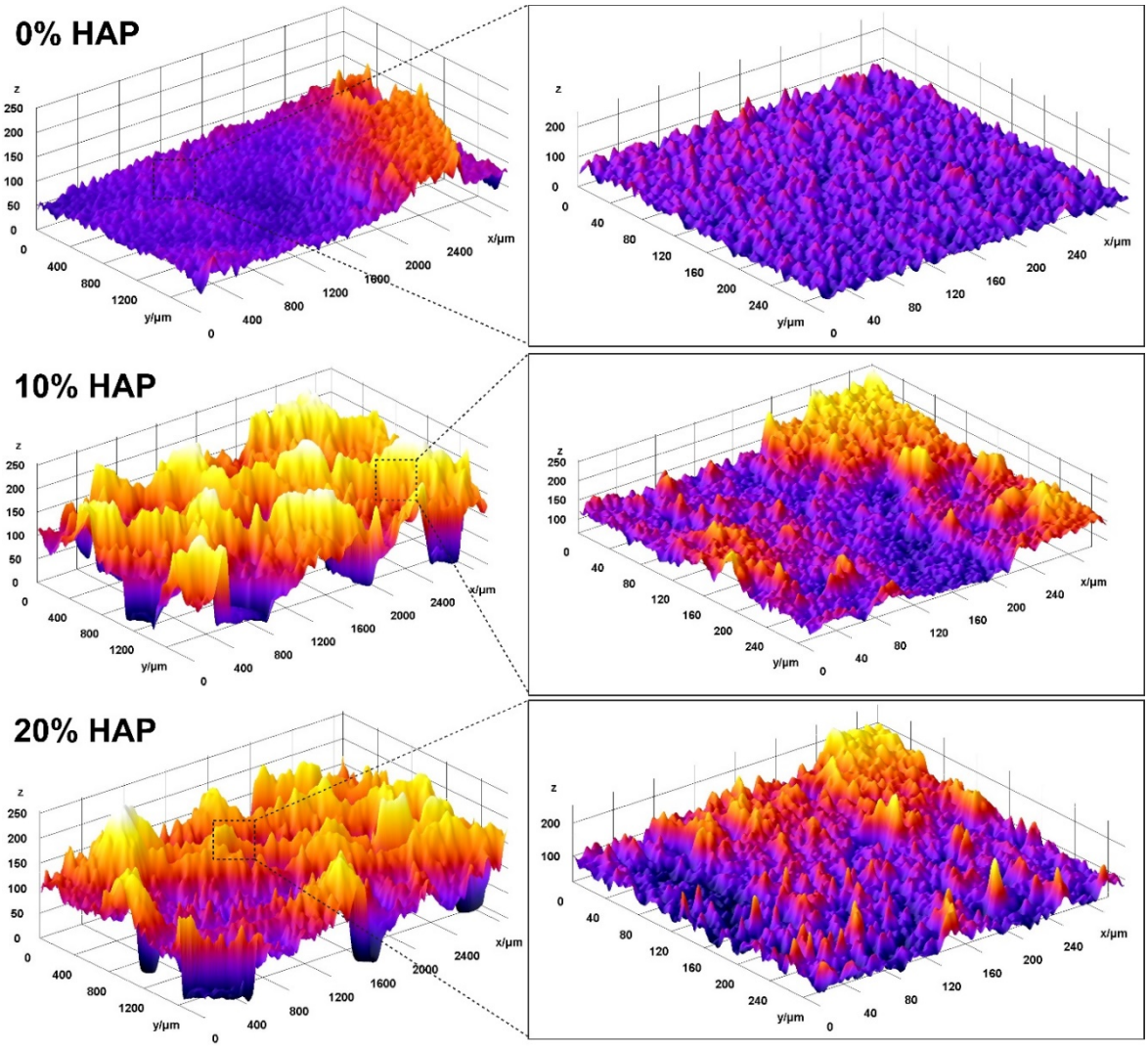


*Figure 83 Surface mapping plots of sHAP-PCLM scaffolds with 0–20% sHAP Mg5Sr5. Left: Larger scaffold region (3 mm × 2 mm). Right: Smaller scaffold region (300 × 300 µm). X-axis and y-axis represent spatial dimensions (µm), z-axis represents grey-scale intensity (arbitrary units).*

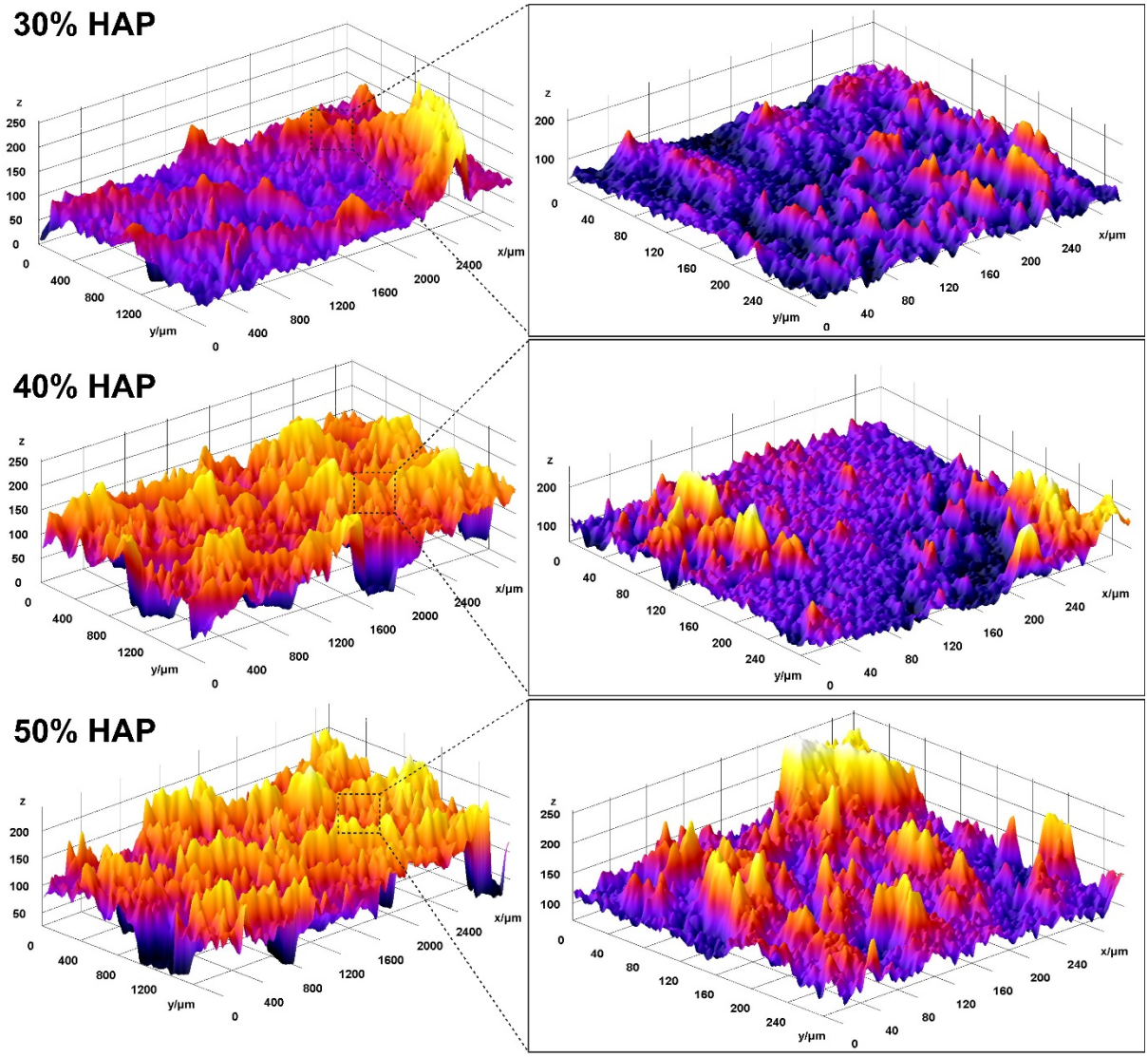


*Figure 84 Surface mapping plots of sHAP-PCLM scaffolds with 30–50% sHAP Mg5Sr5. Left: Larger scaffold region (3 mm × 2 mm). Right: Smaller scaffold region (300 × 300 µm). X-axis and y-axis represent spatial dimensions (µm), z-axis represents grey-scale intensity (arbitrary units).*

### 5.4.5. Good Printability and Shape Retention Achieved with 30 wt% sHAP Mg5Sr5 Ink formulation

Scaffolds containing 30 wt% sHAP Mg5Sr5 and 1.5 wt% $SiO_2$ demonstrated the highest printability among the tested formulations. Figure 85 shows a representative scaffold with clearly defined pores and minimal shape distortion from filament dragging. Other formulations failed to achieve successful printing due to either excessive or insufficient ink viscosity. Modifying printing parameters, including printing speed and platform temperature, influenced printability. Ultimately, scaffolds with 30 wt% sHAP Mg5Sr5 and 1.5 wt% $SiO_2$ exhibited

favourable printing characteristics, providing suitable viscosity for extrusion and shape retention under zero shear conditions.

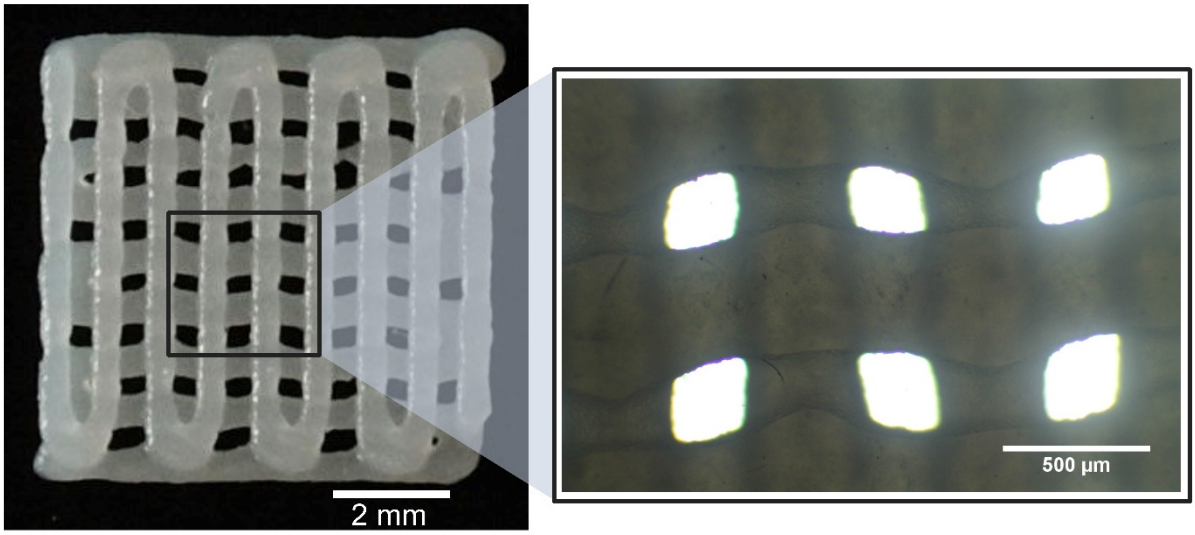


*Figure 85 Printed sHAP-PCLM scaffold containing 30 wt% sHAP Mg5Sr5 and 1.5 wt% $SiO_2$ after crosslinking. Left: Photograph of a scaffold with dimensions of 7.5 × 7.5 mm. Right: Optical microscope image captured at 10× magnification.*

### 5.4.6. Scaffolds with 30 wt% sHAP Mg5Sr5 Supported Y201 MSCs Attachment and Demonstrated No Cytotoxicity

Cell attachment, morphology, and cytotoxicity of scaffolds containing 30 wt% sHAP of Mg5Sr5 and 1.5 wt% $SiO_2$ were evaluated in vitro using Y201 MSCs.

The development of metabolic activity was evaluated using a resazurin assay, with scaffolds assessed at various time points. SCC served as a seeding control (Figure 86). Experiments were conducted in triplicate (n = 3), with results expressed as x-fold change relative to day 1. Shapiro-Wilk testing confirmed normal data distribution across all groups. Statistical analysis employed two-way ANOVA for inter-group and time point comparisons.

All groups exhibited significant increases ($p < 0.0001$) in metabolic activity across time points. The increase in metabolic activity for scaffolds was lower than that of the SCC control, which was cultured under optimised conditions. Nevertheless, scaffold metabolic activity curves exhibited a consistent linear increase, similar to the control group, indicating the non-cytotoxicity of scaffolds.

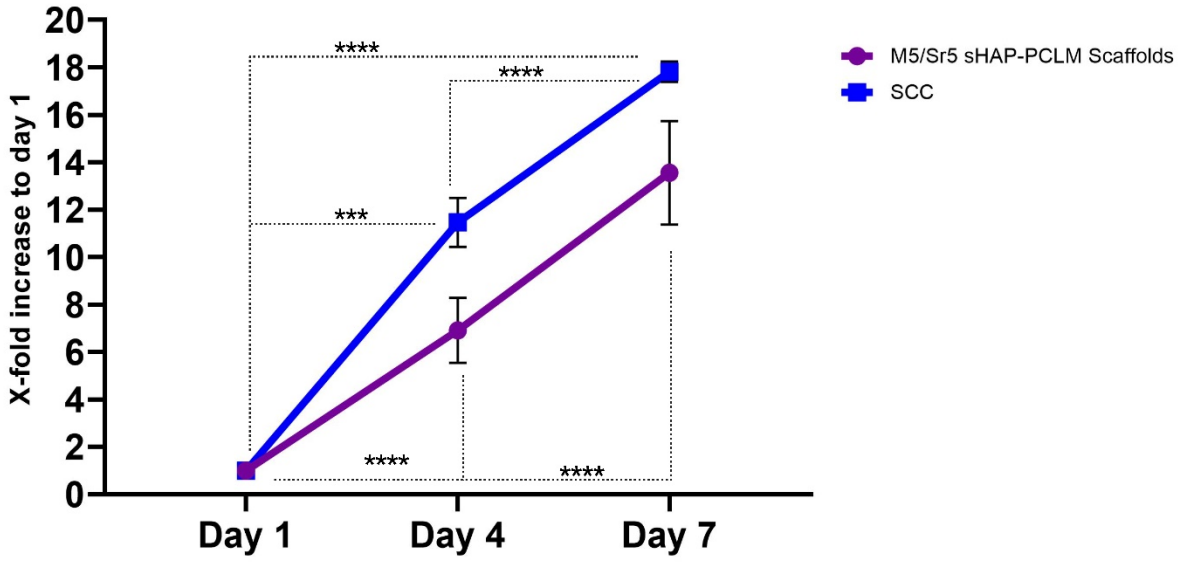


*Figure 86 Y201 MSCs metabolic activity on 30% Mg5Sr5 sHAP-PCLM scaffolds. X-axis: Days 1–7; Y-axis: X-fold increase to day 1. Data presented as mean ± SD (n = 3, *** p < 0.001, **** p < 0.0001).*

By day 28, optical microscopy revealed a notable increase in cell density, with cells progressively colonising scaffold interstitial spaces (Figure 87). Notably, fungal contamination was observed, characterised by distinctive hyphal structures.

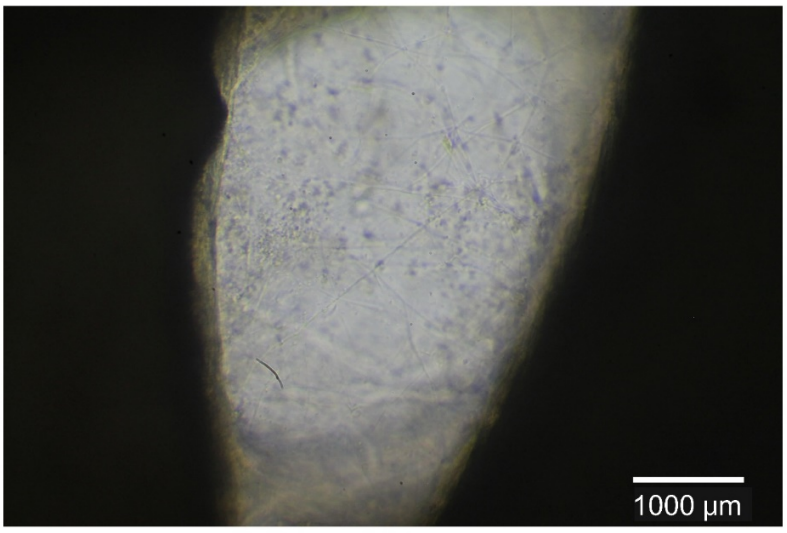


*Figure 87 Optical microscope image of Y201 MSCs cultured on a 30% Mg5Sr5 sHAP-PCLM scaffold at day 28. Captured at 10 × magnification.*

Actin staining on day 7 confirmed cells attached to the scaffold (Figure 88). Cells displayed an elongated fibroblastoid morphology characteristic of this cell type [801]. Distinctive circular voids in nuclear staining regions suggested nuclear presence. However, nuclear staining was unsuccessful, likely due to photobleaching of the DAPI stain. Existing

literature documents DAPI's rapid degradation compared to actin stains and susceptibility to photobleaching under intense fluorescent illumination [803, 804].

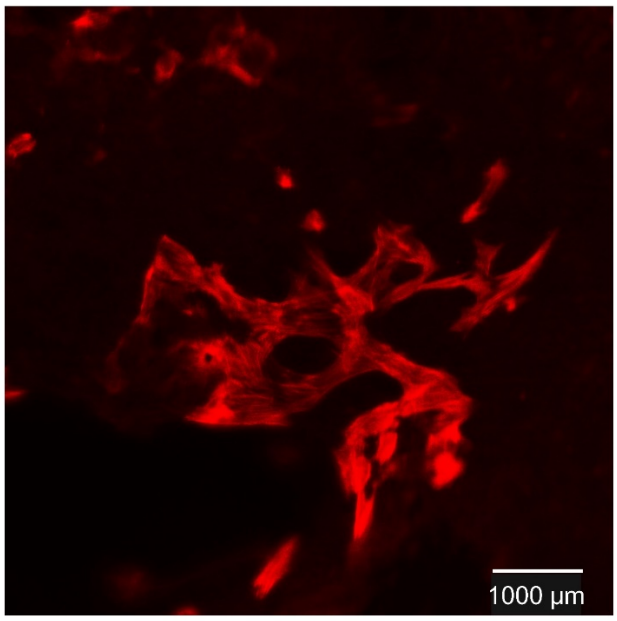


*Figure 88 Confocal fluorescence microscope image of actin-stained Y201 MSCs cultured on a 30% Mg5Sr5 sHAP-PCLM scaffold at day 7. Captured at 100 × magnification.*

Actin staining indicated cell alignment along a preferential orientation in regions of higher cell density. Figure 88 shows cell growth along the filament of the bottom layer of the scaffold, with the gap representing the interstitial space between the filaments.

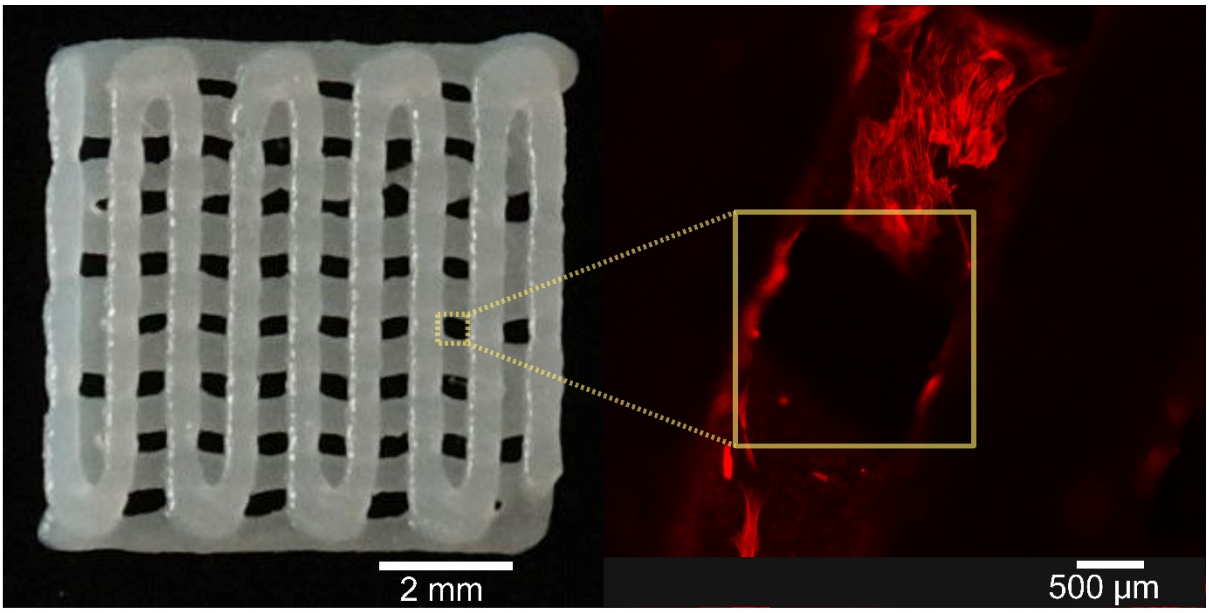


*Figure 89 Confocal fluorescence microscope image of actin-stained Y201 MSCs growing along the filament of a 30% Mg5Sr5 sHAP-PCLM scaffold at day 7. The gap (yellow square) represents the interstitial space between the filaments. Captured at 5 × magnification.*

`

## 5.5. Discussion

In this chapter, synthesised sHAP formulations Mg5Sr5 and Mg10Sr5 were incorporated into PCL for the fabrication of 3D scaffolds. Scaffold fabrication was limited by the temperature sensitivity of sHAP, which led to the selection of extrusion printing to generate precise, customisable 3D structures while avoiding high-temperature processes. This method was successfully employed by multiple research groups for HAP-PCL scaffold fabrication. PCL was synthesised and functionalised with methacrylate groups to enable photocuring for scaffold solidification post-printing. The cytotoxicity of resulting scaffolds was assessed in vitro using Y201 MSCs.

### 5.5.1. Synthesis and Methacrylation of PCL

4-PCL was synthesised via ROP, followed by methacrylate group functionalisation. NMR confirmed successful synthesis and methacrylation through the identification of characteristic functional groups. Additionally, NMR analysis provided insights into molecular conformation, which is critical for understanding its impact on material properties [792, 805].

NMR operates on the principle of nuclear spin quantum transitions. Under an applied magnetic field, nuclei exposed to a specific frequency transition to higher energy states emit detectable resonance signals upon returning to their original states. The local chemical and magnetic environment influences the experienced magnetic field, generating distinct resonance signals. Adjacent protons with varying chemical and magnetic properties interact through nuclear spin coupling, producing characteristic peak splitting in the spectrum. Peak splitting follows the n + 1 rule, where "n" is the number of neighbouring, and "+1" accounts for the proton's own signal. The resulting peak intensity distribution follows Pascal's triangle [806].

Peak analysis of 4-PCL and 4-PCLM spectra revealed complex characteristics: H2, expected to couple only with H3 and generate a triplet according to the n + 1 rule, exhibited an atypical splitting pattern. While resembling a triplet, the peak displayed additional, indistinct splitting. This unusual multiplet pattern potentially arose from "long-range" coupling with protons on other PCL arms, dependent on molecular orbital alignment. Such interactions are typically weak, leading to subtle spectral variations. Existing literature suggests that long-range interactions are more pronounced in polymers with extended chain lengths [807]. H3 protons, characterised by chemical and magnetic equivalence, typically emit a single signal. However, interactions with magnetically distinct H2, H4, and H5/H1 induced second-order coupling, deviating from the n + 1 rule. Each adjacent neighbour splits the signal into a triplet, creating a complex 3×3×3 peak pattern. Peak separation was compromised by similar coupling constants, resulting in peak overlaps and unresolved multiplets. H4, adjacent only to

H3, would expectedly generate a quintuplet following the n + 1 rule. However, the observed spectrum revealed a multiplet. As anticipated, H5 was split by H3, resulting in a triplet pattern. In a 4-PCLM molecule with a single repeat unit (n = 1), H5 would typically appear at approximately 3.4 ppm. The presence of multiple repeat units or methacrylation introduced an ester group nearby, causing deshielding, which relocated H5 to the H1 chemical shift region while preserving its original splitting pattern and coupling constants. Despite automated shift allocation detecting a single signal for the shifted H5, ImageJ analysis confirmed a triplet with consistent coupling constants. Comparing peaks in the H1 region revealed that the original H1 and shifted H5 triplets shared similar coupling constants, measuring approximately 6.64 Hz. H6, comprising a methyl group, produced a singular, strong peak due to the absence of neighbouring protons. H7 and H8, representing germinal alkenyl hydrogen atoms, presented particularly complex spectral characteristics. The carbon-carbon double bond limited spin interactions, rendering each hydrogen on the same carbon diastereotopic with distinct chemical properties. Typically, these hydrogens generate separate signals in proximate chemical shift regions, manifesting as doublets [808]. Contrary to expectations, the NMR spectrum displayed a double, single, and triplet pattern. Given that geminal coupling is inherently weak, this complex pattern likely emerged from combined germinal and allylic "long-range" coupling. The orbital overlap of germinal hydrogens with neighbouring allylic hydrogens likely facilitated these interactions. The observed triplet potentially originated from coupling with two methyl hydrogens, a phenomenon previously reported in the literature [457].

The observed degree of polymerisation exceeded expectations, incorporating three units per pentaerythritol arm instead of the anticipated two. This deviation provides some explanation for the spectral complexity in NMR analysis driven by electron-mediated orbital interactions. Extended PCL arm length could modify orbital configurations, potentially generating unforeseen long-range interactions. Longer arms possess more ester groups, which exhibit a stronger electrostatic attraction to the core due to their higher electronegativity. This attraction induces a slight "leaning" effect, bringing them into proximity with neighbouring protons and facilitating long-range interactions. This preliminary interpretation suggests a more compact polymer configuration, necessitating further comprehensive molecular conformation analysis to validate initial hypotheses.

Methacrylation of PCL utilised a 1:6 molar ratio of PCL to MAA and $Et_3N$, expected to yield a 50% methacrylation degree based on established protocols in literature [457, 459]. Experimental results revealed a 69% methacrylation degree. This deviation potentially stems from multiple factors: incomplete reaction kinetics, temperature variations, impurities, inadequate mixing, or insufficient reaction duration. A more probable explanation involves reduced PCL molecule availability due to elongated arms, resulting in methacrylate excess.

`

Considering the achieved degree of polymerisation, a methacrylation degree of approximately 75% would be anticipated, closely aligning with the calculated value.

## 5.5.2. Metabolic Profiles on HAP-PCLM Discs and Films

Section 5.4.2 confirmed the non-cytotoxicity of HAP-PCLM films on Y201 cells. Metabolic analysis (Figure 76) revealed a steady increase in metabolic activity across time points, albeit lower than in standard plate-seeded cells, potentially due to the inferior cell adhesion on films. Cell-only controls were not intended for direct comparative analysis but to ensure that seeding processes and culture medium did not negatively affect cell viability. Standard cell culture on well plates is highly optimised for cell attachment and proliferation, making it an unsuitable control for evaluating cell growth on scaffolds. Figure 75 shows cell accumulation around the film on the well plate, potentially resulting from the high hydrophilic properties of films promoting viscous spreading. Surface irregularities and external factors such as plate movement could also have influenced cell distribution. The presence of a high number of cells surrounding the scaffold aligns with the metabolic assay results, confirming the non-cytotoxicity of HAP-PCLM films. Cytotoxic materials reduce viable cell numbers by releasing harmful metabolites, affecting the surrounding cellular environment.

Disc scaffolds exhibited markedly different characteristics compared to films. No measurable metabolic activity was detected after washing and sterilisation (Figure 92 in the appendix), suggesting cytotoxicity. Compared to films, this discrepancy could be attributed to structural differences. Discs, produced via moulding without pore encapsulation, have a higher density and greater height, which hinders the removal of unreacted materials. This could result in the release of residual components into the culture medium, potentially inducing cytotoxicity. Existing research indicates that photoinitiator diphenyl-(2,4,6-trimethylbenzoyl)phosphine oxide can induce cytotoxicity via oxidative stress [809, 810]. Additionally, high amounts of HAP might trigger excessive cellular calcium uptake, potentially causing cell death [811].

## 5.5.3. Printing with sHAP-PCLM

Scaffolds were fabricated using Mg5Sr5 and Mg10Sr5 sHAP formulations, which were selected based on their high HAP phase composition and favourable Ca/P ratios demonstrated in the previous chapter.

It was observed that varying concentrations of Mg5Sr5 sHAP in the ink formulations impacted the rheological properties of the inks. These inks exhibited increased viscosity and improved printability and shape retention as the sHAP concentration increased. Specifically,

`

inks with 0% sHAP content exhibited a liquid consistency, whereas those with 50% HAP were notably viscous. Incorporating sHAP into PCL presented challenges due to the high viscosity, necessitating ultrasound-assisted mixing. Manual mixing proved insufficient, particularly with 50% sHAP, where prolonged sonication was essential. While sonication aided in breaking down sHAP agglomerates, it also raised the temperature, reducing the viscosity of the thermosensitive PCL, which aided the mixing process. Efforts to mitigate sHAP agglomeration through dissolution in 100% isopropanol were unsuccessful. Prolonged exposure to elevated temperature and pressure for one week failed to induce solvent evaporation.

The introduction of sHAP into the ink affected the extrudability favourably. Extrusion tests revealed that increasing sHAP concentrations improved filament formation. Inks lacking sHAP exhibited a heterogeneous "drop-like" flow with intermittent interruptions during filament extrusion. However, with higher sHAP content, filament flow became more continuous, reduced interruptions, and improved stream uniformity. This was characterised by a more consistent stream width, primarily due to the increased ink viscosity, which enhanced shape retention. Nevertheless, higher sHAP concentrations necessitated greater extrusion pressure and reduced printing speeds. Furthermore, inks containing 50% sHAP required an ink reservoir temperature of 30°C to achieve extrusion. As the sHAP concentration increased, a more pronounced shear-thinning behaviour was observed in the inks. The extruded filaments initially emerged as a liquid-like stream before transitioning to a more paste-like consistency. Often characterised by filament curling, this behaviour is typical of highly viscous and shear-thinning materials. The observed phenomenon likely resulted from the elevated shear stress during extrusion, which temporarily reduced the viscosity of the extruded filament. Post-extrusion, the shear stress presumably decreased, leading to increased viscosity and improved shape retention, a process previously described by Zhang et al. [449].

These shear-thinning effects could be attributed to sHAP. Previous research has demonstrated that HAP can increase viscosity and exhibit shear-thinning behaviour, with its crystalline structure playing a crucial role [449, 812]. Structures with high crystallinity were found to enhance shear-thinning properties, a phenomenon attributed to the molecular arrangements inherent in crystalline materials [813, 814].

As previously mentioned, a temperature increase was necessary to extrude 50% sHAP inks. Due to PCL's thermos-sensitivity, such a change has likely influenced the pressure drop during extrusion. Ultimately, variations in nozzle geometry, temperature, and input pressure impact the volume flow. Therefore, their direct relationship with ink viscosity in 3D printing with sHAP-PCLM becomes evident.

Printing with Mg10Sr5 and Mg5Sr5 sHAP inks revealed distinct viscosity effects of HAP substitution. Despite comparable HAP content and crystallinity, Mg10Sr5 sHAP inks exhibited less pronounced viscosity increases than Mg5Sr5, even at 80% sHAP, yielding a sticky paste-

like consistency. This difference may be attributed to variations in surface chemistry, HAP morphology, and particle size. PCL exhibits poor polar properties with relatively polar ester groups and non-polar methylene groups. Methacrylation of PCL further decreases its overall polarity by substituting polar end groups. In contrast, standard crystalline non-substituted HAP has a higher polarity of approximately 77% [815], which can be modified by ion substitution. Mg and Sr substitution in HAP induces an elongated rod-like structure, with increasing Sr content correlating with decreased length along the c-axis [366, 371]. This morphological change potentially increases the presence of more polar crystallographic planes (010, 100, or 110, see Figure 16) [816]. Furthermore, Mg substitution facilitates surface adsorption of Mg onto the HAP surface, enhancing surface hydration in aqueous conditions and consequently increasing polarity [340, 342, 691]. This increased hydration effect may also contribute to particle agglomeration, a phenomenon previously reported [339, 340, 346] and observed to become more pronounced with higher levels of Mg substitution [346]. The combination of particle agglomeration and increased polarity potentially results in weaker interactions with the polymer matrix, thereby reducing viscosity. Particle morphology also plays a crucial role in the rheological properties of the composite. Smaller, rounder particles increase viscosity due to higher surface area-to-volume ratios and denser packing, enhancing polymer-particle interactions. Conversely, elongated particles reduce viscosity through lower surface area and less efficient packing [814]. Notably, the radius of hydrated Mg is approximately 400 times larger than its non-hydrated radius [747], which may have contributed to the observed sticky consistency.

Hydrophobic silica was incorporated to enhance the inks' viscosity and shear-thinning behaviour. These nanoparticles form clusters through hydrophobic interactions due to their small size and high surface area. This cluster formation establishes a three-dimensional network within the material, effectively limiting the flow of the polymer and consequently elevating its viscosity. When subjected to shear forces, these clusters of silica particles can undergo partial disruption or reorientation, thereby reducing resistance to flow and causing a decrease in viscosity during shear stress. Subsequently, upon removal of the shear forces, the clusters can reassemble, restoring the material's viscosity [788, 789, 817]. Consequently, the addition of only 1.5% silica effectively increased viscosity and improved the shear-thinning behaviour of sHAP-PCLM inks.

`

### 5.5.4. Shape Fidelity and Topography of Printed sHAP-PCLM Scaffolds

The incorporation of sHAP influenced scaffold shape fidelity and topography. Without sHAP, the ink formulation exhibited poor shape retention, resulting in filament spreading and loss of structural integrity after printing. Increasing sHAP concentration improved filament width homogeneity, initially increasing filament width but decreasing at the highest sHAP concentration. Enhanced filament homogeneity up to 30% sHAP was attributed to more uniform ink flow during printing. The increased filament width resulted from enhanced shear characteristics, reducing extensional forces that cause filament elongation and thinning during printing. The transition from 30% to 50% sHAP exhibited decreased filament width due to improved shape retention and reduced filament collapse through viscous encapsulation. Higher sHAP concentrations also produced more distinct filament junctions at directional changes during printing and enhanced layer separation between lower and upper filaments by minimising viscous spreading. At 50% sHAP, lower filaments displayed a dragging effect potentially attributable to two mechanisms: viscous drag forces from the resistance of the semi-liquid lower layer to flow and layer adhesion from the lack of solidification prior to upper layer extrusion.

Surface mapping of grayscale SEM images revealed topographical changes with varying sHAP concentrations. Higher sHAP concentrations corresponded with increased surface peak frequency, most prominently at 50%. The 50% sHAP scaffolds also exhibited elevated peak heights, suggesting particle agglomeration due to insufficient mixing or agglomerate formation during printing. Previous research has documented similar uneven distribution and HAP aggregate formation due to interactions with positively charged polymer regions [818]. An increase in surface peak frequency could indicate increasing surface roughness, consistent with previous studies demonstrating a positive correlation between HAP concentration and surface roughness [819, 820]. Moghaddaszadeh et al. reported that increasing carbonated nano-HAP concentrations (30–60%) in 3D-printed scaffolds enhanced surface roughness by up to 6.1-fold [445]. Furthermore, coating PCL with HAP has been shown to increase surface roughness and promote osteogenic differentiation [821]. Enhanced surface roughness benefits cell adhesion by providing additional attachment sites, facilitating protein adsorption, and creating favourable microenvironments, as documented in previous studies [451, 822-825].

`

## 5.5.5. Surface Wettability of HAP/sHAP-PCLM Blends

Surface properties of polymer blends with/without sHAP and silica were analysed using thin films. WCA, WoA, and IFT measurements were obtained via drop shape analysis, with SFE calculated using Young's equation. These properties influence biomaterial performance through cell adhesion and protein absorption, enabling cell signalling [826-829].

WCA, a crucial wettability parameter, offers insights into a material's hydrophobic or hydrophilic nature. A higher contact angle indicates reduced wettability and, consequently, greater hydrophobicity. SFE represents the energy per unit surface area, measuring a surface's ability to attract molecules [802]. When liquid contacts a solid surface, their distinct surface energies create wetting, determining the IFT through molecular interactions [830]. The energy required to separate these two surfaces is described as the WoA [831].

The introduction of HAP and silica caused changes in the WCA. Low silica concentrations increased WCA due to silica's partial hydrophobicity. Interestingly, 0.75% silica in PCLM reduced WCA to near-PCLM levels, potentially due to silica cluster formation. Higher silica concentration reduces particle movement due to greater viscosity while increasing particle proximity, thereby promoting intermolecular and electrostatic attractions [832]. This may reduce hydrophobic silica surface exposure, decreasing overall hydrophobicity. Amoabeng et al. demonstrated that fumed silica particles readily form aggregates, transforming from 5-50 nm individual particles to 100-200 nm clusters [833]. The incorporation of HAP into PCLM unexpectedly increased WCA, potentially attributable to the hydrophobic surface characteristics of silica present in the composites. During blend preparation, ns HAP formulations exhibited the highest viscosity and formed large, difficult-to-disperse clusters. Notably, at 30% and 50% concentrations, nsHAP blends displayed lower WCA than substituted HAP blends. This may have resulted from large HAP clusters reducing obstructions that interfere with silica interactions, thereby promoting silica aggregation and decreasing the exposure of hydrophobic silica surfaces. At 50% concentration, the absence of WCA differences was likely due to the increased viscosity of the blends, which impeded particle movement, reducing the probability of silica interactions.

HAP inclusion in PCLM blends did not significantly impact the IFT compared to PCLM alone. However, HAP type and concentration substantially influenced IFT. At 10% and 30% concentrations, nsHAP blends showed higher IFT than substituted HAP, possibly due to reduced hydrophobic silica surface area from large HAP clusters as previously described for WCA measurements. This difference may also stem from varying SFE profiles between HAP and sHAP, influenced by particle size or surface chemistry. Previous studies demonstrated higher surface energy for smaller HAP particles [834]. HAP substitution alters its energy characteristics. HAP's high surface energy originates from oppositely charged $Ca^{2+}$ and $P_4^{3-}$

`

/$O^{2-}$ interactions. Substituting $Ca^{2+}$ with ions of different ionic radii induces shifts in $O^{2-}$ positions, leading to electrostatic repulsion mitigated by oxygen vacancies. This results in parallel hydroxyl dipole alignment, reducing HAP surface free energy through more uniform dipole distribution [327, 835]. At 50% concentration, the nsHAP blend showed a decrease in IFT. This reduction may be attributed to increased viscosity reducing silica agglomeration or stronger HAP particle interactions reducing exposed HAP surface area. A study demonstrated that HAP cluster size influences dipole moment behaviour, with larger clusters exhibiting reduced average polarisation, resulting in internal electric field formation and decreased surface energy [836]. Blends containing Mg5Sr5 exhibited higher IFT than those with Mg10Sr5 at 30% and 50% concentrations. This disparity likely stemmed from the more pronounced energy characteristics of sHAP at higher concentrations. The higher Mg content in Mg10Sr5 presumably caused increased $O^{2-}$ ion loss, reducing surface energy. Silica content significantly influenced IFT, with 0.75% silica more than doubling IFT compared to pure PCLM. Non-polar silica particles may cover polar PCLM regions, disrupting polymer molecule interactions and reducing IFT, as seen with 0.15% silica. While increased silica content promotes aggregation, it could also bring more molecules closer to PCLM. Although individual $SiO_2$ molecules are non-polar due to balanced dipole moments [837], $SiO_2$ clusters acquire a negative charge [832]. This charge potentially fosters dipole-dipole interactions with the polar ester groups of PCLM, reducing dipole force cancellation and increasing surface free energy. The observed IFT increase may result from a combination of forces, including van der Waals and dispersion forces between esters and silica.

WoA was affected by HAP and silica inclusion. HAP/sHAP incorporation reduced WoA, with sHAP demonstrating more pronounced decreases at 10% and 30% concentrations. Silica addition reduced WoA at 0.15% and 0.45% concentrations, while 0.75% exhibited comparable values to pure PCLM. These observations could be attributed to silica's hydrophobic properties and changing surface area during cluster formation, influenced by particle interference and viscosity effects.

No significant differences in SFE were detected between most formulations, except for Mg10Sr5 in the 30% blend, which displayed significantly lower values than PCLM and Mg5Sr5 at 30%. The lack of statistical significance in SFE variations may be attributed to high standard deviations resulting from rapid changes in drop geometry measurements used in the calculations.

## 5.5.6. In Vitro Assessment of sHAP-PCLM Scaffolds

The results in section 5.4.6 confirmed the non-cytotoxicity of 3D HAP-PCLM scaffolds towards Y201 cells, with a low metabolic response, possibly attributed to lower cell numbers.

Microscopic observation (Figure 87) revealed increased cell numbers as cells progressively populated the interstitial spaces between filaments within the scaffold. Notably, potential contamination may have facilitated cell ingrowth by bridging filament gaps.

Actin cytoskeleton staining confirmed cell attachment, though specific alignment was not prominent. Cell alignment becomes more evident with higher cell density and may be influenced by cell differentiation, likely evolving beyond day 14. Localised cell alignment within scaffolds may have resulted from higher cell density in certain scaffold regions. However, variations in scaffold morphology, seeding processes, and post-seeding handling could contribute to heterogeneous cell attachment patterns.

A research group identified moderate SFE (≈ 70 mJ $m^{-2}$) optimal for cell attachment in HeLa cells and a breast cancer cell line [828]. Mg5Sr5 sHAP-PCLM blends used in scaffold cytotoxicity experiments exhibited comparable SFE, suggesting sufficient SFE with no critical need for modification.

## 5.6. Summary and Conclusion

This chapter focused on the development of customisable sHAP-PCLM scaffolds via 3D printing. Four-arm PCL was synthesised and methacrylated to achieve post-extrusion crosslinking. Preliminary in vitro evaluation using HAP-PCLM films confirmed their non-cytotoxicity towards Y201 MSCs.

Multiple ink formulations were investigated, incorporating sHAP concentrations from 0% to 50%. $SiO_2$ was added at 1.5% to improve ink shear-thinning properties, extrudability, and shape retention. Higher sHAP concentrations increased ink viscosity and surface roughness. The Mg10Sr5 formulation demonstrated lower viscosities and a stickier consistency than the Mg5Sr5 formulation. Customisable 3D scaffolds with a woodpile structure were successfully printed using an ink containing 30 wt% sHAP (Mg5Sr5) and 1.5 wt% $SiO_2$. The resultant scaffolds demonstrated good shape fidelity post-printing. Y201 MSCs seeding revealed limited cell attachment, though metabolic activity remained uncompromised.

In conclusion, a sHAP-PCL composite was successfully synthesised and demonstrated potential for custom scaffold fabrication via 3D printing. Although scaffolds with 30 wt% sHAP Mg5Sr5 and 1.5 wt% $SiO_2$ were successfully printed in this project, further refinement of printing parameters and ink formulations is necessary to fabricate scaffolds with various compositions. Cell seeding with Y201 MSCs was successful, with no cytotoxic effects observed, despite the potential for improved cell adhesion.

`

# Chapter VI Conclusions and Further Work

This research project investigated the fabrication of 3D scaffolds composed of Mg and Sr-substituted HAP incorporated into a PCL matrix. The primary objective was to develop scaffolds for potential application as bone graft substitutes, mainly as spinal fusion cage fillers. Additionally, the project aimed to develop and implement an SOP utilising serum-free medium for in vitro experiments throughout the project. The project's goals were successfully achieved.

Firstly, an SOP for Y201 MSC culture that mitigates potential variations arising from batch-to-batch serum differences was established. This development represents an advancement in enhancing the reproducibility of in vitro results and constitutes a crucial step towards more standardised and reliable testing protocols in biomaterial evaluation.

A continuous method for sHAP synthesis was successfully implemented. Compared to batch processing, this approach offers higher synthesis output due to uninterrupted production. This method's potential for large-scale production presents promising opportunities for commercial applications. The project demonstrated the successful ionic substitution of HAP with Mg and Sr at 10 mol% Mg + 5 mol% Sr and 5 mol% Mg + 5 mol% Sr. Importantly, these sHAP formulations exhibited no inherent cytotoxicity towards Y201 MSCs, a finding that is crucial for their potential use in clinical applications.

Incorporation of sHAP into PCLM yielded shear-thinning inks for extrusion printing of 3D composite scaffolds, enabling advancement toward more complex, customisable architectures. In vitro evaluation revealed successful cell attachment and the absence of cytotoxicity, supporting their potential application as bone graft substitutes.

While the achievements described in this thesis represent progress towards the establishment of a bone graft substitute, further optimisation is necessary to meet the stringent requirements for potential clinical applications and commercialisation [838, 839]. The following research priorities have been identified to facilitate a progression toward these goals:

## Synthesis and Evaluation of sHAP

Subsequent research should initially focus on optimising the sHAP synthesis process. A standardised manufacturing process ensures product consistency, quality, and purity before seeking market approval and clinical use [838, 840]. Furthermore, addressing this step at an early stage is advantageous, as it mitigates the need to revisit and re-optimise the synthesis process at later stages of the project.

One key area for improvement is the implementation of pH control throughout the synthesis process. The current methodology lacks such control, resulting in pH variations between formulations and batches, as observed in this project. This is of critical importance

as pH levels influence the stability of different calcium phosphate phases, thereby altering the phase composition of the product [740]. Maintaining a consistent pH would substantially reduce batch-to-batch variability, enhancing the reproducibility and reliability of the synthesis process.

Another proposed enhancement is the introduction of nitrogen flow during synthesis to control atmospheric parameters and mitigate $CO_2$ incorporation, improving the purity and consistency of the final product [368].

Variations in Ca/P ratios were observed in the current project, which can impact the resulting material's mechanical properties, biological response, and degradation rates [841-843]. Introducing a washing step during incubation could address this issue. This step would remove surface-bound ions and initiate precipitation-dissolution processes, potentially leading to more consistent Ca/P ratios [844].

The minimisation of secondary phases is another crucial aspect in synthesising high-purity HAP. The presence of secondary phases can affect in vivo resorption and mechanical properties. For instance, brushite, a frequent secondary phase in this project, has been shown to exhibit reduced biodegradation in vivo due to its conversion to HAP [845]. Moreover, brushite typically demonstrates lower mechanical properties than HAP [846]. Several strategies could be employed to minimise secondary phases, including rapidly decreasing pH after initial incubation to promote dissolution of secondary phases [847], reducing the supersaturation to promote direct HAP formation [848] or increasing synthesis temperature to promote HAP conversion [848].

Following a standardised synthesis process, consistent product quality must be assessed, and acceptance criteria for variability must be established [840].

After optimising sHAP synthesis, a comprehensive characterisation and biological evaluation of the sHAP formulations is essential. This step ensures the safety and efficacy of the material before its incorporation into the PCL matrix and provides valuable insights into its potential performance in bone regeneration applications.

Evaluating the grain size and morphology of the synthesised sHAP powders is crucial, as these physical properties have been demonstrated to influence the biological response. Previous research demonstrated that small needle-shaped particles elicited stronger inflammatory responses than small and large spherical particles [849].

The immunogenicity of different sHAP formulations warrants thorough investigation before their incorporation into PCL. Immunological assessment at this stage is particularly crucial as the particles may elicit varying immunological responses due to their morphology once released from their polymer encapsulation during degradation in vivo. This could be evaluated using an assay that employs bone marrow-derived macrophages with direct cell contact, following the methodology of Lebre et al. [849].

`

Transwell experiments offer a valuable method for evaluating both the cytotoxicity and osteogenic differentiation potential of HAP powders while concurrently monitoring ion concentrations in a cell culture medium. This approach allows for a detailed analysis of the degradation behaviour of the material and its impact on biological responses. Degradation products of sHAP, Ca, P, Mg, and Sr were found to promote osteogenesis [313, 850, 851]. Sr has been shown to have dose-dependent effects on mineralisation, potentially inhibiting it at higher concentrations (20 and 100 µg/mL) [852]. The degree of Mg and Sr substitution in HAP influences its solubility, thereby affecting ion availability and the magnitude of their biological effects [372].

## Synthesis and Evaluation of PCLM

In this project, the synthesis and methacrylation of PCL were performed based on previously established protocols under controlled conditions [457, 459]. However, the anticipated degree of polymerisation and methacrylation could not be achieved. Variations in polymerisation and methacrylation can influence the degradation and mechanical properties of a biomaterial, thereby altering its overall characteristics [459, 462, 853]. Consequently, it is imperative to evaluate the consistency of the product quality. If variations are identified, further optimisation of the synthesis parameters would be necessary to ensure product quality meets the standards for commercialisation and clinical use [840].

## Preliminary Evaluation of sHAP-PCLM

Following synthesis and characterisation of the composite components, the next step in the optimisation process involves incorporating the most promising sHAP formulation into the PCL polymer matrix for preliminary evaluation.

The HAP to PCL ratio is crucial in determining surface properties such as roughness and wettability, which are critical in influencing cell-material interactions and subsequent biological responses [443, 854]. While increasing the HAP content in HAP-PCL composites has been shown to enhance cell proliferation, protein adsorption, and osteogenic differentiation, it is essential to note that it may also result in dose-dependent cytotoxicity through oxidative stress mechanisms [855, 856].

The implementation of an appropriate sterilisation method is essential to meet safety requirements for potential clinical applications [838, 839]. However, different sterilisation techniques can impact the structural and chemical properties of the composite material, which may consequently affect degradation time and key biological responses such as cell adhesion and osteogenic differentiation potential or even induce cytotoxicity [857-860]. A design of experiments (DoE) approach is recommended for the systematic evaluation of HAP/PCL

ratios and sterilisation methods to analyse their effects on composite properties comprehensively.

HAP-PCL films could be used to assess surface characteristics, including roughness and wettability, as well as biological properties, such as protein adsorption, cytotoxicity profiles, and osteogenic differentiation potential. At this stage, a cell line could be seeded directly on the films for biological evaluation, as this approach provides sufficient information for preliminary evaluation.

Sterilisation effectiveness requires evaluation through microbial infection resistance testing to ensure clinical applicability. HAP-PCL discs enable analysis of sterilisation-induced structural changes and material stiffness assessment. Material stiffness matching with native bone is essential to prevent stress shielding and subsequent bone loss in clinical applications [861].

## Fabrication and Evaluation of sHAP-PCLM Scaffolds

Scaffold fabrication optimisation is crucial for bone graft substitute development. This requires refinement of ink formulations and 3D printing parameters for various sHAP-PCL compositions. Proposed modifications include replacing hydrophobic silica with hydrophilic alternatives or other shear-thinning agents (alginate, carboxymethyl cellulose) to enhance cell attachment [862-865]. These modifications are crucial, as the scaffold's surface properties significantly influence cell adhesion and subsequent biological responses [854].

A DoE approach is proposed to establish a comprehensive printability window for various ink formulations. This methodology would involve systematically varying printing parameters such as pressure, temperature, nozzle diameter, and ink formulations. The efficacy of this approach is supported by the work of Reina-Roma et al., who successfully used a DoE methodology to identify optimal nozzle geometries for achieving shear-thinning behaviour in their study [866]. Integration with rheological measurements of different ink formulations would provide insights into flow behaviour for printability parameter optimisation. Upon establishing optimal printing parameters and ink formulations, the initial focus should be on fabricating simpler 3D structures. This stepwise approach allows for thorough scaffold testing before progressing to more complex designs, ensuring that fundamental printing issues are addressed and scaffolds demonstrate biocompatibility and bone regeneration potential before attempting more intricate architectures.

A critical issue identified in the current project is insufficient cell attachment on fabricated scaffolds, attributed to smooth surfaces resulting from 3D printing processes [867], necessitating surface topography and chemistry modifications. One of the most effective methods for improving cell attachment is the enhancement of surface roughness, with NaOH treatment being among the most promising and widely used techniques [445, 455, 868]. NaOH

treatment has been demonstrated to increase surface roughness and create porous structures similar to cancellous bone while maintaining mechanical properties [455]. Moreover, it can enhance the osteogenic potential of PCL scaffolds [868] and remove residual organic contaminants while introducing hydrophilic hydroxyl groups to the surface [869, 870].

Plasma coatings provide another promising strategy for surface modification. They enhance cell attachment by modifying surface chemistry and increasing hydrophilicity. These alterations create a more conducive environment for cell adhesion, thereby improving cell-scaffold interactions [871, 872]. An additional surface treatment option is ε-poly-L-lysine, which has been shown to enhance cell attachment while providing antibacterial properties [873]. Its dual functionality could be particularly beneficial in bone graft substitutes, where infection prevention is a critical concern alongside promoting tissue regeneration.

Prior to in vitro or in vivo testing, scaffold sterilisation must be performed using methods that ensure sterility while minimising material property alterations, thereby maintaining safety and efficacy for potential clinical applications.

Following the optimisation of sHAP synthesis and scaffold fabrication, the next phase involves a comprehensive evaluation using a DoE approach to systematically investigate the effects of varying sHAP-PCL mixing ratios and surface modifications on scaffold performance.

The initial screening should prioritise the assessment of cytotoxicity, cell attachment, and osteogenic differentiation. For this preliminary phase, a continuous cell line is recommended due to its ease of use and reproducibility [874].

Uniform cell seeding distribution requires scaffold stabilisation at the culture vessel bottom, achievable through the application of biocompatible fibrin glue [875].

The ratio of sHAP to PCL in the scaffold composition is a critical factor that could significantly affect the biological response. Previous studies have shown that HAP-PCL composites exhibit higher proliferative and osteogenic capacities than HAP alone in vitro [876]. Furthermore, increased concentrations of HAP in HAP-PCL composites have been associated with enhanced cell proliferation, protein adsorption, and osteogenic differentiation [855]. An in vivo mouse model study has also demonstrated that HAP improves bone regeneration more effectively than PCL alone [877]. However, it is crucial to note that HAP itself can induce dose-dependent cytotoxicity through oxidative stress [856]. Similarly, the photoinitiator diphenyl-(2,4,6-trimethylbenzoyl)phosphine oxide, used in the fabrication process, has also been shown to induce dose-dependent cytotoxicity through oxidative stress [809, 810]. Therefore, careful evaluation and optimisation of these parameters are essential to balance the beneficial effects with potential cytotoxicity risks.

Within the same DoE framework, scaffolds could be evaluated for their degradation behaviour in simulated body fluid. This assessment is crucial, as previous research has indicated that the incorporation of SrHAP increased degradation rates in PCL scaffolds [878].

`

Understanding the degradation kinetics is vital for ensuring the scaffold maintains its structural integrity during bone regeneration while gradually being replaced by newly formed tissue.

Following the initial screening with cell lines, selected scaffolds should undergo testing using primary human stem cells derived from bone marrow. This step is crucial for better predicting in vivo performance and improving translation to clinical applications [874, 879]. These steps should focus on cytotoxicity, immunogenicity, and haemocompatibility, comprehensively assessing the scaffolds' biological interactions.

The scaffold demonstrating the best performance in vitro and exhibiting a degradation time similar to the expected bone regeneration time should be selected for subsequent in vivo testing in an animal model. A critical-sized bone defect model could be employed to evaluate the scaffold's performance in a physiological environment, specifically its ability to support bone regeneration in a defect that would not heal spontaneously [880]. Furthermore, this in vivo model would allow for the evaluation of potential adverse reactions from the host tissue, including immunological, haematological, or toxicological responses, which is essential before considering possible clinical translation [881, 882].

Overall, this project's achievements have laid a strong foundation for the future development of bone graft substitutes, particularly as fillers for spinal fusion cages. The potential utilisation of such engineered bone graft substitutes holds promise to replace conventional autograft and allograft materials, thereby mitigating their inherent risks.

While the essential requirements for direct clinical translation have not been fully realised within the scope of the present work, continued refinement and optimisation could yield a bone graft substitute that enhances the spinal fusion process. Furthermore, the intrinsic customisability could enable the creation of patient-specific graft designs precisely matched to the spinal fusion cages before surgical interventions. This prospective capability for pre-operative planning and preparation has the potential to decrease the overall surgery time, thereby improving surgical outcomes and reducing patient morbidity.

`

# Appendix

## Calculations for Cell Viability Quantification

Cell viability and concentrations of live and dead cells for in vitro assays were quantified using the following equations:

$$\textit{Viable cells/ml} = \frac{\textit{Number of live cells counted}}{\textit{Number of large squares counted}} \times \textit{Dilution factor} \times 10^4$$

$$\textit{Non-viable cells/ml} = \frac{\textit{Number of dead cells counted}}{\textit{Number of large squares counted}} \times \textit{Dilution factor} \times 10^4$$

$$\textit{\% Viability} = \frac{\textit{Number live cells counted}}{\textit{Total number of cells counted}} \times 10$$

`

# SOP for Y201 MSC Expansion and Differentiation in Serum-Free Medium

| | | | |
|---|---|---|---|
| **Task** | SOP for the Expansion and Differentiation of Y201 MSCs in StemMACS™ | | |
| **PI** | Dr Gwendolen Reilly | Lab Location | C+9, Pam Liversidge Building |
| **Issue Date** | 01/02/2022 | Revision Date | |
| **Prepared by** | Denata Syla and Jose Rodriguez | Doc # | #1 |

| | |
|---|---|
| **Purpose** | Establishment of a standardised protocol for the expansion and differentiation of human Y201 MSCs in serum-free medium for in vitro characterisation of HAP-based materials. |
| **Scope** | The following parameters were compared to identify the best conditions for cell expansion and osteogenic differentiation:<br>• Media<br>  ○ DMEM GlutaMAX™ (high glucose) supplemented with 10% FBS<br>  ○ Human Mesenchymal-XF Expansion Medium<br>  ○ StemMACS™ MSC Expansion Medium Kit XF (human)<br>• Plate coatings<br>  ○ No coating<br>  ○ Gelatine coating<br>  ○ Fibronectin coating<br>• Media changes<br>  ○ No media change<br>  ○ Partial media change<br>  ○ Full media change |
| **Background** | Cells require culture medium supplementation with essential bioactive components, including hormones, growth factors, and amino acids [1]. While animal-derived serum, predominantly FBS, represents the standard supplement [1, 2], its undefined composition and inter-lot variability introduce significant challenges through inconsistent cellular responses [1, 2]. |
| **Responsibilities** | Denata Syla investigated cell culture conditions for Y201 MSC expansion, while Jose Rodriguez evaluated the parameters for osteogenic differentiation. |
| **Materials** | • Y201 MSCs<br>• StemMACS™ MSC Expansion Medium Kit XF (human)<br>• P/S antibiotic solution (100 U/ml/100 µg/ml)<br>• Osteogenic supplements: βGP (0.5 M), AA-2P (5 mg/ml), Dex (10 µM)<br>• Well plates/flasks/scaffolds |

`

| | |
|---|---|
| **Methods** | **Cell culture**<br>• Prepare medium by adding StemMACS™ supplement and P/S antibiotic solution to StemMACS™ medium. Aliquot as preferred.<br>• If applicable, pre-soak scaffolds or substrates in medium for at least 30 min, ideally 1 h.<br>• Wash cells twice with 10 ml HBSS.<br>• Detach cells with 5 ml of 0.25% trypsin-EDTA solution for 5–10 min. Cells previously cultured in serum-containing medium might need longer to detach.<br>• Stop trypsin-EDTA by adding 10 ml DMEM supplemented with 10% FBS.<br>• Separate cells by centrifugation at 1000 rpm for 5 min.<br>• Resuspend cell pellet in 1 ml StemMACS™ medium.<br>• Determine the cell concentration and calculate the required volume for 4000 cells/cm$^2$ seeding density:<br>  ○ 2D culture in well plates: Consider the bottom of wells.<br>  ○ 2D culture on scaffolds: Consider the exposed top and lateral surfaces.<br>  ○ 3D culture on scaffolds: Consider the exposed surface areas.<br>• Add the necessary volume of cell suspension to achieve the required cell density; if necessary, supplement with medium to uniformly cover the bottom of the well/ scaffold surface.<br>• Incubate for 45 min to facilitate cell attachment, monitoring every 15 min to prevent drying and adding medium as needed.<br>• Following incubation, adjust the medium volume:<br>  ○ 48-well plate: 400 µl/well<br>  ○ 24-well plate: 800 µl/well<br>  ○ 12-well plate: 1500 µl/well<br>• Scaffold: If treated well plates were used for seeding, transfer the scaffolds to new plates and replace the medium after 24 h.<br>• Cell differentiation: At 48–72 h after seeding, add supplements at a 100:1:1:1 ratio of medium:β-GP:AA-2P:Dex, or replace with osteogenic medium.<br>• Perform full medium changes every 7 days.<br><br>**Methods for Evaluation:**<br>• Cell viability:<br>  ○ Measured via a metabolic assay such as resazurin assay.<br>  ○ Recommended time points for a 4000 cells/cm$^2$ density are days 1, 4 and 7.<br>  ○ DNA quantification can be performed on the same cells after an HBSS wash.<br>• Osteogenic activity:<br>  ○ Evaluated through ALP activity measurement after 14 days and calcium staining after 21 days of cell culture.<br>  ○ It is recommended to analyse metabolic activity and DNA quantity with each osteogenic activity measurement. |
| **References** | [1] N. McGillicuddy, P. Floris, S. Albrecht, J. Bones, Examining the sources of variability in cell culture media used for biopharmaceutical production, Biotechnology Letters 40(1) (2018) 5-21.<br>[2] S. Gottipamula, M.S. Muttigi, U. Kolkundkar, R.N. Seetharam, Serum-free media for the production of human mesenchymal stromal cells: a review, Cell Proliferation 46(6) (2013) 608-627. |

`

# Statistical Results for HAP Substitution in the 5–20% Range

*Table 33 Statistical analysis results of pH values across the 5–20% sHAP range using two-way ANOVA with Tukey's multiple comparisons. The total interaction p-value was <0.0001. All formulations were normally distributed (Kolmogorov-Smirnov test).*

| **Comparisons** | **Significant** | **Adjusted p-value** |
|---|---|---|
| Mg20Sr20 | | |
| $T_0$ vs $T_{24}$ | No | 0.9987 |
| $T_{24}$ vs Wash 3 | Yes | 0.0175 |
| Mg5Sr20 | | |
| $T_0$ vs $T_{24}$ | Yes | <0.0001 |
| $T_{24}$ vs Wash 3 | No | 0.0904 |
| Mg20Sr5 | | |
| $T_0$ vs $T_{24}$ | Yes | 0.0003 |
| $T_{24}$ vs Wash 3 | No | 0.9989 |
| Mg5Sr5 | | |
| $T_0$ vs $T_{24}$ | Yes | 0.0020 |
| $T_{24}$ vs Wash 3 | No | 0.9705 |
| | | |
| $T_0$ | | |
| Mg20Sr20 vs Mg5Sr20 | Yes | <0.0001 |
| Mg20Sr20 vs Mg20Sr5 | Yes | <0.0001 |
| Mg20Sr20 vs Mg5Sr5 | Yes | <0.0001 |
| Mg5Sr20 vs Mg20Sr5 | Yes | <0.0001 |
| Mg5Sr20 vs Mg5Sr5 | No | 0.5977 |
| Mg20Sr5 vs Mg5Sr5 | Yes | <0.0001 |
| $T_{24}$ | | |
| Mg20Sr20 vs Mg5Sr20 | No | 0.3643 |
| Mg20Sr20 vs Mg20Sr5 | Yes | <0.0001 |
| Mg20Sr20 vs Mg5Sr5 | Yes | <0.0001 |
| Mg5Sr20 vs Mg20Sr5 | Yes | <0.0001 |
| Mg5Sr20 vs Mg5Sr5 | Yes | <0.0001 |
| Mg20Sr5 vs Mg5Sr5 | Yes | <0.0001 |

`

*Table 34 Statistical analysis results of ion incorporation efficiency rates [%] across the 5–20% sHAP range using one sample t-test and two-way ANOVA with Tukey's multiple comparisons. The total interaction p-value was <0.0001. All formulations were normally distributed (Kolmogorov-Smirnov test).*

| **One Sample t-test** | **Significant** | **P-value (Two-Tailed)** |
|---|---|---|
| Mg20Sr20 | | |
| Experimental vs Theoretical Ca [wt%] | Yes | <0.0001 |
| Experimental vs Theoretical Mg [wt%] | Yes | <0.0001 |
| Experimental vs Theoretical Sr [wt%] | Yes | <0.0001 |
| Experimental vs Theoretical P [wt%] | Yes | 0.0019 |
| Mg5Sr20 | | |
| Experimental vs Theoretical Ca [wt%] | No | 0.0779 |
| Experimental vs Theoretical Mg [wt%] | Yes | <0.0001 |
| Experimental vs Theoretical Sr [wt%] | Yes | <0.0001 |
| Experimental vs Theoretical P [wt%] | No | 0.7430 |
| Mg20Sr5 | | |
| Experimental vs Theoretical Ca [wt%] | Yes | <0.0001 |
| Experimental vs Theoretical Mg [wt%] | Yes | <0.0001 |
| Experimental vs Theoretical Sr [wt%] | Yes | <0.0001 |
| Experimental vs Theoretical P [wt%] | Yes | <0.0001 |
| Mg5Sr5 | | |
| Experimental vs Theoretical Ca [wt%] | Yes | <0.0001 |
| Experimental vs Theoretical Mg [wt%] | Yes | 0.0327 |
| Experimental vs Theoretical Sr [wt%] | Yes | <0.0001 |
| Experimental vs Theoretical P [wt%] | No | 0.0950 |
| | | |
| **Comparison** | **Significant** | **Adjusted p-value** |
| Ca [wt%] | | |
| Mg20Sr20 vs Mg5Sr20 | Yes | 0.0001 |
| Mg20Sr20 vs Mg20Sr5 | No | 0.3308 |
| Mg20Sr20 vs Mg5Sr5 | No | 0.2414 |
| Mg5Sr20 vs Mg20Sr5 | Yes | <0.0001 |
| Mg5Sr20 vs Mg5Sr5 | No | 0.0829 |
| Mg20Sr5 vs Mg5Sr5 | Yes | 0.0041 |
| Mg [wt%] | | |
| Mg20Sr20 vs Mg5Sr20 | No | 0.4147 |
| Mg20Sr20 vs Mg20Sr5 | Yes | <0.0001 |
| Mg20Sr20 vs Mg5Sr5 | Yes | <0.0001 |
| Mg5Sr20 vs Mg20Sr5 | Yes | 0.0005 |
| Mg5Sr20 vs Mg5Sr5 | Yes | <0.0001 |
| Mg20Sr5 vs Mg5Sr5 | Yes | <0.0001 |
| Sr [wt%] | | |
| Mg20Sr20 vs Mg5Sr20 | No | 0.8561 |
| Mg20Sr20 vs Mg20Sr5 | Yes | 0.0018 |
| Mg20Sr20 vs Mg5Sr5 | Yes | 0.0017 |
| Mg5Sr20 vs Mg20Sr5 | Yes | 0.0201 |
| Mg5Sr20 vs Mg5Sr5 | Yes | 0.0198 |
| Mg20Sr5 vs Mg5Sr5 | No | >0.9999 |
| P [wt%] | | |
| Mg20Sr20 vs Mg5Sr20 | No | 0.4032 |
| Mg20Sr20 vs Mg20Sr5 | Yes | 0.0040 |
| Mg20Sr20 vs Mg5Sr5 | No | >0.9999 |
| Mg5Sr20 vs Mg20Sr5 | Yes | <0.0001 |
| Mg5Sr20 vs Mg5Sr5 | No | 0.3691 |
| Mg20Sr5 vs Mg5Sr5 | Yes | 0.0049 |

`

*Table 35 Statistical analysis results of substitution efficiency rates [%] across the 5–20% sHAP range using one sample t-test and two-way ANOVA with Tukey's multiple comparisons. The total interaction p-value was <0.0001. All formulations were normally distributed (Kolmogorov-Smirnov test).*

| **One Sample t-test** | **Significant** | **P-value (Two-Tailed)** |
|---|---|---|
| Mg20Sr20 | | |
| Experimental vs Theoretical Mg [mol%] | Yes | <0.0001 |
| Experimental vs Theoretical Sr [mol%] | Yes | <0.0001 |
| Mg5Sr20 | | |
| Experimental vs Theoretical Mg [mol%] | Yes | <0.0001 |
| Experimental vs Theoretical Sr [mol%] | Yes | <0.0001 |
| Mg20Sr5 | | |
| Experimental vs Theoretical Mg [mol%] | Yes | 0.0003 |
| Experimental vs Theoretical Sr [mol%] | Yes | 0.0170 |
| Mg5Sr5 | | |
| Experimental vs Theoretical Mg [mol%] | No | 0.1473 |
| Experimental vs Theoretical Sr [mol%] | Yes | <0.0001 |
| | | |
| **Comparison** | **Significant** | **Adjusted p-value** |
| Mg [mol%] | | |
| Mg20Sr20 vs Mg5Sr20 | No | 0.9861 |
| Mg20Sr20 vs Mg20Sr5 | Yes | <0.0001 |
| Mg20Sr20 vs Mg5Sr5 | Yes | <0.0001 |
| Mg5Sr20 vs Mg20Sr5 | Yes | <0.0001 |
| Mg5Sr20 vs Mg5Sr5 | Yes | <0.0001 |
| Mg20Sr5 vs Mg5Sr5 | No | 0.3303 |
| Sr [mol%] | | |
| Mg20Sr20 vs Mg5Sr20 | Yes | 0.0312 |
| Mg20Sr20 vs Mg20Sr5 | Yes | 0.0295 |
| Mg20Sr20 vs Mg5Sr5 | No | 0.8328 |
| Mg5Sr20 vs Mg20Sr5 | Yes | <0.0001 |
| Mg5Sr20 vs Mg5Sr5 | No | 0.1590 |
| Mg20Sr5 vs Mg5Sr5 | Yes | 0.0016 |

`

*Table 36 Statistical analysis results of ratios across the 5–20% sHAP range using two-way ANOVA with Tukey's multiple comparisons. The total interaction p-value was <0.0001. All formulations were normally distributed (Kolmogorov-Smirnov test).*

| Comparison | Significant | Adjusted p-value |
|---|---|---|
| Mg20Sr20 | | |
| Ca/P vs (Ca+Mg)/P | Yes | <0.0001 |
| Ca/P vs (Ca+Sr)/P | Yes | <0.0001 |
| Ca/P vs (Ca+Sr+Mg)/P | Yes | <0.0001 |
| (Ca+Mg)/P vs (Ca+Sr)/P | Yes | <0.0001 |
| (Ca+Mg)/P vs (Ca+Sr+Mg)/P | Yes | <0.0001 |
| (Ca+Sr)/P vs (Ca+Sr+Mg)/P | Yes | 0.0004 |
| Mg5Sr20 | | |
| Ca/P vs (Ca+Mg)/P | No | 0.5177 |
| Ca/P vs (Ca+Sr)/P | Yes | <0.0001 |
| Ca/P vs (Ca+Sr+Mg)/P | Yes | <0.0001 |
| (Ca+Mg)/P vs (Ca+Sr)/P | Yes | <0.0001 |
| (Ca+Mg)/P vs (Ca+Sr+Mg)/P | Yes | <0.0001 |
| (Ca+Sr)/P vs (Ca+Sr+Mg)/P | No | 0.5177 |
| Mg20Sr5 | | |
| Ca/P vs (Ca+Mg)/P | Yes | <0.0001 |
| Ca/P vs (Ca+Sr)/P | Yes | 0.0011 |
| Ca/P vs (Ca+Sr+Mg)/P | Yes | <0.0001 |
| (Ca+Mg)/P vs (Ca+Sr)/P | Yes | <0.0001 |
| (Ca+Mg)/P vs (Ca+Sr+Mg)/P | Yes | 0.0011 |
| (Ca+Sr)/P vs (Ca+Sr+Mg)/P | Yes | <0.0001 |
| Mg5Sr5 | | |
| Ca/P vs (Ca+Mg)/P | Yes | 0.0047 |
| Ca/P vs (Ca+Sr)/P | Yes | 0.0054 |
| Ca/P vs (Ca+Sr+Mg)/P | Yes | <0.0001 |
| (Ca+Mg)/P vs (Ca+Sr)/P | No | >0.9999 |
| (Ca+Mg)/P vs (Ca+Sr+Mg)/P | Yes | 0.0054 |
| (Ca+Sr)/P vs (Ca+Sr+Mg)/P | Yes | 0.0047 |
| | | |
| Ca/P | | |
| Mg20Sr20 vs Mg5Sr20 | Yes | <0.0001 |
| Mg20Sr20 vs Mg20Sr5 | Yes | <0.0001 |
| Mg20Sr20 vs Mg5Sr5 | Yes | <0.0001 |
| Mg5Sr20 vs Mg20Sr5 | Yes | 0.0004 |
| Mg5Sr20 vs Mg5Sr5 | Yes | <0.0001 |
| Mg20Sr5 vs Mg5Sr5 | Yes | <0.0001 |
| (Ca+Mg)/P | | |
| Mg20Sr20 vs Mg5Sr20 | Yes | <0.0001 |
| Mg20Sr20 vs Mg20Sr5 | Yes | <0.0001 |
| Mg20Sr20 vs Mg5Sr5 | Yes | <0.0001 |
| Mg5Sr20 vs Mg20Sr5 | Yes | <0.0001 |
| Mg5Sr20 vs Mg5Sr5 | Yes | <0.0001 |
| Mg20Sr5 vs Mg5Sr5 | Yes | <0.0001 |
| (Ca+Sr)/P | | |
| Mg20Sr20 vs Mg5Sr20 | Yes | <0.0001 |
| Mg20Sr20 vs Mg20Sr5 | Yes | <0.0001 |
| Mg20Sr20 vs Mg5Sr5 | Yes | <0.0001 |
| Mg5Sr20 vs Mg20Sr5 | Yes | <0.0001 |
| Mg5Sr20 vs Mg5Sr5 | Yes | <0.0001 |
| Mg20Sr5 vs Mg5Sr5 | Yes | <0.0001 |
| (Ca+Sr+Mg)/P | | |
| Mg20Sr20 vs Mg5Sr20 | Yes | <0.0001 |
| Mg20Sr20 vs Mg20Sr5 | Yes | <0.0001 |
| Mg20Sr20 vs Mg5Sr5 | Yes | <0.0001 |
| Mg5Sr20 vs Mg20Sr5 | No | 0.4744 |
| Mg5Sr20 vs Mg5Sr5 | Yes | <0.0001 |
| Mg20Sr5 vs Mg5Sr5 | Yes | <0.0001 |

`

# Statistical Results for HAP Substitution in the 5–10% Range

*Table 37 Statistical analysis results of pH values across the 5–10% sHAP range using two-way ANOVA with Tukey's multiple comparisons. The total interaction p-value was <0.0001. Sample size insufficient to achieve normal distribution.*

| **Comparisons** | **Significant** | **Adjusted p-value** |
|---|---|---|
| Mg5Sr5 | | |
| $T_0$ vs $T_{24}$ | Yes | <0.0001 |
| $T_{24}$ vs $T_{PP}$ | No | 0.9883 |
| Mg5Sr10 | | |
| $T_0$ vs $T_{24}$ | Yes | <0.0001 |
| $T_{24}$ vs $T_{PP}$ | Yes | <0.0001 |
| Mg10Sr5 | | |
| $T_0$ vs $T_{24}$ | Yes | <0.0001 |
| $T_{24}$ vs $T_{PP}$ | Yes | <0.0001 |
| Mg10Sr10 | | |
| $T_0$ vs $T_{24}$ | Yes | <0.0001 |
| $T_{24}$ vs $T_{PP}$ | Yes | <0.0001 |
| | | |
| $T_0$ | | |
| Mg5Sr5 vs Mg5Sr10 | Yes | <0.0001 |
| Mg5Sr5 vs Mg10Sr5 | Yes | <0.0001 |
| Mg5Sr5 vs Mg10Sr10 | Yes | <0.0001 |
| Mg5Sr10 vs Mg10Sr5 | Yes | <0.0001 |
| Mg5Sr10 vs Mg10Sr10 | Yes | <0.0001 |
| Mg10Sr5 vs Mg10Sr10 | Yes | <0.0001 |
| $T_{24}$ | | |
| Mg5Sr5 vs Mg5Sr10 | Yes | <0.0001 |
| Mg5Sr5 vs Mg10Sr5 | No | 0.9988 |
| Mg5Sr5 vs Mg10Sr10 | Yes | <0.0001 |
| Mg5Sr10 vs Mg10Sr5 | Yes | <0.0001 |
| Mg5Sr10 vs Mg10Sr10 | Yes | <0.0001 |
| Mg10Sr5 vs Mg10Sr10 | Yes | <0.0001 |
| $T_{PP}$ | | |
| Mg5Sr5 vs Mg5Sr10 | Yes | <0.0001 |
| Mg5Sr5 vs Mg10Sr5 | Yes | <0.0001 |
| Mg5Sr5 vs Mg10Sr10 | Yes | <0.0001 |
| Mg5Sr10 vs Mg10Sr5 | Yes | <0.0001 |
| Mg5Sr10 vs Mg10Sr10 | Yes | <0.0001 |
| Mg10Sr5 vs Mg10Sr10 | Yes | 0.0010 |

`

*Table 38 Statistical analysis results of ion incorporation efficiency rates [%] across the 5–10% sHAP range using one sample t-test and two-way ANOVA with Tukey's multiple comparisons. The total interaction p-value was <0.0001. Sample size insufficient to achieve normal distribution for Sr [wt%] in Mg10Sr10; all other groups were normally distributed (Shapiro-Wilk test).*

| **One Sample t-test** | **Significant** | **P-value (Two-Tailed)** |
|---|---|---|
| Mg5Sr5 | | |
| Experimental vs Theoretical Ca [wt%] | Yes | 0.0025 |
| Experimental vs Theoretical Mg [wt%] | Yes | <0.0001 |
| Experimental vs Theoretical Sr [wt%] | Yes | 0.0005 |
| Experimental vs Theoretical P [wt%] | Yes | 0.0122 |
| Mg5Sr10 | | |
| Experimental vs Theoretical Ca [wt%] | No | 0.0522 |
| Experimental vs Theoretical Mg [wt%] | Yes | 0.0001 |
| Experimental vs Theoretical Sr [wt%] | Yes | 0.0013 |
| Experimental vs Theoretical P [wt%] | No | 0.5810 |
| Mg10Sr5 | | |
| Experimental vs Theoretical Ca [wt%] | Yes | 0.0003 |
| Experimental vs Theoretical Mg [wt%] | Yes | <0.0001 |
| Experimental vs Theoretical Sr [wt%] | Yes | <0.0001 |
| Experimental vs Theoretical P [wt%] | Yes | 0.0064 |
| Mg10Sr10 | | |
| Experimental vs Theoretical Ca [wt%] | Yes | <0.0001 |
| Experimental vs Theoretical Mg [wt%] | Yes | <0.0001 |
| Experimental vs Theoretical Sr [wt%] | Yes | 0.0002 |
| Experimental vs Theoretical P [wt%] | Yes | 0.0003 |
| | | |
| **Comparison** | **Significant** | **Adjusted p-value** |
| Ca [wt%] | | |
| Mg5Sr5 vs Mg5Sr10 | No | 0.1004 |
| Mg5Sr5 vs Mg10Sr5 | No | 0.3756 |
| Mg5Sr5 vs Mg10Sr10 | Yes | <0.0001 |
| Mg5Sr10 vs Mg10Sr5 | Yes | 0.0018 |
| Mg5Sr10 vs Mg10Sr10 | Yes | <0.0001 |
| Mg10Sr5 vs Mg10Sr10 | Yes | <0.0001 |
| Mg [wt%] | | |
| Mg5Sr5 vs Mg5Sr10 | Yes | <0.0001 |
| Mg5Sr5 vs Mg10Sr5 | No | 0.3563 |
| Mg5Sr5 vs Mg10Sr10 | Yes | <0.0001 |
| Mg5Sr10 vs Mg10Sr5 | Yes | <0.0001 |
| Mg5Sr10 vs Mg10Sr10 | No | 0.9748 |
| Mg10Sr5 vs Mg10Sr10 | Yes | <0.0001 |
| Sr [wt%] | | |
| Mg5Sr5 vs Mg5Sr10 | Yes | <0.0001 |
| Mg5Sr5 vs Mg10Sr5 | Yes | 0.0054 |
| Mg5Sr5 vs Mg10Sr10 | Yes | <0.0001 |
| Mg5Sr10 vs Mg10Sr5 | Yes | <0.0001 |
| Mg5Sr10 vs Mg10Sr10 | No | 0.4652 |
| Mg10Sr5 vs Mg10Sr10 | Yes | <0.0001 |
| P [wt%] | | |
| Mg5Sr5 vs Mg5Sr10 | Yes | 0.0363 |
| Mg5Sr5 vs Mg10Sr5 | No | 0.9084 |
| Mg5Sr5 vs Mg10Sr10 | Yes | 0.0158 |
| Mg5Sr10 vs Mg10Sr5 | No | 0.1503 |
| Mg5Sr10 vs Mg10Sr10 | Yes | <0.0001 |
| Mg10Sr5 vs Mg10Sr10 | Yes | 0.0028 |

`

*Table 39 Statistical analysis results of substitution efficiency rates [%] across the 5–10% sHAP range using one sample t-test and two-way ANOVA with Tukey's multiple comparisons. The total interaction p-value was <0.0001. Sample size insufficient to achieve normal distribution for Mg [mol%] in Mg5Sr10; all other groups were normally distributed (Shapiro-Wilk test).*

| **One Sample t-test** | **Significant** | **P-value (two-tailed)** |
|---|---|---|
| Mg5Sr5 | | |
| Experimental vs Theoretical Mg [mol%] | Yes | <0.0001 |
| Experimental vs Theoretical Sr [mol%] | Yes | 0.0005 |
| Mg5Sr10 | | |
| Experimental vs Theoretical Mg [mol%] | Yes | <0.0001 |
| Experimental vs Theoretical Sr [mol%] | Yes | <0.0001 |
| Mg10Sr5 | | |
| Experimental vs Theoretical Mg [mol%] | Yes | <0.0001 |
| Experimental vs Theoretical Sr [mol%] | Yes | 0.0114 |
| Mg10Sr10 | | |
| Experimental vs Theoretical Mg [mol%] | Yes | <0.0001 |
| Experimental vs Theoretical Sr [mol%] | Yes | 0.0019 |
| | | |
| **Comparison** | **Significant** | **Adjusted p-value** |
| Mg [mol%] | | |
| Mg5Sr5 vs Mg5Sr10 | Yes | <0.0001 |
| Mg5Sr5 vs Mg10Sr5 | No | 0.9830 |
| Mg5Sr5 vs Mg10Sr10 | Yes | <0.0001 |
| Mg5Sr10 vs Mg10Sr5 | Yes | <0.0001 |
| Mg5Sr10 vs Mg10Sr10 | Yes | <0.0001 |
| Mg10Sr5 vs Mg10Sr10 | Yes | <0.0001 |
| Sr [mol%] | | |
| Mg5Sr5 vs Mg5Sr10 | Yes | <0.0001 |
| Mg5Sr5 vs Mg10Sr5 | Yes | <0.0001 |
| Mg5Sr5 vs Mg10Sr10 | Yes | <0.0001 |
| Mg5Sr10 vs Mg10Sr5 | Yes | <0.0001 |
| Mg5Sr10 vs Mg10Sr10 | Yes | <0.0001 |
| Mg10Sr5 vs Mg10Sr10 | Yes | <0.0001 |

`

*Table 40 Statistical analysis results of ratios across the 5–10% sHAP range using two-way ANOVA with Tukey's multiple comparisons. The total interaction p-value was <0.0001. All formulations were normally distributed (Shapiro-Wilk test).*

| Comparison | Significant | Adjusted p-value |
|---|---|---|
| Mg5Sr5 | | |
| Ca/P vs (Ca+Mg)/P | Yes | <0.0001 |
| Ca/P vs (Ca+Sr)/P | Yes | <0.0001 |
| Ca/P vs (Ca+Sr+Mg)/P | Yes | <0.0001 |
| (Ca+Mg)/P vs (Ca+Sr)/P | Yes | <0.0001 |
| (Ca+Mg)/P vs (Ca+Sr+Mg)/P | Yes | <0.0001 |
| (Ca+Sr)/P vs (Ca+Sr+Mg)/P | Yes | <0.0001 |
| Mg5Sr10 | | |
| Ca/P vs (Ca+Mg)/P | Yes | <0.0001 |
| Ca/P vs (Ca+Sr)/P | Yes | <0.0001 |
| Ca/P vs (Ca+Sr+Mg)/P | Yes | <0.0001 |
| (Ca+Mg)/P vs (Ca+Sr)/P | Yes | <0.0001 |
| (Ca+Mg)/P vs (Ca+Sr+Mg)/P | Yes | <0.0001 |
| (Ca+Sr)/P vs (Ca+Sr+Mg)/P | Yes | <0.0001 |
| Mg10Sr5 | | |
| Ca/P vs (Ca+Mg)/P | Yes | <0.0001 |
| Ca/P vs (Ca+Sr)/P | Yes | <0.0001 |
| Ca/P vs (Ca+Sr+Mg)/P | Yes | <0.0001 |
| (Ca+Mg)/P vs (Ca+Sr)/P | Yes | <0.0001 |
| (Ca+Mg)/P vs (Ca+Sr+Mg)/P | Yes | <0.0001 |
| (Ca+Sr)/P vs (Ca+Sr+Mg)/P | Yes | <0.0001 |
| Mg10Sr10 | | |
| Ca/P vs (Ca+Mg)/P | Yes | <0.0001 |
| Ca/P vs (Ca+Sr)/P | Yes | <0.0001 |
| Ca/P vs (Ca+Sr+Mg)/P | Yes | <0.0001 |
| (Ca+Mg)/P vs (Ca+Sr)/P | Yes | <0.0001 |
| (Ca+Mg)/P vs (Ca+Sr+Mg)/P | Yes | <0.0001 |
| (Ca+Sr)/P vs (Ca+Sr+Mg)/P | Yes | <0.0001 |
| | | |
| Ca/P | | |
| Mg5Sr5 vs Mg5Sr10 | Yes | <0.0001 |
| Mg5Sr5 vs Mg10Sr5 | Yes | <0.0001 |
| Mg5Sr5 vs Mg10Sr10 | Yes | <0.0001 |
| Mg5Sr10 vs Mg10Sr5 | Yes | <0.0001 |
| Mg5Sr10 vs Mg10Sr10 | Yes | <0.0001 |
| Mg10Sr5 vs Mg10Sr10 | Yes | <0.0001 |
| (Ca+Mg)/P | | |
| Mg5Sr5 vs Mg5Sr10 | Yes | <0.0001 |
| Mg5Sr5 vs Mg10Sr5 | Yes | <0.0001 |
| Mg5Sr5 vs Mg10Sr10 | Yes | <0.0001 |
| Mg5Sr10 vs Mg10Sr5 | Yes | <0.0001 |
| Mg5Sr10 vs Mg10Sr10 | Yes | <0.0001 |
| Mg10Sr5 vs Mg10Sr10 | Yes | <0.0001 |
| (Ca+Sr)/P | | |
| Mg5Sr5 vs Mg5Sr10 | Yes | <0.0001 |
| Mg5Sr5 vs Mg10Sr5 | Yes | <0.0001 |
| Mg5Sr5 vs Mg10Sr10 | Yes | <0.0001 |
| Mg5Sr10 vs Mg10Sr5 | Yes | <0.0001 |
| Mg5Sr10 vs Mg10Sr10 | Yes | <0.0001 |
| Mg10Sr5 vs Mg10Sr10 | Yes | <0.0001 |
| (Ca+Sr+Mg)/P | | |
| Mg5Sr5 vs Mg5Sr10 | Yes | <0.0001 |
| Mg5Sr5 vs Mg10Sr5 | Yes | <0.0001 |
| Mg5Sr5 vs Mg10Sr10 | Yes | <0.0001 |
| Mg5Sr10 vs Mg10Sr5 | Yes | <0.0001 |
| Mg5Sr10 vs Mg10Sr10 | Yes | <0.0001 |
| Mg10Sr5 vs Mg10Sr10 | Yes | <0.0001 |

`

# Statistical Results for Cytotoxicity Testing with MgHAP and sHAP

*Table 41 Statistical analysis results of dose-dependent cytotoxicity testing with SINTlife® at concentrations of 10 (Min), 505 (Med), and 1000 µg/ml medium (Max) compared to a control (SCC) using two-way ANOVA with Tukey's multiple comparisons. The total interaction p-value was 0.0687. All groups were normally distributed (Shapiro-Wilk test).*

| Comparisons | Significant | Adjusted p-value |
|---|---|---|
| Min | | |
| Day 1 vs Day 4 | Yes | <0.0001 |
| Day 4 vs Day 7 | Yes | <0.0001 |
| Med | | |
| Day 1 vs Day 4 | Yes | <0.0001 |
| Day 4 vs Day 7 | Yes | <0.0001 |
| Max | | |
| Day 1 vs Day 4 | Yes | <0.0001 |
| Day 4 vs Day 7 | Yes | <0.0001 |
| SCC | | |
| Day 1 vs Day 4 | Yes | <0.0001 |
| Day 4 vs Day 7 | Yes | <0.0001 |
| | | |
| Day 1 | | |
| Min vs Med | No | 0.9869 |
| Min vs Max | No | >0.9999 |
| Min vs SCC | No | 0.9998 |
| Med vs Max | No | 0.9913 |
| Med vs SCC | No | 0.9756 |
| Max vs SCC | No | 0.9993 |
| Day 4 | | |
| Min vs Med | No | 0.9925 |
| Min vs Max | No | 0.6518 |
| Min vs SCC | Yes | 0.0079 |
| Med vs Max | No | 0.8117 |
| Med vs SCC | Yes | 0.0167 |
| Max vs SCC | No | 0.1290 |
| Day 7 | | |
| Min vs Med | No | 0.9951 |
| Min vs Max | No | 0.9580 |
| Min vs SCC | No | 0.9157 |
| Med vs Max | No | 0.8796 |
| Med vs SCC | No | 0.8115 |
| Max vs SCC | No | 0.9989 |

`

*Table 42 Statistical analysis results of cytotoxicity testing with sHAP Mg5Sr5 and Mg10Sr5 at a concentration of 1000 µg/ml medium compared to a control (SCC) using two-way ANOVA with Tukey's multiple comparisons. The total interaction p-value was <0.0001. All groups were normally distributed (Shapiro-Wilk test).*

| Comparisons | Significant | Adjusted p-value |
|---|---|---|
| Mg5Sr5 | | |
| Day 1 vs Day 4 | Yes | <0.0001 |
| Day 4 vs Day 7 | Yes | <0.0001 |
| Mg10Sr5 | | |
| Day 1 vs Day 4 | Yes | <0.0001 |
| Day 4 vs Day 7 | Yes | <0.0001 |
| SCC | | |
| Day 1 vs Day 4 | Yes | <0.0001 |
| Day 4 vs Day 7 | Yes | <0.0001 |
| | | |
| Day 1 | | |
| Mg5Sr5 vs Mg10Sr5 | No | 0.9876 |
| Mg5Sr5 vs SCC | No | 0.9902 |
| Mg10Sr5 vs SCC | No | 0.9998 |
| Day 4 | | |
| Mg5Sr5 vs Mg10Sr5 | Yes | 0.0251 |
| Mg5Sr5 vs SCC | Yes | <0.0001 |
| Mg10Sr5 vs SCC | Yes | <0.0001 |
| Day 7 | | |
| Mg5Sr5 vs Mg10Sr5 | No | 0.0770 |
| Mg5Sr5 vs SCC | No | 0.1997 |
| Mg10Sr5 vs SCC | Yes | 0.0018 |

# Supplementary Information for NMR Analysis

Peak allocation was performed based on the spectrum in Figure 89. Signal detection and area integration were automated using specialised software. The corresponding raw data are provided in Table 43.

First-generation coupling follows the n+1 rule for protons with homogeneous magnetic properties, with peak intensity distributions conforming to Pascal's triangle. Second-generation coupling deviates from this rule when neighbouring protons exhibit different magnetic properties, leading to multiplicative rather than summative splitting. Peak multiplicity is characterised by coupling constants, which quantify proton-proton interactions. Each coupling partner may exhibit a distinct coupling constant, generating complex splitting patterns. The coupling constant is calculated using the following equation:

$$J = \Delta * F$$

where J represents the coupling constant in Hz, Δ indicates the peak difference in ppm, and F denotes the analysis frequency in Hz. The calculated coupling constants are presented in Table 43.

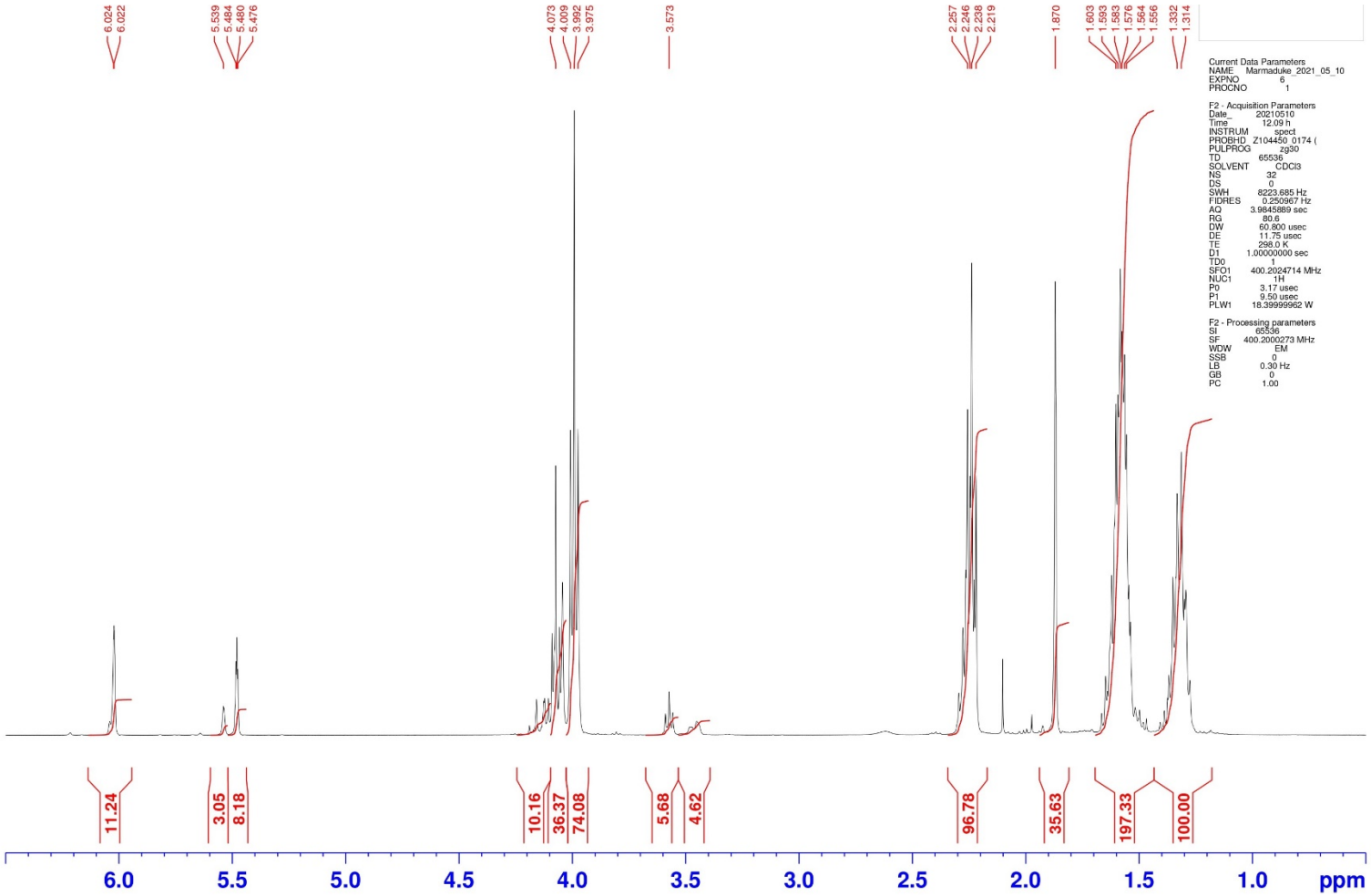


*Figure 90 Full [1]H NMR spectrum of PCLM. Peaks indicate resonances at specific chemical shifts (ppm), with the red-highlighted region indicating the area under the curve.*

`

*Table 43 Raw data of NMR peak regions and intensities with the corresponding calculated coupling constants.*

| Region | Intensity | Coupling Constant |
|---|---|---|
| 6.02411 | 2.318045 | 0.8476 |
| 6.021991 | 2.626033 | |
| 5.53919 | 0.695025 | 22.1184 |
| 5.483894 | 1.770142 | 1.5648 |
| 5.479982 | 2.359038 | 1.5564 |
| 5.476091 | 1.585248 | |
| 4.073392 | 6.495339 | 25.8896 |
| 4.008668 | 7.313168 | 6.686 |
| 3.991953 | 15 | 6.6784 |
| 3.975257 | 7.368292 | |
| 3.573289 | 1.046702 | |
| 3.584 | | 6.8 |
| 3.567 | | 6.4 |
| 3.551 | | 30.8 |
| 3.474 | | 10.4 |
| 3.448 | | |
| 2.257083 | 7.818616 | 4.4628 |
| 2.245926 | 6.21706 | 3.0256 |
| 2.238362 | 11.3291 | 7.6192 |
| 2.219314 | 6.229715 | |
| 1.869834 | 10.88827 | |
| 1.602501 | 7.949426 | 3.6368 |
| 1.593409 | 8.169708 | 4.1356 |
| 1.58307 | 11.19238 | 2.9256 |
| 1.575756 | 9.692421 | 4.654 |
| 1.564121 | 9.132772 | 3.2408 |
| 1.556019 | 7.214326 | |
| 1.332368 | 5.79932 | 7.3848 |
| 1.313906 | 6.795753 | |

`

# Supplementary Information for 3D Printing

## Preliminary Testing with Commercially Available HAP

Preliminary experiments established initial printing parameters using commercially available nano-sized HAP particles (>200 nm). A mixture of 50 wt% HAP and 2 wt% PI was dispersed in liquid PCLM with ultrasonic assistance. Printing at 21°C and 50 psi produced 3D scaffolds with good shape retention (Figure 91).

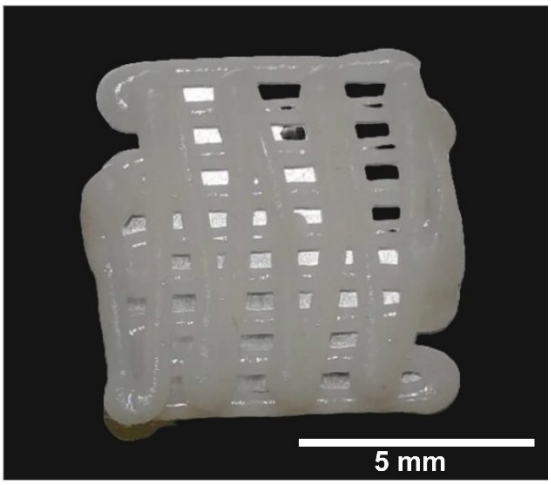


*Figure 91 Photograph of a 3D printed scaffold with 50 wt% HAP and 2 wt% PI after crosslinking. Dimensions: 7.5 × 7.5 mm.*

## Preliminary Testing with Commercially Available MgHAP

Initial experiments exploring printing with substituted HAP utilised commercial MgHAP (SINTlife®). $SiO_2$ was added to increase the viscosity of the liquid ink. An ink formulation of 30 wt% MgHAP, 1.5 wt% $SiO_2$, and 2 wt% PI was prepared and printed at 50 psi and 21°C. The inks demonstrated lower viscosity than commercial HAP, resulting in poor printing performance and an overly liquid consistency that failed to maintain structural integrity.

## Results of HAP-PCLM Discs

After confirming non-cytotoxicity on HAP-PCLM films, HAP-PCLM discs were used to assess bulk material cytotoxicity via a metabolic resazurin assay. Figure 92 presents the Y201 MSCs metabolic activity results. 10% HAP-PCLM exhibited minimal metabolic activity on day 4, undetectable by day 7. No metabolic activity was observed in any other experimental group. The cell-only SCC control demonstrated consistent metabolic activity increase, confirming successful cell seeding.

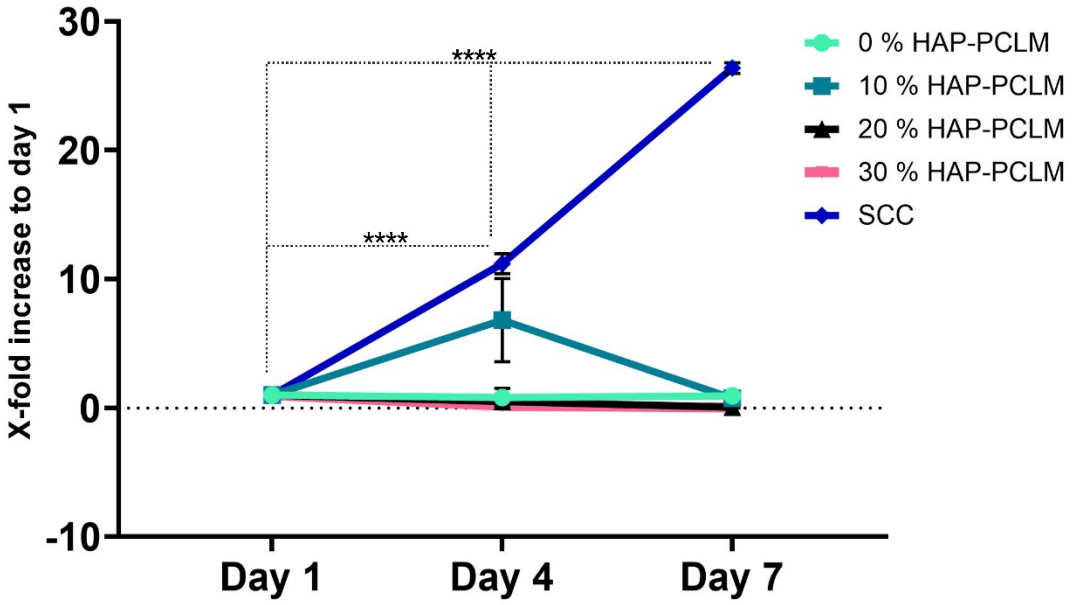


*Figure 92 Y201 MSCs metabolic activity on HAP-PCLM discs. X-axis: Day 1–7; Y-axis: X-fold increase to day 1. Data presented as mean ± SD (n = 3, **** p < 0.0001).*

`

# Bibliography


[1] "Global burden of 369 diseases and injuries in 204 countries and territories, 1990-2019: a systematic analysis for the Global Burden of Disease Study 2019," (in eng), *Lancet,* vol. 396, no. 10258, pp. 1204-1222, Oct 17 2020, doi: 10.1016/s0140-6736(20)30925-9.

[2] "Global, regional, and national burden of low back pain, 1990-2020, its attributable risk factors, and projections to 2050: a systematic analysis of the Global Burden of Disease Study 2021," (in eng), *Lancet Rheumatol,* vol. 5, no. 6, pp. e316-e329, Jun 2023, doi: 10.1016/s2665-9913(23)00098-x.

[3] A. Cieza, K. Causey, K. Kamenov, S. W. Hanson, S. Chatterji, and T. Vos, "Global estimates of the need for rehabilitation based on the Global Burden of Disease study 2019: a systematic analysis for the Global Burden of Disease Study 2019," (in eng), *Lancet,* vol. 396, no. 10267, pp. 2006-2017, Dec 19 2021, doi: 10.1016/s0140-6736(20)32340-0.

[4] W. F. Stewart, J. A. Ricci, E. Chee, D. Morganstein, and R. Lipton, "Lost Productive Time and Cost Due to Common Pain Conditions in the US Workforce," *JAMA,* vol. 290, no. 18, pp. 2443-2454, 2003, doi: 10.1001/jama.290.18.2443.

[5] C. Jo, "Cost-of-illness studies: concepts, scopes, and methods," (in eng), *Clin Mol Hepatol,* vol. 20, no. 4, pp. 327-37, Dec 2014, doi: 10.3350/cmh.2014.20.4.327.

[6] J. N. Katz, "Lumbar disc disorders and low-back pain: socioeconomic factors and consequences," (in eng), *J Bone Joint Surg Am,* vol. 88 Suppl 2, pp. 21-4, Apr 2006, doi: 10.2106/jbjs.E.01273.

[7] S. Wieser *et al.*, "Cost of low back pain in Switzerland in 2005," *The European Journal of Health Economics,* vol. 12, no. 5, pp. 455-467, 2011/10/01 2011, doi: 10.1007/s10198-010-0258-y.

[8] N. Maniadakis and A. Gray, "The economic burden of back pain in the UK," (in eng), *Pain,* vol. 84, no. 1, pp. 95-103, Jan 2000, doi: 10.1016/s0304-3959(99)00187-6.

[9] O. Airaksinen *et al.*, "Chapter 4. European guidelines for the management of chronic nonspecific low back pain," (in eng), *Eur Spine J,* vol. 15 Suppl 2, no. Suppl 2, pp. S192-300, Mar 2006, doi: 10.1007/s00586-006-1072-1.

[10] A. J. Talia, M. L. Wong, H. C. Lau, and A. H. Kaye, "Comparison of the different surgical approaches for lumbar interbody fusion," (in English), *J. Clin. Neurosci.,* Review vol. 22, no. 2, pp. 243-251, Feb 2015, doi: 10.1016/j.jocn.2014.08.008.

[11] K. Malik and A. Nelson, "Chapter 24 - Overview of Low Back Pain Disorders," in *Essentials of Pain Medicine (Fourth Edition)*, H. T. Benzon, S. N. Raja, S. S. Liu, S. M. Fishman, and S. P. Cohen Eds.: Elsevier, 2018, pp. 193-206.e2.

[12] M. S. Tandon and D. Saigal, "Chapter 24 - Spinal Surgery," in *Essentials of Neuroanesthesia*, H. Prabhakar Ed.: Academic Press, 2017, pp. 399-439.

[13] S. T. Canale, F. M. Azar, and J. H. Beaty, *Campbell's Operative Orthopaedics* (no. v. 1). Elsevier, 2017.

[14] V. M. Goldberg and S. Stevenson, "Natural history of autografts and allografts," (in eng), *Clin Orthop Relat Res,* no. 225, pp. 7-16, Dec 1987.

[15] N. A. Shepard, A. J. Rush, 3rd, N. L. Scarborough, A. J. Carter, and F. M. Phillips, "Demineralized Bone Matrix in Spine Surgery: A Review of Current Applications and Future Trends," (in eng), *Int J Spine Surg,* vol. 15, no. s1, pp. 113-119, Apr 2021, doi: 10.14444/8059.

[16] G. Tonk, P. K. Yadav, S. Agarwal, and K. Jamoh, "Donor site morbidity in autologous bone grafting – A comparison between different techniques of anterior iliac crest bone harvesting: A prospective study," *Journal of Orthopaedics, Trauma and Rehabilitation,* vol. 29, no. 1, p. 22104917221092163, 2022, doi: 10.1177/22104917221092163.

[17] G. R. Buttermann, P. A. Glazer, and D. S. Bradford, "The Use of Bone Allografts in the Spine," *Clinical Orthopaedics and Related Research®,* vol. 324, 1996. [Online]. Available: https://journals.lww.com/clinorthop/fulltext/1996/03000/the_use_of_bone_allografts_in_the_spine.10.aspx.

[18] S. S. Jorgenson, T. G. Lowe, J. France, and J. Sabin, "A prospective analysis of autograft versus allograft in posterolateral lumbar fusion in the same patient. A minimum of 1-year follow-up in 144 patients," (in eng), *Spine (Phila Pa 1976),* vol. 19, no. 18, pp. 2048-2053, 1994/09/15 1994, doi: 10.1097/00007632-199409150-00005.

[19] E. R. Carlisle and J. S. Fischgrund, "CHAPTER 27 - Bone Graft and Fusion Enhancement," in *Surgical Management of Spinal Deformities*, T. J. Errico, B. S. Lonner, and A. W. Moulton Eds. Philadelphia: W.B. Saunders, 2009, pp. 433-448.

[20] J. O. Hollinger, J. P. Schmitz, G. E. Friedlaender, C. R. Brown, S. D. Boden, and S. Lynch, "68 - Therapeutic Opportunities for Bone Grafting," in *Principles of Regenerative Medicine*, A. Atala, R. Lanza, J. A. Thomson, and R. M. Nerem Eds. San Diego: Academic Press, 2008, pp. 1164-1175.

[21] L. B. E. Shields *et al.*, "Adverse Effects Associated With High-Dose Recombinant Human Bone Morphogenetic Protein-2 Use in Anterior Cervical Spine Fusion," *Spine,* vol. 31, no. 5, 2006. [Online]. Available: https://journals.lww.com/spinejournal/fulltext/2006/03010/adverse_effects_associated_with_high_dose.9.aspx.

[22] G. C. Comer, M. W. Smith, E. L. Hurwitz, K. A. Mitsunaga, R. Kessler, and E. J. Carragee, "Retrograde ejaculation after anterior lumbar interbody fusion with and without bone morphogenetic protein-2 augmentation: a 10-year cohort controlled study," *The Spine Journal,* vol. 12, no. 10, pp. 881-890, 2012/10/01/ 2012, doi: https://doi.org/10.1016/j.spinee.2012.09.040.

[23] J. D. Smucker, J. M. Rhee, K. Singh, S. T. Yoon, and J. G. Heller, "Increased Swelling Complications Associated With Off-Label Usage of rhBMP-2 in the Anterior Cervical Spine," *Spine,* vol. 31, no. 24, pp. 2813-2819, 2006, doi: 10.1097/01.brs.0000245863.52371.c2.

[24] K. S. Cahill, J. H. Chi, A. Day, and E. B. Claus, "Prevalence, Complications, and Hospital Charges Associated With Use of Bone-Morphogenetic Proteins in Spinal Fusion Procedures," *JAMA,* vol. 302, no. 1, pp. 58-66, 2009, doi: 10.1001/jama.2009.956.

[25] B. J. Williams *et al.*, "Does Bone Morphogenetic Protein Increasethe Incidence of Perioperative Complicationsin Spinal Fusion?: A Comparison of 55,862 Cases of Spinal Fusion With and Without Bone Morphogenetic Protein," *Spine,* vol. 36, no. 20, pp. 1685-1691, 2011, doi: 10.1097/BRS.0b013e318216d825.

[26] D. A. Wong, A. Kumar, S. Jatana, G. Ghiselli, and K. Wong, "Neurologic impairment from ectopic bone in the lumbar canal: a potential complication of off-label PLIF/TLIF use of bone morphogenetic protein-2 (BMP-2)," (in eng), *Spine J,* vol. 8, no. 6, pp. 1011-8, Nov-Dec 2008, doi: 10.1016/j.spinee.2007.06.014.

[27] D. M. Ehrler and A. R. Vaccaro, "The Use of Allograft Bone in Lumbar Spine Surgery," *Clinical Orthopaedics and Related Research®,* vol. 371, pp. 38-45, 2000. [Online]. Available: https://journals.lww.com/clinorthop/fulltext/2000/02000/the_use_of_allograft_bone_in_lumbar_spine_surgery.5.aspx.

[28] G. Hannink and J. J. C. Arts, "Bioresorbability, porosity and mechanical strength of bone substitutes: What is optimal for bone regeneration?," *Injury,* vol. 42, pp. S22-S25, 2011/09/01/ 2011, doi: https://doi.org/10.1016/j.injury.2011.06.008.

[29] T. T. Roberts and A. J. Rosenbaum, "Bone grafts, bone substitutes and orthobiologics: the bridge between basic science and clinical advancements in fracture healing," (in eng), *Organogenesis,* vol. 8, no. 4, pp. 114-24, Oct-Dec 2012, doi: 10.4161/org.23306.

[30] M. S. Katz *et al.*, "Postoperative Morbidity and Complications in Elderly Patients after Harvesting of Iliac Crest Bone Grafts," (in eng), *Medicina (Kaunas),* vol. 57, no. 8, Jul 27 2021, doi: 10.3390/medicina57080759.

[31] A. J. Aboulafia, A. M. Levine, D. Schmidt, and D. Aboulafia, "Surgical Therapy of Bone Metastases," *Seminars in Oncology,* vol. 34, no. 3, pp. 206-214, 2007/06/01/ 2007, doi: https://doi.org/10.1053/j.seminoncol.2007.03.002.

[32] J. A. Sterling and S. A. Guelcher, "Biomaterial scaffolds for treating osteoporotic bone," (in eng), *Curr Osteoporos Rep,* vol. 12, no. 1, pp. 48-54, Mar 2014, doi: 10.1007/s11914-014-0187-2.

[33] C. S. Bahney *et al.*, "Cellular biology of fracture healing," (in eng), *J Orthop Res,* vol. 37, no. 1, pp. 35-50, Jan 2019, doi: 10.1002/jor.24170.

[34] P. J. Mansfield and D. A. Neumann, "Chapter 8 - Structure and Function of the Vertebral Column," in *Essentials of Kinesiology for the Physical Therapist Assistant (Third Edition)*, P. J. Mansfield and D. A. Neumann Eds. St. Louis (MO): Mosby, 2019, pp. 178-232.

[35] G. V. Lawry, H. Hall, C. Ammendolia, and A. G. Fam, "8 - The Spine," in *Fam's Musculoskeletal Examination and Joint Injection Techniques (Second Edition)*, G. V. Lawry, H. J. Kreder, G. A. Hawker, and D. Jerome Eds. Philadelphia: Mosby, 2010, pp. 103-118.

[36] M. W. Devereaux, "Anatomy and Examination of the Spine," *Neurologic Clinics,* vol. 25, no. 2, pp. 331-351, 2007/05/01/ 2007, doi: https://doi.org/10.1016/j.ncl.2007.02.003.

[37] J. C. Lotz, A. J. Fields, and E. C. Liebenberg, "The role of the vertebral end plate in low back pain," (in eng), *Global Spine J,* vol. 3, no. 3, pp. 153-64, Jun 2013, doi: 10.1055/s-0033-1347298.

[38] N. Bogduk, "Chapter 32 - Functional anatomy of the spine," in *Handbook of Clinical Neurology*, vol. 136, J. C. Masdeu and R. G. González Eds.: Elsevier, 2016, pp. 675-688.

[39] T. Bellido, L. I. Plotkin, and A. Bruzzaniti, "Chapter 3 - Bone Cells," in *Basic and Applied Bone Biology (Second Edition)*, D. B. Burr and M. R. Allen Eds.: Academic Press, 2019, pp. 37-55.

[40] M. J. Lopez and M. D. Markel, "Chapter 74 - Bone Biology and Fracture Healing," in *Equine Surgery (Fourth Edition)*, J. A. Auer and J. A. Stick Eds. Saint Louis: W.B. Saunders, 2012, pp. 1025-1040.

[41] J. Kular, J. Tickner, S. M. Chim, and J. Xu, "An overview of the regulation of bone remodelling at the cellular level," *Clinical Biochemistry,* vol. 45, no. 12, pp. 863-873, 2012/08/01/ 2012, doi: https://doi.org/10.1016/j.clinbiochem.2012.03.021.

[42] B. Clarke, "Normal bone anatomy and physiology," (in eng), *Clin J Am Soc Nephrol,* vol. 3 Suppl 3, no. Suppl 3, pp. S131-9, Nov 2008, doi: 10.2215/cjn.04151206.

[43] U. Kini and B. N. Nandeesh, "Physiology of Bone Formation, Remodeling, and Metabolism," in *Radionuclide and Hybrid Bone Imaging*, I. Fogelman, G. Gnanasegaran, and H. van der Wall Eds. Berlin, Heidelberg: Springer Berlin Heidelberg, 2012, pp. 29-57.

[44] L. J. Raggatt and N. C. Partridge, "Cellular and Molecular Mechanisms of Bone Remodeling*," *Journal of Biological Chemistry,* vol. 285, no. 33, pp. 25103-25108, 2010/08/13/ 2010, doi: https://doi.org/10.1074/jbc.R109.041087.

[45] Y. Sun *et al.*, "Macrophage-Osteoclast Associations: Origin, Polarization, and Subgroups," (in eng), *Front Immunol,* vol. 12, p. 778078, 2021, doi: 10.3389/fimmu.2021.778078.

[46] D. B. Burr, "Chapter 1 - Bone Morphology and Organization," in *Basic and Applied Bone Biology (Second Edition)*, D. B. Burr and M. R. Allen Eds.: Academic Press, 2019, pp. 3-26.

[47] S. Kondi and S. R. Gowda, "Principles of bone healing," *Surgery (Oxford),* vol. 41, no. 10, pp. 625-631, 2023/10/01/ 2023, doi: https://doi.org/10.1016/j.mpsur.2023.08.002.

[48] M. R. Allen and D. B. Burr, "Chapter 5 - Bone Growth, Modeling, and Remodeling," in *Basic and Applied Bone Biology (Second Edition)*, D. B. Burr and M. R. Allen Eds.: Academic Press, 2019, pp. 85-100.

[49] M. Ontañón, C. Aparicio, M. P. Ginebra, and J. A. Planell, "Chapter 3 - Structure and Mechanical Properties of Cortical Bone," in *Pergamon Materials Series*, vol. 4, M. Elices Ed.: Pergamon, 2000, pp. 33-71.

[50] E. Hamed, I. Jasiuk, A. Yoo, Y. Lee, and T. Liszka, "Multi-scale modelling of elastic moduli of trabecular bone," *Journal of The Royal Society Interface,* vol. 9, no. 72, pp. 1654-1673, 2012, doi: doi:10.1098/rsif.2011.0814.

[51] N. Reznikov, R. Shahar, and S. Weiner, "Three-dimensional structure of human lamellar bone: The presence of two different materials and new insights into the hierarchical organization," *Bone,* vol. 59, pp. 93-104, 2014/02/01/ 2014, doi: https://doi.org/10.1016/j.bone.2013.10.023.

[52] D. Taylor, "9.02 - Failure Processes in Hard and Soft Tissues," in *Comprehensive Structural Integrity*, I. Milne, R. O. Ritchie, and B. Karihaloo Eds. Oxford: Pergamon, 2003, pp. 35-95.

[53] B. Chang and X. Liu, "Osteon: Structure, Turnover, and Regeneration," (in eng), *Tissue Eng Part B Rev,* vol. 28, no. 2, pp. 261-278, Apr 2022, doi: 10.1089/ten.TEB.2020.0322.

[54] R. B. Kahla and A. Barkaoui, "Chapter 1 - Bone multiscale mechanics," in *Bone Remodeling Process*, R. B. Kahla and A. Barkaoui Eds.: Academic Press, 2021, pp. 1-47.

[55] D. J. Digirolamo and E. L. Germain-Lee, "Chapter 3 - Effects of aging on bone," in *A Comprehensive Guide to Geriatric Rehabilitation (Third Edition)*, T. L. Kauffman, R. Scott, J. O. Barr, and M. L. Moran Eds. Oxford: Churchill Livingstone, 2014, pp. 14-18.

[56] B. Vasilić, C. S. Rajapakse, and F. W. Wehrli, "Classification of trabeculae into three-dimensional rodlike and platelike structures via local inertial anisotropy," (in eng), *Med Phys,* vol. 36, no. 7, pp. 3280-91, Jul 2009, doi: 10.1118/1.3140582.

[57] C. J. Collins, O. G. Andriotis, V. Nedelkovski, M. Frank, O. L. Katsamenis, and P. J. Thurner, "Bone Micro- and Nanomechanics," in *Encyclopedia of Biomedical Engineering*, R. Narayan Ed. Oxford: Elsevier, 2019, pp. 22-44.

[58] Y. Park, E. Cheong, J.-G. Kwak, R. Carpenter, J.-H. Shim, and J. Lee, "Trabecular bone organoid model for studying the regulation of localized bone remodeling," *Science Advances,* vol. 7, no. 4, p. eabd6495, 2021, doi: doi:10.1126/sciadv.abd6495.

[59] H. M. Frost, "On the Trabecular “Thickness”-Number Problem," *Journal of Bone and Mineral Research,* vol. 14, no. 11, pp. 1816-1821, 1999, doi: https://doi.org/10.1359/jbmr.1999.14.11.1816.

[60] U. E. Pazzaglia, T. Congiu, M. Marchese, F. Spagnuolo, and D. Quacci, "Morphometry and Patterns of Lamellar Bone in Human Haversian Systems," *The Anatomical Record,* vol. 295, no. 9, pp. 1421-1429, 2012/09/01 2012, doi: https://doi.org/10.1002/ar.22535.

[61] E. Donnelly, R. M. Williams, S. A. Downs, M. E. Dickinson, S. P. Baker, and M. C. H. van der Meulen, "Quasistatic and dynamic nanomechanical properties of cancellous bone tissue relate to collagen content and organization," *Journal of Materials Research,* vol. 21, no. 8, pp. 2106-2117, 2006/08/01 2006, doi: 10.1557/jmr.2006.0259.

[62] G. Marotti, "A new theory of bone lamellation," *Calcified Tissue International,* vol. 53, no. 1, pp. S47-S56, 1993/02/01 1993, doi: 10.1007/BF01673402.

[63] A. S. Posner, "Relationship between diet and bone mineral ultrastructure," (in eng), *Fed Proc,* vol. 26, no. 6, pp. 1717-22, Nov-Dec 1967.

[64] A. C. Karaplis, "Chapter 3 - Embryonic Development of Bone and Regulation of Intramembranous and Endochondral Bone Formation," in *Principles of Bone Biology (Third Edition)*, J. P. Bilezikian, L. G. Raisz, and T. J. Martin Eds. San Diego: Academic Press, 2008, pp. 53-84.

[65] C. Hartmann and Y. Yang, "Chapter 1 - Molecular and cellular regulation of intramembranous and endochondral bone formation during embryogenesis," in *Principles of Bone Biology (Fourth Edition)*, J. P. Bilezikian, T. J. Martin, T. L. Clemens, and C. J. Rosen Eds.: Academic Press, 2020, pp. 5-44.

[66] C. Cunningham, L. Scheuer, and S. Black, "Chapter 3 - Bone Development," in *Developmental Juvenile Osteology (Second Edition)*, C. Cunningham, L. Scheuer, and S. Black Eds. San Diego: Academic Press, 2016, pp. 19-35.

[67] I. Fernández-Tresguerres-Hernández-Gil, M. A. Alobera-Gracia, M. del-Canto-Pingarrón, and L. Blanco-Jerez, "Physiological bases of bone regeneration II. The remodeling process," (in eng
spa), *Med Oral Patol Oral Cir Bucal,* vol. 11, no. 2, pp. E151-7, Mar 1 2006.

[68] J. A. Siddiqui and N. C. Partridge, "Physiological Bone Remodeling: Systemic Regulation and Growth Factor Involvement," (in eng), *Physiology (Bethesda),* vol. 31, no. 3, pp. 233-45, May 2016, doi: 10.1152/physiol.00061.2014.

[69] S. Bolamperti, I. Villa, and A. Rubinacci, "Bone remodeling: an operational process ensuring survival and bone mechanical competence," *Bone Research,* vol. 10, no. 1, p. 48, 2022/07/18 2022, doi: 10.1038/s41413-022-00219-8.

[70] A. G. Robling, R. Daly, R. K. Fuchs, and D. B. Burr, "Chapter 11 - Mechanical Adaptation," in *Basic and Applied Bone Biology (Second Edition)*, D. B. Burr and M. R. Allen Eds.: Academic Press, 2019, pp. 203-233.

[71] J. Li, M. A. Kacena, and D. L. Stocum, "Chapter 12 - Fracture Healing," in *Basic and Applied Bone Biology (Second Edition)*, D. B. Burr and M. R. Allen Eds.: Academic Press, 2019, pp. 235-253.

[72] R. Marsell and T. A. Einhorn, "The biology of fracture healing," (in eng), *Injury,* vol. 42, no. 6, pp. 551-5, Jun 2011, doi: 10.1016/j.injury.2011.03.031.

[73] C. E. Dionne *et al.*, "A consensus approach toward the standardization of back pain definitions for use in prevalence studies," (in eng), *Spine (Phila Pa 1976),* vol. 33, no. 1, pp. 95-103, Jan 1 2008, doi: 10.1097/BRS.0b013e31815e7f94.

[74] B. W. Koes, M. W. v. Tulder, and S. Thomas, "Diagnosis and treatment of low back pain," *BMJ,* vol. 332, no. 7555, pp. 1430-1434, 2006, doi: 10.1136/bmj.332.7555.1430.

[75] J. Nijs *et al.*, "Low back pain: guidelines for the clinical classification of predominant neuropathic, nociceptive, or central sensitization pain," (in eng), *Pain Physician,* vol. 18, no. 3, pp. E333-46, May-Jun 2015.

[76] T. da Silva *et al.*, "Recurrence of low back pain is common: a prospective inception cohort study," (in eng), *J Physiother,* vol. 65, no. 3, pp. 159-165, Jul 2019, doi: 10.1016/j.jphys.2019.04.010.

[77] J. Hartvigsen *et al.*, "What low back pain is and why we need to pay attention," *The Lancet,* vol. 391, no. 10137, pp. 2356-2367, 2018/06/09/ 2018, doi: https://doi.org/10.1016/S0140-6736(18)30480-X.

[78] J. Hartvigsen *et al.*, "Heritability of spinal pain and consequences of spinal pain: A comprehensive genetic epidemiologic analysis using a population-based sample of 15,328 twins ages 20–71 years," *Arthritis Care & Research,* vol. 61, no. 10, pp. 1343-1351, 2009, doi: https://doi.org/10.1002/art.24607.

[79] M. B. Pinheiro, J. J. Morosoli, L. Colodro-Conde, P. H. Ferreira, and J. R. Ordoñana, "Genetic and environmental influences to low back pain and symptoms of depression and anxiety: A population-based twin study," *Journal of Psychosomatic Research,* vol. 105, pp. 92-98, 2018/02/01/ 2018, doi: https://doi.org/10.1016/j.jpsychores.2017.12.007.

[80] L. Kalichman and D. J. Hunter, "The genetics of intervertebral disc degeneration. Familial predisposition and heritability estimation," (in eng), *Joint Bone Spine,* vol. 75, no. 4, pp. 383-7, Jul 2008, doi: 10.1016/j.jbspin.2007.11.003.

[81] M. C. Battié, T. Videman, E. Levalahti, K. Gill, and J. Kaprio, "Heritability of low back pain and the role of disc degeneration," (in eng), *Pain,* vol. 131, no. 3, pp. 272-280, Oct 2007, doi: 10.1016/j.pain.2007.01.010.

[82] M. B. Freidin *et al.*, "Insight into the genetic architecture of back pain and its risk factors from a study of 509,000 individuals," (in eng), *Pain,* vol. 160, no. 6, pp. 1361-1373, Jun 2019, doi: 10.1097/j.pain.0000000000001514.

[83] A. El-Metwally *et al.*, "Genetic and environmental influences on non-specific low back pain in children: a twin study," (in eng), *Eur Spine J,* vol. 17, no. 4, pp. 502-8, Apr 2008, doi: 10.1007/s00586-008-0605-1.

[84] S. Choi, S. Nah, H. D. Jang, J. E. Moon, and S. Han, "Association between Chronic Low Back Pain and Degree of Stress: A Nationwide Cross-Sectional Study," (in eng), *Sci Rep,* vol. 11, no. 1, p. 14549, Jul 15 2021, doi: 10.1038/s41598-021-94001-1.

[85] D. J. Clauw and D. A. Williams, "Relationship between stress and pain in work-related upper extremity disorders: The hidden role of chronic multisymptom illnesses*," *American Journal of Industrial Medicine,* vol. 41, no. 5, pp. 370-382, 2002, doi: https://doi.org/10.1002/ajim.10068.

[86] V. C. Oliveira, M. L. Ferreira, L. Morso, H. B. Albert, K. M. Refshauge, and P. H. Ferreira, "Patients' perceived level of social isolation affects the prognosis of low back pain," (in eng), *Eur J Pain,* vol. 19, no. 4, pp. 538-45, Apr 2015, doi: 10.1002/ejp.578.

[87] M. Feuerstein, S. Sult, and M. Houle, "Environmental stressors and chronic low back pain: life events, family and work environment," (in eng), *Pain,* vol. 22, no. 3, pp. 295-307, Jul 1985, doi: 10.1016/0304-3959(85)90030-2.

[88] G. Buruck, A. Tomaschek, J. Wendsche, E. Ochsmann, and D. Dörfel, "Psychosocial areas of worklife and chronic low back pain: a systematic review and meta-analysis," *BMC Musculoskeletal Disorders,* vol. 20, no. 1, p. 480, 2019/10/25 2019, doi: 10.1186/s12891-019-2826-3.

[89] D. Pozzobon *et al.*, "Is there an association between diabetes and neck and back pain? A systematic review with meta-analyses," (in eng), *PLoS One,* vol. 14, no. 2, p. e0212030, 2019, doi: 10.1371/journal.pone.0212030.

[90] J. A. Zwart, O. J. Iversen, T. Sand, L. G. Dale, and G. Unsgård, "Higher levels of antibodies against the psoriasis-associated antigen pso p27 in cerebrospinal fluid from patients with low back pain and sciatica," (in eng), *Spine (Phila Pa 1976),* vol. 24, no. 4, pp. 373-7, Feb 15 1999, doi: 10.1097/00007632-199902150-00016.

[91] R. Shiri, J. Karppinen, P. Leino-Arjas, S. Solovieva, and E. Viikari-Juntura, "The Association between Smoking and Low Back Pain: A Meta-analysis," *The American Journal of Medicine,* vol. 123, no. 1, pp. 87.e7-87.e35, 2010/01/01/ 2010, doi: https://doi.org/10.1016/j.amjmed.2009.05.028.

[92] Y. Pasdar *et al.*, "Major dietary patterns in relation to chronic low back pain; a cross-sectional study from RaNCD cohort," (in eng), *Nutr J,* vol. 21, no. 1, p. 28, May 12 2022, doi: 10.1186/s12937-022-00780-2.

[93] H. Heneweer, H. S. Picavet, F. Staes, H. Kiers, and L. Vanhees, "Physical fitness, rather than self-reported physical activities, is more strongly associated with low back pain: evidence from a working population," (in eng), *Eur Spine J,* vol. 21, no. 7, pp. 1265-72, Jul 2012, doi: 10.1007/s00586-011-2097-7.

[94] J. A. Verbunt, R. J. Smeets, and H. M. Wittink, "Cause or effect? Deconditioning and chronic low back pain," (in eng), *Pain,* vol. 149, no. 3, pp. 428-430, Jun 2010, doi: 10.1016/j.pain.2010.01.020.

[95] M. S. Swain, N. Henschke, S. J. Kamper, I. Gobina, V. Ottová-Jordan, and C. G. Maher, "An international survey of pain in adolescents," *BMC Public Health,* vol. 14, no. 1, p. 447, 2014/05/13 2014, doi: 10.1186/1471-2458-14-447.

[96] N. Henschke *et al.*, "Prognosis in patients with recent onset low back pain in Australian primary care: inception cohort study," (in eng), *Bmj,* vol. 337, no. 7662, p. a171, Jul 7 2008, doi: 10.1136/bmj.a171.

[97] M. Krismer and M. van Tulder, "Low back pain (non-specific)," *Best Practice & Research Clinical Rheumatology,* vol. 21, no. 1, pp. 77-91, 2007/02/01/ 2007, doi: https://doi.org/10.1016/j.berh.2006.08.004.

[98] F. Fatoye, T. Gebrye, C. G. Ryan, U. Useh, and C. Mbada, "Global and regional estimates of clinical and economic burden of low back pain in high-income countries: a systematic review and meta-analysis," (in English), *Frontiers in Public Health,* Systematic Review vol. 11, 2023-June-09 2023, doi: 10.3389/fpubh.2023.1098100.

[99] "Global-Metrics." https://www.macrotrends.net/global-metrics/countries (accessed 2024).

[100] G. Olafsson, E. Jonsson, P. Fritzell, O. Hägg, and F. Borgström, "Cost of low back pain: results from a national register study in Sweden," (in eng), *Eur Spine J,* vol. 27, no. 11, pp. 2875-2881, Nov 2018, doi: 10.1007/s00586-018-5742-6.

[101] T. Lallukka *et al.*, "Recurrent back pain during working life and exit from paid employment: a 28-year follow-up of the Whitehall II Study," (in eng), *Occup Environ Med,* vol. 75, no. 11, pp. 786-791, Nov 2018, doi: 10.1136/oemed-2018-105202.

[102] D. J. Schofield, R. N. Shrestha, M. E. Passey, A. Earnest, and S. L. Fletcher, "Chronic disease and labour force participation among older Australians," *Medical Journal of Australia,* vol. 189, no. 8, pp. 447-450, 2008, doi: https://doi.org/10.5694/j.1326-5377.2008.tb02119.x.

[103] M. W. van Tulder, M. Tuut, V. Pennick, C. Bombardier, and W. J. Assendelft, "Quality of primary care guidelines for acute low back pain," (in eng), *Spine (Phila Pa 1976),* vol. 29, no. 17, pp. E357-62, Sep 1 2004, doi: 10.1097/01.brs.0000137056.64166.51.

[104] B. W. Koes, M. van Tulder, C.-W. C. Lin, L. G. Macedo, J. McAuley, and C. Maher, "An updated overview of clinical guidelines for the management of non-specific low back pain in primary care," *European Spine Journal,* vol. 19, no. 12, pp. 2075-2094, 2010/12/01 2010, doi: 10.1007/s00586-010-1502-y.

[105] "How should I assess a person with low back pain?" National Institute for Health and care Excellence. https://cks.nice.org.uk/topics/back-pain-low-without-radiculopathy/diagnosis/assessment/ (accessed 2023).

[106] C. J. Main, C. J. Phillips, and P. J. Watson, "Secondary Prevention in Health-Care and Occupational Settings in Musculoskeletal Conditions Focusing on Low Back Pain," in *Handbook of Complex Occupational Disability Claims: Early Risk Identification, Intervention, and Prevention*, I. Z. Schultz and R. J. Gatchel Eds. Boston, MA: Springer US, 2005, pp. 387-404.

[107] M. K. Nicholas, S. J. Linton, P. J. Watson, C. J. Main, and t. D. o. t. F. W. Group, "Early Identification and Management of Psychological Risk Factors ("Yellow Flags") in Patients With Low Back Pain: A Reappraisal," *Physical Therapy,* vol. 91, no. 5, pp. 737-753, 2011, doi: 10.2522/ptj.20100224.

[108] W. S. Shaw, D. A. van der Windt, C. J. Main, P. Loisel, S. J. Linton, and G. the "Decade of the Flags" Working, "Early Patient Screening and Intervention to Address Individual-Level Occupational Factors ("Blue Flags") in Back Disability," *Journal of Occupational Rehabilitation,* vol. 19, no. 1, pp. 64-80, 2009/03/01 2009, doi: 10.1007/s10926-008-9159-7.

[109] J. Samanta, J. Kendall, and A. Samanta, "10-Minute Consultation: Chronic Low Back Pain," (in eng), *Bmj,* vol. 326, no. 7388, p. 535, Mar 8 2003, doi: 10.1136/bmj.326.7388.535.

[110] L. M. Finucane *et al.*, "International Framework for Red Flags for Potential Serious Spinal Pathologies," *Journal of Orthopaedic & Sports Physical Therapy,* vol. 50, no. 7, pp. 350-372, 2020, doi: 10.2519/jospt.2020.9971.

[111] S. Greenhalgh and J. Selfe, *E-Book-Red Flags: Managing Serious Spinal Pathology*. Elsevier Health Sciences, 2019.

[112] V. Nicol *et al.*, "Chronic Low Back Pain: A Narrative Review of Recent International Guidelines for Diagnosis and Conservative Treatment," (in eng), *J Clin Med,* vol. 12, no. 4, Feb 20 2023, doi: 10.3390/jcm12041685.

[113] D. M. Urquhart, J. L. Hoving, W. W. Assendelft, M. Roland, and M. W. van Tulder, "Antidepressants for Non-Specific Low Back Pain," (in eng), *Cochrane Database Syst Rev,* vol. 2008, no. 1, p. Cd001703, Jan 23 2008, doi: 10.1002/14651858.CD001703.pub3.

[114] J. A. Hayden, J. Ellis, R. Ogilvie, A. Malmivaara, and M. W. van Tulder, "Exercise therapy for chronic low back pain," (in eng), *Cochrane Database Syst Rev,* vol. 9, no. 9, p. Cd009790, Sep 28 2021, doi: 10.1002/14651858.CD009790.pub2.

[115] A. Adamczyk, W. Kiebzak, M. Wilk-Frańczuk, and Z. Sliwiński, "Effectiveness of holistic physiotherapy for low back pain," (in eng), *Ortop Traumatol Rehabil,* vol. 11, no. 6, pp. 562-576, 2009 Nov-Dec 2009. [Online]. Available: http://europepmc.org/abstract/MED/20201159.

[116] G. E. Ferreira *et al.*, "Efficacy and safety of antidepressants for the treatment of back pain and osteoarthritis: systematic review and meta-analysis," *BMJ,* vol. 372, p. m4825, 2021, doi: 10.1136/bmj.m4825.

[117] A. J. Buckland *et al.*, "Anterior Column Reconstruction of the Lumbar Spine in the Lateral Decubitus Position: Anatomical and Patient-Related Considerations for ALIF, Anterior-to-Psoas, and Transpsoas LLIF Approaches," (in eng), *Eur Spine J,* vol. 31, no. 9, pp. 2175-2187, Sep 2022, doi: 10.1007/s00586-022-07127-9.

[118] J. Jiang *et al.*, "Comparative Efficacy of Pharmacological Therapies for Low Back Pain: A Bayesian Network Analysis," (in English), *Frontiers in Pharmacology,* Systematic Review vol. 13, 2022-February-15 2022, doi: 10.3389/fphar.2022.811962.

[119] F. Migliorini *et al.*, "The pharmacological management of chronic lower back pain," (in eng), *Expert Opin Pharmacother,* vol. 22, no. 1, pp. 109-119, Jan 2021, doi: 10.1080/14656566.2020.1817384.

[120] S. Ohtori *et al.*, "L2 spinal nerve-block effects on acute low back pain from osteoporotic vertebral fracture," (in eng), *J Pain,* vol. 10, no. 8, pp. 870-5, Aug 2009, doi: 10.1016/j.jpain.2009.03.002.

[121] S. Dagenais, M. J. Yelland, C. Del Mar, and M. L. Schoene, "Prolotherapy injections for chronic low-back pain," (in eng), *Cochrane Database Syst Rev,* vol. 2007, no. 2, p. Cd004059, Apr 18 2007, doi: 10.1002/14651858.CD004059.pub3.

[122] P. M. Eichen *et al.*, "Nucleoplasty, a minimally invasive procedure for disc decompression: a systematic review and meta-analysis of published clinical studies," (in eng), *Pain Physician,* vol. 17, no. 2, pp. E149-73, Mar-Apr 2014.

[123] I. Gelalis *et al.*, "Current Concepts in Intradiscal Percutaneous Minimally Invasive Procedures for Chronic Low Back Pain," (in eng), *Asian J Neurosurg,* vol. 14, no. 3, pp. 657-669, Jul-Sep 2019, doi: 10.4103/ajns.AJNS_119_17.

[124] B. R. Gabor *et al.*, "Epidural Lysis of Adhesions and Percutaneous Neuroplasty," in *Pain and Treatment*, B. R. Gabor and E. N. Carl Eds. Rijeka: IntechOpen, 2014, p. Ch. 10.

[125] L. Manchikanti, N. N. Knezevic, M. R. Sanapati, M. V. Boswell, A. D. Kaye, and J. A. Hirsch, "Effectiveness of Percutaneous Adhesiolysis in Managing Chronic Central Lumbar Spinal Stenosis: A Systematic Review and Meta-Analysis," (in eng), *Pain Physician,* vol. 22, no. 6, pp. E523-e550, Nov 2019.

[126] L. Kapural and D. A. Sparks, "Chapter 18 - Minimally Invasive Intradiscal Procedures for the Treatment of Discogenic Lower Back and Leg Pain," in *Spinal Injections and*

*Peripheral Nerve Blocks*, vol. 4, M. A. Huntoon, H. T. Benzon, S. Narouze, and T. R. Deer Eds. Philadelphia: W.B. Saunders, 2012, pp. 184-192.

[127] D. Appleby, G. Andersson, and M. Totta, "Meta-analysis of the efficacy and safety of intradiscal electrothermal therapy (IDET)," (in eng), *Pain Med,* vol. 7, no. 4, pp. 308-16, Jul-Aug 2006, doi: 10.1111/j.1526-4637.2006.00172.x.

[128] J. Zhang, Q. Li, Y. Du, Z. Yan, L. Chen, and L. Wang, "Efficacy Analysis of Percutaneous Endoscopic Spinal Surgery for Young Patients with Discogenic Low Back Pain," (in eng), *J Pain Res,* vol. 15, pp. 665-674, 2022, doi: 10.2147/jpr.S351296.

[129] S. Tang *et al.*, "Comparison of clinical and radiological outcomes of full-endoscopic versus microscopic lumbar decompression laminectomy for the treatment of lumbar spinal stenosis: a systematic review and meta-analysis," (in eng), *Ann Palliat Med,* vol. 10, no. 10, pp. 10130-10146, Oct 2021, doi: 10.21037/apm-21-198.

[130] R. Murtagh and A. E. Castellvi, "Motion preservation surgery in the spine," (in eng), *Neuroimaging Clin N Am,* vol. 24, no. 2, pp. 287-94, May 2014, doi: 10.1016/j.nic.2014.01.008.

[131] J. C. Wu, P. C. Hsieh, P. V. Mummaneni, and M. Y. Wang, "Spinal Motion Preservation Surgery," (in eng), *Biomed Res Int,* vol. 2015, p. 372502, 2015, doi: 10.1155/2015/372502.

[132] S. H. Lee, W. G. Choi, S. R. Lim, H. Y. Kang, and S. W. Shin, "Minimally invasive anterior lumbar interbody fusion followed by percutaneous pedicle screw fixation for isthmic spondylolisthesis," (in eng), *Spine J,* vol. 4, no. 6, pp. 644-9, Nov-Dec 2004, doi: 10.1016/j.spinee.2004.04.012.

[133] L. T. Khoo, S. Palmer, D. T. Laich, and R. G. Fessler, "Minimally invasive percutaneous posterior lumbar interbody fusion," (in eng), *Neurosurgery,* vol. 51, no. 5 Suppl, pp. S166-81, Nov 2002.

[134] F. Lovecchio and S. A. Qureshi, "The Current State of Minimally Invasive Approaches to Adult Spinal Deformity," (in eng), *Curr Rev Musculoskelet Med,* vol. 12, no. 3, pp. 318-327, Jul 16 2019, doi: 10.1007/s12178-019-09570-6.

[135] M. Alhashash and M. Shousha, "Minimally Invasive Short-Segment Anteroposterior Surgery for Thoracolumbar Osteoporotic Fractures with Canal Compromise: A Prospective Study with a Minimum 2-Year Follow-up," (in eng), *Asian Spine J,* vol. 16, no. 1, pp. 28-37, Feb 2022, doi: 10.31616/asj.2020.0573.

[136] M. C. Gupta, S. Gupta, M. P. Kelly, and K. H. Bridwell, "Pedicle Subtraction Osteotomy," (in eng), *JBJS Essent Surg Tech,* vol. 10, no. 1, Jan-Mar 2020, doi: 10.2106/jbjs.St.19.00028.

[137] A. Nanda, J. Manghwani, and P. J. Kluger, "Sacropelvic fixation techniques - Current update," (in eng), *J Clin Orthop Trauma,* vol. 11, no. 5, pp. 853-862, Sep-Oct 2020, doi: 10.1016/j.jcot.2020.07.022.

[138] C. Saifi, J. L. Laratta, P. Petridis, J. N. Shillingford, R. A. Lehman, and L. G. Lenke, "Vertebral Column Resection for Rigid Spinal Deformity," (in eng), *Global Spine J,* vol. 7, no. 3, pp. 280-290, May 2017, doi: 10.1177/2192568217699203.

[139] J. E. Bible and J. D. Kang, "Anterior Cervical Discectomy and Fusion: Surgical Indications and Outcomes," *Seminars in Spine Surgery,* vol. 28, no. 2, pp. 80-83, 2016/06/01/ 2016, doi: https://doi.org/10.1053/j.semss.2015.11.002.

[140] C. M. Mikhail, J. E. Dowdell, 3rd, and A. C. Hecht, "Posterior Fusion for the Subaxial Cervical Spine: A Review of the Major Techniques," (in eng), *Hss j,* vol. 16, no. 2, pp. 188-194, Jul 2020, doi: 10.1007/s11420-019-09722-x.

[141] C. Ren, R. Qin, P. Wang, and P. Wang, "Comparison of anterior and posterior approaches for treatment of traumatic cervical dislocation combined with spinal cord injury: Minimum 10-year follow-up," *Scientific Reports,* vol. 10, no. 1, p. 10346, 2020/06/25 2020, doi: 10.1038/s41598-020-67265-2.

[142] D. J. Abraham, H. N. Herkowitz, and J. N. Katz, "INDICATIONS FOR THORACIC AND LUMBAR SPINE FUSION AND TRENDS IN USE," *Orthopedic Clinics of North America,* vol. 29, no. 4, pp. 803-811, 1998/10/01/ 1998, doi: https://doi.org/10.1016/S0030-5898(05)70049-3.

[143] F. R. T. Nelson and C. T. Blauvelt, "Chapter 9 - The Spine," in *A Manual of Orthopaedic Terminology (Seventh Edition)*, F. R. T. Nelson and C. T. Blauvelt Eds. Philadelphia: Mosby, 2007, pp. 263-284.

[144] M. Ruf, J. Drumm, and D. Jeszenszky, "Anterior Instrumented Fusion for Adolescent Idiopathic Scoliosis," (in eng), *Ann Transl Med,* vol. 8, no. 2, p. 31, Jan 2020, doi: 10.21037/atm.2019.11.84.

[145] H. Abbasi and A. Abbasi, "Minimally Invasive Direct Thoracic Interbody Fusion (MIS-DTIF): Technical Notes of a Single Surgeon Study," (in eng), *Cureus,* vol. 8, no. 7, p. e699, Jul 18 2016, doi: 10.7759/cureus.699.

[146] C. Y. Barrey, L. Boissiere, G. D'Acunzi, and G. Perrin, "One-stage combined lumbo-sacral fusion, by anterior then posterior approach: clinical and radiological results," (in eng), *Eur Spine J,* vol. 22 Suppl 6, no. Suppl 6, pp. S957-64, Nov 2013, doi: 10.1007/s00586-013-3017-9.

[147] M. A. Fontana *et al.*, "Presenteeism and absenteeism before and after single-level lumbar spine surgery," (in eng), *Spine J,* vol. 22, no. 5, pp. 776-786, May 2022, doi: 10.1016/j.spinee.2021.10.017.

[148] A. Hansson-Hedblom, E. Jonsson, P. Fritzell, O. Hägg, and F. Borgström, "The Association Between Patient Reported Outcomes of Spinal Surgery and Societal Costs: A Register Based Study," (in eng), *Spine (Phila Pa 1976),* vol. 44, no. 18, pp. 1309-1317, Sep 2019, doi: 10.1097/brs.0000000000003050.

[149] K. Kumar, "Spinal Deformity and Axial Traction," *Spine,* vol. 21, no. 5, pp. 653-655, 1996. [Online]. Available:

https://journals.lww.com/spinejournal/fulltext/1996/03010/spinal_deformity_and_axial_traction.24.aspx.

[150] E. S. Vasiliadis, T. B. Grivas, and A. Kaspiris, "Historical overview of spinal deformities in ancient Greece," *Scoliosis,* vol. 4, no. 1, p. 6, 2009/02/25 2009, doi: 10.1186/1748-7161-4-6.

[151] K. Jang, J. V. Rosenfeld, and A. Di Ieva, "Paulus of Aegina and the Historical Origins of Spine Surgery," *World Neurosurgery,* vol. 133, pp. 291-301, 2020/01/01/ 2020, doi: https://doi.org/10.1016/j.wneu.2019.10.026.

[152] S. M. Tuli, "Historical aspects of Pott's disease (spinal tuberculosis) management," (in eng), *Eur Spine J,* vol. 22 Suppl 4, no. Suppl 4, pp. 529-38, Jun 2013, doi: 10.1007/s00586-012-2388-7.

[153] R. A. Hibbs, "The Classic: An Operation for Progressive Spinal Deformities: A Preliminary Report of Three Cases from the Service of the Orthopaedic Hospital," *Clinical Orthopaedics and Related Research®,* vol. 460, pp. 17-20, 2007, doi: 10.1097/BLO.0b013e3180686b30.

[154] J. C. Risser, "The Application of Body Casts for the Correction of Scoliosis," (in eng), *Instr Course Lect,* vol. 12, pp. 255-9, 1955.

[155] R. A. Hibbs and J. C. Risser, "Treatment of vertebral tuberculosis by the spine fusion operation," *JBJS,* vol. 10, no. 4, pp. 805-815, 1928.

[156] F. H. Albee, "Transplantation of a Portion of the Tibia into the Spine for Pott's Disease: A Preliminary Report," *Journal of the American Medical Association,* vol. LVII, no. 11, pp. 885-886, 1911, doi: 10.1001/jama.1911.04260090107012.

[157] F. H. Albee, "Bone Surgery With Machine Tools," *Scientific American,* vol. 154, no. 4, pp. 178-181, 1936. [Online]. Available: http://www.jstor.org/stable/26144760.

[158] R. B. Cloward, "The treatment of ruptured lumbar intervertebral disc by vertebral body fusion. III. Method of use of banked bone," (in eng), *Ann Surg,* vol. 136, no. 6, pp. 987-92, Dec 1952, doi: 10.1097/00000658-195212000-00011.

[159] R. B. Cloward, "The treatment of ruptured lumbar intervertebral discs by vertebral body fusion. I. Indications, operative technique, after care," (in eng), *J Neurosurg,* vol. 10, no. 2, pp. 154-68, Mar 1953, doi: 10.3171/jns.1953.10.2.0154.

[160] W. J. Mixter and J. S. Barr, "Rupture of the Intervertebral Disc with Involvement of the Spinal Canal," *New England Journal of Medicine,* vol. 211, no. 5, pp. 210-215, 1934, doi: 10.1056/nejm193408022110506.

[161] M. J. Guérin, "Case of Reduction of Dislocation of the Cervical Vertebræ: After Seven Months," (in eng), *Prov Med Surg J (1840),* vol. 1, no. 4, pp. 61-3, Oct 24 1840.

[162] B. E. Hadra, "The classic: Wiring of the vertebrae as a means of immobilization in fracture and Potts' disease. Berthold E. Hadra. Med Times and Register, Vol22, May 23, 1891," (in eng), *Clin Orthop Relat Res,* no. 112, pp. 4-8, Oct 1975.

[163] F. Lange and L. F. Peltier, "The Classic: Support for the Spondylitic Spine by Means of Buried Steel Bars, Attached to the Vertebrae," *Clinical Orthopaedics and Related Research®,* vol. 203, pp. 3-6, 1986. [Online]. Available: https://journals.lww.com/clinorthop/fulltext/1986/02000/the_classic__support_for_the_spondylitic_spine_by.2.aspx.

[164] P. R. Harrington, "Treatment of Scoliosis: Correction and Internal Fixation by Spine Instrumentation," *JBJS,* vol. 44, no. 4, 1962. [Online]. Available: https://journals.lww.com/jbjsjournal/fulltext/1962/44040/treatment_of_scoliosis__correction_and_internal.1.aspx.

[165] R. Roy-Camille, M. Roy-Camille, and C. Demeulenaere, "Osteosynthesis of dorsal, lumbar, and lumbosacral spine with metallic plates screwed into vertebral pedicles and articular apophyses," (in fre), *Presse Med (1893),* vol. 78, no. 32, pp. 1447-8, Jun 1970. Ostéosynthèse du rachis dorsal, lombaire et lombo-sacré par plaques métalliques vissées dans les pédicules vertébraux et les apophyses articulaires.

[166] R. Roy-Camille, G. Saillant, and C. Mazel, "Internal fixation of the lumbar spine with pedicle screw plating," (in eng), *Clin Orthop Relat Res,* no. 203, pp. 7-17, Feb 1986.

[167] P. C. Wagner, B. D. Grant, G. W. Bagby, A. M. Gallina, R. D. Sande, and M. Ratzlaff, "Evaluation of Cervical Spinal Fusion as a Treatment in the Equine “Wobbler” Syndrome," *Veterinary Surgery,* vol. 8, no. 3, pp. 84-88, 1979, doi: https://doi.org/10.1111/j.1532-950X.1979.tb00614.x.

[168] G. W. Bagby, "Arthrodesis by the Distraction-Compression Method Using a Stainless Steel Implant," *Orthopedics,* vol. 11, no. 6, pp. 931-934, 1988, doi: doi:10.3928/0147-7447-19880601-13.

[169] S. D. Kuslich, C. L. Ulstrom, S. L. Griffith, J. W. Ahern, and J. D. Dowdle, "The Bagby and Kuslich Method of Lumbar Interbody Fusion: History, Techniques, and 2-Year Follow-up Results of a United States Prospective, Multicenter Trial," *Spine,* vol. 23, no. 11, pp. 1267-1278, 1998. [Online]. Available: https://journals.lww.com/spinejournal/fulltext/1998/06010/the_bagby_and_kuslich_method_of_lumbar_interbody.19.aspx.

[170] G. Bagby, "Method and apparatus for conjoining bone bodies," ed: Google Patents, 2000.

[171] O. Brink, "The choice between allograft or demineralized bone matrix is not unambiguous in trauma surgery," *Injury,* vol. 52, pp. S23-S28, 2021/06/01/ 2021, doi: https://doi.org/10.1016/j.injury.2020.11.013.

[172] G. Hossein and V. G. Roghayyeh, "Bone Regeneration: Current Status and Future Prospects," in *Advanced Techniques in Bone Regeneration*, Z. Alessandro Rozim and M. Joao Batista de Eds. Rijeka: IntechOpen, 2016, p. Ch. 1.

[173] K. A. Egol, A. Nauth, M. Lee, H.-C. Pape, J. T. Watson, and J. J. Borrelli, "Bone Grafting: Sourcing, Timing, Strategies, and Alternatives," *Journal of Orthopaedic Trauma,* vol. 29, pp. S10-S14, 2015, doi: 10.1097/bot.0000000000000460.

[174] S. N. Parikh, "Bone Graft Substitutes in Modern Orthopedics," *Orthopedics,* vol. 25, no. 11, pp. 1301-1309, 2002, doi: doi:10.3928/0147-7447-20021101-27.

[175] Y. Katsuura, K. Shafi, C. Jacques, S. Virk, S. Iyer, and M. Cunningham, "New Strategies in Enhancing Spinal Fusion," (in eng), *Hss j,* vol. 16, no. 2, pp. 177-182, Jul 2020, doi: 10.1007/s11420-020-09749-5.

[176] M. K. Sen and T. Miclau, "Autologous Iliac Crest Bone Graft: Should It Still Be the Gold Standard for Treating Nonunions?," *Injury,* vol. 38, no. 1, Supplement, pp. S75-S80, 2007/03/01/ 2007, doi: https://doi.org/10.1016/j.injury.2007.02.012.

[177] C. Eder *et al.*, "Autografts for Spinal Fusion: Osteogenic Potential of Laminectomy Bone Chips and Bone Shavings Collected via High Speed Drill," (in eng), *Eur Spine J,* vol. 20, no. 11, pp. 1791-5, Nov 2011, doi: 10.1007/s00586-011-1736-3.

[178] N. Ahmed, V. Eras, A. Pruß, C. Perka, J. Brune, and T. L. Vu-Han, "Allografts: Expanding the Surgeon's Armamentarium," (in eng), *Cell Tissue Bank,* vol. 24, no. 1, pp. 273-283, Mar 2023, doi: 10.1007/s10561-022-10015-7.

[179] J. A. Gruskay, B. A. Basques, D. D. Bohl, M. L. Webb, and J. N. Grauer, "Short-term adverse events, length of stay, and readmission after iliac crest bone graft for spinal fusion," (in eng), *Spine (Phila Pa 1976),* vol. 39, no. 20, pp. 1718-24, Sep 15 2014, doi: 10.1097/brs.0000000000000476.

[180] K. E. Rudisill, P. P. Ratnasamy, G. C. Maloy, and J. N. Grauer, "Decline in Separate Incision Autograft for Spine Surgery Over the Past Decade: A Fading "gold standard"," (in eng), *J Am Acad Orthop Surg,* vol. 31, no. 17, pp. 938-944, Sep 1 2023, doi: 10.5435/jaaos-d-22-01029.

[181] C. F. Hyer, G. C. Berlet, B. W. Bussewitz, T. Hankins, H. L. Ziegler, and T. M. Philbin, "Quantitative Assessment of the Yield of Osteoblastic Connective Tissue Progenitors in Bone Marrow Aspirate from the Iliac Crest, Tibia, and Calcaneus," *JBJS,* vol. 95, no. 14, pp. 1312-1316, 2013, doi: 10.2106/jbjs.L.01529.

[182] A. Oryan, S. Alidadi, A. Moshiri, and N. Maffulli, "Bone regenerative medicine: classic options, novel strategies, and future directions," (in eng), *Journal of Orthopaedic Surgery and Research,* vol. 9, no. 1, p. 18, 2014/03/17 2014, doi: 10.1186/1749-799x-9-18.

[183] M. Mendoza, B. Rosenthal, and W. Hsu, "Biologic Options in Interbody Fusion," 2019, pp. 145-149.

[184] D. Smiler and M. Soltan, "Bone Marrow Aspiration: Technique, Grafts, and Reports," *Implant Dentistry,* vol. 15, no. 3, 2006. [Online]. Available: https://journals.lww.com/implantdent/fulltext/2006/09000/bone_marrow_aspiration__technique,_grafts,_and.6.aspx.

[185] S. N. Khan, F. P. J. Cammisa, H. S. Sandhu, A. D. Diwan, F. P. Girardi, and J. M. Lane, "The Biology of Bone Grafting," *JAAOS - Journal of the American Academy of Orthopaedic Surgeons,* vol. 13, no. 1, pp. 77-86, 2005. [Online]. Available: https://journals.lww.com/jaaos/fulltext/2005/01000/the_biology_of_bone_grafting.10.aspx.

[186] S. B. Goodman and S. Zwingenberger, "Concentrated autologous bone marrow aspirate is not “stem cell” therapy in the repair of nonunions and bone defects," *Biomaterials and Biosystems,* vol. 2, p. 100017, 2021/06/01/ 2021, doi: https://doi.org/10.1016/j.bbiosy.2021.100017.

[187] L. F. Bush and C. Z. Garber, "The Bone Bank," *Journal of the American Medical Association,* vol. 137, no. 7, pp. 588-594, 1948, doi: 10.1001/jama.1948.02890410010003.

[188] S. C. McGinniss, "The Navy Tissue Bank," *The American Journal of Nursing,* vol. 59, no. 5, pp. 666-669, 1959, doi: 10.2307/3417748.

[189] R. Lomas, A. Chandrasekar, and T. N. Board, "Bone allograft in the U.K.: perceptions and realities," (in eng), *Hip Int,* vol. 23, no. 5, pp. 427-33, Sep-Oct 2013, doi: 10.5301/hipint.5000018.

[190] A. G. Sutherland, A. Raafat, P. Yates, and J. D. Hutchison, "Infection associated with the use of allograft bone from the North East Scotland Bone Bank," *Journal of Hospital Infection,* vol. 35, no. 3, pp. 215-222, 1997/03/01/ 1997, doi: https://doi.org/10.1016/S0195-6701(97)90209-7.

[191] M. Zhang, R. M. Powers, Jr., and L. Wolfinbarger, Jr., "A quantitative assessment of osteoinductivity of human demineralized bone matrix," (in eng), *J Periodontol,* vol. 68, no. 11, pp. 1076-84, Nov 1997, doi: 10.1902/jop.1997.68.11.1076.

[192] M. Zhang, R. M. Powers, Jr., and L. Wolfinbarger, Jr., "Effect(s) of the demineralization process on the osteoinductivity of demineralized bone matrix," (in eng), *J Periodontol,* vol. 68, no. 11, pp. 1085-92, Nov 1997, doi: 10.1902/jop.1997.68.11.1085.

[193] H. W. Bae, L. Zhao, L. E. A. Kanim, P. Wong, R. B. Delamarter, and E. G. Dawson, "Intervariability and Intravariability of Bone Morphogenetic Proteins in Commercially Available Demineralized Bone Matrix Products," *Spine,* vol. 31, no. 12, pp. 1299-1306, 2006, doi: 10.1097/01.brs.0000218581.92992.b7.

[194] D. N. Bracey *et al.*, "Bone xenotransplantation: A review of the history, orthopedic clinical literature, and a single-center case series," *Xenotransplantation,* vol. 27, no. 5, p. e12600, 2020, doi: https://doi.org/10.1111/xen.12600.

[195] A. S. Herford, E. Stoffella, and C. M. Stanford, "Chapter 5 - Bone Grafts and Bone Substitute Materials," in *Principles and Practice of Single Implant and Restorations*, M. Torabinejad, M. A. Sabeti, and C. J. Goodacre Eds. Saint Louis: W.B. Saunders, 2014, pp. 75-86.

[196] M. Cascalho and J. L. Platt, "81 - Challenges and Potentials of Xenotransplantation," in *Clinical Immunology (Third Edition)*, R. R. Rich, T. A. Fleisher, W. T. Shearer, H. W. Schroeder, A. J. Frew, and C. M. Weyand Eds. Edinburgh: Mosby, 2008, pp. 1215-1222.

[197] D. Offner *et al.*, "Bone Grafts, Bone Substitutes and Regenerative Medicine Acceptance for the Management of Bone Defects Among French Population: Issues about Ethics, Religion or Fear?," *Cell Medicine,* vol. 11, p. 2155179019857661, 2019, doi: 10.1177/2155179019857661.

[198] P. H. de Azambuja Carvalho, N. de Oliveira Ciaramicolo, O. Ferreira Júnior, and V. A. Pereira-Filho, "Clinical and laboratorial outcomes of xenogeneic biomaterials: literature review," *Frontiers of Oral and Maxillofacial Medicine,* vol. 5, 2021. [Online]. Available: https://fomm.amegroups.org/article/view/56185.

[199] A. Gupta, N. Kukkar, K. Sharif, B. J. Main, C. E. Albers, and S. F. El-Amin Iii, "Bone graft substitutes for spine fusion: A brief review," (in eng), *World J Orthop,* vol. 6, no. 6, pp. 449-56, Jul 18 2015, doi: 10.5312/wjo.v6.i6.449.

[200] T. Albrektsson and C. Johansson, "Osteoinduction, osteoconduction and osseointegration," *European Spine Journal,* vol. 10, no. 2, pp. S96-S101, 2001/10/01 2001, doi: 10.1007/s005860100282.

[201] E. Hjørting-Hansen, "Bone grafting to the jaws with special reference to reconstructive preprosthetic surgery," *Mund-, Kiefer- und Gesichtschirurgie,* vol. 6, no. 1, pp. 6-14, 2002/01/01 2002, doi: 10.1007/s10006-001-0343-6.

[202] D. Donati, C. Zolezzi, P. Tomba, and A. Viganò, "Bone grafting: historical and conceptual review, starting with an old manuscript by Vittorio Putti," *Acta Orthopaedica,* vol. 78, no. 1, pp. 19-25, 2007/01/01 2007, doi: 10.1080/17453670610013376.

[203] W. Macewen and T. H. Huxley, "IV. Observations concerning transplantation of bone. Illustrated by a case of inter-human osseous transplantation, whereby over two-thirds of the shaft of a humerus was restored," *Proceedings of the Royal Society of London,* vol. 32, no. 212-215, pp. 232-247, 1881, doi: doi:10.1098/rspl.1881.0025.

[204] N. Senn, "On the healing of aseptic bone cavities by implantation of antiseptic decalcified bone," *The American Journal of the Medical Sciences (1827-1924),* vol. 98, no. 3, p. 219, 1889.

[205] W. J. Sharrard and D. H. Collins, "The fate of human decalcified bone grafts," (in eng), *Proc R Soc Med,* vol. 54, no. 12, pp. 1101-2, Dec 1961.

[206] H. Dreesmann, "Ueber Knochenplombirung1," *DMW-Deutsche Medizinische Wochenschrift,* vol. 19, no. 19, pp. 445-446, 1893.

[207] S. Weber, Y. P. Acklin, R. Jenni, H. Bereiter, and I. Broger, "Bio-Derived Apatite As a Bone Graft for Vertebral Trauma," (in eng), *Surg Technol Int,* vol. 37, pp. 427-431, Nov 28 2020.

[208] M. R. Urist, "Bone: Formation by Autoinduction," *Science,* vol. 150, no. 3698, pp. 893-899, 1965, doi: doi:10.1126/science.150.3698.893.

[209] M. R. Urist and B. S. Strates, "Bone Morphogenetic Protein," *Journal of Dental Research,* vol. 50, no. 6, pp. 1392-1406, 1971/11/01 1971, doi: 10.1177/00220345710500060601.

[210] J. M. Wozney *et al.*, "Novel Regulators of Bone Formation: Molecular Clones and Activities," *Science,* vol. 242, no. 4885, pp. 1528-1534, 1988, doi: doi:10.1126/science.3201241.

[211] J. K. Burkus, M. F. Gornet, C. A. Dickman, and T. A. Zdeblick, "Anterior Lumbar Interbody Fusion Using rhBMP-2 with Tapered Interbody Cages," *Clinical Spine Surgery,* vol. 15, no. 5, pp. 337-349, 2002. [Online]. Available: https://journals.lww.com/jspinaldisorders/fulltext/2002/10000/anterior_lumbar_interbody_fusion_using_rhbmp_2.1.aspx.

[212] S. D. Boden, J. Kang, H. Sandhu, and J. G. Heller, "Use of Recombinant Human Bone Morphogenetic Protein-2 to Achieve Posterolateral Lumbar Spine Fusion in Humans: A Prospective, Randomized Clinical Pilot Trial 2002 Volvo Award in Clinical Studies," *Spine,* vol. 27, no. 23, 2002. [Online]. Available: https://journals.lww.com/spinejournal/fulltext/2002/12010/use_of_recombinant_human_bone_morphogenetic.5.aspx.

[213] S. Govender *et al.*, "Recombinant human bone morphogenetic protein-2 for treatment of open tibial fractures: a prospective, controlled, randomized study of four hundred and fifty patients," (in eng), *J Bone Joint Surg Am,* vol. 84, no. 12, pp. 2123-34, Dec 2002, doi: 10.2106/00004623-200212000-00001.

[214] J. D. Richmon, A. B. Sage, E. Shelton, B. L. Schumacher, R. L. Sah, and D. Watson, "Effect of growth factors on cell proliferation, matrix deposition, and morphology of human nasal septal chondrocytes cultured in monolayer," (in eng), *Laryngoscope,* vol. 115, no. 9, pp. 1553-60, Sep 2005, doi: 10.1097/01.Mlg.0000175541.31131.A5.

[215] D. S. Mulconrey, K. H. Bridwell, J. Flynn, G. A. Cronen, and P. S. Rose, "Bone morphogenetic protein (RhBMP-2) as a substitute for iliac crest bone graft in multilevel adult spinal deformity surgery: minimum two-year evaluation of fusion," (in eng), *Spine (Phila Pa 1976),* vol. 33, no. 20, pp. 2153-9, Sep 15 2008, doi: 10.1097/BRS.0b013e31817bd91e.

[216] B. P. Dickinson *et al.*, "Reduced morbidity and improved healing with bone morphogenic protein-2 in older patients with alveolar cleft defects," (in eng), *Plast Reconstr Surg,* vol. 121, no. 1, pp. 209-217, Jan 2008, doi: 10.1097/01.prs.0000293870.64781.12.

[217] J. P. Fiorellini *et al.*, "Randomized study evaluating recombinant human bone morphogenetic protein-2 for extraction socket augmentation," (in eng), *J Periodontol,* vol. 76, no. 4, pp. 605-13, Apr 2005, doi: 10.1902/jop.2005.76.4.605.

[218] G. M. Jeffrey and P. L. Morgan, "Class III Spine Grafts," in *Clinical Implementation of Bone Regeneration and Maintenance*, B. Mike, R. Nahum, R. Patrick, K. Željka Perić, and J. Ole Eds. Rijeka: IntechOpen, 2019, p. Ch. 3.

[219] E. M. Agency. "Inductos " https://www.ema.europa.eu/en/medicines/human/EPAR/inductos (accessed 2023).

[220] "The FDA Delivers a Late Warning," *The Back Letter,* vol. 23, no. 10, p. 115, 2008, doi: 10.1097/01.BACK.0000339096.22294.a9.

[221] T. Shima, J. T. Keller, M. M. Alvira, F. H. Mayfield, and S. B. Dunsker, "Anterior Cervical Discectomy and Interbody Fusion: An Experimental Study Using a Synthetic Tricalcium Phosphate," (in English), *Journal of Neurosurgery,* vol. 51, no. 4, pp. 533-538, 01 Jan. 1979 1979, doi: https://doi.org/10.3171/jns.1979.51.4.0533.

[222] S. D. Cook *et al.*, "Evaluation of hydroxylapatite graft materials in canine cervical spine fusions," (in eng), *Spine (Phila Pa 1976),* vol. 11, no. 4, pp. 305-9, May 1986, doi: 10.1097/00007632-198605000-00002.

[223] T. Koyama and J. Handa, "Porous hydroxyapatite ceramics for use in neurosurgical practice," *Surgical Neurology,* vol. 25, no. 1, pp. 71-73, 1986/01/01/ 1986, doi: https://doi.org/10.1016/0090-3019(86)90118-7.

[224] S. Robbins, C. Lauryssen, and M. N. Songer, "Use of Nanocrystalline Hydroxyapatite With Autologous BMA and Local Bone in the Lumbar Spine: A Retrospective CT Analysis of Posterolateral Fusion Results," (in eng), *Clin Spine Surg,* vol. 30, no. 3, pp. E192-e197, Apr 2017, doi: 10.1097/bsd.0000000000000091.

[225] S. Bansal, V. Chauhan, S. Sharma, R. Maheshwari, A. Juyal, and S. Raghuvanshi, "Evaluation of hydroxyapatite and beta-tricalcium phosphate mixed with bone marrow aspirate as a bone graft substitute for posterolateral spinal fusion," (in eng), *Indian J Orthop,* vol. 43, no. 3, pp. 234-9, Jul 2009, doi: 10.4103/0019-5413.49387.

[226] A. S. Greenwald, S. D. Boden, V. M. Goldberg, Y. Khan, C. T. Laurencin, and R. N. Rosier, "Bone-graft substitutes: facts, fictions, and applications," (in eng), *J Bone Joint Surg Am,* vol. 83-A Suppl 2 Pt 2, pp. 98-103, 2001, doi: 10.2106/00004623-200100022-00007.

[227] G. M. Calori, E. Mazza, M. Colombo, and C. Ripamonti, "The use of bone-graft substitutes in large bone defects: Any specific needs?," *Injury,* vol. 42, pp. S56-S63, 2011/09/01/ 2011, doi: https://doi.org/10.1016/j.injury.2011.06.011.

[228] F. P. Cammisa, Jr. *et al.*, "Two-year fusion rate equivalency between Grafton DBM gel and autograft in posterolateral spine fusion: a prospective controlled trial employing a side-by-side comparison in the same patient," (in eng), *Spine (Phila Pa 1976),* vol. 29, no. 6, pp. 660-6, Mar 15 2004, doi: 10.1097/01.brs.0000116588.17129.b9.

[229] H. S. An, J. M. Simpson, J. M. Glover, and J. Stephany, "Comparison Between Allograft Plus Demineralized Bone Matrix Versus Autograft in Anterior Cervical Fusion|A Prospective Multicenter Study," *Spine,* vol. 20, no. 20, pp. 2211-2216, 1995.

[Online]. Available: https://journals.lww.com/spinejournal/fulltext/1995/10001/comparison_between_allograft_plus_demineralized.6.aspx.

[230] P. Korovessis, G. Koureas, S. Zacharatos, Z. Papazisis, and E. Lambiris, "Correlative radiological, self-assessment and clinical analysis of evolution in instrumented dorsal and lateral fusion for degenerative lumbar spine disease. Autograft versus coralline hydroxyapatite," (in eng), *Eur Spine J,* vol. 14, no. 7, pp. 630-8, Sep 2005, doi: 10.1007/s00586-004-0855-5.

[231] J. R. McConnell, B. J. Freeman, U. K. Debnath, M. P. Grevitt, H. G. Prince, and J. K. Webb, "A prospective randomized comparison of coralline hydroxyapatite with autograft in cervical interbody fusion," (in eng), *Spine (Phila Pa 1976),* vol. 28, no. 4, pp. 317-23, Feb 15 2003, doi: 10.1097/01.Brs.0000048503.51956.E1.

[232] K. Vaz, K. Verma, T. Protopsaltis, F. Schwab, B. Lonner, and T. Errico, "Bone grafting options for lumbar spine surgery: a review examining clinical efficacy and complications," (in eng), *Sas j,* vol. 4, no. 3, pp. 75-86, 2010, doi: 10.1016/j.esas.2010.01.004.

[233] R. J. Mobbs, M. Chung, and P. J. Rao, "Bone Graft Substitutes for Anterior Lumbar Interbody Fusion," *Orthopaedic Surgery,* vol. 5, no. 2, pp. 77-85, 2013, doi: https://doi.org/10.1111/os.12030.

[234] A. Ho-Shui-Ling, J. Bolander, L. E. Rustom, A. W. Johnson, F. P. Luyten, and C. Picart, "Bone regeneration strategies: Engineered scaffolds, bioactive molecules and stem cells current stage and future perspectives," *Biomaterials,* vol. 180, pp. 143-162, 2018/10/01/ 2018, doi: https://doi.org/10.1016/j.biomaterials.2018.07.017.

[235] J. G. Wright, M. F. Swiontkowski, and J. D. Heckman, "Introducing Levels of Evidence to The Journal," *JBJS,* vol. 85, no. 1, pp. 1-3, 2003. [Online]. Available: https://journals.lww.com/jbjsjournal/fulltext/2003/01000/introducing_levels_of_evidence_to_the_journal.1.aspx.

[236] J. Yang *et al.*, "Is local autogenous morselized bone harvested from decompression through a posterior-transforaminal approach sufficient for single-level interbody fusion in the lower lumbar spine?," *BMC Musculoskeletal Disorders,* vol. 24, no. 1, p. 12, 2023/01/06 2023, doi: 10.1186/s12891-023-06131-4.

[237] A. Yataganbaba, A. Gahukamble, G. Antoniou, B. J. C. Freeman, and P. J. Cundy, "Local Bone Grafting Is Sufficient for Instrumented Adolescent Idiopathic Scoliosis Surgery: A Preliminary Study," (in eng), *J Pediatr Orthop,* vol. 41, no. 8, pp. e641-e645, Sep 1 2021, doi: 10.1097/bpo.0000000000001865.

[238] W. R. Sassard *et al.*, "Augmenting Local Bone with Grafton Demineralized Bone Matrix for Posterolateral Lumbar Spine Fusion: Avoiding Second Site Autologous Bone Harvest," (in eng), *Orthopedics,* vol. 23, no. 10, pp. 1059-64; discussion 1064-5, Oct 2000, doi: 10.3928/0147-7447-20001001-17.

[239] A. R. Vaccaro, H. A. Stubbs, and J. E. Block, "Demineralized bone matrix composite grafting for posterolateral spinal fusion," (in eng), *Orthopedics,* vol. 30, no. 7, pp. 567-70, Jul 2007, doi: 10.3928/01477447-20070701-06.

[240] J. Kang, H. An, A. Hilibrand, S. T. Yoon, E. Kavanagh, and S. Boden, "Grafton and Local Bone Have Comparable Outcomes to Iliac Crest Bone in Instrumented Single-Level Lumbar Fusions," *Spine,* vol. 37, no. 12, pp. 1083-1091, 2012, doi: 10.1097/BRS.0b013e31823ed817.

[241] T. Lerner, V. Bullmann, T. L. Schulte, M. Schneider, and U. Liljenqvist, "A level-1 pilot study to evaluate of ultraporous beta-tricalcium phosphate as a graft extender in the posterior correction of adolescent idiopathic scoliosis," (in eng), *Eur Spine J,* vol. 18, no. 2, pp. 170-9, Feb 2009, doi: 10.1007/s00586-008-0844-1.

[242] C.-C. Niu, T.-T. Tsai, T.-S. Fu, P.-L. Lai, L.-H. Chen, and W.-J. Chen, "A Comparison of Posterolateral Lumbar Fusion Comparing Autograft, Autogenous Laminectomy Bone With Bone Marrow Aspirate, and Calcium Sulphate With Bone Marrow Aspirate: A Prospective Randomized Study," *Spine,* vol. 34, no. 25, pp. 2715-2719, 2009, doi: 10.1097/BRS.0b013e3181b47232.

[243] D. I. Alexander, N. A. Manson, and M. J. Mitchell, "Efficacy of calcium sulfate plus decompression bone in lumbar and lumbosacral spinal fusion: preliminary results in 40 patients," (in eng), *Can J Surg,* vol. 44, no. 4, pp. 262-6, Aug 2001.

[244] W. J. Chen *et al.*, "The fusion rate of calcium sulfate with local autograft bone compared with autologous iliac bone graft for instrumented short-segment spinal fusion," (in eng), *Spine (Phila Pa 1976),* vol. 30, no. 20, pp. 2293-7, Oct 15 2005, doi: 10.1097/01.brs.0000182087.35335.05.

[245] C. M. Menezes, G. C. Lacerda, G. S. O. do Valle, A. de Oliveira Arruda, and E. G. Menezes, "Ceramic bone graft substitute vs autograft in XLIF: a prospective randomized single-center evaluation of radiographic and clinical outcomes," (in eng), *Eur Spine J,* vol. 31, no. 9, pp. 2262-2269, Sep 2022, doi: 10.1007/s00586-022-07275-y.

[246] A. M. Lehr *et al.*, "Increasing Fusion Rate Between 1 and 2 Years After Instrumented Posterolateral Spinal Fusion and the Role of Bone Grafting," (in eng), *Spine (Phila Pa 1976),* vol. 45, no. 20, pp. 1403-1410, Oct 15 2020, doi: 10.1097/brs.0000000000003558.

[247] P. M. Arnold *et al.*, "i-Factor™ Bone Graft vs Autograft in Anterior Cervical Discectomy and Fusion: 2-Year Follow-up of the Randomized Single-Blinded Food and Drug Administration Investigational Device Exemption Study," (in eng), *Neurosurgery,* vol. 83, no. 3, pp. 377-384, Sep 1 2018, doi: 10.1093/neuros/nyx432.

[248] A. W. Gibson *et al.*, "Cellular allograft for multilevel stand-alone anterior cervical discectomy and fusion," (in eng), *Neurosurg Focus,* vol. 50, no. 6, p. E7, Jun 2021, doi: 10.3171/2021.3.Focus2150.

[249] A. Abdelbary and L. Chang, "6 - Tribology of nonmetals," in *Principles of Engineering Tribology*, A. Abdelbary and L. Chang Eds.: Academic Press, 2023, pp. 235-294.

[250] L. Hattou, X. Morandi, J. Lefebvre, P. J. Le Reste, L. Riffaud, and P. L. Hénaux, "Anterior Cervical Interbody Fusion Using Polyetheretherketone Cage Filled with Synthetic Bone Graft in Acute Cervical Spine Injury," *Orthopaedics & Traumatology: Surgery & Research,* vol. 103, no. 1, pp. 61-66, 2017/02/01/ 2017, doi: https://doi.org/10.1016/j.otsr.2016.09.004.

[251] P. Kim, S. Wakai, S. Matsuo, T. Moriyama, and T. Kirino, "Bisegmental cervical interbody fusion using hydroxyapatite implants: surgical results and long-term observation in 70 cases," (in eng), *Journal of Neurosurgery,* vol. 88, no. 1, pp. 21-7, 1998/01/07 1998, doi: 10.3171/jns.1998.88.1.0021.

[252] S. Hirabayashi and K. Kumano, "Contact of hydroxyapatite spacers with split spinous processes in double-door laminoplasty for cervical myelopathy," (in eng), *J Orthop Sci,* vol. 4, no. 4, pp. 264-8, 1999, doi: 10.1007/s007760050102.

[253] A. Merolli, "11 - Bone repair biomaterials in orthopedic surgery," in *Bone Repair Biomaterials (Second Edition)*, K. M. Pawelec and J. A. Planell Eds.: Woodhead Publishing, 2019, pp. 301-327.

[254] E. Andronescu *et al.*, "Chapter 6 - Nano-hydroxyapatite: Novel approaches in biomedical applications," in *Nanobiomaterials in Hard Tissue Engineering*, A. M. Grumezescu Ed.: William Andrew Publishing, 2016, pp. 189-213.

[255] Z. Sheikh, M.-N. Abdallah, A. A. Hanafi, S. Misbahuddin, H. u. Rashid, and M. Glogauer, "Mechanisms of in Vivo Degradation and Resorption of Calcium Phosphate Based Biomaterials," *Materials,* vol. 8, pp. 7913 - 7925, 2015.

[256] P. Sanaei-Rad, T. S. Jafarzadeh Kashi, E. Seyedjafari, and M. Soleimani, "Enhancement of stem cell differentiation to osteogenic lineage on hydroxyapatite-coated hybrid PLGA/gelatin nanofiber scaffolds," (in eng), *Biologicals,* vol. 44, no. 6, pp. 511-516, Nov 2016, doi: 10.1016/j.biologicals.2016.09.002.

[257] C. Herranz-Diez, A. Crawford, R. L. Goodchild, P. V. Hatton, and C. A. Miller, "Stimulation of Metabolic Activity and Cell Differentiation in Osteoblastic and Human Mesenchymal Stem Cells by a Nanohydroxyapatite Paste Bone Graft Substitute," (in eng), *Materials (Basel),* vol. 15, no. 4, Feb 19 2022, doi: 10.3390/ma15041570.

[258] X. Yang, Y. Li, X. Liu, R. Zhang, and Q. Feng, "In Vitro Uptake of Hydroxyapatite Nanoparticles and Their Effect on Osteogenic Differentiation of Human Mesenchymal Stem Cells," (in eng), *Stem Cells Int,* vol. 2018, p. 2036176, 2018, doi: 10.1155/2018/2036176.

[259] P. Arpornmaeklong and M. J. Pressler, "Effects of ß-TCP scaffolds on neurogenic and osteogenic differentiation of human embryonic stem cells," *Annals of Anatomy - Anatomischer Anzeiger,* vol. 215, pp. 52-62, 2018/01/01/ 2018, doi: https://doi.org/10.1016/j.aanat.2017.09.008.

[260] V. Sollazzo *et al.*, "Calcium sulfate stimulates pulp stem cells towards osteoblasts differentiation," (in eng), *Int J Immunopathol Pharmacol,* vol. 24, no. 2 Suppl, pp. 51-7, Apr-Jun 2011, doi: 10.1177/03946320110240s210.

[261] T. Kim, C. W. See, X. Li, and D. Zhu, "Orthopedic implants and devices for bone fractures and defects: Past, present and perspective," *Engineered Regeneration,* vol. 1, pp. 6-18, 2020/01/01/ 2020, doi: https://doi.org/10.1016/j.engreg.2020.05.003.

[262] M. W. Archunan and S. Petronis, "Bone Grafts in Trauma and Orthopaedics," (in eng), *Cureus,* vol. 13, no. 9, p. e17705, Sep 2021, doi: 10.7759/cureus.17705.

[263] K. Ishikawa, "1.116 - Bioactive Ceramics: Cements," in *Comprehensive Biomaterials*, P. Ducheyne Ed. Oxford: Elsevier, 2011, pp. 267-283.

[264] C. Rey, C. Combes, C. Drouet, and D. Grossin, "1.111 - Bioactive Ceramics: Physical Chemistry," in *Comprehensive Biomaterials*, P. Ducheyne Ed. Oxford: Elsevier, 2011, pp. 187-221.

[265] W. Wang and K. W. K. Yeung, "Bone grafts and biomaterials substitutes for bone defect repair: A review," *Bioactive Materials,* vol. 2, no. 4, pp. 224-247, 2017/12/01/ 2017, doi: https://doi.org/10.1016/j.bioactmat.2017.05.007.

[266] A. Jamali, A. Hilpert, J. Debes, P. Afshar, S. Rahban, and R. Holmes, "Hydroxyapatite/calcium carbonate (HA/CC) vs. plaster of Paris: a histomorphometric and radiographic study in a rabbit tibial defect model," (in eng), *Calcif Tissue Int,* vol. 71, no. 2, pp. 172-8, Aug 2002, doi: 10.1007/s00223-001-1087-x.

[267] M. Canillas, P. Pena, A. H. de Aza, and M. A. Rodríguez, "Calcium phosphates for biomedical applications," *Boletín de la Sociedad Española de Cerámica y Vidrio,* vol. 56, no. 3, pp. 91-112, 2017/05/01/ 2017, doi: https://doi.org/10.1016/j.bsecv.2017.05.001.

[268] "Chapter 1 - General Chemistry of the Calcium Orthophosphates," in *Studies in Inorganic Chemistry*, vol. 18, J. C. Elliott Ed.: Elsevier, 1994, pp. 1-62.

[269] L. Wang and G. H. Nancollas, "Calcium orthophosphates: crystallization and dissolution," (in eng), *Chem Rev,* vol. 108, no. 11, pp. 4628-69, Nov 2008, doi: 10.1021/cr0782574.

[270] J. C. Elliott, "The problems of the composition and structure of the mineral components of the hard tissues," (in eng), *Clin Orthop Relat Res,* no. 93, pp. 313-45, Jun 1973, doi: 10.1097/00003086-197306000-00037.

[271] J. Zhao, Y. Liu, W.-b. Sun, and X. Yang, "First detection, characterization, and application of amorphous calcium phosphate in dentistry," *Journal of Dental Sciences,* vol. 7, no. 4, pp. 316-323, 2012/12/01/ 2012, doi: https://doi.org/10.1016/j.jds.2012.09.001.

[272] C. Combes and C. Rey, "Amorphous Calcium Phosphates: Synthesis, Properties and Uses in Biomaterials," *Acta Biomaterialia,* vol. 6, no. 9, pp. 3362-3378, 2010/09/01/ 2010, doi: https://doi.org/10.1016/j.actbio.2010.02.017.

[273] J. D. Termine and A. S. Posner, "Amorphous/rystalline Interrelationships in Bone Minerals," (in eng), *Calcified Tissue Research,* vol. 1, no. 1, pp. 8-23, 1967/12/01 1967, doi: 10.1007/bf02008070.

[274] J. D. Termine, R. E. Wuthier, and A. S. Posner, "Amorphous-Crystalline Mineral Changes During Endochondral and Periosteal Bone Formation," *Proceedings of the Society for Experimental Biology and Medicine,* vol. 125, no. 1, pp. 4-9, 1967, doi: 10.3181/00379727-125-31999.

[275] E. D. Eanes, I. H. Gillessen, and A. S. Posner, "Intermediate States in the Precipitation of Hydroxyapatite," *Nature,* vol. 208, no. 5008, pp. 365-367, 1965/10/01 1965, doi: 10.1038/208365a0.

[276] J. D. Termine and E. D. Eanes, "Comparative chemistry of amorphous and apatitic calcium phosphate preparations," *Calcified Tissue Research,* vol. 10, no. 1, pp. 171-197, 1972/12/01 1972, doi: 10.1007/BF02012548.

[277] M. S.-A. Johnsson and G. H. Nancollas, "The Role of Brushite and Octacalcium Phosphate in Apatite Formation," *Critical Reviews in Oral Biology & Medicine,* vol. 3, no. 1, pp. 61-82, 1992, doi: 10.1177/10454411920030010601.

[278] M. Bohner, "Calcium orthophosphates in medicine: from ceramics to calcium phosphate cements," *Injury,* vol. 31, pp. D37-D47, 2000/12/01/ 2000, doi: https://doi.org/10.1016/S0020-1383(00)80022-4.

[279] A. S. Posner and F. Betts, "Synthetic amorphous calcium phosphate and its relation to bone mineral structure," *Accounts of Chemical Research,* vol. 8, no. 8, pp. 273-281, 1975/08/01 1975, doi: 10.1021/ar50092a003.

[280] S. V. Dorozhkin, "Calcium Phosphates," in *Handbook of Bioceramics and Biocomposites*, I. V. Antoniac Ed. Cham: Springer International Publishing, 2016, pp. 91-118.

[281] K. Ishikawa and E. D. Eanes, "The Hydrolysis of Anhydrous Dicalcium Phosphate into Hydroxyapatite," *Journal of Dental Research,* vol. 72, no. 2, pp. 474-480, 1993, doi: 10.1177/00220345930720020101.

[282] M. T. Fulmer and P. W. Brown, "Hydrolysis of dicalcium phosphate dihydrate to hydroxyapatite," (in eng), *Journal of Materials Science: Materials in Medicine,* vol. 9, no. 4, pp. 197-202, 1998/04/01 1998, doi: 10.1023/a:1008832006277.

[283] L. Morejón-Alonso, R. García Carrodeguas, and J. A. Delgado García-Menocal, "Transformations in CDHA/OCP/β-TCP scaffold during ageing in simulated body fluid at 36.5°C," *Journal of Biomedical Materials Research Part B: Applied Biomaterials,* vol. 84B, no. 2, pp. 386-393, 2008, doi: https://doi.org/10.1002/jbm.b.30882.

[284] H. Monma and T. Kamiya, "Preparation of hydroxyapatite by the hydrolysis of brushite," *Journal of Materials Science,* vol. 22, no. 12, pp. 4247-4250, 1987/12/01 1987, doi: 10.1007/BF01132015.

[285] S. V. Dorozhkin, "Biphasic, triphasic and multiphasic calcium orthophosphates," *Acta Biomaterialia,* vol. 8, no. 3, pp. 963-977, 2012/03/01/ 2012, doi: https://doi.org/10.1016/j.actbio.2011.09.003.

[286] R. Z. LeGeros, R. Kijkowska, and J. P. LeGeros, "Formation and transformation of octacalcium phosphate, OCP: a preliminary report," (in eng), *Scan Electron Microsc,* no. Pt 4, pp. 1771-7, 1984.

[287] O. Gourgas, J. Marulanda, P. Zhang, M. Murshed, and M. Cerruti, "Multidisciplinary Approach to Understand Medial Arterial Calcification," *Arteriosclerosis, Thrombosis, and Vascular Biology,* vol. 38, no. 2, pp. 363-372, 2018, doi: doi:10.1161/ATVBAHA.117.309808.

[288] M. Umemura *et al.*, "Bone inductive activity of hydroxyapatite-bone morphogenetic protein complex," (in jpn), *Nihon Shishubyo Gakkai Kaishi,* vol. 31, no. 3, pp. 860-9, Sep 1989, doi: 10.2329/perio.31.860.

[289] P. Kasten *et al.*, "Ectopic bone formation associated with mesenchymal stem cells in a resorbable calcium deficient hydroxyapatite carrier," *Biomaterials,* vol. 26, no. 29, pp. 5879-5889, 2005/10/01/ 2005, doi: https://doi.org/10.1016/j.biomaterials.2005.03.001.

[290] R. Wang *et al.*, "Nano-Hydroxyapatite Modulates Osteoblast Differentiation Through Autophagy Induction via mTOR Signaling Pathway," (in eng), *J Biomed Nanotechnol,* vol. 15, no. 2, pp. 405-415, Feb 1 2019, doi: 10.1166/jbn.2019.2677.

[291] L. Chow, "Next Generation Calcium Phosphate-Based Biomaterials," *Dental materials journal,* vol. 28, pp. 1-10, 02/01 2009, doi: 10.4012/dmj.28.1.

[292] M. S. Nickoli and W. K. Hsu, "Ceramic-based bone grafts as a bone grafts extender for lumbar spine arthrodesis: a systematic review," (in eng), *Global Spine J,* vol. 4, no. 3, pp. 211-6, Aug 2014, doi: 10.1055/s-0034-1378141.

[293] K. Lin and J. Chang, "1 - Structure and Properties of Hydroxyapatite for Biomedical Applications," in *Hydroxyapatite (Hap) for Biomedical Applications*, M. Mucalo Ed.: Woodhead Publishing, 2015, pp. 3-19.

[294] A. Fihri, C. Len, R. S. Varma, and A. Solhy, "Hydroxyapatite: A review of syntheses, structure and applications in heterogeneous catalysis," *Coordination Chemistry Reviews,* vol. 347, pp. 48-76, 2017/09/15/ 2017, doi: https://doi.org/10.1016/j.ccr.2017.06.009.

[295] A. Haider, S. Haider, S. S. Han, and I.-K. Kang, "Recent advances in the synthesis, functionalization and biomedical applications of hydroxyapatite: a review," *RSC Advances,* 10.1039/C6RA26124H vol. 7, no. 13, pp. 7442-7458, 2017, doi: 10.1039/C6RA26124H.

[296] S. V. Dorozhkin, "Calcium orthophosphates (CaPO(4)): occurrence and properties," (in eng), *Prog Biomater,* vol. 5, pp. 9-70, 2016, doi: 10.1007/s40204-015-0045-z.

[297] K. J. Münzenberg and M. Gebhardt, "Crystallographic studies of bone minerals," (in ger), *Dtsch Med Wochenschr,* vol. 94, no. 25, pp. 1325-30, Jun 20 1969, doi: 10.1055/s-0028-1111216. Kristallographische Untersuchungen der Knochenminerale.

[298] Z. Zhuang, H. Yoshimura, and M. Aizawa, "Synthesis and ultrastructure of plate-like apatite single crystals as a model for tooth enamel," *Materials Science and Engineering: C,* vol. 33, no. 5, pp. 2534-2540, 2013/07/01/ 2013, doi: https://doi.org/10.1016/j.msec.2013.02.035.

[299] C. Liu, C. Shao, L. Zhang, and Q. Huang, "Chapter 3 - Biomaterials and MSCs composites in regenerative medicine," in *Mesenchymal Stem Cells*, L. Zhang, Z. Han, J. Wang, Z. Li, and Q. Huang Eds.: Academic Press, 2023, pp. 69-99.

[300] T. G. P. Galindo, Y. Chai, and M. Tagaya, "Hydroxyapatite Nanoparticle Coating on Polymer for Constructing Effective Biointeractive Interfaces," *Journal of Nanomaterials,* vol. 2019, p. 6495239, 2019/01/03 2019, doi: 10.1155/2019/6495239.

[301] I. M. Zougrou *et al.*, "Ca L2,3-edge XANES and Sr K-edge EXAFS study of hydroxyapatite and fossil bone apatite," (in eng), *Naturwissenschaften,* vol. 103, no. 7-8, p. 60, Aug 2016, doi: 10.1007/s00114-016-1383-y.

[302] M. Ben Osman *et al.*, "Discrimination of Surface and Bulk Structure of Crystalline Hydroxyapatite Nanoparticles by NMR," *The Journal of Physical Chemistry C,* vol. 119, no. 40, pp. 23008-23020, 2015/10/08 2015, doi: 10.1021/acs.jpcc.5b08732.

[303] H. B. Lu, C. T. Campbell, D. J. Graham, and B. D. Ratner, "Surface characterization of hydroxyapatite and related calcium phosphates by XPS and TOF-SIMS," (in eng), *Anal Chem,* vol. 72, no. 13, pp. 2886-94, Jul 1 2000, doi: 10.1021/ac990812h.

[304] "Chapter 3 - Hydroxyapatite and Nonstoichiometric Apatites," in *Studies in Inorganic Chemistry*, vol. 18, J. C. Elliott Ed.: Elsevier, 1994, pp. 111-189.

[305] G. Ma and X. Y. Liu, "Hydroxyapatite: Hexagonal or Monoclinic?," *Crystal Growth & Design,* vol. 9, no. 7, pp. 2991-2994, 2009/07/01 2009, doi: 10.1021/cg900156w.

[306] J. Elliott, "Further Studies of Structure of Dental Enamel and Carbonate Apatites Using Polarized Infrared Spectroscopy," in *Journal of Dental Research*, 1962, vol. 41, no. 6: Amer Assoc Dental Research 1619 Duke St, Alexandria, VA 22314, pp. 1251-&.

[307] M. I. Kay, R. A. Young, and A. S. Posner, "Crystal Structure of Hydroxyapatite," *Nature,* vol. 204, no. 4963, pp. 1050-1052, 1964/12/01 1964, doi: 10.1038/2041050a0.

[308] M. Vidotto *et al.*, "A Comparative EPR Study of Non-Substituted and Mg-Substituted Hydroxyapatite Behaviour in Model Media and during Accelerated Ageing," *Crystals,* vol. 12, no. 2, p. 297, 2022. [Online]. Available: https://www.mdpi.com/2073-4352/12/2/297.

[309] N. Y. Mostafa and P. W. Brown, "Computer simulation of stoichiometric hydroxyapatite: Structure and substitutions," *Journal of Physics and Chemistry of Solids,* vol. 68, no. 3, pp. 431-437, 2007/03/01/ 2007, doi: https://doi.org/10.1016/j.jpcs.2006.12.011.

[310] E. Boanini, M. Gazzano, and A. Bigi, "Ionic substitutions in calcium phosphates synthesized at low temperature," *Acta Biomaterialia,* vol. 6, no. 6, pp. 1882-1894, 2010/06/01/ 2010, doi: https://doi.org/10.1016/j.actbio.2009.12.041.

[311] Z. Evis and T. J. Webster, "Nanosize hydroxyapatite: doping with various ions," *Advances in Applied Ceramics,* vol. 110, no. 5, pp. 311-321, 2011/07/01 2011, doi: 10.1179/1743676110Y.0000000005.

[312] V. Uskoković, "The Role of Hydroxyl Channel in Defining Selected Physicochemical Peculiarities Exhibited by Hydroxyapatite," (in eng), *RSC Adv,* vol. 5, pp. 36614-36633, 2015, doi: 10.1039/c4ra17180b.

[313] J. Jeong, J. H. Kim, J. H. Shim, N. S. Hwang, and C. Y. Heo, "Bioactive calcium phosphate materials and applications in bone regeneration," *Biomaterials Research,* vol. 23, no. 1, p. 4, 2019/01/14 2019, doi: 10.1186/s40824-018-0149-3.

[314] R. K. Surowiec, M. R. Allen, and J. M. Wallace, "Bone hydration: How we can evaluate it, what can it tell us, and is it an effective therapeutic target?," *Bone Reports,* vol. 16, p. 101161, 2022/06/01/ 2022, doi: https://doi.org/10.1016/j.bonr.2021.101161.

[315] I. S. Harding, N. Rashid, and K. A. Hing, "Surface charge and the effect of excess calcium ions on the hydroxyapatite surface," *Biomaterials,* vol. 26, no. 34, pp. 6818-6826, 2005/12/01/ 2005, doi: https://doi.org/10.1016/j.biomaterials.2005.04.060.

[316] S. Chen, Y. Shi, X. Zhang, and J. Ma, "Biomimetic synthesis of Mg-substituted hydroxyapatite nanocomposites and three-dimensional printing of composite scaffolds for bone regeneration," *Journal of Biomedical Materials Research Part A,* vol. 107, no. 11, pp. 2512-2521, 2019, doi: https://doi.org/10.1002/jbm.a.36757.

[317] R. J. Friederichs, H. F. Chappell, D. V. Shepherd, and S. M. Best, "Synthesis, characterization and modelling of zinc and silicate co-substituted hydroxyapatite," *Journal of The Royal Society Interface,* vol. 12, no. 108, p. 20150190, 2015, doi: doi:10.1098/rsif.2015.0190.

[318] C.-S. Hsu, S. L. Haag, M. T. Bernards, and Q. Li, "Effects of chloride substitution on physical, mechanical, and biological properties of hydroxyapatite," *Ceramics International,* vol. 47, no. 9, pp. 13207-13215, 2021/05/01/ 2021, doi: https://doi.org/10.1016/j.ceramint.2021.01.186.

[319] G.-I. Kontogianni *et al.*, "Osteogenic Potential of Nano-Hydroxyapatite and Strontium-Substituted Nano-Hydroxyapatite," *Nanomaterials,* vol. 13, no. 12, p. 1881, 2023. [Online]. Available: https://www.mdpi.com/2079-4991/13/12/1881.

[320] R. G, B. Venkatesan, S. N. Jaisankar, P. Rajashree, and S. Balakumar, "Interplay between surface chemistry and osteogenic behaviour of sulphate substituted nano-

hydroxyapatite," *Materials Science and Engineering: C,* vol. 120, p. 111617, 2021/01/01/ 2021, doi: https://doi.org/10.1016/j.msec.2020.111617.

[321] A. Bianco, I. Cacciotti, M. Lombardi, L. Montanaro, E. Bemporad, and M. Sebastiani, "F-substituted hydroxyapatite nanopowders: Thermal stability, sintering behaviour and mechanical properties," *Ceramics International,* vol. 36, no. 1, pp. 313-322, 2010/01/01/ 2010, doi: https://doi.org/10.1016/j.ceramint.2009.09.007.

[322] P. H. Oliveira *et al.*, "Manganese behavior in hydroxyapatite crystals revealed by X-ray difference Fourier maps," *Ceramics International,* vol. 46, no. 8, Part A, pp. 10585-10597, 2020/06/01/ 2020, doi: https://doi.org/10.1016/j.ceramint.2020.01.062.

[323] J. P. Lafon, E. Champion, and D. Bernache-Assollant, "Processing of AB-type carbonated hydroxyapatite Ca10−x(PO4)6−x(CO3)x(OH)2−x−2y(CO3)y ceramics with controlled composition," *Journal of the European Ceramic Society,* vol. 28, no. 1, pp. 139-147, 2008/01/01/ 2008, doi: https://doi.org/10.1016/j.jeurceramsoc.2007.06.009.

[324] S. Joseph, K. Genasan, U. Anjaneyalu, A. Livingston, S. Samuel, and S. Sasikumar, "Biomineralization and mechanical studies of sodium substituted hydroxyapatite by a time-saving combustion route," *ChemistrySelect,* vol. 8, no. 41, p. e202302660, 2023/11/06 2023, doi: https://doi.org/10.1002/slct.202302660.

[325] K. Pajor, L. Pajchel, B. Kolodziejska, and J. Kolmas, "Selenium-Doped Hydroxyapatite Nanocrystals–Synthesis, Physicochemical Properties and Biological Significance," *Crystals*, vol. 8, no. 5*,* doi: 10.3390/cryst8050188.

[326] D. A. Nowicki, J. M. S. Skakle, and I. R. Gibson, "Potassium–carbonate co-substituted hydroxyapatite compositions: maximising the level of carbonate uptake for potential CO2 utilisation options," *Materials Advances,* 10.1039/D1MA00676B vol. 3, no. 3, pp. 1713-1728, 2022, doi: 10.1039/D1MA00676B.

[327] K. Matsunaga, "First-principles study of substitutional magnesium and zinc in hydroxyapatite and octacalcium phosphate," *The Journal of Chemical Physics,* vol. 128, no. 24, 2008/06/28 2008, doi: 10.1063/1.2940337.

[328] M. Iafisco, A. Ruffini, A. Adamiano, S. Sprio, and A. Tampieri, "Biomimetic magnesium–carbonate-apatite nanocrystals endowed with strontium ions as anti-osteoporotic trigger," *Materials Science and Engineering: C,* vol. 35, pp. 212-219, 2014/02/01/ 2014, doi: https://doi.org/10.1016/j.msec.2013.11.009.

[329] P. Quint, J. Althoff, H. J. Höhling, A. Boyde, and W. A. Laabs, "Characteristic molar ratios of magnesium, carbon dioxide, calcium and phosphorus in the mineralizing fracture callus and predentine," (in eng), *Calcif Tissue Int,* vol. 32, no. 3, pp. 257-61, 1980, doi: 10.1007/bf02408549.

[330] R. K. Rude, F. R. Singer, and H. E. Gruber, "Skeletal and Hormonal Effects of Magnesium Deficiency," *Journal of the American College of Nutrition,* vol. 28, no. 2, pp. 131-141, 2009/04/01 2009, doi: 10.1080/07315724.2009.10719764.

[331] M. M. Belluci, G. Giro, R. A. L. Del Barrio, R. M. R. Pereira, E. Marcantonio, Jr., and S. R. P. Orrico, "Effects of magnesium intake deficiency on bone metabolism and bone tissue around osseointegrated implants," (in eng), *Clin Oral Implants Res,* vol. 22, no. 7, pp. 716-721, Jul 2011, doi: 10.1111/j.1600-0501.2010.02046.x.

[332] S. Bernick and G. F. Hungerford, "Effect of Dietary Magnesium Deficiency on the Bones and Teeth of Rats," *Journal of Dental Research,* vol. 44, no. 6, pp. 1317-1324, 1965/11/01 1965, doi: 10.1177/00220345650440063401.

[333] G. Stendig-Lindberg, W. Koeller, A. Bauer, and P. M. Rob, "Experimentally induced prolonged magnesium deficiency causes osteoporosis in the rat," *European Journal of Internal Medicine,* vol. 15, no. 2, pp. 97-107, 2004/04/01/ 2004, doi: https://doi.org/10.1016/j.ejim.2004.01.003.

[334] T. Wang *et al.*, "miR-765 inhibits the osteogenic differentiation of human bone marrow mesenchymal stem cells by targeting BMP6 via regulating the BMP6/Smad1/5/9 signaling pathway," *Stem Cell Research & Therapy,* vol. 11, no. 1, p. 62, 2020/02/14 2020, doi: 10.1186/s13287-020-1579-0.

[335] Finceramica and T. Holding. "Sintlife: moldable bone substitute." (accessed 2nd June 2019, 2019).

[336] G. B. Bròdano *et al.*, "Hydroxyapatite-Based Biomaterials Versus Autologous Bone Graft in Spinal Fusion: An In Vivo Animal Study," *Spine,* vol. 39, no. 11, pp. E661-E668, 2014, doi: 10.1097/brs.0000000000000311.

[337] C. Griffoni *et al.*, "Ceramic bone graft substitute (Mg-HA) in spinal fusion: A prospective pilot study," (in English), *Frontiers in Bioengineering and Biotechnology,* Original Research vol. 10, 2022-November-17 2022, doi: 10.3389/fbioe.2022.1050495.

[338] Z. Zhao, M. Espanol, J. Guillem-Marti, D. Kempf, A. Diez-Escudero, and M. P. Ginebra, "Ion-doping as a strategy to modulate hydroxyapatite nanoparticle internalization," *Nanoscale,* 10.1039/C5NR05262A vol. 8, no. 3, pp. 1595-1607, 2016, doi: 10.1039/C5NR05262A.

[339] M. Mehrjoo, J. Javadpour, M. Shokrgozar, M. Farokhi, S. Javadian, and S. Bonakdar, "Effect of magnesium substitution on structural and biological properties of synthetic hydroxyapatite powder," *Materials Express,* vol. 5, 02/01 2015, doi: 10.1166/mex.2015.1205.

[340] N. C. Andrés, N. L. D'Elía, J. M. Ruso, A. E. Campelo, V. L. Massheimer, and P. V. Messina, "Manipulation of Mg2+–Ca2+ Switch on the Development of Bone Mimetic Hydroxyapatite," *ACS Applied Materials & Interfaces,* vol. 9, no. 18, pp. 15698-15710, 2017/05/10 2017, doi: 10.1021/acsami.7b02241.

[341] X. Lijuan, J. Liuyun, X. Chengdong, and J. Lixin, "Effect of different synthesis conditions on the microstructure, crystallinity and solubility of Mg-substituted hydroxyapatite nanopowder," *Advanced Powder Technology,* vol. 25, no. 3, pp. 1142-1146, 2014/05/01/ 2014, doi: https://doi.org/10.1016/j.apt.2014.02.019.

[342] A. Farzadi, F. Bakhshi, M. Solati-Hashjin, M. Asadi-Eydivand, and N. A. a. Osman, "Magnesium incorporated hydroxyapatite: Synthesis and structural properties characterization," *Ceramics International,* vol. 40, no. 4, pp. 6021-6029, 2014/05/01/ 2014, doi: https://doi.org/10.1016/j.ceramint.2013.11.051.

[343] I. Cacciotti, A. Bianco, M. Lombardi, and L. Montanaro, "Mg-substituted hydroxyapatite nanopowders: Synthesis, thermal stability and sintering behaviour," *Journal of the European Ceramic Society,* vol. 29, no. 14, pp. 2969-2978, 2009/11/01/ 2009, doi: https://doi.org/10.1016/j.jeurceramsoc.2009.04.038.

[344] D. Predoi, S. L. Iconaru, M. V. Predoi, G. E. Stan, and N. Buton, "Synthesis, Characterization, and Antimicrobial Activity of Magnesium-Doped Hydroxyapatite Suspensions," *Nanomaterials,* vol. 9, no. 9, p. 1295, 2019. [Online]. Available: https://www.mdpi.com/2079-4991/9/9/1295.

[345] S. Adzila, R. Singh, I. Sopyan, C. Y. Tan, M. Abd Shukor, and W. Teng, *Mechanochemical Synthesis of Magnesium Doped Hydroxyapatite: Powder Characterization*. 2013.

[346] E. Landi, G. Logroscino, L. Proietti, A. Tampieri, M. Sandri, and S. Sprio, "Biomimetic Mg-substituted hydroxyapatite: from synthesis to in vivo behaviour," *Journal of Materials Science: Materials in Medicine,* vol. 19, no. 1, pp. 239-247, 2008/01/01 2008, doi: 10.1007/s10856-006-0032-y.

[347] P. J. Marie *et al.*, "An uncoupling agent containing strontium prevents bone loss by depressing bone resorption and maintaining bone formation in estrogen-deficient rats," *Journal of Bone and Mineral Research,* vol. 8, no. 5, pp. 607-615, 1993/05/01 1993, doi: https://doi.org/10.1002/jbmr.5650080512.

[348] S. G. Dahl *et al.*, "Incorporation and distribution of strontium in bone," *Bone,* vol. 28, no. 4, pp. 446-453, 2001/04/01/ 2001, doi: https://doi.org/10.1016/S8756-3282(01)00419-7.

[349] P. J. Marie, P. Ammann, G. Boivin, and C. Rey, "Mechanisms of action and therapeutic potential of strontium in bone," (in eng), *Calcif Tissue Int,* vol. 69, no. 3, pp. 121-9, Sep 2001, doi: 10.1007/s002230010055.

[350] P. J. Marie, "Strontium as therapy for osteoporosis," *Current Opinion in Pharmacology,* vol. 5, no. 6, pp. 633-636, 2005/12/01/ 2005, doi: https://doi.org/10.1016/j.coph.2005.05.005.

[351] G. Boivin, A. Doublier, and D. Farlay, "Strontium ranelate – a promising therapeutic principle in osteoporosis," *Journal of Trace Elements in Medicine and Biology,* vol. 26, no. 2, pp. 153-156, 2012/06/01/ 2012, doi: https://doi.org/10.1016/j.jtemb.2012.03.013.

[352] P. J. Meunier *et al.*, "The Effects of Strontium Ranelate on the Risk of Vertebral Fracture in Women with Postmenopausal Osteoporosis," *New England Journal of Medicine,* vol. 350, no. 5, pp. 459-468, 2004, doi: 10.1056/NEJMoa022436.

[353] S. Peng *et al.*, "Osteoprotegerin deficiency attenuates strontium-mediated inhibition of osteoclastogenesis and bone resorption," *Journal of Bone and Mineral Research,* vol. 26, no. 6, pp. 1272-1282, 2011, doi: 10.1002/jbmr.325.

[354] E. Bonnelye, A. Chabadel, F. Saltel, and P. Jurdic, "Dual effect of strontium ranelate: Stimulation of osteoblast differentiation and inhibition of osteoclast formation and resorption in vitro," *Bone,* vol. 42, no. 1, pp. 129-138, 2008/01/01/ 2008, doi: https://doi.org/10.1016/j.bone.2007.08.043.

[355] S. J. S. Flora and P. Vidhu, "Chapter 22 - Metals," in *Side Effects of Drugs Annual*, vol. 37, S. D. Ray Ed.: Elsevier, 2015, pp. 243-257.

[356] M. S. Ali *et al.*, "Comparative cardiovascular safety of strontium ranelate and bisphosphonates: a multi-database study in 5 EU countries by the EU-ADR Alliance," (in eng), *Osteoporos Int,* vol. 31, no. 12, pp. 2425-2438, Dec 2020, doi: 10.1007/s00198-020-05580-0.

[357] J.-Y. Reginster, "Cardiac concerns associated with strontium ranelate," *Expert Opinion on Drug Safety,* vol. 13, no. 9, pp. 1209-1213, 2014/09/01 2014, doi: 10.1517/14740338.2014.939169.

[358] "Protelos/Osseor to remain available but with further restrictions." The European Medicines Agency. https://www.ema.europa.eu/en/medicines/human/referrals/protelos-osseor (accessed 2023).

[359] W.-H. Ren *et al.*, "Strontium-Doped Hydroxyapatite Promotes Osteogenic Differentiation of Bone Marrow Mesenchymal Stem Cells in Osteoporotic Rats through the CaSR-JAK2/STAT3 Signaling Pathway," *Advanced NanoBiomed Research,* vol. 2, no. 9, p. 2200018, 2022, doi: https://doi.org/10.1002/anbr.202200018.

[360] M.-D. Yan *et al.*, "Does the incorporation of strontium into calcium phosphate improve bone repair? A meta-analysis," *BMC Oral Health,* vol. 22, no. 1, p. 62, 2022/03/08 2022, doi: 10.1186/s12903-022-02092-7.

[361] E. Landi, A. Tampieri, G. Celotti, S. Sprio, M. Sandri, and G. Logroscino, "Sr-substituted hydroxyapatites for osteoporotic bone replacement," *Acta Biomaterialia,* vol. 3, no. 6, pp. 961-969, 2007/11/01/ 2007, doi: https://doi.org/10.1016/j.actbio.2007.05.006.

[362] Z. Y. Li *et al.*, "Chemical composition, crystal size and lattice structural changes after incorporation of strontium into biomimetic apatite," *Biomaterials,* vol. 28, no. 7, pp. 1452-1460, 2007/03/01/ 2007, doi: https://doi.org/10.1016/j.biomaterials.2006.11.001.

[363] S.-W. Tsai *et al.*, "Fabrication and Characterization of Strontium-Substituted Hydroxyapatite-CaO-$CaCO_3$ Nanofibers with a Mesoporous Structure as Drug Delivery Carriers," (in eng), *Pharmaceutics,* vol. 10, no. 4, p. 179, 2018, doi: 10.3390/pharmaceutics10040179.

[364] A. Mocanu *et al.*, "Ion release from hydroxyapatite and substituted hydroxyapatites in different immersion liquids: in vitro experiments and theoretical modelling study," (in eng), *R Soc Open Sci,* vol. 8, no. 1, p. 201785, Jan 2021, doi: 10.1098/rsos.201785.

[365] N. D. Ravi, R. Balu, and T. S. Sampath Kumar, "Strontium-Substituted Calcium Deficient Hydroxyapatite Nanoparticles: Synthesis, Characterization, and Antibacterial Properties," *Journal of the American Ceramic Society,* vol. 95, no. 9, pp. 2700-2708, 2012, doi: https://doi.org/10.1111/j.1551-2916.2012.05262.x.

[366] L. Stipniece *et al.*, "Strontium substituted hydroxyapatite promotes direct primary human osteoblast maturation," *Ceramics International,* vol. 47, no. 3, pp. 3368-3379, 2021/02/01/ 2021, doi: https://doi.org/10.1016/j.ceramint.2020.09.182.

[367] A. Ressler, M. Cvetnić, M. Antunović, I. Marijanović, M. Ivanković, and H. Ivanković, "Strontium substituted biomimetic calcium phosphate system derived from cuttlefish bone," *Journal of Biomedical Materials Research Part B: Applied Biomaterials,* vol. 108, no. 4, pp. 1697-1709, 2020, doi: https://doi.org/10.1002/jbm.b.34515.

[368] A. Bigi, E. Boanini, C. Capuccini, and M. Gazzano, "Strontium-substituted hydroxyapatite nanocrystals," *Inorganica Chimica Acta,* vol. 360, no. 3, pp. 1009-1016, 2007/02/15/ 2007, doi: https://doi.org/10.1016/j.ica.2006.07.074.

[369] Y. Zhuang *et al.*, "Promoting vascularized bone regeneration via strontium-incorporated hydroxyapatite bioceramic," *Materials & Design,* vol. 234, p. 112313, 2023/10/01/ 2023, doi: https://doi.org/10.1016/j.matdes.2023.112313.

[370] V. Aina *et al.*, "Magnesium- and strontium-co-substituted hydroxyapatite: the effects of doped-ions on the structure and chemico-physical properties," *Journal of materials science. Materials in medicine,* vol. 23, 09/29 2012, doi: 10.1007/s10856-012-4767-3.

[371] Z. Geng *et al.*, "Synthesis, characterization and the formation mechanism of magnesium- and strontium-substituted hydroxyapatite," *Journal of Materials Chemistry B,* 10.1039/C4TB02148G vol. 3, no. 18, pp. 3738-3746, 2015, doi: 10.1039/C4TB02148G.

[372] I. R. de Lima *et al.*, "Understanding the impact of divalent cation substitution on hydroxyapatite: An in vitro multiparametric study on biocompatibility," *Journal of Biomedical Materials Research Part A,* vol. 98A, no. 3, pp. 351-358, 2011, doi: 10.1002/jbm.a.33126.

[373] Z. Geng *et al.*, "Synthesis, characterization and biological evaluation of strontium/magnesium-co-substituted hydroxyapatite," (in eng), *J Biomater Appl,* vol. 31, no. 1, pp. 140-51, Jul 2016, doi: 10.1177/0885328216633892.

[374] E. Landi, J. Uggeri, V. Medri, and S. Guizzardi, "Sr, Mg cosubstituted HA porous macro-granules: potentialities as resorbable bone filler with antiosteoporotic functions," (in eng), *J Biomed Mater Res A,* vol. 101, no. 9, pp. 2481-90, Sep 2013, doi: 10.1002/jbm.a.34553.

[375] F. Scalera, B. Palazzo, A. Barca, and F. Gervaso, "Sintering of magnesium-strontium doped hydroxyapatite nanocrystals: Towards the production of 3D biomimetic bone scaffolds," *Journal of Biomedical Materials Research Part A,* vol. 108, no. 3, pp. 633-644, 2020, doi: https://doi.org/10.1002/jbm.a.36843.

[376] M. M. Kadhim, H. A. AlMashhadani, R. D. Hashim, A. A. Khadom, K. A. Salih, and A. W. Salman, "Effect of Sr/Mg co-substitution on corrosion resistance properties of hydroxyapatite coated on Ti–6Al–4V dental alloys," *Journal of Physics and Chemistry of Solids,* vol. 161, p. 110450, 2022/02/01/ 2022, doi: https://doi.org/10.1016/j.jpcs.2021.110450.

[377] P. de Alcântara Pessôa Filho, G. A. Medeiros Hirata, É. O. Watanabe, and E. A. Miranda, "2.49 - Precipitation and Crystallization," in *Comprehensive Biotechnology (Third Edition)*, M. Moo-Young Ed. Oxford: Pergamon, 2019, pp. 725-738.

[378] J. W. Mullin, "3 - Solutions and Solubility," in *Crystallization (Fourth Edition)*, J. W. Mullin Ed. Oxford: Butterworth-Heinemann, 2001, pp. 86-134.

[379] P. H. Karpinski and J. S. Wey, "6 - Precipitation Processes," in *Handbook of Industrial Crystallization (Second Edition)*, A. S. Myerson Ed. Woburn: Butterworth-Heinemann, 2002, pp. 141-160.

[380] J. W. Mullin, "5 - Nucleation," in *Crystallization (Fourth Edition)*, J. W. Mullin Ed. Oxford: Butterworth-Heinemann, 2001, pp. 181-215.

[381] M. Celikbilek Ersundu, A. E. Ersundu, and Ş. Aydın, "Crystallization Kinetics of Amorphous Materials," 2012, pp. 127-162.

[382] T. B. Massalski, "Phase Diagrams," in *Encyclopedia of Materials: Science and Technology*, K. H. J. Buschow *et al.* Eds. Oxford: Elsevier, 2001, pp. 6842-6851.

[383] Y. Wang, J. He, C. Liu, W. H. Chong, and H. Chen, "Thermodynamics versus Kinetics in Nanosynthesis," *Angewandte Chemie International Edition,* vol. 54, no. 7, pp. 2022-2051, 2015, doi: https://doi.org/10.1002/anie.201402986.

[384] M. Nicol, N. Welham, and G. Senanayake, "3 - Precipitation and Crystallization," in *Hydrometallurgy*, M. Nicol, N. Welham, and G. Senanayake Eds.: Elsevier, 2022, pp. 85-115.

[385] D. Gebauer, M. Kellermeier, J. D. Gale, L. Bergström, and H. Cölfen, "Pre-nucleation clusters as solute precursors in crystallisation," *Chemical Society Reviews,* 10.1039/C3CS60451A vol. 43, no. 7, pp. 2348-2371, 2014, doi: 10.1039/C3CS60451A.

[386] D. J. Pietrzyk and C. W. Frank, "Chapter Seven - Precipitation Methods," in *Analytical Chemistry*, D. J. Pietrzyk and C. W. Frank Eds.: Academic Press, 1979, pp. 90-130.

[387] "Anti-Solvent Crystallization," in *Crystallization of Organic Compounds*, 2023, pp. 223-252.

[388] D. Erdemir, A. Y. Lee, and A. S. Myerson, "Crystal Nucleation," in *Handbook of Industrial Crystallization*, D. Erdemir, A. Y. Lee, and A. S. Myerson Eds., 3 ed. Cambridge: Cambridge University Press, 2019, pp. 76-114.

[389] D. Winter, P. Virnau, and K. Binder, "Heterogeneous nucleation at a wall near a wetting transition: a Monte Carlo test of the classical theory," *Journal of Physics: Condensed Matter,* vol. 21, no. 46, p. 464118, 2009/10/29 2009, doi: 10.1088/0953-8984/21/46/464118.

[390] W. Ostwald, "Studien über die Bildung und Umwandlung fester Körper," *1. Abhandlung: Übersättigung und Überkaltung,* vol. 22U, no. 1, pp. 289-330, 1897, doi: doi:10.1515/zpch-1897-2233.

[391] P. T. Cardew, "Ostwald Rule of Stages–Myth or Reality?," *Crystal Growth & Design,* vol. 23, no. 6, pp. 3958-3969, 2023/06/07 2023, doi: 10.1021/acs.cgd.2c00141.

[392] M. Volmer and A. Weber, "Keimbildung in übersättigten Gebilden," vol. 119U, no. 1, pp. 277-301, 1926, doi: doi:10.1515/zpch-1926-11927.

[393] R. Becker and W. Döring, "Kinetische Behandlung der Keimbildung in übersättigten Dämpfen," *Annalen der Physik,* vol. 416, no. 8, pp. 719-752, 1935, doi: https://doi.org/10.1002/andp.19354160806.

[394] D. W. Oxtoby, "Homogeneous nucleation: theory and experiment," *Journal of Physics: Condensed Matter,* vol. 4, no. 38, p. 7627, 1992/09/21 1992, doi: 10.1088/0953-8984/4/38/001.

[395] D. Erdemir, A. Y. Lee, and A. S. Myerson, "Nucleation of Crystals from Solution: Classical and Two-Step Models," *Accounts of Chemical Research,* vol. 42, no. 5, pp. 621-629, 2009/05/19 2009, doi: 10.1021/ar800217x.

[396] T. P. Feenstra and P. L. De Bruyn, "The ostwald rule of stages in precipitation from highly supersaturated solutions: a model and its application to the formation of the nonstoichiometric amorphous calcium phosphate precursor phase," *Journal of Colloid and Interface Science,* vol. 84, no. 1, pp. 66-72, 1981/11/01/ 1981, doi: https://doi.org/10.1016/0021-9797(81)90260-5.

[397] W. J. E. M. Habraken *et al.*, "Ion-association complexes unite classical and non-classical theories for the biomimetic nucleation of calcium phosphate," *Nature Communications,* vol. 4, no. 1, p. 1507, 2013/02/19 2013, doi: 10.1038/ncomms2490.

[398] X. Yang, M. Wang, Y. Yang, B. Cui, Z. Xu, and X. Yang, "Physical origin underlying the prenucleation-cluster-mediated nonclassical nucleation pathways for calcium phosphate," *Physical Chemistry Chemical Physics,* 10.1039/C9CP00919A vol. 21, no. 27, pp. 14530-14540, 2019, doi: 10.1039/C9CP00919A.

[399] G. Mancardi, U. Terranova, and N. H. de Leeuw, "Calcium Phosphate Prenucleation Complexes in Water by Means of ab Initio Molecular Dynamics Simulations," *Crystal Growth & Design,* vol. 16, no. 6, pp. 3353-3358, 2016/06/01 2016, doi: 10.1021/acs.cgd.6b00327.

[400] D. Gebauer and H. Cölfen, "Prenucleation clusters and non-classical nucleation," *Nano Today,* vol. 6, no. 6, pp. 564-584, 2011/12/01/ 2011, doi: https://doi.org/10.1016/j.nantod.2011.10.005.

[401] A. L. Boskey and A. S. Posner, "Conversion of amorphous calcium phosphate to microcrystalline hydroxyapatite. A pH-dependent, solution-mediated, solid-solid conversion," *The Journal of Physical Chemistry,* vol. 77, no. 19, pp. 2313-2317, 1973/09/01 1973, doi: 10.1021/j100638a011.

[402] C.-G. Wang *et al.*, "Crystallization at Multiple Sites inside Particles of Amorphous Calcium Phosphate," *Crystal Growth & Design,* vol. 9, no. 6, pp. 2620-2626, 2009/06/03 2009, doi: 10.1021/cg801069t.

[403] J. J. De Yoreo *et al.*, "CRYSTAL GROWTH. Crystallization by particle attachment in synthetic, biogenic, and geologic environments," (in eng), *Science,* vol. 349, no. 6247, p. aaa6760, Jul 31 2015, doi: 10.1126/science.aaa6760.

[404] G. Satchanska, S. Davidova, and P. D. Petrov, "Natural and Synthetic Polymers for Biomedical and Environmental Applications," (in eng), *Polymers (Basel),* vol. 16, no. 8, Apr 20 2024, doi: 10.3390/polym16081159.

[405] S. Mathews, P. K. Gupta, R. Bhonde, and S. Totey, "Chitosan enhances mineralization during osteoblast differentiation of human bone marrow-derived mesenchymal stem cells, by upregulating the associated genes," (in eng), *Cell Prolif,* vol. 44, no. 6, pp. 537-49, Dec 2011, doi: 10.1111/j.1365-2184.2011.00788.x.

[406] Y. Li, J. H. Kim, E. H. Choi, and I. Han, "Promotion of osteogenic differentiation by non-thermal biocompatible plasma treated chitosan scaffold," *Scientific Reports,* vol. 9, no. 1, p. 3712, 2019/03/06 2019, doi: 10.1038/s41598-019-40371-6.

[407] J. Cai *et al.*, "Enzymatic preparation of chitosan from the waste Aspergillus niger mycelium of citric acid production plant," *Carbohydrate Polymers,* vol. 64, no. 2, pp. 151-157, 2006/05/11/ 2006, doi: https://doi.org/10.1016/j.carbpol.2005.11.004.

[408] T. K. Eom and K. M. Lee, "Characteristics of chitosanases fromAspergillus fumigatus KB-1," *Archives of Pharmacal Research,* vol. 26, no. 12, pp. 1036-1041, 2003/12/01 2003, doi: 10.1007/BF02994755.

[409] I.-Y. Kim *et al.*, "Chitosan and its derivatives for tissue engineering applications," *Biotechnology Advances,* vol. 26, no. 1, pp. 1-21, 2008/01/01/ 2008, doi: https://doi.org/10.1016/j.biotechadv.2007.07.009.

[410] Z. Huang *et al.*, "In vivo bone regeneration with injectable chitosan/hydroxyapatite/collagen composites and mesenchymal stem cells," *Frontiers of Materials Science,* vol. 5, pp. 301-310, 09/01 2011, doi: 10.1007/s11706-011-0142-4.

[411] K. Y. Lee and D. J. Mooney, "Alginate: Properties and Biomedical Applications," *Progress in Polymer Science,* vol. 37, no. 1, pp. 106-126, 2012/01/01/ 2012, doi: https://doi.org/10.1016/j.progpolymsci.2011.06.003.

[412] N. A. Kamalaldin, B. H. Yahya, and A. Nurazreena, "Cell Evaluation on Alginate/Hydroxyapatite Block for Biomedical Application," *Procedia Chemistry,* vol. 19, pp. 297-303, 2016/01/01/ 2016, doi: https://doi.org/10.1016/j.proche.2016.03.012.

[413] S. Sancilio *et al.*, "Alginate/Hydroxyapatite-Based Nanocomposite Scaffolds for Bone Tissue Engineering Improve Dental Pulp Biomineralization and Differentiation," (in eng), *Stem Cells Int,* vol. 2018, p. 9643721, 2018, doi: 10.1155/2018/9643721.

[414] F. Paula, I. Barreto, M. H. Rocha-Leão, A. Rossi, F. Paim Rosa, and M. Farina, "Hydroxyapatite-alginate biocomposite promotes bone mineralization in different length scales in vivo," *Frontiers of Materials Science in China,* vol. 3, pp. 145-153, 06/01 2009, doi: 10.1007/s11706-009-0029-9.

[415] M. G. Albu, I. Titorencu, and M. V. Ghica, *Collagen-based drug delivery systems for tissue engineering*. chapter, 2011.

[416] D. Olsen *et al.*, "Recombinant collagen and gelatin for drug delivery," *Advanced Drug Delivery Reviews,* vol. 55, no. 12, pp. 1547-1567, 2003/11/28/ 2003, doi: https://doi.org/10.1016/j.addr.2003.08.008.

[417] G. Calabrese *et al.*, "Collagen-Hydroxyapatite Scaffolds Induce Human Adipose Derived Stem Cells Osteogenic Differentiation In Vitro," *PLOS ONE,* vol. 11, no. 3, p. e0151181, 2016, doi: 10.1371/journal.pone.0151181.

[418] S. Trivedi *et al.*, "Hydroxyapatite-Collagen Augments Osteogenic Differentiation of Dental Pulp Stem Cells," (in eng), *Odontology,* vol. 108, no. 2, pp. 251-259, Apr 2020, doi: 10.1007/s10266-019-00464-0.

[419] M. K. Di Pillo, P. G. Montagner, L. N. Teixeira, and E. F. Martinez, "In vivo evaluation of a collagen membrane in bone neoformation: A morphological and histomorphometric study," *Journal of Stomatology, Oral and Maxillofacial Surgery,* vol. 124, no. 1, Supplement, p. 101372, 2023/02/01/ 2023, doi: https://doi.org/10.1016/j.jormas.2022.101372.

[420] J. Chen *et al.*, "Enhanced osteogenesis of human mesenchymal stem cells by periodic heat shock in self-assembling peptide hydrogel," (in eng), *Tissue Eng Part A,* vol. 19, no. 5-6, pp. 716-28, Mar 2013, doi: 10.1089/ten.TEA.2012.0070.

[421] Y. Iwai, Y. Matsuda, M. Nakatsuka, Y. Mikami, and S. Kumabe, "A preliminary study of the dental implant therapy--initial osteogenesis of human mesenchymal stem (HMS0014) cells on titanium discs with different surface modifications," (in eng), *Okajimas Folia Anat Jpn,* vol. 88, no. 4, pp. 133-40, Feb 2012, doi: 10.2535/ofaj.88.133.

[422] H. Misawa *et al.*, "PuraMatrix facilitates bone regeneration in bone defects of calvaria in mice," (in eng), *Cell Transplant,* vol. 15, no. 10, pp. 903-10, 2006, doi: 10.3727/000000006783981369.

[423] Z. Li *et al.*, "Bone marrow enriched graft, modified by self-assembly peptide, repairs critically-sized femur defects in goats," *International Orthopaedics,* vol. 38, no. 11, pp. 2391-2398, 2014/11/01 2014, doi: 10.1007/s00264-014-2388-9.

[424] M. S. Namini *et al.*, "A comparison study on the behavior of human endometrial stem cell-derived osteoblast cells on PLGA/HA nanocomposite scaffolds fabricated by electrospinning and freeze-drying methods," *Journal of Orthopaedic Surgery and Research,* vol. 13, no. 1, p. 63, 2018/03/27 2018, doi: 10.1186/s13018-018-0754-9.

[425] M. P. Bernardo *et al.*, "PLA/Hydroxyapatite scaffolds exhibit in vitro immunological inertness and promote robust osteogenic differentiation of human mesenchymal stem cells without osteogenic stimuli," *Scientific Reports,* vol. 12, no. 1, p. 2333, 2022/02/11 2022, doi: 10.1038/s41598-022-05207-w.

[426] F. Cestari, M. Petretta, Y. Yang, A. Motta, B. Grigolo, and V. M. Sglavo, "3D Printing of PCL/Nano-Hydroxyapatite Scaffolds Derived from Biogenic Sources for Bone Tissue Engineering," *Sustainable Materials and Technologies,* vol. 29, p. e00318, 2021/09/01/ 2021, doi: https://doi.org/10.1016/j.susmat.2021.e00318.

[427] V. Guarino, G. Gentile, L. Sorrentino, and L. Ambrosio, "Polycaprolactone: Synthesis, Properties, and Applications," in *Encyclopedia of Polymer Science and Technology*, pp. 1-36.

[428] P. S. Tan and S. H. Teoh, "Effect of stiffness of polycaprolactone (PCL) membrane on cell proliferation," *Materials Science and Engineering: C,* vol. 27, no. 2, pp. 304-308, 2007/03/01/ 2007, doi: https://doi.org/10.1016/j.msec.2006.03.010.

[429] M. Hakkarainen and A.-C. Albertsson, "Degradation Products of Aliphatic and Aliphatic–Aromatic Polyesters," in *Chromatography for Sustainable Polymeric Materials: Renewable, Degradable and Recyclable*, A.-C. Albertsson and M. Hakkarainen Eds. Berlin, Heidelberg: Springer Berlin Heidelberg, 2008, pp. 85-116.

[430] Y. You, B.-M. Min, S. J. Lee, T. S. Lee, and W. H. Park, "In vitro degradation behavior of electrospun polyglycolide, polylactide, and poly(lactide-co-glycolide)," *Journal of Applied Polymer Science,* vol. 95, no. 2, pp. 193-200, 2005, doi: https://doi.org/10.1002/app.21116.

[431] C. X. Lam, M. M. Savalani, S. H. Teoh, and D. W. Hutmacher, "Dynamics of in vitro polymer degradation of polycaprolactone-based scaffolds: accelerated versus simulated physiological conditions," (in eng), *Biomed Mater,* vol. 3, no. 3, p. 034108, Sep 2008, doi: 10.1088/1748-6041/3/3/034108.

[432] C. X. Lam, D. W. Hutmacher, J. T. Schantz, M. A. Woodruff, and S. H. Teoh, "Evaluation of polycaprolactone scaffold degradation for 6 months in vitro and in vivo," (in eng), *J Biomed Mater Res A,* vol. 90, no. 3, pp. 906-19, Sep 1 2009, doi: 10.1002/jbm.a.32052.

[433] T. Yeo, Y.-G. Ko, E. J. Kim, O. K. Kwon, H. Y. Chung, and O. H. Kwon, "Promoting bone regeneration by 3D-printed poly(glycolic acid)/hydroxyapatite composite

scaffolds," *Journal of Industrial and Engineering Chemistry,* vol. 94, pp. 343-351, 2021/02/25/ 2021, doi: https://doi.org/10.1016/j.jiec.2020.11.004.

[434] S. Lin *et al.*, "PLGA/β-TCP composite scaffold incorporating salvianolic acid B promotes bone fusion by angiogenesis and osteogenesis in a rat spinal fusion model," *Biomaterials,* vol. 196, pp. 109-121, 2019/03/01/ 2019, doi: https://doi.org/10.1016/j.biomaterials.2018.04.004.

[435] Y. Liu *et al.*, "Clinical application of 3D-printed biodegradable lumbar interbody cage (polycaprolactone/β-tricalcium phosphate) for posterior lumbar interbody fusion," (in eng), *J Biomed Mater Res B Appl Biomater,* vol. 111, no. 7, pp. 1398-1406, Jul 2023, doi: 10.1002/jbm.b.35244.

[436] R. E. Cameron and A. Kamvari-Moghaddam, "5 - Synthetic Bioresorbable Polymers," in *Durability and Reliability of Medical Polymers*, M. Jenkins and A. Stamboulis Eds.: Woodhead Publishing, 2012, pp. 96-118.

[437] X. Zhang, X. Peng, and S. W. Zhang, "7 - Synthetic Biodegradable Medical Polymers: Polymer Blends," in *Science and Principles of Biodegradable and Bioresorbable Medical Polymers*, X. Zhang Ed.: Woodhead Publishing, 2017, pp. 217-254.

[438] J. W. Park *et al.*, "A randomized, participant- and evaluator-blinded, matched-pair prospective study to compare the safety and efficacy between polycaprolactone-based fillers in the correction of nasolabial folds," (in eng), *Dermatol Ther,* vol. 35, no. 7, p. e15508, Jul 2022, doi: 10.1111/dth.15508.

[439] P. D. Darney, C. M. Klaisle, S. E. Monroe, C. E. Cook, N. R. Phillips, and A. Schindler, "Evaluation of a 1-year levonorgestrel-releasing contraceptive implant: side effects, release rates, and biodegradability," (in eng), *Fertil Steril,* vol. 58, no. 1, pp. 137-43, Jul 1992, doi: 10.1016/s0015-0282(16)55150-4.

[440] J. Ruiz-Tovar, C. Llavero, M. Jimenez-Fuertes, M. Duran, M. Perez-Lopez, and A. Garcia-Marin, "Incisional Surgical Site Infection after Abdominal Fascial Closure with Triclosan-Coated Barbed Suture vs Triclosan-Coated Polydioxanone Loop Suture vs Polydioxanone Loop Suture in Emergent Abdominal Surgery: A Randomized Clinical Trial," (in eng), *J Am Coll Surg,* vol. 230, no. 5, pp. 766-774, May 2020, doi: 10.1016/j.jamcollsurg.2020.02.031.

[441] X. Jing, H.-Y. Mi, and L.-S. Turng, "Comparison between PCL/hydroxyapatite (HA) and PCL/halloysite nanotube (HNT) composite scaffolds prepared by co-extrusion and gas foaming," *Materials Science and Engineering: C,* vol. 72, pp. 53-61, 2017/03/01 2017, doi: https://doi.org/10.1016/j.msec.2016.11.049.

[442] L. A. Bosworth and S. Downes, "Physicochemical characterisation of degrading polycaprolactone scaffolds," *Polymer Degradation and Stability,* vol. 95, no. 12, pp. 2269-2276, 2010/12/01/ 2010, doi: https://doi.org/10.1016/j.polymdegradstab.2010.09.007.

[443] Z. Ebrahimi, S. Irani, A. Ardeshirylajimi, and E. Seyedjafari, "Enhanced osteogenic differentiation of stem cells by 3D printed PCL scaffolds coated with collagen and

hydroxyapatite," *Scientific Reports,* vol. 12, no. 1, p. 12359, 2022/07/20 2022, doi: 10.1038/s41598-022-15602-y.

[444] T. D. Szucs and D. Brabazon, "Effect of Saturation and Post Processing on 3D Printed Calcium Phosphate Scaffolds," *Key Engineering Materials,* vol. 396-398, pp. 663-666, 2009, doi: 10.4028/www.scientific.net/KEM.396-398.663.

[445] A. Moghaddaszadeh, H. Seddiqi, N. Najmoddin, S. Abbasi Ravasjani, and J. Klein-Nulend, "Biomimetic 3D-printed PCL scaffold containing a high concentration carbonated-nanohydroxyapatite with immobilized-collagen for bone tissue engineering: enhanced bioactivity and physicomechanical characteristics," *Biomedical Materials,* vol. 16, p. 065029, November 01, 2021 2021, doi: 10.1088/1748-605X/ac3147.

[446] Y. S. Cho, S. Choi, S.-H. Lee, K. K. Kim, and Y.-S. Cho, "Assessments of Polycaprolactone/Hydroxyapatite Composite Scaffold with Enhanced Biomimetic Mineralization by Exposure to Hydroxyapatite via a 3D-Printing System and Alkaline Erosion," *European Polymer Journal,* vol. 113, pp. 340-348, 2019/04/01/ 2019, doi: https://doi.org/10.1016/j.eurpolymj.2019.02.006.

[447] S. Biscaia *et al.*, "3D Printed Poly(ε-caprolactone)/Hydroxyapatite Scaffolds for Bone Tissue Engineering: A Comparative Study on a Composite Preparation by Melt Blending or Solvent Casting Techniques and the Influence of Bioceramic Content on Scaffold Properties," (in eng), *Int J Mol Sci,* vol. 23, no. 4, Feb 19 2022, doi: 10.3390/ijms23042318.

[448] S. Eosoly, S. Lohfeld, and D. Brabazon, "Effect of Hydroxyapatite on Biodegradable Scaffolds Fabricated by SLS," *Key Engineering Materials,* vol. 396-398, pp. 659-662, 01/01 2009, doi: 10.4028/0-87849-353-0.659.

[449] B. Zhang, A. K. Nguyen, R. J. Narayan, and J. Huang, "Direct ink writing of vancomycin-loaded polycaprolactone/ polyethylene oxide/ hydroxyapatite 3D scaffolds," *Journal of the American Ceramic Society,* vol. 105, no. 3, pp. 1821-1840, 2022, doi: https://doi.org/10.1111/jace.18048.

[450] Z. Jiao, B. Luo, S. Xiang, H. Ma, Y. Yu, and W. Yang, "3D Printing of HA/PCL Composite Tissue Engineering Scaffolds," *Advanced Industrial and Engineering Polymer Research,* vol. 2, no. 4, pp. 196-202, 2019/10/01/ 2019, doi: https://doi.org/10.1016/j.aiepr.2019.09.003.

[451] J. Qian, M. Xu, A. Suo, T. Yang, and X. Yong, "An innovative method to fabricate honeycomb-like poly(ε-caprolactone)/nano-hydroxyapatite scaffolds," *Materials Letters,* vol. 93, pp. 72-76, 2013/02/15/ 2013, doi: https://doi.org/10.1016/j.matlet.2012.11.046.

[452] C. Cao, P. Huang, A. Prasopthum, A. J. Parsons, F. Ai, and J. Yang, "Characterisation of bone regeneration in 3D printed ductile PCL/PEG/hydroxyapatite scaffolds with high ceramic microparticle concentrations," *Biomaterials Science,* 10.1039/D1BM01645H vol. 10, no. 1, pp. 138-152, 2022, doi: 10.1039/D1BM01645H.

[453] B.-S. Kim, S.-S. Yang, and J. Lee, "A polycaprolactone/cuttlefish bone-derived hydroxyapatite composite porous scaffold for bone tissue engineering," *Journal of Biomedical Materials Research Part B: Applied Biomaterials,* vol. 102, no. 5, pp. 943-951, 2014, doi: https://doi.org/10.1002/jbm.b.33075.

[454] M. I. Hassan, M. Mokhtar, N. Sultana, and T. H. Khan, "Production of hydroxyapatite(HA) nanoparticle and HA/PCL tissue engineering scaffolds for bone tissue engineering," in *2012 IEEE-EMBS Conference on Biomedical Engineering and Sciences*, 17-19 Dec. 2012 2012, pp. 239-242, doi: 10.1109/IECBES.2012.6498024.

[455] M. Janmohammadi, M. S. Nourbakhsh, M. Bahraminasab, and L. Tayebi, "Effect of Pore Characteristics and Alkali Treatment on the Physicochemical and Biological Properties of a 3D-Printed Polycaprolactone Bone Scaffold," *ACS Omega,* vol. 8, no. 8, pp. 7378-7394, 2023/02/28 2023, doi: 10.1021/acsomega.2c05571.

[456] L. Elomaa, S. Teixeira, R. Hakala, H. Korhonen, D. W. Grijpma, and J. V. Seppälä, "Preparation of poly(ε-caprolactone)-based tissue engineering scaffolds by stereolithography," *Acta Biomaterialia,* vol. 7, no. 11, pp. 3850-3856, 2011/11/01/ 2011, doi: https://doi.org/10.1016/j.actbio.2011.06.039.

[457] B. Aldemir Dikici, G. C. Reilly, and F. Claeyssens, "Boosting the Osteogenic and Angiogenic Performance of Multiscale Porous Polycaprolactone Scaffolds by In Vitro Generated Extracellular Matrix Decoration," *ACS Applied Materials & Interfaces,* vol. 12, no. 11, pp. 12510-12524, 2020/03/18 2020, doi: 10.1021/acsami.9b23100.

[458] B. Aldemir Dikici, C. Sherborne, G. C. Reilly, and F. Claeyssens, "Emulsion templated scaffolds manufactured from photocurable polycaprolactone," *Polymer,* vol. 175, pp. 243-254, 2019/06/26/ 2019, doi: https://doi.org/10.1016/j.polymer.2019.05.023.

[459] J. Field, J. W. Haycock, F. M. Boissonade, and F. Claeyssens, "A Tuneable, Photocurable, Poly(Caprolactone)-Based Resin for Tissue Engineering—Synthesis, Characterisation and Use in Stereolithography," *Molecules,* vol. 26, no. 5, p. 1199, 2021. [Online]. Available: https://www.mdpi.com/1420-3049/26/5/1199.

[460] P. Bhatt, S. Trehan, N. Inamdar, V. K. Mourya, and A. Misra, "Chapter 1 - Polymers in Drug Delivery: An Update," in *Applications of Polymers in Drug Delivery (Second Edition)*, A. Misra and A. Shahiwala Eds.: Elsevier, 2021, pp. 1-42.

[461] H. Li *et al.*, "Star-shaped PCL/PLLA blended fiber membrane via electrospinning," (in eng), *J Biomater Sci Polym Ed,* vol. 26, no. 7, pp. 420-32, 2015, doi: 10.1080/09205063.2015.1015865.

[462] M. D. Doganci, "Effects of star-shaped PCL having different numbers of arms on the mechanical, morphological, and thermal properties of PLA/PCL blends," *Journal of Polymer Research,* vol. 28, no. 1, p. 11, 2021/01/05 2021, doi: 10.1007/s10965-020-02380-2.

[463] K. D. Samson, V. Hidalgo-Alvarez, T. R. Dargaville, and F. P. Melchels, "Tough, Resorbable Polycaprolactone-Based Bimodal Networks for Vat Polymerization 3D

Printing," *Advanced Functional Materials,* vol. 33, no. 25, p. 2213797, 2023, doi: https://doi.org/10.1002/adfm.202213797.

[464] M. Meister *et al.*, "A Meta-Review about Medical 3D Printing," *medRxiv,* p. 2024.04.11.23300674, 2024, doi: 10.1101/2024.04.11.23300674.

[465] M. Fogarasi, K. L. Snodderly, and M. A. Di Prima, "A survey of additive manufacturing trends for FDA-cleared medical devices," *Nature Reviews Bioengineering,* vol. 1, no. 10, pp. 687-689, 2023/10/01 2023, doi: 10.1038/s44222-023-00109-6.

[466] G. Prashar, H. Vasudev, and D. Bhuddhi, "Additive manufacturing: expanding 3D printing horizon in industry 4.0," *International Journal on Interactive Design and Manufacturing (IJIDeM),* vol. 17, no. 5, pp. 2221-2235, 2023/10/01 2023, doi: 10.1007/s12008-022-00956-4.

[467] A. Kumar and A. Jacob, "Techniques in scaffold fabrication process for tissue engineering applications: A review," *Journal of Applied Biology & Biotechnology,* 2022.

[468] J. P. Kruth, "Material Incress Manufacturing by Rapid Prototyping Techniques," *CIRP Annals,* vol. 40, no. 2, pp. 603-614, 1991/01/01/ 1991, doi: https://doi.org/10.1016/S0007-8506(07)61136-6.

[469] D. Godec *et al.*, "Introduction to Additive Manufacturing," in *A Guide to Additive Manufacturing*, D. Godec, J. Gonzalez-Gutierrez, A. Nordin, E. Pei, and J. Ureña Alcázar Eds. Cham: Springer International Publishing, 2022, pp. 1-44.

[470] A. Behera, "Additive Manufacturing Materials," in *Advanced Materials: An Introduction to Modern Materials Science*, A. Behera Ed. Cham: Springer International Publishing, 2022, pp. 667-700.

[471] F. Li, J. Li, G. Xu, G. Liu, H. Kou, and L. Zhou, "Fabrication, pore structure and compressive behavior of anisotropic porous titanium for human trabecular bone implant applications," *Journal of the Mechanical Behavior of Biomedical Materials,* vol. 46, pp. 104-114, 2015/06/01/ 2015, doi: https://doi.org/10.1016/j.jmbbm.2015.02.023.

[472] M. Elsheikh, R. Kishida, K. Hayashi, A. Tsuchiya, M. Shimabukuro, and K. Ishikawa, "Effects of pore interconnectivity on bone regeneration in carbonate apatite blocks," (in eng), *Regen Biomater,* vol. 9, no. 1, p. rbac010, 2022, doi: 10.1093/rb/rbac010.

[473] S.-W. Choi, Y. Zhang, and Y. Xia, "Three-Dimensional Scaffolds for Tissue Engineering: The Importance of Uniformity in Pore Size and Structure," *Langmuir,* vol. 26, no. 24, pp. 19001-19006, 2010/12/21 2010, doi: 10.1021/la104206h.

[474] M. Costantini *et al.*, "Correlation between porous texture and cell seeding efficiency of gas foaming and microfluidic foaming scaffolds," *Materials Science and Engineering: C,* vol. 62, pp. 668-677, 2016/05/01/ 2016, doi: https://doi.org/10.1016/j.msec.2016.02.010.

[475] T. Lu, S. Feng, F. He, and J. Ye, "Enhanced osteogenesis of honeycomb β-tricalcium phosphate scaffold by construction of interconnected pore structure: An in vivo study," *Journal of Biomedical Materials Research Part A,* vol. 108, no. 3, pp. 645-653, 2020, doi: https://doi.org/10.1002/jbm.a.36844.

[476] C. Mota, D. Puppi, F. Chiellini, and E. Chiellini, "Additive manufacturing techniques for the production of tissue engineering constructs," *Journal of Tissue Engineering and Regenerative Medicine,* vol. 9, no. 3, pp. 174-190, 2015, doi: https://doi.org/10.1002/term.1635.

[477] "OsteoFab." https://www.oxfordpm.com/biomedical-3dp (accessed 11 July 2024, 2024).

[478] "3D printed bone approved for patients in Europe." Cerhum. https://www.cerhum.com/news/26-3d-printed-bone-approved-for-patients-in-europe (accessed 11 July 2024, 2024).

[479] S. Systermans *et al.*, "An innovative 3D hydroxyapatite patient-specific implant for maxillofacial bone reconstruction: A case series of 13 patients," *Journal of Cranio-Maxillofacial Surgery,* vol. 52, no. 4, pp. 420-431, 2024/04/01/ 2024, doi: https://doi.org/10.1016/j.jcms.2024.02.026.

[480] "Dimension Inx Announces First Surgical Cases Utilizing CMFlex™ Synthetic Bone Graft - The First 3D-printed Regenerative Bone Graft Product Cleared by the FDA." Dimension Inx. https://www.dimensioninx.com/pr-cmflex (accessed 11 July 2024, 2024).

[481] "Patient-Matched and Bio-integrative Orthopedic Implant Solutions." Ossiform. https://ossiform.com/p3d-bone/ (accessed 11 July 2024, 2024).

[482] "510(k) Premarket Notification." U.S. Food and Drug Administration. https://www.accessdata.fda.gov/scripts/cdrh/cfdocs/cfpmn/pmn.cfm?ID=k020720 (accessed 11 July 2024, 2024).

[483] "Critical-Sized Defect." Osteopore. https://www.osteopore.com/surgeons/critical-sized-defect# (accessed 11 July 2024, 2024).

[484] M. Laubach *et al.*, "Clinical translation of a patient-specific scaffold-guided bone regeneration concept in four cases with large long bone defects," (in eng), *J Orthop Translat,* vol. 34, pp. 73-84, May 2022, doi: 10.1016/j.jot.2022.04.004.

[485] "Granted Market Access." BellaSeno https://www.bellaseno.com/press-release/granted-market-access-europe-excavatum-scaffolds/ (accessed 11 July 2024, 2024).

[486] "Products." BellaSeno. https://www.bellaseno.com/products/ (accessed 11 July 2024, 2024).

[487] P. Mommsen *et al.*, "Reconstruction of an Extensive Segmental Radial Shaft Bone Defect by Vascularized 3D-Printed Graft Cage," *Journal of Personalized Medicine*, vol. 14, no. 2, doi: 10.3390/jpm14020178.

[488] M. Qu *et al.*, "Multi-Dimensional Printing for Bone Tissue Engineering," (in eng), *Adv Healthc Mater,* vol. 10, no. 11, p. e2001986, Jun 2021, doi: 10.1002/adhm.202001986.

[489] I. Gibson, D. Rosen, B. Stucker, and M. Khorasani, "Material Extrusion," in *Additive Manufacturing Technologies*, I. Gibson, D. Rosen, B. Stucker, and M. Khorasani Eds. Cham: Springer International Publishing, 2021, pp. 171-201.

[490] A. Sola, "Materials Requirements in Fused Filament Fabrication: A Framework for the Design of Next-Generation 3D Printable Thermoplastics and Composites," *Macromolecular Materials and Engineering,* vol. 307, no. 10, p. 2200197, 2022, doi: https://doi.org/10.1002/mame.202200197.

[491] J. A. Lewis, "Direct Ink Writing of 3D Functional Materials," *Advanced Functional Materials,* vol. 16, no. 17, pp. 2193-2204, 2006, doi: https://doi.org/10.1002/adfm.200600434.

[492] H. K. Dave and S. T. Patel, "Introduction to Fused Deposition Modeling Based 3D Printing Process," in *Fused Deposition Modeling Based 3D Printing*, H. K. Dave and J. P. Davim Eds. Cham: Springer International Publishing, 2021, pp. 1-21.

[493] N. Kumar, P. K. Jain, P. Tandon, and P. M. Pandey, "Investigation on the effects of process parameters in CNC assisted pellet based fused layer modeling process," *Journal of Manufacturing Processes,* vol. 35, pp. 428-436, 2018/10/01/ 2018, doi: https://doi.org/10.1016/j.jmapro.2018.08.029.

[494] T. Shen, H. Xiong, Z. Li, L. Zhang, and K. Zhou, "Fused deposition fabrication of high-quality zirconia ceramics using granular feedstock," *Ceramics International,* vol. 47, no. 24, pp. 34352-34360, 2021/12/15/ 2021, doi: https://doi.org/10.1016/j.ceramint.2021.08.348.

[495] J. Lee, C. Song, I. Noh, S. Song, and Y.-S. Rhee, "Hot-Melt 3D Extrusion for the Fabrication of Customizable Modified-Release Solid Dosage Forms," *Pharmaceutics,* vol. 12, no. 8, p. 738, 2020. [Online]. Available: https://www.mdpi.com/1999-4923/12/8/738.

[496] H.-W. Cho, S.-H. Baek, B.-J. Lee, and H.-E. Jin, "Orodispersible Polymer Films with the Poorly Water-Soluble Drug, Olanzapine: Hot-Melt Pneumatic Extrusion for Single-Process 3D Printing," *Pharmaceutics,* vol. 12, no. 8, p. 692, 2020. [Online]. Available: https://www.mdpi.com/1999-4923/12/8/692.

[497] M. A. S. R. Saadi *et al.*, "Direct Ink Writing: A 3D Printing Technology for Diverse Materials," *Advanced Materials,* vol. 34, no. 28, p. 2108855, 2022, doi: https://doi.org/10.1002/adma.202108855.

[498] X. Yuan *et al.*, "Recent Advances in 3D Printing of Smart Scaffolds for Bone Tissue Engineering and Regeneration," (in eng), *Adv Mater,* vol. 36, no. 34, p. e2403641, Aug 2024, doi: 10.1002/adma.202403641.

[499] K. Willson, A. Atala, and J. J. Yoo, "Bioprinting Au Natural: The Biologics of Bioinks," (in eng), *Biomolecules,* vol. 11, no. 11, Oct 28 2021, doi: 10.3390/biom11111593.

[500] A. Held, G. Puchas, F. Müller, and W. Krenkel, "Direct ink writing of water-based C–SiC pastes for the manufacturing of SiSiC components," *Open Ceramics,* vol. 5, p. 100054, 2021/03/01/ 2021, doi: https://doi.org/10.1016/j.oceram.2020.100054.

[501] I. Chiesa *et al.*, "Modeling the Three-Dimensional Bioprinting Process of β-Sheet Self-Assembling Peptide Hydrogel Scaffolds," (in eng), *Front Med Technol,* vol. 2, p. 571626, 2020, doi: 10.3389/fmedt.2020.571626.

[502] S. Malik *et al.*, "Robotic Extrusion of Algae-Laden Hydrogels for Large-Scale Applications," (in eng), *Glob Chall,* vol. 4, no. 1, p. 1900064, Jan 2020, doi: 10.1002/gch2.201900064.

[503] L. Ning *et al.*, "Process-induced cell damage: pneumatic versus screw-driven bioprinting," *Biofabrication,* vol. 12, no. 2, p. 025011, 2020/02/13 2020, doi: 10.1088/1758-5090/ab5f53.

[504] M. Costantini *et al.*, "Microfluidic-enhanced 3D bioprinting of aligned myoblast-laden hydrogels leads to functionally organized myofibers in vitro and in vivo," *Biomaterials,* vol. 131, pp. 98-110, 2017/07/01/ 2017, doi: https://doi.org/10.1016/j.biomaterials.2017.03.026.

[505] C. Colosi *et al.*, "Microfluidic Bioprinting of Heterogeneous 3D Tissue Constructs Using Low-Viscosity Bioink," (in eng), *Adv Mater,* vol. 28, no. 4, pp. 677-84, Jan 27 2016, doi: 10.1002/adma.201503310.

[506] T. J. Hensen *et al.*, "Additive manufacturing of ceramic nanopowder by direct coagulation printing," *Additive Manufacturing,* vol. 23, pp. 140-150, 2018/10/01/ 2018, doi: https://doi.org/10.1016/j.addma.2018.07.010.

[507] R. Karyappa, A. Ohno, and M. Hashimoto, "Immersion precipitation 3D printing (ip3DP)," *Materials Horizons,* 10.1039/C9MH00730J vol. 6, no. 9, pp. 1834-1844, 2019, doi: 10.1039/C9MH00730J.

[508] Y. Wang *et al.*, "Direct writing alginate bioink inside pre-polymers of hydrogels to create patterned vascular networks," *Journal of Materials Science,* vol. 54, no. 10, pp. 7883-7892, 2019/05/01 2019, doi: 10.1007/s10853-019-03447-2.

[509] T. Gonzalez-Fernandez, A. J. Tenorio, K. T. Campbell, E. A. Silva, and J. K. Leach, "Alginate-Based Bioinks for 3D Bioprinting and Fabrication of Anatomically Accurate Bone Grafts," (in eng), *Tissue Eng Part A,* vol. 27, no. 17-18, pp. 1168-1181, Sep 2021, doi: 10.1089/ten.TEA.2020.0305.

[510] S.-Z. Guo, M.-C. Heuzey, and D. Therriault, "Properties of Polylactide Inks for Solvent-Cast Printing of Three-Dimensional Freeform Microstructures," *Langmuir,* vol. 30, no. 4, pp. 1142-1150, 2014/02/04 2014, doi: 10.1021/la4036425.

[511] H. Kim, G. H. Yang, C. H. Choi, Y. S. Cho, and G. Kim, "Gelatin/PVA scaffolds fabricated using a 3D-printing process employed with a low-temperature plate for hard tissue regeneration: Fabrication and characterizations," *International Journal of Biological Macromolecules,* vol. 120, pp. 119-127, 2018/12/01/ 2018, doi: https://doi.org/10.1016/j.ijbiomac.2018.07.159.

[512] B. Stolz, M. Mader, L. Volk, T. Steinberg, and R. Mülhaupt, "Cryo-3D Printing of Hierarchically Porous Polyhydroxymethylene Scaffolds for Hard Tissue Regeneration," *Macromolecular Materials and Engineering,* vol. 306, no. 1, p. 2000541, 2021, doi: https://doi.org/10.1002/mame.202000541.

[513] A. Cochis *et al.*, "3D Printing of Thermo-Responsive Methylcellulose Hydrogels for Cell-Sheet Engineering," *Materials,* vol. 11, no. 4, p. 579, 2018. [Online]. Available: https://www.mdpi.com/1996-1944/11/4/579.

[514] O. D. Yirmibesoglu *et al.*, "Multi-material direct ink writing of photocurable elastomeric foams," *Communications Materials,* vol. 2, no. 1, p. 82, 2021/07/30 2021, doi: 10.1038/s43246-021-00186-3.

[515] L. E. Bertassoni *et al.*, "Direct-write bioprinting of cell-laden methacrylated gelatin hydrogels," *Biofabrication,* vol. 6, no. 2, p. 024105, 2014/04/03 2014, doi: 10.1088/1758-5082/6/2/024105.

[516] Y. Sun *et al.*, "3D printing of thermosets with diverse rheological and functional applicabilities," *Nature Communications,* vol. 14, no. 1, p. 245, 2023/01/16 2023, doi: 10.1038/s41467-023-35929-y.

[517] S. Noh, K. Kim, J.-I. Kim, J. H. Shin, and H.-W. Kang, "Direct-write printing for producing biomimetic patterns with self-aligned neurites," *Additive Manufacturing,* vol. 32, p. 101072, 2020/03/01/ 2020, doi: https://doi.org/10.1016/j.addma.2020.101072.

[518] A. T. Banigo, L. Nauta, B. Zoetebier, and M. Karperien, "Coaxial Bioprinting of Enzymatically Crosslinkable Hyaluronic Acid-Tyramine Bioinks for Tissue Regeneration," (in eng), *Polymers (Basel),* vol. 16, no. 17, Aug 30 2024, doi: 10.3390/polym16172470.

[519] Q. Zheng, B. Xie, Z. Xu, and H. Wu, "A systematic printability study of direct ink writing towards high-resolution rapid manufacturing," *International Journal of Extreme Manufacturing,* vol. 5, no. 3, p. 035002, 2023/05/16 2023, doi: 10.1088/2631-7990/acd090.

[520] A. Patti, S. Acierno, G. Cicala, and D. Acierno, "Predicting the Printability of Poly(Lactide) Acid Filaments in Fused Deposition Modeling (FDM) Technology: Rheological Measurements and Experimental Evidence," *ChemEngineering,* vol. 7, no. 1, p. 1, 2023. [Online]. Available: https://www.mdpi.com/2305-7084/7/1/1.

[521] M. Alsoufi and A. El-Sayed, "Warping Deformation of Desktop 3D Printed Parts Manufactured by Open Source Fused Deposition Modeling (FDM) System," *International Journal of Mechanical & Mechatronics Engineering,* vol. 17, pp. 7-16, 08/21 2017.

[522] P. Czyżewski, D. Marciniak, B. Nowinka, M. Borowiak, and M. Bieliński, "Influence of Extruder's Nozzle Diameter on the Improvement of Functional Properties of 3D-Printed PLA Products," *Polymers,* vol. 14, no. 2, p. 356, 2022. [Online]. Available: https://www.mdpi.com/2073-4360/14/2/356.

[523] P. A. Amorim, M. A. d'Ávila, R. Anand, P. Moldenaers, P. Van Puyvelde, and V. Bloemen, "Insights on shear rheology of inks for extrusion-based 3D bioprinting," *Bioprinting,* vol. 22, p. e00129, 2021/06/01/ 2021, doi: https://doi.org/10.1016/j.bprint.2021.e00129.

[524] N. Majumder, A. Mishra, and S. Ghosh, "Effect of varying cell densities on the rheological properties of the bioink," *Bioprinting,* vol. 28, p. e00241, 2022/12/01/ 2022, doi: https://doi.org/10.1016/j.bprint.2022.e00241.

[525] W. M. S. Russell and R. L. Burch, *The principles of humane experimental technique*. Methuen, 1959.

[526] "The Principles of Humane Experimental Technique," *Medical Journal of Australia,* vol. 1, no. 13, pp. 500-500, 1960, doi: https://doi.org/10.5694/j.1326-5377.1960.tb73127.x.

[527] A. Cacciamali, R. Villa, and S. Dotti, "3D Cell Cultures: Evolution of an Ancient Tool for New Applications," (in English), *Frontiers in Physiology,* Review vol. 13, 2022-July-22 2022, doi: 10.3389/fphys.2022.836480.

[528] A. Pizzoferrato *et al.*, "Cell culture methods for testing Biocompatibility," *Clinical Materials,* vol. 15, no. 3, pp. 173-190, 1994/01/01/ 1994, doi: https://doi.org/10.1016/0267-6605(94)90081-7.

[529] M. P. Ferraz, "An Overview on the Big Players in Bone Tissue Engineering: Biomaterials, Scaffolds and Cells," *International Journal of Molecular Sciences*, vol. 25, no. 7, doi: 10.3390/ijms25073836.

[530] A. Przekora, "The summary of the most important cell-biomaterial interactions that need to be considered during in vitro biocompatibility testing of bone scaffolds for tissue engineering applications," *Materials Science and Engineering: C,* vol. 97, pp. 1036-1051, 2019/04/01/ 2019, doi: https://doi.org/10.1016/j.msec.2019.01.061.

[531] S. Metwally *et al.*, "Surface potential and roughness controlled cell adhesion and collagen formation in electrospun PCL fibers for bone regeneration," *Materials & Design,* vol. 194, p. 108915, 2020/09/01/ 2020, doi: https://doi.org/10.1016/j.matdes.2020.108915.

[532] A. J. Friedenstein, S. Piatetzky, II, and K. V. Petrakova, "Osteogenesis in transplants of bone marrow cells," (in eng), *J Embryol Exp Morphol,* vol. 16, no. 3, pp. 381-90, Dec 1966.

[533] M. F. Pittenger *et al.*, "Multilineage Potential of Adult Human Mesenchymal Stem Cells," *Science,* vol. 284, no. 5411, pp. 143-147, 1999, doi: doi:10.1126/science.284.5411.143.

[534] X. Li, J. Bai, X. Ji, R. Li, Y. Xuan, and Y. Wang, "Comprehensive characterization of four different populations of human mesenchymal stem cells as regards their immune properties, proliferation and differentiation," *Int J Mol Med,* vol. 34, no. 3, pp. 695-704, 2014/09/01 2014, doi: 10.3892/ijmm.2014.1821.

[535] A. M. Billing *et al.*, "Comprehensive transcriptomic and proteomic characterization of human mesenchymal stem cells reveals source specific cellular markers," (in eng), *Sci Rep,* vol. 6, p. 21507, Feb 9 2016, doi: 10.1038/srep21507.

[536] S. Kern, H. Eichler, J. Stoeve, H. Klüter, and K. Bieback, "Comparative Analysis of Mesenchymal Stem Cells from Bone Marrow, Umbilical Cord Blood, or Adipose Tissue," *Stem Cells,* vol. 24, no. 5, pp. 1294-1301, 2006, doi: 10.1634/stemcells.2005-0342.

[537] H. J. Jin *et al.*, "Comparative Analysis of Human Mesenchymal Stem Cells from Bone Marrow, Adipose Tissue, and Umbilical Cord Blood as Sources of Cell Therapy," *International Journal of Molecular Sciences*, vol. 14, no. 9*,* pp. 17986-18001doi: 10.3390/ijms140917986.

[538] E. M. Horwitz *et al.*, "Clarification of the nomenclature for MSC: The International Society for Cellular Therapy position statement," *Cytotherapy,* vol. 7, no. 5, pp. 393-395, 2005/01/01/ 2005, doi: https://doi.org/10.1080/14653240500319234.

[539] M. Dominici *et al.*, "Minimal criteria for defining multipotent mesenchymal stromal cells. The International Society for Cellular Therapy position statement," *Cytotherapy,* vol. 8, no. 4, pp. 315-317, 2006/01/01 2006, doi: 10.1080/14653240600855905.

[540] O. Uysal, T. Sevimli, M. Sevimli, S. Gunes, and A. Eker Sariboyaci, "Chapter 17 - Cell and Tissue Culture: The Base of Biotechnology," in *Omics Technologies and Bio-Engineering*, D. Barh and V. Azevedo Eds.: Academic Press, 2018, pp. 391-429.

[541] C. Zhao, "Cell culture: in vitro model system and a promising path to in vivo applications," *Journal of Histotechnology,* vol. 46, no. 1, pp. 1-4, 2023/01/02 2023, doi: 10.1080/01478885.2023.2170772.

[542] A. Verma, M. Verma, and A. Singh, "Chapter 14 - Animal tissue culture principles and applications," in *Animal Biotechnology (Second Edition)*, A. S. Verma and A. Singh Eds. Boston: Academic Press, 2020, pp. 269-293.

[543] A. Ramakrishnan, B. Torok-Storb, and M. M. Pillai, "Primary marrow-derived stromal cells: isolation and manipulation," (in eng), *Methods Mol Biol,* vol. 1035, pp. 75-101, 2013, doi: 10.1007/978-1-62703-508-8_8.

[544] P. J. Price, "Best practices for media selection for mammalian cells," *In Vitro Cellular & Developmental Biology - Animal,* vol. 53, no. 8, pp. 673-681, 2017/09/01 2017, doi: 10.1007/s11626-017-0186-6.

[545] L. Hayflick and P. S. Moorhead, "The serial cultivation of human diploid cell strains," *Experimental Cell Research,* vol. 25, no. 3, pp. 585-621, 1961/12/01/ 1961, doi: https://doi.org/10.1016/0014-4827(61)90192-6.

[546] "Replicative Aging and Gene Expression in Long-Term Cultures of Human Bone Marrow Stromal Cells," *Tissue Engineering,* vol. 8, no. 6, pp. 901-910, 2002, doi: 10.1089/107632702320934001.

[547] S. Mohamed-Ahmed *et al.*, "Adipose-Derived and Bone Marrow Mesenchymal Stem Cells: A Donor-Matched Comparison," *Stem Cell Research & Therapy,* vol. 9, no. 1, p. 168, 2018/06/19 2018, doi: 10.1186/s13287-018-0914-1.

[548] G. Detela *et al.*, "Donor Variability in Growth Kinetics of Healthy hMSCs Using Manual Processing: Considerations for Manufacture of Cell Therapies," *Biotechnology Journal,* vol. 13, no. 2, p. 1700085, 2018, doi: https://doi.org/10.1002/biot.201700085.

[549] K. Kaastrup and K. Grønbæk, "The Impact of Sedentary Lifestyle, High-fat Diet, Tobacco Smoke, and Alcohol Intake on the Hematopoietic Stem Cell Niches," (in eng), *Hemasphere,* vol. 5, no. 8, p. e615, Aug 2021, doi: 10.1097/hs9.0000000000000615.

[550] M. A. Baxter, R. F. Wynn, S. N. Jowitt, J. E. Wraith, L. J. Fairbairn, and I. Bellantuono, "Study of Telomere Length Reveals Rapid Aging of Human Marrow Stromal Cells following In Vitro Expansion," *Stem Cells,* vol. 22, no. 5, pp. 675-682, 2004, doi: 10.1634/stemcells.22-5-675.

[551] R. I. Dmitrieva, I. R. Minullina, A. A. Bilibina, O. V. Tarasova, S. V. Anisimov, and A. Y. Zaritskey, "Bone marrow- and subcutaneous adipose tissue-derived mesenchymal stem cells: Differences and similarities," *Cell Cycle,* vol. 11, no. 2, pp. 377-383, 2012/01/15 2012, doi: 10.4161/cc.11.2.18858.

[552] M. Carter and J. Shieh, "Chapter 14 - Cell Culture Techniques," in *Guide to Research Techniques in Neuroscience (Second Edition)*, M. Carter and J. Shieh Eds. San Diego: Academic Press, 2015, pp. 295-310.

[553] G. Kaur and J. M. Dufour, "Cell lines: Valuable tools or useless artifacts," (in eng), *Spermatogenesis,* vol. 2, no. 1, pp. 1-5, Jan 1 2012, doi: 10.4161/spmg.19885.

[554] N. Y. Souren *et al.*, "Cell line authentication: a necessity for reproducible biomedical research," (in eng), *Embo j,* vol. 41, no. 14, p. e111307, 2022/07/19 2022, doi: 10.15252/embj.2022111307.

[555] S. James *et al.*, "Multiparameter Analysis of Human Bone Marrow Stromal Cells Identifies Distinct Immunomodulatory and Differentiation-Competent Subtypes," (in eng), *Stem Cell Reports,* vol. 4, no. 6, pp. 1004-15, Jun 9 2015, doi: 10.1016/j.stemcr.2015.05.005.

[556] H. Eagle, "Amino Acid Metabolism in Mammalian Cell Cultures," *Science,* vol. 130, no. 3373, pp. 432-437, 1959.

[557] D. F. Gruber and D. W. Jayme, "Cell and Tissue Culture Media: History and Terminology," in *Cell Biology*, J. E. Celis Ed.: Academic Press, 1994, pp. 451-458.

[558] P. Tonarova, K. Lochovska, R. Pytlik, and M. Hubalek Kalbacova, "The Impact of Various Culture Conditions on Human Mesenchymal Stromal Cells Metabolism," *Stem Cells International,* vol. 2021, no. 1, p. 6659244, 2021, doi: https://doi.org/10.1155/2021/6659244.

[559] K. Turnovcova, K. Ruzickova, V. Vanecek, E. Sykova, and P. Jendelova, "Properties and growth of human bone marrow mesenchymal stromal cells cultivated in different media," *Cytotherapy,* vol. 11, no. 7, pp. 874-885, 2009/01/01 2009, doi: 10.3109/14653240903188947.

[560] J. C. Fitzgerald, G. Shaw, J. M. Murphy, and F. Barry, "Media matters: culture medium-dependent hypervariable phenotype of mesenchymal stromal cells," *Stem Cell Research & Therapy,* vol. 14, no. 1, p. 363, 2023/12/12 2023, doi: 10.1186/s13287-023-03589-w.

[561] T. R. J. Heathman *et al.*, "Serum-free process development: improving the yield and consistency of human mesenchymal stromal cell production," *Cytotherapy,* vol. 17, no. 11, pp. 1524-1535, 2015/11/01/ 2015, doi: https://doi.org/10.1016/j.jcyt.2015.08.002.

[562] P. J. Price and E. A. Gregory, "Relationship between in vitro growth promotion and biophysical and biochemical properties of the serum supplement," *In Vitro,* vol. 18, no. 6, pp. 576-584, 1982/06/01 1982, doi: 10.1007/BF02810081.

[563] S. Ansari, K. Ito, and S. Hofmann, "Alkaline Phosphatase Activity of Serum Affects Osteogenic Differentiation Cultures," *ACS Omega,* vol. 7, no. 15, pp. 12724-12733, 2022/04/19 2022, doi: 10.1021/acsomega.1c07225.

[564] S. Liu, W. Yang, Y. Li, and C. Sun, "Fetal bovine serum, an important factor affecting the reproducibility of cell experiments," *Scientific Reports,* vol. 13, no. 1, p. 1942, 2023/02/02 2023, doi: 10.1038/s41598-023-29060-7.

[565] J. R. Vetsch, S. J. Paulsen, R. Müller, and S. Hofmann, "Effect of fetal bovine serum on mineralization in silk fibroin scaffolds," *Acta Biomaterialia,* vol. 13, pp. 277-285, 2015/02/01/ 2015, doi: https://doi.org/10.1016/j.actbio.2014.11.025.

[566] C. E. Jochems, J. B. van der Valk, F. R. Stafleu, and V. Baumans, "The use of fetal bovine serum: ethical or scientific problem?," (in eng), *Altern Lab Anim,* vol. 30, no. 2, pp. 219-27, Mar-Apr 2002, doi: 10.1177/026119290203000208.

[567] A. Shahdadfar, K. Frønsdal, T. Haug, F. P. Reinholt, and J. E. Brinchmann, "In Vitro Expansion of Human Mesenchymal Stem Cells: Choice of Serum Is a Determinant of Cell Proliferation, Differentiation, Gene Expression, and Transcriptome Stability," *Stem Cells,* vol. 23, no. 9, pp. 1357-1366, 2005, doi: 10.1634/stemcells.2005-0094.

[568] N. Stute, K. Holtz, M. Bubenheim, C. Lange, F. Blake, and A. R. Zander, "Autologous serum for isolation and expansion of human mesenchymal stem cells for clinical use,"

*Experimental Hematology,* vol. 32, no. 12, pp. 1212-1225, 2004/12/01/ 2004, doi: https://doi.org/10.1016/j.exphem.2004.09.003.

[569] A. Blázquez Prunera, J. Diez, R. Gajardo, and S. Grancha, "Human mesenchymal stem cells maintain their phenotype, multipotentiality, and genetic stability when cultured using a defined xeno-free human plasma fraction," *Stem Cell Research & Therapy,* vol. 8, 04/27 2017.

[570] B. W. M. de Wildt, K. Ito, and S. Hofmann, "Human Platelet Lysate as Alternative of Fetal Bovine Serum for Enhanced Human In Vitro Bone Resorption and Remodeling," (in eng), *Front Immunol,* vol. 13, p. 915277, 2022, doi: 10.3389/fimmu.2022.915277.

[571] S. Ansari, K. Ito, and S. Hofmann, "Development of serum substitute medium for bone tissue engineering," *Journal of Biomedical Materials Research Part A,* vol. 111, no. 9, pp. 1423-1440, 2023, doi: https://doi.org/10.1002/jbm.a.37544.

[572] S. Bhat, P. Viswanathan, S. Chandanala, S. J. Prasanna, and R. N. Seetharam, "Expansion and characterization of bone marrow derived human mesenchymal stromal cells in serum-free conditions," *Scientific Reports,* vol. 11, no. 1, p. 3403, 2021/02/09 2021, doi: 10.1038/s41598-021-83088-1.

[573] F. Langenbach and J. Handschel, "Effects of dexamethasone, ascorbic acid and β-glycerophosphate on the osteogenic differentiation of stem cells in vitro," (in eng), *Stem Cell Res Ther,* vol. 4, no. 5, p. 117, 2013, doi: 10.1186/scrt328.

[574] D. Schop *et al.*, "Growth, Metabolism, and Growth Inhibitors of Mesenchymal Stem Cells," *Tissue Engineering Part A,* vol. 15, no. 8, pp. 1877-1886, 2009/08/01 2009, doi: 10.1089/ten.tea.2008.0345.

[575] A. Winkel *et al.*, "Cell culture media notably influence properties of human mesenchymal stroma/stem-like cells from different tissues," *Cytotherapy,* vol. 22, no. 11, pp. 653-668, 2020/11/01/ 2020, doi: https://doi.org/10.1016/j.jcyt.2020.07.005.

[576] D. F. Stroncek *et al.*, "Human Mesenchymal Stromal Cell (MSC) Characteristics Vary Among Laboratories When Manufactured From the Same Source Material: A Report by the Cellular Therapy Team of the Biomedical Excellence for Safer Transfusion (BEST) Collaborative," (in English), *Frontiers in Cell and Developmental Biology,* Original Research vol. 8, 2020-June-16 2020, doi: 10.3389/fcell.2020.00458.

[577] J. Zullo, K. Matsumoto, S. Xavier, B. Ratliff, and M. S. Goligorsky, "The cell secretome, a mediator of cell-to-cell communication," (in eng), *Prostaglandins Other Lipid Mediat,* vol. 120, pp. 17-20, Jul 2015, doi: 10.1016/j.prostaglandins.2015.03.012.

[578] W. Wu and J. Krijgsveld, "Secretome Analysis: Reading Cellular Sign Language to Understand Intercellular Communication," *Molecular & Cellular Proteomics,* vol. 23, no. 1, 2024, doi: 10.1016/j.mcpro.2023.100692.

[579] M. Paprocka *et al.*, "From Primary MSC Culture of Adipose Tissue to Immortalized Cell Line Producing Cytokines for Potential Use in Regenerative Medicine Therapy or

Immunotherapy," (in eng), *Int J Mol Sci,* vol. 22, no. 21, Oct 23 2021, doi: 10.3390/ijms222111439.

[580] S. K. Sze *et al.*, "Elucidating the secretion proteome of human embryonic stem cell-derived mesenchymal stem cells," (in eng), *Mol Cell Proteomics,* vol. 6, no. 10, pp. 1680-9, Oct 2007, doi: 10.1074/mcp.M600393-MCP200.

[581] A. Vilar *et al.*, "Substrate mechanical properties bias MSC paracrine activity and therapeutic potential," *Acta Biomaterialia,* vol. 168, pp. 144-158, 2023/09/15/ 2023, doi: https://doi.org/10.1016/j.actbio.2023.06.041.

[582] E. Müller *et al.*, "Distinguishing autocrine and paracrine signals in hematopoietic stem cell culture using a biofunctional microcavity platform," *Scientific Reports,* vol. 6, no. 1, p. 31951, 2016/08/18 2016, doi: 10.1038/srep31951.

[583] V. Jakl *et al.*, "Effect of Expansion Media on Functional Characteristics of Bone Marrow-Derived Mesenchymal Stromal Cells," (in eng), *Cells,* vol. 12, no. 16, Aug 19 2023, doi: 10.3390/cells12162105.

[584] G. Sagaradze *et al.*, "Conditioned Medium from Human Mesenchymal Stromal Cells: Towards the Clinical Translation," (in eng), *Int J Mol Sci,* vol. 20, no. 7, Apr 3 2019, doi: 10.3390/ijms20071656.

[585] J. Shin *et al.*, "Comparative analysis of differentially secreted proteins in serum-free and serum-containing media by using BONCAT and pulsed SILAC," *Scientific Reports,* vol. 9, no. 1, p. 3096, 2019/02/28 2019, doi: 10.1038/s41598-019-39650-z.

[586] S. Nonnis *et al.*, "Effect of fetal bovine serum in culture media on MS analysis of mesenchymal stromal cells secretome," *EuPA Open Proteomics,* vol. 10, pp. 28-30, 2016/03/01/ 2016, doi: https://doi.org/10.1016/j.euprot.2016.01.005.

[587] C. Giannasi, S. Niada, E. Della Morte, S. R. Casati, C. De Palma, and A. T. Brini, "Serum starvation affects mitochondrial metabolism of adipose-derived stem/stromal cells," *Cytotherapy,* vol. 25, no. 7, pp. 704-711, 2023/07/01/ 2023, doi: https://doi.org/10.1016/j.jcyt.2023.03.004.

[588] J. Mauney and V. Volloch, "Progression of human bone marrow stromal cells into both osteogenic and adipogenic lineages is differentially regulated by structural conformation of collagen I matrix via distinct signaling pathways," *Matrix Biology,* vol. 28, no. 5, pp. 239-250, 2009/06/01/ 2009, doi: https://doi.org/10.1016/j.matbio.2009.04.003.

[589] G. Higuera, D. Schop, F. Janssen, R. van Dijkhuizen-Radersma, T. van Boxtel, and C. A. van Blitterswijk, "Quantifying In Vitro Growth and Metabolism Kinetics of Human Mesenchymal Stem Cells Using a Mathematical Model," *Tissue Engineering Part A,* vol. 15, no. 9, pp. 2653-2663, 2009/09/01 2009, doi: 10.1089/ten.tea.2008.0328.

[590] R. Noverina *et al.*, "Growth factors profile in conditioned medium human adipose tissue-derived mesenchymal stem cells (CM-hATMSCs)," *Clinical Nutrition Experimental,* vol. 24, pp. 34-44, 2019, doi: 10.1016/j.yclnex.2019.01.002.

[591] B. Gharibi and F. J. Hughes, "Effects of Medium Supplements on Proliferation, Differentiation Potential, and In Vitro Expansion of Mesenchymal Stem Cells," *Stem Cells Translational Medicine,* vol. 1, no. 11, pp. 771-782, 2012, doi: 10.5966/sctm.2010-0031.

[592] A. Al-Ani, D. Toms, D. Kondro, J. Thundathil, Y. Yu, and M. Ungrin, "Oxygenation in cell culture: Critical parameters for reproducibility are routinely not reported," (in eng), *PLoS One,* vol. 13, no. 10, p. e0204269, 2018, doi: 10.1371/journal.pone.0204269.

[593] J. Tan *et al.*, "Limited oxygen in standard cell culture alters metabolism and function of differentiated cells," (in eng), *Embo j,* vol. 43, no. 11, pp. 2127-2165, Jun 2024, doi: 10.1038/s44318-024-00084-7.

[594] E. Mestres *et al.*, "Factors of the human embryo culture system that may affect media evaporation and osmolality," *Human Reproduction,* vol. 36, no. 3, pp. 605-613, 2021, doi: 10.1093/humrep/deaa370.

[595] B. A. Wagner, S. Venkataraman, and G. R. Buettner, "The rate of oxygen utilization by cells," *Free Radical Biology and Medicine,* vol. 51, no. 3, pp. 700-712, 2011/08/01/ 2011, doi: https://doi.org/10.1016/j.freeradbiomed.2011.05.024.

[596] J. Paquet, M. Deschepper, A. Moya, D. Logeart-Avramoglou, C. Boisson-Vidal, and H. Petite, "Oxygen Tension Regulates Human Mesenchymal Stem Cell Paracrine Functions," *Stem Cells Translational Medicine,* vol. 4, no. 7, pp. 809-821, 2015, doi: 10.5966/sctm.2014-0180.

[597] H. Ren *et al.*, "Proliferation and differentiation of bone marrow stromal cells under hypoxic conditions," (in eng), *Biochem Biophys Res Commun,* vol. 347, no. 1, pp. 12-21, Aug 18 2006, doi: 10.1016/j.bbrc.2006.05.169.

[598] Y.-M. Li *et al.*, "Effects of high glucose on mesenchymal stem cell proliferation and differentiation," *Biochemical and Biophysical Research Communications,* vol. 363, no. 1, pp. 209-215, 2007/11/09/ 2007, doi: https://doi.org/10.1016/j.bbrc.2007.08.161.

[599] M. Pawar *et al.*, "Glucose and Serum Deprivation Led to Altered Proliferation, Differentiation Potential and AMPK Activation in Stem Cells from Human Deciduous Tooth," (in eng), *J Pers Med,* vol. 12, no. 1, Dec 30 2021, doi: 10.3390/jpm12010018.

[600] A. Lage, R. Rodríguez, D. Valdés, and J. Lombardero, "Early effects of medium change in cultured cells: evidences for the existence of negative modulators of cell proliferation," (in eng), *Neoplasma,* vol. 30, no. 6, pp. 701-10, 1983.

[601] M. Filipak *et al.*, "Integrated control of proliferation and differentiation of mesenchymal stem cells," *Environmental Health Perspectives,* vol. 80, pp. 117-125, 1989, doi: doi:10.1289/ehp.8980117.

[602] V. Jossen, F. Muoio, S. Panella, Y. Harder, T. Tallone, and R. Eibl, "An Approach towards a GMP Compliant In-Vitro Expansion of Human Adipose Stem Cells for Autologous Therapies," *Bioengineering*, vol. 7, no. 3, doi: 10.3390/bioengineering7030077.

[603] A. M. Kolkmann, M. J. Post, M. A. M. Rutjens, A. L. M. van Essen, and P. Moutsatsou, "Serum-free media for the growth of primary bovine myoblasts," *Cytotechnology,* vol. 72, no. 1, pp. 111-120, 2020/02/01 2020, doi: 10.1007/s10616-019-00361-y.

[604] "StemMACS™ MSC Expansion Medium Kit XF, human." Miltenyi Biotec. https://www.miltenyibiotec.com/AT-en/products/stemmacs-msc-expansion-medium-kit-xf-human.html (accessed 28 July 2024, 2024).

[605] "DMEM, high glucose, GlutaMAX™ Supplement, pyruvate." Thermo Fisher Scientific. https://www.thermofisher.com/order/catalog/product/31966047 (accessed 28 June 2024, 2024).

[606] H. Yako *et al.*, "Role of pyruvate in maintaining cell viability and energy production under high-glucose conditions," *Scientific Reports,* vol. 11, no. 1, p. 18910, 2021/09/23 2021, doi: 10.1038/s41598-021-98082-w.

[607] "Fetal Bovine Serum, qualified, heat inactivated, Brazil." https://www.thermofisher.com/order/catalog/product/10500064 (accessed 2024).

[608] "Xeno-free mesenchymal stem cell media specially formulated for the rapid expansion of human mesenchymal stem cells isolated from a variety of sources, including adipose and bone marrow tissues.
Human Mese." Merck. https://www.merckmillipore.com/AT/de/product/Human-Mesenchymal-XF-Expansion-Medium,MM_NF-SCM045?ReferrerURL=https%3A%2F%2Fwww.google.com%2F (accessed 28 June 2024, 2024).

[609] H. X. Zhang, G. H. Du, and J. T. Zhang, "Assay of Mitochondrial Functions by Resazurin In Vitro," (in eng), *Acta Pharmacol Sin,* vol. 25, no. 3, pp. 385-9, Mar 2004.

[610] M. M. Lieberman, G. M. Patterson, and R. E. Moore, "In vitro bioassays for anticancer drug screening: effects of cell concentration and other assay parameters on growth inhibitory activity," (in eng), *Cancer Lett,* vol. 173, no. 1, pp. 21-29, 2001/11// 2001, doi: 10.1016/s0304-3835(01)00681-4.

[611] R. Hamid, Y. Rotshteyn, L. Rabadi, R. Parikh, and P. Bullock, "Comparison of alamar blue and MTT assays for high through-put screening," (in eng), *Toxicol In Vitro,* vol. 18, no. 5, pp. 703-10, Oct 2004, doi: 10.1016/j.tiv.2004.03.012.

[612] P. Wang, C. Li, H. Gong, X. Jiang, H. Wang, and K. Li, "Effects of synthesis conditions on the morphology of hydroxyapatite nanoparticles produced by wet chemical process," *Powder Technology,* vol. 203, no. 2, pp. 315-321, 2010/11/10/ 2010, doi: https://doi.org/10.1016/j.powtec.2010.05.023.

[613] S. C. Cox, P. Jamshidi, L. M. Grover, and K. K. Mallick, "Low temperature aqueous precipitation of needle-like nanophase hydroxyapatite," *Journal of Materials Science: Materials in Medicine,* vol. 25, no. 1, pp. 37-46, 2014/01/01 2014, doi: 10.1007/s10856-013-5042-y.

[614] T. Hielscher, "Ultrasonic Production of Nano-Size Dispersions and Emulsions," in *ENS 2005*, Paris, France, 2005-12 2005: TIMA Editions, https://hal.archives-ouvertes.fr/hal-00166996/document
https://hal.archives-ouvertes.fr/hal-00166996/file/1048.pdf, pp. 138-143. [Online]. Available: https://hal.archives-ouvertes.fr/hal-00166996. [Online]. Available: https://hal.archives-ouvertes.fr/hal-00166996

[615] K. F. Khan, "Application, Principle and Operation of ICP-OES in Pharmaceutical Analysis," vol. 8, pp. 281-282, 11/25 2019.

[616] K. Ashley, "Sonication as a sample preparation method for elemental analysis," in *Comprehensive Analytical Chemistry*, vol. 41: Elsevier, 2003, pp. 353-369.

[617] P. Koczoń *et al.*, "The Analytical Possibilities of FT-IR Spectroscopy Powered by Vibrating Molecules," (in eng), *Int J Mol Sci,* vol. 24, no. 2, Jan 5 2023, doi: 10.3390/ijms24021013.

[618] "How to Properly Use and Maintain Laboratory Equipment," in *Molecular Biology Problem Solver*, pp. 49-111.

[619] A. Grunenwald, C. Keyser, A. M. Sautereau, E. Crubézy, B. Ludes, and C. Drouet, "Revisiting carbonate quantification in apatite (bio)minerals: a validated FTIR methodology," *Journal of Archaeological Science,* vol. 49, pp. 134-141, 2014/09/01/ 2014, doi: https://doi.org/10.1016/j.jas.2014.05.004.

[620] F. Wu, D. D. W. Lin, J. H. Chang, C. Fischbach, L. A. Estroff, and D. Gourdon, "Effect of the Materials Properties of Hydroxyapatite Nanoparticles on Fibronectin Deposition and Conformation," *Crystal Growth & Design,* vol. 15, no. 5, pp. 2452-2460, 2015/05/06 2015, doi: 10.1021/acs.cgd.5b00231.

[621] G. Dal Sasso, Y. Asscher, I. Angelini, L. Nodari, and G. Artioli, "A universal curve of apatite crystallinity for the assessment of bone integrity and preservation," *Scientific Reports,* vol. 8, no. 1, p. 12025, 2018/08/13 2018, doi: 10.1038/s41598-018-30642-z.

[622] C. M. Hüls, H. Erlenkeuser, M. J. Nadeau, P. M. Grootes, and N. Andersen, "Experimental Study on the Origin of Cremated Bone Apatite Carbon," *Radiocarbon,* vol. 52, no. 2, pp. 587-599, 2010, doi: 10.1017/S0033822200045628.

[623] S. Weiner and O. Bar-Yosef, "States of preservation of bones from prehistoric sites in the Near East: A survey," *Journal of Archaeological Science,* vol. 17, no. 2, pp. 187-196, 1990/03/01/ 1990, doi: https://doi.org/10.1016/0305-4403(90)90058-D.

[624] A. Chauhan and P. Chauhan, "Powder XRD Technique and its Applications in Science and Technology," *Journal of analytical and bioanalytical techniques,* vol. 5, pp. 1-5, 2014.

[625] B. Diehl, "Chapter 1 - Principles in NMR Spectroscopy," in *NMR Spectroscopy in Pharmaceutical Analysis*, U. Holzgrabe, I. Wawer, and B. Diehl Eds. Amsterdam: Elsevier, 2008, pp. 1-41.

[626] G. Chinga, P. O. Johnsen, R. Dougherty, E. L. Berli, and J. Walter, "Quantification of the 3D microstructure of SC surfaces," (in eng), *J Microsc,* vol. 227, no. Pt 3, pp. 254-65, Sep 2007, doi: 10.1111/j.1365-2818.2007.01809.x.

[627] M. Parvinzadeh Gashti, S. Moradian, A. Rashidi, and M. Yazdanshenas, "Dispersibility of Hydrophilic and Hydrophobic Nano-Silica Particles in Polyethylene Terephthalate Films: Evaluation of Morphology and Thermal Properties," *Polymers and Polymer Composites,* vol. 23, pp. 285-296, 05/01 2015, doi: 10.1177/096739111502300502.

[628] T. Young, "III. An essay on the cohesion of fluids," *Philosophical Transactions of the Royal Society of London,* vol. 95, pp. 65-87, 1805, doi: doi:10.1098/rstl.1805.0005.

[629] S. Minardi *et al.*, "Evaluation of the osteoinductive potential of a bio-inspired scaffold mimicking the osteogenic niche for bone augmentation," *Biomaterials,* vol. 62, pp. 128-137, 2015/09/01/ 2015, doi: https://doi.org/10.1016/j.biomaterials.2015.05.011.

[630] M. Godino Izquierdo, "Osteogenic in vitro training of bone marrow mesenquimal cells for application in segmentary bone resections," *Revista Española de Cirugía Ortopédica y Traumatología (English Edition),* vol. 64, no. 4, pp. 236-243, 2020, doi: 10.1016/j.recote.2020.06.001.

[631] I. H. Song and J. E. Dennis, "Simple evaluation method for osteoinductive capacity of cells or scaffolds using ceramic cubes," (in eng), *Tissue Cell,* vol. 46, no. 5, pp. 372-8, Oct 2014, doi: 10.1016/j.tice.2014.06.009.

[632] B. W. M. d. Wildt, L. A. B. Cuypers, E. E. A. Cramer, A. S. Wentzel, K. Ito, and S. Hofmann, "The impact of culture variables on 3D human in vitro bone remodeling; a design of experiments approach," *bioRxiv,* p. 2022.11.11.516134, 2022, doi: 10.1101/2022.11.11.516134.

[633] P. Su *et al.*, "Mesenchymal Stem Cell Migration during Bone Formation and Bone Diseases Therapy," (in eng), *Int J Mol Sci,* vol. 19, no. 8, Aug 9 2018, doi: 10.3390/ijms19082343.

[634] F. Cal, T. Sezgin Arslan, B. Derkus, F. Kiran, U. Cengiz, and Y. E. Arslan, "Synthesis of Silica-Based Boron-Incorporated Collagen/Human Hair Keratin Hybrid Cryogels with the Potential Bone Formation Capability," *ACS Applied Bio Materials,* vol. 4, no. 9, pp. 7266-7279, 2021/09/20 2021, doi: 10.1021/acsabm.1c00805.

[635] Y. Tang, L. Zhu, J. S. Cho, X. Y. Li, and S. J. Weiss, "Matrix remodeling controls a nuclear lamin A/C-emerin network that directs Wnt-regulated stem cell fate," (in eng), *Dev Cell,* vol. 57, no. 4, pp. 480-495.e6, Feb 28 2022, doi: 10.1016/j.devcel.2022.01.015.

[636] U. Bjare, "Serum-free cell culture," *Pharmacology & Therapeutics,* vol. 53, no. 3, pp. 355-374, 1992/01/01/ 1992, doi: https://doi.org/10.1016/0163-7258(92)90056-6.

[637] J. van der Valk *et al.*, "Fetal Bovine Serum (FBS): Past - Present - Future," (in eng), *Altex,* vol. 35, no. 1, pp. 99-118, 2018, doi: 10.14573/altex.1705101.

[638] E. Altrock *et al.*, "Significant improvement of bone marrow-derived MSC expansion from MDS patients by defined xeno-free medium," (in eng), *Stem Cell Res Ther,* vol. 14, no. 1, p. 156, Jun 7 2023, doi: 10.1186/s13287-023-03386-5.

[639] K. Godthardt *et al.*, *Improved clinical-scale MSC isolation from primary tissue and expansion with a GMP matrix- and xeno-free medium*. 2016.

[640] S. Parvin Nejad *et al.*, "Serum- and xeno-free culture of human umbilical cord perivascular cells for pediatric heart valve tissue engineering," *Stem Cell Research & Therapy,* vol. 14, no. 1, p. 96, 2023/04/19 2023, doi: 10.1186/s13287-023-03318-3.

[641] O. Guillame-Gentil *et al.*, "Engineering the Extracellular Environment: Strategies for Building 2D and 3D Cellular Structures," *Advanced Materials,* vol. 22, no. 48, pp. 5443-5462, 2010, doi: https://doi.org/10.1002/adma.201001747.

[642] P. Silva Couto, S. A. Molina, D. O'Sullivan, L. O'Neill, A. M. Lyness, and Q. A. Rafiq, "Understanding the impact of bioactive coating materials for human mesenchymal stromal cells and implications for manufacturing," (in eng), *Biotechnol Lett,* vol. 45, no. 8, pp. 1013-1027, Aug 2023, doi: 10.1007/s10529-023-03369-9.

[643] R. Pal, M. Hanwate, M. Jan, and S. Totey, "Phenotypic and functional comparison of optimum culture conditions for upscaling of bone marrow-derived mesenchymal stem cells," *Journal of Tissue Engineering and Regenerative Medicine,* vol. 3, no. 3, pp. 163-174, 2009, doi: https://doi.org/10.1002/term.143.

[644] Z. Gong, G. Calkins, E.-c. Cheng, D. Krause, and L. E. Niklason, "Influence of Culture Medium on Smooth Muscle Cell Differentiation from Human Bone Marrow–Derived Mesenchymal Stem Cells," *Tissue Engineering Part A,* vol. 15, no. 2, pp. 319-330, 2009/02/01 2008, doi: 10.1089/ten.tea.2008.0161.

[645] D. Mushahary, A. Spittler, C. Kasper, V. Weber, and V. Charwat, "Isolation, cultivation, and characterization of human mesenchymal stem cells," *Cytometry Part A,* vol. 93, no. 1, pp. 19-31, 2018, doi: https://doi.org/10.1002/cyto.a.23242.

[646] M. Dhanasekaran, S. Indumathi, R. P. Lissa, R. Harikrishnan, J. S. Rajkumar, and D. Sudarsanam, "A comprehensive study on optimization of proliferation and differentiation potency of bone marrow derived mesenchymal stem cells under prolonged culture condition," *Cytotechnology,* vol. 65, no. 2, pp. 187-197, 2013/03/01 2013, doi: 10.1007/s10616-012-9471-0.

[647] R. Arredondo *et al.*, "Fibronectin-coating enhances attachment and proliferation of mesenchymal stem cells on a polyurethane meniscal scaffold," (in eng), *Regen Ther,* vol. 18, pp. 480-486, Dec 2021, doi: 10.1016/j.reth.2021.11.001.

[648] C. Linsley, B. Wu, and B. Tawil, "The Effect of Fibrinogen, Collagen Type I, and Fibronectin on Mesenchymal Stem Cell Growth and Differentiation into Osteoblasts," *Tissue Engineering Part A,* vol. 19, pp. 1416-1423, 06/01 2013, doi: 10.1089/ten.tea.2012.0523.

[649] C. Obara *et al.*, "Differentiation and Molecular Properties of Mesenchymal Stem Cells Derived from Murine Induced Pluripotent Stem Cells Derived on Gelatin or Collagen," (in eng), *Stem Cells Int,* vol. 2016, p. 9013089, 2016, doi: 10.1155/2016/9013089.

[650] K. A. Davis, H. Peng, L. Chelvarajan, A. Abdel-Latif, and B. J. Berron, "Increased yield of gelatin coated therapeutic cells through cholesterol insertion," *Journal of Biomedical Materials Research Part A,* vol. 109, no. 3, pp. 326-335, 2021, doi: https://doi.org/10.1002/jbm.a.37025.

[651] N. Ogura *et al.*, "Differentiation of the human mesenchymal stem cells derived from bone marrow and enhancement of cell attachment by fibronectin," (in eng), *J Oral Sci,* vol. 46, no. 4, pp. 207-13, Dec 2004, doi: 10.2334/josnusd.46.207.

[652] L. Chen *et al.*, "Effect of fibronectin, FGF-2, and BMP4 in the stemness maintenance of BMSCs and the metabolic and proteomic cues involved," *Stem Cell Research & Therapy,* vol. 12, no. 1, p. 165, 2021/03/06 2021, doi: 10.1186/s13287-021-02227-7.

[653] V. Basoli, E. Della Bella, E. J. Kubosch, M. Alini, and M. J. Stoddart, "Effect of expansion media and fibronectin coating on growth and chondrogenic differentiation of human bone marrow-derived mesenchymal stromal cells," *Scientific Reports,* vol. 11, no. 1, p. 13089, 2021/06/22 2021, doi: 10.1038/s41598-021-92270-4.

[654] C. J. Sherr and R. A. DePinho, "Cellular senescence: mitotic clock or culture shock?," (in eng), *Cell,* vol. 102, no. 4, pp. 407-10, Aug 18 2000, doi: 10.1016/s0092-8674(00)00046-5.

[655] X. Ren *et al.*, "Osteogenic ability using porous hydroxyapatite scaffold-based delivery of human placenta-derived mesenchymal stem cells," (in eng), *Exp Ther Med,* vol. 22, no. 4, p. 1091, Oct 2021, doi: 10.3892/etm.2021.10525.

[656] N. A. R. Putranti *et al.*, "Combination of Carbonate Hydroxyapatite and Stem Cells from Human Deciduous Teeth Promotes Bone Regeneration by Enhancing BMP-2, VEGF and CD31 Expression in Immunodeficient Mice," *Cells,* vol. 11, no. 12, p. 1914, 2022. [Online]. Available: https://www.mdpi.com/2073-4409/11/12/1914.

[657] V. M. Wu and V. Uskoković, "Is there a relationship between solubility and resorbability of different calcium phosphate phases in vitro?," (in eng), *Biochim Biophys Acta,* vol. 1860, no. 10, pp. 2157-2168, 2016, doi: 10.1016/j.bbagen.2016.05.022.

[658] J.-H. Ryu *et al.*, "Synergistic Effect of Porous Hydroxyapatite Scaffolds Combined with Bioactive Glass/Poly(lactic-co-glycolic acid) Composite Fibers Promotes Osteogenic Activity and Bioactivity," *ACS Omega,* vol. 4, no. 1, pp. 2302-2310, 2019/01/31 2019, doi: 10.1021/acsomega.8b02898.

[659] A. El-Ghannam and P. Ducheyne, "1.109 - Bioactive Ceramics," in *Comprehensive Biomaterials*, P. Ducheyne Ed. Oxford: Elsevier, 2011, pp. 157-179.

[660] A. Ressler, A. Žužić, I. Ivanišević, N. Kamboj, and H. Ivanković, "Ionic substituted hydroxyapatite for bone regeneration applications: A review," 2021.

[661] C. Garbo *et al.*, "Advanced Mg, Zn, Sr, Si Multi-Substituted Hydroxyapatites for Bone Regeneration," (in eng), *Int J Nanomedicine,* vol. 15, pp. 1037-1058, 2020, doi: 10.2147/ijn.S226630.

[662] H. Yang *et al.*, "In vitro and in vivo studies on zinc-hydroxyapatite composites as novel biodegradable metal matrix composite for orthopedic applications," *Acta Biomaterialia,* vol. 71, pp. 200-214, 2018/04/15/ 2018, doi: https://doi.org/10.1016/j.actbio.2018.03.007.

[663] J. Pan, S. Prabakaran, and M. Rajan, "In-vivo assessment of minerals substituted hydroxyapatite / poly sorbitol sebacate glutamate (PSSG) composite coating on titanium metal implant for orthopedic implantation," *Biomedicine & Pharmacotherapy,* vol. 119, p. 109404, 2019/11/01/ 2019, doi: https://doi.org/10.1016/j.biopha.2019.109404.

[664] J. Li *et al.*, "Osteogenesis effects of strontium-substituted hydroxyapatite coatings on true bone ceramic surfaces in vitro and in vivo," *Biomedical Materials,* vol. 13, no. 1, p. 015018, 2017/12/20 2018, doi: 10.1088/1748-605X/aa89af.

[665] D. S. Yoo, J. S. Cho, Y.-C. Chung, and S.-H. Rhee, "Defect structures of sodium and chloride co-substituted hydroxyapatite and its osseointegration capacity," *Journal of Materials Science,* vol. 56, no. 9, pp. 5493-5508, 2021/03/01 2021, doi: 10.1007/s10853-020-05645-9.

[666] L. Yang *et al.*, "Bioactive Sr2+/Fe3+ co-substituted hydroxyapatite in cryogenically 3D printed porous scaffolds for bone tissue engineering," *Biofabrication,* vol. 13, no. 3, p. 035007, 2021/04/02 2021, doi: 10.1088/1758-5090/abcf8d.

[667] J. M. Burnell, E. J. Teubner, and A. G. Miller, "Normal maturational changes in bone matrix, mineral, and crystal size in the rat," *Calcified Tissue International,* vol. 31, no. 1, pp. 13-19, 1980/12/01 1980, doi: 10.1007/BF02407162.

[668] B. J. Hunt, "Age and Magnesium Deficiency in the Rat with Emphasis on Bone and Muscle Magnesium," *American Journal of Physiology-Legacy Content,* vol. 221, no. 6, pp. 1809-1817, 1971.

[669] S. Zaichick and V. Zaichick, "The effect of age and gender on 38 chemical element contents in human iliac crest investigated by instrumental neutron activation analysis," *Journal of Trace Elements in Medicine and Biology,* vol. 24, no. 1, pp. 1-6, 2010/01/01/ 2010, doi: https://doi.org/10.1016/j.jtemb.2009.07.002.

[670] Ż. Ciosek, K. Kot, D. Kosik-Bogacka, N. Łanocha-Arendarczyk, and I. Rotter, "The Effects of Calcium, Magnesium, Phosphorus, Fluoride, and Lead on Bone Tissue," *Biomolecules,* vol. 11, no. 4, p. 506, 2021. [Online]. Available: https://www.mdpi.com/2218-273X/11/4/506.

[671] I. D. McCarthy and S. P. F. Hughes, "Inhibition of bone cell metabolism increases strontium-85 uptake," *Calcified Tissue International,* vol. 39, no. 6, pp. 386-389, 1986/11/01 1986, doi: 10.1007/BF02555176.

[672] E. Canalis, M. Hott, P. Deloffre, Y. Tsouderos, and P. J. Marie, "The divalent strontium salt S12911 enhances bone cell replication and bone formation in vitro," *Bone,* vol. 18, no. 6, pp. 517-523, 1996/06/01/ 1996, doi: https://doi.org/10.1016/8756-3282(96)00080-4.

[673] A. A. Chaudhry *et al.*, "Instant nano-hydroxyapatite: a continuous and rapid hydrothermal synthesis," *Chemical Communications,* 10.1039/B518102J no. 21, pp. 2286-2288, 2006, doi: 10.1039/B518102J.

[674] A. Anwar, I. U. Rehman, and J. A. Darr, "Low-Temperature Synthesis and Surface Modification of High Surface Area Calcium Hydroxyapatite Nanorods Incorporating Organofunctionalized Surfaces," *The Journal of Physical Chemistry C,* vol. 120, no. 51, pp. 29069-29076, 2016/12/29 2016, doi: 10.1021/acs.jpcc.6b05878.

[675] A. A. Chaudhry *et al.*, "Synthesis and characterisation of magnesium substituted calcium phosphate bioceramic nanoparticles made via continuous hydrothermal flow synthesis," *Journal of Materials Chemistry,* 10.1039/B807920J vol. 18, no. 48, pp. 5900-5908, 2008, doi: 10.1039/B807920J.

[676] S. Lala, M. Ghosh, P. K. Das, D. Das, T. Kar, and S. K. Pradhan, "Magnesium substitution in carbonated hydroxyapatite: Structural and microstructural characterization by Rietveld's refinement," *Materials Chemistry and Physics,* vol. 170, pp. 319-329, 2016/02/15/ 2016, doi: https://doi.org/10.1016/j.matchemphys.2015.12.058.

[677] P. Rajkumar and B. K. Sarma, "Role of Zn and Mg substitutions on the mechanical behaviour of biomimetic hydroxyapatite and insight of the emergence of hydroxyapatite-ZnO nanocomposite," *Materials Characterization,* vol. 176, p. 111107, 2021/06/01/ 2021, doi: https://doi.org/10.1016/j.matchar.2021.111107.

[678] B.-C. Liga and B. Natalija, "Research of Calcium Phosphates Using Fourier Transform Infrared Spectroscopy," in *Infrared Spectroscopy*, T. Theophile Ed. Rijeka: IntechOpen, 2012, p. Ch. 6.

[679] I. Petrov, B. Šoptrajanov, N. Fuson, and J. R. Lawson, "Infra-red investigation of dicalcium phosphates," *Spectrochimica Acta Part A: Molecular Spectroscopy,* vol. 23, no. 10, pp. 2637-2646, 1967/10/01/ 1967, doi: https://doi.org/10.1016/0584-8539(67)80155-7.

[680] A. Antonakos, E. Liarokapis, and T. Leventouri, "Micro-Raman and FTIR studies of synthetic and natural apatites," *Biomaterials,* vol. 28, no. 19, pp. 3043-3054, 2007/07/01/ 2007, doi: https://doi.org/10.1016/j.biomaterials.2007.02.028.

[681] S. Von Euw *et al.*, "Bone mineral: new insights into its chemical composition," *Scientific Reports,* vol. 9, no. 1, p. 8456, 2019/06/11 2019, doi: 10.1038/s41598-019-44620-6.

[682] B. O. Fowler, "Infrared studies of apatites. I. Vibrational assignments for calcium, strontium, and barium hydroxyapatites utilizing isotopic substitution," *Inorganic Chemistry,* vol. 13, no. 1, pp. 194-207, 1974/01/01 1974, doi: 10.1021/ic50131a039.

[683] B. O. Fowler, E. C. Moreno, and W. E. Brown, "Infra-red spectra of hydroxyapatite, octacalcium phosphate and pyrolysed octacalcium phosphate," *Archives of Oral Biology,* vol. 11, no. 5, pp. 477-492, 1966/05/01/ 1966, doi: https://doi.org/10.1016/0003-9969(66)90154-3.

[684] I. u. Rehman and W. Bonfield, "Characterization of hydroxyapatite and carbonated apatite by photo acoustic FTIR spectroscopy," *Journal of Materials Science: Materials in Medicine,* vol. 8, pp. 1-4, 1997.

[685] F. Casciani and R. A. Condrate, "The Vibrational Spectra of Brushite, CaHPO4·2H2O," *Spectroscopy Letters,* vol. 12, no. 10, pp. 699-713, 1979/01/01 1979, doi: 10.1080/00387017908069196.

[686] A. Hirsch *et al.*, "Infrared Absorption Spectrum of Brushite from First Principles," *Chemistry of Materials,* vol. 26, no. 9, pp. 2934-2942, 2014/05/13 2014, doi: 10.1021/cm500650t.

[687] K. J. Wali, A. T. Saleh, and G. F. Huseien, "Preparation of Injectable Dicalcium Phosphate Bone Cement for Potential Orthopedic Applications," *Eng,* vol. 5, no. 2, pp. 1028-1042, 2024. [Online]. Available: https://www.mdpi.com/2673-4117/5/2/56.

[688] L. Tortet, J. R. Gavarri, G. Nihoul, and A. J. Dianoux, "Study of Protonic Mobility in CaHPO4·2H2O (Brushite) and CaHPO4(Monetite) by Infrared Spectroscopy and Neutron Scattering," *Journal of Solid State Chemistry,* vol. 132, no. 1, pp. 6-16, 1997/08/01/ 1997, doi: https://doi.org/10.1006/jssc.1997.7383.

[689] C. Drouet, "Apatite Formation: Why It May Not Work as Planned, and How to Conclusively Identify Apatite Compounds," *BioMed Research International,* vol. 2013, p. 490946, 2013/07/29 2013, doi: 10.1155/2013/490946.

[690] Z. Hua Cheng, A. Yasukawa, K. Kandori, and T. Ishikawa, "FTIR Study on incorporation of CO2 into calcium hydroxyapatite," *Journal of the Chemical Society, Faraday Transactions,* 10.1039/A708581H vol. 94, no. 10, pp. 1501-1505, 1998, doi: 10.1039/A708581H.

[691] W. L. Suchanek, K. Byrappa, P. Shuk, R. E. Riman, V. F. Janas, and K. S. TenHuisen, "Preparation of magnesium-substituted hydroxyapatite powders by the mechanochemical–hydrothermal method," *Biomaterials,* vol. 25, no. 19, pp. 4647-4657, 2004/08/01/ 2004, doi: https://doi.org/10.1016/j.biomaterials.2003.12.008.

[692] S. Meejoo, W. Maneeprakorn, and P. Winotai, "Phase and thermal stability of nanocrystalline hydroxyapatite prepared via microwave heating," *Thermochimica Acta,* vol. 447, no. 1, pp. 115-120, 2006/08/01/ 2006, doi: https://doi.org/10.1016/j.tca.2006.04.013.

[693] Z. H. Cheng, A. Yasukawa, K. Kandori, and T. Ishikawa, "FTIR Study of Adsorption of CO2 on Nonstoichiometric Calcium Hydroxyapatite," *Langmuir,* vol. 14, no. 23, pp. 6681-6686, 1998/11/01 1998, doi: 10.1021/la980339n.

[694] S. C. Cox, P. Jamshidi, L. M. Grover, and K. K. Mallick, "Preparation and characterisation of nanophase Sr, Mg, and Zn substituted hydroxyapatite by aqueous precipitation," *Materials Science and Engineering: C,* vol. 35, pp. 106-114, 2014/02/01/ 2014, doi: https://doi.org/10.1016/j.msec.2013.10.015.

[695] H. Madupalli, B. Pavan, and M. M. J. Tecklenburg, "Carbonate substitution in the mineral component of bone: Discriminating the structural changes, simultaneously imposed by carbonate in A and B sites of apatite," *Journal of Solid State Chemistry,* vol. 255, pp. 27-35, 2017/11/01/ 2017, doi: https://doi.org/10.1016/j.jssc.2017.07.025.

[696] E. Landi *et al.*, "Biomimetic Mg- and Mg, CO3-substituted hydroxyapatites: synthesis characterization and in vitro behaviour," *Journal of the European Ceramic Society,* vol. 26, no. 13, pp. 2593-2601, 2006/01/01/ 2006, doi: https://doi.org/10.1016/j.jeurceramsoc.2005.06.040.

[697] A. J. Hoeher, S. T. Mergelsberg, O. J. Borkiewicz, and F. M. Michel, "Impacts of Initial Ca/P on Amorphous Calcium Phosphate," *Crystal Growth & Design,* vol. 21, no. 7, pp. 3736-3745, 2021/07/07 2021, doi: 10.1021/acs.cgd.1c00058.

[698] C. Reynaud, C. Thomas, and G. Costentin, "On the Comprehensive Precipitation of Hydroxyapatites Unraveled by a Combined Kinetic–Thermodynamic Approach," *Inorganic Chemistry,* vol. 61, no. 7, pp. 3296-3308, 2022/02/21 2022, doi: 10.1021/acs.inorgchem.1c03884.

[699] Y. Sa *et al.*, "Are Different Crystallinity-Index-Calculating Methods of Hydroxyapatite Efficient and Consistent?," *New Journal of Chemistry,* vol. 41, pp. 5723-5731, 2017.

[700] S. J. Gadaleta, E. P. Paschalis, F. Betts, R. Mendelsohn, and A. L. Boskey, "Fourier transform infrared spectroscopy of the solution-mediated conversion of amorphous calcium phosphate to hydroxyapatite: New correlations between X-ray diffraction and infrared data," *Calcified Tissue International,* vol. 58, no. 1, pp. 9-16, 1996/01/01 1996, doi: 10.1007/BF02509540.

[701] M. S. Tung and W. E. Brown, "An Intermediate State in Hydrolysis of Amorphous Calcium Phosphate," *Calcified Tissue International,* vol. 35, no. 1, pp. 783-790, 1983/12/01 1983, doi: 10.1007/BF02405124.

[702] H. Ding, H. Pan, X. Xu, and R. Tang, "Toward a Detailed Understanding of Magnesium Ions on Hydroxyapatite Crystallization Inhibition," *Crystal Growth & Design,* vol. 14, no. 2, pp. 763-769, 2014/02/05 2014, doi: 10.1021/cg401619s.

[703] C. Holt *et al.*, "Preparation of amorphous calcium-magnesium phosphates at pH 7 and characterization by x-ray absorption and fourier transform infrared spectroscopy," *Journal of Crystal Growth,* vol. 92, no. 1, pp. 239-252, 1988/10/01/ 1988, doi: https://doi.org/10.1016/0022-0248(88)90455-1.

[704] J. M. Stutman, J. D. Termine, and A. S. Posner, "Vibrational Spectra and Structure of the Phosphate Ion in Some Calcium Phosphates," (in eng), *Trans N Y Acad Sci,* vol. 27, pp. 669-75, Apr 1965, doi: 10.1111/j.2164-0947.1965.tb02224.x.

[705] N. C. Blumenthal, A. S. Posner, and J. M. Holmes, "Effect of preparation conditions on the properties and transformation of amorphous calcium phosphate," *Materials Research Bulletin,* vol. 7, no. 11, pp. 1181-1189, 1972/11/01/ 1972, doi: https://doi.org/10.1016/0025-5408(72)90097-9.

[706] M. E. Tadros, J. Skalny, and R. S. Kalyoncu, "Kinetics of calcium hydroxide crystal growth from solution," *Journal of Colloid and Interface Science,* vol. 55, no. 1, pp. 20-24, 1976/04/01/ 1976, doi: https://doi.org/10.1016/0021-9797(76)90004-7.

[707] G. R. Osorio-Celestino, M. Hernandez, D. Solis-Ibarra, S. Tehuacanero-Cuapa, A. Rodríguez-Gómez, and A. P. Gómora-Figueroa, "Influence of Calcium Scaling on Corrosion Behavior of Steel and Aluminum Alloys," (in eng), *ACS Omega,* vol. 5, no. 28, pp. 17304-17313, Jul 21 2020, doi: 10.1021/acsomega.0c01538.

[708] H. Visser, "The Role of Surface Forces in Fouling of Stainless Steel in the Dairy Industry," *Journal of Dispersion Science and Technology,* vol. 19, no. 6-7, pp. 1127-1150, 1998/01/01 1998, doi: 10.1080/01932699808913233.

[709] L. Armelao, A. Bassan, R. Bertoncello, G. Biscontin, S. Daolio, and A. Glisenti, "Silica glass interaction with calcium hydroxide: a surface chemistry approach," *Journal of Cultural Heritage,* vol. 1, no. 4, pp. 375-384, 2000/12/01/ 2000, doi: https://doi.org/10.1016/S1296-2074(00)01093-1.

[710] C. L. Briant, Z. F. Wang, and N. Chollocoop, "Hydrogen embrittlement of commercial purity titanium," *Corrosion Science,* vol. 44, pp. 1875-1888, 08/01 2002, doi: 10.1016/S0010-938X(01)00159-7.

[711] D. Prando *et al.*, "Corrosion of Titanium: Part 1: Aggressive Environments and Main Forms of Degradation," *Journal of Applied Biomaterials & Functional Materials,* vol. 15, no. 4, pp. e291-e302, 2017, doi: 10.5301/jabfm.5000387.

[712] E. Łunarska, O. Chernyayeva, and D. Lisovytskiy, "Hydride Formation at Cathodic Charging of α-Ti," *Advances in Materials Sciences,* vol. 8, pp. 105-114, 09/01 2008, doi: 10.2478/v10077-008-0012-7.

[713] G. Ranjith Kumar, G. Rajyalakshmi, and S. Swaroop, "A critical appraisal of laser peening and its impact on hydrogen embrittlement of titanium alloys," *Proceedings of the Institution of Mechanical Engineers, Part B: Journal of Engineering Manufacture,* vol. 233, no. 13, pp. 2371-2398, 2019, doi: 10.1177/0954405419838956.

[714] P. W. Arnold, "The nature of precipitated calcium phosphates," *Transactions of the Faraday Society,* 10.1039/TF9504601061 vol. 46, no. 0, pp. 1061-1072, 1950, doi: 10.1039/TF9504601061.

[715] M. Boulet and J. R. Marier, "Precipitation of calcium phosphates from solutions at near physiological concentrations," *Archives of Biochemistry and Biophysics,* vol. 93, no. 1, pp. 157-165, 1961/04/01/ 1961, doi: https://doi.org/10.1016/0003-9861(61)90329-0.

[716] C. Verwilghen, S. Rio, A. Nzihou, D. Gauthier, G. Flamant, and P. J. Sharrock, "Preparation of high specific surface area hydroxyapatite for environmental

applications," *Journal of Materials Science,* vol. 42, no. 15, pp. 6062-6066, 2007/08/01 2007, doi: 10.1007/s10853-006-1160-y.

[717] E. D. Eanes, J. D. Termine, and M. U. Nylen, "An electron microscopic study of the formation of amorphous calcium phosphate and its transformation to crystalline apatite," *Calcified Tissue Research,* vol. 12, no. 1, pp. 143-158, 1973/12/01 1973, doi: 10.1007/BF02013730.

[718] X. Yang, B. Xie, L. Wang, Y. Qin, Z. J. Henneman, and G. H. Nancollas, "Influence of magnesium ions and amino acids on the nucleation and growth of hydroxyapatite," *CrystEngComm,* vol. 13, no. 4, pp. 1153-1158, 2011, doi: 10.1039/C0CE00470G.

[719] M. S. Tung, "Calcium Phosphates: Structure, Composition, Solubility, and Stability," in *Calcium Phosphates in Biological and Industrial Systems*, Z. Amjad Ed. Boston, MA: Springer US, 1998, pp. 1-19.

[720] J. D. Termine and A. S. Posner, "Calcium phosphate formation in vitro: I. Factors affecting initial phase separation," *Archives of Biochemistry and Biophysics,* vol. 140, no. 2, pp. 307-317, 1970/10/01/ 1970, doi: https://doi.org/10.1016/0003-9861(70)90071-8.

[721] F. Lagno, S. D. F. Rocha, L. Katsarou, and G. P. Demopoulos, "Supersaturation-Controlled Synthesis of Dicalcium Phosphate Dihydrate and Nanocrystalline Calcium-Deficient Hydroxyapatite," *Industrial & Engineering Chemistry Research,* vol. 51, no. 19, pp. 6605-6612, 2012/05/16 2012, doi: 10.1021/ie300059d.

[722] M. Córdova-Udaeta, Y. Kim, K. Yasukawa, Y. Kato, T. Fujita, and G. Dodbiba, "Study on the Synthesis of Hydroxyapatite under Highly Alkaline Conditions," *Industrial & Engineering Chemistry Research,* vol. 60, no. 11, pp. 4385-4396, 2021/03/24 2021, doi: 10.1021/acs.iecr.0c05969.

[723] D. P. McDonogh, P. Kirupananthan, and D. Gebauer, "Counterintuitive Crystallization: Rate Effects in Calcium Phosphate Nucleation at Near-Physiological pH," *Crystal Growth & Design,* vol. 23, no. 10, pp. 7037-7043, 2023/10/04/ 2023, doi: 10.1021/acs.cgd.3c00851.

[724] E. Landi, G. Celotti, G. Logroscino, and A. Tampieri, "Carbonated hydroxyapatite as bone substitute," *Journal of the European Ceramic Society,* vol. 23, no. 15, pp. 2931-2937, 2003/01/01/ 2003, doi: https://doi.org/10.1016/S0955-2219(03)00304-2.

[725] M. Elassfouri, B. E. ouatli, F. Abida, M. Jamil, A. Kheribech, and Z. Hatim, "Ions Traces Substitution in Stoichiometric Calcium-Hydroxyapatite: Structural Analysis by Rietveld Refinement," *chemistry and materials research,* vol. 8, pp. 8-15, 2016.

[726] L. T. Bang, B. D. Long, and R. Othman, "Carbonate Hydroxyapatite and Silicon-Substituted Carbonate Hydroxyapatite: Synthesis, Mechanical Properties, and Solubility Evaluations," *The Scientific World Journal,* vol. 2014, p. 969876, 2014/03/02 2014, doi: 10.1155/2014/969876.

[727] S. Gomes *et al.*, "Thorough analysis of silicon substitution in biphasic calcium phosphate bioceramics: A multi-technique study," *Acta Biomaterialia,* vol. 6, no. 8, pp. 3264-3274, 2010/08/01/ 2010, doi: https://doi.org/10.1016/j.actbio.2010.02.034.

[728] M. Kikuchi, A. Yamazaki, R. Otsuka, M. Akao, and H. Aoki, "Crystal Structure of Sr-Substituted Hydroxyapatite Synthesized by Hydrothermal Method," *Journal of Solid State Chemistry,* vol. 113, no. 2, pp. 373-378, 1994/12/01/ 1994, doi: https://doi.org/10.1006/jssc.1994.1383.

[729] T. T. T. Pham *et al.*, "Impact of physical and chemical parameters on the hydroxyapatite nanopowder synthesized by chemical precipitation method," *Advances in Natural Sciences: Nanoscience and Nanotechnology,* vol. 4, no. 3, p. 035014, 2013/07/01 2013, doi: 10.1088/2043-6262/4/3/035014.

[730] H. Takeyama *et al.*, "Fabrication of bioresorbable hydroxyapatite bone grafts through the setting reaction of calcium phosphate cement," (in eng), *Dent Mater J,* vol. 41, no. 6, pp. 882-888, Nov 30 2022, doi: 10.4012/dmj.2022-045.

[731] J. L. Meyer and E. D. Eanes, "A thermodynamic analysis of the amorphous to crystalline calcium phosphate transformation," *Calcified Tissue Research,* vol. 25, no. 1, pp. 59-68, 1978/12/01 1978, doi: 10.1007/BF02010752.

[732] J. L. Meyer and C. C. Weatherall, "Amorphous to Crystalline Calcium Phosphate Phase Transformation at Elevated pH," *Journal of Colloid and Interface Science,* vol. 89, no. 1, pp. 257-267, 1982/09/01/ 1982, doi: https://doi.org/10.1016/0021-9797(82)90139-4.

[733] U. Amornkitbamrung *et al.*, "Interface-Controlled Biomimetic Intrafibrillar Mineralization of Collagen: Effect of Ca2+/[PO4]3− Concentration Ratio," *Advanced Materials Interfaces,* vol. 10, no. 24, p. 2300384, 2023, doi: https://doi.org/10.1002/admi.202300384.

[734] O. Rybalkina *et al.*, "Partial Fluxes of Phosphoric Acid Anions through Anion-Exchange Membranes in the Course of NaH2PO4 Solution Electrodialysis," *International Journal of Molecular Sciences,* vol. 20, no. 14, p. 3593, 2019. [Online]. Available: https://www.mdpi.com/1422-0067/20/14/3593.

[735] F. Vassallo *et al.*, "A pilot-plant for the selective recovery of magnesium and calcium from waste brines," *Desalination,* vol. 517, p. 115231, 2021/12/01/ 2021, doi: https://doi.org/10.1016/j.desal.2021.115231.

[736] A. Moghal, S. Mohammed, and M. Al-Shamrani, "State-of-the-Art Review on Strontium Toxicokinetics, Mechanistic Response, Alterations and Regulations," *International Journal of GEOMATE,* vol. 16, pp. 204-213, 01/01 2019, doi: 10.21660/2019.53.71462.

[737] J. Parks and M. Edwards, "Precipitative Removal of As, Ba, B, Cr, Sr, and V Using Sodium Carbonate," *Journal of Environmental Engineering-asce - J ENVIRON ENG-ASCE,* vol. 132, 05/01 2006, doi: 10.1061/(ASCE)0733-9372(2006)132:5(489).

[738] P. Fellner *et al.*, "Preparation of magnesium hydroxide from nitrate aqueous solution," *Chemical Papers,* vol. 65, pp. 454-459, 08/01 2011, doi: 10.2478/s11696-011-0038-x.

[739] C. Jaeger, S. Maltsev, and A. Karrasch, "Progress of Structural Elucidation of Amorphous Calcium Phosphate(ACP)and Hydroxyapatite (HAp): Disorder and Surfaces as Seen by Solid State NMR," *Key Engineering Materials,* vol. 309-311, pp. 69 - 72, 2006.

[740] M. S. Tung, L. C. Chow, and W. E. Brown, "Basic Biological Sciences Hydrolysis of Dicalcium Phosphate Dihydrate in the Presence or Absence of Calcium Fluoride," *Journal of Dental Research,* vol. 64, no. 1, pp. 2-5, 1985, doi: 10.1177/00220345850640010301.

[741] N. S. Al-Qasas and S. Rohani, "Synthesis of Pure Hydroxyapatite and the Effect of Synthesis Conditions on its Yield, Crystallinity, Morphology and Mean Particle Size," *Separation Science and Technology,* vol. 40, no. 15, pp. 3187-3224, 2005/11/01 2005, doi: 10.1080/01496390500385400.

[742] E. D. Eanes, "Amorphous Calcium Phosphate: Thermodynamic and Kinetic Considerations," in *Calcium Phosphates in Biological and Industrial Systems*, Z. Amjad Ed. Boston, MA: Springer US, 1998, pp. 21-39.

[743] L. Montastruc, C. Azzaro-Pantel, B. Biscans, M. Cabassud, and S. Domenech, "A thermochemical approach for calcium phosphate precipitation modeling in a pellet reactor," *Chemical Engineering Journal,* vol. 94, no. 1, pp. 41-50, 2003/07/15/ 2003, doi: https://doi.org/10.1016/S1385-8947(03)00044-5.

[744] C. Holt *et al.*, "Amorphous Calcium Phosphates Prepared at pH 6.5 and 6.0," *Materials Research Bulletin,* vol. 24, no. 1, pp. 55-62, 1989/01/01/ 1989, doi: https://doi.org/10.1016/0025-5408(89)90008-1.

[745] J. Zhang, L. Wang, and C. V. Putnis, "Underlying Role of Brushite in Pathological Mineralization of Hydroxyapatite," *The Journal of Physical Chemistry B,* vol. 123, no. 13, pp. 2874-2881, 2019/04/04 2019, doi: 10.1021/acs.jpcb.9b00728.

[746] J. Terra, E. R. Dourado, J.-G. Eon, D. E. Ellis, G. Gonzalez, and A. M. Rossi, "The structure of strontium-doped hydroxyapatite: an experimental and theoretical study," *Physical Chemistry Chemical Physics,* 10.1039/B802841A vol. 11, no. 3, pp. 568-577, 2009, doi: 10.1039/B802841A.

[747] W. Jahnen-Dechent and M. Ketteler, "Magnesium basics," (in eng), *Clin Kidney J,* vol. 5, no. Suppl 1, pp. i3-i14, Feb 2012, doi: 10.1093/ndtplus/sfr163.

[748] M. R. Christoffersen, J. Christoffersen, and W. Kibalczyc, "Apparent Solubilities of Two Amorphous Calcium Phosphates and of Octacalcium Phosphate in the Temperature Range 30–42°C," *Journal of Crystal Growth,* vol. 106, no. 2, pp. 349-354, 1990/11/01/ 1990, doi: https://doi.org/10.1016/0022-0248(90)90079-Z.

[749] Å. Bengtsson, A. Shchukarev, P. Persson, and S. Sjöberg, "A solubility and surface complexation study of a non-stoichiometric hydroxyapatite," *Geochimica et*

*Cosmochimica Acta,* vol. 73, no. 2, pp. 257-267, 2009/01/15/ 2009, doi: https://doi.org/10.1016/j.gca.2008.09.034.

[750] M. Sayahi *et al.*, "Brushite (Ca,M)HPO4, 2H2O doping with bioactive ions (M = Mg2+, Sr2+, Zn2+, Cu2+, and Ag+): a new path to functional biomaterials?," *Materials Today Chemistry,* vol. 16, p. 100230, 2020/06/01/ 2020, doi: https://doi.org/10.1016/j.mtchem.2019.100230.

[751] E. Boanini, F. Silingardi, M. Gazzano, and A. Bigi, "Synthesis and Hydrolysis of Brushite (DCPD): The Role of Ionic Substitution," *Crystal Growth & Design,* vol. 21, no. 3, pp. 1689-1697, 2021/03/03 2021, doi: 10.1021/acs.cgd.0c01569.

[752] J. L. Giocondi, B. S. El-Dasher, G. H. Nancollas, and C. A. Orme, "Molecular mechanisms of crystallization impacting calcium phosphate cements," (in eng), *Philos Trans A Math Phys Eng Sci,* vol. 368, no. 1917, pp. 1937-61, Apr 28 2010, doi: 10.1098/rsta.2010.0006.

[753] R. Gelli, L. Briccolani-Bandini, M. Pagliai, G. Cardini, F. Ridi, and P. Baglioni, "Exploring the effect of Mg2+ substitution on amorphous calcium phosphate nanoparticles," *Journal of Colloid and Interface Science,* vol. 606, pp. 444-453, 2022/01/15/ 2022, doi: https://doi.org/10.1016/j.jcis.2021.08.033.

[754] F. Abbona and A. Baronnet, "A XRD and TEM study on the transformation of amorphous calcium phosphate in the presence of magnesium," *Journal of Crystal Growth,* vol. 165, no. 1, pp. 98-105, 1996/07/02/ 1996, doi: https://doi.org/10.1016/0022-0248(96)00156-X.

[755] M. D. O'Donnell, Y. Fredholm, A. de Rouffignac, and R. G. Hill, "Structural analysis of a series of strontium-substituted apatites," *Acta Biomaterialia,* vol. 4, no. 5, pp. 1455-1464, 2008/09/01/ 2008, doi: https://doi.org/10.1016/j.actbio.2008.04.018.

[756] V. Bystrov, E. Paramonova, L. Avakyan, J. Coutinho, and N. Bulina, "Simulation and Computer Study of Structures and Physical Properties of Hydroxyapatite with Various Defects," *Nanomaterials,* vol. 11, no. 10, p. 2752, 2021. [Online]. Available: https://www.mdpi.com/2079-4991/11/10/2752.

[757] S. Jiang, Y. Chen, H. Pan, Y.-J. Zhang, and R. Tang, "Faster nucleation at lower pH: amorphous phase mediated nucleation kinetics," *Physical Chemistry Chemical Physics,* 10.1039/C3CP51466H vol. 15, no. 30, pp. 12530-12533, 2013, doi: 10.1039/C3CP51466H.

[758] J. Christoffersen, M. R. Christoffersen, W. Kibalczyc, and F. A. Andersen, "A contribution to the understanding of the formation of calcium phosphates," *Journal of Crystal Growth,* vol. 94, no. 3, pp. 767-777, 1989/03/01/ 1989, doi: https://doi.org/10.1016/0022-0248(89)90102-4.

[759] A. L. Boskey and A. S. Posner, "Magnesium stabilization of amorphous calcium phosphate: A kinetic study," *Materials Research Bulletin,* vol. 9, no. 7, pp. 907-916, 1974/07/01/ 1974, doi: https://doi.org/10.1016/0025-5408(74)90169-X.

[760] E. D. Eanes and A. S. Posner, "Intermediate phases in the basic solution preparation of alkaline earth phosphates," *Calcified Tissue Research,* Article vol. 2, no. 1, pp. 38-48, 1968, doi: 10.1007/BF02279192.

[761] W. F. Neuman and B. J. Mulryan, "Synthetic hydroxyapatite crystals," *Calcified Tissue Research,* vol. 7, no. 1, pp. 133-138, 1971/12/01 1971, doi: 10.1007/BF02062601.

[762] M. H. Salimi, J. C. Heughebaert, and G. H. Nancollas, "Crystal growth of calcium phosphates in the presence of magnesium ions," *Langmuir,* vol. 1, no. 1, pp. 119-122, 1985/01/01 1985, doi: 10.1021/la00061a019.

[763] P. A. M. De Bruyne, R. M. H. Verbeeck, and F. Verbeek, "The Solubility of Calcium Hydrogen Phosphate Dihydrate and Magnesium Hydrogen Phosphate Trihydrate and Ion Pair Formation in the System M(OH)2-H3Po4-H2O (M = Ca or Mg) at 37°C," *Bulletin des Sociétés Chimiques Belges,* vol. 99, no. 8, pp. 543-552, 1990, doi: https://doi.org/10.1002/bscb.19900990805.

[764] W. Kibalczyc, J. Christoffersen, M. R. Christoffersen, A. Zielenkiewicz, and W. Zielenkiewicz, "The effect of magnesium ions on the precipitation of calcium phosphates," *Journal of Crystal Growth,* vol. 106, no. 2, pp. 355-366, 1990/11/01/ 1990, doi: https://doi.org/10.1016/0022-0248(90)90080-5.

[765] J. C. Heughebaert and G. Montel, "Conversion of amorphous tricalcium phosphate into apatitic tricalcium phosphate," (in eng), *Calcified tissue international,* vol. 34 Suppl 2, pp. S103-8, 1982 1982. [Online]. Available: http://europepmc.org/abstract/MED/6293671.

[766] K. Vasylenko, Y. Sakhno, D. Jaisi, and M. Nikolenko, "Determination of the Activation Energies of Phase Transition for Calcium Orthophosphates Based on Powder X-Ray Diffraction Data," *Crystal Research and Technology,* vol. 57, no. 3, p. 2100215, 2022, doi: https://doi.org/10.1002/crat.202100215.

[767] B. A. E. Ben-Arfa and R. C. Pullar, "A Comparison of Bioactive Glass Scaffolds Fabricated by Robocasting from Powders Made by Sol–Gel and Melt-Quenching Methods," *Processes,* vol. 8, no. 5, p. 615, 2020. [Online]. Available: https://www.mdpi.com/2227-9717/8/5/615.

[768] E. Waleed, "Biocompatibility," in *Advances in Ceramics*, Costas Sikalidis Ed. Rijeka: IntechOpen, 2011, p. Ch. 15.

[769] F. Liu *et al.*, "Nanocellulose-Reinforced Hydroxyapatite Nanobelt Membrane as a Stem Cell Multi-Lineage Differentiation Platform for Biomimetic Construction of Bioactive 3D Osteoid Tissue In Vitro," *Advanced Healthcare Materials,* vol. 10, no. 8, p. 2001851, 2021, doi: https://doi.org/10.1002/adhm.202001851.

[770] B. N. L. Costa, R. M. R. Adão, C. Maibohm, A. Accardo, V. F. Cardoso, and J. B. Nieder, "Cellular Interaction of Bone Marrow Mesenchymal Stem Cells with Polymer and Hydrogel 3D Microscaffold Templates," *ACS Applied Materials & Interfaces,* vol. 14, no. 11, pp. 13013-13024, 2022/03/23 2022, doi: 10.1021/acsami.1c23442.

[771] M. Domingos *et al.*, "The first systematic analysis of 3D rapid prototyped poly(ε-caprolactone) scaffolds manufactured through BioCell printing: the effect of pore size and geometry on compressive mechanical behaviour and in vitro hMSC viability," *Biofabrication,* vol. 5, no. 4, p. 045004, 2013/11/06 2013, doi: 10.1088/1758-5082/5/4/045004.

[772] M. Gharibshahian *et al.*, "Recent advances on 3D-printed PCL-based composite scaffolds for bone tissue engineering," (in English), *Frontiers in Bioengineering and Biotechnology,* Review vol. 11, 2023-June-19 2023, doi: 10.3389/fbioe.2023.1168504.

[773] R. Dwivedi *et al.*, "Polycaprolactone as biomaterial for bone scaffolds: Review of literature," (in eng), *J Oral Biol Craniofac Res,* vol. 10, no. 1, pp. 381-388, Jan-Mar 2020, doi: 10.1016/j.jobcr.2019.10.003.

[774] H. Shao, J. He, T. Lin, Z. Zhang, Y. Zhang, and S. Liu, "3D Gel-Printing of Hydroxyapatite Scaffold for Bone Tissue Engineering," *Ceramics International,* vol. 45, no. 1, pp. 1163-1170, 2019/01/01/ 2019, doi: https://doi.org/10.1016/j.ceramint.2018.09.300.

[775] N. Raja, A. Sung, H. Park, and H.-s. Yun, "Low-temperature fabrication of calcium deficient hydroxyapatite bone scaffold by optimization of 3D printing conditions," *Ceramics International,* vol. 47, no. 5, pp. 7005-7016, 2021/03/01/ 2021, doi: https://doi.org/10.1016/j.ceramint.2020.11.051.

[776] H. Liang, Y. Wang, S. Chen, Y. Liu, Z. Liu, and J. Bai, "Nano-Hydroxyapatite Bone Scaffolds with Different Porous Structures Processed by Digital Light Processing 3D Printing," (in eng), *Int J Bioprint,* vol. 8, no. 1, p. 502, 2022, doi: 10.18063/ijb.v8i1.502.

[777] X. Li *et al.*, "3D Printing of Hydroxyapatite/Tricalcium Phosphate Scaffold with Hierarchical Porous Structure for Bone Regeneration," *Bio-Design and Manufacturing,* vol. 3, no. 1, pp. 15-29, 2020/03/01 2020, doi: 10.1007/s42242-019-00056-5.

[778] D. Van hede *et al.*, "3D-Printed Synthetic Hydroxyapatite Scaffold with In Silico Optimized Macrostructure Enhances Bone Formation In Vivo," *Advanced Functional Materials,* vol. 32, no. 6, p. 2105002, 2022, doi: https://doi.org/10.1002/adfm.202105002.

[779] G.-I. Kontogianni *et al.*, "Promotion of In Vitro Osteogenic Activity by Melt Extrusion-Based PLLA/PCL/PHBV Scaffolds Enriched with Nano-Hydroxyapatite and Strontium Substituted Nano-Hydroxyapatite," *Polymers,* vol. 15, no. 4, p. 1052, 2023. [Online]. Available: https://www.mdpi.com/2073-4360/15/4/1052.

[780] R. Singh, R. Kumar, and I. Singh, "Investigations on 3D printed thermosetting and ceramic-reinforced recycled thermoplastic-based functional prototypes," *Journal of Thermoplastic Composite Materials,* vol. 34, no. 8, pp. 1103-1122, 2021/08/01 2019, doi: 10.1177/0892705719864623.

[781] B. Huang, G. Caetano, C. Vyas, J. J. Blaker, C. Diver, and P. Bártolo, "Polymer-Ceramic Composite Scaffolds: The Effect of Hydroxyapatite and β-tri-Calcium

Phosphate," *Materials,* vol. 11, no. 1, p. 129, 2018. [Online]. Available: https://www.mdpi.com/1996-1944/11/1/129.

[782] Y. Yang *et al.*, "Photocrosslinkable nanocomposite ink for printing strong, biodegradable and bioactive bone graft," *Biomaterials,* vol. 263, p. 120378, 2020/12/01/ 2020, doi: https://doi.org/10.1016/j.biomaterials.2020.120378.

[783] M. A. Sarabia-Vallejos *et al.*, "Biocompatible and bioactive PEG-Based resin development for additive manufacturing of hierarchical porous bone scaffolds," *Materials & Design,* vol. 234, p. 112315, 2023/10/01/ 2023, doi: https://doi.org/10.1016/j.matdes.2023.112315.

[784] M. Domingos, A. Gloria, J. Coelho, P. Bartolo, and J. Ciurana, "Three-dimensional printed bone scaffolds: The role of nano/micro-hydroxyapatite particles on the adhesion and differentiation of human mesenchymal stem cells," *Proceedings of the Institution of Mechanical Engineers, Part H: Journal of Engineering in Medicine,* vol. 231, no. 6, pp. 555-564, 2017, doi: 10.1177/0954411916680236.

[785] J. Ma *et al.*, "Modification of 3D printed PCL scaffolds by PVAc and HA to enhance cytocompatibility and osteogenesis," *RSC Advances,* vol. 9, no. 10, pp. 5338 - 5346, 2019, doi: 10.1039/C8RA06652C.

[786] S. E. El-Habashy, A. H. El-Kamel, M. M. Essawy, E.-Z. A. Abdelfattah, and H. M. Eltaher, "Engineering 3D-printed core–shell hydrogel scaffolds reinforced with hybrid hydroxyapatite/polycaprolactone nanoparticles for in vivo bone regeneration," *Biomaterials Science,* 10.1039/D1BM00062D vol. 9, no. 11, pp. 4019-4039, 2021, doi: 10.1039/D1BM00062D.

[787] E. I. Dorozhkina and S. V. Dorozhkin, "Mechanism of the Solid-State Transformation of a Calcium-Deficient Hydroxyapatite (CDHA) into Biphasic Calcium Phosphate (BCP) at Elevated Temperatures," *Chemistry of Materials,* vol. 14, no. 10, pp. 4267-4272, 2002/10/01 2002, doi: 10.1021/cm0203060.

[788] J. K. M. B. Daguano *et al.*, "Shear-thinning sacrificial ink for fabrication of Biosilicate® osteoconductive scaffolds by material extrusion 3D printing," *Materials Chemistry and Physics,* vol. 287, p. 126286, 2022/08/01/ 2022, doi: https://doi.org/10.1016/j.matchemphys.2022.126286.

[789] R. Woo, G. Chen, J. Zhao, and J. Bae, "Structure–Mechanical Property Relationships of 3D-Printed Porous Polydimethylsiloxane," *ACS Applied Polymer Materials,* vol. 3, no. 7, pp. 3496-3503, 2021/07/09 2021, doi: 10.1021/acsapm.1c00417.

[790] C. Xiong and D. Wen, "Polypropylene/Sn-Pb Alloy Nanocomposites," *Transactions of the Nonferrous Metals Society of China(China),* vol. 9, no. 2, pp. 312-317, 1999.

[791] M. A. Baghbadorani, A. Bigham, M. Rafienia, and H. Salehi, "In vitro Studies of Polycaprolactone Nanofibrous Scaffolds Containing Novel Gehlenite Nanoparticles," (in eng), *J Med Signals Sens,* vol. 11, no. 2, pp. 131-137, Apr-Jun 2021, doi: 10.4103/jmss.JMSS_42_20.

[792] A. C. Dona *et al.*, "A guide to the identification of metabolites in NMR-based metabonomics/metabolomics experiments," (in eng), *Comput Struct Biotechnol J,* vol. 14, pp. 135-53, 2016, doi: 10.1016/j.csbj.2016.02.005.

[793] A. M. Bhayo, R. Abdul-Karim, S. G. Musharraf, and M. I. Malik, "Synthesis and characterization of 4-arm star-shaped amphiphilic block copolymers consisting of poly(ethylene oxide) and poly(ε-caprolactone)," *RSC Advances,* 10.1039/C8RA05000G vol. 8, no. 50, pp. 28569-28580, 2018, doi: 10.1039/C8RA05000G.

[794] F. Wang, T. K. Bronich, A. V. Kabanov, R. D. Rauh, and J. Roovers, "Synthesis and Characterization of Star Poly(ε-caprolactone)-b-Poly(ethylene glycol) and Poly(l-lactide)-b-Poly(ethylene glycol) Copolymers: Evaluation as Drug Delivery Carriers," *Bioconjugate Chemistry,* vol. 19, no. 7, pp. 1423-1429, 2008/07/01 2008, doi: 10.1021/bc7004285.

[795] R. Diez-Ahedo *et al.*, "UV-Casting on Methacrylated PCL for the Production of a Peripheral Nerve Implant Containing an Array of Porous Aligned Microchannels," (in eng), *Polymers (Basel),* vol. 12, no. 4, Apr 22 2020, doi: 10.3390/polym12040971.

[796] K. Maji, S. Dasgupta, R. Bhaskar, and M. K. Gupta, "Photo-crosslinked alginate nano-hydroxyapatite paste for bone tissue engineering," (in eng), *Biomed Mater,* vol. 15, no. 5, p. 055019, Aug 21 2020, doi: 10.1088/1748-605X/ab9551.

[797] F. Yousefi, S. Kandel, and N. Pleshko, "Infrared Spectroscopic Quantification of Methacrylation of Hyaluronic Acid: A Scaffold for Tissue Engineering Applications," *Appl. Spectrosc.,* vol. 72, no. 10, pp. 1455-1466, 2018/10/01 2018, doi: 10.1364/AS.72.001455.

[798] A. H. Van Hove, B. D. Wilson, and D. S. Benoit, "Microwave-assisted functionalization of poly(ethylene glycol) and on-resin peptides for use in chain polymerizations and hydrogel formation," (in eng), *J Vis Exp,* no. 80, p. e50890, Oct 29 2013, doi: 10.3791/50890.

[799] K.-J. Liu, "NMR studies of polymer solutions. VI. Molecular weight determination of poly(ethylene glycol) by NMR analysis of near-end groups," *Die Makromolekulare Chemie,* vol. 116, no. 1, pp. 146-151, 1968, doi: https://doi.org/10.1002/macp.1968.021160115.

[800] J. U. Izunobi and C. L. Higginbotham, "Polymer Molecular Weight Analysis by 1H NMR Spectroscopy," *Journal of Chemical Education,* vol. 88, no. 8, pp. 1098-1104, 2011/08/01 2011, doi: 10.1021/ed100461v.

[801] F. Haasters *et al.*, "Morphological and immunocytochemical characteristics indicate the yield of early progenitors and represent a quality control for human mesenchymal stem cell culturing," (in eng), *J Anat,* vol. 214, no. 5, pp. 759-67, May 2009, doi: 10.1111/j.1469-7580.2009.01065.x.

[802] K.-Y. Law, "Definitions for Hydrophilicity, Hydrophobicity, and Superhydrophobicity: Getting the Basics Right," *The Journal of Physical Chemistry Letters,* vol. 5, no. 4, pp. 686-688, 2014/02/20 2014, doi: 10.1021/jz402762h.

[803] J. M. Laubach and R. K. Sani, "Thermophilic Exopolysaccharide Films: A Potential Device for Local Antibiotic Delivery," (in eng), *Pharmaceutics,* vol. 15, no. 2, Feb 7 2023, doi: 10.3390/pharmaceutics15020557.

[804] K. Liu *et al.*, "Hyperspectral microscopy combined with DAPI staining for the identification of hepatic carcinoma cells," (in eng), *Biomed Opt Express,* vol. 12, no. 1, pp. 173-180, Jan 1 2021, doi: 10.1364/boe.412158.

[805] W. F. Reynolds, "NMR Pulse Sequences," in *Encyclopedia of Spectroscopy and Spectrometry*, J. C. Lindon Ed. Oxford: Elsevier, 1999, pp. 1554-1567.

[806] M. K. Singh and A. Singh, "Chapter 14 - Nuclear magnetic resonance spectroscopy," in *Characterization of Polymers and Fibres*, M. K. Singh and A. Singh Eds.: Woodhead Publishing, 2022, pp. 321-339.

[807] K.-J. Liu, "NMR studies of polymer solutions. VII. Effects of chain length on polymer NMR measurements," *Die Makromolekulare Chemie,* vol. 126, no. 1, pp. 187-196, 1969, doi: https://doi.org/10.1002/macp.1969.021260121.

[808] M. Barfield, V. J. Hruby, and J. P. Meraldi, "The dependence of geminal hydrogen-hydrogen spin-spin coupling constants on .phi. and .psi. angles of peptides in solution," *Journal of the American Chemical Society,* vol. 98, no. 6, pp. 1308-1314, 1976/03/01 1976, doi: 10.1021/ja00422a002.

[809] K. L. Van Landuyt *et al.*, "Evaluation of cell responses toward adhesives with different photoinitiating systems," (in eng), *Dent Mater,* vol. 31, no. 8, pp. 916-27, Aug 2015, doi: 10.1016/j.dental.2015.04.016.

[810] B. Zeng *et al.*, "Cytotoxic and cytocompatible comparison among seven photoinitiators-triggered polymers in different tissue cells," (in eng), *Toxicol In Vitro,* vol. 72, p. 105103, Apr 2021, doi: 10.1016/j.tiv.2021.105103.

[811] N. L. D'Elía, C. Mathieu, C. D. Hoemann, J. A. Laiuppa, G. E. Santillán, and P. V. Messina, "Bone-repair properties of biodegradable hydroxyapatite nano-rod superstructures," *Nanoscale,* 10.1039/C5NR04850H vol. 7, no. 44, pp. 18751-18762, 2015, doi: 10.1039/C5NR04850H.

[812] J. Adhikari, M. S. Perwez, A. Das, and P. Saha, "Development of hydroxyapatite reinforced alginate–chitosan based printable biomaterial-ink," *Nano-Structures & Nano-Objects,* vol. 25, p. 100630, 2021/02/01/ 2021, doi: https://doi.org/10.1016/j.nanoso.2020.100630.

[813] Y. Deng, Z. Dan, X. Yan, Q. Wang, and S. He, "Investigation of rheological behavior for commercial mold slags," *Journal of Materials Research and Technology,* vol. 9, no. 5, pp. 9568-9575, 2020/09/01/ 2020, doi: https://doi.org/10.1016/j.jmrt.2020.06.082.

[814] S. Kajiyama *et al.*, "Shear-induced liquid-crystalline phase transition behaviour of colloidal solutions of hydroxyapatite nanorod composites," *Nanoscale,* 10.1039/C9NR10996J vol. 12, no. 21, pp. 11468-11479, 2020, doi: 10.1039/C9NR10996J.

[815] S. B. Lang *et al.*, "Ferroelectric Polarization in Nanocrystalline Hydroxyapatite Thin Films on Silicon," *Scientific Reports,* vol. 3, no. 1, p. 2215, 2013/07/25 2013, doi: 10.1038/srep02215.

[816] J. Zeglinski, M. Nolan, D. Thompson, and S. A. M. Tofail, "Reassigning the most stable surface of hydroxyapatite to the water resistant hydroxyl terminated (010) surface," *Surface Science,* vol. 623, pp. 55-63, 2014/05/01/ 2014, doi: https://doi.org/10.1016/j.susc.2014.01.008.

[817] Y. Sugino and M. Kawaguchi, "Fumed and Precipitated Hydrophilic Silica Suspension Gels in Mineral Oil: Stability and Rheological Properties," (in eng), *Gels,* vol. 3, no. 3, 2017/08/09 2017, doi: 10.3390/gels3030032.

[818] R. Rial, Z. Liu, and J. M. Ruso, "Soft Actuated Hybrid Hydrogel with Bioinspired Complexity to Control Mechanical Flexure Behavior for Tissue Engineering," (in eng), *Nanomaterials (Basel),* vol. 10, no. 7, Jul 3 2020, doi: 10.3390/nano10071302.

[819] N. L. D'Elía, A. N. Gravina, J. M. Ruso, J. A. Laiuppa, G. E. Santillán, and P. V. Messina, "Manipulating the bioactivity of hydroxyapatite nano-rods structured networks: Effects on mineral coating morphology and growth kinetic," *Biochimica et Biophysica Acta (BBA) - General Subjects,* vol. 1830, no. 11, pp. 5014-5026, 2013/11/01/ 2013, doi: https://doi.org/10.1016/j.bbagen.2013.07.020.

[820] S. Bhumiratana *et al.*, "Nucleation and growth of mineralized bone matrix on silk-hydroxyapatite composite scaffolds," *Biomaterials,* vol. 32, no. 11, pp. 2812-2820, 2011/04/01/ 2011, doi: https://doi.org/10.1016/j.biomaterials.2010.12.058.

[821] M.-E. Grigora *et al.*, "3D Printed Poly(Lactic Acid)-Based Nanocomposite Scaffolds with Bioactive Coatings for Tissue Engineering Applications," *Journal of Materials Science,* vol. 58, no. 6, pp. 2740-2763, 2023/02/01 2023, doi: 10.1007/s10853-023-08149-4.

[822] G. Kumar, M. S. Waters, T. M. Farooque, M. F. Young, and C. G. Simon, Jr., "Freeform fabricated scaffolds with roughened struts that enhance both stem cell proliferation and differentiation by controlling cell shape," (in eng), *Biomaterials,* vol. 33, no. 16, pp. 4022-30, Jun 2012, doi: 10.1016/j.biomaterials.2012.02.048.

[823] A. V. Singh *et al.*, "Bottom-up engineering of the surface roughness of nanostructured cubic zirconia to control cell adhesion," *Nanotechnology,* vol. 23, no. 47, p. 475101, 2012/10/30 2012, doi: 10.1088/0957-4484/23/47/475101.

[824] H. Amani *et al.*, "Controlling Cell Behavior through the Design of Biomaterial Surfaces: A Focus on Surface Modification Techniques," *Advanced Materials Interfaces,* vol. 6, no. 13, p. 1900572, 2019, doi: https://doi.org/10.1002/admi.201900572.

[825] D. D. Deligianni, N. D. Katsala, P. G. Koutsoukos, and Y. F. Missirlis, "Effect of surface roughness of hydroxyapatite on human bone marrow cell adhesion, proliferation, differentiation and detachment strength," (in eng), *Biomaterials,* vol. 22, no. 1, pp. 87-96, Jan 2001, doi: 10.1016/s0142-9612(00)00174-5.

[826] R. Tzoneva, N. Faucheux, and T. Groth, "Wettability of substrata controls cell-substrate and cell-cell adhesions," (in eng), *Biochim Biophys Acta,* vol. 1770, no. 11, pp. 1538-47, Nov 2007, doi: 10.1016/j.bbagen.2007.07.008.

[827] Y. Arima and H. Iwata, "Effect of wettability and surface functional groups on protein adsorption and cell adhesion using well-defined mixed self-assembled monolayers," (in eng), *Biomaterials,* vol. 28, no. 20, pp. 3074-82, Jul 2007, doi: 10.1016/j.biomaterials.2007.03.013.

[828] B. Majhy, P. Priyadarshini, and A. K. Sen, "Effect of surface energy and roughness on cell adhesion and growth – facile surface modification for enhanced cell culture," *RSC Advances,* 10.1039/D1RA02402G vol. 11, no. 25, pp. 15467-15476, 2021, doi: 10.1039/D1RA02402G.

[829] A. Shamloo and M. Sarmadi, "Investigation of the adhesive characteristics of polymer–protein systems through molecular dynamics simulation and their relation to cell adhesion and proliferation," *Integrative Biology,* vol. 8, no. 12, pp. 1276-1295, 2016, doi: 10.1039/c6ib00159a.

[830] A. F. M. Barton, "Cohesion Parameters," in *Encyclopedia of Physical Science and Technology (Third Edition)*, R. A. Meyers Ed. New York: Academic Press, 2003, pp. 233-251.

[831] J. Zhang, "Work of Adhesion and Work of Cohesion," in *Encyclopedia of Tribology*, Q. J. Wang and Y.-W. Chung Eds. Boston, MA: Springer US, 2013, pp. 4127-4132.

[832] T. Wang, M. Ni, Z. Luo, C. Shou, and K. Cen, "Viscosity and aggregation structure of nanocolloidal dispersions," *Chinese Science Bulletin,* vol. 57, no. 27, pp. 3644-3651, 2012/09/01 2012, doi: 10.1007/s11434-012-5150-y.

[833] D. Amoabeng, A. Tempalski, B. A. Young, B. P. Binks, and S. S. Velankar, "Fumed silica induces co-continuity across a wide composition range in immiscible polymer blends," *Polymer,* vol. 186, p. 121831, 2020/01/09/ 2020, doi: https://doi.org/10.1016/j.polymer.2019.121831.

[834] S.-H. Um and S.-H. Rhee, "In vivo evaluations of hydroxyapatites with small and large grain sizes," *Advances in Applied Ceramics,* vol. 118, no. 8, pp. 484-490, 2019/11/17 2019, doi: 10.1080/17436753.2019.1667176.

[835] Y. Miao *et al.*, "Oxygen vacancy-induced hydroxyl dipole reorientation in hydroxyapatite for enhanced piezocatalytic activity," *Nano Energy,* vol. 100, p. 107473, 2022/09/01/ 2022, doi: https://doi.org/10.1016/j.nanoen.2022.107473.

[836] V. S. Bystrov *et al.*, "Computational and experimental studies of size and shape related physical properties of hydroxyapatite nanoparticles," *Journal of Physics: Condensed*

*Matter,* vol. 23, no. 6, p. 065302, 2011/01/25 2011, doi: 10.1088/0953-8984/23/6/065302.

[837] G. Rossmy, P. Gimmnich, B. Grüning, H. Schator, and J. Venzmer, "Amphiphilic Particles or Molecules with Predominantly Hydrophilic and Predominantly Hydrophobic Domains Distributed Anisotropically on their Surface," ed: Google Patents, 2003.

[838] M. H. Lee *et al.*, "Considerations for Tissue-Engineered and Regenerative Medicine Product Development Prior to Clinical Trials in the United States," *Tissue Engineering Part B: Reviews,* vol. 16, no. 1, pp. 41-54, 2010/02/01 2009, doi: 10.1089/ten.teb.2009.0449.

[839] J. J. Tobin, "7 - Global marketing authorisation of biomaterials and medical devices," in *Regulatory Affairs for Biomaterials and Medical Devices*, S. F. Amato and R. M. Ezzell Eds.: Woodhead Publishing, 2015, pp. 93-114.

[840] P. Chandra, J. J. Yoo, and S. J. Lee, "Chapter 13 - Biomaterials in Regenerative Medicine: Challenges in Technology Transfer from Science to Process Development," in *Translational Regenerative Medicine*, A. Atala and J. G. Allickson Eds. Boston: Academic Press, 2015, pp. 151-167.

[841] S. Ramesh, C. Y. Tan, M. Hamdi, I. Sopyan, and W. D. Teng, "The influence of Ca/P ratio on the properties of hydroxyapatite bioceramics," in *International Conference on Smart Materials and Nanotechnology in Engineering*, 2007.

[842] H. Liu, H. Yazici, C. Ergun, T. J. Webster, and H. Bermek, "An in vitro evaluation of the Ca/P ratio for the cytocompatibility of nano-to-micron particulate calcium phosphates for bone regeneration," *Acta Biomaterialia,* vol. 4, no. 5, pp. 1472-1479, 2008/09/01/ 2008, doi: https://doi.org/10.1016/j.actbio.2008.02.025.

[843] H. Wang, J. K. Lee, A. Moursi, and J. J. Lannutti, "Ca/P ratio effects on the degradation of hydroxyapatite in vitro," (in eng), *J Biomed Mater Res A,* vol. 67, no. 2, pp. 599-608, Nov 1 2003, doi: 10.1002/jbm.a.10538.

[844] M. V. Nikolenko, K. V. Vasylenko, V. D. Myrhorodska, A. Kostyniuk, and B. Likozar, "Synthesis of Calcium Orthophosphates by Chemical Precipitation in Aqueous Solutions: The Effect of the Acidity, Ca/P Molar Ratio, and Temperature on the Phase Composition and Solubility of Precipitates," *Processes*, vol. 8, no. 9*,* doi: 10.3390/pr8091009.

[845] Z. Sheikh, Y. L. Zhang, L. Grover, G. E. Merle, F. Tamimi, and J. Barralet, "In vitro degradation and in vivo resorption of dicalcium phosphate cement based grafts," *Acta Biomaterialia,* vol. 26, pp. 338-346, 2015/10/15/ 2015, doi: https://doi.org/10.1016/j.actbio.2015.08.031.

[846] E. Charrière *et al.*, "Mechanical characterization of brushite and hydroxyapatite cements," *Biomaterials,* vol. 22, no. 21, pp. 2937-2945, 2001/11/01/ 2001, doi: https://doi.org/10.1016/S0142-9612(01)00041-2.

[847] W.-C. Chen, C. Ju, W. Cheng, and J. Chernlin, "Green synthesis of calcium and phosphate compounds by varying ph value and ca/p atomic ratio using aqueous precipitations," *Ceramics - Silikaty,* vol. 57, pp. 14-21, 03/01 2013.

[848] D. N. d. Rocha *et al.*, "Kinetics of conversion of brushite coatings to hydroxyapatite in alkaline solution," *Journal of Materials Research and Technology,* vol. 7, no. 4, pp. 479-486, 2018/10/01/ 2018, doi: https://doi.org/10.1016/j.jmrt.2018.02.002.

[849] F. Lebre, R. Sridharan, M. J. Sawkins, D. J. Kelly, F. J. O'Brien, and E. C. Lavelle, "The shape and size of hydroxyapatite particles dictate inflammatory responses following implantation," *Scientific Reports,* vol. 7, no. 1, p. 2922, 2017/06/07 2017, doi: 10.1038/s41598-017-03086-0.

[850] J. M. Díaz-Tocados *et al.*, "Magnesium Chloride promotes Osteogenesis through Notch signaling activation and expansion of Mesenchymal Stem Cells," *Scientific Reports,* vol. 7, no. 1, p. 7839, 2017/08/10 2017, doi: 10.1038/s41598-017-08379-y.

[851] F. Yang, D. Yang, J. Tu, Q. Zheng, L. Cai, and L. Wang, "Strontium enhances osteogenic differentiation of mesenchymal stem cells and in vivo bone formation by activating Wnt/catenin signaling," (in eng), *Stem Cells,* vol. 29, no. 6, pp. 981-91, Jun 2011, doi: 10.1002/stem.646.

[852] S. C. Verberckmoes, M. E. De Broe, and P. C. D'Haese, "Dose-dependent effects of strontium on osteoblast function and mineralization," *Kidney International,* vol. 64, no. 2, pp. 534-543, 2003/08/01/ 2003, doi: https://doi.org/10.1046/j.1523-1755.2003.00123.x.

[853] C. J. Blackwell, K. Haernvall, G. M. Guebitz, M. Groombridge, D. Gonzales, and E. Khosravi, "Enzymatic Degradation of Star Poly(ε-Caprolactone) with Different Central Units," (in eng), *Polymers (Basel),* vol. 10, no. 11, Nov 14 2018, doi: 10.3390/polym10111266.

[854] S. Guo *et al.*, "Parallel Control over Surface Charge and Wettability Using Polyelectrolyte Architecture: Effect on Protein Adsorption and Cell Adhesion," *ACS Applied Materials & Interfaces,* vol. 8, no. 44, pp. 30552-30563, 2016/11/09 2016, doi: 10.1021/acsami.6b09481.

[855] Y. Li *et al.*, "Characterization and evaluation of polycaprolactone/hydroxyapatite composite scaffolds with extra surface morphology by cryogenic printing for bone tissue engineering," *Materials & Design,* vol. 205, p. 109712, 2021/07/01/ 2021, doi: https://doi.org/10.1016/j.matdes.2021.109712.

[856] Y. Jin *et al.*, "Oxidative stress-induced apoptosis of osteoblastic MC3T3-E1 cells by hydroxyapatite nanoparticles through lysosomal and mitochondrial pathways," *RSC Advances,* 10.1039/C7RA01008G vol. 7, no. 21, pp. 13010-13018, 2017, doi: 10.1039/C7RA01008G.

[857] J. Horakova *et al.*, "Impact of Various Sterilization and Disinfection Techniques on Electrospun Poly-ε-caprolactone," (in eng), *ACS Omega,* vol. 5, no. 15, pp. 8885-8892, Apr 21 2020, doi: 10.1021/acsomega.0c00503.

[858] Y. Dai *et al.*, "Optimization of sterilization methods for electrospun poly(ε-caprolactone) to enhance pre-osteoblast cell behaviors for guided bone regeneration," *Journal of Bioactive and Compatible Polymers,* vol. 31, no. 2, pp. 152-166, 2016/03/01 2015, doi: 10.1177/0883911515598795.

[859] Y. Zhao, B. Zhu, Y. Wang, C. Liu, and C. Shen, "Effect of different sterilization methods on the properties of commercial biodegradable polyesters for single-use, disposable medical devices," *Materials Science and Engineering: C,* vol. 105, p. 110041, 2019/12/01/ 2019, doi: https://doi.org/10.1016/j.msec.2019.110041.

[860] K. Havlickova *et al.*, "The Impacts of the Sterilization Method and the Electrospinning Conditions of Nanofibrous Biodegradable Layers on Their Degradation and Hemocompatibility Behavior," *Polymers*, vol. 16, no. 8, doi: 10.3390/polym16081029.

[861] A. Chmielewska and D. Dean, "The role of stiffness-matching in avoiding stress shielding-induced bone loss and stress concentration-induced skeletal reconstruction device failure," *Acta Biomaterialia,* vol. 173, pp. 51-65, 2024/01/01/ 2024, doi: https://doi.org/10.1016/j.actbio.2023.11.011.

[862] J. Penfold, E. Staples, and I. Tucker, "On the Consequences of Surface Treatment on the Adsorption of Nonionic Surfactants at the Hydrophilic Silica−Solution Interface," *Langmuir,* vol. 18, no. 8, pp. 2967-2970, 2002/04/01 2002, doi: 10.1021/la011575s.

[863] S. Tuladhar, S. Clark, and A. Habib, "Tuning Shear Thinning Factors of 3D Bio-Printable Hydrogels Using Short Fiber," (in eng), *Materials (Basel),* vol. 16, no. 2, Jan 6 2023, doi: 10.3390/ma16020572.

[864] Y. B. Kim *et al.*, "Mechanically reinforced cell-laden scaffolds formed using alginate-based bioink printed onto the surface of a PCL/alginate mesh structure for regeneration of hard tissue," *Journal of Colloid and Interface Science,* vol. 461, pp. 359-368, 2016/01/01/ 2016, doi: https://doi.org/10.1016/j.jcis.2015.09.044.

[865] M. E. Alemán-Domínguez *et al.*, "Polycaprolactone–carboxymethyl cellulose composites for manufacturing porous scaffolds by material extrusion," *Bio-Design and Manufacturing,* vol. 1, no. 4, pp. 245-253, 2018/12/01 2018, doi: 10.1007/s42242-018-0024-z.

[866] E. Reina-Romo, S. Mandal, P. Amorim, V. Bloemen, E. Ferraris, and L. Geris, "Towards the Experimentally-Informed In Silico Nozzle Design Optimization for Extrusion-Based Bioprinting of Shear-Thinning Hydrogels," (in eng), *Front Bioeng Biotechnol,* vol. 9, p. 701778, 2021, doi: 10.3389/fbioe.2021.701778.

[867] D. Gupta, A. K. Singh, N. Kar, A. Dravid, and J. Bellare, "Modelling and optimization of NaOH-etched 3-D printed PCL for enhanced cellular attachment and growth with minimal loss of mechanical strength," *Materials Science and Engineering: C,* vol. 98, pp. 602-611, 2019/05/01/ 2019, doi: https://doi.org/10.1016/j.msec.2018.12.084.

[868] S. Wang *et al.*, "Fabrication and Application of a 3D-Printed Poly-ε-Caprolactone Cage Scaffold for Bone Tissue Engineering," *BioMed Research International,* vol. 2020, p. 2087475, 2020/01/30 2020, doi: 10.1155/2020/2087475.

[869] D. E. MacDonald, B. E. Rapuano, N. Deo, M. Stranick, P. Somasundaran, and A. L. Boskey, "Thermal and chemical modification of titanium–aluminum–vanadium implant materials: effects on surface properties, glycoprotein adsorption, and MG63 cell attachment," *Biomaterials,* vol. 25, no. 16, pp. 3135-3146, 2004/07/01/ 2004, doi: https://doi.org/10.1016/j.biomaterials.2003.10.029.

[870] A. Nanci *et al.*, "Chemical modification of titanium surfaces for covalent attachment of biological molecules," (in eng), *J Biomed Mater Res,* vol. 40, no. 2, pp. 324-35, May 1998, doi: 10.1002/(sici)1097-4636(199805)40:2<324::aid-jbm18>3.0.co;2-l.

[871] F. Intranuovo *et al.*, "Plasma Modification of PCL Porous Scaffolds Fabricated by Solvent-Casting/Particulate-Leaching for Tissue Engineering," *Plasma Processes and Polymers,* vol. 11, no. 2, pp. 184-195, 2014, doi: https://doi.org/10.1002/ppap.201300149.

[872] W. Janvikul, P. Uppanan, B. Thavornyutikarn, W. Kosorn, and P. Kaewkong, "Effects of Surface Topography, Hydrophilicity and Chemistry of Surface-treated PCL Scaffolds on Chondrocyte Infiltration and ECM Production," *Procedia Engineering,* vol. 59, pp. 158-165, 2013/01/01/ 2013, doi: https://doi.org/10.1016/j.proeng.2013.05.106.

[873] L. Tian, Z. Zhang, B. Tian, X. Zhang, and N. Wang, "Study on antibacterial properties and cytocompatibility of EPL coated 3D printed PCL/HA composite scaffolds," *RSC Advances,* 10.1039/C9RA10275B vol. 10, no. 8, pp. 4805-4816, 2020, doi: 10.1039/C9RA10275B.

[874] T. Groth, P. Falck, and R.-R. Miethke, "Cytotoxicity of Biomaterials — Basic Mechanisms and In Vitro Test Methods: A Review," *Alternatives to Laboratory Animals,* vol. 23, no. 6, pp. 790-799, 1995, doi: 10.1177/026119299502300609.

[875] H. Fang, S. Peng, A. Chen, F. Li, K. Ren, and N. Hu, "Biocompatibility studies on fibrin glue cultured with bone marrow mesenchymal stem cells in vitro," (in eng), *J Huazhong Univ Sci Technolog Med Sci,* vol. 24, no. 3, pp. 272-4, 2004, doi: 10.1007/bf02832010.

[876] S. E. El-Habashy, H. M. Eltaher, A. Gaballah, E. I. Zaki, R. A. Mehanna, and A. H. El-Kamel, "Hybrid bioactive hydroxyapatite/polycaprolactone nanoparticles for enhanced osteogenesis," *Materials Science and Engineering: C,* vol. 119, p. 111599, 2021/02/01/ 2021, doi: https://doi.org/10.1016/j.msec.2020.111599.

[877] N. A. Luchman, R. Megat Abdul Wahab, S. H. Zainal Ariffin, N. S. Nasruddin, S. F. Lau, and F. Yazid, "Comparison between hydroxyapatite and polycaprolactone in inducing osteogenic differentiation and augmenting maxillary bone regeneration in rats," (in eng), *PeerJ,* vol. 10, p. e13356, 2022, doi: 10.7717/peerj.13356.

[878] E. V. Melnik *et al.*, "In vitro degradation behaviour of hybrid electrospun scaffolds of polycaprolactone and strontium-containing hydroxyapatite microparticles," *Polymer Degradation and Stability,* vol. 167, pp. 21-32, 2019/09/01/ 2019, doi: https://doi.org/10.1016/j.polymdegradstab.2019.06.017.

[879] T. Steger-Hartmann and M. Raschke, "Translating in vitro to in vivo and animal to human," *Current Opinion in Toxicology,* vol. 23-24, pp. 6-10, 2020/10/01/ 2020, doi: https://doi.org/10.1016/j.cotox.2020.02.003.

[880] Y. Li, S. K. Chen, L. Li, L. Qin, X. L. Wang, and Y. X. Lai, "Bone defect animal models for testing efficacy of bone substitute biomaterials," (in eng), *J Orthop Translat,* vol. 3, no. 3, pp. 95-104, Jul 2015, doi: 10.1016/j.jot.2015.05.002.

[881] C. A. Labarrere, A. E. Dabiri, and G. S. Kassab, "Thrombogenic and Inflammatory Reactions to Biomaterials in Medical Devices," (in eng), *Front Bioeng Biotechnol,* vol. 8, p. 123, 2020, doi: 10.3389/fbioe.2020.00123.

[882] G. Thrivikraman, G. Madras, and B. Basu, "In vitro/In vivo assessment and mechanisms of toxicity of bioceramic materials and its wear particulates," *RSC Advances,* 10.1039/C3RA44483J vol. 4, no. 25, pp. 12763-12781, 2014, doi: 10.1039/C3RA44483J.